Uncertainty Analyses in Computational Electromagnetism

Submitted in accordance to the requirements of the University of York for the degree of Doctor of Philosophy.

Robert Stephen Edwards

March 15, 2009

THE UNIVERSITY of York
Department of Electronics

Abstract

Uncertainty Analyses provide the quantitative level of confidence that can be held in the results of a measurement or computational simulation. Different Error and Uncertainty Analysis methods are used to estimate the error and uncertainty in the output of Computational Electromagnetic simulations in this thesis. The Uncertainty Analysis methods are compared in terms of their ability to accurately quantify the mean, uncertainty and ninety five per cent confidence intervals in the output of the simulations, as well as in terms of their computational expense.

Through this work the Monte Carlo Method, the Method of Moments and the Polynomial Chaos Method are implemented into the Finite Difference Time Domain method. The Monte Carlo Method and the Method of Moments are also implemented into the Intermediate Level Circuit Model. These Uncertainty Analysis methods are applied to a number of specific examples, from simple examples that have analytic solutions, to more realistic and complex Electromagnetic Compatibility scenarios.

Performing both Error and Uncertainty Analyses enables an investigation on the relationship between the errors and uncertainties, in the output of simulations, to be conducted. Different Computational Electromagnetic methods are also used in this thesis to determine the differences in the uncertainty in the output of simulations performed using the different methods.

In Electromagnetic Compatibility the output of interest is often a curve viewed in the frequency domain. The Feature Selective Validation method is used in this thesis to compare the mean, uncertainty and ninety five percent confidence interval curves formed from the different Uncertainty Analysis methods. Curve Alignment techniques are also used to determine the extent to which the errors and uncertainties in the output curves are amplitude and frequency errors and uncertainties.

The results obtained in this thesis show that, of the three uncertainty analysis meth-

ods investigated, the Monte Carlo Method is the most accurate method providing the best estimates of the uncertainty in various Computational Electromagnetic simulations. As expected, this method is also shown to be the most computationally expensive method. The Method of Moments is the most practical method to use, to obtain an estimate of the uncertainty, due to its computational efficiency. However, at resonant frequencies the Method of Moments forms large peak overestimations of the uncertainty. The research in this thesis explains that these overestimations arise in part because of the resonant nature of the output curves, which is a common feature of data formed in Electromagnetic Compatibility studies. The Polynomial Chaos Method can provide slightly more accurate estimates of the output uncertainty than the Method of Moments, but there are situations when this method cannot be used. The Polynomial Chaos Method is also found to be computationally more expensive than the Method of Moments.

The work in this thesis shows that there is no relationship between the overall size of the output uncertainty in a simulation and the underlying model used to form this simulation, or the accuracy with which the simulation is performed. It may therefore be possible to use computationally efficient, less accurate Computational Electromagnetic methods to efficiently estimate the uncertainty in the output of a simulation formed using a computationally more expensive, more accurate method. If a fast Computational Electromagnetic method is used then the Monte Carlo Method is preferred as it will keep the accuracy of the uncertainty estimate as high as possible. One of the most consistent findings of this work is that the Uncertainty Analyses are computationally expensive when compared to performing a single simulation using only the mean input parameters of the system. Researching computationally efficient ways of quantifying the output uncertainty is one of the key areas of future work.

The results in this thesis highlight the importance of quantifying the frequency errors and uncertainties as well as the amplitude errors and uncertainties. This is especially important in Electromagnetic Compatibility where small frequency variations can cause large amplitude variations due to the resonant nature of the output data. The novel curve alignment methods proposed in this thesis enable the successful analysis of these frequency errors and uncertainties. It is also suggested that considering the frequency or x-domain differences between two curves provides a useful additional measure that can be used within the Feature Selective Validation method.

Contents

List of Figures

List of Tables

Acknowledgments

I would primarily like to thank Prof. A.C. Marvin and Dr. S.J. Porter for their invaluable advise and support in the course of this project. In particular I would like to thank Dr. Porter for the time he has spent reading and providing feedback on this thesis. Thanks also goes to Dr. I.D. Flintoft for his advice on many of the Computational Electromagnetic methods that were used. I would like to extend a big thank you to all members of the Applied Electromagnetics Group at York for all their support throughout this project. This PhD would not have been possible without the financial support provided by the EPSRC, for which I am very grateful.

To my parents, Steve and Sheila, I would like to say a special thank you for your unending support, love and encouragement, which has always driven me to try my best at everything that I do. I would also like to thank my sisters, Nicola and Katie, for their love, encouragement and for always being there when I needed them.

Finally I would like to thank my wife Debbie for going through all the different experiences with me, for listening to my incessant ramblings and for her love and support, always and forever. Debbie, words can not describe how much I love and appreciate you, and how thankful I am that we have been able to share this journey together.

Declaration

Selected aspects of the research described in this report have been documented or published elsewhere:

Robert S. Edwards, Martin P. Robinson, John F. Dawson, Andy C. Marvin and Stuart J. Porter. Aligning Curves for More Accurate Curve Comparisons. In *23rd Annual Review of Progress in Applied Computational Electromagnetics, Verona, Italy, March 19-23, 2007.*

Robert S. Edwards, Andy C. Marvin and Stuart J. Porter. Quantifying Errors and Uncertainty in CEM. In *Applied Computational Electromagnetics Newsletter, Vol. 22(3), November 2007.*

Robert S. Edwards, Andy C. Marvin and Stuart J. Porter. Uncertainty Analysis in Computational Electromagnetism. In *The European Consortium For Mathematics In Industry (ECMI), University College London, London, England June 30 - July 4, 2008.*

Robert S. Edwards, Andy C. Marvin and Stuart J. Porter. Towards the Development of Uncertainty Analyses in FDTD Simulations. In *European Electromagnetics (EUROEM), Swiss Federal Institute of Technology (EPFL), Lausanne, Switzerland, July 21-25, 2008.*

Robert S. Edwards, Andy C. Marvin and Stuart J. Porter. Uncertainty Analyses in the Finite Difference Time Domain Method. Submitted to *IEEE Transactions on Electromagnetic Compatibility.* (Appendix A)

Chapter 1

Introduction

Contents

1.1 Background to the Research

Electromagnetic Compatibility (EMC) involves the study of the electromagnetic interactions that occur between different electronic and biological systems. An electronic system must be immune to external sources of electromagnetic interference, and should not interfere with the normal operation of other electronic or biological systems. The immunity and interference of electronic systems is determined by performing different laboratory experiments, from which measurements are obtained. EMC practitioners are required to follow many standards and guidelines. One such standard (ISO/IEC 17025 [1]) requires that laboratory EMC measurements are accompanied by an appropriate estimate of the uncertainty in the measurements [2].

In recent years computational resources have advanced at a tremendous rate. This advancement has allowed many sophisticated Computational Electromagnetic (CEM) methods to be developed. It is now common practice to use CEM simulations to obtain estimates of EMC measurements that may be too difficult or expensive to obtain from a laboratory experiment. Currently no standards exist that require the results obtained from computational simulations to be accompanied by an appropriate estimate of the uncertainty in the results. Recently an IEEE standard has been approved for the "Validation of Computational

Electromagnetics Computer Modeling and Simulations" [3]. This standard outlines the necessary steps for validating CEM models and simulations. One step in this process involves the use of the Feature Selective Validation (FSV) method to compare the results of a CEM simulation with some other reference data in order to validate the CEM model used. The current standard does not require that an approximate estimate of the uncertainty in the output of a CEM simulation must be formed during the validation process. Quantifying this uncertainty is important as it provides the quantitative level of confidence that may be held in the results and thus allows for a statistical comparison with other reference data, such as the results obtained from an equivalent experimental measurement. Future editions of this standard should require that the results of all CEM simulations are accompanied by an approximate estimate of the uncertainty in the results. This thesis investigates different methods that may be used to quantify the uncertainty in the output of CEM simulations. The work carried out in this thesis may provide useful contributions for future editions of the IEEE standard.

Researchers from many other scientific fields already form uncertainty estimates for the results of their computational simulations. Examples of these scientific fields include Climate modelling [4–7], Meteorology [8; 9] and Computational Fluid Dynamics (CFD) [10–15], amongst many others. To enable a discussion of the different forms of uncertainty analysed in computational models, the terms error and uncertainty must first be defined. These definitions are used in this thesis to identify some of the sources of error and uncertainty that exist in CEM simulations. There has been a significant amount of research on Error and Uncertainty Analyses in CFD [10–15], and so this discipline is chosen to provide the formal definition of the errors and uncertainties in computer models. The following definitions come from the *American Institute of Aeronautics and Astronautics (AIAA)* report on the verification and validation of CFD simulations [11].

Definition 1.1 *Error: A recognisable deficiency in any phase or activity of modelling and simulation that is not due to lack of knowledge.*

Errors are introduced into computer models via the approximations and assumptions that are made in forming the model. Since these approximations and assumptions are known, the errors they produce can be analysed [10].

Definition 1.2 *Uncertainty: A potential deficiency in any phase or activity of the modelling process that is due to lack of knowledge.*

This definition of uncertainty is also known as epistemic or systematic uncertainty and is often referred to as a "Type B" uncertainty [2]. Epistemic uncertainty is the uncertainty that arises due to lack of knowledge [16], this type of uncertainty can be reduced by gaining more knowledge. Aleatory uncertainty is another type of uncertainty which arises from stochastic or random behaviour in the system. This uncertainty, which is often referred to as a "Type A" uncertainty, does not exist in deterministic computational simulations.

Epistemic uncertainties arising in computational simulations can be further categorised into two groups. The first, is the uncertainty in how well the mathematical model represents the true behaviour of the real physical system [15]. This uncertainty, which is known as model form uncertainty, is very difficult to determine [15] but can be reduced by verifying the model against physical measurements. The second type of uncertainty is the uncertainty that arises due to a lack of precise input parameter data [15]. If there are uncertainties in the input parameter data, then there will be uncertainties in the output. This type of uncertainty is often known as parameter uncertainty [15]. It is the parameter uncertainty that will be investigated throughout this thesis.

Climate models suffer from a large amount of model form uncertainty [5]. This uncertainty arises because it is very difficult to determine how well the climate models represent the real physical climate. The time scales involved in climate forecasts are of the order of decades, making it difficult to verify the results of the forecast against physical measurements [5]. In contrast to climate models the time scales involved in weather forecasts are of the order of days [5]. This makes it much easier to verify the weather models against physical measurements and subsequently modify the models, reducing the amount of model form uncertainty.

Both climate modelling and weather forecasts suffer from parameter uncertainties. It is well known that weather systems are chaotic and a small change in an input parameter can form large changes in the output: this is perhaps most well known as the Butterfly Effect. The uncertainty in the state of weather and climate systems therefore increases with the temporal length of the forecasts. Monte Carlo approaches form the basis of all current Numerical Weather Prediction (NWP) systems that are used to forecast the weather, and estimate the uncertainty in the forecast [8]. Monte Carlo simulations use many selected input parameters to estimate the output Probability Distribution Function (PDF) of the system. Performing many Monte Carlo simulations can be computationally expensive [8], different sampling strategies have therefore been formed that reduce the computational expense.

Since the uncertainty in the output grows with the time of the forecast, inputs are selected that are known to maximise the uncertainty in the output [8]. This results in a reduction of the parameter space and therefore a reduction in the cost of the Monte Carlo simulations. The resulting simulations are known as an ensemble of simulations [5; 8]. The uncertainty in CEM simulations will not necessarily increase with the time of the simulation. The sampling methods used in NWP systems are therefore not necessarily applicable to the quantification of uncertainty in CEM.

The model form uncertainty in both CFD and CEM is smaller than for climate and weather forecasts. The mathematical models that are used to explain the different phenomena occurring in CFD and CEM have been verified by many people over many years. The Uncertainty Analyses in CFD concentrate on the uncertainties due to a lack of precise knowledge of the input parameters [10–15]. These analyses use probabilistic methods such as the Monte Carlo Method (MCM), Bayesian Inference, the Polynomial Chaos Method (PCM) and the Method of Moments (MoM). The MoM should not be confused with the CEM technique, known as the Moment Method and described in detail by Harrington [17]. The probabilistic MoM is the method outlined in the internationally accepted *Guide to the Expression of Uncertainty in Measurement* (GUM) [16]. The MoM is also used in the *United Kingdom Accreditation Service* (UKAS) guide to quantifying the uncertainty in physical EMC measurements [2].

The output formed from CEM simulations normally involve resonant peaks with large Q-factors. These resonances are not present in data obtained from Climatology, Meteorology or CFD. It is therefore necessary to determine whether the different Uncertainty Analyses, used within these different disciplines, may be applied to the results of CEM simulations. The main aim of this thesis is to investigate possible methods that may be used to quantify the uncertainty in the output of CEM simulations. These different methods are compared in terms of their accuracy and computational expense.

Definitions 1.1 and 1.2 may be used to identify the sources of error and uncertainty in different CEM methods. One example of an error that may exist in Finite Difference Time Domain (FDTD) simulations is the error formed from modelling a curved surface in the discrete FDTD mesh. It is *known* that the surface is not modelled correctly, this results in an error in the output. Uncertainties arise due to *lack of knowledge*, for example the *lack* of precise information on the material properties of some dielectric that is being modelled computationally. The *lack of knowledge* in the material parameter results in an uncertainty in the output of the model. Each CEM simulation requires a set of inputs which may or

may not have some associated uncertainty. If the PDFs associated with the uncertain input parameters are known, then the uncertainty in the output of the CEM simulation may be found using probabilistic Uncertainty Analysis (UA) methods.

There has already been a significant amount of research analysing the errors that exist in CEM simulations, such as the FDTD method. Some of this previous work is discussed in Chapter 2. From this work it appears that many of the errors, arising in the FDTD method, are reduced when the cell size and temporal step size used in the simulations are reduced. Approximate Error Analyses are formed using this fact in Chapter 4. It is apparent that less work has attempted to quantify the uncertainty in the output of CEM simulations. The principle aim of this thesis is to investigate different methods that may be used to quantify parameter uncertainty. Some of the previous research into uncertainty in CEM is outlined below.

During the course of this project, there has been a recent increase in the number of researchers attempting to formulate methods of uncertainty quantification in CEM. In 2006 Chauvière published work involving the implementation of the PCM into a higher order discontinuous Galerkin solution of Maxwell's equations [18]. The PCM approximates the quantity of interest as a sum of orthogonal polynomials, which are selected from specific basis sets. Chauvière found that the PCM could accurately quantify the output uncertainty, giving results that were in good agreement with results obtained from the MCM [18]. The PCM was also shown to be much more computationally efficient than the MCM. Chauvière's work however only estimated the output uncertainty due to one uncertain input parameter. The accuracy of this method with increased numbers of uncertain input parameters needs to be analysed. The computational expense of the PCM will increase significantly for more complex CEM simulations, which have multiple uncertain input parameters. A novel implementation of the PCM into the FDTD method is outlined in Section 4.7.4 of this thesis. This method is analysed for a variety of simulations, with multiple uncertain input parameters.

Researchers at Nottingham University have also recently attempted to formulate methods to efficiently quantify the uncertainty in CEM simulations [19–22]. Recent publications [19–21] propose two methods that may be used to efficiently quantify uncertainty in CEM. Ajayi discusses the use of a Direct Solution Technique (DST) to quantify uncertainty [19]. This technique is simply the application of the well known MoM, outlined in GUM [16] and by UKAS [2], into simple electronic circuit theory and the Transmission Line Matrix (TLM) method. Ajayi used this method to estimate the uncertainty in the first resonant frequency

of simple electromagnetic problems [19]. This work can also be found in Ajayi's thesis [23]; Ajayi's work has been carried out in parallel to and independently from the research in the present thesis. Ajayi found that the computationally efficient MoM works well for small parameter variations, giving results that are in agreement with results obtained from the MCM [19]. This work concentrates on the performance of the MoM at the first resonance. In the present thesis uncertainties are quantified between 0GHz and 3GHz for electrically large problems, encompassing many more of the resonant features that are present in EMC data. The different UAs are also applied to more realistic examples from EMC, in the present thesis. These EMC scenarios are simulated using two different CEM techniques. Through this work it is shown that the approximations used to form the MoM can cause the method to underestimate and overestimate the uncertainty in the results of resonant EMC data.

The use of Unscented Transforms (UT) to efficiently estimate uncertainties has also been proposed by researchers at Nottingham University [20; 21]. This technique uses specified points to discretise the continuous PDFs associated with the different input parameters. Using this technique the uncertainty can be quantified more efficiently but once again the method is only accurate for smaller input parameter variations [21]. The methods efficiency also decreases for more complex simulations containing many uncertain input parameters [21].

1.2 Aims and Objectives

The main aim of this thesis is to determine the accuracy and computational efficiency of a number of well known UA techniques, when applied to CEM simulations of realistic EMC scenarios. The probabilistic UA techniques analysed in this thesis are the MCM, the MoM and the PCM. These different UA methods are used to analyse the uncertainty in the output of FDTD and Intermediate Level Circuit Model (ILCM) simulations. The errors and uncertainties arising from the CEM simulations will be quantified for frequencies from 0GHz to 3GHz. This broad frequency range will include many of the highly resonant features that are often present in EMC data.

Since the output of interest is evaluated at a number of frequencies, the output of the CEM simulations forms a curve in the frequency domain. This curve is referred to as the output curve in this thesis. Different methods are used, in this thesis, that aid in the analysis of curves. The FSV method is used to compare two different curves in terms of

their amplitude and feature differences. The method returns a metric that describes how similar the two curves are. In this thesis the FSV method is used in a novel way to test for the convergence of the MCM. It is also used to compare the means and uncertainties produced by the different UA methods with benchmark results. These comparisons help determine the performance of the different UA methods in the various examples.

Research into different probabilistic UA methods has found that the methods are all computationally expensive, especially when applied to complex computational simulations involving many uncertain input parameters. The computational expense of the UA methods may be reduced by using less accurate computationally cheaper CEM simulations to estimate the uncertainty in more accurate computationally more expensive simulations. The uncertainty estimate will be accurate if the uncertainty in the output is independent of the CEM technique used or the accuracy with which the CEM technique is implemented. An additional aim of this thesis is to determine the relationships between the errors and uncertainties arising from different CEM simulations.

Currently Error and Uncertainty Analysis methods concentrate on quantifying the errors and uncertainties in the amplitude of the various output curves. Often errors and uncertainties arise as frequency shift errors and uncertainties as well as amplitude errors and uncertainties. The final aim of this thesis is to investigate possible ways of quantifying the frequency errors and uncertainties that arise in CEM simulations. The frequency errors and uncertainties may be calculated by aligning the curves used to obtain the output errors and uncertainties. Once the curves are aligned the aligned amplitude errors and uncertainties may be obtained. Different methods are investigated in this thesis that attempt to align the output curves. The errors and uncertainties calculated without aligning the output curves are referred to as the unaligned amplitude errors and uncertainties in this thesis. In Chapter 4 a relationship between the unaligned amplitude errors and the aligned amplitude and frequency errors is derived. Similar novel derivations are given for the relationship between the aligned and unaligned uncertainties formed using the MCM. These relationships show that no information is lost by considering the aligned amplitude and frequency errors and uncertainties.

The remaining structure of this thesis is as follows:

Chapter 2 describes a number of CEM methods that are used to study EMC. A consideration of some of the sources of error and uncertainty that may exist in different FDTD simulations are given.

Chapter 3 introduces the different methods that aid in the analysis of errors and uncertainties when the output of interest is a curve. This discussion begins with a description of the FSV method, and the ways in which this method is used in this thesis. Following this a number of novel curve alignment techniques are introduced that have been previously published in [24].

Chapter 4 considers the different methods that may be used to quantify the error and uncertainty in the output of CEM simulations. The novel implementation of the PCM into the FDTD method is discussed in detail. The different Error and Uncertainty Analysis methods that are used in this thesis are identified.

Chapter 5 contains the first example that is used to test the different Error and Uncertainty Analysis methods. This one dimensional example has an analytic solution from which the analytic error and uncertainty in the output can be obtained. These analytic errors and uncertainties are used to test the accuracy of the different approximate Error and Uncertainty Analysis methods.

Chapter 6 introduces a more complicated three dimensional example that also has an analytic solution. Once again the different Error and Uncertainty Analysis methods are compared in terms of their accuracy and computational expense. From these first two examples it is concluded that the MCM provides the best estimates of the mean and uncertainty in the output of the CEM simulations. This method is therefore used as the benchmark method in the remaining examples, which do not have analytic solutions. At the end of this chapter another example is introduced, which shows that the PCM is not suitable in all situations.

Chapter 7 contains more realistic EMC examples that are used to compare the different UA methods. It is found that the methods are in excellent agreement in some EMC scenarios. However in other more complex EMC examples the more efficient MoM is shown to overestimate the uncertainty in the output, when compared to the benchmark MCM. The resonant nature of the output curves exacerbates the overestimations at particular frequencies.

Chapter 8 provides the major conclusions that are drawn from this work. The future continuation of this work is also considered.

Chapter 2

Computational Electromagnetism in Electromagnetic Compatibility

Contents

2.1 Introduction

Electromagnetic Compatibility concerns itself with the interaction of electronic systems with other electrical and biological systems. The electronic system under consideration must not be susceptible to Electromagnetic Interference (EMI) caused by the fields radiated from other electrical systems. At the same time the electronic system should not interfere with the performance of other electronic or biological systems.

The satisfactory operation of a device is usually tested by ascertaining how immune the device is to certain levels of interference [25, p.5]. This is often done experimentally in the lab, however there are often cases where it is too expensive or awkward to perform these experiments physically. An example of such a case is in the EMC analysis of aircraft. The time and money required to conduct a full EMC analysis of an aircraft is extremely costly. A European project is due to begin soon, which will attempt to transfer some of the experimental EMC analyses to computational simulation. This project aims to computationally model High Intensity Radiated Fields in Synthetic Environments (HIRF SE) [26], making use of existing CEM models and developing new models. The output of these computational models will be subject to some level of uncertainty, and will contain some amount of error. It is the aim of this thesis to investigate different ways to quantify the errors and uncertainties in such CEM simulations.

Excellent progress in electromagnetic field modelling has been made in recent history [27]. From the advent of digital computers in the 1960s, the first computational electromagnetic models were formed to provide insight into engineering problems [25, p.4]. Over the years, as computer hardware has become more powerful, computational models have developed into sophisticated methods used to study different scenarios in EMC. This chapter introduces previous work summarising some of the main methodologies that are used in CEM. In recent years these CEM techniques have been modified and improved, however for the purposes of the discussion in this chapter it is sufficient to consider only the unmodified conventional techniques. It is fairly simple to apply the MCM and the MoM to all of these CEM methods, because the MCM and the MoM simply use the output formed from the CEM simulations. When applying the PCM to different CEM simulations a modification of the CEM technique is required. The PCM may therefore be harder to implement into the different CEM simulations. This thesis concentrates on applying the Error and Uncertainty Analyses to the FDTD method. As such the majority of this chapter is devoted to the FDTD method: how it works, the different boundary conditions that are used and the stability

criteria.

Using Definition 1.1, some of the sources of error in the FDTD method are identified. There has already been a significant amount of previous work providing understanding into how these errors affect the output of FDTD simulations. Some aspects of this work are outlined in this chapter. Using Definition 1.2, some possible sources of parameter uncertainty that arise in CEM simulations are identified. Compared to the amount of previous work on the errors in CEM simulations, significantly fewer formal studies have been carried out on the affects of parameter uncertainty. It is the main aim of this thesis to investigate methods that can be used to quantify the parameter uncertainty in different CEM simulations.

2.2 Computational Electromagnetic Methods

Many CEM methods that are used to solve specific EMC problems have implementations that allow a solution to be calculated in either the frequency or time domain. Often however, the methods are more computationally efficient when used in one or other of the domains. The CEM methods may therefore be split into two groups: the frequency domain and time domain methods. If a CEM method is more computationally efficient when used in the frequency domain then it is referred to as a frequency domain method; a similar statement can be formed for time domain methods.

Frequency domain methods used in EMC include the Integral Equation Method of Moments (IEMoM), the Finite Element Method (FEM) and the ILCM method. The ILCM method is a more recent method that has shown some success in modelling different EMC scenarios, such as the Shielding Effectiveness (SE) of a shielded enclosure [28]. The time domain methods include the Transmission Line Matrix (TLM) method and the FDTD method. There are many other methods that are used in CEM, however it may be argued that the methods described in this chapter comprise the most popular methods that are used. Two other high frequency techniques that are used in EMC are the Geometrical Theory of Diffraction (GTD) [29] and the Uniform Geometrical Theory of Diffraction (UTD) [30]. These two methods will not be discussed in this chapter. The majority of this thesis is devoted to the errors and uncertainties in the FDTD method. This method is therefore described in detail in Sections 2.3 and 2.4.

The frequency and time domain methods produce frequency and time responses of the output quantity of interest. In EMC the output of interest is usually shown in the fre-

quency domain. For example, the output of interest may be the SE of a structure at particular frequencies. The time responses of the output quantity of interest, produced by the time domain methods, are therefore usually transformed into frequency responses via a Fast Fourier Transform (FFT). In the majority of this thesis the quantity of interest is the frequency response of the absolute value of the electric field, relative to a 1V/m input excitation. This quantity is referred to as the normalised electric field in this thesis. In EMC this frequency response curve is often converted into decibels, however in this thesis the normalised fields remain in linear units. In the latter part of this thesis the output of interest is the frequency response of the SE of a structure, in decibel units.

The following sections provide the details of some of the main CEM methods used in EMC. Throughout these discussions references are made to the problem space of a certain CEM model. The problem space is the three dimensional geometric space that contains the electromagnetic problem for which the solution is sought.

2.2.1 Integral Equation Method of Moments

The IEMoM makes use of the integral form of Maxwell's equations. A usual EMC scenario often involves electromagnetic waves scattering from certain geometric structures. The integral form of Maxwell's equations may be solved numerically to obtain the values of the resulting surface charges and currents that exist on the geometric structures. The surface charges and currents are used to obtain quantities of interest such as the near field, far field or radar cross section. The integral equations are solved numerically using the Method of Moments, which is different from the probabilistic UA method used later in this thesis. Harrington describes the use of this method to solve electromagnetic problems in an early paper [31] and more recently in [17]. Perhaps the most widely used computer software that uses the IEMoM is the Numerical Electromagnetics Code (NEC) [32].

The Electric Field Integral Equation (EFIE) and the Magnetic Field Integral Equation (MFIE) are obtained from Maxwell's equations. Using the EFIE, the surface currents induced on an obstacle may be calculated given knowledge of the incident electric field **E**. This is achieved by representing the integral as a linear operator L, operating on the surface current **J**. This reduces the EFIE to

$$L\mathbf{J} = \hat{\mathbf{n}} \times \mathbf{E} \tag{2.1}$$

where $\hat{\mathbf{n}}$ is the unit normal to the surface of interest. By expanding the surface current in

terms of some known basis polynomials $\mathbf{J}_i$ as

$$\mathbf{J} = \sum_{i=1}^{N} \alpha_i \mathbf{J}_i \tag{2.2}$$

equation (2.1) becomes

$$\sum_{i=1}^{N} \alpha_i L\mathbf{J}_i = \hat{\mathbf{n}} \times \mathbf{E}. \tag{2.3}$$

The α_i in the above equations represent coefficients that need to be found in order to solve for $\mathbf{J}$. Taking inner products of the above equation with some weighting functions w_i produces a set of N simultaneous equations that may be rewritten in matrix form as

$$\left(\langle w_i L\mathbf{J}_j \rangle\right)\left(\alpha_j\right) = \left(\langle w_i \hat{\mathbf{n}} \times \mathbf{E} \rangle\right). \tag{2.4}$$

where $i, j = 1, \ldots, N$. The matrix on the right hand side of this equation contains the excitation fields and the vector (α_j) contains the coefficients required to calculate the currents $\mathbf{J}$. Equation (2.4) may be considered as being analogous to Ohm's law, with the first matrix on the left hand side representing the mutual impedances of the system. This matrix is referred to as the impedance matrix. If the impedance matrix is nonsingular then it may be inverted and multiplied to the matrix on the right hand side of equation (2.4). This provides a means of calculating the coefficients α_j and hence the surface currents may be calculated using (2.2).

In more general problems there may be many conducting bodies. The surface currents induced on these bodies will form fields that scatter onto other bodies in the problem space. The interaction of these different bodies may be represented using other integral equations. For wires it is possible to derive a Thin Wire Integral Equation (TWIE); integral equations can also be derived for conducting surface patches and volumes. In reality it is impossible to determine the current density at every point in the problem space. The structures in the problem space are therefore split up into a series of wire segments, patch segments and volume segments. For every pair of segments the mutual impedances may be calculated using the different integral equations and the Moment Method. These impedance terms form an impedance matrix similar to that given above. Incorporating the incident electric fields into another matrix yields a matrix equation which is equivalent to (2.4). This matrix equation may be solved to obtain the different current densities on the individual segments.

Since the impedance matrix is formed from the impedance terms for each pair of seg-

ments, the computational expense of the IEMoM increases as the number of segments increases. The larger the impedance matrix the more time and memory is required to perform the matrix inversion required to solve the matrix equation. The accuracy of the IEMoM relies on the segmentation of the obstacles in the problem space, and on the choice of basis functions used for each section. Details of the different basis functions that may be used can be found in [33, p.192-198].

Thus far the use of the IEMoM has been described for the specific case where the bodies involved are electrically conducting. The method may be modified to include dielectric bodies [17, p.97-99] and magnetic bodies [17, p.99-101] (with permeabilities other than the free space value). More generalisable hybrid techniques have also been developed that include bodies that are both dielectric and magnetic [17, p.101-105]. Using the generalised hybrid IEMoM it is possible to form a solution to any electromagnetic problem [17, p.104]. This generalised technique is however more computationally expensive. The large computational expense limits the applications for which the IEMoM is generally used. If for example a $1m^3$ dielectric and magnetic cube were to be modelled using subcubes of $0.1m^3$ then there would be 1,000 interacting terms [17, p.105]. If this cube has three electric current bases and three magnetic current bases then the resulting matrix operators would contain nine million elements [17, p.105]. Storage and inversion of these matrices would be extremely computationally costly [17, p.105].

The IEMoM is most widely used to study the performance of antennas, which can be constructed easily out of electrically conducting wires and surfaces. These types of problem can be solved accurately and extremely efficiently by the IEMoM, because the matrix inversions involved are small. The IEMoM can determine the size of the electric field at any arbitrary distance from an antenna being modelled, at any given set of frequencies. In EMC scenarios such as this the IEMoM is computationally more efficient than time domain techniques. To obtain the same electric field using time domain solvers the calculation of all electromagnetic field components, at all mesh points in the problem space, and for many time steps, is required. This is computationally intensive, especially if the resulting field is only required at a number of specific frequencies.

2.2.2 Finite Element Method

Brauer [34] suggests that the FEM was first established by Turner, Clough, Martin and Topp [35] in 1956. In this seminal paper, the method was used to analyse structural problems

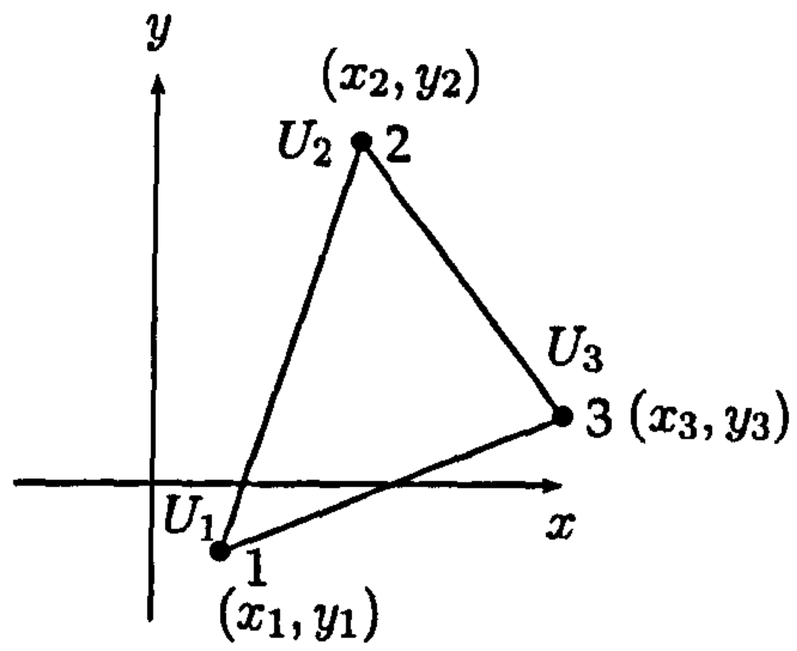

Figure 2.1: A typical triangular finite element in 2D.

in the aircraft industry. The term Finite Element was first associated with this method by Clough in 1960 [36]. The method is based on splitting the volume of the problem space into elements. These elements may be shaped arbitrarily so long as the elements fill the whole problem space. The vertices of these elements are often referred to as the nodes or mesh points, and the edges and surfaces of the elements are known as the finite element mesh.

Electromagnetic fields that exist in the mesh can be described in terms of their associated potentials. The potential at a point inside an element is represented as a function of the position inside the element. The functions that are commonly used are linear or quadratic functions. Each element will also have associated material properties, representing the material that is being modelled. Excitations may be applied to points in the finite element mesh, and constraints may be applied to certain edges and surfaces to represent different boundary conditions. A detailed account of the FEM is given by Silvester and Ferrari [37]. The discussion that follows considers the FEM in 2D, following reference [37, p.28-39] closely.

Consider a triangular element in 2D space. Figure 2.1 shows this element in the x-y plane, a similar figure is given in [37, p.32]. The potential U within the element can be approximated linearly as [37, p.32]

$$U = a + bx + cy \tag{2.5}$$

where a, b and c are constants that need to be determined. If the potentials U_1, U_2 and U_3, corresponding to the nodes at (x_1, y_1), (x_2, y_2) and (x_3, y_3) respectively, are known then the

objective is to solve the matrix equation [37, p.40]

$$\begin{pmatrix} U_1 \\ U_2 \\ U_3 \end{pmatrix} = \begin{pmatrix} 1 & x_1 & y_1 \\ 1 & x_2 & y_2 \\ 1 & x_3 & y_3 \end{pmatrix} \begin{pmatrix} a \\ b \\ c \end{pmatrix} \tag{2.6}$$

to obtain a, b and c. This results in the following relation for the potential inside the element

$$U = \begin{pmatrix} 1 & x & y \end{pmatrix} \begin{pmatrix} 1 & x_1 & y_1 \\ 1 & x_2 & y_2 \\ 1 & x_3 & y_3 \end{pmatrix}^{-1} \begin{pmatrix} U_1 \\ U_2 \\ U_3 \end{pmatrix}. \tag{2.7}$$

This may be rewritten as the sum [37, p.39]

$$U(x,y) = \sum_{i=1}^{3} U_i \alpha_i(x,y) \tag{2.8}$$

where

$$\alpha_1(x,y) = \frac{1}{2A}\left[(x_2y_3 - x_3y_2) + (y_2 - y_3)x + (x_3 - x_2)y\right] \tag{2.9}$$

A is the area of the element and the indices may be clyclically interchanged to form equations for $\alpha_2(x,y)$ and $\alpha_3(x,y)$.

The energy $W^{(e)}$ stored inside element e may be related to the potential U (to within a constant multiplier) as [37, p.34]

$$W^{(e)} = \frac{1}{2}\int_e \nabla U \nabla U d\mathbf{A} \tag{2.10}$$

where the integral is performed over the 2D area of the element e. Substituting in equation (2.8) yields

$$W^{(e)} = \frac{1}{2}\sum_{i=1}^{3}\sum_{j=1}^{3} U_i U_j \int_e \nabla\alpha_i \nabla\alpha_j d\mathbf{A}. \tag{2.11}$$

Defining the elements of the *stiffness matrix* $\mathbf{S}^{(e)}$ as

$$S_{ij}^{(e)} = \int_e \nabla\alpha_i \nabla\alpha_j d\mathbf{A} \tag{2.12}$$

the energy may be expressed as

$$W^{(e)} = \frac{1}{2}\mathbf{U}^{\mathbf{T}}\mathbf{S}^{(e)}\mathbf{U} \tag{2.13}$$

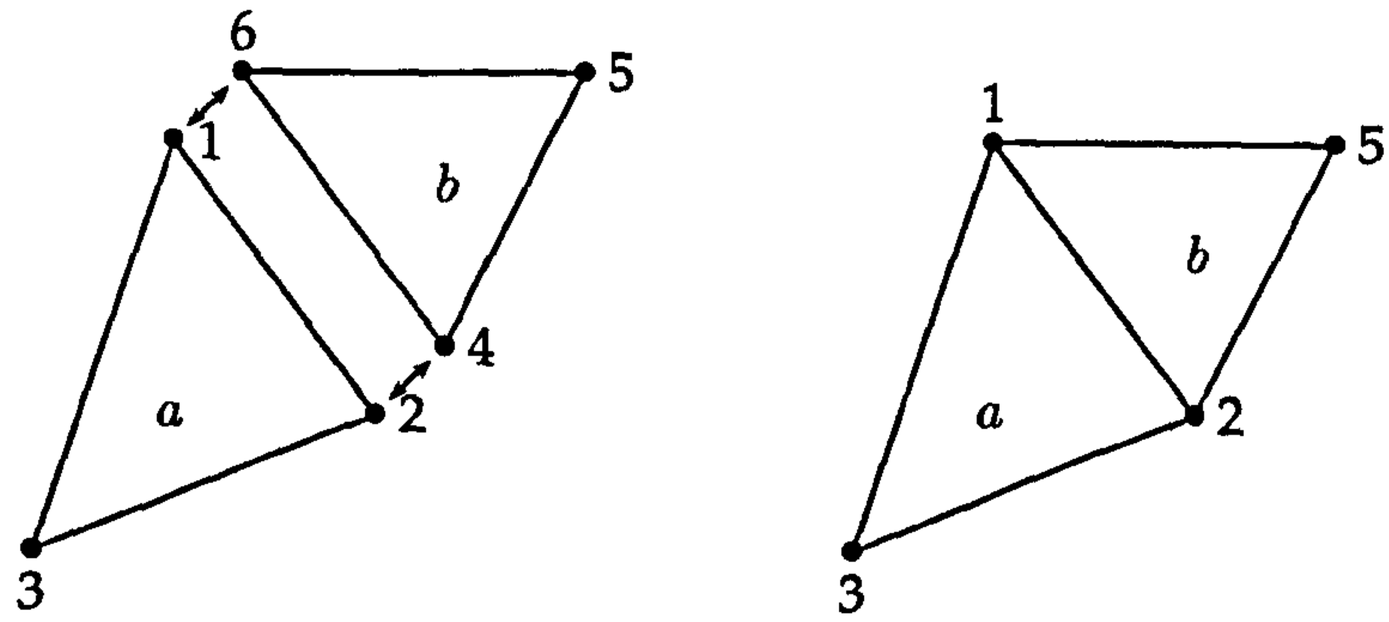

Figure 2.2: Joining two triangular finite elements in 2D; nodes are renumbered to account for continuity across elements.

where **U** is the column vector containing the vector potentials [37, p.34]. The elements of $\mathbf{S}^{(e)}$ are easily calculated since the terms $\nabla\alpha_i$ in the integral are simply constants. Note that $\mathbf{S}^{(e)}$ is called the stiffness matrix as the FEM originated from structural analysis.

The discussion above outlines how to determine the energy stored in each element given the potentials at the nodes. In the FEM the problem space is split into many joined elements. The energy stored in all of these elements may be found by considering the joining of the elements. Consider the two elements being joined in Figure 2.2, this figure is similar to one given in [37, p.35]. These two elements share common nodes at the joining edge and by continuity the potential at these nodes must be the same. The combined stiffness matrix is formed by adding the matrix elements of the individual stiffness matrices $\mathbf{S}^{(a)}$ and $\mathbf{S}^{(b)}$ (corresponding to elements a and b) where the nodes touch, and adding a new row and column for the extra potential. This yields the combined stiffness matrix [37, p.37]

$$\mathbf{S} = \begin{pmatrix} S_{11}^{(a)} + S_{66}^{(b)} & S_{12}^{(a)} + S_{64}^{(b)} & S_{13}^{(a)} & S_{65}^{(b)} \\ S_{21}^{(a)} + S_{46}^{(b)} & S_{22}^{(a)} + S_{44}^{(b)} & S_{23}^{(a)} & S_{45}^{(b)} \\ S_{31}^{(a)} & S_{32}^{(a)} & S_{33}^{(a)} & 0 \\ S_{56}^{(b)} & S_{54}^{(b)} & 0 & S_{55}^{(b)} \end{pmatrix}. \tag{2.14}$$

This joining of elements may be repeated until a stiffness matrix is formed for the whole problem space.

The principle of minimum potential energy asserts that the potential U will distribute itself in such a way as to minimize the stored energy in the field [37, p.29]. The total stored energy W is quadratic in each component of the potential vector **U** [37, p.37]. Thus to

minimise the stored energy it is sufficient to set [37, p.37]

$$\frac{\partial W}{\partial U_k} = 0 \tag{2.15}$$

where k refers to one of the nodal potentials. Some of the nodal potentials will be constrained by boundary conditions or excitations. To account for this the combined stiffness matrix, representing the whole problem space, may be partitioned to separate out the terms related to the constrained terms. If f and p relate to free and prescribed nodes, then the total stored energy may be written as [37, p.38]

$$W = \frac{1}{2}\begin{pmatrix} \mathbf{U_f^T} & \mathbf{U_p^T} \end{pmatrix}\begin{pmatrix} \mathbf{S_{ff}} & \mathbf{S_{fp}} \\ \mathbf{S_{pf}} & \mathbf{S_{pp}} \end{pmatrix}\begin{pmatrix} \mathbf{U_f} \\ \mathbf{U_p} \end{pmatrix}. \tag{2.16}$$

To solve for the minimum stored energy, this matrix equation must be differentiated with respect to the free nodal potentials and the resulting differential must be set to zero. Doing this results in the matrix equation [37, p.38]

$$\begin{pmatrix} \mathbf{S_{ff}} & \mathbf{S_{fp}} \end{pmatrix}\begin{pmatrix} \mathbf{U_f} \\ \mathbf{U_p} \end{pmatrix} = 0. \tag{2.17}$$

This can be rearranged to give the full solution of the unconstrained nodal potentials

$$\mathbf{U_f} = -\mathbf{S_{ff}}^{-1}\mathbf{S_{fp}}\mathbf{U_p}. \tag{2.18}$$

Now that the electric potentials are known at the nodes, the electric potential anywhere inside the problem space may be interpolated. This method is easily generalisable to three dimensions, where tetrahedral elements can be used in place of the triangular elements used in the two dimensional case. Different materials and sources may also be incorporated into the FEM: for more details on the FEM the reader is referred to [37].

The FEM is capable of modelling complex geometric shapes [25, p.91], such as an aircraft. The triangular and tetrahedral elements, used in the two and three dimensional FEM, conform accurately to different shapes. The FEM generally models complex geometries more accurately than conventional FDTD and TLM methods, which use orthogonal meshes [25, p.91]. More recently however FDTD and TLM schemes have been developed with variable grid sizes. These modified methods model different structures more accurately.

The FEM is less computationally efficient than the IEMoM when modelling simple

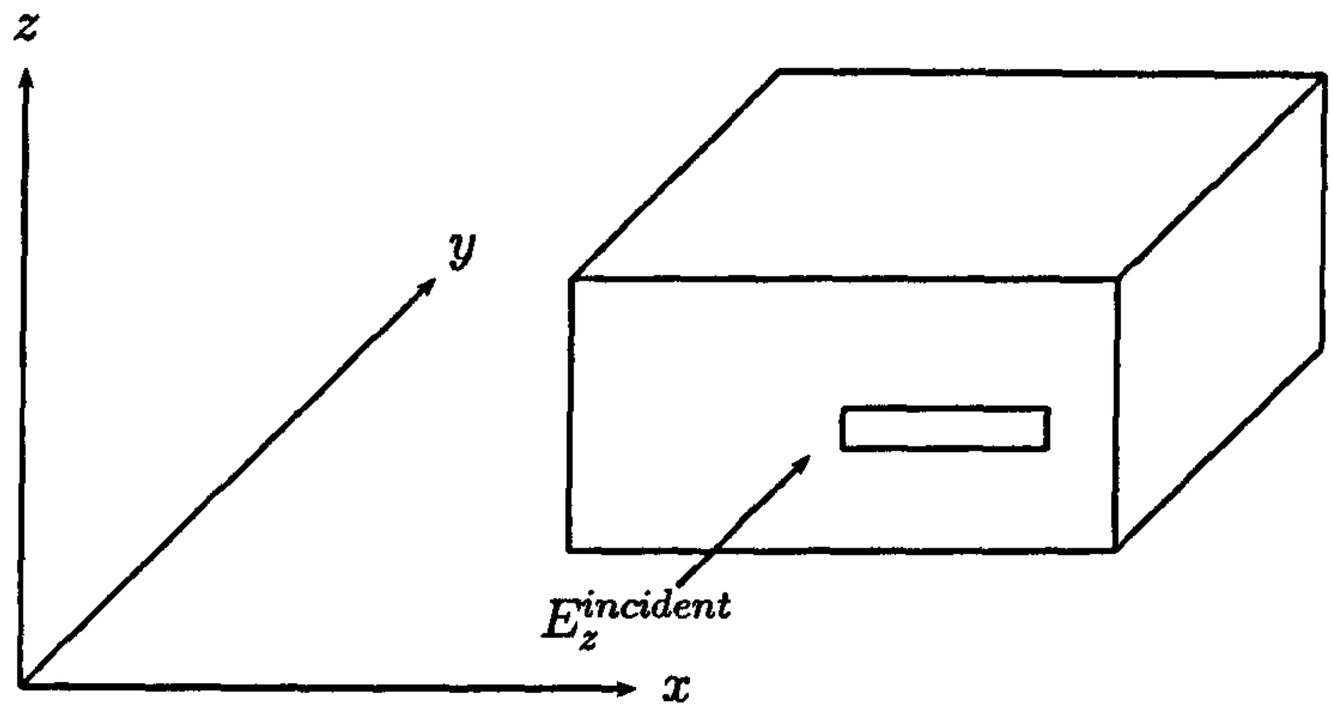

Figure 2.3: A metal box with an aperture undergoing scattering from an incident field $E_z^{incident}$.

structures in a large problem space containing mainly free space. The FEM is however better if large volumes of dielectric are being modelled. In this case the IEMoM requires a large amount of storage to model the dielectric bodies, as discussed in the previous section. The FEM is therefore best suited to bounded problems containing complex geometries and many different materials.

2.2.3 The Intermediate Level Circuit Model

The ILCM method uses circuit models to represent the electromagnetic interactions that occur in different EMC scenarios. One particular use of this method is for the efficient prediction of the SE of a rectangular box containing a rectangular aperture [28]: Figure 2.3 represents the type of box being modelled. This particular implementation of the ILCM method expands on previous ILCM approaches [38–40]. In Chapter 7 the uncertainty analyses will be applied to this implementation of the ILCM method and the FDTD method to determine whether the uncertainty in the output is dependent on the CEM method used. From now on, in this thesis, the shielded box implementation of the ILCM method is referred to simply as the ILCM method. A brief description of the ILCM method is given below. The mathematical arguments required to form this method are complex and detailed and they have been omitted here for brevity.

The ILCM method models the shielding enclosure as an equivalent circuit made up of coupled transmission lines. The equivalent circuit diagram is represented in Figure 2.4, which is similar to the diagram given in [28]. The incident electric field is represented as a potential V_{in} producing a free space current I_{FS} that flows through a resistor, with a resistance of free space (377Ω). This portion of the equivalent circuit model is known as the free

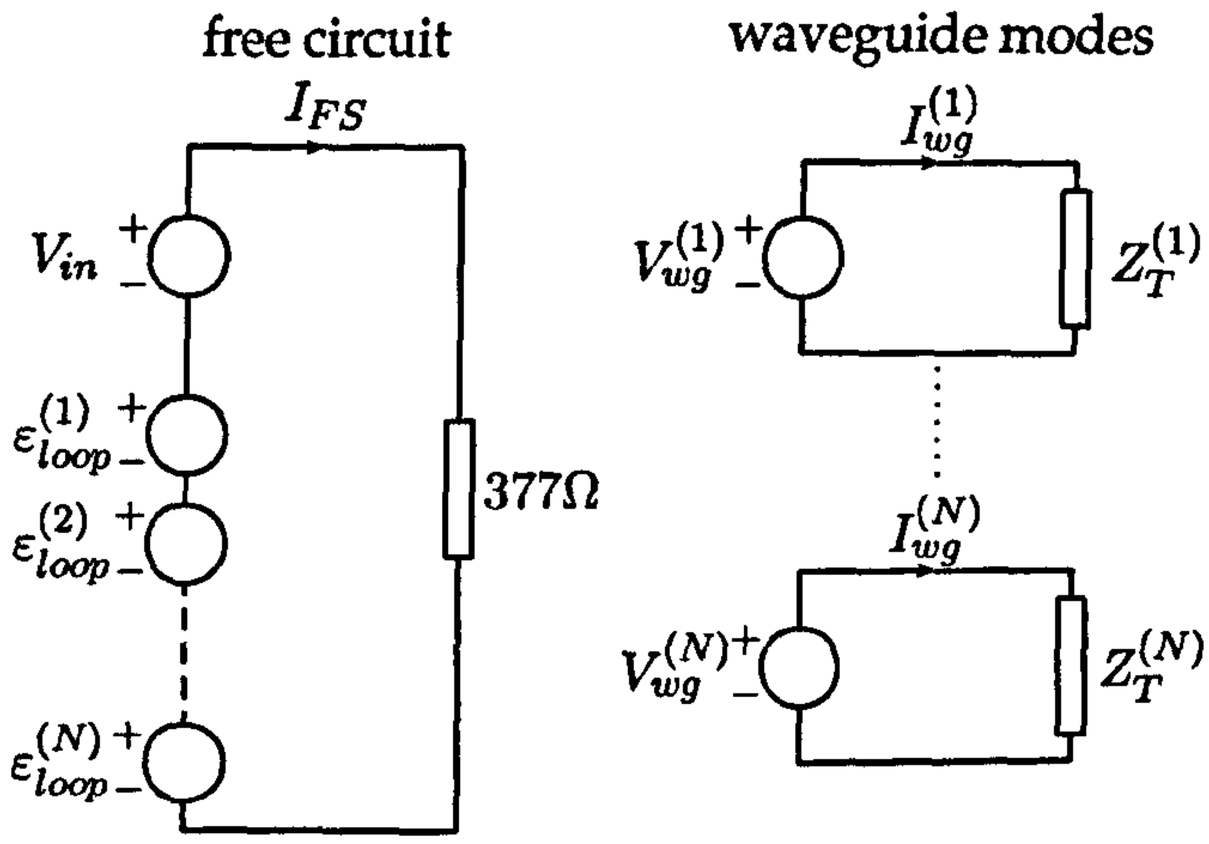

Figure 2.4: The equivalent circuit model for a metal box excited by an incident field.

space circuit [28]. The rest of the box is modelled as a waveguide, which supports different modes of excitation. These waveguide modes are represented in the equivalent circuit model as a series of transmission lines, one for each mode. The characteristic impedances of the transmission lines $Z_c^{(i)}$ are equal to the transverse ratio of the electric and magnetic fields for the particular mode.

The aperture is itself considered to be a transmission line, which has at its centre a resistance representing the radiation resistance of the aperture in the box. Babinet's Principle [41] is used to relate the resistance of a dipole antenna to the resistance at the centre of the aperture. The dipole resistance can be calculated using NEC [32] for a dipole formed by the metal remaining from cutting the aperture out of the box. Once the resistance across the slot has been calculated, the electric field in the aperture is calculated when it is subjected to some incident field [28]. By considering the coupling of the aperture with the rest of the box, the initial excitation of each wave guide mode may be found [28].

The initial potential of each waveguide mode $V_{wg}^{(i)}$ is related to the free space current I_{FS} via a transimpedance $Z_{\text{Trans}}^{(i)}$ as $V_{wg}^{(i)} = Z_{\text{Trans}}^{(i)} I_{FS}$ [28]. The initial modal excitation and the free space current are used to calculate the transimpedances of the system via this relationship. The fields set up in the waveguide will reflect back towards the aperture, increasing the potential in the free space circuit. Using the principle of reciprocity, reactive electromotive forces $\varepsilon_{loop}^{(i)}$ are set up in the free space circuit, one for each mode [28]. This ensures that mode coupling takes place by altering the current I_{FS} flowing through the free space resistor and hence altering the excitation of all modes in the waveguide. The transimpedances of the system are used to determine the change in the free space current

arising from the fields reflected back up the waveguide towards the aperture. The resultant voltages of the different waveguide modes $V_{wg}^{(i)}$ are then calculated and used to obtain the the electric field at any point within the box. This electric field is then used to calculate the SE of the box.

This method has been shown to efficiently obtain the SE of a number of different boxes. The simulations performed using the ILCM method by Konefal [28] were over 3900 times faster than the same simulations performed using the TLM method. The results of the TLM simulations were used to validate this ILCM method. Konefal noted that the method's accuracy relies on the aperture of the box having a small ratio for the aperture height to the aperture length.

The ILCM method may be applied to more general EMC scenarios. The formation of different models is however not as simple as for the other CEM methods described in this chapter. Different ILCM models have to be formed depending on the setup of the EMC scenario. The method described above can be used to estimate the SE of a shielded box of any size. Its use is however limited to that of a shielded box. To apply the method to different EMC scenarios the whole system must first be modelled as a set of coupled circuits.

2.2.4 Transmission Line Matrix Method

The TLM method was proposed by Johns and Beurle [42] in 1971. Initially the method was implemented into 2D. In this 2D method Telegrapher's equations for a lossless 2D transmission line are identical to Maxwell's equations in 2D, under transformations of electromagnetic fields into transmission line currents and potentials, and physical material parameters into the capacitance and inductance of a transmission line. This implies that 2D electromagnetic problems can be modelled by a 2D transmission line. In the TLM method a mesh of transmission line segments, connected in parallel, are used to approximate the continuous space in a discrete way. These segments connections are known as shunt connections. It is also possible to connect the segments in series, as outlined in [43, p.71-90], however the underlying mathematics is identical for both the series and shunt connections.

Figure 2.5 shows a shunt connection of two transmission lines. Each of these lines has an equal impedance Z_l in free space. Scattering of the electromagnetic field in the TLM mesh is considered by relating the four incident voltages $V^{j,in}$ at each node to the scattered

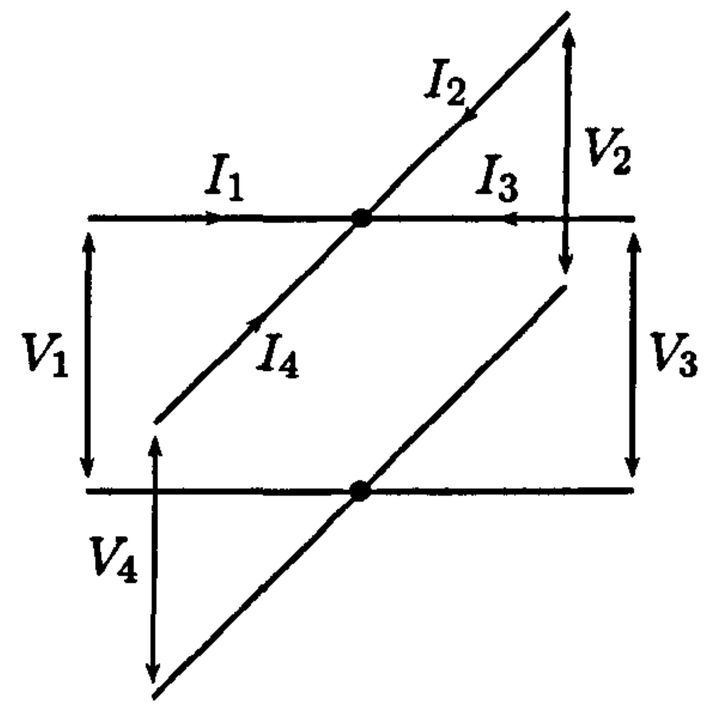

Figure 2.5: A shunt connection: the junction of two transmission lines for the 2D TLM method.

voltages $V^{j,scat}$ by a scattering matrix S as

$$\begin{pmatrix} V^{1,scat} \\ V^{2,scat} \\ V^{3,scat} \\ V^{4,scat} \end{pmatrix} = \begin{pmatrix} S_{11} & S_{12} & S_{13} & S_{14} \\ S_{21} & S_{22} & S_{23} & S_{24} \\ S_{31} & S_{32} & S_{33} & S_{34} \\ S_{41} & S_{42} & S_{43} & S_{44} \end{pmatrix} \begin{pmatrix} V^{1,in} \\ V^{2,in} \\ V^{3,in} \\ V^{4,in} \end{pmatrix}. \tag{2.19}$$

This matrix equation can be investigated by considering a pulse incident on one of the lines connected to the node. The load seen by this line is the combination of the loads on the remaining three lines, which are connected in parallel. These lines each have an impedance Z_l, and therefore the load seen by the line with the incident pulse is $Z_l/3$. The reflection coefficient of the incoming pulse, which is represented by the diagonal elements of S, is

$$S_{jj} = \frac{Z_l/3 - Z_l}{Z_l/3 + Z_l} = -\frac{1}{2}. \tag{2.20}$$

The non diagonal elements of S represent the transmission coefficients to the other three lines. In the case of the pulse this produces transmission coefficients

$$S_{jk} = 1 + S_{jj} = \frac{1}{2}. \tag{2.21}$$

Thus the scattered voltages on each of the lines due to the incident pulse are calculated by

$$\begin{pmatrix} V^{1,scat} \\ V^{2,scat} \\ V^{3,scat} \\ V^{4,scat} \end{pmatrix} = \frac{1}{2} \begin{pmatrix} -1 & 1 & 1 & 1 \\ 1 & -1 & 1 & 1 \\ 1 & 1 & -1 & 1 \\ 1 & 1 & 1 & -1 \end{pmatrix} \begin{pmatrix} V^{1,in} \\ V^{2,in} \\ V^{3,in} \\ V^{4,in} \end{pmatrix}. \tag{2.22}$$

In the TLM mesh these nodes are all connected, thus the scattered voltage pulses from one node become the incident voltages for the adjacent nodes. Different boundary conditions may be added into the TLM mesh, and material properties within the mesh may be introduced by altering the scattering matrix. Details on the implementation of the boundary conditions and materials properties into the 2D method are given in [43, p.95-105].

In 1986 Johns [44] proposed a successful 3D implementation of the TLM method. This 3D implementation is fairly complex because two independent electromagnetic polarisations are possible in each direction, thus a 3D TLM mesh must have two transmission lines for each direction. Johns suggested the symmetrical condensed node, which has 12 transmission lines entering it. These transmission lines are assigned to the two possible polarisations on each of the six faces of the cube containing it. Using this node the TLM method works in much the same way as for the 2D case, using scattering matrices to relate the incident and scattered voltages at each node. These incident and scattered voltage pulses are calculated at discrete time steps. The voltage at each time step is then transformed to the corresponding field at that time step, resulting in the time domain response of the electromagnetic fields, at discrete points in the mesh. For more details on the 3D TLM method see [43, Ch.6].

Previous work has shown that the TLM method is numerically equivalent to the FDTD method [45]. In much of the work in this thesis the Error and Uncertainty analyses are applied to the FDTD method. The similarities between the TLM and FDTD methods mean that these UAs should also be applicable to the TLM method. Time domain methods such as the TLM method and the FDTD method are most suitable to bounded electromagnetic problems containing many regular geometric bodies. Since these time domain methods are converted into the frequency domain via a FFT the frequency response obtained is broad. The frequency domain methods are often more suitable for forming frequency responses over narrower frequency bands. To increase the accuracy of the TLM and FDTD methods, or to obtain reliable data at higher frequencies, more nodes need to be introduced into the TLM and FDTD meshes. Introducing more nodes increases the computational expense of

these time domain methods.

This section has considered a number of popular CEM methods that are used in EMC analyses. The UAs introduced in Chapter 4 may be used to estimate the uncertainty in all of these CEM methods. In the next section the FDTD method is described in detail. The error and uncertainty in different FDTD simulations are determined in Chapters 5-7.

2.3 The Finite Difference Time Domain Method

In 1966 Yee [46] published a numerical method for solving electromagnetic problems in the time domain. This method, known as the Finite Difference Time Domain (FDTD) method, is based on Maxwell's equations for electric and magnetic fields. The differential operators in Maxwell's equations are approximated by finite difference equations. These approximate equations can be solved for numerically subject to some general input parameters. What follows is a detailed discussion of the FDTD algorithm.

2.3.1 Finite Difference Time Domain in One Dimension

The propagation of electromagnetic waves is determined by Maxwell's two curl equations. In their most general form these equations are [47, p.341]

$$\nabla \times \mathbf{E} = -\frac{\partial \mathbf{B}}{\partial t} \tag{2.23}$$

$$\text{and } \nabla \times \mathbf{H} = \frac{\partial \mathbf{D}}{\partial t} + \mathbf{J} \tag{2.24}$$

where $\mathbf{E}$ is the electric field, $\mathbf{D}$ is the electric displacement field, $\mathbf{H}$ is the magnetic field, $\mathbf{B}$ is the magnetic flux density and $\mathbf{J}$ is the electric current density. For simplicity, consider the case where the electromagnetic fields are propagating through a linear, isotropic, homogeneous dielectric with a permittivity, permeability and conductivity denoted by ϵ, μ and σ respectively. In such a media the following relations hold:

$$\mathbf{D} = \epsilon \mathbf{E} \tag{2.25}$$

$$\mathbf{B} = \mu \mathbf{H} \tag{2.26}$$

$$\text{and } \mathbf{J} = \sigma \mathbf{E}. \tag{2.27}$$

Substituting equations (2.25)-(2.27) into equations (2.23) and (2.24) yields

$$\nabla \times \mathbf{E} = -\mu \frac{\partial \mathbf{H}}{\partial t} \tag{2.28}$$

$$\text{and } \nabla \times \mathbf{H} = \epsilon \frac{\partial \mathbf{E}}{\partial t} + \sigma \mathbf{E}. \tag{2.29}$$

Equations (2.28) and (2.29) can be rewritten in index notation as

$$\frac{\partial H_x}{\partial t} = \frac{1}{\mu}\left(\frac{\partial E_y}{\partial z} - \frac{\partial E_z}{\partial y}\right) \tag{2.30}$$

$$\frac{\partial H_y}{\partial t} = \frac{1}{\mu}\left(\frac{\partial E_z}{\partial x} - \frac{\partial E_x}{\partial z}\right) \tag{2.31}$$

$$\frac{\partial H_z}{\partial t} = \frac{1}{\mu}\left(\frac{\partial E_x}{\partial y} - \frac{\partial E_y}{\partial x}\right) \tag{2.32}$$

and

$$\frac{\partial E_x}{\partial t} = \frac{1}{\epsilon}\left(\frac{\partial H_z}{\partial y} - \frac{\partial H_y}{\partial z} - \sigma E_x\right) \tag{2.33}$$

$$\frac{\partial E_y}{\partial t} = \frac{1}{\epsilon}\left(\frac{\partial H_x}{\partial z} - \frac{\partial H_z}{\partial x} - \sigma E_y\right) \tag{2.34}$$

$$\frac{\partial E_z}{\partial t} = \frac{1}{\epsilon}\left(\frac{\partial H_y}{\partial x} - \frac{\partial H_x}{\partial y} - \sigma E_z\right). \tag{2.35}$$

Consider an electromagnetic wave propagating in the negative x-direction, with its electric field component oriented in the z-direction, and its magnetic field component oriented in the y-direction. For this particular electromagnetic wave Maxwell's equations reduce to

$$\frac{\partial H_y}{\partial t} = \frac{1}{\mu}\frac{\partial E_z}{\partial x} \tag{2.36}$$

$$\text{and } \frac{\partial E_z}{\partial t} = \frac{1}{\epsilon}\left(\frac{\partial H_y}{\partial x} - \sigma E_z\right). \tag{2.37}$$

The above two equations are a set of hyperbolic partial differential equations. In 1960 Lax and Wendroff [48] proposed the use of a central derivative approximation to solve such equations. For a function $f(x)$ the central derivative approximation takes the form

$$\frac{\partial f(x)}{\partial x} \approx \frac{f(x + h/2) - f(x - h/2)}{h} \tag{2.38}$$

where h represents a small constant. This approximation is a finite difference approximation, and is the origin of the first half of the name of the FDTD scheme. Applying the finite

difference approximation to equations (2.36) and (2.37) yields

$$\frac{H_y(x,t+\Delta t/2)-H_y(x,t-\Delta t/2)}{\Delta t}=\frac{1}{\mu}\frac{E_z(x+\Delta x/2,t)-E_z(x-\Delta x/2,t)}{\Delta x} \tag{2.39}$$

and

$$\frac{E_z(x,t+\Delta t/2)-E_z(x,t-\Delta t/2)}{\Delta t}=\frac{1}{\epsilon}\left(\frac{H_y(x+\Delta x/2,t)-H_y(x-\Delta x/2,t)}{\Delta x}-\sigma E_z(x,t)\right). \tag{2.40}$$

Here Δt represents a small interval in time and Δx represents a small interval in space. Notice that E_z is evaluated at three different points in time, in equation (2.40). If another approximation is made, namely

$$E_z(x,t)\approx\frac{E_z(x,t+\Delta t/2)+E_z(x,t-\Delta t/2)}{2} \tag{2.41}$$

then equation (2.40) can be rewritten as

$$\frac{E_z(x,t+\Delta t/2)-E_z(x,t-\Delta t/2)}{\Delta t}=\frac{1}{\epsilon}\left(\frac{H_y(x+\Delta x/2,t)-H_y(x-\Delta x/2,t)}{\Delta x}-\sigma\,\frac{E_z(x,t+\Delta t/2)+E_z(x,t-\Delta t/2)}{2}\right), \tag{2.42}$$

The electric field is only evaluated at two places in equation (2.42). Equations (2.39) and (2.42) may be rewritten as

$$H_y(x,t+\Delta t/2)=H_y(x,t-\Delta t/2)+\frac{\Delta t}{\mu}\frac{E_z(x+\Delta x/2,t)-E_z(x-\Delta x/2,t)}{\Delta x} \tag{2.43}$$

and

$$E_z(x,t+\Delta t/2)=\frac{1-\Delta t\sigma/2\epsilon}{1+\Delta t\sigma/2\epsilon}E_z(x,t-\Delta t/2)+\frac{\Delta t}{\epsilon(1+\Delta t\sigma/2\epsilon)}\left(\frac{H_y(x+\Delta x/2,t)-H_y(x-\Delta x/2,t)}{\Delta x}\right). \tag{2.44}$$

Using equation (2.43) the magnetic field can be calculated at a position x and time $t+\Delta t/2$, on the condition that the magnetic field is known at the same position and a time Δt before, and the electric fields are known at positions $\Delta x/2$ either side of x and at a time $\Delta t/2$ before. The electric field can be calculated, at a position x and time $t+\Delta t/2$, in a similar way by using equation (2.44).

To calculate the electric fields and magnetic fields along some interval of the x-axis for some interval in time, space and time must first be discretised [49, p.75-79]. Spatially the interval on the x-axis can be split up into points that are separated by Δx, where the i'th point is given by $x_i = i\Delta x$. Similarly time can be split into time steps Δt, where the n'th time step is denoted as $t_n = n\Delta t$ [49, p.75-79]. This forms a mesh of points in space and time. If the electric field is evaluated at the points x_i and at times t_n then the magnetic fields may be calculated at points $x_{i+1/2}$ and times $t_{n+1/2}$ by using equation (2.43). The fields $E_z(x_i, t_n)$ are denoted as $E_z^n(i)$ from now on for ease of notation. Applying this discretisation to equations (2.43) and (2.44) yields [46]

$$H_y^{n+1/2}(i+1/2) = H_y^{n-1/2}(i+1/2) + \frac{\Delta t}{\mu}\frac{E_z^n(i+1) - E_z^n(i-1)}{\Delta x} \tag{2.45}$$

and

$$\begin{aligned} E_z^{n+1}(i) =& \frac{1-\Delta t\sigma/2\epsilon}{1+\Delta t\sigma/2\epsilon}E_z^n(i) + \\ & \frac{\Delta t}{\epsilon(1+\Delta t\sigma/2\epsilon)}\left(\frac{H_y^{n+1/2}(i+1/2) - H_y^{n+1/2}(i-1/2)}{\Delta x}\right). \end{aligned} \tag{2.46}$$

It is convenient to collect the material parameters and the time and spatial steps together to give

$$\alpha = \frac{1-\Delta t\sigma/2\epsilon}{1+\Delta t\sigma/2\epsilon} \tag{2.47}$$

$$\beta = \frac{\Delta t}{\Delta x\epsilon(1+\Delta t\sigma/2\epsilon)} \tag{2.48}$$

$$\text{and} \quad \gamma = \frac{\Delta t}{\mu\Delta x}. \tag{2.49}$$

Using these terms the FDTD update equations become

$$H_y^{n+1/2}(i+1/2) = H_y^{n-1/2}(i+1/2) + \gamma\left(E_z^n(i+1) - E_z^n(i-1)\right) \tag{2.50}$$

and

$$E_z^{n+1}(i) = \alpha E_z^n(i) + \beta\left(H_y^{n+1/2}(i+1/2) - H_y^{n+1/2}(i-1/2)\right). \tag{2.51}$$

If the electric fields are known at positions x_i and $x_i + \Delta x$, at time t_n, and the magnetic field is known at position $x_i + \Delta x/2$, at time $t_n - \Delta t/2$, then the magnetic field can be calculated at position $x_i + \Delta x/2$ and time $t_n + \Delta t/2$, using equation (2.50). Similarly the

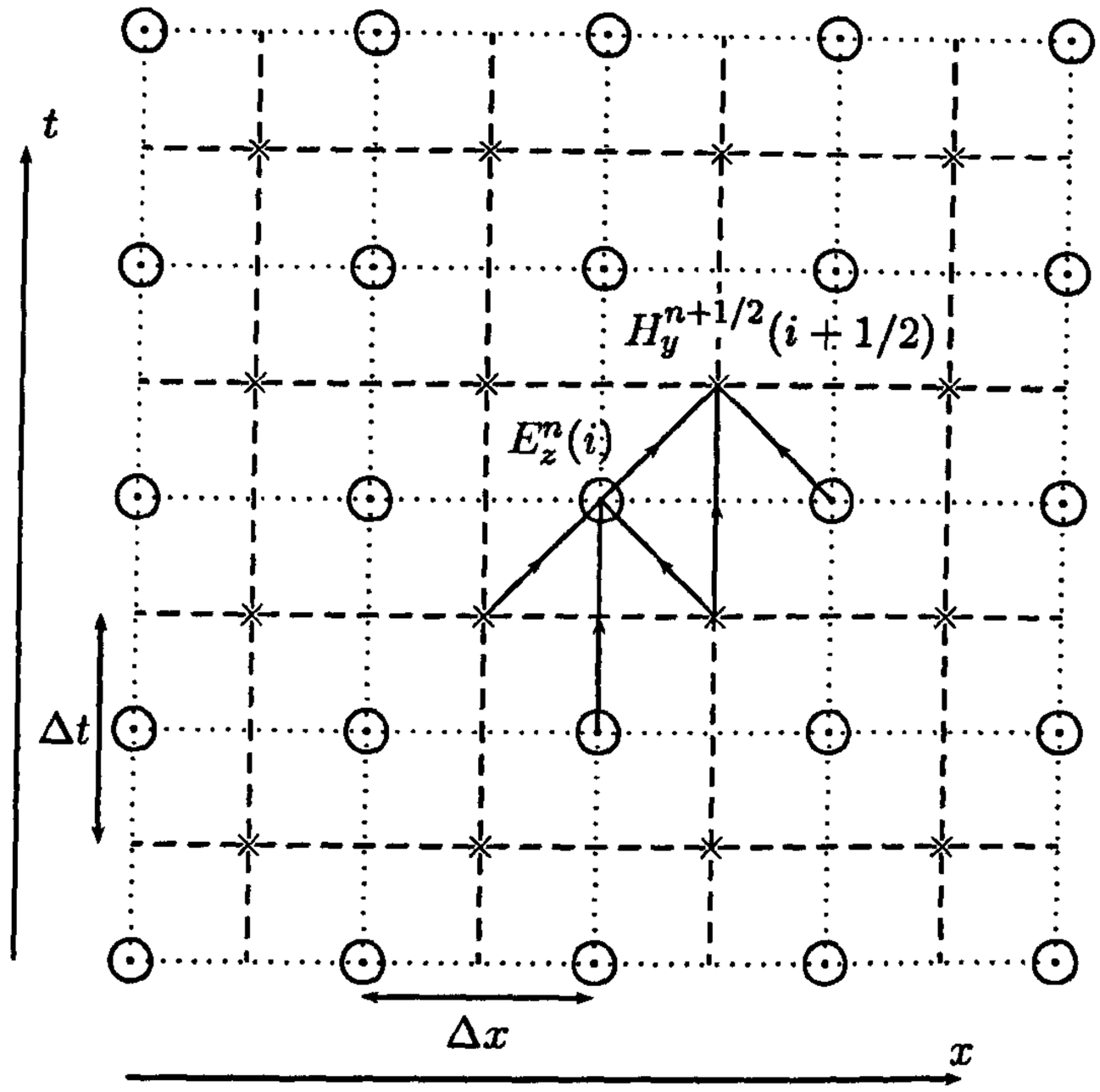

Figure 2.6: The FDTD mesh points in one dimensional space and time. The electric field is evaluated at the dots (⊙) and the magnetic field is evaluated at the crosses (×). The arrows represent the three field values that are used to calculate the next field point in time.

electric field can be calculated using knowledge of the fields at previous time steps using equation (2.51). This forms the basis of the staggered (or leap-frog) FDTD scheme [49, p.77]: electric and magnetic fields are updated at spatial positions set at half a cell apart and at alternating half integer time steps. Figure 2.6 represents the space-time mesh points in 1D, and shows how each field is updated by using other field values from previous time steps.

The update equations (2.50) and (2.51) represent the FDTD algorithm for the propagation of electromagnetic waves along the x-axis. To use these equations the electric and magnetic field values need to be given initial values at time $t = 0$. Initially the field values are set to zero to represent free space. To initialise an electromagnetic wave in the one dimensional mesh a certain amount of electric field is added in at certain points in the mesh over a number of time steps. The amount of field added in at each time step, and the points at which the field is added, depends on the input excitation that is being modelled. The input excitation for position i and time step n may be represented as $E^n_{exc}(i)$. Adding this input excitation into the FDTD update equation (2.51) yields

$$E_z^{n+1}(i) = \alpha E_z^n(i) + \beta \left(H_y^{n+1/2}(i+1/2) - H_y^{n+1/2}(i-1/2) \right) + E^n_{exc}(i). \tag{2.52}$$

It is possible to add in other input excitations such as the fields arising from currents and

potential differences.

The 1D FDTD update equations (2.50) and (2.52) are relatively easy to implement into a computer code, and can be used to provide an efficient and accurate way of studying 1D electromagnetic problems. In the real world however, electromagnetic experiments are performed in 3D. The 3D FDTD update equations are introduced in the next section.

2.3.2 The Finite Difference Time Domain Method in Three Dimensions

So far the FDTD update equations have been derived for the case of a 1D electromagnetic wave polarised in the z direction. The derivation can be easily scaled up to form the FDTD scheme in 2D and 3D. To obtain the 3D FDTD scheme, central derivative approximations are applied to equations (2.30)-(2.35). These equations are then discretised into time $t = n\Delta t$, and space $x = i\Delta x$, $y = j\Delta y$ and $z = k\Delta z$. By using a uniform spatial step size Δl in all spatial directions, the 3D FDTD update equations may be written as

$$H_x^{n+\frac{1}{2}}(i, j+\tfrac{1}{2}, k+\tfrac{1}{2}) = H_x^{n-\frac{1}{2}}(i, j+\tfrac{1}{2}, k+\tfrac{1}{2}) + \gamma \Big(E_y^n(i, j+\tfrac{1}{2}, k+1) - E_y^n(i, j+\tfrac{1}{2}, k) + E_z^n(i, j, k+\tfrac{1}{2}) - E_z^n(i, j+1, k+\tfrac{1}{2}) \Big) \tag{2.53}$$

$$H_y^{n+\frac{1}{2}}(i+\tfrac{1}{2}, j, k+\tfrac{1}{2}) = H_y^{n-\frac{1}{2}}(i+\tfrac{1}{2}, j, k+\tfrac{1}{2}) + \gamma \Big(E_z^n(i+1, j, k+\tfrac{1}{2}) - E_z^n(i, j, k+\tfrac{1}{2}) + E_x^n(i+\tfrac{1}{2}, j, k) - E_x^n(i+\tfrac{1}{2}, j, k+1) \Big) \tag{2.54}$$

$$H_z^{n+\frac{1}{2}}(i+\tfrac{1}{2}, j+\tfrac{1}{2}, k) = H_z^{n-\frac{1}{2}}(i+\tfrac{1}{2}, j+\tfrac{1}{2}, k) + \gamma \Big(E_x^n(i+\tfrac{1}{2}, j+1, k) - E_x^n(i+\tfrac{1}{2}, j, k) + E_y^n(i, j+\tfrac{1}{2}, k) - E_y^n(i+1, j+\tfrac{1}{2}, k) \Big) \tag{2.55}$$

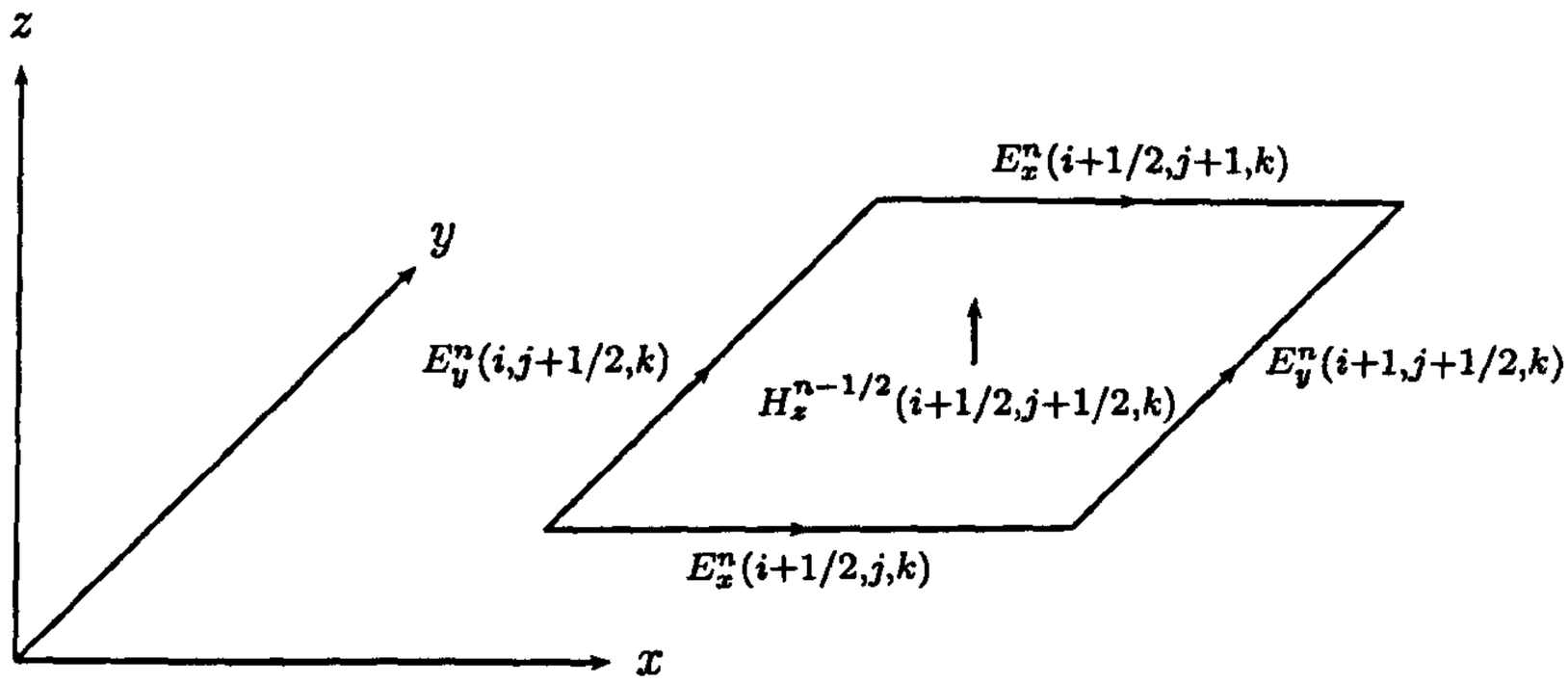

Figure 2.7: Electromagnetic field values required to calculate $H_z^{n+1/2}(i+1/2, j+1/2, k)$.

$$E_x^{n+1}(i+\tfrac{1}{2},j,k) = \alpha E_x^n(i+\tfrac{1}{2},j,k) + \beta\Big(H_z^{n+\frac{1}{2}}(i+\tfrac{1}{2},j+\tfrac{1}{2},k) - H_z^{n+\frac{1}{2}}(i+\tfrac{1}{2},j-\tfrac{1}{2},k) + H_y^{n+\frac{1}{2}}(i+\tfrac{1}{2},j,k-\tfrac{1}{2}) - H_y^{n+\frac{1}{2}}(i+\tfrac{1}{2},j,k+\tfrac{1}{2})\Big) \quad (2.56)$$

$$E_y^{n+1}(i,j+\tfrac{1}{2},k) = \alpha E_y^n(i,j+\tfrac{1}{2},k) + \beta\Big(H_x^{n+\frac{1}{2}}(i,j+\tfrac{1}{2},k+\tfrac{1}{2}) - H_x^{n+\frac{1}{2}}(i,j+\tfrac{1}{2},k-\tfrac{1}{2}) + H_z^{n+\frac{1}{2}}(i-\tfrac{1}{2},j+\tfrac{1}{2},k) - H_z^{n+\frac{1}{2}}(i+\tfrac{1}{2},j+\tfrac{1}{2},k)\Big) \quad (2.57)$$

$$E_z^{n+1}(i,j,k+\tfrac{1}{2}) = \alpha E_z^n(i,j,k+\tfrac{1}{2}) + \beta\Big(H_y^{n+\frac{1}{2}}(i+\tfrac{1}{2},j,k+\tfrac{1}{2}) - H_y^{n+\frac{1}{2}}(i-\tfrac{1}{2},j,k+\tfrac{1}{2}) + H_x^{n+\frac{1}{2}}(i,j-\tfrac{1}{2},k+\tfrac{1}{2}) - H_x^{n+\frac{1}{2}}(i,j+\tfrac{1}{2},k+\tfrac{1}{2})\Big) \quad (2.58)$$

where the material parameters and temporal and spatial step sizes are combined to form

$$\alpha = \frac{1-\Delta t\sigma/2\epsilon}{1+\Delta t\sigma/2\epsilon} \quad (2.59)$$

$$\beta = \frac{\Delta t}{\Delta l\epsilon(1+\Delta t\sigma/2\epsilon)} \quad (2.60)$$

$$\text{and} \quad \gamma = \frac{\Delta t}{\mu\Delta l}. \quad (2.61)$$

The material parameters in equations (2.59)-(2.61) need not be isotropic nor homogeneous. To model an inhomogeneous anisotropic material, different material parameter values need to be stored for different cell positions and for the different field directions.

The 3D FDTD update equations use field values calculated at staggered cell positions and half integer time steps to update the next set of field values. Starting at time $t = 0$ with

all electric and magnetic field values equal to zero, the magnetic field values at positions half a step away from the nodes of the FDTD mesh may be calculated. These are then used to calculate the electric field at the next half integer time step at the nodes of the FDTD mesh. A certain amount of input excitation may then be added into the electric field values. This field will propagate through the mesh in space and time as the field values are updated at each time step. Figure 2.7 shows the field values required to calculate the H_z field component: the required field values surround the H_z component. This is the case for the update of all the field components.

To complete the FDTD update scheme, the update of the fields near the boundary of the problem space needs to be considered. It is impossible to calculate the field values over an infinite problem space as this would require an infinite amount of computer time and memory. Instead the problem space is confined to a bounded volume. This volume forms a cuboid, the edges of which correspond to the nodes of the mesh, where the electric field values are calculated. Since FDTD update equations use field values surrounding a node to calculate the electric field at the node, some value of the magnetic field outside of the problem space is required to update the electric field at a node on the boundary. The magnetic field is not known outside the problem space, and so the FDTD update equations cannot be used to update the electric field at the boundary. Certain boundary conditions are required to enable the calculation of the electric field at the boundary. These boundary conditions are described in more detail in the next section.

2.3.3 Boundary Conditions for the Finite Difference Time Domain Method

There are a number of boundary conditions that may be used alongside the FDTD method. Three such methods are described briefly in this section. These are a Perfectly Electrically Conducting (PEC) boundary, Mur's Absorbing Boundary Condition (ABC) and Bérenger's Perfectly Matched Layers (PML).

Perfectly Electrically Conducting Boundaries

PEC boundaries are perhaps the simplest type of boundaries. These boundaries are used to simulate the enclosure of the problem space in a metal structure such as a reverberation chamber. To implement these boundary conditions the electric field is set to zero at the nodes on the boundary. These boundaries will have zero transmission, reflecting all waves

that are incident upon them.

Mur's Absorbing Boundary Conditions

Often CEM simulations are used to model the scattering of electromagnetic fields in free space. In these cases boundary conditions are required that give no reflection of electromagnetic waves back into the problem space. The required boundaries must transmit (or radiate) all outgoing waves to simulate what would happen in free space. Engquist and Majda [50] considered the use of one-way wave equations to simulate outgoing waves at the boundary [49, p.244]. Mur [51] formed simple ABCs by applying finite-differences to these wave equations. These boundary conditions are really radiating boundary conditions, however Mur referred to them as absorbing boundaries because the boundary effectively absorbs all the waves that radiate out of the problem space.

To derive the Mur ABC in 3D at the free space boundary $x = 0$, consider the wave equation

$$\frac{\partial^2 f}{\partial x^2} + \frac{\partial^2 f}{\partial y^2} + \frac{\partial^2 f}{\partial z^2} - \frac{1}{c^2}\frac{\partial^2 f}{\partial t^2} = 0 \tag{2.62}$$

where f is a scalar field component and c represents the speed of light in free space [49, p.247]. Defining a differential operator

$$L \equiv \frac{\partial^2}{\partial x^2} + \frac{\partial^2}{\partial y^2} + \frac{\partial^2}{\partial z^2} - \frac{1}{c^2}\frac{\partial^2}{\partial t^2} = D_x^2 + D_y^2 + D_z^2 - \frac{1}{c^2}D_t^2 \tag{2.63}$$

equation (2.62) may be rewritten as

$$Lf = 0. \tag{2.64}$$

It is possible to factorise this equation [52, p.244-247] to give

$$Lf = L^+ L^- f = 0 \tag{2.65}$$

where

$$L^+ = D_x + \frac{D_t}{c}\sqrt{1 - S^2} \tag{2.66}$$

$$L^- = D_x - \frac{D_t}{c}\sqrt{1 - S^2} \tag{2.67}$$

$$S = \sqrt{\left(\frac{cD_y}{D_t}\right)^2 + \left(\frac{cD_z}{D_t}\right)^2}. \tag{2.68}$$

Equation (2.65) can be separated into two equations as

$$L^+ f = 0 \tag{2.69}$$

$$L^- f = 0. \tag{2.70}$$

At this point the Taylor series expansion of $\sqrt{1-S^2}$ may be truncated to form simplified approximate solutions of (2.69) and (2.70). The so called first order Mur ABCs are formed by truncating the square root as

$$\sqrt{1-S^2} \cong 1. \tag{2.71}$$

This truncation is valid for small values of S, or more physically when the outgoing wave is normal to the $x = 0$ boundary, and the partial derivatives in the y and z direction are therefore equal to zero. In reality outgoing waves are not always normal to the boundaries in 3D. This results in a reflection of some of the outgoing wave back into the problem space, which creates an error in the final result.

Substituting the Taylor series truncation (2.71) into equations (2.69) and (2.70) yields

$$\left(D_x + \frac{D_t}{c}\right) f = 0 \tag{2.72}$$

$$\left(D_x - \frac{D_t}{c}\right) f = 0. \tag{2.73}$$

Applying finite differences to these equations at the $x = 0$ boundary leads to

$$f^{n+1}(0) = f^n(1) + \frac{c\Delta t - \Delta x}{c\Delta t + \Delta x}\left(f^{n+1}(1) - f^n(0)\right). \tag{2.74}$$

A similar equation is obtained for the upper boundary $x = N_x \Delta x$, namely

$$f^{n+1}(N_x) = f^n(N_x - 1) + \frac{c\Delta t - \Delta x}{c\Delta t + \Delta x}\left(f^{n+1}(N_x - 1) - f^n(N_x)\right) \tag{2.75}$$

where N_x is the highest cell position in the x direction. The scalar field component f may be substituted with E_y or E_z to obtain the update equations for the field components at the boundary $x = 0$. Similar equations are obtained for the update of the electric field at the exterior boundaries in the y and z directions.

Mur's simple ABC has been shown to be successful [49, p.248] when implemented within the FDTD method. These ABCs will be used in the implementation of the FDTD method in this thesis. The inaccuracy of the Taylor series approximation used to form these

first order ABCs has already been highlighted. Further errors will be introduced into the FDTD simulation by the finite difference approximations that are used in forming the ABCs. The errors formed by the approximations used to form the Mur ABCs will be discussed in more detail in Section 2.4.2.

A considerable number of alternative boundary conditions have been proposed since Mur's ABC. Trefethen and Halpern [53] generalised Mur's ABCs for higher order approximations to give better accuracy. Higdon [54] proposed a method to cancel out the outgoing waves, which are incident upon the boundary at different angles, using a linear combination of plane waves. These methods, and other similar methods showed some small success in increasing the accuracy of the boundary conditions. However it was not until 1994 that a significant improvement in the accuracy of boundary conditions was made by Bérenger [55]. Bérenger proposed the use of a PML to absorb all outgoing waves. This method is described in more detail in the next section.

Bérenger's Perfectly Matched Layers

Bérenger's PML produces significantly less unwanted reflections at the boundary of a FDTD mesh than Mur's ABC [33, p.516]. The PML is based on the fact that a plane wave incident on a half space has zero reflection (perfectly matched), so long as the material parameters of the half space are [33, p.516]

$$\frac{\sigma}{\epsilon_0} = \frac{\sigma^*}{\mu_0}. \tag{2.76}$$

In the above equation ϵ_0 and μ_0 are the usual permeability and permittivity of free space respectively, and σ and σ^* are the electrical and magnetic conductivity of the half space material respectively. The use of magnetic conductivity assumes the existence of magnetic monopoles, which cause Maxwell's equations to become symmetric: a phenomenon known as electromagnetic duality. The existence of magnetic charge may be an exciting concept for mathematicians and theoretical physicists, however for Bérenger's PML the physical existence of magnetic monopoles is immaterial. Assuming the existence of magnetic charge at the boundary does not affect the physics of the interior of the FDTD mesh except to reduce the unwanted reflections from the boundary.

The above condition works well to reduce the reflection of normally incident plane waves. However, a wave that is not normally incident on the exterior boundary will not

be perfectly matched [33, p.516]. To overcome this problem Bérenger proposed that the magnetic field components may be artificially split into two subcomponents each with an associated magnetic conductivity [33, p.516]. Bérenger originally proposed the use of a PML in 2D. By splitting the magnetic fields near the 2D boundary, Maxwell's equations become

$$\epsilon_0 \frac{\partial E_x}{\partial t} = \frac{\partial H_z}{\partial y} - \sigma_y E_x \tag{2.77}$$

$$\epsilon_0 \frac{\partial E_y}{\partial t} = -\frac{\partial H_z}{\partial x} - \sigma_x E_y \tag{2.78}$$

$$\mu_0 \frac{\partial H_{zx}}{\partial t} = -\frac{\partial E_y}{\partial x} - \sigma_x^* H_{zx} \tag{2.79}$$

$$\mu_0 \frac{\partial H_{zy}}{\partial t} = \frac{\partial E_x}{\partial y} - \sigma_y^* H_{zy} \tag{2.80}$$

where the magnetic field is split into $H_z = H_{zx} + H_{zy}$, and the conductivities associated with different components are represented by σ_x, σ_y, σ_x^* and σ_y^* [33, p.516]. This splitting of the magnetic field allows waves, which are incident on the PML at any arbitrary angle of incidence, to be perfectly matched. Incident waves are in effect decomposed into their different oriented components, which are then matched separately by setting

$$\frac{\sigma_x}{\epsilon_0} = \frac{\sigma_x^*}{\mu_0} \quad \text{and} \quad \frac{\sigma_y}{\epsilon_0} = \frac{\sigma_y^*}{\mu_0}. \tag{2.81}$$

To implement the PML at the upper x boundary set $\sigma_y = \sigma_y^* = 0$ and let $\sigma_x = \sigma_x^* \epsilon_0 / \mu_0$ be a constant [33, p.516]. Under these conditions, the solution of the modified Maxwell's equations (2.77)-(2.80) become [33, p.516]

$$H_z = H_0 e^{\sqrt{-1}(\omega t)} e^{-\sqrt{-1}(\omega/c)(x\cos\phi + y\sin\phi)} e^{-(\sigma_x \cos\phi/\epsilon_0 c)x} \tag{2.82}$$

$$\mathbf{E} = (-\hat{x}\sin\phi + \hat{y}\cos\phi)\sqrt{\frac{\mu_0}{\epsilon_0}} H_z \tag{2.83}$$

for a wave travelling with an angular frequency ω, at an angle of ϕ to the positive x-axis, in the x-y plane. The constant c in equation (2.82) represents the speed of light and H_0 is the amplitude of the magnetic field. The energy of the outgoing wave is dissipated through the exponential decay factor, thus zero reflections are obtained so long as the values of x are allowed to be infinitely large [33, p.516]. Since the fields decay exponentially with x, exponential differencing must be used to discretise equations (2.77)-(2.80). The update equation

obtained for equation (2.78) is [33, p.516]

$$E_y^{n+1}(i,j+\tfrac{1}{2}) = E_y^n(i,j+\tfrac{1}{2}) - \frac{1}{\sigma_x}(1-e^{-\sigma_x \Delta t/\epsilon_0})\frac{H_z^{n+1/2}(i+\tfrac{1}{2},j+\tfrac{1}{2}) - H_z^{n+1/2}(i-\tfrac{1}{2},j+\tfrac{1}{2})}{\Delta x}. \tag{2.84}$$

This 2D derivation of the PML was later extended to 3D by Katz, Thiele and Taflove [56].

For practical implementations the PML thickness is truncated, at some distance where most of the outgoing energy is absorbed [33, p.517]. A PEC boundary is then used at the outermost points, which causes some reflection of outgoing waves back into the mesh. These reflections, however, are significantly smaller than the reflections produced by Mur's ABCs. The thicker the PML boundary, the smaller the reflections back into the FDTD mesh, but the larger the computational expense. Research has been carried out to obtain the optimal thickness of the PML boundary required to balance the accuracy with the computational expense of the boundary condition [57]. Although the PML has been shown to be more accurate than Mur's ABC, it is also more complicated to implement and requires extra computational expense. Therefore, the Mur ABC is used in the implementation of the FDTD method in this thesis.

The different boundary conditions that may be implemented into the FDTD have been discussed in this section. The next section describes a more accurate FDTD scheme, which makes use of higher order finite difference approximations of the partial derivatives in Maxwell's equations.

2.3.4 A Higher Order Finite Difference Time Domain Method

This section briefly outlines a higher order FDTD method first introduced by Fang [58] in 1989. This method relies on higher order finite difference approximations of the derivatives in Maxwell's equations. These higher order derivatives make Fang's FDTD scheme more accurate than the original scheme proposed by Yee. The order of accuracy of Yee's FDTD method and Fang's higher order method are discussed in more detail in Section 2.4. The following discussion of Fang's higher order scheme is as given by Taflove in [52, p.76-77].

Fang proposed the use of the higher order temporal derivative

$$\left(\frac{\partial f}{\partial t}\right)^{n+1/2} = \frac{f^{n+1}-f^n}{\Delta t} - \frac{(\Delta t)^2}{24}\left(\frac{\partial^3 f}{\partial t^3}\right)^{n+1/2} + O(\Delta t)^4 \tag{2.85}$$

in Maxwell's equations. If f is a variable representing the electric or magnetic field then its third order derivative with respect to time can be related to different spatial derivatives, of the electric and magnetic fields, using Maxwell's equations. This results in the relations [52, p.77]

$$\frac{\partial^3 \mathbf{H}}{\partial t^3} = \frac{1}{\mu}\nabla \times \left[\frac{1}{\epsilon}\nabla \times \left(\frac{1}{\mu}\nabla \times \mathbf{E}\right) + \frac{\sigma}{\epsilon^2}\left(\nabla \times \mathbf{H} - \sigma \mathbf{E}\right)\right] \tag{2.86}$$

$$\begin{aligned}\epsilon\frac{\partial^3 \mathbf{E}}{\partial t^3} = &-\nabla \times \left\{\frac{1}{\mu}\nabla \times \left[\frac{1}{\epsilon}\left(\nabla \times \mathbf{H} - \sigma \mathbf{E}\right)\right]\right\} \\ &\frac{\sigma}{\epsilon}\nabla \times \left(\frac{1}{\mu}\nabla \times \mathbf{E}\right) + \frac{\sigma^2}{\epsilon^2}\left(\nabla \times \mathbf{H} - \sigma \mathbf{E}\right).\end{aligned} \tag{2.87}$$

These expressions are greatly reduced for the 1D case, or for the case where the permeability, permittivity and conductivity are constant. The spatial derivatives in equations (2.86) and (2.87) are approximated by second order central derivatives in Fang's FDTD scheme. The other spatial derivatives appearing in Maxwell's equations are approximated by a higher order spatial derivative, namely

$$\frac{\partial f}{\partial x} = \frac{27\left(f(i+\frac{1}{2}) - f(i-\frac{1}{2})\right) - \left(f(i+\frac{3}{2}) - f(i-\frac{3}{2})\right)}{24\Delta x} + O(\Delta x^4) \tag{2.88}$$

where f denotes the scalar field components used in Maxwell's equations. These derivative approximations are chosen to maintain the order of accuracy of the higher order FDTD scheme.

This higher order FDTD scheme provides higher order derivative approximations for the derivatives in Maxwell's equations. Once again only the fields from the previous half integer time step are required to update the fields at the next time step. The scheme may well be more accurate than Yee's original FDTD scheme, however the scheme is more difficult to implement and more computationally expensive, especially in 3D and when the material parameters vary spatially.

Fang's higher order FDTD scheme will be investigated as a possible method that may be used to analyse the error in simulations performed using Yee's original scheme. This is described in more detail in Chapter 4. In the next section the stability criteria is introduced. This criteria maintains certain physical laws within the FDTD schemes.

2.3.5 Stability Criteria

In one time step the FDTD scheme allows the field at one point to affect the field values at only the nearest points. It is therefore important that the time step is small enough to record the effects of a wave passing through the problem space. If the time step is too large, then a wave may have passed over a number of points before the field values at these points are updated: this causes the simulated solution to become unstable. To maintain stability in 3D the time step is chosen so that a wave travelling at the speed of light c will not pass by one cell before the field values are updated at the next time step. This causes the time step to take on a maximum value, namely

$$\Delta t \leq \frac{1}{c}\left(\frac{1}{\Delta x^2}+\frac{1}{\Delta y^2}+\frac{1}{\Delta z^2}\right)^{-\frac{1}{2}}. \tag{2.89}$$

This temporal step size limit is known as the Courant limit [49]. The Courant stability criteria asserts that the speed of light limits the rate at which information is propagated through the FDTD mesh [33, p.503]. If a uniform spatial step Δl is used in each direction then

$$\Delta t \leq \frac{\Delta l}{c\sqrt{3}}. \tag{2.90}$$

Similar stability criteria may be obtained for the 1D and 2D FDTD methods. For the 1D case stability is maintained so long as

$$\Delta t \leq \frac{\Delta l}{c} \tag{2.91}$$

and in the 2D case the stability is maintained so long as

$$\Delta t \leq \frac{\Delta l}{c\sqrt{2}}. \tag{2.92}$$

Thus, the temporal step size required to maintain stability is inversely proportional to the square root of the dimension of the FDTD simulation. In practice a step size of

$$\Delta t = \frac{\Delta l}{2c} \tag{2.93}$$

is used in 3D, however this step size satisfies the Courant condition for FDTD simulations of all dimensions. Using this time step a wave will propagate from an electric field node to the nearest magnetic field and then to the next electric field node in two time steps.

There are many other considerations that must be taken into account when forming

a reliable FDTD scheme. Different implementations of the FDTD method will produce different sources of error. Some of these sources of error will be identified in the next section, using Definition 1.1.

2.4 Sources of Errors in Finite Difference Time Domain Simulations

The sources of errors described in this section are meant to act as a general introduction to some of the main errors that should be analysed in any general FDTD simulation. These errors are by no means a complete error taxonomy for the FDTD scheme. Each simulation and application of FDTD introduces different types of error. To discuss some of the sources of errors, the definition of the order of accuracy is required. A similar definition can be found in [49, p.63].

Definition 2.1 *Let f be a smooth function that depends on some variable x, which when operated on by the continuous operator A gives*

$$Af(x) = F_{exact}. \tag{2.94}$$

Suppose $A_{\Delta x}$ is a discretised approximation of A, which depends on the discrete interval Δx of x, and let the operation of $A_{\Delta x}$ on $f(x)$ be given by

$$A_{\Delta x} f(x) = F_{\Delta x}. \tag{2.95}$$

The order of accuracy of the approximate operator $A_{\Delta x}$ is said to be p if the error in the operation on $f(x)$ by $A_{\Delta x}$ satisfies

$$Error = F_{\Delta x} - F_{exact} \propto (\Delta x)^p. \tag{2.96}$$

This definition will be used to obtain the order of accuracy of the conventional FDTD method in the next section.

2.4.1 Truncation, Discretisation and Dispersion Errors

In the derivation of the field update equations (equations (2.45) and (2.46)) the derivatives in Maxwell's equations were approximated by using the central difference approximation (2.38)

$$\frac{\partial f(x)}{\partial x} \approx \frac{f(x+\Delta x/2) - f(x-\Delta x/2)}{\Delta x}$$

where f is a smooth function dependent on x. In accordance with Definition 2.1, the continuous operator $A_{exact} = \partial/\partial x$ is approximated by the discrete operator

$$A_{\Delta x} = \frac{T^{1/2} - T^{-1/2}}{\Delta x} \tag{2.97}$$

where T is a translation operator defined by $Tf(x) = f(x + \Delta x)$ [59, p.3].

Performing the Taylor series expansion of $f(x+\Delta x/2)$ and $f(x-\Delta x/2)$ gives [49][p.38]

$$f(x + \Delta x/2) = f(x) + \frac{\Delta x}{2} f'(x) + \frac{\Delta x^2}{2!2^2} f''(x) + \frac{\Delta x^3}{3!2^3} f^{(3)}(x) + \frac{\Delta x^3}{4!2^4} f^{(4)}(x) \ldots \tag{2.98}$$

and

$$f(x - \Delta x/2) = f(x) - \frac{\Delta x}{2} f'(x) + \frac{\Delta x^2}{2!2^2} f''(x) - \frac{\Delta x^3}{3!2^3} f^{(3)}(x) + \frac{\Delta x^4}{4!2^4} f^{(4)}(x) \ldots . \tag{2.99}$$

Using these expansions $A_{\Delta x} f(x)$ can be rewritten as

$$\begin{aligned} A_{\Delta x} f(x) = &\left[f(x) + \frac{\Delta x}{2} f'(x) + \frac{\Delta x^2}{2!2^2} f''(x) + \frac{\Delta x^3}{3!2^3} f^{(3)}(x) + \frac{\Delta x^3}{4!2^4} f^{(4)}(x) \right. \\ &\left. - \left(f(x) - \frac{\Delta x}{2} f'(x) + \frac{\Delta x^2}{2!2^2} f''(x) - \frac{\Delta x^3}{3!2^3} f^{(3)}(x) + \frac{\Delta x^4}{4!2^4} f^{(4)}(x) \right) \right] / \Delta x + \ldots \\ = &f'(x) + \frac{\Delta x^2}{24} f^{(3)}(x) + \ldots . \end{aligned} \tag{2.100}$$

The error in the finite difference approximation is

$$\begin{aligned} Error &= A_{\Delta x} f(x) - A_{exact} f(x) \\ &= (f'(x) + \frac{\Delta x^2}{24} f^{(3)}(x) + \ldots) - f'(x) \\ &= \frac{\Delta x^2}{24} f^{(3)}(x) \propto \Delta x^2. \end{aligned} \tag{2.101}$$

Using Definition 2.1 it is clear that the central difference approximation is second order accu-

rate. Since the FDTD method uses central differences for the temporal and spatial derivative, the method is second order accurate in time and second order accurate in space [49, p.39]. FDTD simulations performed with this order of accuracy are referred to as (2,2) FDTD simulations; the numbers in the brackets referring to the order of accuracy in space and time respectively. Using a similar argument to that given above, it can be shown that Fang's higher order FDTD method [58] is 4th order accurate in both space and time. Simulations performed using Fang's higher order method are referred to as (4,4) FDTD simulations.

In forming the central difference approximations, which are used in the FDTD method, the Taylor series expansion of a function is truncated. The error introduced by the central difference approximation is therefore known as the truncation error. The FDTD method also requires the discretisation of Maxwell's equations, which introduces a finite mesh size. This approximation of Maxwell's equations introduces errors that are known as discretisation errors. The discretisation error is related to the truncation error because the truncation error of each first derivative is dependent on the mesh size (Δx in the above equations). Both the discretisation and truncation errors tend to zero as the mesh size becomes infinitesimally small.

There are a number of ways to analyse the truncation and discretisation errors in a FDTD simulation, these will be discussed in more detail later. Researchers have previously gained an insight into the truncation and discretisation errors by analysing the dispersion error [60],[61]. Dispersion is a direct consequence of the central difference approximation which introduces discretisation and truncation errors. The discretisation and truncation errors cause the phase velocity of a wave, travelling through an FDTD mesh, to be lower than the speed of light. In higher dimensional problem spaces the wave speed is dependent on the angle at which the wave propagates with respect to the mesh axis [49, p.110-123]. Therefore, a wave travelling in two or three dimensions will have different propagation velocities in different directions causing the wave to disperse. The extent of the dispersion is also affected by the wavelength of the waves propagating through the FDTD mesh. The derivation of the dispersion relation for FDTD is given below. This derivation and the results that follow from it are well documented: the reader is referred to [49, p.110-123] and [33, p.502-506].

Consider a wave with an angular frequency ω and wavenumber k, travelling in a lossless 2D space. The electromagnetic wave will satisfy Maxwell's equations, which in 2D

are

$$\frac{\partial H_x}{\partial t} = -\frac{1}{\mu}\frac{\partial E_z}{\partial y} \tag{2.102}$$

$$\frac{\partial H_y}{\partial t} = \frac{1}{\mu}\frac{\partial E_z}{\partial x} \tag{2.103}$$

$$\frac{\partial E_z}{\partial t} = \frac{1}{\epsilon}\left(\frac{\partial H_y}{\partial x} - \frac{\partial H_x}{\partial y}\right). \tag{2.104}$$

Discretising and using central difference approximations, these equations become

$$\frac{H_x^{n+1/2}(i,j+\frac{1}{2}) - H_x^{n-1/2}(i,j+\frac{1}{2})}{\Delta t} = -\frac{1}{\mu}\frac{E_z^n(i,j+1) - E_z^n(i,j)}{\Delta y} \tag{2.105}$$

$$\frac{H_y^{n+1/2}(i+\frac{1}{2},j) - H_y^{n-1/2}(i+\frac{1}{2},j)}{\Delta t} = \frac{1}{\mu}\frac{E_z^n(i+1,j) - E_z^n(i,j)}{\Delta x} \tag{2.106}$$

$$\begin{aligned}\frac{E_z^{n+1}(i,j) - E_z^n(i,j)}{\Delta t} = \frac{1}{\epsilon}\Bigg(&\frac{H_y^{n+1/2}(i+\frac{1}{2},j) - H_y^{n+1/2}(i-\frac{1}{2},j)}{\Delta x} \\ &- \frac{H_x^{n+1/2}(i,j+\frac{1}{2}) - H_x^{n+1/2}(i,j-\frac{1}{2})}{\Delta y}\Bigg).\end{aligned} \tag{2.107}$$

Numerical dispersion relationships can be derived by substituting the solution of a single frequency planar wave into the above FDTD update equations [49, p.110]. A 2D plane wave solution that may be used for this purpose takes the form:

$$E_z^n(i,j) = E_{z_0} e^{\sqrt{-1}(\omega n\Delta t - k\cos\phi i\Delta x - k\sin\phi j\Delta y)} \tag{2.108}$$

$$H_x^n(i,j) = H_{x_0} e^{\sqrt{-1}(\omega n\Delta t - k\cos\phi i\Delta x - k\sin\phi j\Delta y)} \tag{2.109}$$

$$H_y^n(i,j) = H_{y_0} e^{\sqrt{-1}(\omega n\Delta t - k\cos\phi i\Delta x - k\sin\phi j\Delta y)} \tag{2.110}$$

where E_{z_0}, H_{x_0} and H_{y_0} are constant coefficients, and ϕ is the angle of propagation of the wave relative to the x-axis. Substituting this plane wave solution into equations (2.105)-(2.107) and using the relation

$$\sin x = \frac{1}{2\sqrt{-1}}\left(e^{\sqrt{-1}x} - e^{-\sqrt{-1}x}\right) \tag{2.111}$$

yields [49, p.111]

$$H_{x_0} = \frac{\Delta t E_{z_0}}{\mu \Delta y} \frac{\sin\left(k \sin\phi \Delta y/2\right)}{\sin\left(\omega \Delta t/2\right)} \tag{2.112}$$

$$H_{y_0} = -\frac{\Delta t E_{z_0}}{\mu \Delta x} \frac{\sin\left(k \cos\phi \Delta x/2\right)}{\sin\left(\omega \Delta t/2\right)} \tag{2.113}$$

$$E_{z_0} \sin\left(\frac{\omega \Delta t}{2}\right) = \frac{\Delta t}{\epsilon}\left[\frac{H_{x_0}}{\Delta y} \sin\left(\frac{k \sin\phi \Delta y}{2}\right) - \frac{H_{y_0}}{\Delta x} \sin\left(\frac{k \cos\phi \Delta x}{2}\right)\right]. \tag{2.114}$$

Equations (2.112) and (2.113) are then substituted into equation (2.114) to obtain [49, p.111]

$$\left[\frac{1}{c\Delta t} \sin\left(\frac{\omega \Delta t}{2}\right)\right]^2 = \left[\frac{1}{\Delta x} \sin\left(\frac{k \cos\phi \Delta x}{2}\right)\right]^2 + \left[\frac{1}{\Delta y} \sin\left(\frac{k \sin\phi \Delta y}{2}\right)\right]^2 \tag{2.115}$$

where $c = 1/\sqrt{\mu\epsilon}$ is the speed of the travelling wave in the material. Equation (2.115) represents the numerical dispersion relation of the 2D FDTD algorithm [49, p.111]. Notice that as Δt, Δx and Δy tend to zero, equation (2.115) tends to the numerical dispersion relation for the continuous case [33, p.504]:

$$\left(\frac{\omega}{c}\right)^2 = k^2. \tag{2.116}$$

It is possible to compare the discrete and continuous numerical dispersion relations for different wave propagation angles ϕ, and different cell sizes Δx. To do this consider the case where the 2D mesh has square cells such that $\Delta l = \Delta x = \Delta y$. Using the Courant stability criteria derived earlier, the time step may be written in terms of the spatial step as $\Delta t = \Delta l/2c$. In reality the phase velocity of the travelling wave should be

$$c = \frac{\omega}{k} \tag{2.117}$$

which is independent of the angle of propagation of the wave. The phase velocity of the wave in the discrete case is found by rearranging equation (2.115) to obtain ω in terms of the wavenumber k or vice-versa, and then using the definition of the phase velocity $v_p = \omega/k$. Figure 2.8 shows the ratio of this phase velocity to the continuous wave speed c, for different propagation angles: this figure is as found in [33, p.506] and [49, p.118]. From this figure it can be seen that the ratio of the wave speeds differ from the ideal value of one, for propagation angles closer to the FDTD mesh axes. The ratio of the wave speeds also differs for larger cell sizes. Using a smaller cell size is more accurate, producing phase velocities that are closer to the continuous wave speed c. Usually it is accepted that using a cell size that gives a ratio of $\Delta l/\lambda = 1/10$, is sufficiently accurate.

This section has discussed the truncation, discretisation and dispersion errors. The fact that these errors decrease as the cell size of the FDTD mesh decreases is used in Chapter 4 when considering approximate Error Analysis methods.

2.4.2 Boundary Errors

The errors produced by the approximations made when forming the Mur ABCs may be analysed in a similar way to the dispersion errors in the previous section. Consider a monochromatic plane wave propagating in 2D towards the $x = 0$ Mur boundary at an angle of ϕ to the normal of the boundary. The 2D plane wave can be represented by [33, p.514-515]

$$E_z^n(i,j) = E_0 \exp\left\{\sqrt{-1}(\omega n\Delta t + k\cos\phi i\Delta x + k\sin\phi j\Delta y)\right\} \tag{2.118}$$

where E_0, ω and k are the amplitude, angular frequency and wavenumber of the wave respectively. The error in the Mur ABC causes the plane wave to reflect at the $x = 0$ boundary. Thus the electric field solution at the boundary is the sum of the incident wave and the reflected wave in the positive x direction:

$$E_z^n(i,j) = E_0 e^{\sqrt{-1}(\omega n\Delta t + k\sin\phi j\Delta y)}\left(e^{\sqrt{-1}(k\cos\phi i\Delta x)} + Re^{-\sqrt{-1}(k\cos\phi i\Delta x)}\right). \tag{2.119}$$

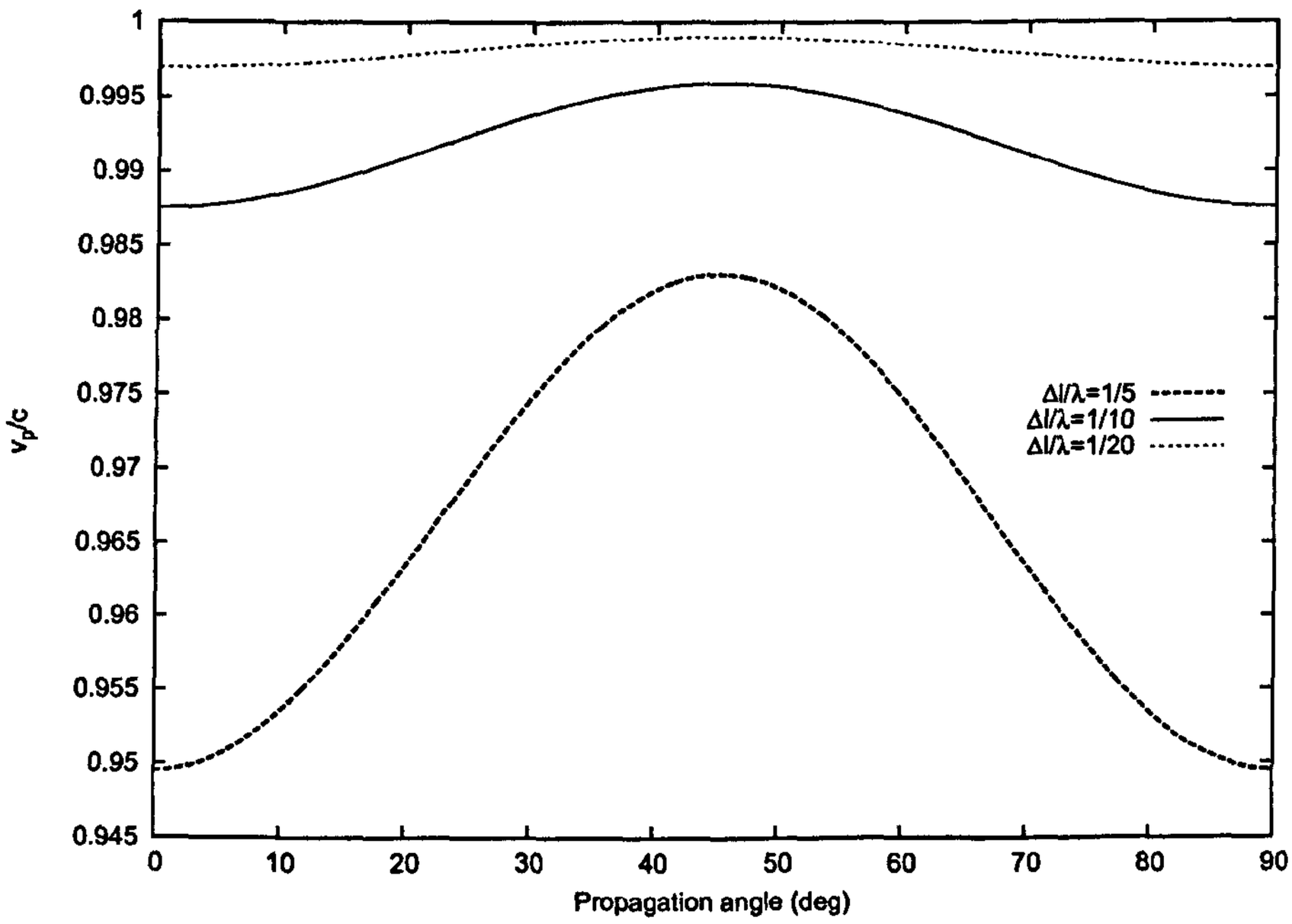

Figure 2.8: Ratio of the discrete phase velocity to the continuous wave speed for different propagation angles.

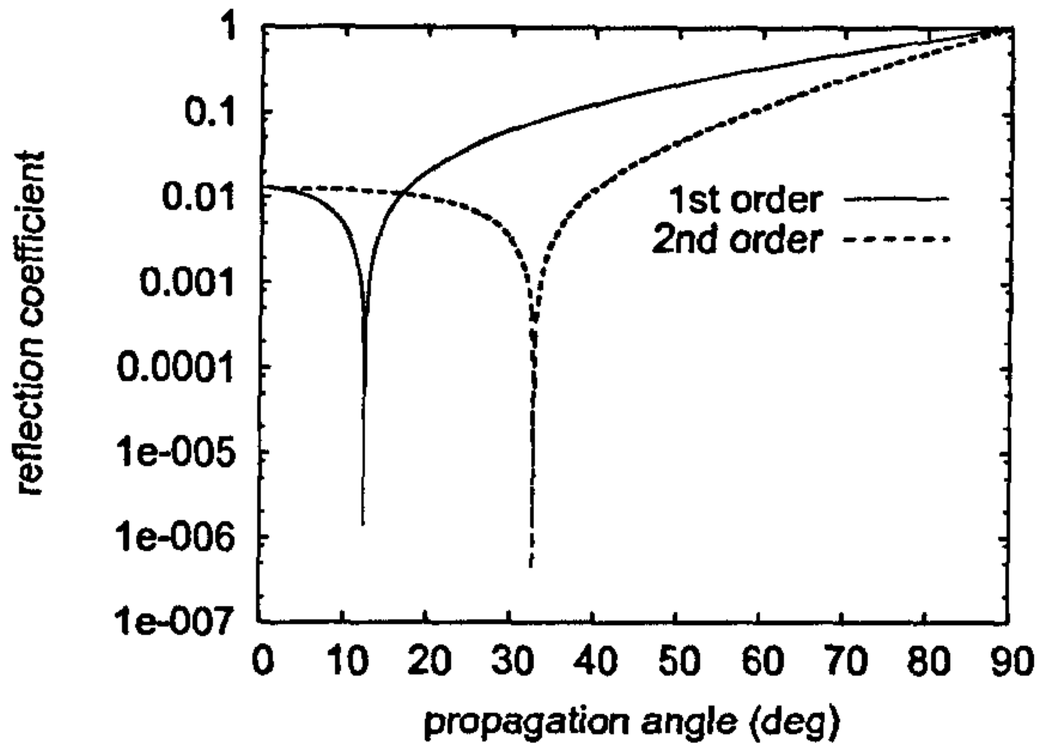

Figure 2.9: Absolute value of the reflection coefficient for Mur ABCs.

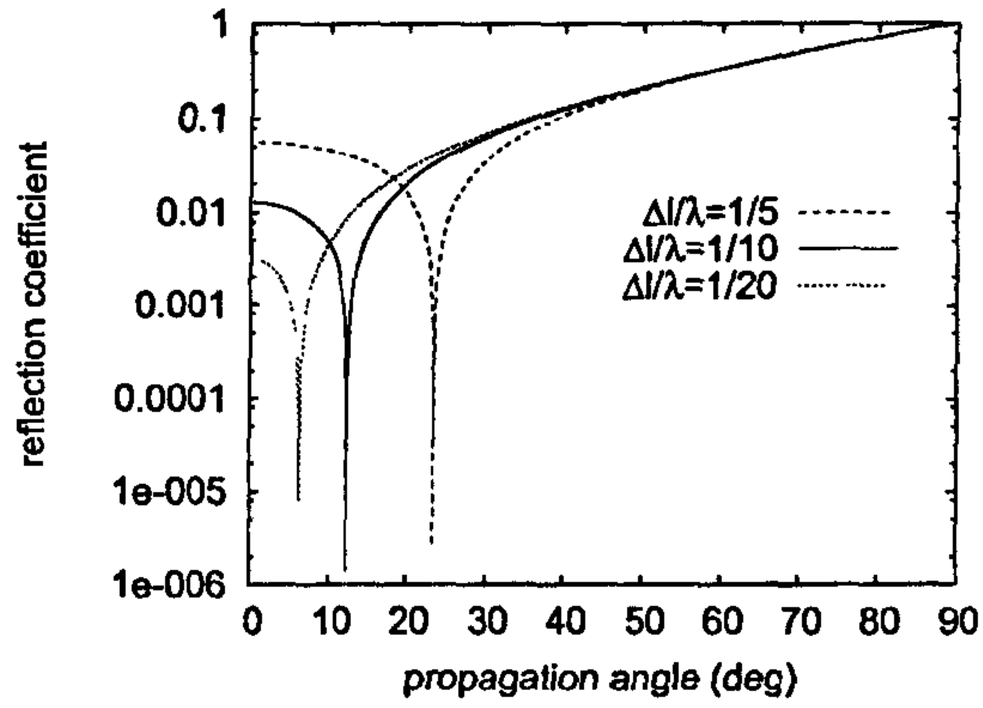

Figure 2.10: Absolute value of the reflection coefficient for different cell sizes.

The constant R is the reflection coefficient, which is determined by substituting (2.119) into the Mur ABC update equation (2.74). For the first order Mur ABCs this substitution yields [33, p.514]

$$R = -e^{jk\cos\phi\Delta x}\frac{\Delta x\sin(\omega\Delta t/2)\cos(k\cos\phi\Delta x/2) - c\Delta t\cos(\omega\Delta t/2)\sin(k\cos\phi\Delta x/2)}{\Delta x\sin(\omega\Delta t/2)\cos(k\cos\phi\Delta x/2) + c\Delta t\cos(\omega\Delta t/2)\sin(k\cos\phi\Delta x/2)}. \tag{2.120}$$

It is possible to obtain a similar expression for the reflection coefficient of the higher order Mur ABC. Setting $c\Delta t = \Delta x$ in equation (2.120) gives the desired zero value for the reflection coefficient. However setting $c\Delta t = \Delta x$ violates the Courant stability criteria for the 2D FDTD method [33, p.515]. By ensuring that the Courant stability condition is maintained, errors from the Mur ABC will appear in the output of the FDTD simulation.

Consider the case where $\Delta l = \Delta x = \Delta y$, and the time step is $\Delta t = \Delta l/2c$. Figure 2.9 shows the magnitude of the reflection coefficient for the first and second order Mur ABCs, for different propagation angles [33, p.515]. This figure shows that the reflection coefficient is smaller in general for the second order Mur ABC, however the reflection coefficient increases to one for waves with grazing incidence upon the boundary. Figure 2.10 shows the magnitude of the reflection coefficient for the first order Mur ABC, for different angles and different cell sizes. Figure 2.10 shows that the reflection coefficient decreases as the ratio of the cell size to the wavelength of the propagating wave decreases. However the reflection coefficient increases to one for plane waves with grazing incidence upon the boundary, no matter how small this ratio is.

An approximate Error Analysis is introduced in Chapter 4 that considers the use of smaller mesh cells to provide more accurate FDTD simulated output. It has been shown

in this section that reducing the cell size will reduce the boundary error to some extent; however in this thesis no explicit method is used to quantify the error in the output due to boundary errors.

As discussed previously the PML boundary conditions are more accurate than the Mur ABCs. The Mur ABCs introduce more unwanted reflections back into the FDTD mesh than the PML. It would therefore be possible to estimate the error in the output of an FDTD simulation due to the Mur ABC, by using an equivalent simulation that uses PML boundaries. The difference between the output of the simulation using Mur ABCs and the output of the simulation using a PML will provide an estimate of the output error due to the Mur boundary. It may be argued that since a simulation using a PML has been performed then the more accurate output formed from this simulation should be used in place of the output from the simulation with Mur ABCs. If however many simulations were to be performed, it may be computationally cheaper to use the Mur ABCs and to estimate the error in these simulations using one simulation performed with a PML. This method of error estimation is not investigated in this thesis.

The error estimation methods introduced in Chapter 4 attempt to quantify the error in the output of FDTD simulations due to the truncation and discretisation errors. These Error Analyses are used in Chapters 5 and 6 to obtain the error estimate for a number of FDTD simulations. The error estimations are compared to the true error, which is obtained analytically, to determine the accuracy of the approximate Error Analyses. The analytical error includes all errors, it is therefore possible to determine whether the Error Analyses are accurate despite ignoring some of the sources of error (such as the error due to the boundary conditions).

2.4.3 Staircasing Errors

Staircasing errors arise from introducing a mesh to numerically solve Maxwell's equations. Unfortunately material parameters can only be defined at the discrete spatial points of the mesh. If a circle is modelled on the 2D mesh then it is constructed out of the squares that make up the mesh. The circle appears in the simulation with a stair-stepped boundary (as shown in Figure 2.11) and is therefore not circular. The stair-stepped boundary may act quite differently from a smooth circular boundary. Thus errors are introduced when simulating curved surfaces in discrete orthogonal meshes. These errors are called staircasing errors.

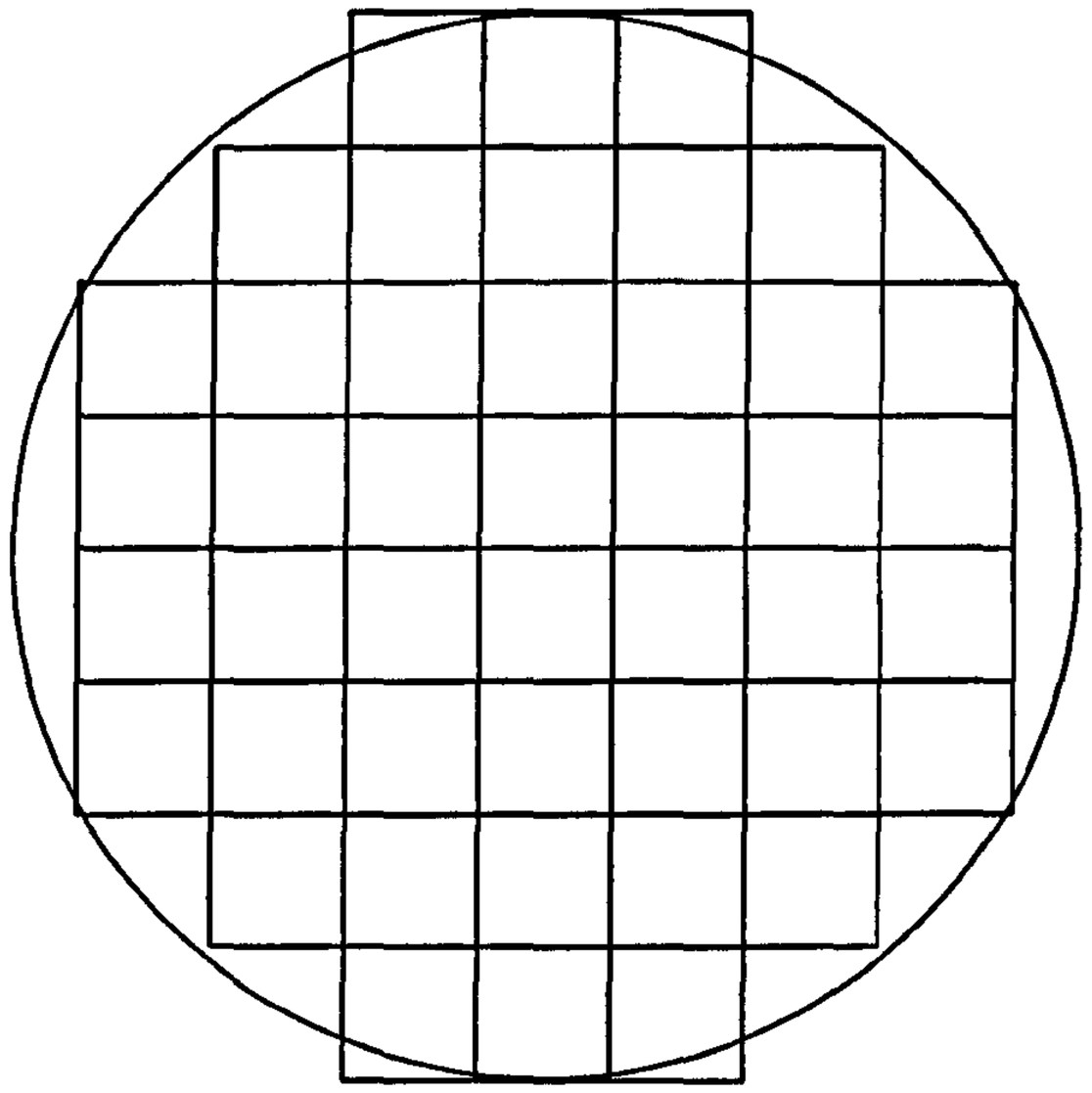

Figure 2.11: Simulation of a circle on a two dimensional mesh. The perimeter of the squares will be the simulated circle when applied to the mesh.

Much work has already been carried out on the analysis of staircasing errors, including work by Cangellaris and Wright [62], Akyurtlu [63] and Holland [64]. Cangellaris and Wright compared the results obtained by sending electromagnetic waves at a perfect electrical conductor that was aligned parallel to and at 45 degrees to the axis of the mesh. They found that the propagation of the waves was dependent on the wavelength of the waves used and the cell size of the mesh [62]. Akyurtlu gives a similar analysis of the staircasing errors for a general air-dielectric boundary. They found that as the relative permittivity of the dielectric is increased the errors converge to the results for an air-PEC interface [63]. Holland compared two different meshes, a stair-stepped orthogonal mesh and a coarse conformal mesh, to model a conducting strip and a conducting circular cylinder. The model using the stair-stepped mesh was found to be less accurate than the model using the coarse conformal mesh, which fitted the canonical results much more closely [64].

These staircasing errors are introduced by the discretisation of Maxwell's equations: an approximation that was required to form the FDTD method. By using a more refined mesh, with cells of a smaller size, curved surfaces will be modelled more accurately. Thus, the staircasing error also decreases for more refined FDTD meshes.

2.4.4 Numerical Round-off Errors

Numerical round-off errors arise from the numerical precision used to record the field values at each point in space and time [65, p.100-103]. This precision must be finite as only a finite amount of computer memory exists [65, p.100-103]. When field values are rounded off errors are introduced. These errors are propagated through the simulation as field values are updated using previously rounded off field values. Normally field values are stored as floats which can hold up to six significant figures [65, p.100-103]. Some idea of the numerical round-off errors could be obtained for a simulation that uses floats by performing a second simulation using doubles to store the field values, and comparing the two simulations. Doubles will hold approximately twice as many significant figures as floats, which will increase the accuracy of the simulation. Roache argues that numerical round-off errors are negligible compared to other forms of error [65, p.100-103]. Thus, no analysis of the numerical errors in FDTD simulations is made in this thesis.

2.5 Sources of Parameter Uncertainty in Computational Electromagnetism

This thesis aims to investigate the uncertainty in the output of CEM simulations due to the uncertainty in the input parameters. This type of uncertainty is known as parameter uncertainty. Quantifying the uncertainty in a result indicates the level of confidence that may be held in that result. Examples of the types of inputs that may have an associated uncertainty are the:

- geometric positions of materials in the problem space,
- physical sizes of these materials,
- material parameter values such as the permittivity, permeability and conductivity,
- input excitation parameters such as amplitude and phase,
- position of the output (measurement) points.

The values of some of these inputs may not be exactly known, for example there may be an uncertainty in the value of the permittivity of a dielectric being modelled. Other inputs may be known to certain tolerances, such as the length of a metal sheet. As with determining

the uncertainty in the results of physical EMC experiments, expert knowledge is required to determine the sizes of these input uncertainties, and the associated PDFs. The work in this thesis concentrates on investigating different methods to quantify the uncertainty in the output of CEM simulations when given a set of uncertain input parameters, and does not consider the accurate determination of these uncertain input parameters. The material parameters of free space are used in the examples in this thesis, for simplicity these values are assumed to have a zero associated uncertainty.

As discussed in Chapter 1 there has already been some previous research into uncertainty in CEM. This research includes work by Chauvière, Hesthaven and Lurati [18] and Ajayi, Ingrey, Sewell, and Christopoulos [19]. Chauvière et al concentrated on implementing Polynomial Chaos into a high-order discontinuous Galerkin method, which was proposed by Hesthaven and Warburton [66] as a possible method for solving Maxwell's equations in the time domain. Ajayi et al used another approximate method to determine parameter uncertainty, known as the Method of Moments (MoM) [16]. This method is not the same as the well known method used in CEM (referred to as IEMoM in this thesis), but is a statistical method for determining the output uncertainty given a set of input uncertainties. Despite this previous work it is evident that there has been considerably more research analysing the errors in CEM simulations. This thesis aims to investigate different methods that may be used to quantify parameter uncertainty in CEM simulations.

2.6 Discussion

This chapter has introduced a number of CEM methods that are used within EMC research. In particular this chapter has discussed the FDTD method in detail. The boundary conditions used in the FDTD method have been described, as well as a higher order FDTD method and the stability criteria.

Some of the sources of error and uncertainty that exist in the FDTD method have been discussed. It is clear that there has been a significant amount of research analysing the errors in the FDTD method. From this work it may be concluded that many of the errors arising in the FDTD method are reduced when the cell size and time step used in the FDTD simulations are reduced. This fact will be used later in the thesis to form approximate Error Analysis methods.

Less work has been carried out on the uncertainty in the output of CEM simulations.

This thesis will concentrate primarily on quantifying the uncertainties in the output of CEM simulations. The MCM, MoM and PCM are used in this thesis to quantify parameter uncertainty. The MCM and MoM use the output of CEM simulations to quantify the uncertainty: these two methods may therefore be used to analyse the uncertainty in any of the CEM techniques discussed in this chapter. The PCM requires a modification to the different CEM techniques before it can be used to quantify the uncertainty. More work is therefore required to implement the PCM into the various CEM techniques described in this chapter.

The discretised FDTD mesh, which introduces errors into the output of the FDTD simulations, will also affect the accuracy of the chosen UA methods. Consider the quantification of the output uncertainty due to a geometric uncertain input parameter. Using the MCM to quantify this uncertainty will result in many sample coordinates being formed for the uncertain parameter. These coordinates may not necessarily coincide with the FDTD mesh. To perform the different MCM simulations the coordinates must be reassigned to the nearest mesh node, introducing an error into the UA. The discretisation, used in the FDTD method, therefore has the potential to introduce errors into the different UA methods.

As discussed in Section 2.2 the output from a CEM simulation is usually a frequency response curve. The error and uncertainty in this output will also be a curve. The next chapter introduces a number of numerical methods that are used in this thesis to help analyse the error and uncertainty in output curves.

Chapter 3

Numerical Analysis of Curves

Contents

3.1 Introduction

As discussed in Chapter 2, the output of CEM simulations are often frequency response curves. In this thesis the error and uncertainty in these output curves will be determined. In order to facilitate this a number of different numerical techniques are needed to analyse the output curves; these techniques will be discussed in this chapter.

Firstly the Feature Selective Validation (FSV) method will be discussed. This is a method for comparing curves, first proposed by Martin in his thesis [67]. The method, which is described in Section 3.2.1, compares curves in terms of their amplitude and feature differences. The FSV method is used in a number of different ways in this thesis, as outlined in Section 3.2.3.

Curve alignments are used alongside the Error and Uncertainty Analyses, in this thesis, to determine the manifestation of the errors and uncertainties in the output frequency response curves. The errors and uncertainties in the output curves manifest themselves as amplitude and frequency errors and uncertainties. Section 3.3 provides more details on the need for curve alignments, when performing Error and Uncertainty Analyses. Three different methods that may be used to align curves are introduced in this section. The first two methods (Peak Matching and Interval Correlation) are novel methods that are shown to align different curves well. The third method (Dynamic Time Warping) also aligns curves very well, however the alignment process distorts the curves severely. These severe distortions will affect the results of subsequent Error and Uncertainty Analyses. The Peak Matching (PM) method is shown to provide better alignments than the Interval Correlation (IC) method in the majority of test cases. The PM method is also shown to be computationally faster than the IC method. Much of this work on curve alignment has already been published in [24].

3.2 The Feature Selective Validation Method

The Feature Selective Validation (FSV) method was developed as a tool for validating Computational Electromagnetic (CEM) models [67]. One step in validating CEM models involves comparing the results of CEM simulations with results obtained by laboratory experiments. The FSV method provides a way of comparing output curves produced by a CEM simulation with similar curves produced by physical measurement. If the comparison determines that the curves are in good agreement then support is provided for the validity of the CEM model. Often an experimenter will compare two curves visually, using their experience and knowledge to determine how similar the two curves are [68]. These visual comparisons may not be consistent; different experimenters may come to different conclusions about the similarity of the curves. The FSV method attempts to provide a consistent way of comparing two curves in a nonsubjective way.

The FSV method is outlined in detail in [68]. Comparisons provided by the method have been validated against comparisons given by approximately 50 EMC engineers from several countries [69]. More recently, improvements have been made to the FSV method [70]. In the next section details of the FSV method are given, following the work in [68] and [70].

3.2.1 Details of the Feature Selective Validation Method

The FSV method was developed using evidence from the psychology of visual perception [68]. This evidence suggests that when individuals study pictures, their eyes are drawn to the areas of high "feature density" [68]. When asked different questions about the picture, the individual's eyes move to different parts of the picture [68]. This knowledge can be used to help determine how people compare curves. Curves are made up of individual features that are ordered and spaced in a particular way [68]. An engineer comparing two curves will be drawn to the individual features of the two curves. Whilst comparing the curves the engineer will ask themselves questions such as "How similar are the amplitudes of the curves?" and "Do the features of the curves align?" [68]. This will draw the engineer's attention to different parts of the curves.

Using these concepts it was suggested that a useful way to compare curves would be to determine the differences in the overall amplitudes of the curves seperately from the differences in the "high frequency" features of the curves [68]. This is done by separating the original curves, under comparison, into their low frequency and high frequency components. The low frequency components represent the overall amplitude of each curve, whilst the high frequency components represent the features of each curve. These components are used to determine an Amplitude Difference Measure (ADM) and a Feature Difference Measure (FDM), for the two curves being compared. These difference measures are then combined to give an overall Global Difference Measure (GDM) [68]. The ADM has more recently been modified to include an Offset Difference Measure (ODM). The ODM represents the "dc offset" of the two curves; including this measure improves the performance of the FSV method [70].

The difference measures are determined on a point by point basis, it may therefore be necessary to interpolate one of the curves so that the two curves are evaluated at the same points. If the curves are sufficiently sampled and the interpolation does not produce a curve that is significantly different from the original curve, then the interpolation will not affect the results [68]. Duffy noted that there are a number of weighting factors that are required to calculate the difference measures [68]. These weighting factors have been obtained by optimising the method, so that the results of the FSV comparisons are in agreement with the results obtained via visual interpretation [68].

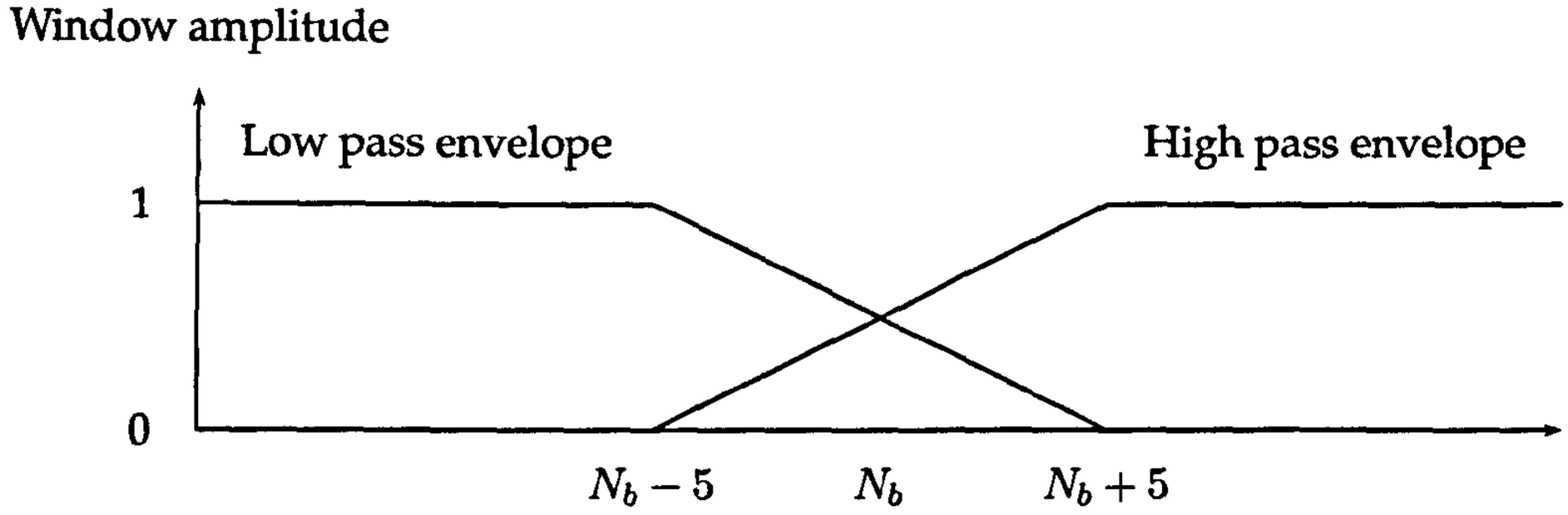

Figure 3.1: The low and high pass filters.

Implementing the Feature Selective Validation Method

The following procedure provides all the details needed to implement the FSV method: these details are as in [68] and [70]. The two curves will be referred to as datasets 1 and 2 in the following algorithm:

1. Read in the datasets 1 and 2 and interpolate, if necessary, over the same data points.

2. Fourier Transform both datasets. In this thesis a FFT is used to do this.

3. Obtain the "dc" datasets by taking the inverse Fourier transform of the first four points in the transformed datasets. These "dc" datasets are referred to as dc_1 and dc_2, corresponding to the original datasets 1 and 2.

4. Obtain the "low" datasets from the transformed data.

   (a) Sum the intensities of the remaining transformed datasets (from point 5 onwards), to produce the Total Intensity of each dataset.

   (b) Obtain a 40% cutoff point (for each dataset) by summing the intensities, again from point 5, until the total reaches 40% of the Total Intensity. The 40% cutoff point used in the FSV method is the lowest of the two cutoff points calculated for each dataset. A "break-point" five data points above the cutoff point is then found. This break point, referred to as point N_b here, provides a transition window between the low and high data regions. Duffy [68] notes that the 40% value was determined from sensitivity tests aimed to ensure that the FSV method was in agreement with visual comparisons.

   (c) Window the transformed datasets using a linearly decreasing envelope from point $N_b - 5$ to point $N_b + 5$ (as illustrated in Figure 3.1, taken from [68]). This essentially

low pass filters the transformed datasets.

(d) Inverse Fourier transform the windowed data to obtain the "low" datasets Lo_1 and Lo_2, corresponding to the original datasets 1 and 2.

5. Obtain the "high" datasets from the transformed data by first windowing the data using the high pass envelope (as illustrated in Figure 3.1), essentially high pass filtering the datasets. The "high" datasets are obtained by taking the inverse Fourier transform of the windowed data. The "high" datasets, corresponding to the original datasets 1 and 2, are referred to as Hi_1 and Hi_2 respectively.

6. Calculate the ODM on a point-by-point basis using

$$\mathrm{ODM}(i) = \mathrm{ODM}_i = \left|\frac{\chi}{\delta}\right| \exp\left\{\left|\frac{\chi}{\delta}\right|\right\} \tag{3.1}$$

where

$$\chi = |\mathrm{dc}_1(i)| - |\mathrm{dc}_2(i)| \tag{3.2}$$

$$\delta = \frac{1}{N}\sum_{n=1}^{N}(|\mathrm{dc}_1(n)| + |\mathrm{dc}_2(n)|) \tag{3.3}$$

i represents the ith data point and N is the total number of data points. The point-by-point representation of the ODM is represented by ODM_i here.

7. Calculate the ADM on a point-by-point basis using

$$\mathrm{ADM}(i) = \mathrm{ADM}_i = \left|\frac{\alpha}{\beta}\right| + \mathrm{ODM}_i \tag{3.4}$$

where

$$\alpha = |\mathrm{Lo}_1(i)| - |\mathrm{Lo}_2(i)| \tag{3.5}$$

$$\text{and} \quad \beta = \frac{1}{N}\sum_{n=1}^{N}(|\mathrm{Lo}_1(n)| + |\mathrm{Lo}_2(n)|). \tag{3.6}$$

Again i represents the ith data point and the point-by-point representation of the ADM is represented by ADM_i here.

8. Calculate the mean value of ADM, to give an overall difference measure, using

$$\mathrm{ADM} = \frac{\sum_{i=1}^{N}\mathrm{ADM}_i}{N}. \tag{3.7}$$

FSV value (e.g. ADM_i)	FSV interpretation
$ADM_i \leq 0.1$	Excellent
$0.1 \leq ADM_i < 0.2$	Very good
$0.2 \leq ADM_i < 0.4$	Good
$0.4 \leq ADM_i < 0.8$	Fair
$0.8 \leq ADM_i < 1.6$	Poor
$1.6 \leq ADM_i$	Very poor

Table 3.1: FSV Interpretation Scale.

9. Calculate the ADM histogram. The values of the ADM, FDM and GDM can be divided into six groups each with an associated language descriptor: *excellent*, *very good*, *good*, *fair*, *poor* and *very poor*. The histogram is formed by determining the proportion of points that have ADM_i values that belong to each of the six groups. Table 3.1 shows the six groups that the ADM_i (or FDM_i or GDM_i) belong to, and the qualitative description for each group. This table was originally published in [68].

10. Calculate the derivatives required to form the FDM. These derivatives accentuate the high rate of change features in the original curves [68]. The first derivatives of the Lo and Hi datasets are formed using a central difference scheme as

$$\mathrm{Lo}'(i) = \mathrm{Lo}(i + N_d) - \mathrm{Lo}(i - N_d) \tag{3.8}$$

$$\text{and} \quad \mathrm{Hi}'(i) = \mathrm{Hi}(i + N_d) - \mathrm{Hi}(i - N_d) \tag{3.9}$$

$$\tag{3.10}$$

where $N_d = 2$ here. The second derivatives of the Hi datasets are also required to form the FDM, these are calculated as

$$\mathrm{Hi}''(i) = \mathrm{Hi}'(i + N_d) - \mathrm{Hi}'(i - N_d) \tag{3.11}$$

where $N_d = 3$ here.

11. Calculate FDM_i, the point-by-point value for the FDM. The FDM_i are formed from three components: FDM1(i), FDM2(i) and FDM3(i). These three components are cal-

FSV Value (X)	Visual Scale Value V	Qualitative Descriptor
$X \leq 0.1$	$V = 1 + 10X$	Excellent
$0.1 < X \leq 0.2$	$V = 2 + 10(X - 0.099)$	Very good
$0.2 < X \leq 0.4$	$V = 3 + 5(X - 0.199)$	Good
$0.4 < X \leq 0.8$	$V = 4 + 2.5(X - 0.399)$	Fair
$0.8 < X \leq 1.6$	$V = 5 + 1.25(X - 0.799)$	Poor
$1.6 < X$	$V = 6$	Very poor

Table 3.2: Rule base for the conversion of FSV values to a visual scale [68].

culated using the derivatives calculated in step 10 as

$$\mathrm{FDM1}(i) = \frac{|\mathrm{Lo}_1'(i)| - |\mathrm{Lo}_2'(i)|}{\frac{2}{N}\sum_{n=1}^{N}(|\mathrm{Lo}_1'(n)| + |\mathrm{Lo}_2'(n)|)} \tag{3.12}$$

$$\mathrm{FDM2}(i) = \frac{|\mathrm{Hi}_1'(i)| - |\mathrm{Hi}_2'(i)|}{\frac{6}{N}\sum_{n=1}^{N}(|\mathrm{Hi}_1'(n)| + |\mathrm{Hi}_2'(n)|)} \tag{3.13}$$

$$\mathrm{FDM3}(i) = \frac{|\mathrm{Hi}_1''(i)| - |\mathrm{Hi}_2''(i)|}{\frac{7.2}{N}\sum_{n=1}^{N}(|\mathrm{Hi}_1''(n)| + |\mathrm{Hi}_2''(n)|)}. \tag{3.14}$$

The FDM_i is then obtained using

$$\mathrm{FDM}(i) = \mathrm{FDM}_i = 2|\mathrm{FDM1}(i) + \mathrm{FDM2}(i) + \mathrm{FDM3}(i)|. \tag{3.15}$$

12. Calculate the mean value of FDM in the same way as for the ADM.

13. Calculate the FDM histogram in the same way as for the ADM.

14. Calculate GDM_i, the point-by-point GDM as

$$\mathrm{GDM}_i = \sqrt{\mathrm{ADM}_i^2 + \mathrm{FDM}_i^2}. \tag{3.16}$$

15. Calculate the mean value of the GDM and the GDM histogram in the same way as for the ADM and FDM.

16. Convert the ADM, FDM and GDM mean values to the visual scale, with values from 1-6 (1 corresponding to an "excellent" match and 6 to a "very poor" match). This scale is useful as it gives the qualitative description for the comparison, and the degree to which the comparison belongs to this group descriptive. For example a comparison may be determined to be "fair", and using the visual scale it may be determined that the comparison is closer to being "good" than "poor". Table 3.2 shows the conversion of the ADM, FDM or GDM value (represented by X) to the visual scale value V.

This ends the algorithm for the FSV method. In the next section some results of FSV comparisons will be given to show the strengths and weaknesses of the method. Following this an improvement to the FSV method is proposed.

3.2.2 Results of Feature Selective Validation Comparisons

Figure 3.2 shows two datasets that shall be compared using the FSV method. These datasets are taken from [69]. Visually it looks like these two curves are fairly similar, especially at lower frequencies. At higher frequencies the curves become less similar. Figure 3.3 shows the point-by-point GDM values for the two curves, calculated using the FSV method. This figure agrees qualitatively with our visual comparison of the curves showing that at lower frequencies the GDM takes on lower values, implying that the curves are good matches in this region. The GDM values are much larger at the higher frequencies, which implies that the two curves are not similar in this region.

The histogram in Figure 3.4 shows the proportion of points that belong to the six individual qualitative groups. The majority of the points lie in the "good" and "fair" group. This agrees with the visual comparisons collected by 50 engineers [70]. In fact the 50 engineers concluded that the two curves, in this case, were slightly more similar than the comparison determined by the FSV method. The FSV gave a mean GDM value on the visual scale of

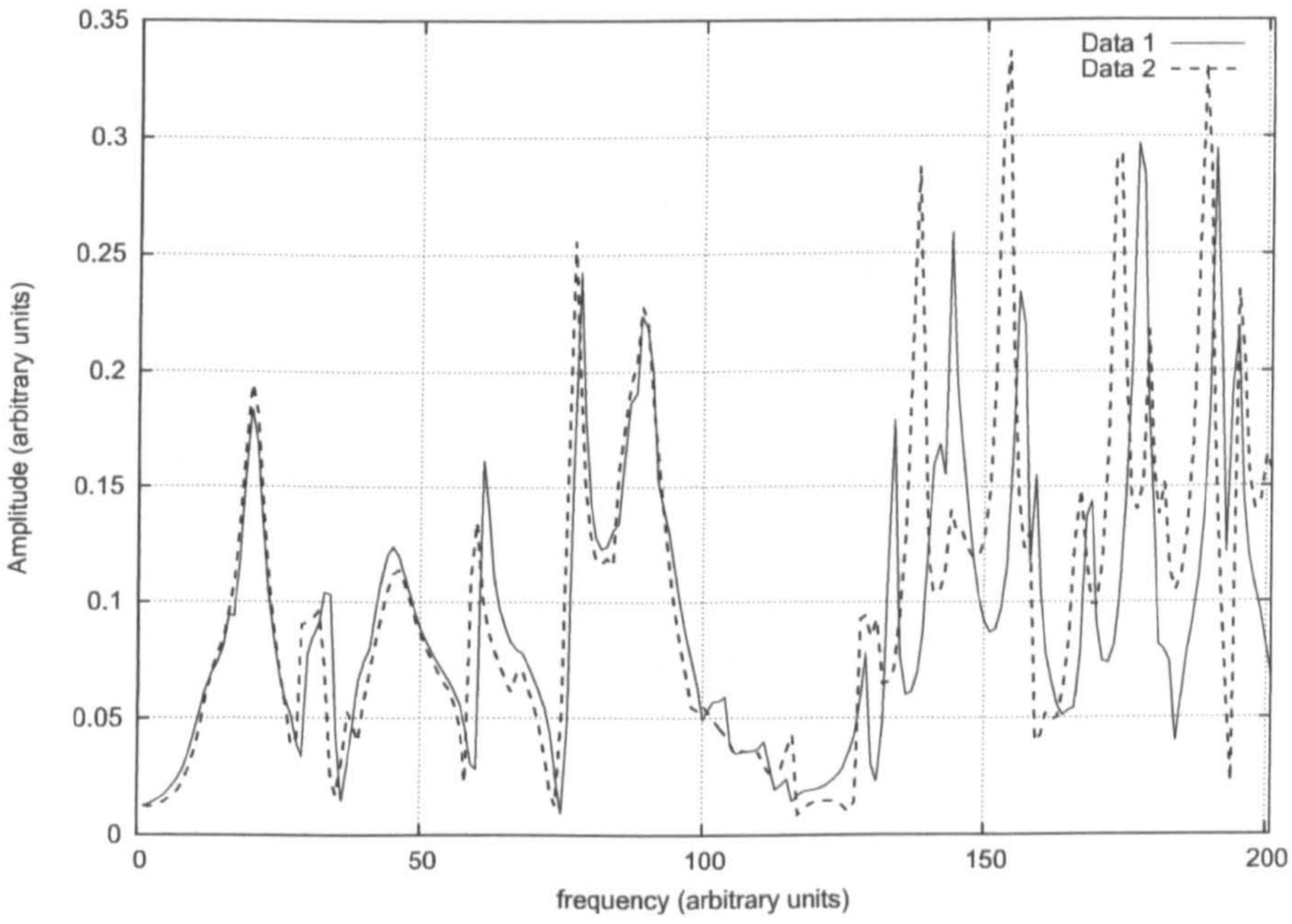

Figure 3.2: Datasets 1 and 2.

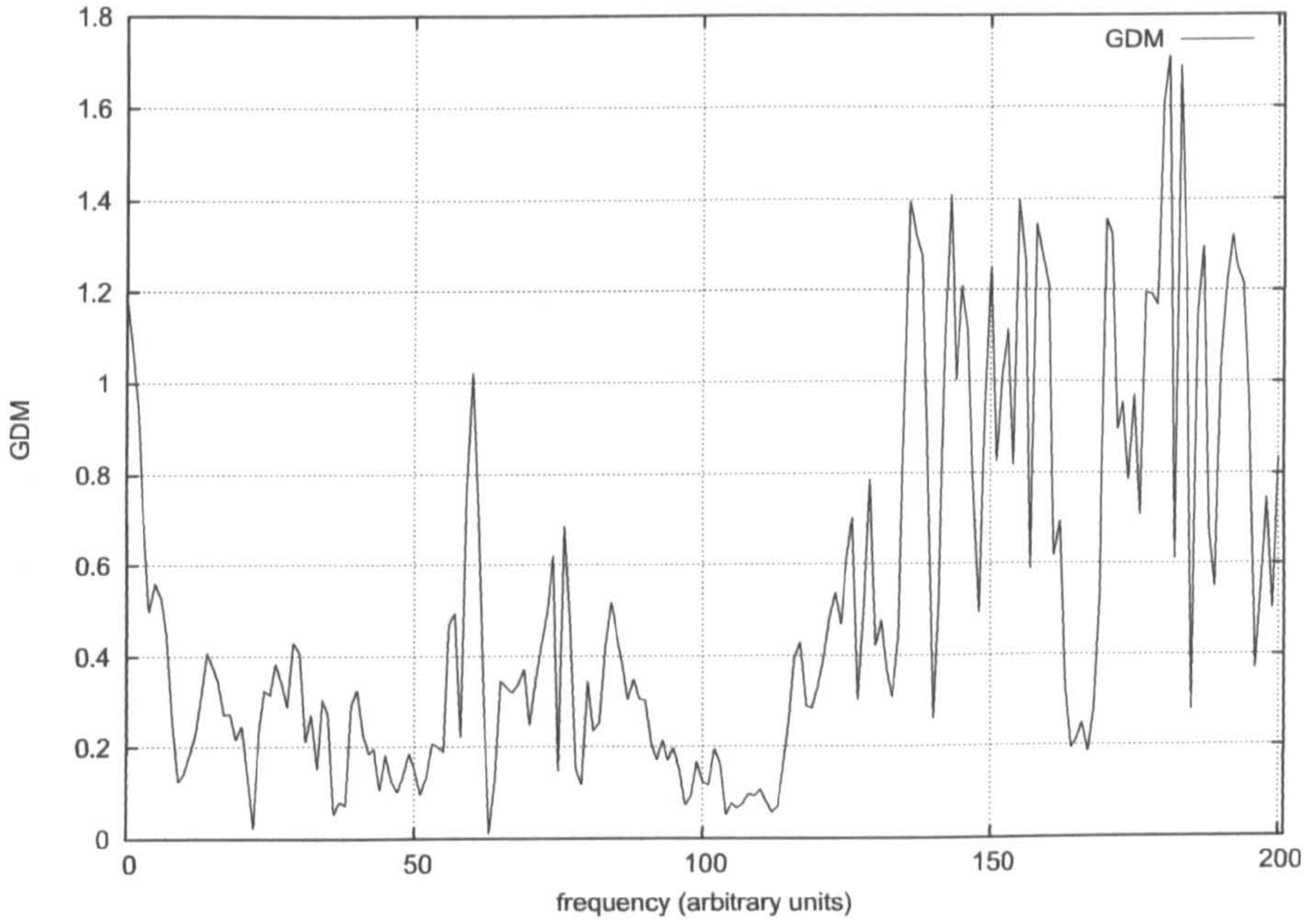

Figure 3.3: GDM_i for the comparison of datasets 1 and 2 on a point-by-point basis.

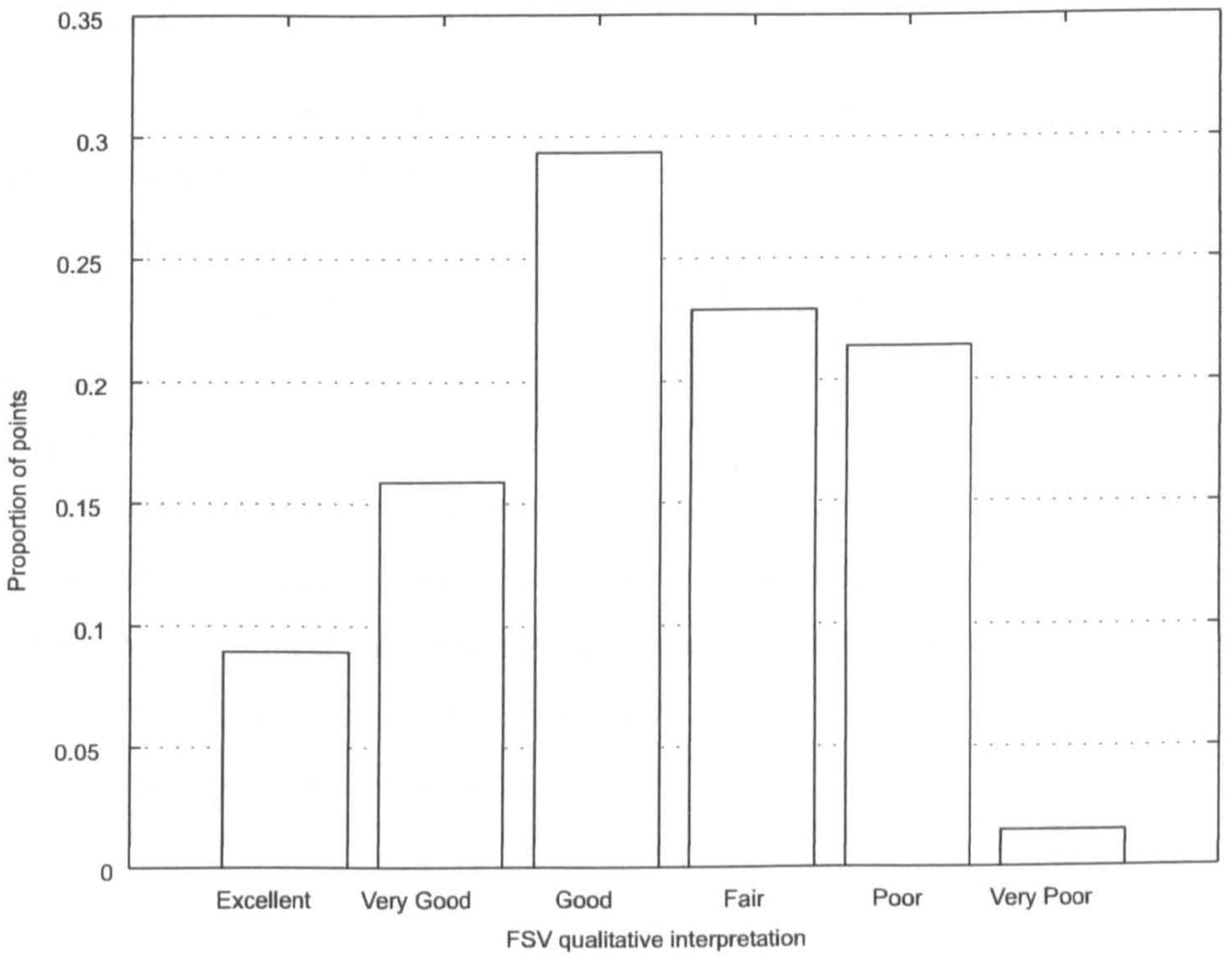

Figure 3.4: GDM histogram for the comparison of datasets 1 and 2.

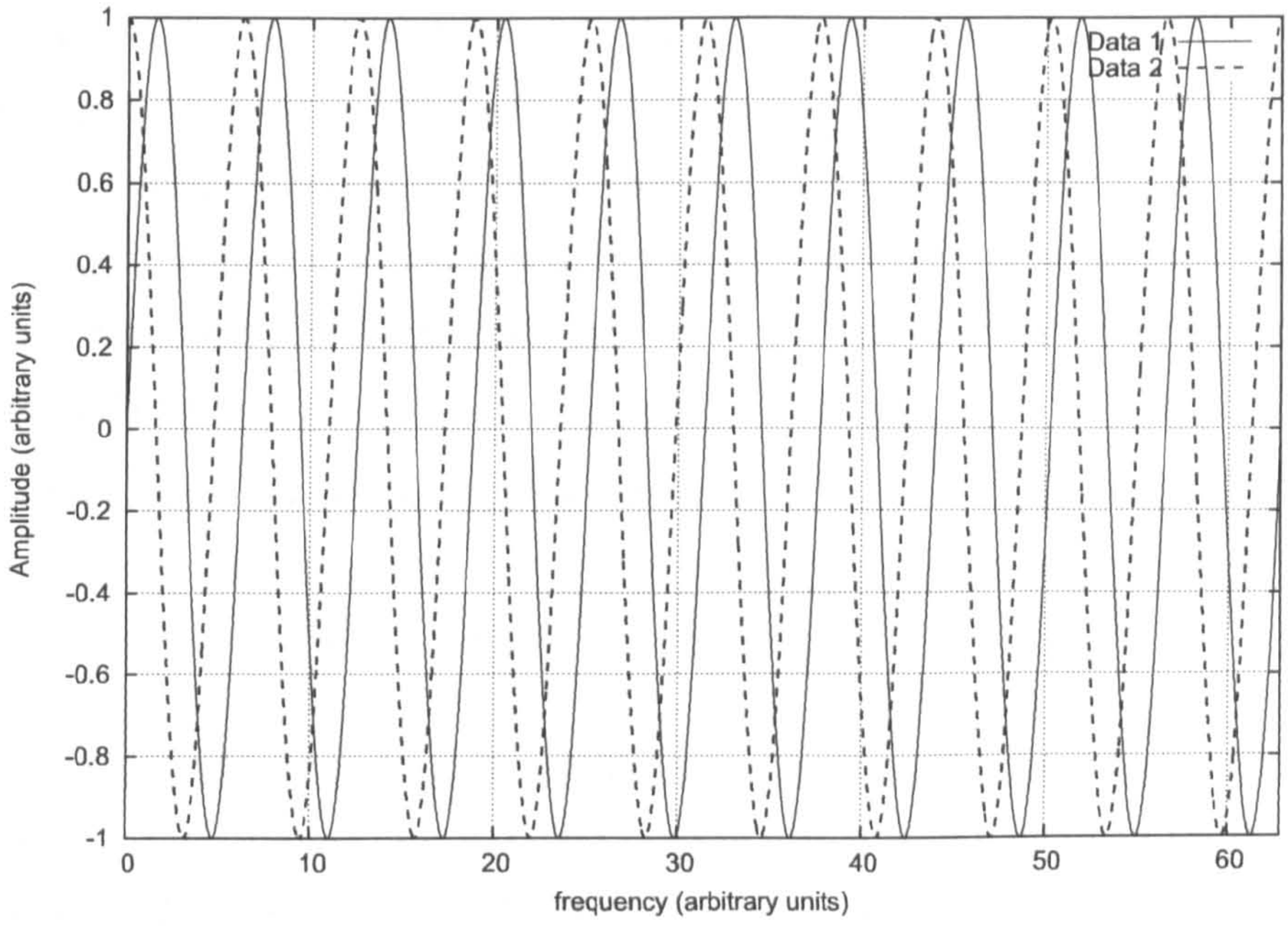

Figure 3.5: The sin and cosine functions.

4.2847, which implies that the curves are a "fair" match, and are closer to being a "good" match than a "poor" match.

The datasets in Figure 3.2 are fairly well aligned. When curves are not aligned, it may be argued that the FSV method does not provide a comprehensive comparison of the two curves. The two curves in Figure 3.5 are the sine and cosine functions. These two curves are exactly the same, apart from being shifted in the frequency domain by a constant phase shift of $\pi/2$. Comparing these two curves using the FSV method results in a GDM of six, implying that the curves are a "very poor" match. However, it is clear that these two curves share more similarities than is determined by the FSV comparison. The FSV method may be improved by first aligning the two curves under comparison. The frequency shifts $F(i)$ (at each point i) required to align the two curves can be used to form a frequency (or x-domain) Difference Measure (XDM). This XDM can be calculated on a point-by-point basis in a similar manner as for the ADM:

$$\mathrm{XDM}_i = \frac{|F(i)|}{\frac{1}{N}\sum_{n=1}^{N}(|f_1(n)| + |f_2(n)|)} \tag{3.17}$$

where $f_1(n)$ and $f_2(n)$ are the frequencies of the two respective curves at the point n. The FSV method may then be used in the same manner as before, but using the aligned curves. It is important that the curves are still analysed over their shared domain, for the sine and cosine curves some of the domain will be lost in aligning the curves (assuming they are

originally fixed to the domain illustrated in Figure 3.5, and not continuous over an infinite domain as is actually the case). If the curves are aligned properly then the ADM and FDM should reduce, because a proportion of the amplitude and feature differences will appear in the XDM instead. Using curve alignment in this way provides more information as to the differences between the curves; determining whether the differences are amplitude, feature or frequency differences.

Under this new scheme the GDM is redefined as

$$\mathrm{GDM}_i = c\sqrt{\mathrm{ADM}_i^2 + \mathrm{FDM}_i^2 + \mathrm{XDM}_i^2}. \tag{3.18}$$

The coefficient c may be varied to allow better agreements with visual comparisons. If we take c to be one, then the new mean GDM (on the visual scale) obtained for the sine and cosine curves will be 1.250. This implies that the curves are an excellent comparison with a small shift in the x-domain. More work is needed to refine this new scheme; work which is beyond the scope of this research project and is left for future work. For the purposes of the comparisons in this thesis the original FSV method is used. The next section briefly outlines where the FSV method will be used in this thesis.

3.2.3 Using the Feature Selective Validation Method

There are three main ways that the FSV method is used in this thesis. Firstly it is used to test the performance of different Error and Uncertainty Analysis methods. The results of different analyses are compared with benchmark results. If the results of the different analyses are similar to the benchmark results then it may be concluded that the analyses are providing accurate results.

Secondly the FSV method is used, in a novel way, to determine when FDTD simulations undergoing progressive mesh refinements form a converged solution. It is well known that FDTD simulations are more accurate when performed on finer meshes. To obtain good accuracy of FDTD simulations whilst minimising the computational expense of the method, the FDTD simulations are often performed on progressively refined meshes. The meshes may be refined by a factor two, so that the number of cells in each axis and the number of time steps is doubled and the cell size and the time steps are halved in size. If the results of an FDTD simulation do not differ by much before and after a refinement then it is concluded that convergence has been reached. In EMC the results of interest are often frequency

domain curves. In this thesis the FSV method is used to compare the results of the FDTD simulations obtained before and after each refinement. If the FSV method determines that the results are good matches then it may be concluded that the FDTD simulations have converged for that mesh refinement. The FSV method has never before been used in this way to test for convergence.

In general, convergence is tested by performing a subjective visual comparison of the curves formed after successive refinements. Testing for convergence in this way is less reliable than using the FSV method because different experimenters may disagree on the extent to which the curves match. Other more standard methods of testing for convergence involve determining when the difference between the curves has decreased to a certain value. It may be argued that using the FSV provides a more rigorous assessment of the overall comparison of the output curves.

The FSV method is also used in this thesis to test the convergence of MCM simulations. The MCM will be discussed in more detail later, a brief description is given here. In this thesis the MCM is used to estimate the uncertainty in a simulation by performing many simulations with different input parameters. The outputs of these many simulations (also curves in the frequency domain) are used to form the mean and standard deviation of the output. The uncertainty in the outputs is the standard deviation of the different output curves, formed on a point-by-point basis. In this thesis the mean and uncertainty in the simulations are both frequency domain curves. The accuracy of the MCM increases with the number of simulations that are used to construct the mean and uncertainty. After many simulations have been performed the MCM will reach convergence. At convergence the mean and uncertainty curves will not change significantly even if more simulations are performed. The FSV method is used in this thesis to compare the mean and uncertainty curves produced after N simulations with the same curves produced after $N+50$ simulations. If the curves are determined to be excellent matches then it may be concluded that the curves have not changed much even after 50 extra simulations were performed, and therefore convergence has been reached. The FSV method has never before been used to test for convergence in this way. The benefits of using the FSV method in this way is that the comparisons are consistent and nonsubjective. Since visual comparisons are not needed, the MCM simulations can be stopped automatically when it has been determined that convergence has been reached.

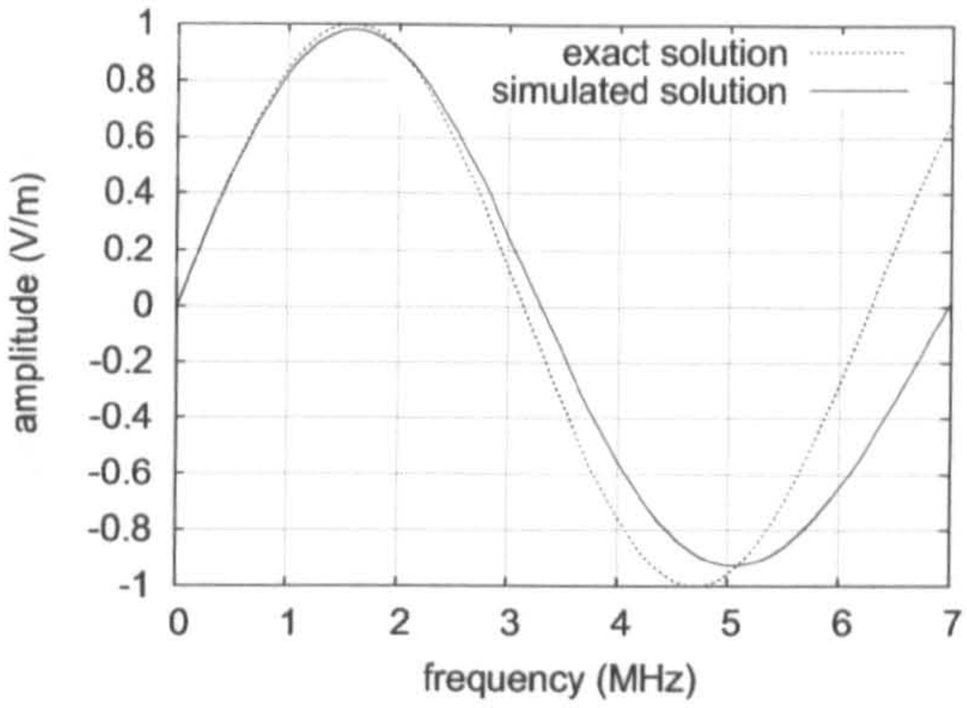

Figure 3.6: Unaligned exact solution and simulated solution.

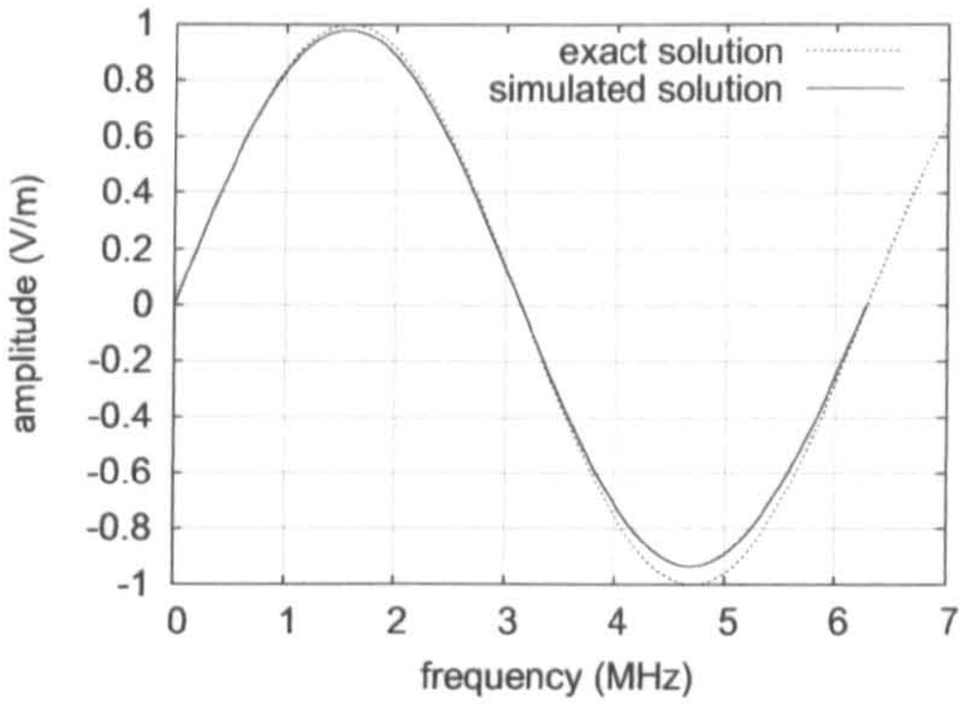

Figure 3.7: Aligned exact solution and simulated solution.

3.3 Curve Alignment Methods

In Chapters 5-7 it is shown that curve alignments may be used to decompose the error and uncertainty in an output curve into the aligned amplitude error, aligned frequency error, and aligned amplitude and frequency uncertainties. This provides more information about the manner in which the errors and uncertainties, in an output curve, manifest themselves. For example an error in a simulation may manifest itself as a frequency shift in the output curve [71]. In this case the results of the simulation will have a frequency shift with respect to the exact solution: an example of this is shown in Figure 3.6. By taking the difference between the two curves in Figure 3.6 the unaligned amplitude error is obtained, which is shown in Figure 3.8. This error is an overestimation of the amplitude error, caused by the frequency shift between the curves. The overestimation can be reduced by first aligning the curves: the aligned curves are shown in Figure 3.7. The frequency shifts required to align the curves are the aligned frequency errors. Taking the difference between the aligned curves results in the aligned amplitude error. The aligned amplitude and frequency errors are shown in Figures 3.9 and 3.10 respectively. It is clear that for this example the error in the simulated solution is due to both an amplitude and frequency shift. The amplitude error formed before aligning the curves (Figure 3.8) is much bigger than the amplitude error after alignment (Figure 3.9). The overestimation of the unaligned amplitude error is greater at the higher frequencies, where there are greater frequency shifts (frequency errors). By aligning the curves it is possible to decompose the error in the simulated solution into the frequency and amplitude errors.

In the next three sections, three methods are introduced that can be used to align

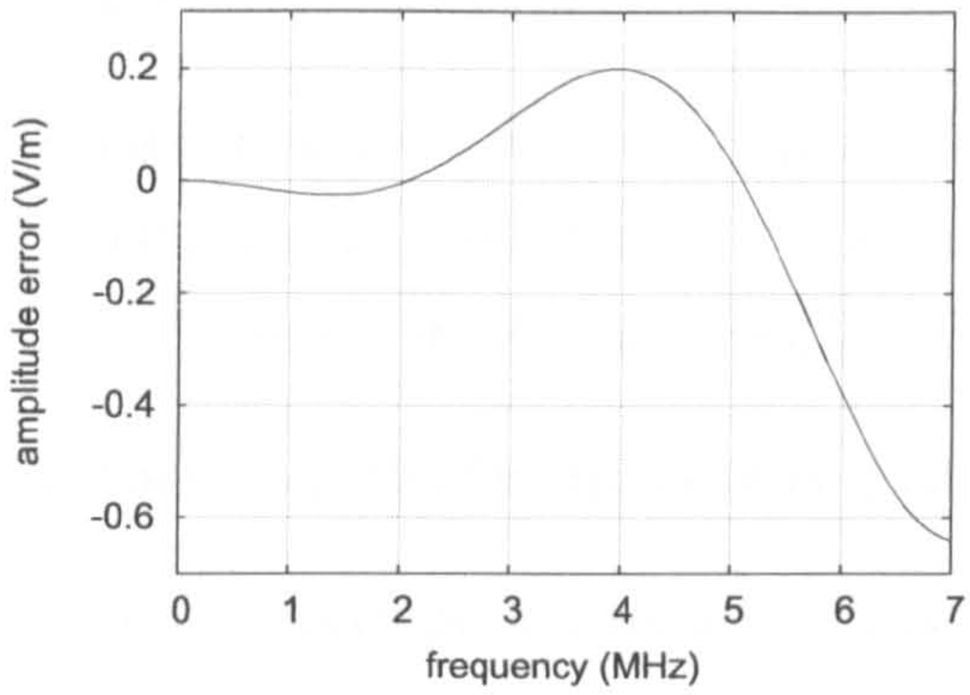

Figure 3.8: Frequency response of the unaligned amplitude error.

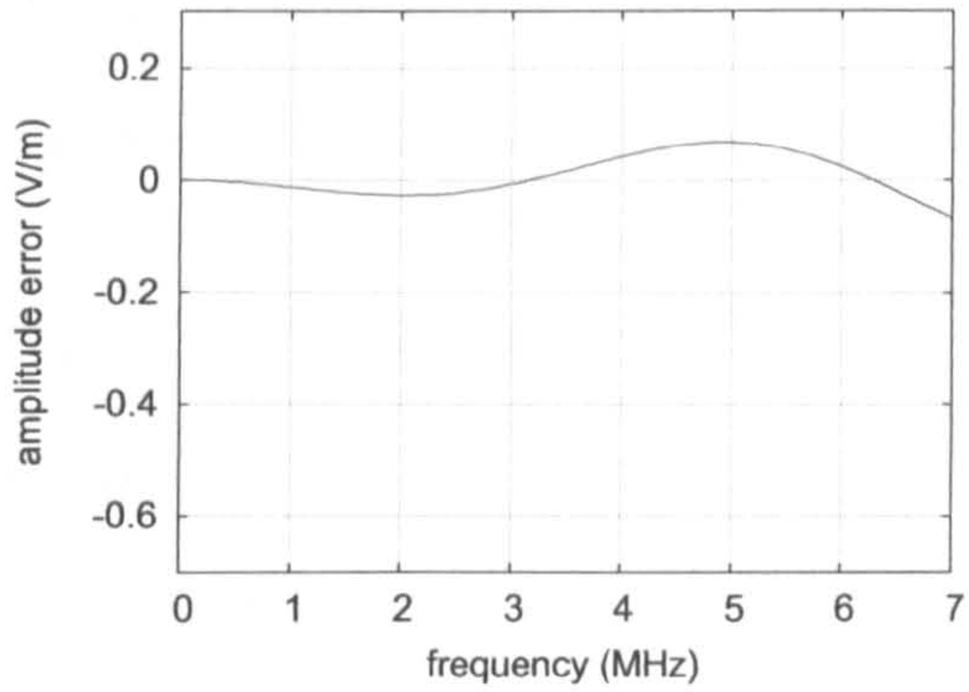

Figure 3.9: Frequency response of the aligned amplitude error.

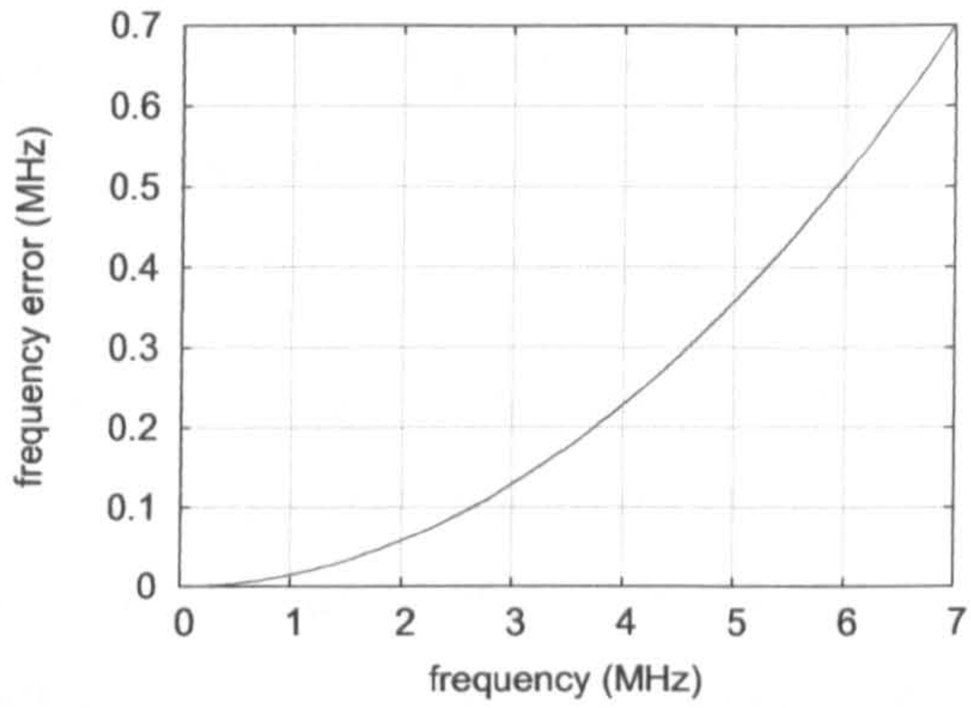

Figure 3.10: Frequency response of the aligned frequency error.

curves. The first two methods, Peak Matching (PM) and Interval Correlation (IC), are novel methods that have been previously published in the *Applied Computational Electromagnetic Society Conference 2007* [24]. In the discussion that follows, references will be made to a target curve being aligned to a reference curve. The reference curve may be chosen as the data set which is known to be more accurate, or it may be chosen arbitrarily. The objective assessment is the frequency shift between features in the curves.

3.3.1 Curve Alignment via Peak Matching

This method calculates the frequency shifts required to align two curves by linearly interpolating the frequency differences between the corresponding maxima and minima of the curves. In the following algorithm the maxima and minima of the curves are referred to as peaks with positive and negative sense respectively. The algorithm is as follows:

1. Find the maxima and minima of the curves by determining where the derivatives of

the curves change from a positive value to a negative value or vice-versa.

2. Find the characteristics of the peaks. These are the peak amplitude, frequency, Q value, left fall off and right fall off. The left and right fall off are the number of points between the peak and the neighbouring left and right peak of opposite sense.

3. For each peak (denoted as peak j) on the first curve:
   (a) For each peak (denoted as peak k) on the second curve:
      i. Determine how many peak characteristics the two selected peaks are most similar on. This number represents a score for the two peaks, so a score of three may mean that peak j and peak k are the closest in amplitude, Q-factor and left fall off, but not frequency or right fall off. The maximum possible score for two peaks is five.
      ii. Assign this score to the (j, k)'th element of a score matrix.

4. Loop through the score matrix and match any pair of peaks that have a score of five, and remove them from the data set. Before matching ensure that the peaks are close enough in frequency. For the curves aligned in this thesis, peaks are matched if they are less than five percent of the total frequency range apart.

5. Repeat step 4 for peaks with a score of four, and then for peaks with a score of three.

6. Whilst there are still peaks in the data set that can be matched, repeat steps 3, 4 and 5 using these remaining peaks.

7. For each pair of matched peaks calculate the frequency difference between the peaks, referencing it as the frequency difference occurring at the frequency of the peak on the target curve.

8. Use this data to linearly interpolate frequency shifts all along the target curve.

9. Shift the target curve by the interpolated amounts to align it with the reference curve.

It is possible to sort through the peaks (after step 1) removing the peaks that are due to noise. This can be done by removing peaks that are less than a certain distance away from neighbouring peaks of opposite sense and/or peaks that are less than a certain height. The PM method used in this thesis does not attempt to remove peaks that are due to noise.

After the target curve is shifted, a cubic spline of this curve may be required to ensure that it is being evaluated at the same frequency points as the reference curve. If the target curve is shifted so that its endpoint is at a lower value than the endpoint of the reference curve, then the cubic spline will produce errors after this endpoint. The aligned curves must therefore be cropped at the points preceding these errors.

Once the curves are aligned, the aligned amplitude difference can be calculated at each frequency. The frequency shifts required to align the two curves provide the frequency differences between the curves. In cases where the target curve needs to be shifted by a significant amount, the PM method may not exactly align the curves in the first instance. However, by repeatedly applying the PM method to the aligned curves, an even better alignment may be achieved. It is important to test whether the repeated application of the PM results in a better alignment. This test is carried out by calculating the absolute amplitude difference between the curves before and after each application of the PM method. If the amplitude difference is lower after alignment it is assumed that the application of the PM method has provided a better alignment of the curves. Otherwise, the PM method has not provided a better alignment and the curves fed into the PM method are chosen as the final aligned curves.

3.3.2 Curve Alignment via Interval Correlation

The second method of aligning curves is based on the use of cross correlation to align curve segments. Some of the numbers in the following algorithm are quite specific, they were obtained by optimising the performance of the method through a number of trials. The algorithm is as follows:

1. For numbers of intervals N ranging from 9 to 12.

   (a) Split the curves into N intervals, each with an equal number of points.

   (b) For linear stretching factors α from 0.9 to 1.11 (incrementing by 0.01).

      i. Stretch the target curve in the frequency domain by the stretching factor α. Since the stretchings/compressions are linear, the first point on the target curve is not stretched at all whereas the last point is stretched by the maximum amount.

      ii. Obtain the correlation coefficient of the two curves, in the first interval.

(c) Find the stretching factor α_{max} which maximises the correlation coefficient between the target and reference curves, for the first interval.

(d) Stretch the target curve linearly in the frequency domain by α_{max}.

(e) Fix the points in the first interval and move onto the next interval.

(f) Repeat steps (b)-(e) for all intervals using the data beginning at the end of the last fixed interval, to the end of the data set.

(g) Store these two aligned curves

(h) Calculate the correlation coefficient of the aligned curves.

2. Find the number of intervals N_{max} that gave the maximum correlation coefficient of the curves after alignment.

3. The curves aligned using N_{max} intervals represent the final aligned curves.

This algorithm has been modified since its publication in [24]. The modification was introduced to determine whether the curves could be aligned further using the same method. After the curves are aligned, the correlation coefficient of the two curves is obtained. The whole alignment process is then repeated using these two aligned curves. After each alignment the correlation coefficient of the newly aligned curves is calculated. If this correlation coefficient is greater than the correlation coefficients of the two curves before alignment, then the alignment process is repeated again, otherwise the two curves before this last alignment are taken to be the final aligned curves. Performing multiple alignments in this way is computationally costly, the number of alignments has therefore been limited to ten to reduce the computational expense.

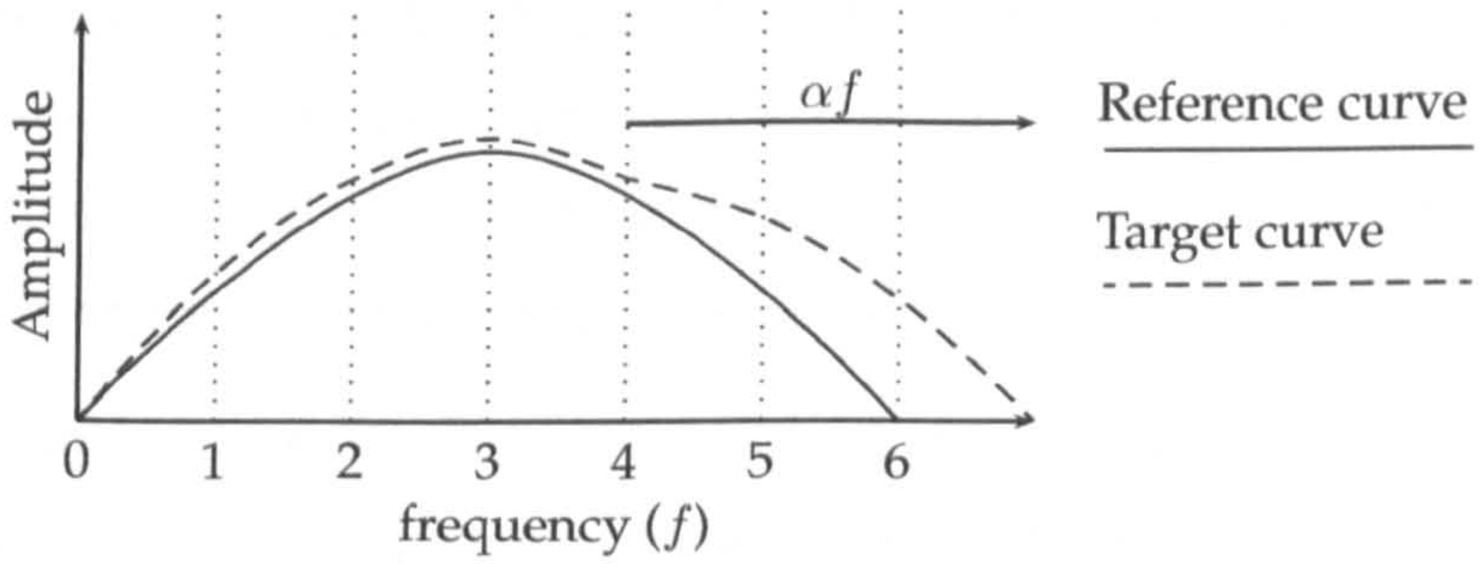

Figure 3.11: The Interval Correlation technique. The first four intervals have been realigned and fixed. The target curve is being stretched by a factor α to obtain the highest correlation for the fifth interval.

Figure 3.11 represents the alignment process for a simple example. The amount the curve has to be stretched provides information on the frequency difference at each fre-

quency. Once the curves are aligned a more accurate determination of the amplitude difference can be obtained.

This method relies on the range of the stretching factors α used. If two curves do not align well then more severe stretching factors are required. If the curves are allowed to stretch too far then an incorrect alignment may result. By performing a number of alignments using different stretching factors it was found that using stretching factors $0.9 \leq \alpha \leq 1.11$ gave optimal performance. The quality of the alignment is also dependent on the number of intervals used, so the alignment process is performed for different numbers of intervals (typically 9-12). Of these alignments, the alignment which gives the highest correlation between the two curves is used. The numbers of intervals that are used in the alignment process were chosen as they seemed to produce the best alignments, other intervals could also be looped through but this would add to the computational expense of the method.

3.3.3 Curve Alignment via Dynamic Time Warping

Dynamic Time Warping (DTW) is a very successful method, first used in speech recognition, to align waveforms in the time domain [72]. The DTW method involves finding a match between the points on two curves, which minimises the distance between the two curves. The end points of both curves are always matched in DTW [72]. One of the main limitations of DTW is that it does not cope well with the case where one curve has more features (maxima/minima) than the other [67].

The following algorithm describes how the DTW method works. This algorithm is based on two curves, one with n points and the other with m points.

1. For each point on one curve find the absolute difference between the amplitude of the point and the amplitude of all other points on the other curve. These differences form a matrix where the (i, j)'th element is the absolute difference between the amplitude at the i'th point on one curve and the amplitude at the j'th point on the other curve.

2. Starting at (1,1) form paths that will end up at (n, m). For each path construct a cumulative path value, called the path cost c, by cumulatively summing the absolute difference values of all the points in the path and dividing by the number of points in the path.

3. A path can only reach the point (i, j) in the matrix by stepping from the points $(i - 1, j - 1)$, $(i - 1, j)$ or $(i, j - 1)$.

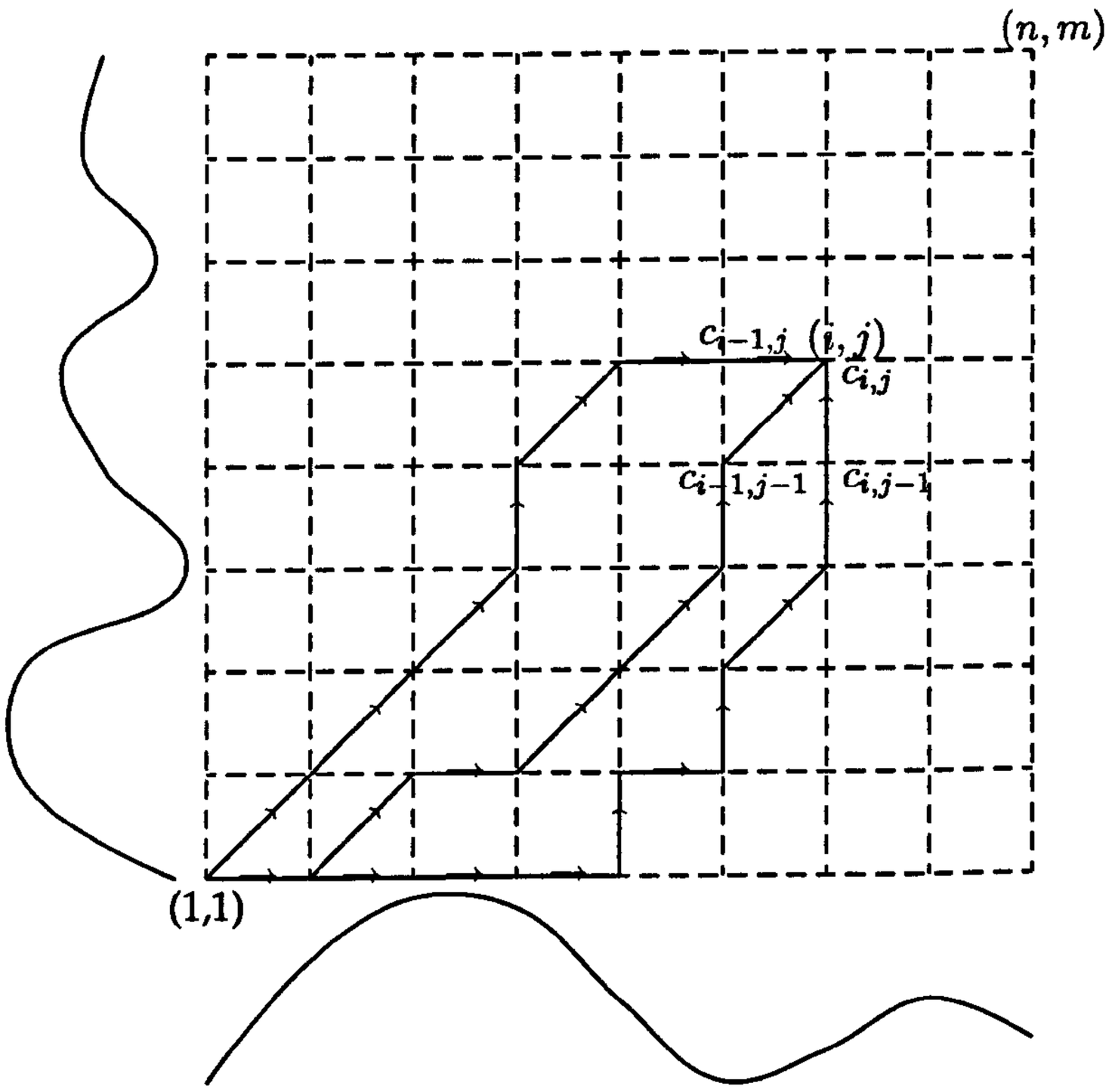

Figure 3.12: An example of the Dynamic Time Warping process applied to two curves. Here $c_{i,j}$ is the cumulative path cost for the path that passes through (i, j). The path that passes through (i, j) is the path that has the minimum path cost out of $c_{i-1,j}$, $c_{i,j-1}$ or $c_{i-1,j-1}$.

4. Minimise the differences between the points in the curves by picking the path with the smallest path value. So the path that involves the point (i, j) will be the path ending at $(i-1, j-1)$, $(i-1, j)$ or $(i, j-1)$, with the minimum path value and the point (i, j).

5. Using this method calculate the path that joins $(1, 1)$ and (n, m) with the minimum path value.

The frequency domain of the target curve is warped so that the points on the two curves match up according to the minimum path. The amount the target curve is shifted in frequency represents the frequency difference between the two curves. Once the target curve is aligned to the reference curve the aligned amplitude difference between the two curves may be calculated. Warping the axes of the target curve can cause violations of monotonicity, where a number of points are warped so that they occur at a single frequency. At these frequency points it is possible to replace the value of the curve on the y-axis with the mean

value of all the points that now occur at the single frequency. Processing the data in this way may cause the form of the target curve to change slightly, which would introduce errors into the results of subsequent error and uncertainty analyses.

3.3.4 Comparing the Performance of the Curve Alignment Methods

The three methods of curve alignment were applied to four sets of example curves that appear later in this thesis, and one set that is taken from an EMC validation example [24],[28]. These five sets of example curves are referred to as Case 1-Case 5 in the following discussion. To test the performance of the three alignment methods, three metrics are calculated before and after alignment. The first metric that is used is the GDM on the visual scale, calculated using the FSV method. If the GDM reduces after alignment then the curves are more similar after alignment, which provides support that the alignment process has worked. The second metric used is the correlation coefficient: the closer the correlation coefficient is to one, the better the alignment. Lastly the Average Absolute Amplitude Difference (AAAD) is calculated before and after alignment. This AAAD metric is defined as

$$\text{AAAD} = \frac{\sum_{i=1}^{n} |a_{2i} - a_{1i}|}{\sum_{i=1}^{n} |a_{1i}|} \tag{3.19}$$

where n is the number of points on the two curves, and a_{1i} and a_{2i} are the amplitudes of the reference and target curve respectively, at the i'th point. This AAAD gives us a measure of the amplitude difference between the curves before and after alignment. Curves that are aligned better should have a lower AAAD value in general. The three curve alignment methods are also compared in terms of the amount of computational time they take.

The results obtained using the curve alignment methods, when applied to the curves from Case 3, are shown in Figures 3.13-3.15. All three methods work well here to align the target curve to the reference curve. The DTW method may however be too severe, distorting the target curve through the alignment process. An example of one of these severe distortions is found at 750MHz in Figure 3.15; at this frequency the target curve is stretched to a horizontal line taking a constant value over the surrounding frequencies. Some of the information in the target curve will be lost through this distortion. The IC and PM alignments distort the curves less severely because the frequency shifts used to align the curves are smaller.

Figures 3.16-3.18 show the FSV comparisons, the correlation coefficients and the AAAD

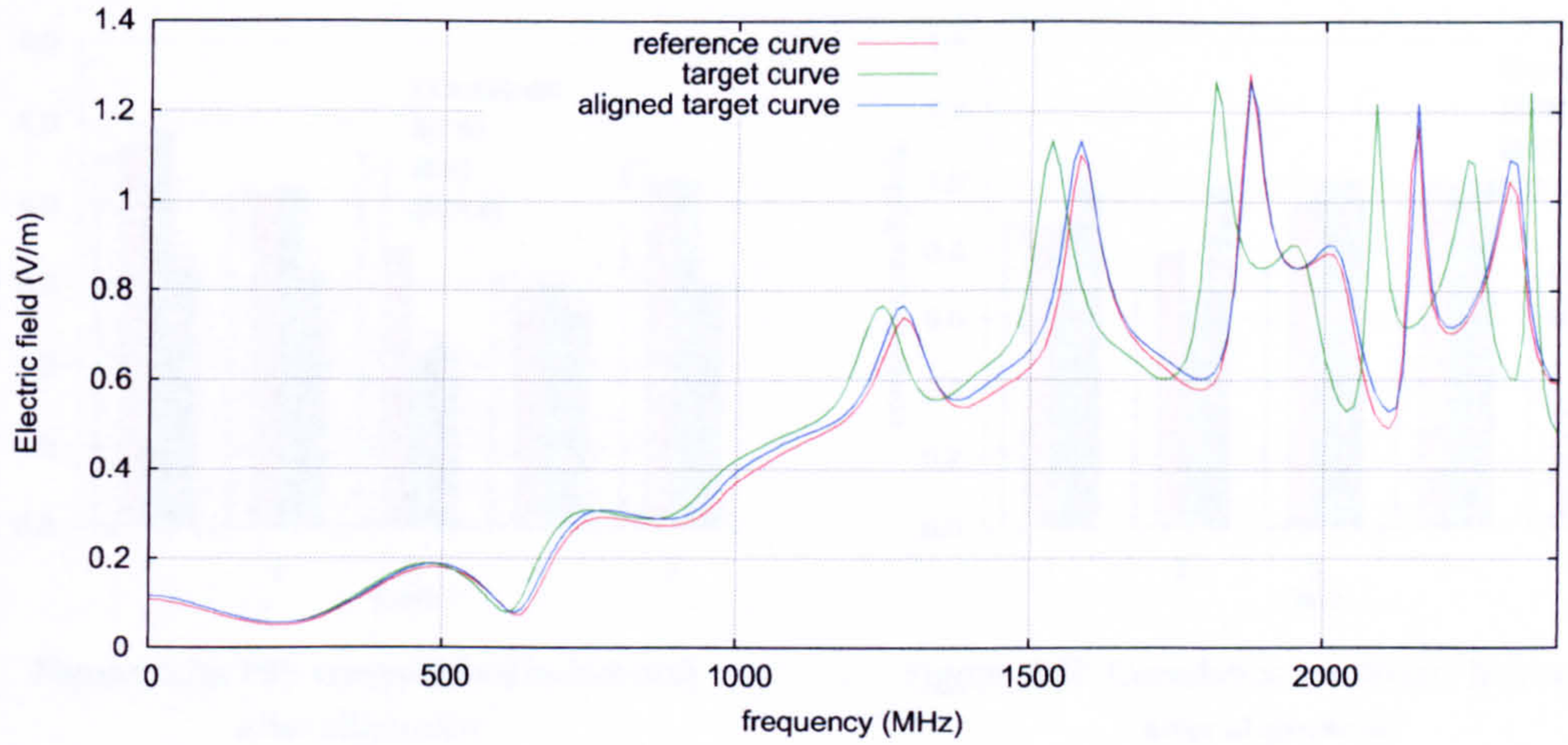

Figure 3.13: Case 3 curves aligned via the PM method.

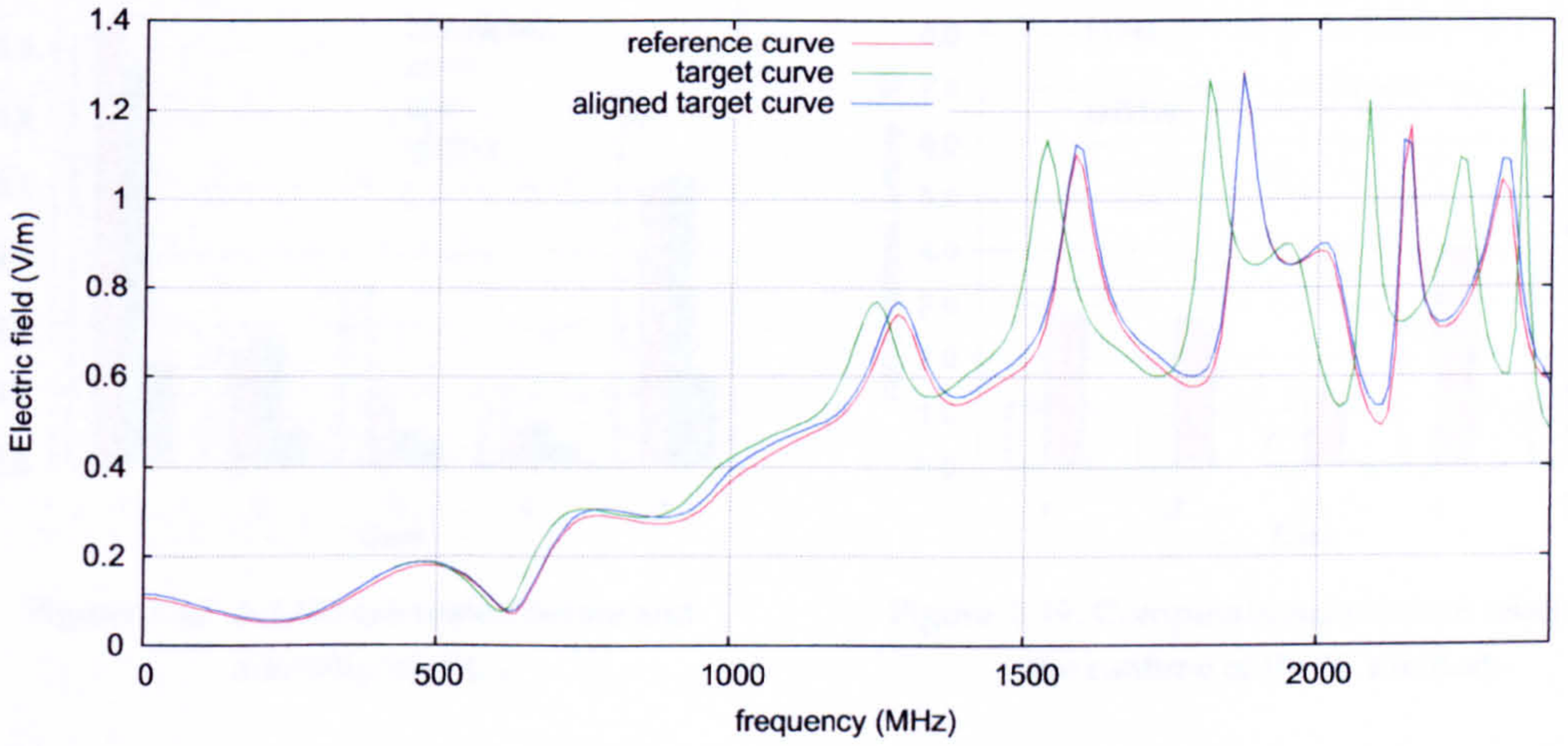

Figure 3.14: Case 3 curves aligned via the IC method.

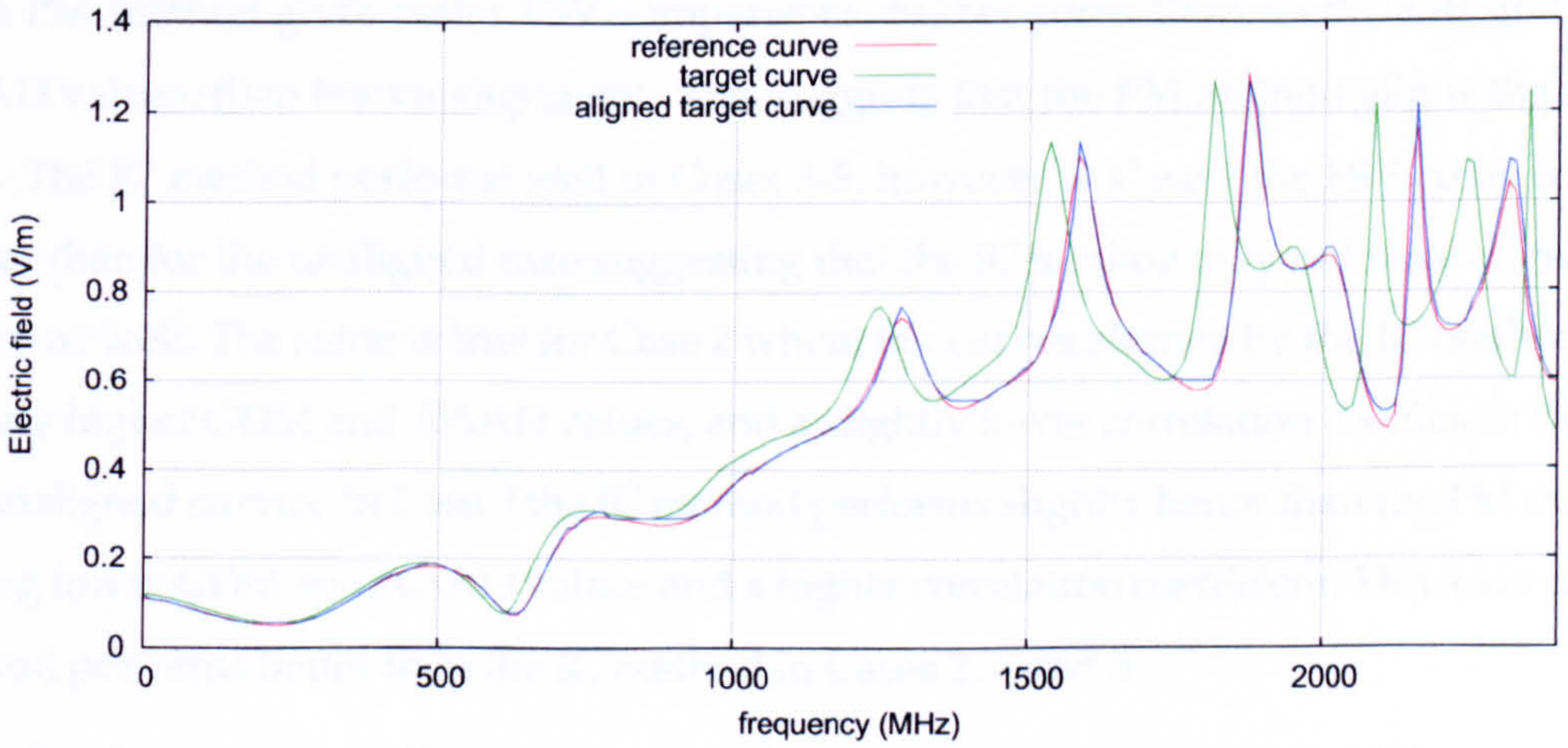

Figure 3.15: Case 3 curves aligned via the DTW method.

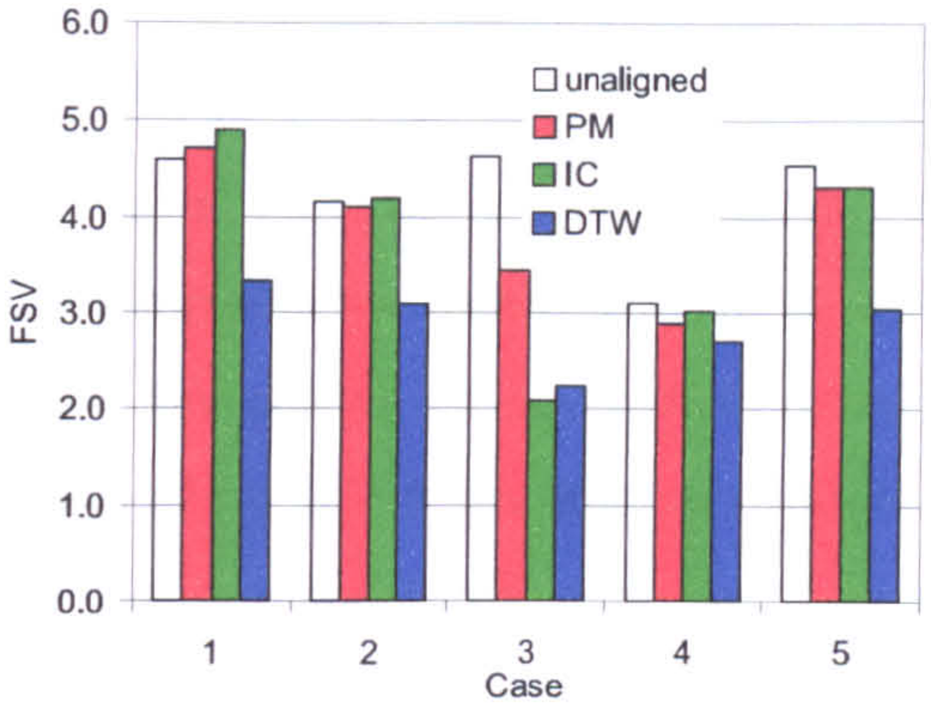

Figure 3.16: FSV comparisons before and after alignment.

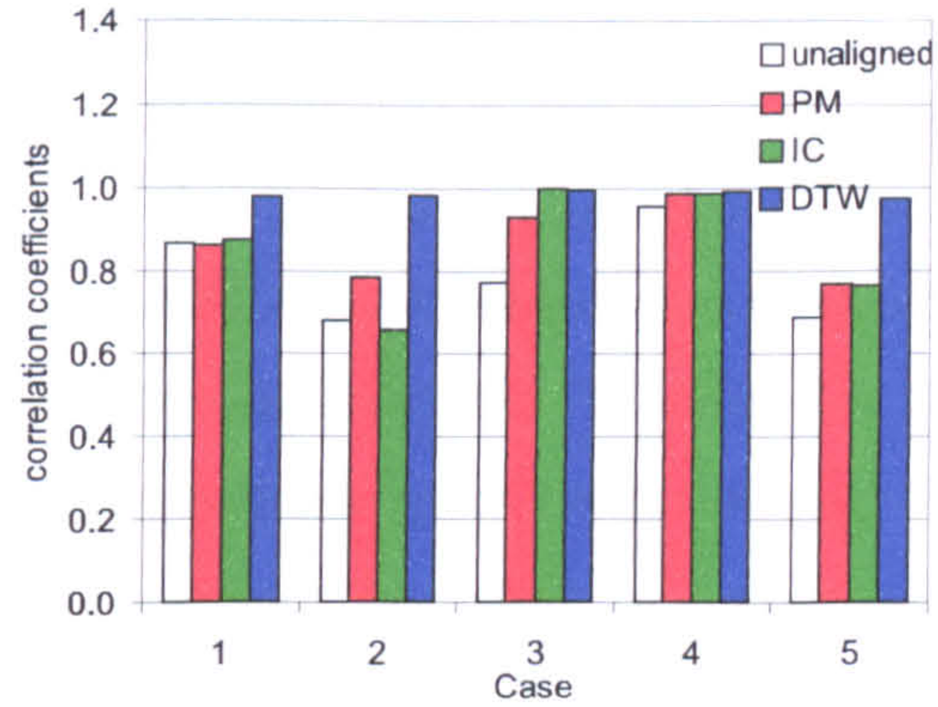

Figure 3.17: Correlation coefficient before and after alignment.

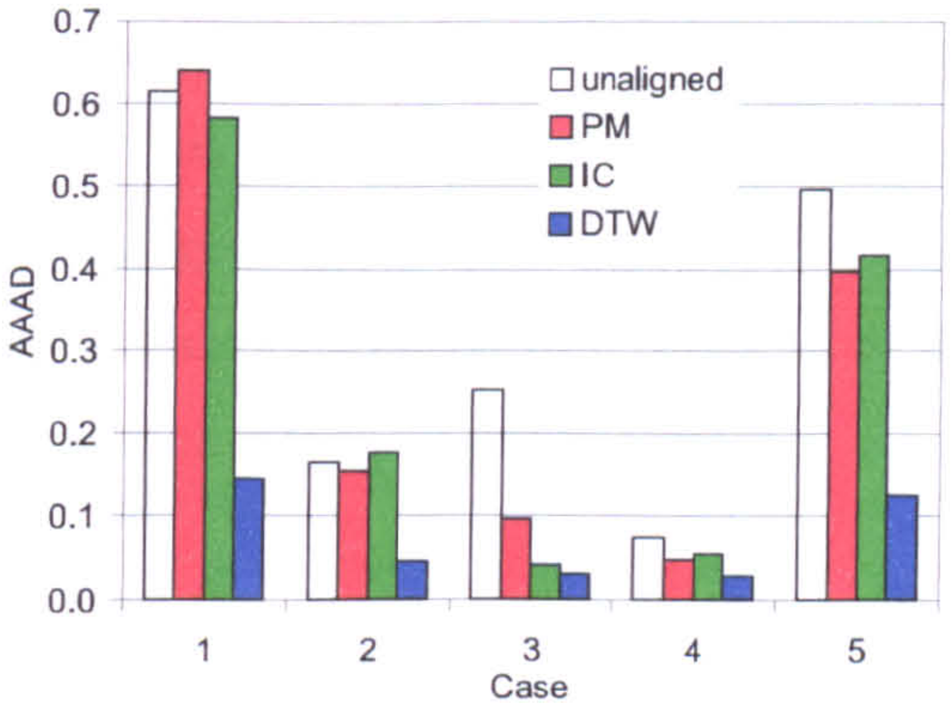

Figure 3.18: AAAD calculated before and after alignment.

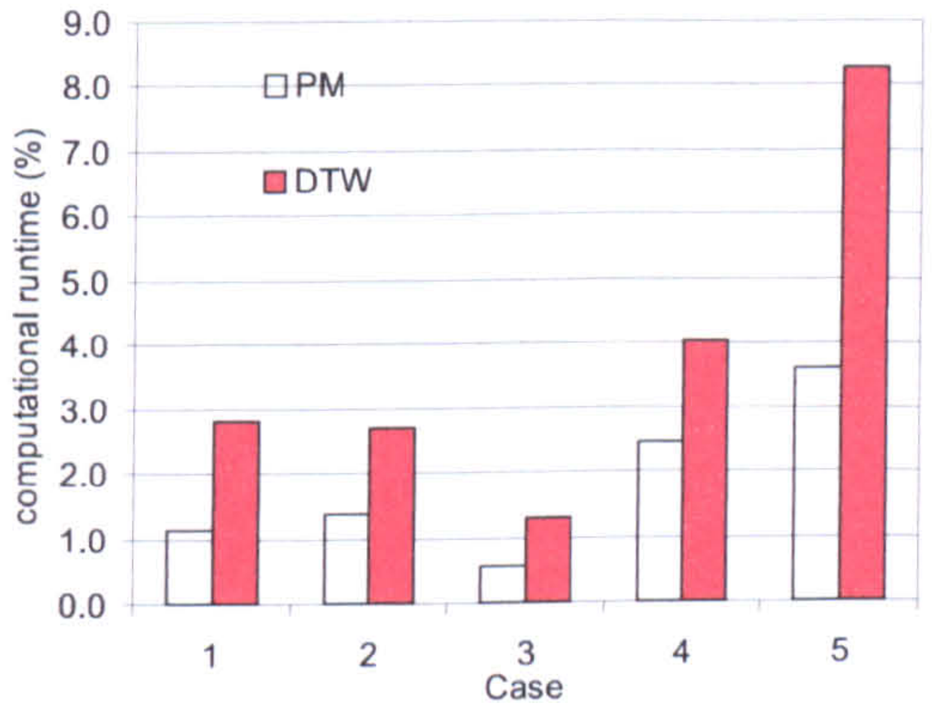

Figure 3.19: Computational runtime relative to the runtime of the IC method.

for the five test cases, before and after alignment with each method. In all cases except Case 1 the PM method gives better FSV comparisons, higher correlation coefficients and lower AAAD values, than before alignment. This suggests that the PM method aligns the curves well. The IC method performs well in Cases 3-5, however in Case 1 the FSV comparison is higher than for the unaligned case suggesting that the IC method may not have aligned the curves as well. The same is true for Case 2 where the curves aligned by the IC method have slightly higher GDM and AAAD values, and a slightly lower correlation coefficient than for the unaligned curves. In Case 3 the IC method performs slightly better than the PM method, having lower GDM and AAAD values and a higher correlation coefficient. However the PM method performs better than the IC method in Cases 2, 4 and 5.

In all five cases the DTW method produces very good alignments of the curves, however as discussed earlier and in [24] the DTW method can warp the curves severely. The

Error and Uncertainty Analyses performed on curves aligned via the DTW method suffer from this severe warping of the curves.

Figure 3.19 shows the computational runtime of the PM and DTW methods relative to the computational runtime of the IC method. It is clear that the PM method is the fastest method. For all five cases shown here the computational runtime of the PM method is less than 4% of the IC computational runtime. The PM method also gives better comparisons than the IC method in the majority of cases, and does not severely distort the curves as the DTW method does. Therefore in the majority of cases in this thesis the PM method will be used to align the curves. In Chapter 7 there is one case where the IC method provides a better alignment than the PM method; the IC method is used to align the curves in this case. As mentioned earlier in Case 1 both the PM and IC method fail to provide a better alignment of the curves, when tested using the three metrics. This may be the case for other curves that undergo alignment in this thesis. If the AAAD is larger after alignment than before alignment, for curves aligned in this thesis, then it is concluded that the alignment process has not worked well. In this case the original curves are used instead of the aligned curves in any subsequent analyses.

3.4 Discussion

The output of a CEM simulation is often a frequency response curve. In this chapter a number of numerical analyses have been introduced, which are useful when determining the errors and uncertainties in output curves.

The FSV method may be used to compare two curves in terms of their overall amplitude and feature differences. This method is used, in this thesis, to test for the convergence of the FDTD under increasing mesh refinements. The method is also used to test for the convergence of the MCM. This is a novel way of testing for convergence, it is useful because the comparisons are consistent and nonsubjective. The comparisons also provide a quantitative measure of the similarity of two curves, which may be used to automatically terminate the MCM when a convergence criteria has been reached. The FSV method is also used to compare the results of the different Error and Uncertainty Analysis methods with benchmark results. These comparisons are used to test the accuracy of the different methods.

In some cases, in this thesis, it will be necessary to align curves to determine the extent to which the errors and uncertainty in the outputs of CEM simulations are amplitude and

frequency errors and uncertainties. Without curve alignment it is impossible to tell whether or not the errors and uncertainties are due to frequency shifts.

A number of curve alignment techniques have been introduced in this chapter. From the analysis in this chapter it may be concluded that the DTW method aligns curves the best, but large frequency shifts make its use for subsequent Error and Uncertainty Analyses questionable. The PM method has been shown to effectively align curves without excessively distorting them, and is also the computationally fastest method considered here. It is therefore the method that is used in the majority of cases to align the output curves. The quality of the alignment will be tested using the AAAD. If the AAAD is larger after alignment then the alignment is concluded to be poor, and the original curves are used in any analyses that follow.

This chapter has introduced a number of numerical techniques for analysing curves. The next chapter discusses the application of these techniques to different Error and Uncertainty Analyses.

Chapter 4

Errors and Uncertainty

Contents

4.1 Introduction

Different methods of determining the error and uncertainty in the output of CEM simulations will be outlined in this chapter. In Chapter 2 a number of sources of error that exist in FDTD simulations were described. Many of these errors have been found to decrease in size when the cell size used in the FDTD simulations reduces. This observation is used in the error estimation methods of this chapter. The difference between more accurate and less accurate FDTD simulations provides an estimation of the error in the less accurate simulations. The more accurate simulations are performed with smaller cell sizes and higher order FDTD methods. This chapter begins with a description of how to determine errors analytically in certain special cases. Following this, more general approaches for estimating the error in the output of FDTD simulations are given.

The sources of parametric uncertainty were also discussed in Chapter 2. An example of a parametric uncertainty is the uncertainty in the material parameters, or the geometric positions, of a structure being modelled. The uncertainty in the input will propagate through the simulation to produce an uncertainty in the output. The MCM, MoM and PCM are used in this thesis to determine such output uncertainties. These UA methods are introduced in this chapter and their application to the FDTD method is discussed. The implementation of the PCM into FDTD is entirely novel. Since the uncertainty in the output is a curve (usually in the frequency domain), the numerical analyses described in Chapter 3 are used when developing the UA methods in this chapter.

This chapter also provides novel derivations of the relationships between aligned and unaligned errors and uncertainties. Using these relationships it is shown that the unaligned errors can be reconstructed from the aligned errors. Similarly, it is shown that unaligned uncertainties can be reconstructed from the aligned uncertainties. The aligned errors and uncertainties provide the user with insight into what proportion of the output errors and uncertainties are due to differences in amplitude, and what proportion are due to frequency differences. Since it is possible to reconstruct the unaligned errors and uncertainties from the aligned errors and uncertainties, it may be concluded that no information is lost by

analysing aligned errors and uncertainties.

4.2 Error Quantification Methods for Finite Difference Time Domain Simulations

This section introduces some possible methods of determining the error in the output of FDTD simulations. The most accurate determination of the error in a simulation is formed by taking the difference between the results of the simulation and the analytical solution of the same scenario [73]. Unfortunately analytic solutions can only be formed for relatively simple problems. The examples in Chapters 5 and 6 have analytic solutions that are used to form the exact error in the results of FDTD simulations. These exact errors are then compared to error estimates formed from other Error Analysis methods to determine the accuracy of these methods. The two approximate Error Analysis methods used are discussed in the next two sections.

4.2.1 Determining Errors by Using Refined Meshes

As described in Section 2.4 the truncation, discretisation, dispersion and staircasing errors of (2,2) FDTD simulations decrease as the size of the cells in the FDTD mesh decrease. Taking the difference between the results of FDTD simulations performed on coarse and fine meshes provides a quantitative estimation of how the truncation, discretisation, dispersion and staircasing errors introduce errors in the results of the coarse FDTD simulation. The finer the mesh used (for the simulation performed on the fine mesh), the more accurate the FDTD simulation and therefore the more accurate the estimation of the errors in the coarse simulation.

It may seem pointless to use more accurate simulations to determine the errors in less accurate simulations, because the more accurate results may be used instead of the less accurate results. However, if many simulations are to be performed (as with a Monte Carlo Simulation) the computational expense of using the more accurate methods may be too great. It may be more practical to use less accurate simulations, and determine the error in one of these simulations using a more accurate simulation. This will provide a useful quantitative estimate of the error that will occur in each of the subsequent simulations.

4.2.2 Determining Errors by Using Higher Order Finite Difference Time Domain Simulations

In 1989 Fang [58] published his thesis on higher order FDTD methods. Fang's (4,4) FDTD scheme is described in detail in Section 2.3.4. This scheme is based on using higher order central difference approximations when discretising Maxwell's equations. These higher order approximations make the results of higher order FDTD simulations more accurate than the results of standard (2,2) FDTD simulations. Thus higher order methods may be used to estimate the truncation errors in the results of standard FDTD simulations. In the example in Chapter 5, Fang's (4,4) FDTD scheme is used to determine estimates of the error in a (2,2) FDTD simulation. Mesh refinements will make the higher order simulations even more accurate, and thus provide a better estimation of the errors in the (2,2) simulations. Once these error estimates are formed, it is possible to determine how similar they are to the exact error, formed using the analytic solution of the example in Chapter 5. The Feature Selective Validation method [68] is used to compare the error estimates, with the exact errors formed using analytic solutions.

The Error Analysis methods described in this section and in Section 4.2.1 concentrate on quantifying the truncation, discretisation, dispersion and staircasing error. The truncation and discretisation errors are two of the main sources of error in FDTD simulations. No analyses of the errors due to boundary approximations or numerical precision are made by the two Error analysis methods. Errors produced by the Mur boundaries may be estimated by comparing the results of simulations using the Mur boundary condition with results obtained when the more accurate PML boundary condition is used. Numerical round off errors may be estimated by using the results of simulations performed using doubles instead of floats. The examples in Chapters 5 and 6 will investigate how well the above two approximate error estimation methods estimate the full exact errors.

4.3 Using Curve Alignment when Determining Errors

The error in a simulated frequency response curve is calculated by taking the difference between two curves. These curves should be fairly similar however it is possible that they may be shifted in frequency with respect to each other. This implies that the error between the curves is a frequency shift error as well as an amplitude error. If the curves are aligned so that the features of the curves match up, then the frequency shift required to align

the curves will be the error in the frequency domain. Once aligned, the aligned amplitude difference may be calculated to obtain the aligned amplitude error. It is useful to analyse the aligned amplitude and frequency errors, as well as the unaligned amplitude errors, as they provide more information on how the errors manifest themselves in the results.

4.3.1 The Relationship Between the Error Calculated Using Aligned and Unaligned Curves

This section will provide a relationship between the unaligned amplitude error, and the aligned amplitude and frequency error. To the author's knowledge, the mathematical arguments set out in this section are entirely novel.

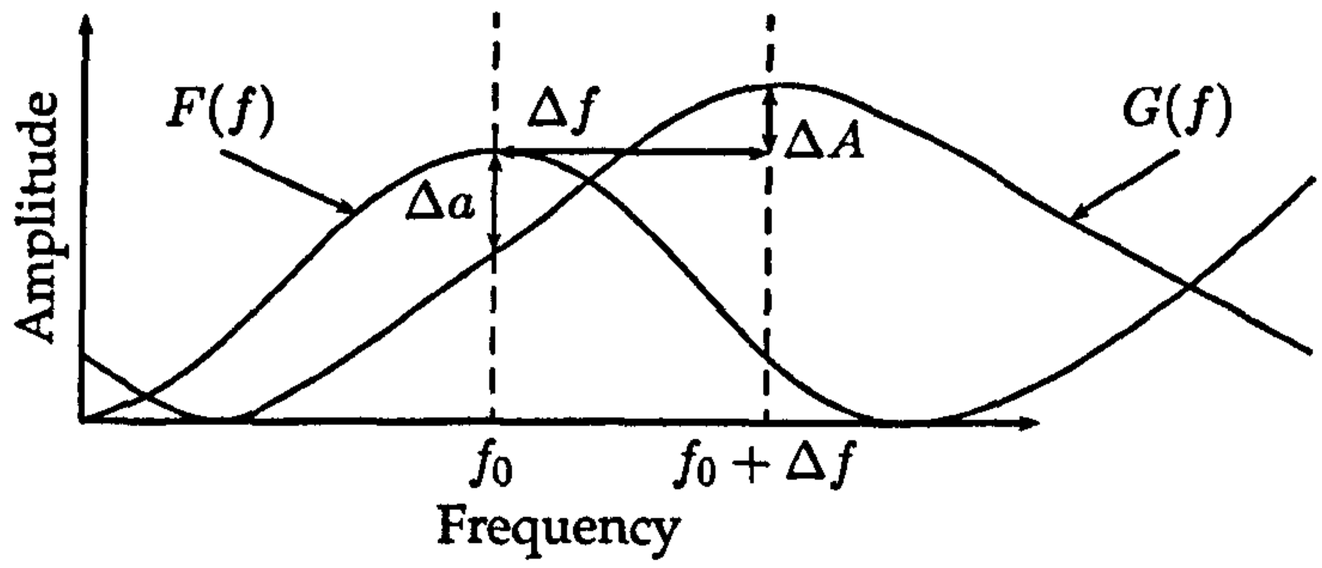

Figure 4.1: Two unaligned curves with amplitude difference Δa, aligned amplitude difference ΔA and aligned frequency difference Δf at f_0.

Let $F(f)$ be the reference curve to which a target curve $G(f)$ is aligned, in the frequency domain f. Figure 4.1 shows the aligned and unaligned differences between the curves $G(f)$ and $F(f)$, at the frequency f_0. The difference in the amplitudes of the unaligned curves may be calculated as

$$\Delta a(f_0) = G(f_0) - F(f_0). \tag{4.1}$$

From Figure 4.1 it can be seen that the difference in the amplitudes of the aligned curves at f_0 may be calculated as

$$\Delta A(f_0) = G(f_0 + \Delta f) - F(f_0) \tag{4.2}$$

where Δf is the difference in the frequencies of the matched points on the two curves.

The differential of the curve $G(f)$, at the frequency f_0, can be defined as

$$\left.\frac{\partial G(f)}{\partial f}\right|_{f=f_0} = \lim_{\delta f \to 0} \frac{G(f_0 + \delta f) - G(f_0)}{\delta f}. \tag{4.3}$$

If the frequency difference Δf is assumed to be small then we may approximate the derivative of G as

$$\left.\frac{\partial G(f)}{\partial f}\right|_{f=f_0} \approx \frac{G(f_0+\Delta f)-G(f_0)}{\Delta f}. \tag{4.4}$$

This approximation is inaccurate in the case where the frequency shifts Δf are large. Using equations (4.1) and (4.2), equation (4.4) may be rewritten as

$$\left.\frac{\partial G(f)}{\partial f}\right|_{f=f_0} \approx \frac{(\Delta A(f_0)+F(f_0))-(\Delta a(f_0)+F(f_0))}{\Delta f}. \tag{4.5}$$

Equation (4.5) may be rearranged to obtain

$$\Delta a(f_0) \approx \Delta A(f_0) - \Delta f \left.\frac{\partial G(f)}{\partial f}\right|_{f=f_0}. \tag{4.6}$$

Equation (4.6) gives the relationship between the unaligned amplitude error, and the aligned amplitude and frequency errors of the two curves. The equation is second order accurate in the frequency shifts Δf. The term Δa in equation (4.6) is referred to as the reconstructed unaligned error. The relationship between the aligned and unaligned errors, given by equation (4.6), may be tested by comparing the reconstructed unaligned error with the actual unaligned error.

Figure 4.2 shows a target curve being aligned to a reference curve: these curves are taken from Chapter 6. The reference curve is the analytic solution of the electric field backscattered from a dielectric sphere. The target curve is the (2,2) FDTD simulation of the same scenario. Only small frequency shifts were required to align the curves, which were

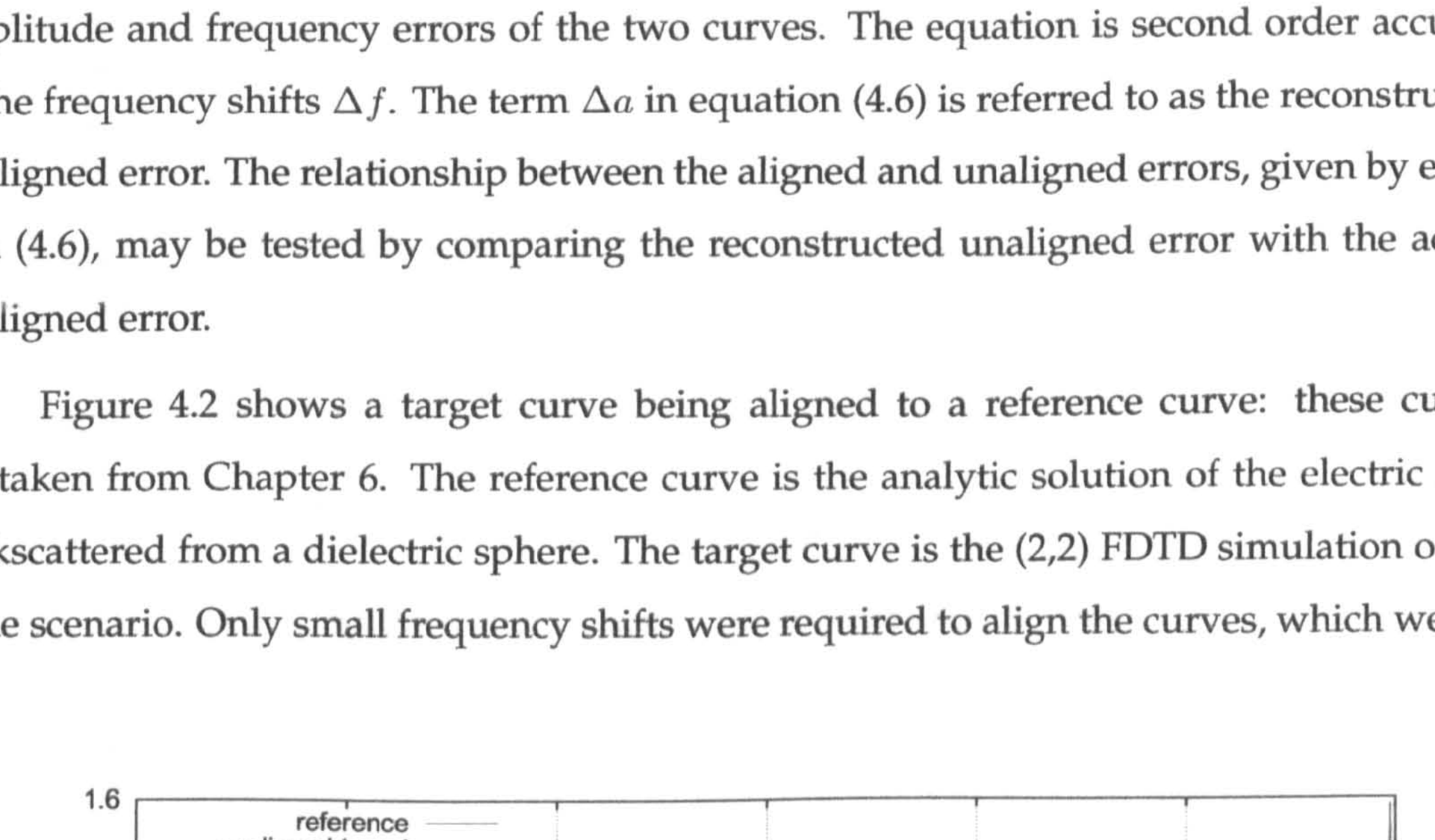

Figure 4.2: Aligning the target curve to the reference curve.

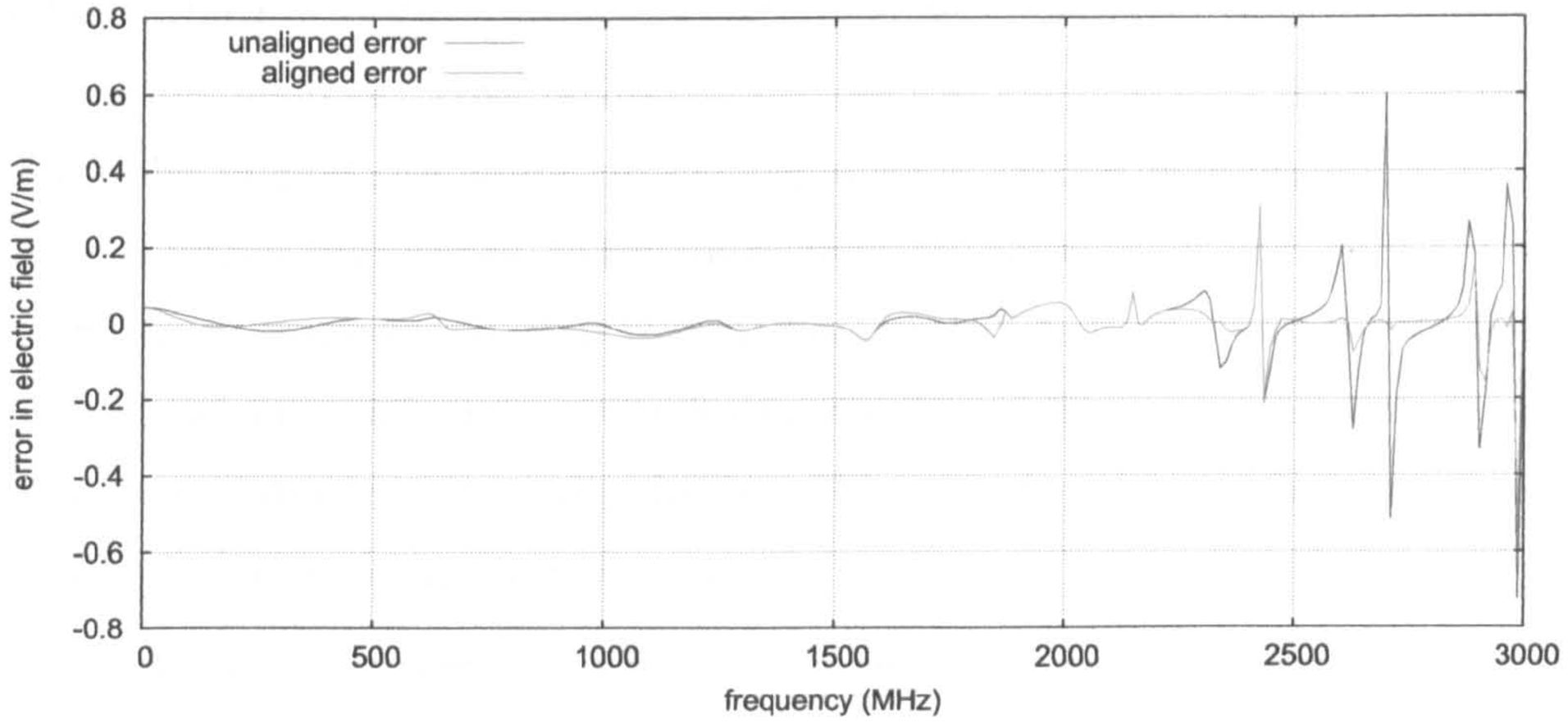

Figure 4.3: Amplitude error calculated using aligned and unaligned curves.

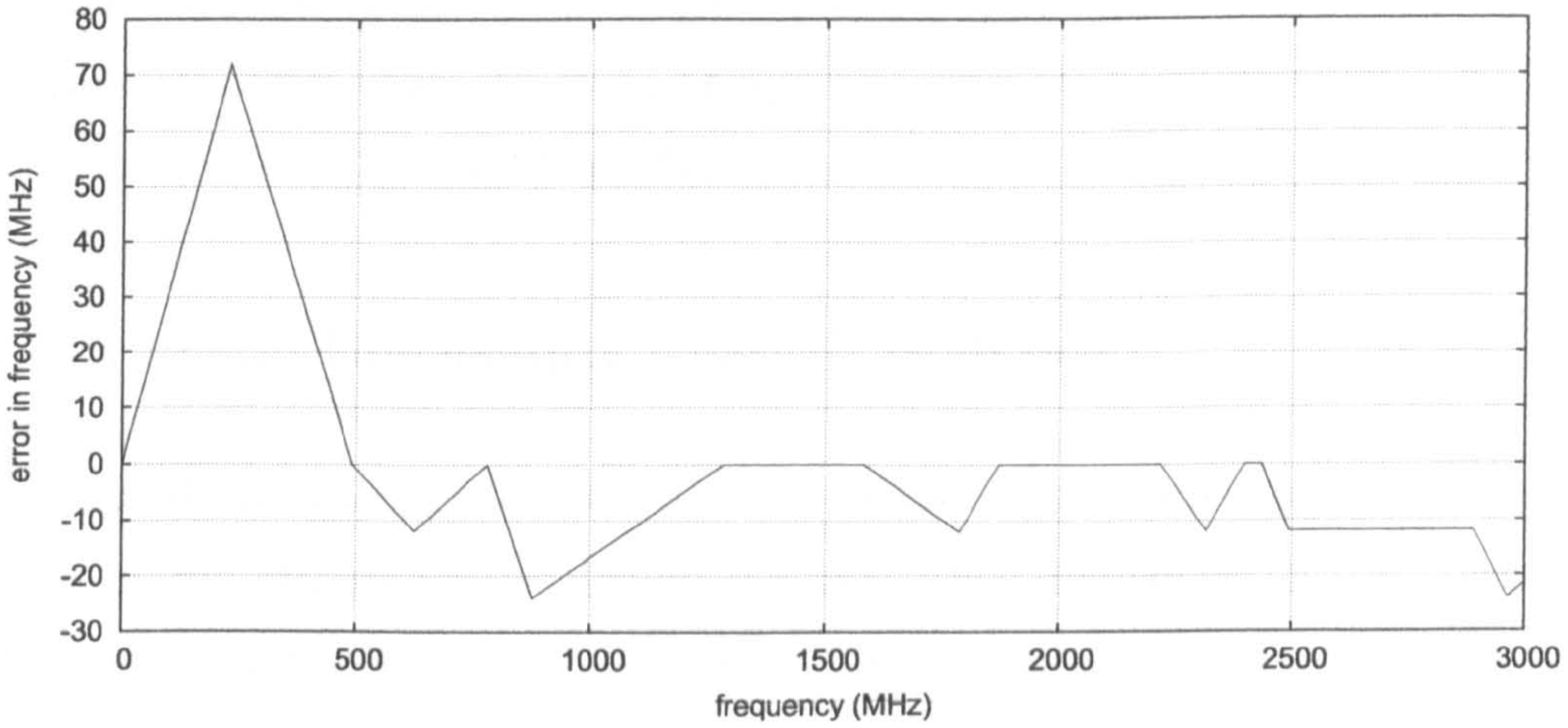

Figure 4.4: The frequency response of the frequency error.

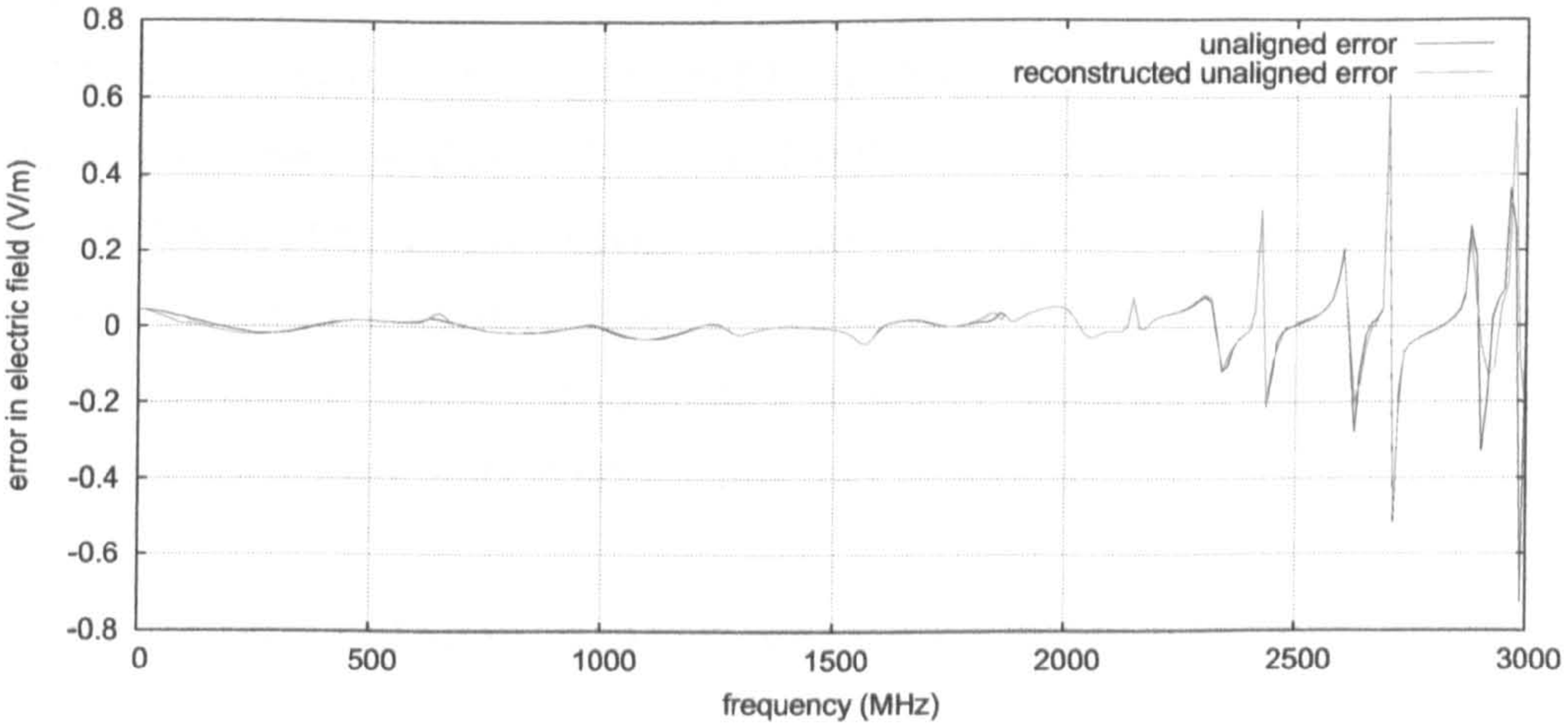

Figure 4.5: Unaligned amplitude error and reconstructed unaligned amplitude error.

aligned using the PM method. The aligned and unaligned amplitude error are shown in Figure 4.3, and the frequency error is shown in Figure 4.4. The frequency errors are relatively small, and the aligned amplitude error is significantly smaller than the unaligned amplitude error at higher frequencies. To test the relationship between the unaligned and aligned errors, the reconstructed unaligned uncertainty is calculated according to equation (4.6). Figure 4.5 shows the unaligned amplitude uncertainty and the reconstructed unaligned uncertainty, these two curves are very similar. This provides support that the relationship between aligned and unaligned errors, given by equation (4.6), is valid.

Using curve alignments, it is possible to obtain more information on the nature of the error in output curves. Often the error in the output of a CEM simulation will be a frequency shift in the output curve, caused perhaps by dispersion errors. Without alignment it is impossible to quantify this frequency error. Curve alignments will be used in Chapters 5-7 to determine the aligned amplitude and frequency errors (and uncertainties) in the output curves formed from (2,2) FDTD simulations.

4.4 Parameter Uncertainty Analysis Methods

A significant amount of work has already been carried out on parameter uncertainties in the output of Computational Fluid Dynamic (CFD) simulations [10–15]. This section reviews some of the methods used to analyse parameter uncertainty in CFD models. These methods are of two types, probabilistic methods and nonprobabilistic methods [10]. Nonprobabilistic methods (also called possibilistic methods) include Interval Analysis (IA) and Fuzzy Logic applied to Membership Functions [15]. The probabilistic methods are Monte Carlo, Moment methods and Polynomial Chaos. These methods are referred to as probabilistic methods because they make use of the PDFs associated with the uncertain input parameters. These PDFs are propagated through the simulation to produce an output PDF, from which the mean, uncertainty and 95% Confidence Intervals (CI) may be calculated. The three probabilistic methods are described in detail in Sections 4.5-4.7. The next section discusses how the analytic output uncertainty may be formed.

4.4.1 Analytically Calculating the Output Uncertainty

Let $f(p_1, \ldots, p_n)$ be a known function of n uncertain parameters $p_1, \ldots, p_n$. Each uncertain input parameter p_i follows a specific probability distribution with a corresponding

weighting function w_i, and is defined over the probability space S_i. The mean value μ is the expected value $E(f(x))$, and is obtained by integrating f over the different parameter probability spaces as

$$\mu = E(f(x)) = \int_{S_1} \dots \int_{S_n} f(p_1, \dots, p_n) w_1 \dots w_n dp_1 \dots dp_n. \tag{4.7}$$

The variance σ^2 is obtained similarly using

$$\sigma^2 = E((f(x) - \mu)^2) = \int_{S_1} \dots \int_{S_n} (f(p_1, \dots, p_n) - \mu)^2 w_1 \dots w_n dp_1 \dots dp_n. \tag{4.8}$$

The analytic uncertainty in the output is the square root of this variance. In Chapters 5 and 6 it is possible to calculate the analytic uncertainty because the analytic solution of the output is known. This analytic uncertainty is used as a benchmark to test the performance of the other Uncertainty Analysis methods.

In the next two sections, the possibilistic methods IA and Fuzzy Logic are described. These two methods are simple to implement into CEM codes, however they do not provide as much information on the output uncertainty as the probabilistic methods.

4.4.2 Interval Analysis

Interval Analysis involves setting an interval bound for each input, and using interval arithmetic [74] to propagate the input intervals through the model, producing an output interval. This output interval acts as an uncertainty bound for the output value based on the uncertainty bounds of the input values. Rao and Berke [75] give an example of how to use IA to analyse uncertain structural systems. IA is very simple to implement, it can however give uncertainty bounds that are too conservative, representing the worst case scenario [15].

The large output uncertainty bounds are due in part to the dependency problem. The dependency problem arises from the fact that different interval variables are assumed to be independent in each interval arithmetic evaluation. Ignoring the dependency of these variables results in an overestimation of the resultant interval [76, p.31]. For example, let $X = [0, 1]$ be an interval variable. Subtracting X from itself using interval arithmetic yields

$$[0, 1] - [0, 1] = [-1, 1] \tag{4.9}$$

an overestimation of the true interval $X - X = [0, 0]$. Similarly if $X = [-1, 1]$ then interval

arithmetic asserts that $X^2 = [-1, 1]$, when in reality $X^2 = [0, 1]$. Ignoring the dependency of X with itself results in unwanted expansions of the output intervals.

This dependency problem may result in overestimations of the output intervals of FDTD simulations. Suppose one of the material parameters is uncertain, and is therefore represented as an interval variable in the FDTD update equations. The FDTD method will make multiple calculations using this interval variable, and the interval arithmetic will ignore the dependency of this variable with itself. Every time the uncertain interval is used, the output interval will increase, providing an overestimation of the actual output interval.

Not much knowledge of the input values is required to use IA, only an expected input value is required for each parameter. Using these expected values, intervals that are say ten percent above and below the expected values can be created. The resulting output intervals do not provide much information on the uncertainty in the output values compared to the information obtained from probabilistic methods [15]. Since not as much information is gained from IA, and the output intervals produced suffer from the dependency problem, this method will not be used to quantify uncertainty in this thesis.

4.4.3 Fuzzy Logic

Fuzzy Logic was first introduced by Zadeh [77] in 1965. It is a useful means of dealing with sets of variables with vague definitions [78, p.1]. These sets are called fuzzy sets, an example of such a set is the set of all tall people. This set is not a conventional "crisp" set as there is a vagueness about who will belong to this set. A "crisp" set is a set with distinct members that definitely belong to the set, and definitely do not belong to the complement of the set. An example of a crisp set is the set of all people that are taller than 190cm [78, p.1].

If A represents a crisp set of the universal set X, then the characteristic function χ_A for A can be defined as the mapping [78, p.9]

$$\chi_A : X \to [0, 1]$$

such that

$$\chi_A(x) = \begin{cases} 1 & \text{if } x \in A, \\ 0 & \text{if } x \notin A. \end{cases}$$

A similar function for fuzzy sets exists called a Membership Function. The Membership Function of a fuzzy set B assigns real values, between zero and one to each member of the

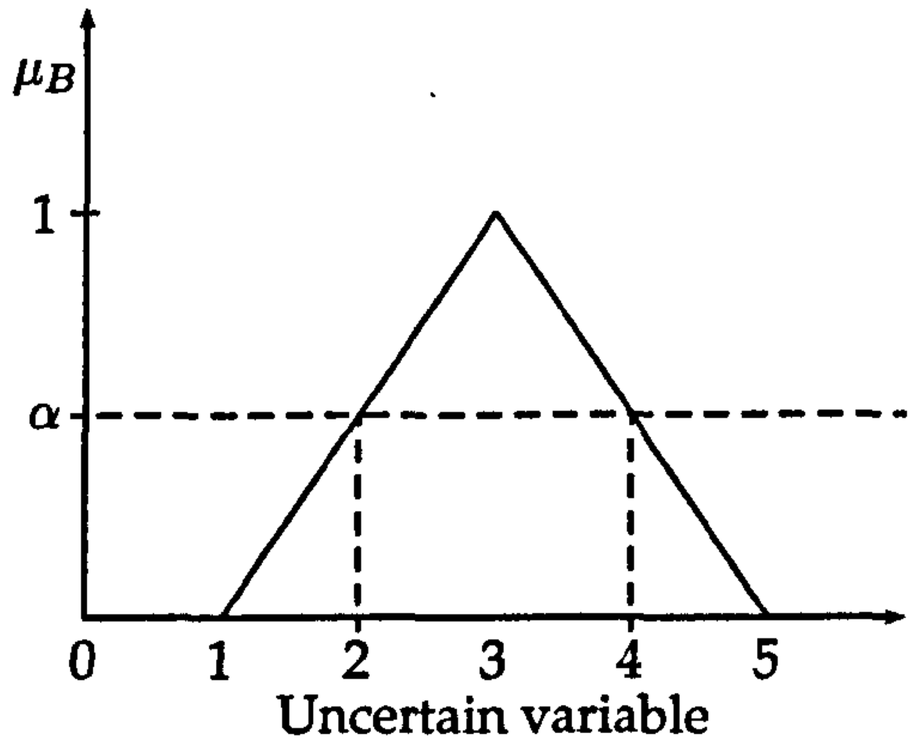

Figure 4.6: An example Membership Function; the uncertain variables are given a value between zero and one. An α cut is taken at $\alpha = 0.5$, the corresponding interval for this alpha cut is [2,4].

universal set X [78, p.9-13]. This value describes the degree to which the member belongs to the set B. If a certain element of the universal set has a zero value for the Membership Function of B, then it definitely does not belong to B. Conversely, if the element has a value of one for the Membership Function of B, then it definitely belongs to B. If the element has a value in between zero and one then it may belong to B, the degree to which it belongs to B depends on how close this value is to one. An example of a Membership Function μ_B is shown in Figure 4.6.

To perform an uncertainty analysis using fuzzy logic, α cuts of the Membership Function are taken between zero and one. An α cut is a set of variables x_i, from the fuzzy set B, for which $\mu_B(x_i) \geq \alpha$ [79]. For each value of α, between zero and one, an interval of input values is obtained from the corresponding α cut. The output interval values, corresponding to the different input interval values, are calculated using interval arithmetic [74]. These interval output values are output α cuts, which can be transformed into an output fuzzy set. The expected value for the output, and some idea of the uncertainty in this value, can be obtained from the output fuzzy set.

This method is easy to implement and provides more information on the output values than IA. The Fuzzy Logic method is not as accurate as probabilistic methods, but it is easier to implement and less computationally expensive [15]. Since interval arithmetic is used, Fuzzy Logic will also suffer from overestimated intervals due to the dependency problem. Thus, Fuzzy Logic will not be investigated further in this thesis. The next three sections give detailed descriptions of the three UA methods that are used in this thesis.

4.5 The Monte Carlo Method

The MCM is perhaps the best known UA method described in this thesis. Historically the method has been used for hundreds of years, however the name "Monte Carlo" has only been used since the 1940s [15]. The name refers to a casino in Monte Carlo, and was given to the method because of the use of probability and repetition that is shared by the UA method and gambling in casinos. The MCM works by taking a number of sets of random samples from the input parameter space, systematically computing the output that is formed from each set of inputs, and combining these outputs to form the mean and standard deviation.

Suppose that the output of a simulation depends on K uncertain inputs. Each of the K uncertain inputs will have an associated PDF. The PDFs can be used to calculate the probability that each input parameter takes on certain values. In the MCM, the PDFs are sampled many times to produce multiple sets of input parameter values. The PDFs are used to determine which input values are more probable; the more probable values are sampled more often. The individual samples of the input parameters are then combined to form sets of input parameter values. There are many ways to form these sets of input parameter values. In this thesis Latin Hypercube Sampling is used to form the sets of input values. This method is described in more detail in the next section.

If N outputs $E_1, \ldots, E_N$ are formed from N FDTD simulations using N sets of sampled inputs, then the sample mean output μ is

$$\mu = \frac{1}{N} \sum_{i=1}^{N} E_i \tag{4.10}$$

and the sample variance σ^2 is

$$\sigma^2 = \frac{1}{N-1} \sum_{i=1}^{N} (E_i - \mu)^2. \tag{4.11}$$

The uncertainty σ in the output of the FDTD simulation is the square root of the variance.

The mean and uncertainty formed from the N simulations will converge as N tends towards infinity. It is important that N is large enough so that the results of the Monte Carlo simulations have reached an acceptable level of convergence. A novel way of determining when an acceptable level of convergence has been reached is discussed in Section 4.5.2. Since the MCM has a slow convergence N is generally large; performing a large number of FDTD

simulations is computationally expensive. Different sampling methods may be used to help improve the rate of convergence and thus decrease the computational expense of the MCM. The next section outlines one such method called Latin Hypercube Sampling.

4.5.1 Latin Hypercube Sampling

There have been many sampling methods proposed to reduce the expense of the MCM [80]-[81]. Latin Hypercube Sampling (LHS) is one such method proposed by McKay et al [80]. This technique works by splitting up each input parameter PDF into equal regions of probability [80]. Suppose there are K uncertain inputs $X_1, \ldots, X_K$. The PDF of the kth uncertain input X_k is split into N segments of equal probability. One random sample is taken from each segment, producing N samples for parameter k that span the whole of the PDF. This process is repeated for all K parameters. By then randomly combining the N samples from the K parameters, N sets of input parameter values are produced.

Splitting the PDFs in this way is equivalent to splitting the whole probability set into N^K cells of equal probability. These cells form a hypercube in the multidimensional probability space. From this probability space N cells are selected and one random sample is taken from each cell [15]. The cells are selected so that each segment from each parameter PDF is selected once and only once [15]. This selection criteria corresponds to a K-dimensional extension of Latin Square sampling [80]. Using LHS with the MCM has been shown to increase the rate of convergence compared to using Random Sampling or Stratified Sampling [80]. LHS will be used in this thesis to obtain the sets of input parameters for the MCM.

4.5.2 Testing for Convergence Using the Feature Selective Validation Method

The MCM is known to be slow to converge. It is important to determine when the MCM has reached an acceptable level of convergence. This section describes the novel use of the FSV method, to determine when the MCM has reached convergence.

The output of interest in CEM is often a curve, such as the frequency response of the electric field in dB V/m. The mean and uncertainty of the outputs are also curves. Suppose that N simulations have been performed and the mean and uncertainty curves of the N outputs are calculated. If more simulations are performed and the mean and uncertainty of the outputs formed using these extra simulations are very similar to the respective mean and uncertainty curves produced from the N simulations, then convergence has been reached.

The FSV method may be used to determine whether the respective curves are similar or not.

The convergence of the MCM, in this thesis, is determined as follows:

1. Perform $50n$ simulations (initially $n = 1$) and calculate the mean and standard deviation of the different output curves, on a point-by-point basis.

2. If $n > 1$ compare the mean and standard deviation curves produced after $50n$ simulations with the respective curves produced after $50(n-1)$ simulations, using the FSV method.

3. If the FSV comparison determines that one/both of the GDM values, for these comparisons, is/are greater than 1.5 then increase n by one and repeat the process from Step 1.

4. Or else if the GDM values are both less than or equal to 1.5 then the mean and standard deviation curves are "excellent" matches to the respective curves formed 50 simulations previously, and therefore convergence has been reached.

This is a novel way of determining the convergence of the MCM when the output of interest is a complex curve. The benefits of this method are that the FSV comparisons are consistent, quantitative and nonsubjective. A consistent quantitative convergence criteria can therefore be set for the similarity of curves produced after certain numbers of simulations. The FSV comparisons can be performed automatically and therefore the MCM simulations can be stopped automatically when convergence has been reached. This automation ensures that enough simulations are performed for convergence, without performing more simulations than is necessary. This helps to minimise the computational expense of the MCM. In this thesis the convergence criteria (GDM$\leq$1.5) is tested after 50 simulations. This number of simulations is small enough to prevent unnecessary simulations from being performed, and is large enough to ensure that individual variances (from each set of 50 simulations) do not affect the output mean and uncertainty.

Other automised methods that test for convergence involve looking at the least square difference between the respective means or standard deviations. These methods are arguably less reliable for EMC data, which often has narrow resonant features. The FSV method is more useful as it provides a metric that can be used to determine when the respective curves are very similar over all frequencies.

4.5.3 Using the Monte Carlo Method to Calculate Confidence Intervals

The results of the multiple MCM simulations may be used to calculate 95% CI, by first forming the cumulative probability distribution function from the results. The 95% CI is the interval that begins when the cumulative probability distribution function is at 2.5% and ends when the distribution function equals 97.5%.

In this thesis the cumulative distribution function is approximated using the Kaplan-Meier empirical cumulative density function [82]. This function does not follow any particular distribution, it therefore represents the results more accurately. Kaplan and Meier's original work focused on estimating the probability that a member from a population (of human patients) has a lifetime exceeding time t given a sample of lifetimes from the population [82]. Let $P(t)$ denote this probability and let the N observed lifetimes, sampled from the population, be

$$t_1 \leq t_2 \leq t_3 \leq \ldots \leq t_N. \tag{4.12}$$

If d is the number of deaths at time t then the probability $P(t)$ may be approximated by the Kaplan-Meier estimator $\hat{P}(t)$, which takes the form [82]

$$\hat{P}(t) = \prod_{r=1}^{d} \frac{N-r}{N-r+1}. \tag{4.13}$$

Since $\hat{P}(t)$ is the estimate of the probability that a member of the population has a lifetime that exceeds t, the cumulative distribution function for the lifetime is

$$F(t) = 1 - \hat{P}(t). \tag{4.14}$$

This cumulative distribution function is known as an Empirical Cumulative Distribution Function (ECDF), because it is formed out of the evidence from the population.

To obtain the ECDF for the N simulations, the outputs E_i must first be sorted in numerical order to give

$$E_1 \leq E_2 \leq \ldots \leq E_N. \tag{4.15}$$

If d is the number of output values that are less than or equal to E, then the ECDF is

$$F(E) = 1 - \prod_{r=1}^{d} \frac{N-r}{N-r+1}. \tag{4.16}$$

For the examples given later in this thesis, the ECDF is calculated for the output curves at each frequency. The 95% CI is then calculated as $[E_{low}, E_{high}]$, where the ECDF is 0.025 (2.5%) at E_{low} and 0.975 (97.5%) at E_{high}. These 95% CIs are based on the empirical evidence formed from the MCM simulations; there is no assumption that the output follows a particular distribution.

4.5.4 The Relationship Between the Uncertainty Calculated Using Aligned and Unaligned Curves via the Monte Carlo Method

This section will provide a relationship between the uncertainties calculated when the curves are not aligned, and the uncertainties calculated after the curves have been aligned. Using curve alignment provides more information as to what is the dominant source of the uncertainty: amplitude differences in the curves or frequency differences. It will be shown that once the aligned uncertainties have been found, the unaligned uncertainties may be reconstructed using these aligned uncertainties. To the author's knowledge, the mathematical arguments set out in this section are entirely novel.

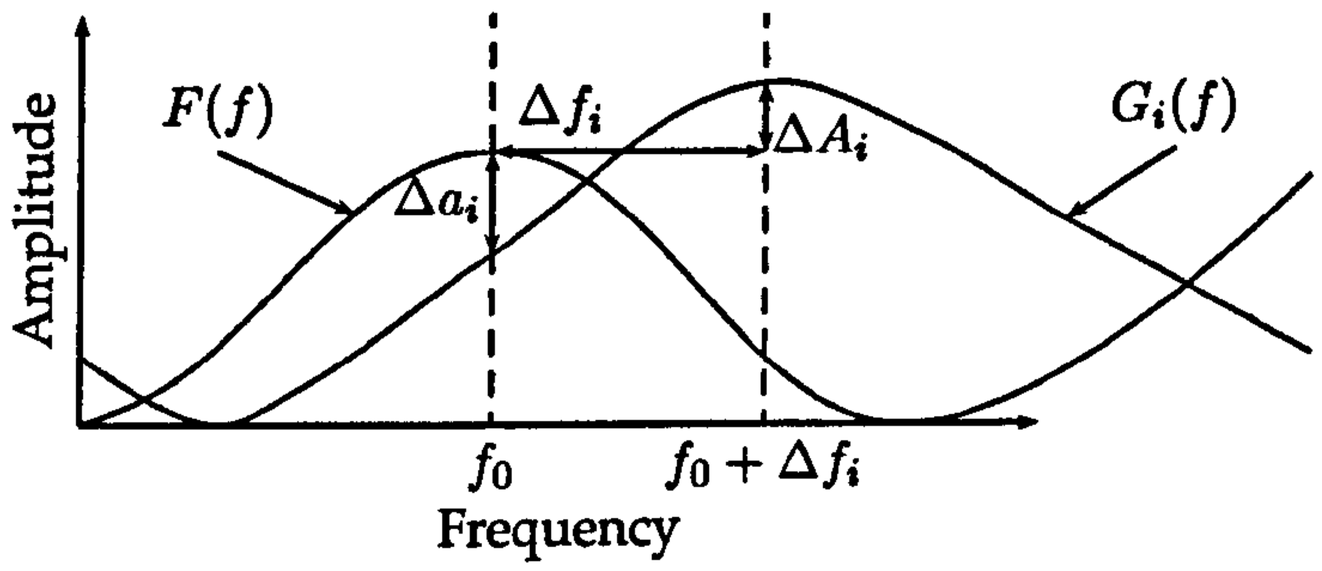

Figure 4.7: Two unaligned curves with amplitude difference Δa_i, aligned amplitude difference ΔA_i and aligned frequency difference Δf_i at f_0.

Suppose that N simulations have been performed and the N outputs are used to calculate the uncertainty via the MCM. If these simulations are performed in the frequency domain f then the N outputs may be frequency response curves. The N output curves, denoted as $G_1(f), \ldots, G_N(f)$, may be aligned to some reference curve $F(f)$. The reference curve could, for example, be the curve produced by performing a simulation using the mean input values. Figure 4.7 shows the aligned and unaligned differences between the curves $G_i(f)$ and $F(f)$, at the frequency f_0. The difference in the amplitudes of the unaligned curves may be calculated as

$$\Delta a_i(f_0) = G_i(f_0) - F(f_0). \tag{4.17}$$

From Figure 4.7 it can be seen that the difference in the amplitudes of the aligned curves at f_0 may be calculated as

$$\Delta A_i(f_0) = G_i(f_0 + \Delta f_i) - F(f_0) \tag{4.18}$$

where Δf_i is the difference in the frequencies of the matched points on the two curves, at f_0. In equation (4.6) of Section 4.3.1 the unaligned amplitude difference between two curves was related to the aligned amplitude and frequency differences. A similar equation may be derived for the curves in Figure 4.7, that is

$$\Delta a_i(f_0) = \Delta A_i(f_0) - \Delta f_i \left.\frac{\partial G_i(f)}{\partial f}\right|_{f=f_0}. \tag{4.19}$$

This equation is inaccurate if the frequency shifts Δf_i are large.

The uncertainty σ_{ua}, calculated using the unaligned curves $G_i(f)$, is the standard deviation in the amplitude of the unaligned curves, which at a frequency f_0 is defined as

$$\sigma_{ua}^2(f_0) = \frac{1}{N(N-1)}\left[N\sum_{i=0}^{N} G_i^2(f_0) - \left(\sum_{i=0}^{N} G_i(f_0)\right)^2\right]. \tag{4.20}$$

Using equation (4.17), equation (4.20) may be rewritten as

$$\sigma_{ua}^2(f_0) = \frac{1}{N(N-1)}\left[N\sum_{i=0}^{N} (\Delta a_i(f_0) + F(f_0))^2 - \left(\sum_{i=0}^{N} (\Delta a_i(f_0) + F(f_0))\right)^2\right]. \tag{4.21}$$

This equation may be expanded as

$$\sigma_{ua}^2 = \frac{1}{N(N-1)}\left[N\sum_{i=0}^{N} (\Delta a_i^2 + 2\Delta a_i F + F^2) - \left(\sum_{i=0}^{N} \Delta a_i\right)^2 - 2NF\sum_{i=0}^{N} \Delta a_i - N^2F^2\right]. \tag{4.22}$$

In the above equation all functions are evaluated at f_0, to aid notation the f_0 have been removed. Equation (4.22) reduces to

$$\sigma_{ua}^2 = \frac{1}{N(N-1)}\left[N\sum_{i=0}^{N} \Delta a_i^2 - \left(\sum_{i=0}^{N} \Delta a_i\right)^2\right]. \tag{4.23}$$

Using equation (4.19), equation (4.23) may be rewritten as

$$\sigma_{ua}^2 = \frac{1}{N(N-1)}\left[N\sum_{i=0}^{N} \left(\Delta A_i - \Delta f_i \frac{\partial G_i}{\partial f}\right)^2 - \left(\sum_{i=0}^{N} \left(\Delta A_i - \Delta f_i \frac{\partial G_i}{\partial f}\right)\right)^2\right], \tag{4.24}$$

which may be expanded to obtain

$$\sigma_{ua}^2 = \frac{1}{N(N-1)}\left[N\sum_{i=0}^{N}\left(\Delta A_i^2 - 2\Delta A_i \Delta f_i \frac{\partial G_i}{\partial f} + \left(\Delta f_i \frac{\partial G_i}{\partial f}\right)^2\right) - \left(\sum_{i=0}^{N}\Delta A_i\right)^2 + 2\sum_{i=0}^{N}\Delta A_i \sum_{j=0}^{N}\Delta f_j \frac{\partial G_j}{\partial f} - \left(\sum_{i=0}^{N}\Delta f_i \frac{\partial G_i}{\partial f}\right)^2\right]. \quad (4.25)$$

The standard deviation in the amplitude σ_A obtained using the aligned curves is defined as

$$\begin{aligned}\sigma_A^2 &= \frac{1}{N(N-1)}\left[N\sum_{i=0}^{N}G_i^2(f_0+\Delta f_i) - \left(\sum_{i=0}^{N}G_i(f_0+\Delta f_i)\right)^2\right] \\ &= \frac{1}{N(N-1)}\left[N\sum_{i=0}^{N}(\Delta A_i(f_0)+F(f_0))^2 - \left(\sum_{i=0}^{N}(\Delta A_i(f_0)+F(f_0))\right)^2\right] \quad (4.26)\end{aligned}$$

where equation (4.18) has been used. Expanding the terms in equation (4.26) gives

$$\sigma_A^2 = \frac{1}{N(N-1)}\left[N\sum_{i=0}^{N}(\Delta A_i)^2 - \left(\sum_{i=0}^{N}\Delta A_i\right)^2\right]. \quad (4.27)$$

The standard deviation σ_{Af} in the amplitude due to the frequency shifts Δf_i is

$$\sigma_{Af}^2 = \frac{1}{N(N-1)}\left[N\sum_{i=0}^{N}\left(\Delta f_i \frac{\partial G_i}{\partial f}\right)^2 - \left(\sum_{i=0}^{N}\Delta f_i \frac{\partial G_i}{\partial f}\right)^2\right]. \quad (4.28)$$

The covariance C, of the aligned amplitudes $G_i(f_0+\Delta f_i)$ and the amplitude change due to shifts in the frequency Δf_i, can be shown to be

$$C = \frac{1}{N(N-1)}\left[N\sum_{i=0}^{N}\Delta A_i \Delta f_i \frac{\partial G_i}{\partial f} - \left(\sum_{i=0}^{N}\Delta A_i\right)\left(\sum_{j=0}^{N}\Delta f_j \frac{\partial G_j}{\partial f}\right)\right]. \quad (4.29)$$

Using equations (4.27)-(4.29), equation (4.25) may be rewritten as

$$\sigma_{ua}^2 = \sigma_A^2 + \sigma_{Af}^2 - 2C. \quad (4.30)$$

Thus the uncertainty in the amplitude of the unaligned curves is related to: the uncertainty in the amplitude of the aligned curves; the uncertainty in the amplitude due to frequency shifts between the curves; and the covariance of the amplitudes of the aligned curves and

the amplitude differences caused by the frequency shifts. More information about the uncertainty in the output is obtained using curve alignment. After alignment it is possible to determine what proportion of the uncertainty is due to amplitude differences and what proportion is due to frequency shifts between the different curves. Equation (4.30) is second order accurate in the frequency shifts Δf_i.

It is possible to test the relationship between the aligned and unaligned uncertainties given by equation (4.30). The unaligned uncertainty in equation (4.30) may be referred to as the reconstructed unaligned uncertainty. Figures 4.8 and 4.9 show the unaligned and aligned uncertainties calculated using the MCM with 800 simulations. These uncertainties are the uncertainties in the output electric field backscattered from a PEC sphere, with an uncertain radius, from Chapter 6.

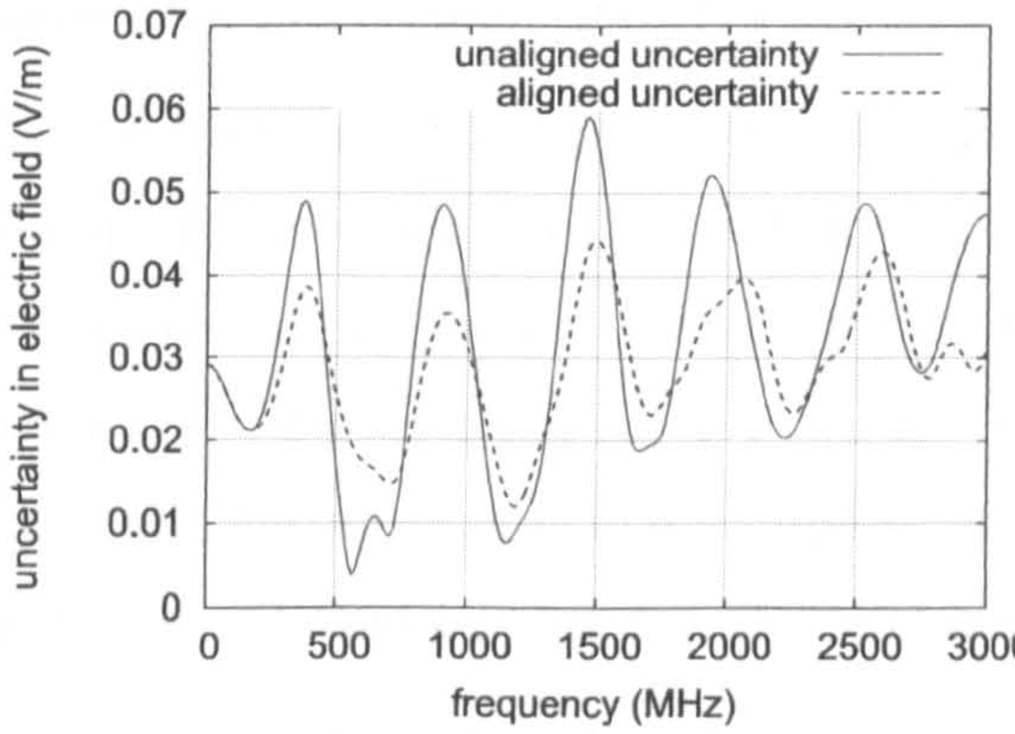

Figure 4.8: Aligned and unaligned amplitude uncertainty.

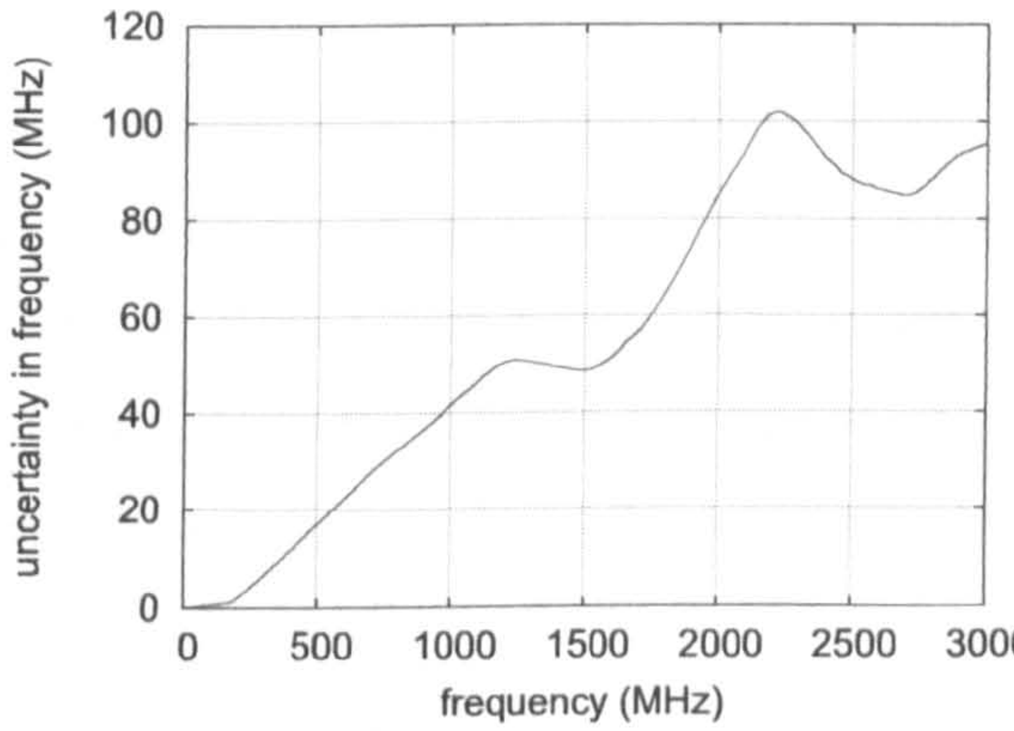

Figure 4.9: Uncertainty in the frequency.

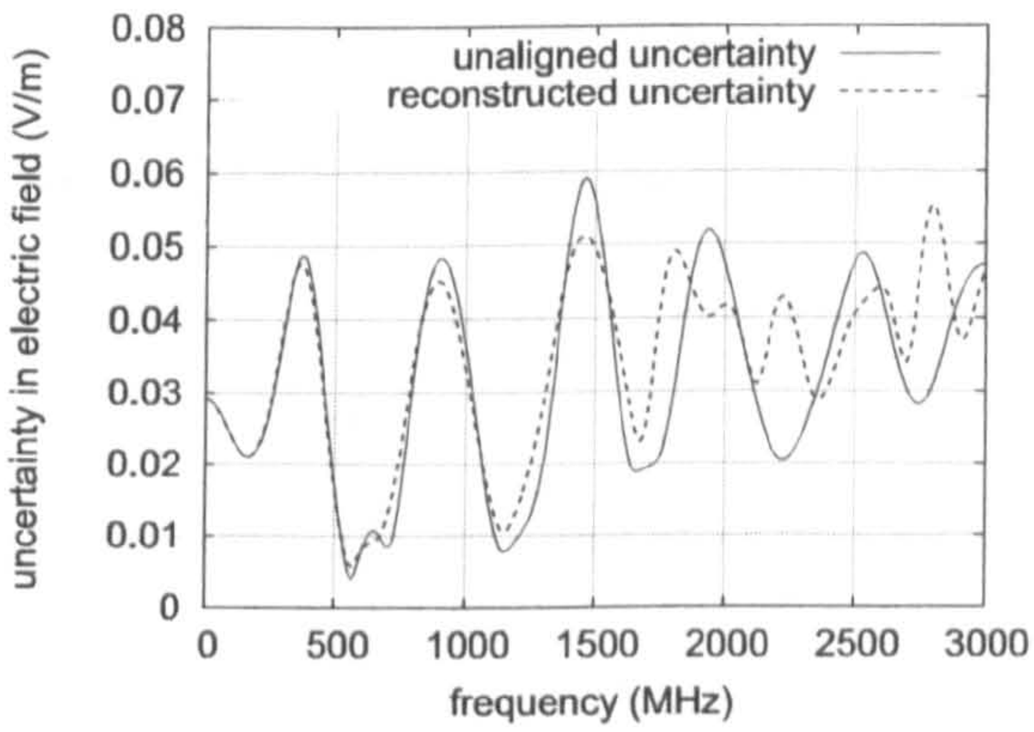

Figure 4.10: Unaligned amplitude uncertainty and reconstructed unaligned amplitude uncertainty

Figure 4.8 shows that the aligned amplitude uncertainty is smaller than the unaligned amplitude uncertainty. This is because the overestimations in the amplitude uncertainty, due to frequency differences between the curves, have been removed. The uncertainty in

the frequency shown in Figure 4.9 increases with the frequency. This means that larger frequency shifts were required to align the curves at the higher frequencies. The relationship between the aligned and unaligned uncertainties is based on the assumption that the frequency shifts between the curves are small. The relationship given by equation (4.30) will therefore be less accurate at the higher frequencies in this case.

Figure 4.10 shows the uncertainty calculated using the unaligned curves, and the unaligned uncertainty reconstructed using equation (4.30). The curves in this figure are in good agreement at the lower frequencies, providing support for equation (4.30). At higher frequencies the reconstructed unaligned uncertainty agrees less well with the unaligned uncertainty. As discussed earlier, at the higher frequencies larger frequency shifts are required to align the curves. The relationship between the unaligned and aligned uncertainties will therefore be less accurate at higher frequencies.

To form the relationship between the aligned and unaligned uncertainties, using equation (4.30), the derivatives $\partial G_i/\partial f$ need to be calculated for all N curves. It is possible to obtain a similar relation between the aligned and unaligned uncertainties that uses the derivative of the reference curve $F(f)$, and the uncertainty in the frequency obtained after alignment, the uncertainty in the amplitudes obtained after alignment and the covariance of the frequencies and amplitudes after alignment.

Equation (4.17) may be evaluated at a frequency $f_0 + \Delta f_i$ to obtain

$$\Delta a_i(f_0 + \Delta f_i) = G_i(f_0 + \Delta f_i) - F(f_0 + \Delta f_i). \tag{4.31}$$

As before, if the frequency shifts Δf_i are assumed to be small, then the derivative of the reference curve with respect to the frequency may be approximated as

$$\left.\frac{\partial F(f)}{\partial f}\right|_{f=f_0} \approx \frac{F(f_0 + \Delta f) - F(f_0)}{\Delta f_i}. \tag{4.32}$$

Using equation (4.31) and equation (4.18), this derivative may be rewritten as

$$\left.\frac{\partial F(f)}{\partial f}\right|_{f=f_0} = \frac{(G_i(f_0 + \Delta f_i) - \Delta a_i(f_0 + \Delta f_i)) - (G_i(f_0 + \Delta f_i) - \Delta A_i(f_0))}{\Delta f_i} \tag{4.33}$$

which may be rearranged to obtain

$$\Delta a_i(f_0 + \Delta f_i) = \Delta A_i(f_0)) - \Delta f_i \left.\frac{\partial F(f)}{\partial f}\right|_{f=f_0}. \tag{4.34}$$

Since Δf_i is assumed to be small, $\Delta a_i(f_0)$ may be approximated by

$$\Delta a_i(f_0) \approx \Delta a_i(f_0 + \Delta f_i) = \Delta A_i(f_0)) - \Delta f_i \left.\frac{\partial F(f)}{\partial f}\right|_{f=f_0}. \tag{4.35}$$

Using equations (4.23) and (4.35), the uncertainty in the unaligned curves at a frequency f_0 may be approximated by

$$\sigma_{ua}^2 \approx \frac{1}{N(N-1)} \left[N \sum_{i=0}^{N} \left(\Delta A_i - \Delta f_i \frac{\partial F}{\partial f} \right)^2 - \left(\sum_{i=0}^{N} \Delta A_i - \Delta f_i \frac{\partial F}{\partial f} \right)^2 \right]. \tag{4.36}$$

Expanding the squared terms in this equation yields

$$\begin{aligned} \sigma_{ua}^2 \approx \quad & \frac{1}{N(N-1)} \left[N \sum_{i=0}^{N} \left(\Delta A_i^2 - 2\Delta A_i \Delta f_i \frac{\partial F}{\partial f} + \left(\Delta f_i \frac{\partial F}{\partial f} \right)^2 \right) \right. \\ & \left. - \left(\sum_{i=0}^{N} \Delta A_i \right)^2 + 2 \left(\sum_{i=0}^{N} \Delta A_i \right) \left(\sum_{j=0}^{N} \Delta f_j \frac{\partial F}{\partial f} \right) - \left(\sum_{i=0}^{N} \Delta f_i \frac{\partial F}{\partial f} \right)^2 \right]. \end{aligned} \tag{4.37}$$

Equation (4.27) defines the standard deviation in the amplitude of the aligned curves σ_A. Similarly the standard deviation σ_f, in the frequency $f_i(f_0) = f_0 + \Delta f_i(f_0)$, after alignment may be defined as

$$\sigma_f^2 = \frac{1}{N(N-1)} \left[N \sum_{i=0}^{N} \Delta f_i^2 - \left(\sum_{i=0}^{N} \Delta f_i \right)^2 \right]. \tag{4.38}$$

The covariance C_{Af} of the amplitudes and frequencies of the aligned curves is

$$C_{Af} = \frac{1}{N(N-1)} \left[N \sum_{i=0}^{N} (\Delta A_i \Delta f_i)^2 - \left(\sum_{i=0}^{N} \Delta A_i \right) \left(\sum_{j=0}^{N} \Delta f_j \right) \right]. \tag{4.39}$$

Substituting equations (4.27), (4.38) and (4.39) into equation (4.37) yields

$$\sigma_{ua}^2 \approx \sigma_A^2 + \sigma_f^2 \frac{\partial F}{\partial f}^2 - 2 \frac{\partial F}{\partial f} C_{Af}. \tag{4.40}$$

The unaligned uncertainty has been successfully related to: the uncertainty in the amplitude of the aligned curves; the uncertainty in the frequency of the aligned curves; and the covariance of the amplitudes and frequencies of the aligned curves. Equation (4.40) is first order accurate in the frequency shifts Δf_i. Figure 4.11 shows the unaligned uncertainty, and the uncertainty predicted using equation (4.40) for the field backscattered from a PEC sphere with an uncertain radius. Once again there is good agreement between the unaligned

uncertainty and the unaligned uncertainty reconstructed using equation (4.40) at the lower frequencies. However at the higher frequencies, where the assumption that Δf_i is small is worse, the agreement between the unaligned uncertainty and reconstructed unaligned uncertainty is also worse. The mathematical arguments described here, along with the comparisons made by Figures 4.10 and 4.11, show that there is a relationship between the uncertainty calculated using unaligned curves, and the uncertainties calculated after the curves are aligned. These mathematical relationships show that aligning the curves provides more information on whether the uncertainty is due to amplitude or frequency differences. Curve alignments will therefore be used in this thesis to quantify the amplitude and frequency uncertainties in the output curves.

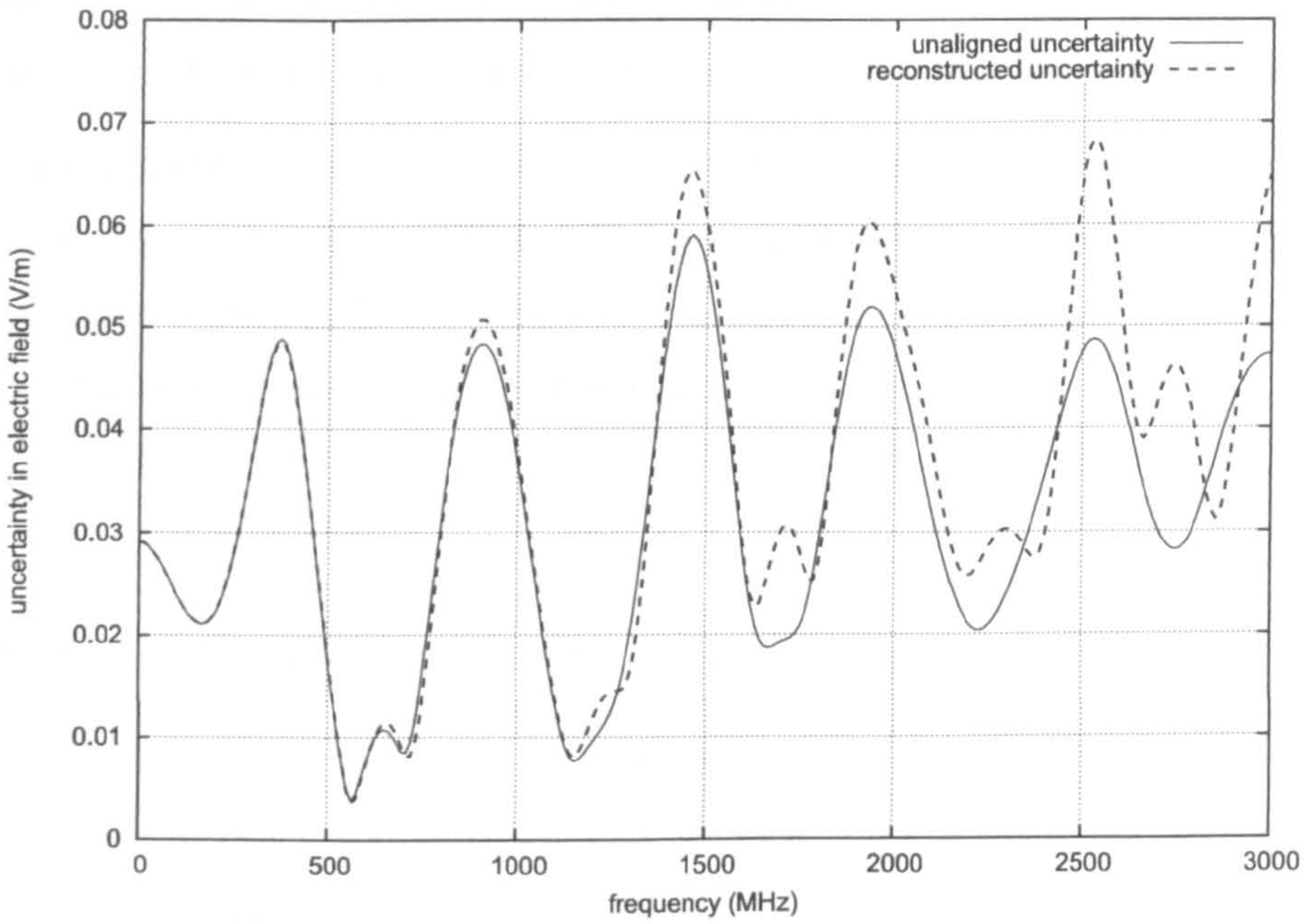

Figure 4.11: Unaligned amplitude uncertainty and reconstructed unaligned amplitude uncertainty

This section has described the MCM, the sampling method that is used with the MCM, the way in which the convergence of the MCM is tested in this thesis, and the relationship between aligned and unaligned uncertainties calculated using the MCM. The next section introduces the second probabilistic method of estimating the uncertainty in the output of CEM simulations called the Method of Moments (MoM). The MoM is computationally much faster than the MCM, however its estimates of the output uncertainty are less accurate than those provided by the MCM.

4.6 Method of Moments

The MoM is an approximate method for estimating the mean and uncertainty in some output quantity. The first order method uses the mean and variance to analyse the output uncertainty [83]. The MoM is the internationally accepted method outlined in GUM [16] for the propagation of uncertainties through a model. A similar method is outlined in UKAS [2] for the estimation of the uncertainty in practical EMC measurements. The MoM has previously been applied to a 2D-TLM method [84], and was shown to be accurate for small parameter variations, whilst being computationally more efficient than the MCM. In this section a brief overview of the method will be given. The method will then be analysed empirically using a set of analytically solvable examples. These examples will be used to show situations where the MoM underestimates and overestimates the uncertainty.

Moment methods provide approximations to the mean and variance, of a specified output value, by constructing truncated Taylor series expansions about the expected value of the input parameters [10]. Let y be a function of only one variable denoted by x. The function y may be expanded about the mean input value $\bar{x}$ to give

$$y(x) = y(\bar{x}) + \left.\frac{dy}{dx}\right|_{x=\bar{x}} (x-\bar{x}) + \left.\frac{d^2y}{dx^2}\right|_{x=\bar{x}} \frac{(x-\bar{x})^2}{2} + \ldots. \tag{4.41}$$

Taking the expected value of both sides of equation (4.41) yields

$$E(y) = y(\bar{x}) + \frac{1}{2}\left.\frac{d^2y}{dx^2}\right|_{x=\bar{x}} \sigma_x^2 + \ldots \tag{4.42}$$

where σ_x is the uncertainty in x. The first order estimate of the mean μ_{1st} is given by

$$\mu_{1st} = y(\bar{x}). \tag{4.43}$$

This first order estimate is obtained by truncating the initial Taylor series to first order. In doing this it is assumed that y depends linearly on x. This assumption will only be valid for values of x close to the mean value. The second order estimate of the mean μ_{2nd} is obtained by truncating the Taylor series to second order, to give

$$\mu_{2nd} = y(\bar{x}) + \frac{1}{2}\left.\frac{d^2y}{dx^2}\right|_{x=\bar{x}} \sigma_x^2. \tag{4.44}$$

This second order estimate of the mean is more accurate than the first order estimate. It will

however only be accurate if the higher order moments of x are small. Forming the second order estimate of the mean is more computationally expensive, than forming the first order estimate, because more simulations are required to estimate the second order derivative in equation (4.44).

The variance in y may be obtained by first finding the expected value of y^2 [85]. Replacing y with y^2 in equation (4.44) yields

$$E(y^2) = y^2(\bar{x}) + \frac{1}{2}\left.\frac{d^2(y^2)}{dx^2}\right|_{x=\bar{x}} \sigma_x^2 \tag{4.45}$$

$$= y^2(\bar{x}) + \left.\left[\left(\frac{dy}{dx}\right)^2 + \frac{dy}{dx}\frac{d^2y}{dx^2}\right]\right|_{x=\bar{x}} \sigma_x^2. \tag{4.46}$$

The first order estimate of the uncertainty in y, denoted by $\sigma_{1st}(y)$, is calculated using the standard definition of the variance:

$$\sigma_{1st}(y)^2 = E(y^2) - E(y)^2 \tag{4.47}$$

$$= y^2(\bar{x}) + \left.\left[\left(\frac{dy}{dx}\right)^2 + y(\bar{x})\frac{d^2y}{dx^2}\right]\right|_{x=\bar{x}} \sigma_x^2 - \left(y(\bar{x}) + \frac{1}{2}\left.\frac{d^2y}{dx^2}\right|_{x=\bar{x}} \sigma_x^2\right)^2 \tag{4.48}$$

$$= \sigma_x^2 \left(\frac{dy}{dx}\right)^2 \tag{4.49}$$

where terms involving σ_x^4 are ignored. The second order estimate of the variance is obtained similarly [10] as

$$\sigma_{2nd}(y)^2 = \sigma_x^2 \left(\frac{dy}{dx}\right)^2 + \frac{1}{2}\left(\frac{d^2y}{dx^2}\sigma_x^2\right)^2. \tag{4.50}$$

The uncertainties are the square roots of these variances. These estimates of the uncertainty are formed using truncated Taylor series expansions, they will therefore only be accurate if the input uncertainty σ_x is small [85].

These mean and uncertainty estimates are easily generalised for functions that depend on multiple input parameters. Let y depend on n uncertain input parameters $\mathbf{p} = p_1, \ldots, p_n$, with mean values $\bar{\mathbf{p}} = \bar{p}_1, \ldots, \bar{p}_n$ and associated uncertainties (standard deviations) $\mathbf{u} = u_1, \ldots, u_n$. The first order estimates of the mean $\bar{y}_{1st}$ and uncertainty $\sigma_{1st}(y)$ are

$$\bar{y}_{1st} = y(\bar{\mathbf{p}}) \tag{4.51}$$

$$\text{and} \quad \sigma_{1st}(y) = \sqrt{\sum_{i=1}^{n}\left(\frac{\partial y}{\partial p_i}u_i\right)^2 + \sum_{i\neq j}^{n}\frac{\partial y}{\partial p_i}\frac{\partial y}{\partial p_j}\mathrm{cov}(p_i, p_j)}, \tag{4.52}$$

where all the sensitivity derivatives are evaluated at the mean parameter values $\bar{\mathbf{p}}$. In practical EMC measurements, input parameters that have a nonzero covariance are grouped together so that the term involving the covariance of different parameters in (4.52) can be ignored [2]. Throughout this thesis, the uncertain input parameters are independent, and therefore their covariance is zero. This reduces equation (4.52) to

$$\sigma_{1st}(y) = \sqrt{\sum_{i=1}^{n} \left(\frac{\partial y}{\partial p_i} u_i \right)^2}. \tag{4.53}$$

It is possible that in some scenarios the input parameters will not be independent. For example if a parallel plate capacitor, filled with a dielectric, is being modelled then moving the position of one of the capacitor plates will also move the boundary of the dielectric. The position of the capacitor plates and the dielectric are therefore dependent with a nonzero covariance.

It is important to remember that the uncertainty estimates formed in this section rely on truncated Taylor series expansions. The first order truncated Taylor series is used to obtain the first order estimates of the mean and uncertainty. Thus the output y is assumed to depend linearly on the input parameters. If the output depends on the input in a nonlinear manner, then the first order MoM estimate of uncertainty will only be accurate for small input uncertainties [85]. EMC data is often highly nonlinear at certain frequencies. At these frequencies the output of interest may also depend on the inputs in a highly nonlinear way. The MoM will provide poor estimates of the mean and uncertainty in these cases.

4.6.1 The Method of Moments in Computational Electromagnetic Simulations

The MoM can be easily applied to all areas of Computational Electromagnetism. A brief description of the application of the method to FDTD simulations is given here. Suppose the output E of an FDTD simulation depends on the frequency f and n uncertain input parameters $p_1, \ldots, p_n$. The output may then be written as a function of the frequency and the uncertain parameters:

$$E = E(f, p_1, \ldots, p_n). \tag{4.54}$$

To calculate the variance in the output due to the variance in the input parameters, the sensitivity derivative of the output with respect to each individual input parameter must first be found. The sensitivity of the output to parameter p_i is approximated using a forward

difference approximation to give

$$\left.\frac{\partial E}{\partial p_i}\right|_{(f,\bar{p_1},\ldots,\bar{p_n})} = \frac{E(f,\bar{p_1},\ldots,\bar{p_i}+\delta_i,\ldots,\bar{p_n}) - E(f,\bar{p_1},\ldots,\bar{p_i},\ldots,\bar{p_n})}{\delta_i}. \tag{4.55}$$

For a FDTD simulation this amounts to performing one simulation with the input parameters taking on their mean values to obtain $E(f,\bar{p_1},\ldots,\bar{p_i},\ldots,\bar{p_n})$, and one simulation with the ith parameter value perturbed by a small value δ_i. To obtain all n sensitivity derivatives, which are required to calculate the variance in E, $n+1$ simulations must be performed. For simulations with many different input parameters, this could equate to a large amount of computer runtime. The computational runtime should however be significantly less than that required for the MCM.

The appropriate size of the perturbation δ_i has been suggested to be of a similar size to the input uncertainty $\sigma(p_i)$ [2]. It is well known that the forward difference approximation is more accurate when smaller perturbations are used. However, the mathematical accuracy of the sensitivity derivative is not always the prime concern when performing the UA. The MoM uses the sensitivity derivative to convert the uncertainty in the input to an uncertainty in the output [2]. Using a larger perturbation of $\delta_i = \sigma(p_i)$ will account for how the output varies for larger (possible) changes in the input parameter.

This thesis includes examples that use FDTD simulations to model EMC scenarios involving uncertain geometric input parameters. The perturbations in these geometric parameters must coincide with the FDTD mesh, this results in perturbations that may differ in size from the size of the input uncertainty. For the examples in this thesis, the perturbation does not always take on a value that is exactly the same as the input uncertainty. The chosen perturbations are of a similar size to that of the input uncertainties, but are often slightly smaller to maintain the numerical accuracy of the sensitivity derivative.

In the previous section it was noted that the MoM is only valid if the uncertainties in the input parameters take on small values. In the next section a number of examples will be used to show how the MoM performs for different nonlinear functions, with different sized uncertainties in the input parameters.

4.6.2 Empirical Analysis of the Method of Moments

The MoM is known to be valid for small input parameter uncertainties [84], [85]. The first order MoM is based on the assumption that the output depends linearly on the input

parameters. In this section an analysis of the performance of the MoM for nonlinear functions will be given. In all of these examples the functions will depend on one variable only.

A Small Input Uncertainty

Consider a function y that depends on an uncertain input parameter x as

$$y = 2x^2. \tag{4.56}$$

If x is uniformly distributed over the interval $[0.3, 0.4]$, then it has a mean value $\bar{x} = 0.35$ and an uncertainty

$$\sigma_x = \sqrt{\frac{(0.4 - 0.3)^2}{12}} = 0.02887. \tag{4.57}$$

This uncertainty is relatively small; only 0.8% of the mean. Since the uncertainty is small and the values of x are confined to a relatively small interval, the MoM should estimate the mean and uncertainty in y fairly well.

The mean may be calculated analytically using

$$\bar{y} = \int_{0.3}^{0.4} y(x) f(x) dx. \tag{4.58}$$

The function $f(x)$ in the above equation represents the PDF of x, in this case $f(x) = 10$ over the interval $x = [0.3, 0.4]$. The mean value of y is therefore

$$\bar{y} = \int_{0.3}^{0.4} 20x^2 dx = \left[\frac{20x^3}{3}\right]_{0.3}^{0.4} = 0.2467. \tag{4.59}$$

In a similar way the variance σ_y^2 in y is analytically calculated using

$$\sigma_y^2 = \int_{0.3}^{0.4} (y(x) - \bar{y})^2 f(x) dx \tag{4.60}$$

$$= \int_{0.3}^{0.4} 10(2x^2 - \bar{y})^2 dx \tag{4.61}$$

$$= 2\left[4x^5 - \frac{20}{3}x^3\bar{y} + 5\bar{y}^2 x\right]_{0.3}^{0.4} = 1.636 \times 10^{-3}. \tag{4.62}$$

Thus the uncertainty in y calculated analytically is $\sigma_y = 0.04044$. The mean and uncertainty calculated above may be used to test the performance of the MoM for this example.

The mean estimated by the MoM to first order is

$$\bar{y}_{1st} = y(\bar{x}) = 0.245. \tag{4.63}$$

This estimated mean is very close to the actual value of 0.2467 calculated above. The first order estimate of the uncertainty is

$$\sigma_{1st} = \sqrt{\left.\frac{dy}{dx}\right|^2_{x=\bar{x}} \sigma_x^2}. \tag{4.64}$$

A forward difference approximation is used in practical applications of the MoM. It is important to use small perturbations in calculating this finite difference approximation to keep the accuracy of the derivative approximation as high as possible. The first order estimate of the uncertainty calculated using the actual derivative is

$$\sigma_{1st} = \sqrt{(4\bar{x})^2 \sigma_x^2} = 0.04042. \tag{4.65}$$

This value is very close to the uncertainty calculated analytically. Therefore the MoM gives a very good prediction of the mean and uncertainty when the input uncertainty is small and the derivative used in the prediction of the uncertainty is accurate. Using a forward difference approximation for the derivative with a small perturbation ($\Delta x = 0.001$) yields

$$\sigma_{1st} = \sqrt{\left(\frac{2(0.351)^2 - 2(0.35)^2}{0.001}\right)^2 \sigma_x^2} = 0.04048. \tag{4.66}$$

This estimate of the uncertainty is still very close to the uncertainty calculated analytically. If a larger perturbation ($\Delta x = \sigma_x$) is used in the forward difference approximation then the uncertainty predicted is

$$\sigma_{1st} = \sqrt{\left(\frac{2(0.37887)^2 - 2(0.35)^2}{0.5}\right)^2 \sigma_x^2} = 0.04208. \tag{4.67}$$

This uncertainty estimate is less accurate, but is still fairly close to the analytically calculated uncertainty. In this example the uncertainty in the input is fairly small, in the next example a larger input uncertainty is considered. Through the next example it is shown that the MoM can both underestimate and overestimate the output uncertainty.

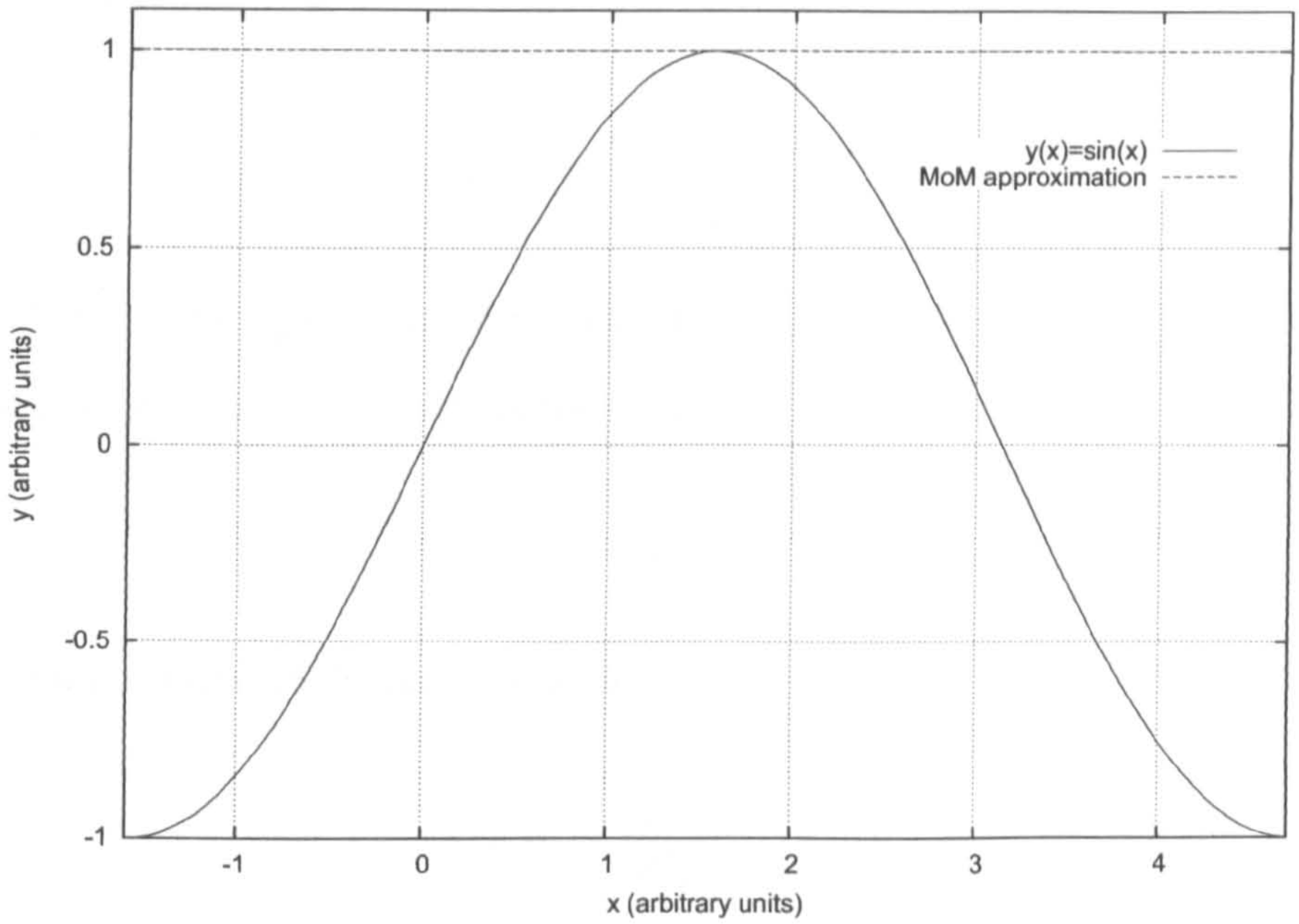

Figure 4.12: The function $y = \sin(x)$, and the MoM approximation of y at $x = \pi/2$.

A Larger Input Uncertainty

This example is used to show situations in which the MoM underestimates the output uncertainty, and situations in which the MoM overestimates the output uncertainty. These inaccurate estimations arise from the assumptions used to form the MoM.

Let y be a function that depends on an uncertain variable x as

$$y = \sin(x). \tag{4.68}$$

The uncertain variable x is Normally distributed with a mean $\bar{x} = \pi/2$ and an uncertainty $\sigma_x = \pi/4$. This point is at a maxima: the first derivative at this point is zero and the second derivative takes on its largest absolute value. Figure 4.12 shows the values of y for a range of x values, and the first order MoM approximation of y about the point $x = \bar{x}$. It is clear from this figure that for values of x that are further from $\bar{x}$, the MoM approximation is poor.

The mean value of y is

$$\bar{y} = \int_{-\infty}^{\infty} \sin(x) \frac{\exp\left(-\frac{(x-\pi/2)^2}{2(\pi/4)^2}\right)}{\frac{\pi}{4}\sqrt{2\pi}} dx = 0.7346. \tag{4.69}$$

Similarly the variance σ_y^2 is

$$\sigma_y^2 = \int_{-\infty}^{\infty} (\sin(x) - \bar{y})^2 \frac{\exp\left(-\frac{(x-\pi/2)^2}{2(\pi/4)^2}\right)}{\frac{\pi}{4}\sqrt{2\pi}} dx = 0.1060. \tag{4.70}$$

The uncertainty is the square root of this variance: $\sigma_y = 0.3255$.

The first order MoM estimate of the mean is

$$\bar{y}_{1st} = y(\bar{x}) = 1 \tag{4.71}$$

and first order estimate of the uncertainty is

$$\sigma_{1st} = \sqrt{\left.\frac{dy}{dx}\right|_{x=\bar{x}}^2 \sigma_x^2} = 0. \tag{4.72}$$

The estimated uncertainty is an underestimation of the actual uncertainty. This is because in the first order estimate, the sine wave is assumed to be linear at the point $x = \bar{x}$. At the mean value of x the function has a zero gradient. It is therefore assumed that around this point the value of the function does not change, and therefore the uncertainty in the output is zero. However, at this point the second derivative takes on its largest value. For a large input uncertainty it is possible for the output to vary significantly. The output uncertainty is therefore nonzero and the first order MoM estimate of the uncertainty is less than the actual value.

The second order MoM estimates of the mean and uncertainty are 0.6916 and 0.4362 respectively. These also differ from the actual mean and uncertainty, however they are better estimates than the first order estimates. The first order estimates of uncertainty are underestimations of the actual uncertainty at points where the first derivative (of the function with respect to the uncertain input variable) is low, the size of the second derivatives are relatively large, and the input uncertainty is also relatively large.

Using a forward difference approximation to the sensitivity derivative, with a perturbation equal to the input uncertainty yields

$$\sigma_{1st} = \sqrt{\left(\frac{\sin 3\pi/2 - \sin \pi/4}{\pi/4}\right)^2 (\pi/4)^2} = 0.2929. \tag{4.73}$$

This is much closer to the actual uncertainty since some of the variation of the output due to the uncertain input has been taken into account. The predicted uncertainty still underes-

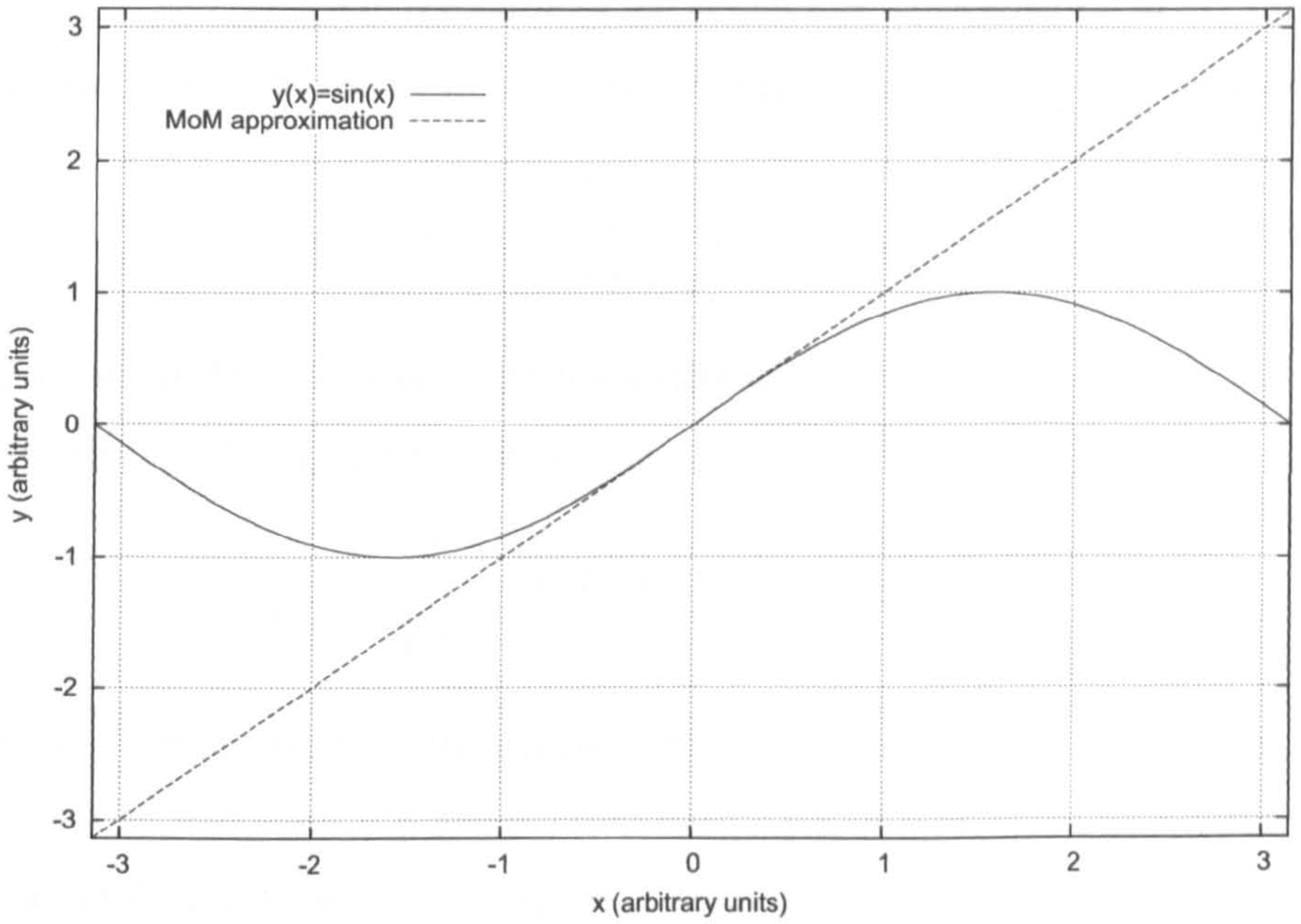

Figure 4.13: The function $y = \sin(x)$, and the MoM approximation of y at $x = 0$.

timates the actual uncertainty.

In the next example the uncertain variable x has a mean value $\bar{x} = 0$ and an uncertainty of $\pi/4$. At this point the first derivative takes on its largest value. Figure 4.13 shows the values of y for a range of x values about the point $x = \bar{x}$. This figure also shows the first order MoM approximation of y about the same point. It is clear from this figure that for values of x that are further from $\bar{x}$, the MoM approximation is poor.

The mean value of y is

$$\bar{y} = \int_{-\infty}^{\infty} \sin(x) \frac{\exp\left(-\frac{(x-0)^2}{2(\pi/4)^2}\right)}{\frac{\pi}{4}\sqrt{2\pi}} dx = 0 \tag{4.74}$$

the variance σ_y^2 is

$$\sigma_y^2 = \int_{-\infty}^{\infty} (\sin(x) - \bar{y})^2 \frac{\exp\left(-\frac{(x-0)^2}{2(\pi/4)^2}\right)}{\frac{\pi}{4}\sqrt{2\pi}} dx = 0.3544 \tag{4.75}$$

and the uncertainty is therefore $\sigma_y = 0.5953$.

The first order MoM estimate of the mean is

$$\bar{y}_{1st} = y(\bar{x}) = 0. \tag{4.76}$$

The estimated mean is exactly the same as the actual mean. This is due to the antisymmetry of the sine function at the mean input point. The first order estimate of the uncertainty is

$$\sigma_{1st} = \sqrt{\left.\frac{dy}{dx}\right|_{x=\bar{x}}^{2} \sigma_x^2} = 0.7854. \tag{4.77}$$

Using a forward difference approximation to the sensitivity derivative, with a perturbation equal to the the input uncertainty, yields

$$\sigma_{1st} = \sqrt{\left(\frac{\sin \pi/4 - \sin 0}{\pi/4}\right)^2 (\pi/4)^2} = 0.7071. \tag{4.78}$$

Notice that the estimated uncertainty is considerably larger than the actual uncertainty. This is because at this mean input point the first derivative of y takes on its largest value. The MoM assumes that y depends linearly on x, therefore at this point it is assumed that the output is sensitive to changes in the input, and the output uncertainty is predicted to be large. The sine function is however nonlinear, and the output points around this point of largest gradient do not vary by as much as if the function was linear. The actual uncertainty is therefore considerably less than the uncertainty predicted by the MoM.

These empirical analyses have shown that when the output of interest depends on the uncertain inputs in a nonlinear manner, and when the input uncertainties are not small, the MoM can underestimate and overestimate the uncertainty in the output. In the examples in Chapters 5-7 the output is shown to be related to the uncertain inputs in a highly non-linear manner, at certain frequencies. The MoM provides large peak overestimations of the uncertainty at these frequencies.

4.6.3 Using the Method of Moments to Calculate Confidence Intervals

The mean and uncertainty calculated using the MoM can be used to calculate 95% CI. To do this it is assumed that the output probability distribution is, or is very similar to, a Normal distribution. This assumption is based on the Central Limit Theorem, which states that the linear sum of a large set of independent identically distributed variables is approximately Normally distributed [16]. If μ is the mean output and σ is the uncertainty in this value calculated at a frequency f, then the upper and lower 95% CI values (represented

as CI_{upper} and CI_{lower} respectively) may be calculated as [16]

$$CI_{upper} = \mu(f) + 1.96\sigma(f) \tag{4.79}$$

$$CI_{lower} = \mu(f) - 1.96\sigma(f). \tag{4.80}$$

These CI are less accurate, in general, than those calculated for the MCM. This is because here the probability distribution of the output is assumed to be a Normal distribution, but the output is not always Normally distributed. No such assumption is made when forming the CI using data obtained from the MCM.

4.7 Polynomial Chaos

The concept of Homogeneous Chaos was first introduced by Wiener [86] in 1938 [87]. Ghanom and Spanos [88] pioneered Polynomial Chaos and applied it to problems in mechanics [12]. In the generalised method the output of interest is approximated as a function of certain orthogonal basis polynomials. The choice of the basis polynomials is dependent on the probability distributions of the uncertain input parameters [12]. It is possible to solve stochastic differential equations, involving the approximate function, by using the orthogonality of the polynomial basis set. The orthogonality of the basis polynomials reduces the stochastic differential equations to a set of deterministic differential equations, which can be solved numerically. Xiu and Karniadakis [12] found this approach to be computationally cheaper than the Monte Carlo Method. They found the mean and variance for a specific problem 500 times faster than the Monte Carlo Method, for the same accuracy [15]. They noted however that the methods efficiency is problem specific [15].

The following sections outline the theory behind Polynomial Chaos and how it is used to quantify uncertainty. The Homogeneous Chaos expansion is introduced in the next section. This expansion is then generalised to the Wiener-Askey Chaos expansion. General Polynomial Chaos uses the Wiener-Askey Chaos expansion to solve stochastic differential equations, and to quantify the uncertainty in this solution.

4.7.1 Homogeneous Chaos

Wiener [86] proposed the use of a Homogeneous Chaos expansion to represent a process, which depends on Normally distributed uncertain input parameters, in terms of Her-

mite polynomials. Cameron and Martin [89] proved that the expansion can be used to approximate any second order linear function. This means that the Homogeneous expansion can be used to expand second order random processes in terms of Hermite polynomials [12]. Second order random processes are processes with finite variance, which encompasses most physical processes [12].

If θ is a Normally distributed random event and $X(\theta)$ is a general second order random process, then the Homogeneous Chaotic expansion of $X(\theta)$ is [12]

$$\begin{aligned} X(\theta) =& a_0 H_0 \\ &+ \sum_{i_1=1}^{\infty} a_{i_1} H_1(\xi_{i_1}(\theta)) \\ &+ \sum_{i_1=1}^{\infty} \sum_{i_2=1}^{i_1} a_{i_1 i_2} H_2(\xi_{i_1}(\theta), \xi_{i_2}(\theta)) \\ &+ \sum_{i_1=1}^{\infty} \sum_{i_2=1}^{i_1} a_{i_1 i_2} \sum_{i_3=1}^{i_2} a_{i_1 i_2 i_3} H_3(\xi_{i_1}(\theta), \xi_{i_2}(\theta), \xi_{i_3}(\theta)) \\ &+ \dots . \end{aligned} \tag{4.81}$$

In the above expansion $H_n(\xi_{i_1}(\theta), \dots, \xi_{i_n}(\theta))$ is the nth Hermite polynomial, written in terms of the n standard Normally distributed variables $(\xi_{i_1}(\theta), \dots, \xi_{i_n}(\theta))$, which have zero mean and unit variance [12]. Using the notation $\boldsymbol{\xi} = (\xi_{i_1}(\theta), \dots, \xi_{i_n}(\theta))$, the Hermite polynomials are defined as

$$H_n(\boldsymbol{\xi}) = e^{\frac{1}{2}\boldsymbol{\xi}^T \boldsymbol{\xi}} (-1)^n \frac{\partial^n}{\partial \xi_{i_1} \dots \partial \xi_{i_n}} e^{-\frac{1}{2}\boldsymbol{\xi}^T \boldsymbol{\xi}}. \tag{4.82}$$

The a's in equation (4.81) are constant coefficients of the expansion. Equation (4.81) can be rewritten in a more convenient form as

$$X(\theta) = \sum_{j=0}^{\infty} \tilde{a}_j \phi_j(\boldsymbol{\xi}) \tag{4.83}$$

where there is a one-to-one correspondence between H_j and ϕ_j, and the $\tilde{a}_j$ represent the constant coefficients of the expansion [12]. The polynomial basis is orthogonal, which means that

$$< \phi_i \phi_j > = < \phi_i^2 > \delta_{ij} \tag{4.84}$$

where δ_{ij} is the Kronecker delta [12]. The inner product $< ., . >$ is defined as

$$< f(\xi)g(\xi) >= \int f(\xi)g(\xi)w(\xi)d\xi \tag{4.85}$$

where the function $w(\xi)$ is a weighting function corresponding to the chosen polynomial basis set. For the Hermite polynomial basis set, the weighting function is

$$w(\xi) = \frac{1}{\sqrt{(2\pi)^n}} e^{\frac{1}{2}\xi^T\xi}. \tag{4.86}$$

Ghanom and Spanos [88] applied this theory to problems in mechanics that involved Normally distributed random variables. A more general expansion is required to accurately represent stochastic processes that depend on random variables, which are not necessarily Normally distributed. Xiu and Karniadakis [12] proposed the Wiener-Askey Chaos expansion, which is based on polynomial bases from the Askey-scheme.

4.7.2 Wiener-Askey Chaos

Any second order random process X depending on some random event θ, can be represented as

$$X(\theta) = \sum_{j=0}^{\infty} c_j \psi_j(\zeta(\theta)) \tag{4.87}$$

where c_j are constant coefficients and $\zeta(\theta) = (\zeta_1(\theta), \zeta_2(\theta), \ldots)$ represents a vector containing an infinite number of independent random variables [12]. This summation is known as the Wiener-Askey Chaos expansion (or sometimes the Polynomial Chaos expansion). The polynomial basis set $\{\psi_j\}$, corresponding to the random variables $\zeta(\theta)$, are chosen from the Askey-scheme as shown in Table 4.1.

The polynomial basis sets are all orthogonal, which implies that

$$< \psi_i\psi_j >=< \psi_i^2 > \delta_{ij} \tag{4.88}$$

where once again δ_{ij} is the Kronecker delta and the inner product $< ., . >$ is defined as [12]

$$< f(\zeta)g(\zeta) >= \int f(\zeta)g(\zeta)w(\zeta)d\zeta. \tag{4.89}$$

Here the weighting function $w(\zeta)$ will correspond to the choice of the polynomial basis $\{\psi_j\}$.

	Random Variable ζ	Polynomial Basis Set ψ_j	Support
Continuous	Normal	Hermite	$(-\infty, \infty)$
	Gamma	Laguerre	$[0, \infty)$
	Beta	Jacobi	$[a, b]$
	Uniform	Legendre	$[a, b]$
Discrete	Poisson	Charlier	$\{0, 1, 2, \ldots\}$
	Binomial	Krawtchouk	$\{0, 1, \ldots, N\}$
	Negative Binomial	Meixner	$\{0, 1, 2, \ldots\}$
	Hypergeometric	Hahn	$\{0, 1, \ldots, N\}$

Table 4.1: The polynomial basis sets corresponding to the different types of random variables. The support is the domain over which the variables are defined, the symbols a and b are real constants and N is a positive finite integer.

4.7.3 General Polynomial Chaos

The Polynomial Chaos expansion can be used to solve stochastic differential equations [12]. Let $u(x, t, \theta)$ be a solution of the stochastic differential equation

$$\mathcal{L}(x, t, \theta)u(x, t, \theta) = f(x, t, \theta) \tag{4.90}$$

where x, t and θ represent position, time and some random event respectively. The symbol $\mathcal{L}$ represents some differential operator and f is a source term [12]. The solution u may be regarded as a random process and expanded as [12]

$$u(x, t, \theta) = \sum_{i=0}^{P} u_i(x, t)\psi_i(\zeta(\theta)). \tag{4.91}$$

Notice here that the infinite sum has been truncated at P. If d is the order of the highest order polynomial used in the expansion, and n is the dimension of the random variable ζ, then [12]

$$P + 1 = \frac{(n + d)!}{n!d!}. \tag{4.92}$$

Substituting the expansion of u into equation (4.90) yields

$$\mathcal{L}(x, t, \theta) \sum_{i=0}^{P} u_i(x, t)\psi_i(\zeta(\theta)) = f(x, t, \theta). \tag{4.93}$$

The inner product of both sides of this equation can be formed with ψ_k to give

$$\left\langle \mathcal{L}(x, t, \theta) \sum_{i=0}^{P} u_i(x, t)\psi_i(\zeta(\theta)), \psi_k \right\rangle =< f(x, t, \theta), \psi_k > . \tag{4.94}$$

The orthogonality of the polynomials from the basis set causes this equation to be reduced to a set of $(P+1)$ differential equations, one for each u_i [12]. These equations no longer contain any random components and are therefore deterministic [12]. The set of deterministic differential equations can be numerically solved to find each u_i. Once each u_i is found the mean and variance of $u(x,t,\theta)$ can be calculated. The mean μ is calculated as [18]

$$\begin{aligned}\mu =& < u(x,t,\theta),1 >= \sum_{i=0}^{P} u_i < \psi_i,1 > \\ &= \sum_{i=0}^{P} u_i < \psi_i,\psi_0 >= \sum_{i=0}^{P} u_i\delta_{i0} = u_0 \end{aligned} \tag{4.95}$$

using the fact that for all the distributions the lowest order polynomial $\psi_0 = 1$. The variance σ^2 can be obtained in a similar way by first calculating

$$\begin{aligned}< u(x,t,\theta),u(x,t,\theta) > &= \sum_{i=0}^{P}\sum_{j=0}^{P} u_iu_j < \psi_i,\psi_j > \\ &= \sum_{i=0}^{P}\sum_{j=0}^{P} u_iu_j\delta_{ij} < \psi_i^2 >= \sum_{i=0}^{P} u_i^2 < \psi_i^2 > . \end{aligned} \tag{4.96}$$

The variance σ^2 of $u(x,t,\theta)$ is [18]

$$\begin{aligned}\sigma^2 =& < u(x,t,\theta),u(x,t,\theta) > - < u(x,t,\theta),1 >^2 \\ &= \sum_{i=0}^{P} u_i^2 < \psi_i^2 > -u_0^2 = \sum_{i=1}^{P} u_i^2 < \psi_i^2 > . \end{aligned} \tag{4.97}$$

The uncertainty in $u(x,t,\theta)$ is defined as the standard deviation of $u(x,t,\theta)$, which is simply the square root of the above variance.

4.7.4 Generalised Polynomial Chaos in One Dimensional Finite Difference Time Domain

Generalised Polynomial Chaos has already been successfully applied to CFD [13],[14], and to specific areas of CEM [18]. Generalised Polynomial Chaos has yet to be applied to the FDTD method. A new application of Generalised Polynomial Chaos to the 1D FDTD method is given here, these arguments can easily be generalised to 3D.

Maxwell's equations can be written in 1D as

$$\frac{\partial H_z}{\partial t} = -\frac{1}{\mu}\frac{\partial E_y}{\partial x} \tag{4.98}$$

$$\frac{\partial E_y}{\partial t} = -\frac{1}{\epsilon}\left(\frac{\partial H_z}{\partial x} + \sigma E_y\right). \tag{4.99}$$

As usual $H_z(x,t)$ represents the magnetic field oriented in the z direction, at a position x and time t, similarly E_y represents the electric field. The symbols μ, ϵ and σ represent the permeability, permittivity and conductivity of the medium in which the electromagnetic fields propagate. CEM models seek to solve the coupled equations (4.98) and (4.99) to find approximations for $H_z(x,t)$ and $E_y(x,t)$. If there are uncertain input parameters then the solutions will depend on a random event θ. Thus, the output field solutions can be represented as $H_z(x,t,\theta)$ and $E_y(x,t,\theta)$. Maxwell's equations may be solved approximately using the 1D FDTD scheme, first proposed by Yee in 1966 [46]. The FDTD scheme is described in detail in Section 2.3, it is summarised again here.

In Yee's scheme central difference approximations are used for the partial derivatives of space and time. The problem space is discretised into cells of length Δx, and time is split into discrete intervals Δt. This yields two update equations, which form the basis of the 1D FDTD solution. The update equations formed are

$$H_z^{n+\frac{1}{2}}\left(j+\frac{1}{2},\theta\right) = H_z^{n-\frac{1}{2}}\left(j+\frac{1}{2},\theta\right) - \gamma[E_y^n(j+1,\theta) - E_y^n(j,\theta)] \tag{4.100}$$

and

$$E_y^{n+1}(j,\theta) = \alpha E_y^n(j,\theta) + \beta\left[H_z^{n+\frac{1}{2}}\left(j-\frac{1}{2},\theta\right) - H_z^{n+\frac{1}{2}}\left(j+\frac{1}{2},\theta\right)\right]. \tag{4.101}$$

The shorthand notation $H_z^n(j,\theta) = H_z(j\Delta x, n\Delta t, \theta)$, is used in the above equations, where j and n are positive integers. The material properties of the medium in which the fields propagate are represented by

$$\alpha = \alpha(x,\theta) = \frac{1-\sigma(x,\theta)\Delta t/2\epsilon(x,\theta)}{1+\sigma(x,\theta)\Delta t/2\epsilon(x,\theta)} \tag{4.102}$$

$$\beta = \beta(x,\theta) = \frac{\Delta t}{\Delta x\epsilon(x,\theta)(1+\sigma(x,\theta)\Delta t/2\epsilon(x,\theta)} \tag{4.103}$$

$$\gamma = \gamma(x,\theta) = \frac{\Delta t}{\Delta x\mu(x,\theta)}. \tag{4.104}$$

The material properties μ, ϵ and σ all depend on the uncertain parameter θ. This dependence

is defined by the PDFs of the input parameters.

The 1D FDTD update equations defined above are used to obtain solutions for the electric and magnetic field, subject to some input excitation. The field solutions can be expanded in terms of the appropriate orthogonal polynomials $\{\psi_i\}$, to separate the dependence of the field on the random parameter θ from the dependence on time and position. Using the Wiener-Askey Chaos expansion, the field solutions become

$$E_y^n(j,\theta) = \sum_{i=0}^{P} e_i^n(j)\psi_i(\zeta(\theta)) \tag{4.105}$$

$$H_z^n(j,\theta) = \sum_{i=0}^{P} h_i^n(j)\psi_i(\zeta(\theta)) \tag{4.106}$$

where $e_i^n(j)$ and $h_i^n(j)$ are coefficients that need to be found. These expanded expressions can be substituted into equations (4.100) and (4.101) to obtain

$$\sum_{i=0}^{P} h_i^{n+\frac{1}{2}}(j+1/2)\psi_i(\zeta(\theta)) = \sum_{i=0}^{P}\Big[h_i^{n-\frac{1}{2}}(j+1/2)\psi_i(\zeta(\theta)) - \gamma\left(e_i^n(j+1) - e_i^n(j)\right)\psi_i(\zeta(\theta))\Big] \tag{4.107}$$

and

$$\sum_{i=0}^{P} e_i^{n+1}(j)\psi_i(\zeta(\theta)) = \sum_{i=0}^{P}\Big[\alpha e_i^n(j)\psi_i(\zeta(\theta)) + \beta\left(h_i^{n+\frac{1}{2}}(j-1/2) - h_i^{n+\frac{1}{2}}(j+1/2)\right)\psi_i(\zeta(\theta))\Big]. \tag{4.108}$$

At this point an electric field source E_s may be added into equation (4.108). If this field source has some associated uncertainty then it may be expanded as

$$E_s^n(j,\theta) = \sum_{i=0}^{P} e_{i,s}^n(j)\psi_i(\zeta(\theta)). \tag{4.109}$$

Adding this source term into equation (4.108) yields

$$\sum_{i=0}^{P} e_i^{n+1}(j)\psi_i = \sum_{i=0}^{P}\Big[\alpha e_i^n(j)\psi_i + e_{i,s}^n(j)\psi_i + \beta\left(h_i^{n+\frac{1}{2}}(j-1/2) - h_i^{n+\frac{1}{2}}(j+1/2)\right)\psi_i\Big]. \tag{4.110}$$

Taking the inner product of both sides of equations (4.107) and (4.110) with some test polynomial $\psi_k(\boldsymbol{\zeta}(\theta))$, where $0 \leq k \leq P$, reduces the expressions to

$$h_k^{n+\frac{1}{2}}(j+1/2) = h_k^{n-\frac{1}{2}}(j+1/2) - \frac{1}{<\psi_k^2>}\sum_{i=0}^{P}\left[\left(e_i^n(j+1) - e_i^n(j)\right) < \gamma\psi_i\psi_k >\right] \tag{4.111}$$

and

$$e_k^{n+1}(j) = e_{k,s}^{n+1}(j) + \frac{1}{<\psi_k^2>}\sum_{i=0}^{P}\left[e_i^n(j) < \alpha\psi_i\psi_k > + \left(h_i^{n+\frac{1}{2}}(j-1/2) - h_i^{n+\frac{1}{2}}(j+1/2)\right) < \beta\psi_i\psi_k >\right]. \tag{4.112}$$

The above two equations make use of the orthogonality relation

$$< \psi_i\psi_k >= \delta_{ik} < \psi_k^2 > . \tag{4.113}$$

The material properties α, β and γ enter the inner products in equations (4.111) and (4.112) due to their dependence on θ.

Equations (4.111) and (4.112) can be used to calculate $e_i^n(j)$ and $h_i^{n+1/2}(j+1/2)$ for all n and j, and for $i = 0, \ldots, P$. In order to do this the inner products $< \alpha\psi_i\psi_k >$, $< \beta\psi_i\psi_k >$ and $< \gamma\psi_i\psi_k >$ must first be calculated for all $i, k = 0, \ldots, P$. These can be calculated as a preprocess, the update equations can then be used in a similar manner to the leapfrog scheme used in conventional FDTD. The source term must also be calculated at each time step as

$$e_{k,s}^n(j) = \frac{1}{<\psi_k^2>} < e_s^n(j,\theta)\psi_k(\boldsymbol{\zeta}(\theta)) > . \tag{4.114}$$

Lastly, update equations are required at the boundary. Here we shall consider using the 1st order Mur ABC [51]. If the lower boundary is at $j = 0$, then the usual update equation is

$$E_y^{n+1}(0) = E_y^n(1) + \sqrt{\frac{\beta(1)\gamma(1)-1}{\beta(1)\gamma(1)+1}}\left(E_y^{n+1}(1) - E_y^n(0)\right). \tag{4.115}$$

Introducing uncertainty into this equation via dependence on θ yields

$$E_y^{n+1}(0,\theta) = E_y^n(1,\theta) + \sqrt{\frac{\beta(1,\theta)\gamma(1,\theta)-1}{\beta(1,\theta)\gamma(1,\theta)+1}}\left(E_y^{n+1}(1,\theta) - E_y^n(0,\theta)\right).$$

As before, the field terms can be expanded using the chaotic expansion and an inner product of both sides of the resulting equation can be taken with some polynomial ψ_k from the basis set. Carrying out these two steps produces

$$e_k^{n+1}(0) = e_k^n(1) + \frac{1}{<\psi_k^2>}\sum_{i=0}^{P}\left(e_i^{n+1}(1) - e_i^n(0)\right) <\xi(1,\theta)\psi_i\psi_k> \tag{4.116}$$

where ξ is defined as

$$\xi(1,\theta) = \sqrt{\frac{\beta(1,\theta)\gamma(1,\theta)-1}{\beta(1,\theta)\gamma(1,\theta)+1}}. \tag{4.117}$$

Usually at the boundaries the properties of the medium are that of free space and therefore there is usually no uncertainty in these parameter values. Thus ξ will have no θ dependence and $<\xi\psi_i\psi_k> = \xi <\psi_k^2>$. This simplifies the update equation for the electric field at the lower boundary to

$$e_k^{n+1}(0) = e_k^n(1) + \xi(1)\left(e_k^{n+1}(1) - e_k^n(0)\right) \tag{4.118}$$

for $k = 0,\ldots,P$. Using a similar argument the electric field update equation at the upper boundary ($j = N$) is found to be

$$e_k^{n+1}(N) = e_k^n(N-1) + \xi(N-1)\left(e_k^{n+1}(N-1) - e_k^n(N)\right). \tag{4.119}$$

This completes the set of equations required to calculate $e_k^n(j)$ at each time step n, each spatial position j and for $k = 0,\ldots,P$. Similar equations to (4.95)-(4.97) may be formed to calculate the mean value μ of $E_y^n(j,\zeta(\theta))$ as

$$\mu = e_0^n(j) \tag{4.120}$$

and the variance σ^2 as

$$\sigma^2 = \sum_{i=1}^{P}(e_i^n(j))^2 <\psi_i^2> . \tag{4.121}$$

This mean and uncertainty can be used to calculate 95% CI, in the same manner as for the

MoM (see Section 4.6.3).

Polynomial chaos is easily applied to the FDTD method because the update equations follow a very similar form to those in the ordinary FDTD method. The only extra step comes in calculating the integrals that correspond to the inner products defined in the update equations (4.111) and (4.112). The PCM is computationally cheaper than the MCM, requiring fewer calculations overall to provide an estimate of the uncertainty. The PCM will however require more computational memory than the MoM and the MCM. This is because the PCM calculates the numerous chaotic field coefficients using one large simulation, storing a factor $P+1$ more field values and $(P+1)^2$ more material parameter values (via the inner products) than the MCM and the MoM.

One problem with the PCM arises when trying to form the mean and uncertainty of some related quantity, which does not depend linearly on $E_y^n(j,\theta)$. For example the output of interest may be the absolute value of $E_y^n(j,\theta)$. The mean μ of this output is formed as

$$\mu =< |E_y^n(j,\theta)|, 1 >= \left\langle \left| \sum_{i=0}^{P} e_i^n(j)\psi_i(\zeta(\theta)) \right| \psi_0 \right\rangle . \tag{4.122}$$

The absolute value within the inner product prevents the orthogonality of the basis polynomials from being used to form a simple relationship for the mean. The mean will have to be calculated using a numerical integration over the uncertain parameter space θ. This presents a problem with the PCM; the calculation of the mean of the output of interest quantity is not always trivial. Some of the mathematical simplicity of the PCM has been lost by trying to form the mean of the quantity $|E_y^n(j,\theta)|$. The mean must be calculated using a numerical integration at each frequency point, this requires extra computational time. This extra computational expense is however small compared to the PCM simulation runtime. Once this mean has been calculated the variance σ^2 may be calculated using the standard definition

$$\sigma^2(|E_y^n(j,\theta)|) =< (|E_y^n(j,\theta)| - \mu)^2 > . \tag{4.123}$$

Further numerical integrations are required to obtain this variance. The uncertainty in $|E_y^n(j,\theta)|$ is the square root of this variance.

4.8 Discussion

This chapter has introduced the different Error and Uncertainty Analysis methods that are used to quantify the error and uncertainty in the output of CEM simulations in Chapters 5-7. In cases where the analytical solution of the simulated scenario is known, the analytical error and uncertainty can be calculated. These can be used as benchmarks by which the performance of the other Error and Uncertainty Analysis methods can be compared.

An estimation of some of the errors may be obtained by calculating more accurate FDTD results using higher order techniques and mesh refinements. The difference between the results of the FDTD simulations and the more accurate FDTD simulations should provide an estimate of the error in the output of the less accurate FDTD simulations. This error will be an estimate of the unaligned amplitude error. Using curve alignments it is possible to calculate the aligned amplitude and frequency errors. In this chapter a relationship between the aligned and unaligned errors has been derived and shown to be valid for small frequency errors. The aligned errors provide more information on whether the error in an output curve is an amplitude or frequency error.

The probabilistic uncertainty analysis methods that are used in this thesis are the MCM, the MoM and the PCM. LHS is used alongside the MCM, since it has been shown to be more efficient than other sampling methods [80]. The MCM requires a large number of simulations to reach convergence, and is therefore computationally expensive. The convergence of the MCM is determined in a novel way using the FSV method. The results of the MCM simulations are used to form the sample mean, uncertainty and 95% CI. These CI are formed empirically using the Kaplan-Meier ECDF [82].

Using curve alignment it is possible to obtain the aligned amplitude and frequency uncertainty. These aligned uncertainties provide more information on the way in which the uncertainty in the output manifests itself: uncertainty in the frequency or uncertainty in the amplitude. In this chapter relationships between the aligned and unaligned uncertainties (formed using the MCM) have been derived. These relationships were shown to be valid so long as the uncertainty in the frequency is not too large.

The MoM is computationally much faster than the MCM. The first order MoM uses a linear approximation to represent the dependence of the output on the individual input parameters. This linear approximation is inaccurate in cases where the output depends non-

linearly on the input parameters and the uncertainty in the input parameters is large. These inaccuracies have been investigated in this chapter using a number of examples. Through these examples it has been shown that the MoM can both overestimate and underestimate the actual uncertainty. The MoM may also be used to calculate the 95% CI about the mean value. These CI are calculated using the assumption that the output PDF is a Normal distribution: this will not always be the case. The 95% CI calculated using the PCM are formed in a similar way as for the MoM.

The novel implementation of the PCM into the FDTD method was presented in this chapter. The implementation results in similar update equations to those used in the conventional FDTD method. Extra numerical integrations are required to obtain the inner products of the uncertain input parameters, which appear in the modified FDTD update equations. If the mean and uncertainty of the absolute value of the electric field is the quantity of interest, then more numerical integrations are required. These numerical integrations add to the computational expense of this method. The PCM can be used to calculate the mean and uncertainty more efficiently than the MCM. The method will however require extra computational memory.

In the next three chapters, the Error and Uncertainty Analysis methods are applied to a number of CEM simulations. The performance of these methods will be tested in terms of their accuracy at predicting the errors and uncertainties, and in terms of their computational expense.

Chapter 5

Error and Uncertainty Analyses Applied to a One Dimensional Finite Difference Time Domain Simulation

Contents

5.1 Introduction

Error and Uncertainty Analyses are applied to an analytically solvable example in this chapter. The chosen example considers the scattering of a Gaussian pulse from a dielectric slab, in one dimension. The output electric field is recorded at some distance from the slab in the time domain. This electric field is transformed into the frequency domain, and the error and uncertainty in this frequency response are calculated using the methods outlined in Chapter 4.

The analytical solution of this example is used to calculate the exact error in the output of FDTD simulations. Comparing this exact error to the results of other error prediction methods helps determine the accuracy of the methods. The results of these methods are compared to the exact error using the FSV method. The methods are also compared in terms of their computational expense.

The FSV method is also used to compare the results of progressively refined FDTD simulations to determine when convergence has been reached. Using the FSV method in this novel way provides a consistent, automatic and nonsubjective way of determining the convergence of the refined FDTD simulations. To start with a relatively coarse FDTD mesh is considered, the simulation performed on this mesh is referred to as the coarse simulation in this chapter. This coarse mesh is refined by factors of two, four, eight and sixteen (halving the cell size each time). The FSV method determines that the simulations performed on meshes refined by factors of eight and sixteen are "excellent" matches. The FDTD simulation performed on the mesh that was refined by a factor sixteen represents the converged FDTD simulation. This simulation is performed on a relatively fine mesh and is therefore referred to as the fine simulation in this chapter. The Error Analyses, in this chapter, are applied to both the coarse and fine FDTD simulations.

The analytic solution, of the example in this chapter, is used to form the analytic mean and uncertainty. The three uncertainty analyses (the MCM, the MoM and the PCM) are all applied to the analytic solution, and their predictions of the mean and uncertainty are compared to the analytic mean and uncertainty. The FSV method is again used to obtain a nonsubjective comparison of these means and uncertainties. These comparisons are used to determine which UA method most accurately predicts the analytic uncertainty for this example. It is found that the MCM provides the best estimates of the uncertainty in the analytic solution for this example. The MCM is therefore used as a benchmark for the uncertainty

predictions obtained for the FDTD simulations of the same example.

The three UAs are applied to the coarse and fine FDTD simulations. The uncertainties predicted by the MoM and the PCM are compared to those calculated using the benchmark MCM, to determine their respective ability to accurately predict the uncertainty in the output. The FSV method is used to compare the output curves produced by the three UA methods. All three UAs are also compared in terms of their computational expense.

The uncertainties predicted by the MCM for the analytic solution and the coarse and fine FDTD simulations are also compared. This helps determine whether there is a relationship between the errors and uncertainties in these FDTD simulations. If the uncertainties in the output of a simulation do not depend on the accuracy with which that simulation was performed, then computationally cheaper, less accurate solutions may be used to determine the uncertainty in more accurate simulations. This will reduce the computational expense of the UAs. For the example in this chapter, the overall size of the output uncertainty has only a small dependence on the accuracy of the simulation.

Finally, curve alignment is used to obtain the aligned uncertainties via the MCM and the MoM. This helps determine how the uncertainties in the output manifest themselves. For this example the uncertainty in the output is a combination of the uncertainty in the amplitude and the frequencies of the curves. Without curve alignment it is impossible to differentiate between the uncertainties in the amplitude and the uncertainties in the frequencies. Once again the uncertainties in the coarse, fine and analytical solutions are compared to determine whether there is a relationship between the error and the aligned uncertainties. Following this conclusions are drawn on the main findings of this work.

5.2 A Dielectric Slab in One Dimension

In this example, a Gaussian pulse is introduced to a one dimensional problem space. The problem space contains a dielectric slab, which has an uncertain length and permittivity. The left hand end of the slab is assumed to be fixed at $x = 0.1$m, while the right hand end follows a Normal distribution with mean position $\bar{x}_{end} = 0.2$m and standard deviation $\sigma(x_{end}) = 0.005$m. The relative permittivity of the slab also follows a Normal distribution with a mean $\bar{\epsilon}_r = 4$ and a standard deviation $\sigma(\epsilon_r) = 0.5$. Notice that the uncertainty in the permittivity of the slab is relatively large, it is 12.5% of the mean value. This large input uncertainty may cause the first order MoM estimations of the output mean and uncertainty

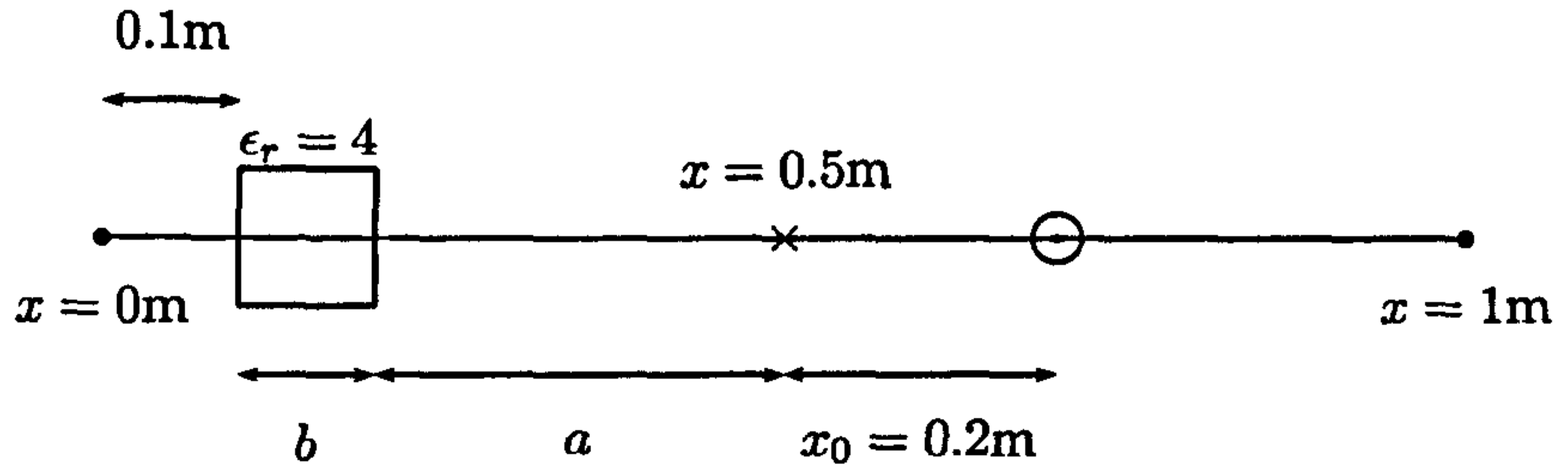

Figure 5.1: A one dimensional problem space containing a dielectric slab. A Gaussian pulse is excited at ⊙ and the resulting fields are observed at ×.

to be less accurate, as discussed in Section 4.6.2. Figure 5.1 represents the geometry of this example. In this figure the average length of b is $\bar{b} = 0.1$m and the average length of a is $\bar{a} = 0.3$m.

The output electric field is recorded at the centre of the problem space. For this example, the quantity of interest is the absolute value of the frequency response of the output electric field component E_z, relative to a 1 V/m input excitation. This quantity is referred to as the normalised electric field throughout this discussion. The analytical solution of this example is obtained in the next section.

5.2.1 The Analytic Solution

For this example, a Gaussian pulse is propagated from the point $x = 0.7$m in a 1D problem space. The input excitation takes the form

$$E_z(x = 0.7, t) = E_0 \exp\left(\frac{-(t_0 - t)^2}{2\beta^2}\right) \tag{5.1}$$

where E_0 is the maximum amplitude of the pulse, t_0 is the onset time delay of the pulse in seconds, t is the time in seconds and β represents the width of the pulse at half its maximum height, in seconds. For this simulation $E_0 = 1$ (V/m), $t_0 = 40\Delta t$ and the duration $\beta = 5\sqrt{2}\Delta t$, where $\Delta t = 16.67$ps. This excitation is a broad Gaussian pulse, which is chosen so that the electric field can be calculated over a broad frequency range. The time response of the electric field is recorded at $x = 0.5$m for times from zero to 83.3ns.

The analytical solution to this problem, for the electric field at the specified observa-

tion point, is

$$E_z(x=0.5,t) = E_0\left[\exp\left(\frac{-(x_0/c_0+t_0-t)^2}{2\beta^2}\right) + R_{12}\exp\left(\frac{-(x_0/c_0+2a/c_0+t_0-t)^2}{2\beta^2}\right)\right.$$
$$\left. + \sum_{m=1}^{\infty}\left[T_{12}R_{21}^{2m-1}T_{21}\times\exp\left(\frac{-((x_0+2a)/c_0+2mb/c_d+t_0-t)^2}{2\beta^2}\right)\right]\right]. \quad (5.2)$$

The first term in equation (5.2) arises from the pulse propagating from the excitation point straight to the observation point. The second term represents the pulse travelling from the excitation point and reflecting off the right hand side of the dielectric slab and then travelling to the observation point. Finally the last summation term represents the pulse passing through the right hand side of the dielectric slab, making $2m-1$ reflections inside the slab (where m is a positive integer) and then passing out to the observation point. In this analytic solution, T_{12} and R_{12} represent the transmission and reflection coefficients for a wave passing from free space to the dielectric slab. Similarly T_{21} and R_{21} represent the transmission and reflection coefficients for a wave passing from the dielectric slab to free space. The speed of the electromagnetic wave in the dielectric is represented by c_d. The last term contains an infinite sum, which is approximated by taking the sum to $m=30$. Truncating this series at $m=30$ means that the accuracy of the final solution is of the order of 61 in R_{21}. The coefficient R_{21} is less than one, and therefore the error in the truncated series solution is extremely small.

The analytic time response may be transformed into the frequency domain via a Continuous Fourier Transform. To do this the following standard Fourier Transforms are needed:

$$e^{-t^2/\tau^2} \rightarrow \tau\sqrt{2\pi}e^{-\tau^2\omega^2/2} \quad (5.3)$$

$$x(t-\tau) \rightarrow X(\omega)e^{-j\omega\tau} \quad (5.4)$$

where t represents time, ω is the angular frequency, τ is a constant with units of time, and $X(\omega)$ is the Fourier transform of $x(t)$. Using these transforms, the analytic solution (represented by equation (5.2)) may be transformed to the frequency domain to obtain

$$E(t) \rightarrow E(\omega) = 2E_0\beta\sqrt{\pi}e^{-\beta^2\omega^2}\left[e^{-j\omega A} + R_{12}e^{-j\omega B} + \sum_{m=1}^{30}T_{12}R_{21}^{2m-1}T_{21}e^{-j\omega C_m}\right] \quad (5.5)$$

where

$$A = x_0/c_0 + t_0 \tag{5.6}$$

$$B = x_0/c_0 + 2a/c_0 + t_0 \tag{5.7}$$

$$\text{and} \quad C_m = (x_0 + 2a)/c_0 + 2mb/c_d + t_0. \tag{5.8}$$

This electric field is transformed to the normalised electric field by taking the absolute value of this field relative to the absolute value of the incident pulse. The incident pulse, given in equation (5.1), is easily transformed into the frequency domain. The resulting normalised electric field $\tilde{E}(\omega)$ is

$$\tilde{E}(\omega) = \left| e^{-j\omega\tilde{A}} + R_{12}e^{-j\omega\tilde{B}} + \sum_{m=1}^{30} T_{12}R_{21}^{2m-1}T_{21}e^{-j\omega\tilde{C}_m} \right| \tag{5.9}$$

where

$$\tilde{A} = x_0/c_0 \tag{5.10}$$

$$\tilde{B} = x_0/c_0 + 2a/c_0 \tag{5.11}$$

$$\text{and } \tilde{C}_m = (x_0 + 2a)/c_0 + 2mb/c_d. \tag{5.12}$$

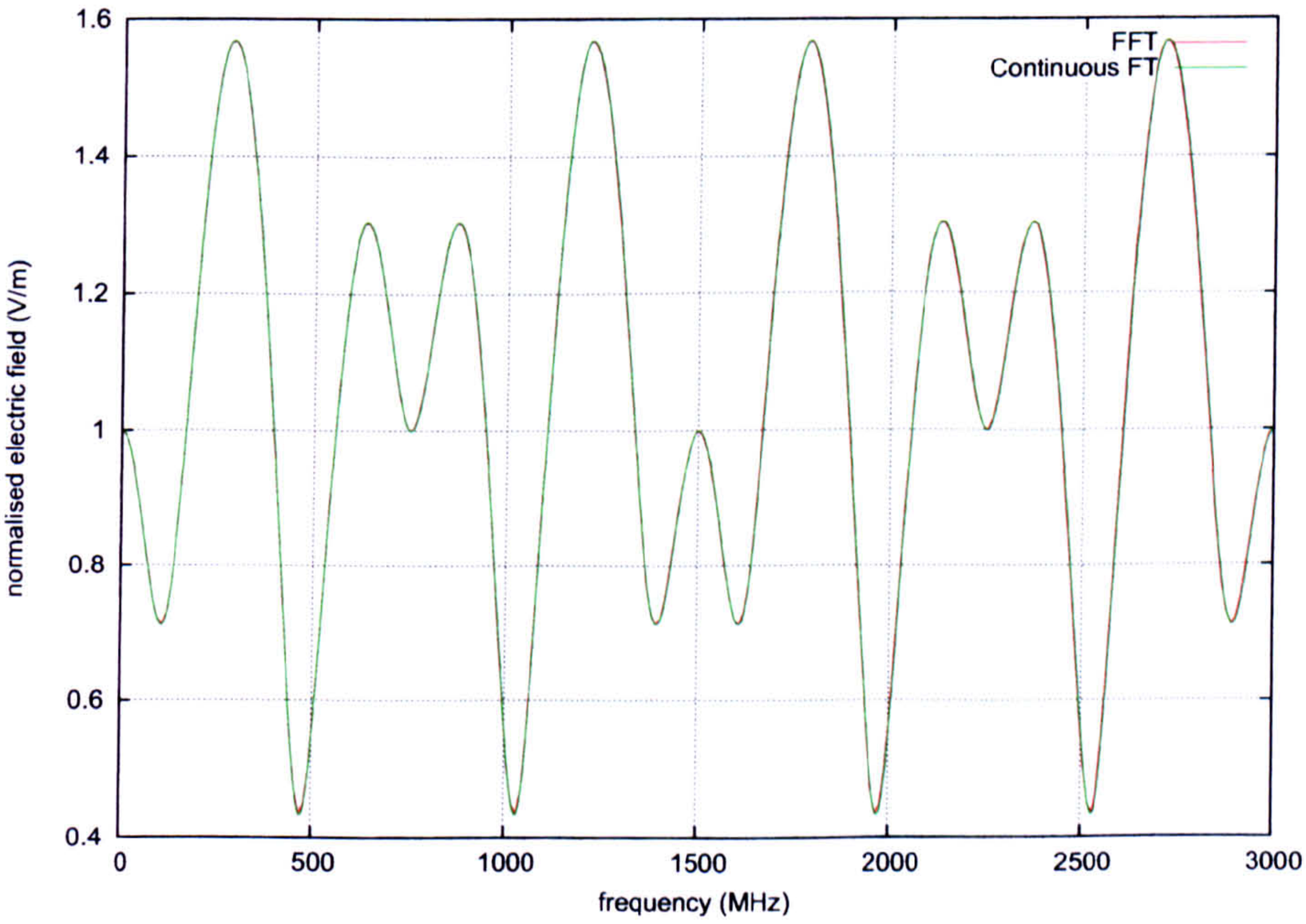

Figure 5.2: Frequency response of the analytic solution formed via an FFT and a Continuous Fourier Transform.

Figure 5.2 shows the analytic solution of the normalised electric field. The analytic solution (equation (5.9)) is simply a sum of complex exponentials, this results in the periodicity of the solution as shown in the figure. Figure 5.2 also displays the normalised electric field formed from the FFT of the time domain solution sampled at time intervals $\Delta t = 16.67$ ps. This time step corresponds to the time step used in an FDTD simulation with a cell size of $\Delta x = 0.01$m. The analytic solution formed from the Continuous Fourier Transform and the FFT, in Figure 5.2, are in excellent agreement (the two curves are coincident). No aliasing or sampling problems arise from using the specified time step for the FFT. This means that there will be no sampling or aliasing problems formed from the FFT of the FDTD simulation results if the same (or a smaller) time step is used for the FDTD simulations.

5.2.2 Frequency Response of the Normalised Electric Field

In the discussion that follows reference is made to certain refinement factors. These factors represent the extent to which a mesh is refined with respect to the coarse FDTD mesh size of $\Delta x = 0.01$m. Thus, a mesh refinement factor of two refers to a refined mesh of size $\Delta x = 0.01\text{m}/2 = 0.005$m, and a sampling time of $\Delta t = 16.67\text{ps}/2 = 8.335$ps. The FDTD simulation performed on a mesh with a refinement factor of one is referred to as the coarse simulation in the following discussion.

The frequency response of the electric field was calculated for the analytic solution, three (2,2) FDTD simulations with mesh refinement factors of one, two and four, and three (4,4) FDTD simulations also with mesh refinement factors of one, two and four. The computational time taken for each of the simulations can be found in Table 5.1. This table shows that the (4,4) simulations take longer to run than corresponding (2,2) simulations. With each factor two mesh refinement, twice as many field positions are being evaluated and for twice as many times; the runtime of the refined simulations should therefore increase by a factor

Method	time (s)
analytic	0.12
(2,2) refine=1	0.06
(4,4) refine=1	0.15
(2,2) refine=2	0.13
(4,4) refine=2	0.55
(2,2) refine=4	0.33
(4,4) refine=4	2.11

Table 5.1: Time taken to perform the respective simulations.

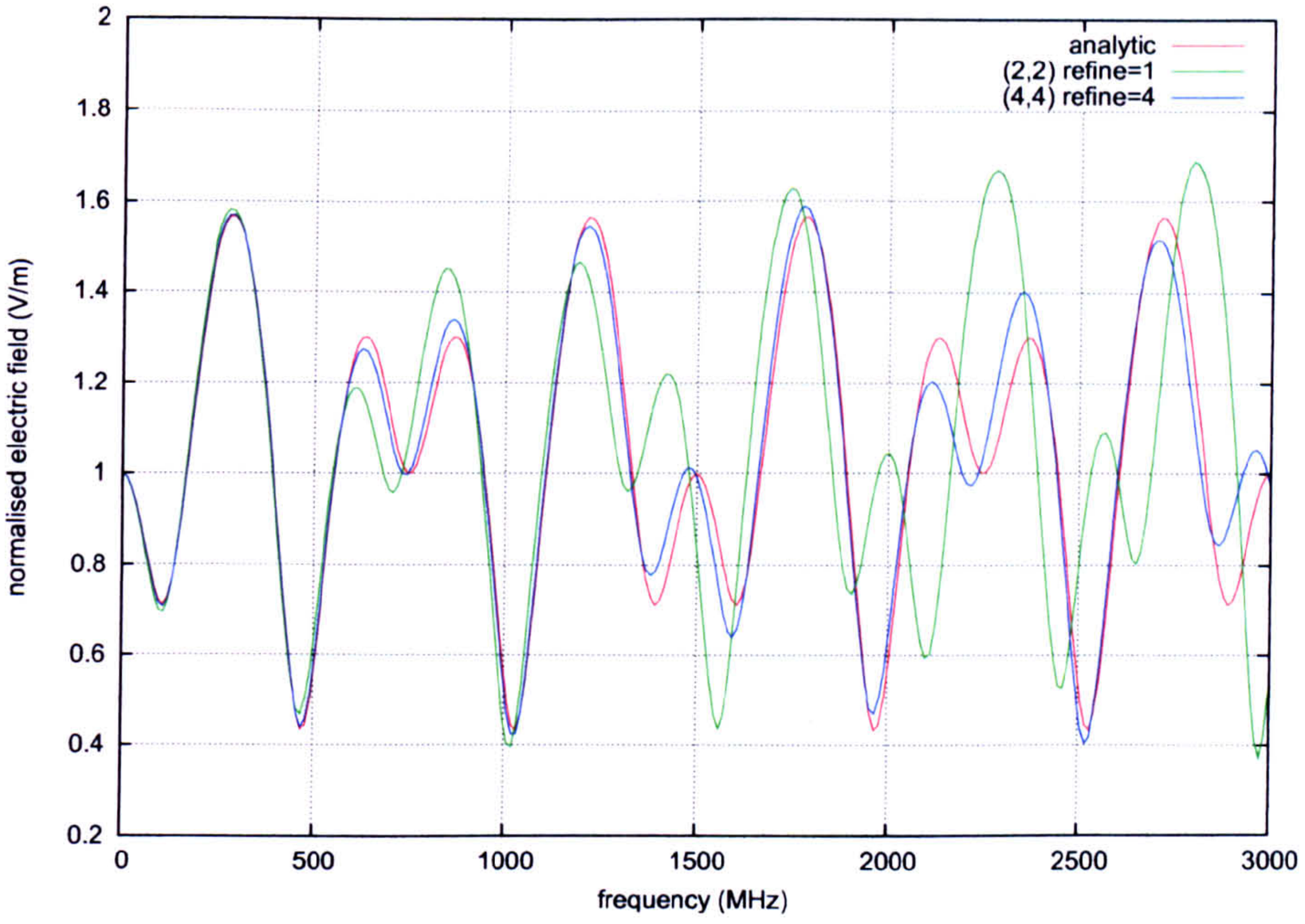

Figure 5.3: Frequency response of the normalised electric field, calculated analytically, using a (2,2) FDTD simulation with a refinement factor of one (refine=1) and a (4,4) simulation with a refinement factor of four (refine=4).

four. This is the case for the (4,4) simulations (as can be seen from Table 5.1), however for the (2,2) simulations the runtimes are so small that other processes dominate (such as the time taken to write output data to files).

In Section 2.4.1 it was shown that FDTD simulations are usually accepted as being accurate for wavelengths above $\lambda = 10\Delta x$. The coarse (2,2) FDTD simulation used a cell size of $\Delta x = 0.01$m, therefore the FDTD simulations should be valid for frequencies up to 3GHz. Figure 5.3 shows the frequency response of the electric field for the analytic solution, the coarse (2,2) FDTD simulated data and the more accurate (4,4) FDTD simulation using a mesh refinement factor of four. It is clear from the figure that the more accurate (4,4) simulation gives results much closer to the analytic result. The (2,2) simulated results are acceptable at lower frequencies but contain larger errors at the higher frequencies.

5.3 Error Analysis of the FDTD Simulation

The exact errors in the coarse (2,2) simulation may be found by taking the difference between the frequency response, formed from the simulation, and the analytical result. Other error predictions may be calculated by taking the difference between the frequency response of the coarse (2,2) simulation and the responses formed from more accurate sim-

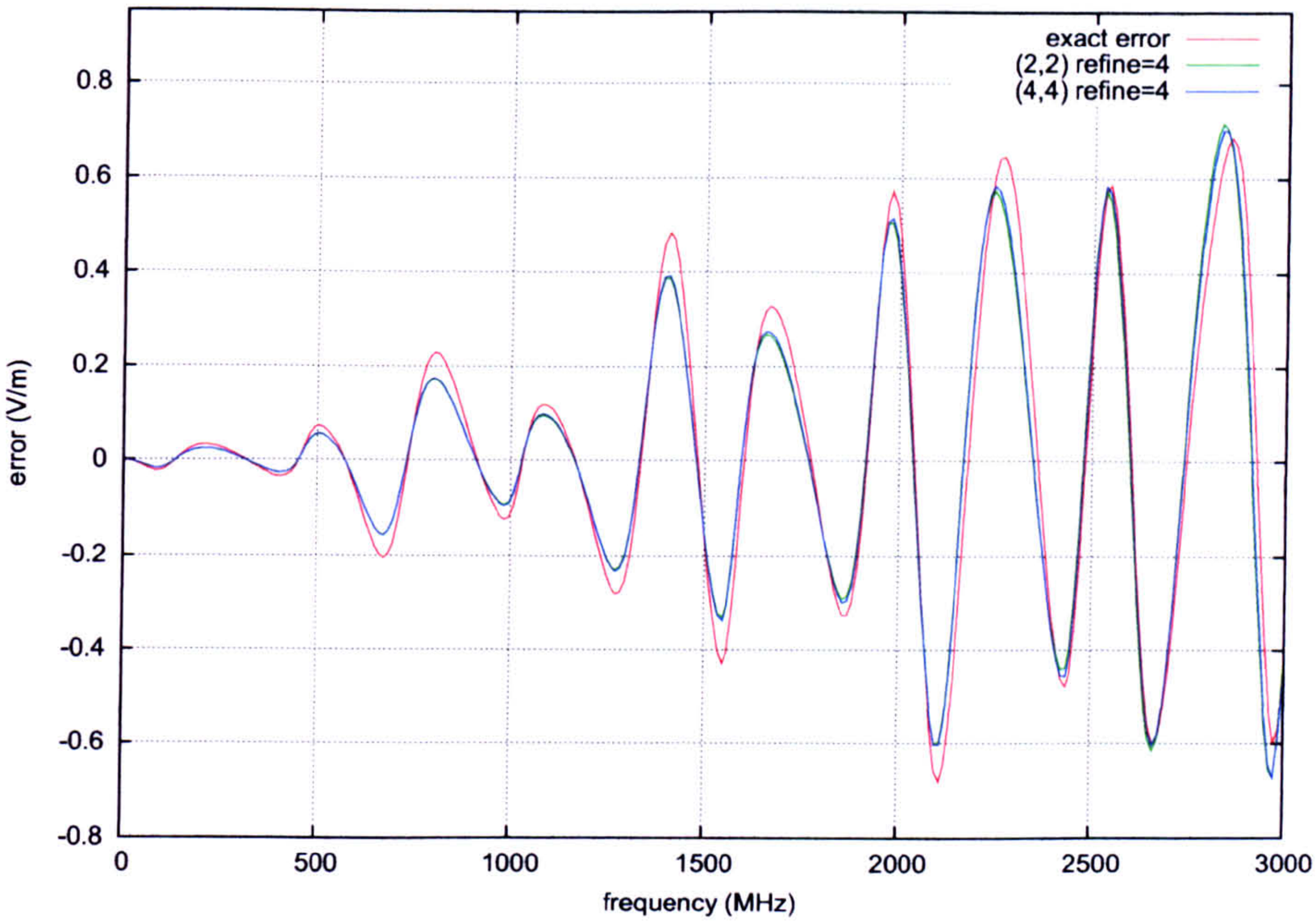

Figure 5.4: Error in the normalised electric field calculated analytically and using refined FDTD simulations.

ulations. Figure 5.4 displays the exact errors, in the coarse FDTD simulation, and the two most accurate error predictions. The curve labelled as "(2,2) refine=4", in Figure 5.4, refers to the error in the coarse FDTD simulation formed by taking the difference between the results of the coarse simulation and the results of a more accurate (2,2) simulation performed on a mesh with a refinement factor of four. Figure 5.4 shows that the errors increase as the frequency increases. The error predictions in Figure 5.4 are very similar to the exact errors. The errors predicted by the more complex (4,4) simulation are of a similar accuracy to the errors predicted using the (2,2) simulation, when a refinement factor of four is used for both.

The predicted errors may be compared to the exact errors using the FSV method: Table 5.2 displays the results of these comparisons. This table shows that the error predictions are better when the simulations used to form them are performed on more refined meshes. It may be concluded that there is a marginal benefit from using the (4,4) FDTD method as opposed to the (2,2) FDTD method, to predict errors. This benefit is very small though, and

Prediction Method	ADM	FDM	GDM	GDM (1-6)	Qualitative
(4,4) refine=1	1.2074	0.5549	1.4481	5.8114	Poor
(2,2) refine=2	0.6795	0.3025	0.7971	4.9953	Fair
(4,4) refine=2	0.5002	0.2287	0.5949	4.4899	Fair
(2,2) refine=4	0.2616	0.1241	0.3105	3.5577	Good
(4,4) refine=4	0.2218	0.1091	0.2658	3.3340	Good

Table 5.2: FSV comparisons of the predicted errors with the exact error.

Refinements compared	ADM	FDM	GDM	GDM (1-6)	Qualitative
1 and 2	0.2681	0.3368	0.4747	4.1892	Fair
2 and 4	0.1133	0.1571	0.2176	3.0932	Good
4 and 8	0.0558	0.0767	0.0.1059	2.0693	Very Good
8 and 16	0.0223	0.0287	0.0407	1.4066	Excellent

Table 5.3: FSV comparisons of simulated results calculated with different mesh refinements.

the (4,4) method is more complex to implement and more computationally expensive. It may therefore be concluded that using a (2,2) simulation with a mesh refinement factor of four or higher is the preferred error prediction method, in this example.

Figure 5.3 displays the large differences between the frequency response of the coarse (2,2) simulation and the analytic result. These differences are large because the coarse (2,2) FDTD simulation is not the converged simulation. This lack of convergence presents a need for further work to determine the accuracy of the Error Analysis methods when applied to converged simulations. The next section describes how to determine when a converged solution has been reached, and analyses the accuracy of the error prediction methods when applied to converged simulations.

5.3.1 Converged Simulations

It is possible to compare the results of a simulation with the results of the same simulation performed on a refined mesh using the FSV method. If the output curves are shown to be in good agreement (i.e. the curves are very good or excellent matches) then it can be concluded that convergence has been reached. This is a novel way of determining when convergence has been reached in FDTD simulations. Its advantage lies in that it does not rely on the subjective opinion of the experimenter and thus provides a more consistent method of obtaining the convergence of the FDTD simulations.

Table 5.3 shows the FSV comparisons of the simulated results formed from progressive mesh refinements. The results of the simulations performed on meshes with refinement factors of 8 and 16 are in excellent agreement; a mesh refinement of 16 therefore provides a solution that has sufficiently converged. An error analysis was performed on the results of this converged simulation. The exact error was calculated by taking the difference between the analytic solution and the output formed from the FDTD simulation. Previously, in this section, it was found that an accurate error prediction was formed by using FDTD simulations which were refined by a factor four. Thus, simulations using a mesh refinement of 64

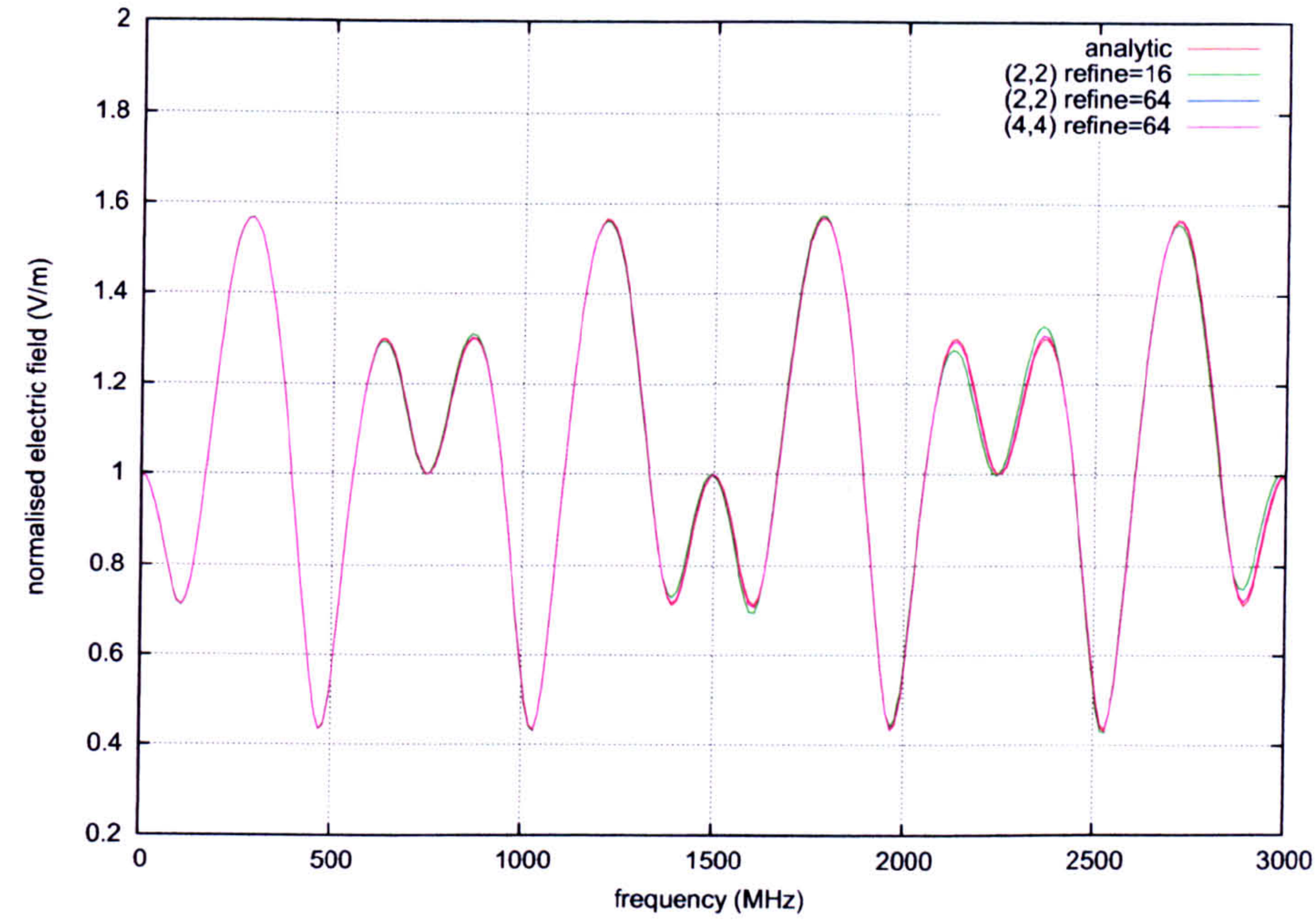

Figure 5.5: Frequency response of the normalised electric field calculated analytically and using (2,2) and (4,4) FDTD simulations with different mesh refinement factors.

were used to estimate the errors in the converged simulation. These error predictions were performed using both the (2,2) and (4,4) FDTD methods. The frequency responses formed from these simulations and the analytic solution are presented in Figure 5.5. The different curves in this figure are all very similar.

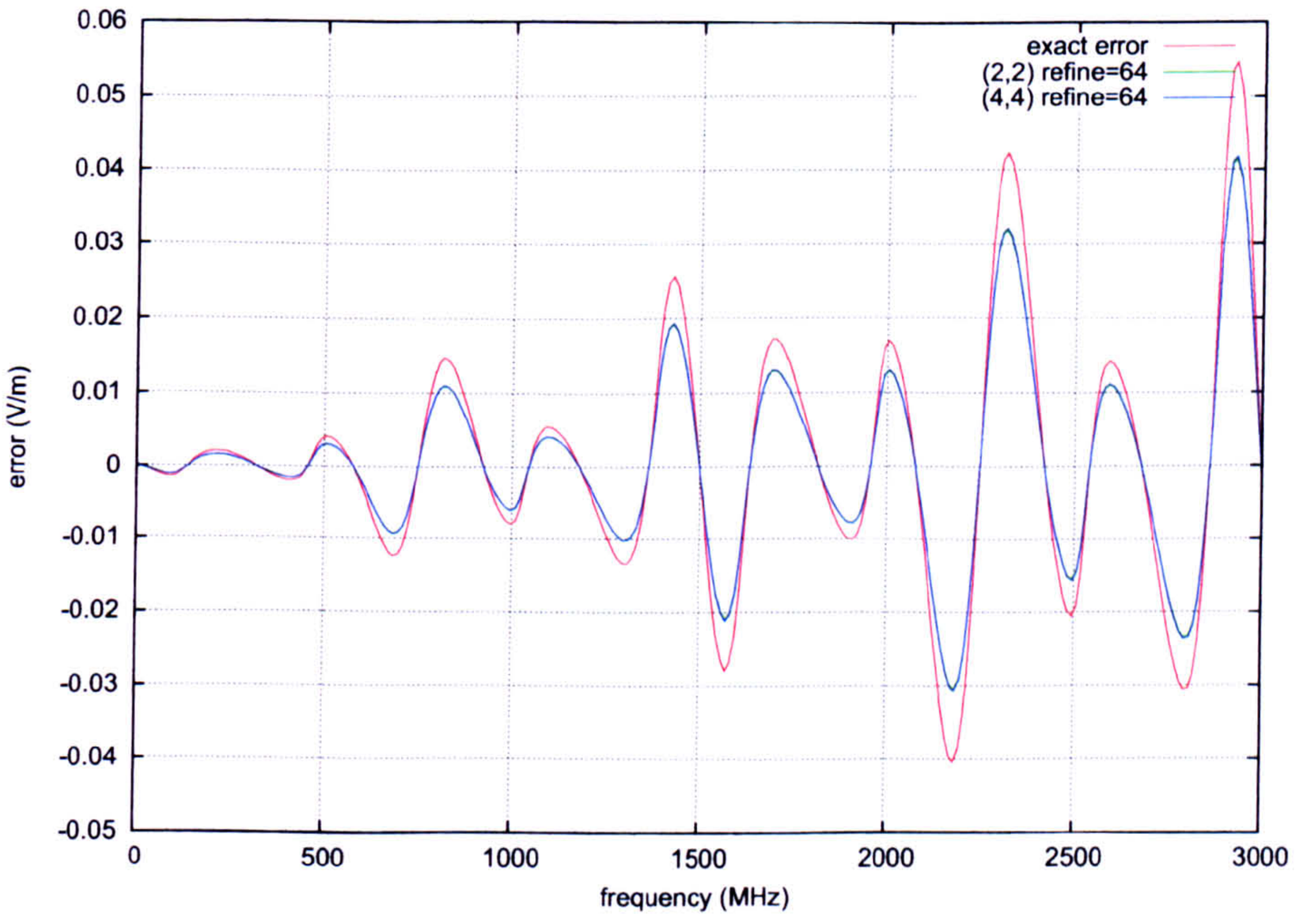

Figure 5.6: Error in the normalised electric field formed from the (2,2) FDTD simulation with a mesh with a refinement factor of 16.

Prediction Method	ADM	FDM	GDM	GDM (1-6)	Qualitative
(2,2) refine=64	0.3373	0.2226	0.4351	4.0901	Fair
(4,4) refine=64	0.3264	0.2172	0.4219	4.0572	Fair

Table 5.4: FSV comparisons of the predicted errors with the exact error.

Figure 5.6 shows the error in the converged FDTD simulation. This error is a factor of 10 smaller in magnitude than the error in the (2,2) simulation (shown in Figure 5.4), which was performed on a mesh with a refinement factor of one. This is as expected since the converged simulation is more accurate. The errors predicted by the (4,4) and (2,2) simulations are very similar. The FSV method was used to determine how similar the error predictions are to the exact error, the results of these comparisons may be found in Table 5.4. The FSV comparisons show that the two error prediction methods give a "fair" estimate of the exact error. However the GDM values obtained from these comparisons are close to four, thus the error predictions are much closer to being "good" estimates than "poor" estimates. Figure 5.6 shows that the features of the error predictions agree with the features of the exact error, however overall the error prediction methods underestimate the actual error. The (4,4) method does marginally better than the (2,2) method, having a slightly lower GDM value. The (4,4) method took 523 seconds to calculate the error, whilst the (2,2) method took only 40 seconds. Since both error prediction methods give fairly similar results and the (2,2) method is computationally quicker, it is the preferred method to use in this example. The error prediction method that uses the (2,2) refined FDTD simulations is applied to 3D FDTD simulations in the next chapter.

In the next section Uncertainty Analyses are applied to this example. The uncertainty is calculated for the analytic case, the coarse FDTD simulation and the converged (fine) FDTD simulation. Comparing the uncertainties calculated for these different cases will determine whether the uncertainty is related to the accuracy of the results, and thus whether there is a relationship between error and uncertainty.

5.4 Uncertainty Analyses Applied to the One Dimensional Example

The uncertainty in the output frequency response is determined in this section. Firstly the application of each of the UA methods to this specific example is described, the methods are then compared in terms of their accuracy and their computational expense. The

uncertainties for the coarse, fine and analytic solutions are compared to determine whether there is a relationship between the errors and uncertainties in these FDTD simulations. The results of the UAs are then used to construct the 95% Confidence Intervals (CI).

5.4.1 The Analytic Uncertainty

The mean $\bar{\tilde{E}}(f)$ and uncertainty $\sigma(\tilde{E}(f))$, of the normalised electric field $\tilde{E}(f)$, may be calculated analytically as

$$\bar{\tilde{E}}(f) = \int_{-\infty}^{\infty}\int_{-\infty}^{\infty} \tilde{E}(f) \frac{\exp\left(\frac{-(x-\bar{x}_{end})^2}{2\sigma(x_{end})^2}\right)}{\sigma(x_{end})\sqrt{2\pi}} \frac{\exp\left(\frac{-(\epsilon_r-\bar{\epsilon}_r)^2}{2\sigma(\epsilon_r)^2}\right)}{\sigma(\epsilon_r)\sqrt{2\pi}} dx\, d\epsilon_r \tag{5.13}$$

$$\sigma(\tilde{E}(f))^2 = \int_{-\infty}^{\infty}\int_{-\infty}^{\infty} (\tilde{E}(f) - \bar{\tilde{E}}(f))^2 \frac{\exp\left(\frac{-(x-\bar{x}_{end})^2}{2\sigma(x_{end})^2}\right)}{\sigma(x_{end})\sqrt{2\pi}} \frac{\exp\left(\frac{-(\epsilon_r-\bar{\epsilon}_r)^2}{2\sigma(\epsilon_r)^2}\right)}{\sigma(\epsilon_r)\sqrt{2\pi}} dx\, d\epsilon_r. \tag{5.14}$$

These two integrations are fairly complex and are therefore calculated approximately using numerical integrations. A numerical integration is performed at each frequency point f, this is quite costly and so the midpoint rule is used to approximate the integration. The midpoint rule is chosen to perform the integration because it is simple and computationally efficient. It must also be noted that the integrations are not defined over the whole domain. Using the whole domain would result in possible values for the end of the slab and the relative permittivity at positive and negative *infinity* (albeit with infinitesimal probabilities), which is unphysical. It is reasonable to truncate the domains of integration at more plausible values since the standard deviations are not too large. This also aids the computational efficiency of the numerical integrations. These numerical integrations have been verified against integrations performed using MAPLE.

5.4.2 The Monte Carlo Method

The LHS method was used to create 500 samples of the input parameters, based on their associated PDFs. These input parameter samples were used in the analytical solution and the 1D FDTD simulations to create numerous output frequency responses of the normalised electric field. The mean and standard deviation (uncertainty) of these outputs were then calculated. The FSV method was used to determine when the MCM has reached convergence, as described in Sections 3.2.3 and 4.5.2. For this example it was found that convergence was reached after 300 simulations for the analytic solution and both the coarse and fine (2,2) FDTD simulations. The MCM is the most rigorous method, it is also the most

computationally expensive method. However for this simple example the computational expense is not too large. The results of the 300 Monte Carlo simulations were also used to to form the Kaplan-Meier empirical cumulative distribution function [82], from which the 95% CI were calculated.

5.4.3 The Method of Moments

The MoM may be used in the manner described below to obtain the mean and uncertainty in the analytic solution and the FDTD simulations. For the purposes of the discussion below, "simulation" refers to both the calculation of the analytic result and an FDTD simulation, depending on which one the MoM is being applied to.

Three simulations are required to calculate the uncertainty using the MoM. One simulation was performed with the input parameters taking on their mean values, this is referred to as the reference simulation. The output of this reference simulation represents the mean of the normalised electric field. The second simulation was performed with the relative permittivity perturbed by $\Delta\epsilon_r = 0.1$. The final simulation was performed with the end position of the slab being perturbed from its mean value by one cell position $\Delta x = 0.01$m. In accordance with the calculation of uncertainty in practical EMC experiments [2], these perturbations are of a similar order of magnitude to the corresponding parameter uncertainties. Notice that the perturbation in the end position of the slab is confined to the FDTD mesh.

The frequency responses obtained from these three simulations are used to calculate the sensitivity derivatives of the output with respect to individual perturbations in the input parameters. The sensitivity derivatives are combined with the input uncertainties to calculate the uncertainty in the output, according to equations (4.51) and (4.53). Since only three simulations are required here, this method is computationally much cheaper than the MCM.

The 95% CI are calculated using the mean and uncertainty as outlined in Section 4.6.3. To calculate the CI the probability distribution of the output is assumed to be a Normal distribution, this will not always be the case. These CI may therefore be less accurate than those calculated for the MCM.

5.4.4 The Polynomial Chaos Method

This section describes the steps required to calculate the uncertainty using the PCM. Firstly the application of the PCM to the FDTD simulations is described. Following this the

details of the application of the PCM to the analytic solution are given.

Application to the Finite Difference Time Domain Simulations

The PCM requires the input uncertainties to be related to the material parameters in the FDTD chaotic update equations (4.111) and (4.112). In order to do this inner products must be formed, the values of which are calculated using numerical integrations. The numerical integrations can be quite costly, adding to the overall computational cost of this method.

Firstly the uncertainty in the permittivity of the slab must be related to θ_1, which follows a Normal distribution with mean equal to zero and standard deviation equal to one. The following relation fits this purpose

$$\epsilon_r = \bar{\epsilon}_r + \sigma(\epsilon_r)\theta_1 = 4 + 0.5\theta_1. \tag{5.15}$$

The uncertainty in the end point of the slab must be related to θ_2, another standard Normal. The following relation fits this purpose

$$x_{end} = \bar{x}_{end} + \sigma(x_{end})\theta_2 = 20\Delta x + 0.005\theta_2. \tag{5.16}$$

This uncertainty in the end position of the slab must now be related to the uncertainty in the permittivity at positions around the end of the slab. If a point in the problem space is inside the slab then $\epsilon_r = 4 + 0.5\theta_1$ otherwise $\epsilon_r = 1$. Consider a point $x = i\Delta x$, which is near the end point of the slab, this point is in the slab if

$$i\Delta x \leq x_{end} = 20\Delta x + 0.005\theta_2. \tag{5.17}$$

Thus x is in the slab if

$$\theta_2 \geq \frac{(i-20)\Delta x}{0.005}. \tag{5.18}$$

The relative permittivity at position $x = i\Delta x$ is represented by $\epsilon_r(i\Delta x, \theta_1, \theta_2)$ (the dependence on θ_1 and θ_2 represents the dependence on the two uncertain input parameters), and can be defined as

$$\epsilon_r(i\Delta x, \theta_1, \theta_2) = \begin{cases} 4 + 0.5\theta_1 & \text{for } \theta_2 \geq \frac{(i-20)\Delta x}{0.005} \\ 1 & \text{otherwise.} \end{cases} \tag{5.19}$$

Thus, the material parameter $\beta(i\Delta x, \theta_1, \theta_2)$, used in the FDTD Polynomial Chaos update equations (4.111) and (4.112), is defined as

$$\beta = \beta(i\Delta x, \theta_1, \theta_2) = \begin{cases} \frac{\Delta t}{(4+0.5\theta_1)\Delta x \epsilon_0} & \text{for } \theta_2 \geq \frac{(i-20)\Delta x}{0.005} \\ \frac{\Delta t}{\Delta x \epsilon_0} & \text{otherwise.} \end{cases} \tag{5.20}$$

In the above equation, the symbol ϵ_0 represents the permittivity of free space.

The input uncertainties follow Normal distributions, thus Hermite Polynomials must be used in the chaotic expansion of the electric fields. If the uncertainty is sought to first order, then the chaotic expansion is terminated at $P = 2$ for this example. Thus the Hermite polynomials required are

$$H_0 = 1 \tag{5.21}$$

$$H_1(\theta_1) = \theta_1 \tag{5.22}$$

$$\text{and } H_1(\theta_2) = \theta_2. \tag{5.23}$$

The inner product of these polynomials is

$$< H_i(\theta_k) H_j(\theta_l) >= \delta_{ij}\delta_{kl}(i)!. \tag{5.24}$$

The electric and magnetic fields are calculated using the update equations (4.111) and (4.112). Before these equations can be used the inner products, of the material parameters α, β and γ with the Hermite polynomials, need to be calculated. Since α and γ have no θ_1 or θ_2 dependence, their inner products reduce to

$$< \alpha H_i(\theta_k) H_j(\theta_l) > = \alpha < H_i(\theta_k) H_j(\theta_l) >= \alpha\delta_{ij}\delta_{kl}(i)! \tag{5.25}$$

$$\text{and } < \gamma H_i(\theta_k) H_j(\theta_l) > = \gamma < H_i(\theta_k) H_j(\theta_l) >= \gamma\delta_{ij}\delta_{kl}(i)!. \tag{5.26}$$

For ease of notation we may represent the polynomials in the chaotic expansion as $\psi_0 = H_0$,

$\psi_1 = H_1(\theta_1)$ and $\psi_2 = H_1(\theta_2)$. The inner products required for β are

$$
\begin{aligned}
< \beta\psi_0\psi_0 > &= \int_{-\infty}^{\infty}\left(\int_{-\infty}^{\infty}\beta\frac{\exp(-\frac{\theta_1^2}{2})}{\sqrt{2\pi}}d\theta_1\right)\frac{\exp(-\frac{\theta_2^2}{2})}{\sqrt{2\pi}}d\theta_2 \\
&= \frac{\Delta t}{\Delta x\epsilon_0}\int_{-\infty}^{\frac{(i-20)\Delta x}{0.005}}\left(\int_{-\infty}^{\infty}\frac{\exp(-\frac{\theta_1^2}{2})}{\sqrt{2\pi}}d\theta_1\right)\frac{\exp(-\frac{\theta_2^2}{2})}{\sqrt{2\pi}}d\theta_2 \\
&+ \int_{\frac{(i-20)\Delta x}{0.005}}^{\infty}\left(\int_{-\infty}^{\infty}\frac{\Delta t}{(4+0.5\theta_1)\Delta x\epsilon_0}\frac{\exp(-\frac{\theta_1^2}{2})}{\sqrt{2\pi}}d\theta_1\right)\frac{\exp(-\frac{\theta_2^2}{2})}{\sqrt{2\pi}}d\theta_2
\end{aligned}
\tag{5.27}
$$

$$
\begin{aligned}
< \beta\psi_0\psi_1 > =< \beta\psi_1\psi_0 > &= \int_{-\infty}^{\infty}\left(\int_{-\infty}^{\infty}\beta\theta_1\frac{\exp(-\frac{\theta_1^2}{2})}{\sqrt{2\pi}}d\theta_1\right)\frac{\exp(-\frac{\theta_2^2}{2})}{\sqrt{2\pi}}d\theta_2 \\
&= \frac{\Delta t}{\Delta x\epsilon_0}\int_{-\infty}^{\frac{(i-20)\Delta x}{0.005}}\left(\int_{-\infty}^{\infty}\theta_1\frac{\exp(-\frac{\theta_1^2}{2})}{\sqrt{2\pi}}d\theta_1\right)\frac{\exp(-\frac{\theta_2^2}{2})}{\sqrt{2\pi}}d\theta_2 \\
&+ \int_{\frac{(i-20)\Delta x}{0.005}}^{\infty}\left(\int_{-\infty}^{\infty}\frac{\Delta t}{(4+0.5\theta_1)\Delta x\epsilon_0}\theta_1\frac{\exp(-\frac{\theta_1^2}{2})}{\sqrt{2\pi}}d\theta_1\right)\frac{\exp(-\frac{\theta_2^2}{2})}{\sqrt{2\pi}}d\theta_2
\end{aligned}
\tag{5.28}
$$

$$
\begin{aligned}
< \beta\psi_1\psi_1 > &= \int_{-\infty}^{\infty}\left(\int_{-\infty}^{\infty}\beta\theta_1^2\frac{\exp(-\frac{\theta_1^2}{2})}{\sqrt{2\pi}}d\theta_1\right)\frac{\exp(-\frac{\theta_2^2}{2})}{\sqrt{2\pi}}d\theta_2 \\
&= \frac{\Delta t}{\Delta x\epsilon_0}\int_{-\infty}^{\frac{(i-20)\Delta x}{0.005}}\left(\int_{-\infty}^{\infty}\theta_1^2\frac{\exp(-\frac{\theta_1^2}{2})}{\sqrt{2\pi}}d\theta_1\right)\frac{\exp(-\frac{\theta_2^2}{2})}{\sqrt{2\pi}}d\theta_2 \\
&+ \int_{\frac{(i-20)\Delta x}{0.005}}^{\infty}\left(\int_{-\infty}^{\infty}\frac{\Delta t}{(4+0.5\theta_1)\Delta x\epsilon_0}\theta_1^2\frac{\exp(-\frac{\theta_1^2}{2})}{\sqrt{2\pi}}d\theta_1\right)\frac{\exp(-\frac{\theta_2^2}{2})}{\sqrt{2\pi}}d\theta_2
\end{aligned}
\tag{5.29}
$$

$$
\begin{aligned}
< \beta\psi_0\psi_2 > =< \beta\psi_2\psi_0 > &= \int_{-\infty}^{\infty}\left(\int_{-\infty}^{\infty}\beta\frac{\exp(-\frac{\theta_1^2}{2})}{\sqrt{2\pi}}d\theta_1\right)\theta_2\frac{\exp(-\frac{\theta_2^2}{2})}{\sqrt{2\pi}}d\theta_2 \\
&= \frac{\Delta t}{\Delta x\epsilon_0}\int_{-\infty}^{\frac{(i-20)\Delta x}{0.005}}\left(\int_{-\infty}^{\infty}\frac{\exp(-\frac{\theta_1^2}{2})}{\sqrt{2\pi}}d\theta_1\right)\theta_2\frac{\exp(-\frac{\theta_2^2}{2})}{\sqrt{2\pi}}d\theta_2 \\
&+ \int_{\frac{(i-20)\Delta x}{0.005}}^{\infty}\left(\int_{-\infty}^{\infty}\frac{\Delta t}{(4+0.5\theta_1)\Delta x\epsilon_0}\frac{\exp(-\frac{\theta_1^2}{2})}{\sqrt{2\pi}}d\theta_1\right)\theta_2\frac{\exp(-\frac{\theta_2^2}{2})}{\sqrt{2\pi}}d\theta_2
\end{aligned}
\tag{5.30}
$$

$$
\begin{aligned}
< \beta\psi_2\psi_2 > &= \int_{-\infty}^{\infty}\left(\int_{-\infty}^{\infty}\beta\frac{\exp(-\frac{\theta_1^2}{2})}{\sqrt{2\pi}}d\theta_1\right)\theta_2^2\frac{\exp(-\frac{\theta_2^2}{2})}{\sqrt{2\pi}}d\theta_2 \\
&= \frac{\Delta t}{\Delta x\epsilon_0}\int_{-\infty}^{\frac{(i-20)\Delta x}{0.005}}\left(\int_{-\infty}^{\infty}\frac{\exp(-\frac{\theta_1^2}{2})}{\sqrt{2\pi}}d\theta_1\right)\theta_2^2\frac{\exp(-\frac{\theta_2^2}{2})}{\sqrt{2\pi}}d\theta_2 \\
&+ \int_{\frac{(i-20)\Delta x}{0.005}}^{\infty}\left(\int_{-\infty}^{\infty}\frac{\Delta t}{(4+0.5\theta_1)\Delta x\epsilon_0}\frac{\exp(-\frac{\theta_1^2}{2})}{\sqrt{2\pi}}d\theta_1\right)\theta_2^2\frac{\exp(-\frac{\theta_2^2}{2})}{\sqrt{2\pi}}d\theta_2 \qquad (5.31)
\end{aligned}
$$

$$
\begin{aligned}
\text{and} \quad < \beta\psi_1\psi_2 > =< \beta\psi_2\psi_1 > &= \int_{-\infty}^{\infty}\left(\int_{-\infty}^{\infty}\beta\theta_1\frac{\exp(-\frac{\theta_1^2}{2})}{\sqrt{2\pi}}d\theta_1\right)\theta_2\frac{\exp(-\frac{\theta_2^2}{2})}{\sqrt{2\pi}}d\theta_2 \\
&= \frac{\Delta t}{\Delta x\epsilon_0}\int_{-\infty}^{\frac{(i-20)\Delta x}{0.005}}\left(\int_{-\infty}^{\infty}\theta_1\frac{\exp(-\frac{\theta_1^2}{2})}{\sqrt{2\pi}}d\theta_1\right)\theta_2\frac{\exp(-\frac{\theta_2^2}{2})}{\sqrt{2\pi}}d\theta_2 \\
&+ \int_{\frac{(i-20)\Delta x}{0.005}}^{\infty}\left(\int_{-\infty}^{\infty}\frac{\Delta t}{(4+0.5\theta_1)\Delta x\epsilon_0}\theta_1\frac{\exp(-\frac{\theta_1^2}{2})}{\sqrt{2\pi}}d\theta_1\right)\theta_2\frac{\exp(-\frac{\theta_2^2}{2})}{\sqrt{2\pi}}d\theta_2. \qquad (5.32)
\end{aligned}
$$

The orthogonal polynomials θ_1 have the following properties

$$\int_{-\infty}^{\infty}\frac{\exp(-\frac{\theta_1^2}{2})}{\sqrt{2\pi}}d\theta_1 = 1 \qquad (5.33)$$

$$\int_{-\infty}^{\infty}\frac{\theta_1\exp(-\frac{\theta_1^2}{2})}{\sqrt{2\pi}}d\theta_1 = 0 \qquad (5.34)$$

$$\text{and} \quad \int_{-\infty}^{\infty}\frac{\theta_1^2\exp(-\frac{\theta_1^2}{2})}{\sqrt{2\pi}}d\theta_1 = 1. \qquad (5.35)$$

These can be used to reduce equations (5.27)-(5.32) to

$$
\begin{aligned}
< \beta\psi_0\psi_0 > &= \frac{\Delta t}{\Delta x\epsilon_0}\int_{-\infty}^{\frac{(i-20)\Delta x}{0.005}}\frac{\exp(-\frac{\theta_2^2}{2})}{\sqrt{2\pi}}d\theta_2 \\
&+ \int_{\frac{(i-20)\Delta x}{0.005}}^{\infty}\left(\int_{-\infty}^{\infty}\frac{\Delta t}{(4+0.5\theta_1)\Delta x\epsilon_0}\frac{\exp(-\frac{\theta_1^2}{2})}{\sqrt{2\pi}}d\theta_1\right)\frac{\exp(-\frac{\theta_2^2}{2})}{\sqrt{2\pi}}d\theta_2 \qquad (5.36)
\end{aligned}
$$

$$< \beta\psi_0\psi_1 > = \int_{\frac{(i-20)\Delta x}{0.005}}^{\infty}\left(\int_{-\infty}^{\infty}\frac{\Delta t}{(4+0.5\theta_1)\Delta x\epsilon_0}\theta_1\frac{\exp(-\frac{\theta_1^2}{2})}{\sqrt{2\pi}}d\theta_1\right)\frac{\exp(-\frac{\theta_2^2}{2})}{\sqrt{2\pi}}d\theta_2 \qquad (5.37)$$

$$< \beta\psi_1\psi_1 > = \frac{\Delta t}{\Delta x \epsilon_0} \int_{-\infty}^{\frac{(i-20)\Delta x}{0.005}} \frac{\exp(-\frac{\theta_2^2}{2})}{\sqrt{2\pi}} d\theta_2 + \int_{\frac{(i-20)\Delta x}{0.005}}^{\infty} \left(\int_{-\infty}^{\infty} \frac{\Delta t}{(4+0.5\theta_1)\Delta x \epsilon_0} \theta_1^2 \frac{\exp(-\frac{\theta_1^2}{2})}{\sqrt{2\pi}} d\theta_1 \right) \frac{\exp(-\frac{\theta_2^2}{2})}{\sqrt{2\pi}} d\theta_2 \quad (5.38)$$

$$< \beta\psi_0\psi_2 > = \frac{\Delta t}{\Delta x \epsilon_0} \int_{-\infty}^{\frac{(i-20)\Delta x}{0.005}} \theta_2 \frac{\exp(-\frac{\theta_2^2}{2})}{\sqrt{2\pi}} d\theta_2 + \int_{\frac{(i-20)\Delta x}{0.005}}^{\infty} \left(\int_{-\infty}^{\infty} \frac{\Delta t}{(4+0.5\theta_1)\Delta x \epsilon_0} \frac{\exp(-\frac{\theta_1^2}{2})}{\sqrt{2\pi}} d\theta_1 \right) \theta_2 \frac{\exp(-\frac{\theta_2^2}{2})}{\sqrt{2\pi}} d\theta_2 \quad (5.39)$$

$$< \beta\psi_2\psi_2 > = \frac{\Delta t}{\Delta x \epsilon_0} \int_{-\infty}^{\frac{(i-20)\Delta x}{0.005}} \theta_2^2 \frac{\exp(-\frac{\theta_2^2}{2})}{\sqrt{2\pi}} d\theta_2 + \int_{\frac{(i-20)\Delta x}{0.005}}^{\infty} \left(\int_{-\infty}^{\infty} \frac{\Delta t}{(4+0.5\theta_1)\Delta x \epsilon_0} \frac{\exp(-\frac{\theta_1^2}{2})}{\sqrt{2\pi}} d\theta_1 \right) \theta_2^2 \frac{\exp(-\frac{\theta_2^2}{2})}{\sqrt{2\pi}} d\theta_2 \quad (5.40)$$

$$\text{and} \quad < \beta\psi_1\psi_2 > = \int_{\frac{(i-20)\Delta x}{0.005}}^{\infty} \left(\int_{-\infty}^{\infty} \frac{\Delta t}{(4+0.5\theta_1)\Delta x \epsilon_0} \theta_1 \frac{\exp(-\frac{\theta_1^2}{2})}{\sqrt{2\pi}} d\theta_1 \right) \theta_2 \frac{\exp(-\frac{\theta_2^2}{2})}{\sqrt{2\pi}} d\theta_2. \quad (5.41)$$

The above improper integrals are calculated using the extended midpoint rule [90, p.141-147]. The accuracy of the integration is increased by iteratively adding $(2/3) \times 3^{n-1}$ interior points at iteration step n [90, p.142]. The infinite limits, of the improper integrals, are transformed to finite limits using a change of variables [90, p.144]. The results of a number of integrations calculated using these numerical techniques were validated against results obtained using the software package MAPLE.

The values of all these integrals are substituted into the update equations (4.111) and (4.112), which are used to find the mean and uncertainty in the electric field at the output point. In this example the output quantity of interest is the absolute value of the electric field in the frequency domain relative to a 1 V/m input excitation. More numerical integrations are required to calculate the mean and uncertainty in this output, which adds to the overall computational cost of this method. The 95% CI are obtained using the mean and uncertainty, in the same way as for the MoM.

Application of the Polynomial Chaos Method to the Analytic Solution

The normalised output electric field $\tilde{E}(f)$ is expanded in terms of the uncertain input parameters θ_1 and θ_2 as

$$\tilde{E}(f,\theta_1,\theta_2) = e_0(f) + e_1(f)\theta_1 + e_2(f)\theta_2. \tag{5.42}$$

The uncertain parameters θ_1 and θ_2 are related to the uncertain parameters ϵ_r and x_{end} in the same manner as described by equations (5.15) and (5.16). The coefficients e_0, e_1 and e_2 are calculated using the inner products

$$e_0(f) = <\tilde{E}(f,\theta_1,\theta_2),1> = \int_{-\infty}^{\infty}\int_{-\infty}^{\infty}\tilde{E}(f,\theta_1,\theta_2)\frac{\exp(-\frac{\theta_1^2}{2})}{\sqrt{2\pi}}\frac{\exp(-\frac{\theta_2^2}{2})}{\sqrt{2\pi}}d\theta_1\, d\theta_2 \tag{5.43}$$

$$e_1(f) = \frac{<\tilde{E}(f,\theta_1,\theta_2),\theta_1>}{<\theta_1^2>} = \int_{-\infty}^{\infty}\int_{-\infty}^{\infty}\tilde{E}(f,\theta_1,\theta_2)\theta_1\frac{\exp(-\frac{\theta_1^2}{2})}{\sqrt{2\pi}}\frac{\exp(-\frac{\theta_2^2}{2})}{\sqrt{2\pi}}d\theta_1\, d\theta_2 \tag{5.44}$$

$$\text{and}\quad e_2(f) = \frac{<\tilde{E}(f,\theta_1,\theta_2),\theta_2>}{<\theta_2^2>} = \int_{-\infty}^{\infty}\int_{-\infty}^{\infty}\tilde{E}(f,\theta_1,\theta_2)\theta_2\frac{\exp(-\frac{\theta_1^2}{2})}{\sqrt{2\pi}}\frac{\exp(-\frac{\theta_2^2}{2})}{\sqrt{2\pi}}d\theta_1\, d\theta_2. \tag{5.45}$$

These are calculated by numerically integrating the analytical solution over the specified domain. A numerical integration must be performed for each frequency point, thus the mid-point rule is used due to its computational efficiency and simplicity. Once the coefficients e_0, e_1 and e_2 are found, the mean normalised electric field $\bar{E}(f)$ and uncertainty $\sigma(\tilde{E}(f))$ may be calculated as

$$\bar{E}(f) = e_0 \tag{5.46}$$

$$\text{and}\quad \sigma(\tilde{E}(f)) = \sqrt{e_1^2 + e_2^2}. \tag{5.47}$$

Notice that the definition of the mean here is exactly the same as the definition of the analytic mean given by equation (5.13). This is not the case when the PCM is applied to the FDTD simulations.

5.4.5 Comparing the Results of the Uncertainty Analysis Methods

This section provides the results of the UAs, beginning with the uncertainty in the analytic solution.

The Uncertainty in the Analytic Solution

Figures 5.7 and 5.8 display the mean and uncertainty in the analytic solution of the normalised electric field, as predicted by the different UA methods. The mean predicted by the PCM is exactly the same as the analytic solution of the mean. This is as expected since

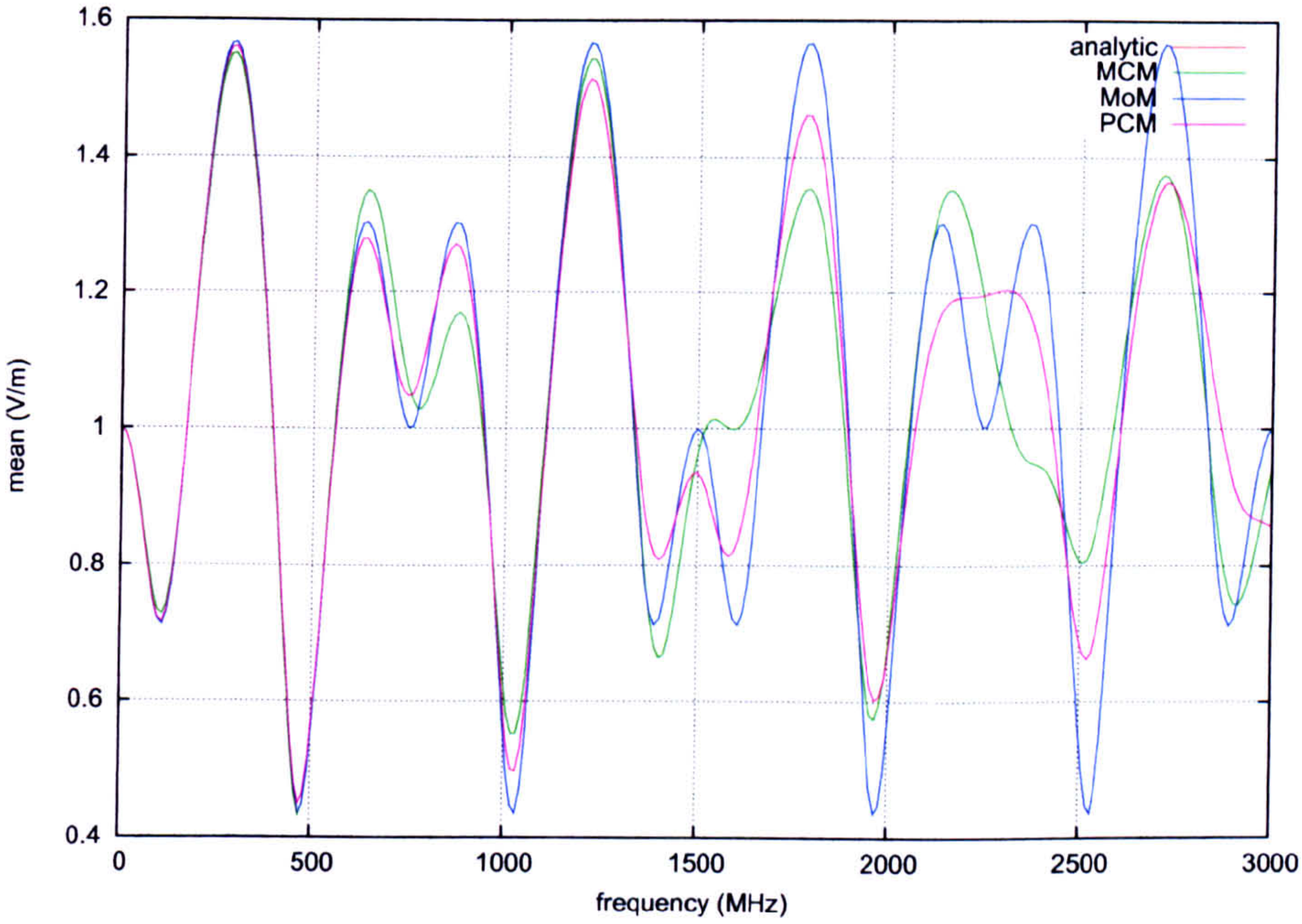

Figure 5.7: Mean normalised electric field calculated using the different UA methods, for the analytic solution.

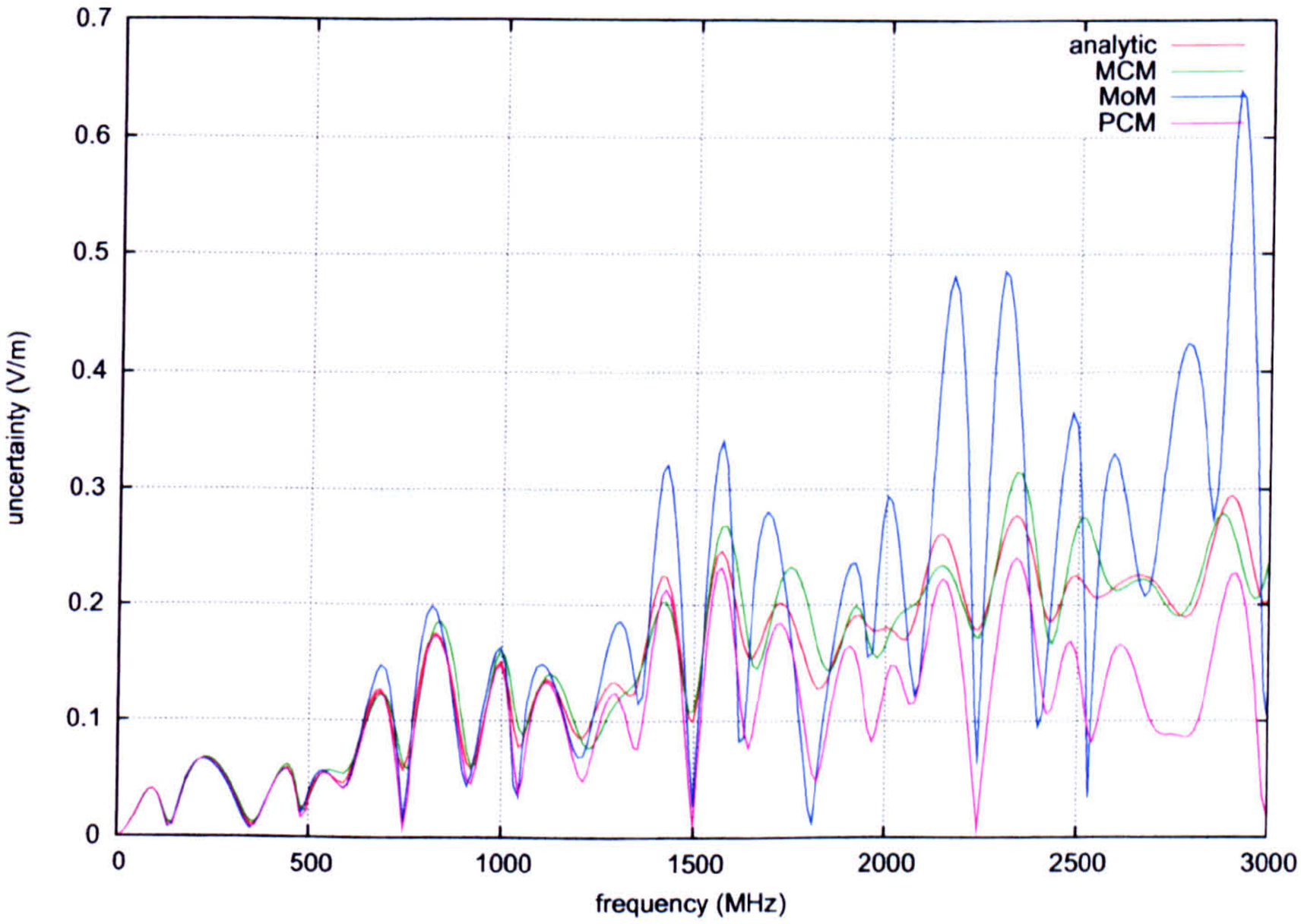

Figure 5.8: Uncertainty in the normalised electric field calculated using the different UA methods, for the analytic solution.

Comparing the Predictions of the Means					
Method	ADM	FDM	GDM	GDM (1-6)	Qualitative
MCM	0.1457	0.1793	0.2526	3.2682	Good
MoM	0.1114	0.2660	0.3039	3.5245	Good
PCM	0	0	0	1	Excellent
Comparing the Predictions of the Uncertainty					
MCM	0.2074	0.1770	0.3015	3.5127	Good
MoM	0.5257	0.6567	0.9220	5.1538	Poor
PCM	0.3980	0.3127	0.5453	4.3658	Fair

Table 5.5: FSV comparisons of the analytic solution of the mean and uncertainty in the normalised electric field, with the means and uncertainties predicted by the three UA methods.

the analytic solution of the mean (5.13) and the equation representing the PCM prediction of the mean (5.46) are equivalent. It is difficult to tell, from Figure 5.7, which of the means predicted by the MCM and the MoM are closer to the analytic mean. To overcome this problem the FSV method was used to compare the various predictions with the analytic solution: Table 5.5 gives the results of these comparisons. Using this table it is clear that the PCM provides the best prediction of the mean. The MCM and MoM both provide "good" predictions of the mean when compared to the analytic mean. The MCM provides a slightly more accurate prediction of the mean, than the MoM, having a slightly lower GDM. In terms of the predictions of the uncertainty, Table 5.5 shows that the MCM provides the best estimation of the analytic uncertainty followed by the PCM. The MoM provides a "poor" estimation of the uncertainty having a fairly large GDM of 5.1538 on the visual scale. These comparisons agree with the visual comparisons of the uncertainties in Figure 5.8. From this figure it can be seen that the MCM uncertainty is closest to the analytic uncertainty, followed by the PCM.

Since the MCM provides the best estimations of the uncertainty for the analytic solutions it is chosen as the benchmark method by which the performance of the other two UA methods are compared, when all three UA methods are applied to the FDTD simulations. It is important to note that the PCM may not give as good predictions of the mean and uncertainty when applied to the FDTD simulations. This is because the application of the PCM to the analytic solution is quite different from its application to FDTD simulations.

Figure 5.8 shows that the MoM both underestimates and overestimates the analytic uncertainty at the higher frequencies. At these higher frequencies, perturbations in the uncertain input parameters cause the output curves to be shifted slightly in frequency. The more the input parameter is perturbed the larger the frequency shifts. At a certain frequency the output value will increase and decrease in a non linear way as it moves up and down the

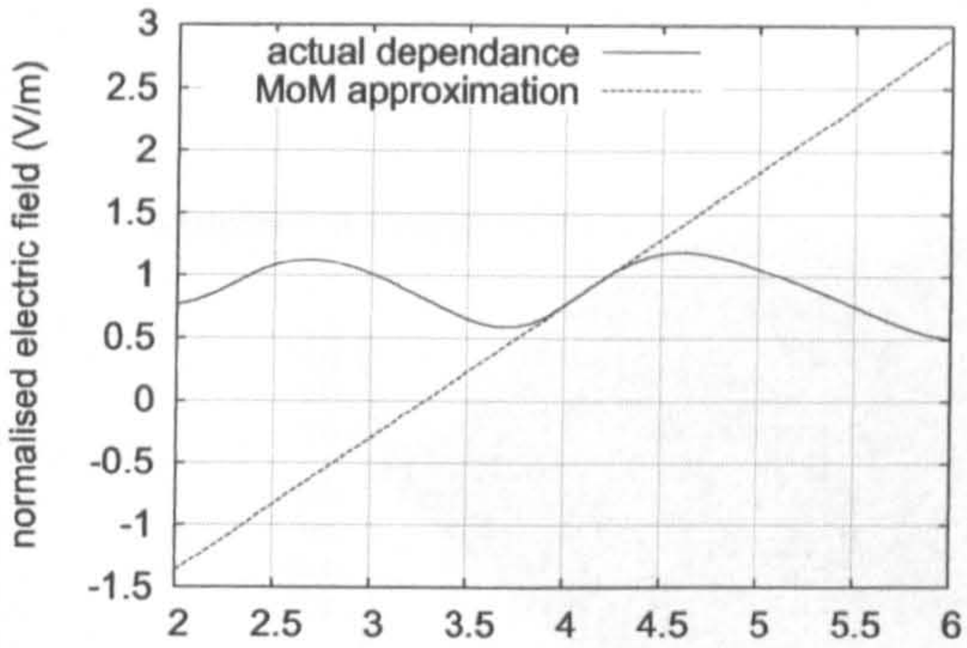

Figure 5.9: Dependence of the normalised field on the relative permittivity, at 2.91GHz.

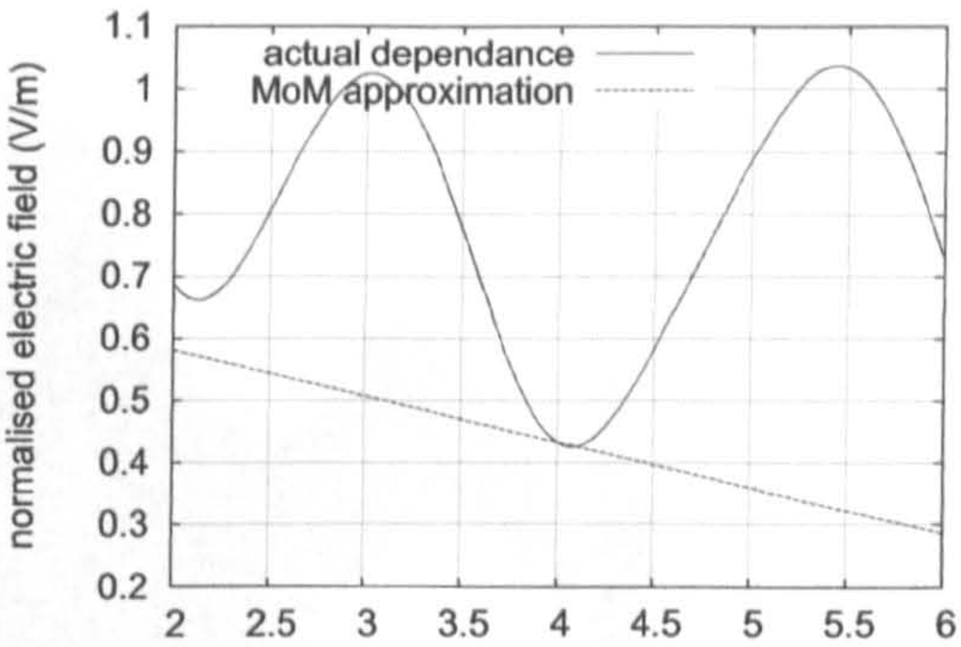

Figure 5.10: Dependence of the normalised field on the relative permittivity, at 2.53GHz.

shifted curves. Thus the output will depend nonlinearly on the input parameters. Figure 5.9 illustrates the dependence of the output normalised electric field on the relative permittivity of the slab, at the frequency 2.91GHz. This frequency corresponds to the final peak overestimation of the uncertainty for the MoM. It is clear from Figure 5.9 that the output depends nonlinearly on the relative permittivity. This figure also shows the MoM approximation of the relationship between the output and the relative permittivity. At the mean permittivity $\bar{\epsilon}_r = 4$, the MoM assumes that the output depends linearly on the input. At this point it is clear that the first derivative is larger than surrounding values. It has already been noted that the size of the uncertainty in the relative permittivity is not small (but may be realistic). As discussed in Section 4.6.2 the large input uncertainty, the nonlinear relationship between the output and the input parameter, and the larger sensitivity derivative at the mean input parameter value, all cause the first order MoM prediction of the uncertainty to be an overestimation of the actual value. Figure 5.8 confirms that this overestimation has occurred.

From Figure 5.8 it is clear that the MoM also underestimates the uncertainty at certain frequencies, such as at 2.53GHz. In Section 4.6.2 it was explained that if the input uncertainties are large, then the MoM underestimates the actual uncertainty at points where the sensitivity of the output with respect to the input parameters is small compared to the sensitivity at nearby points. Figure 5.10 illustrates the dependence of the normalised electric field on the relative permittivity at 2.53GHz, and the linear approximation made by the MoM. It is clear from this figure that the sensitivity derivative at the mean relative permittivity value is smaller than at surrounding permittivity values. The uncertainty in the relative permittivity is also quite large. This causes the MoM to underestimate the uncertainty at this frequency.

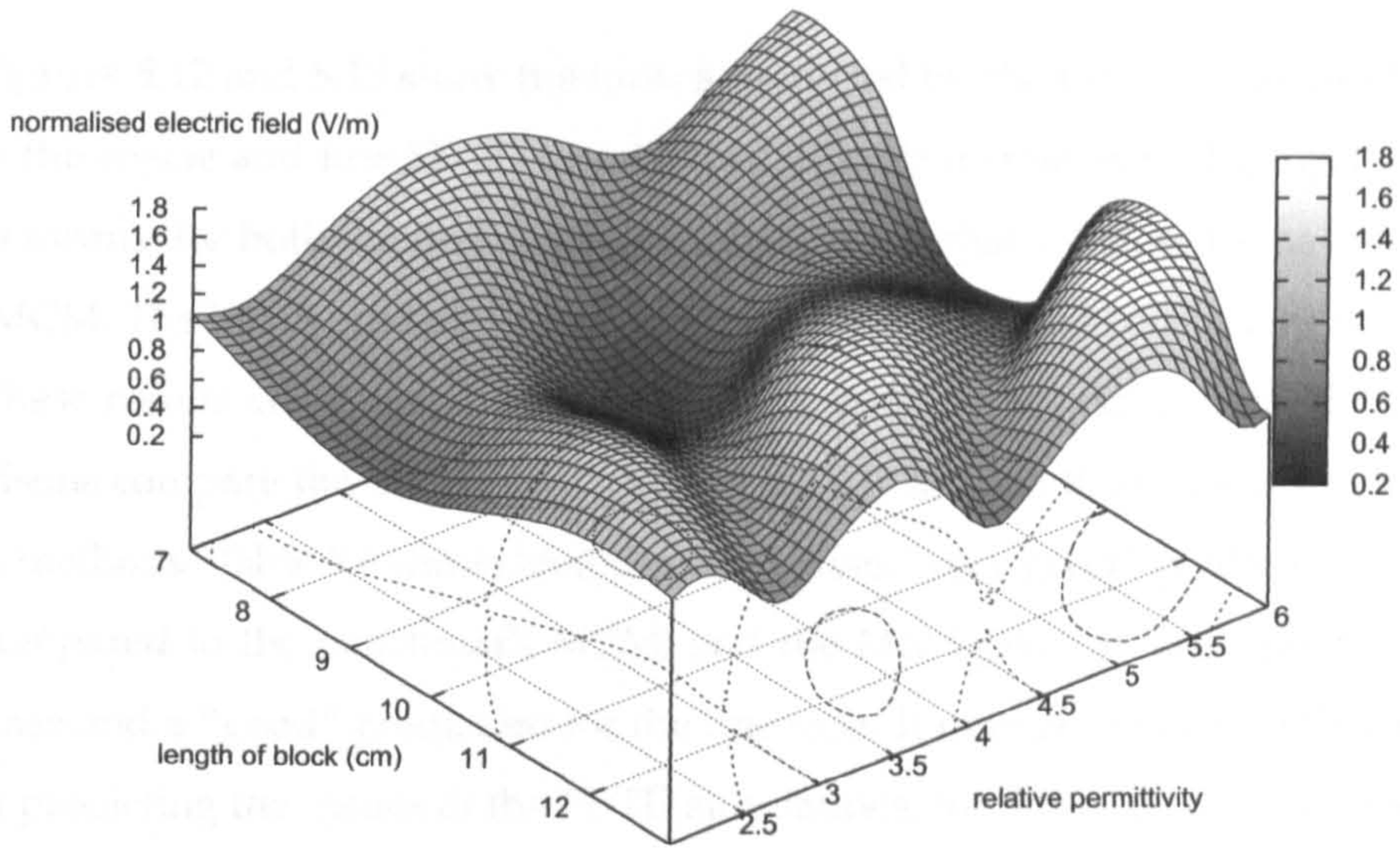

Figure 5.11: Dependence of the electric field on the length and the relative permittivity of the slab, at 2.914GHz.

The MoM disregards the nonlinear dependence of the electric field on the simultaneous change of the length and relative permittivity of the slab. Figure 5.11 shows the nonlinear relationship between the electric field and the input parameters at 2.91GHz. The MoM approximates this surface as a linear plane, which is inaccurate for larger input uncertainties. The MCM allows for the simultaneous change of both input parameter values, and is therefore more accurate than the MoM. For this example, the PCM also assumes that the output electric field depends linearly on the inputs. The PCM does however allow for the simultaneous change of the input parameters when obtaining the coefficients of the linear relationship. Equation (5.20) shows how both uncertain input parameters are combined to form one uncertain parameter that is propagated through the FDTD simulation. This prevents the effect of changing the input parameters on the output uncertainty from being simply the additive effect of changing the input parameters separately as in the MoM.

By applying the UA methods to the analytic solution it has been shown that the MCM provides the best prediction of the uncertainty in the output of this example. Some of the errors that arise from the MoM have also been discussed. The performance of the UAs when applied to the FDTD simulations is discussed in the next section.

The Uncertainty in the Finite Difference Time Domain Simulations

Figures 5.12 and 5.13 show the means predicted by the three UA methods when applied to the coarse and fine FDTD simulations. It is clear from these figures that the PCM predicts means, for both the fine and coarse simulation, that are close to the benchmark set by the MCM. The MoM predicts means that are farther from the benchmark result than the PCM. These results are confirmed by the FSV comparisons set out in Table 5.6. These FSV comparisons compare the means predicted by the MCM with those predicted by the other two UA methods. Table 5.6 shows that the PCM gives "very good" predictions of the mean when compared to the benchmark MCM, and the MoM gives a "fair" prediction for the coarse case and a "good" prediction for the fine case. It may be concluded that the PCM is better at predicting the means of the FDTD simulations, for this example, than the MoM.

Figures 5.14 and 5.15 show the uncertainty predicted by the three methods for the

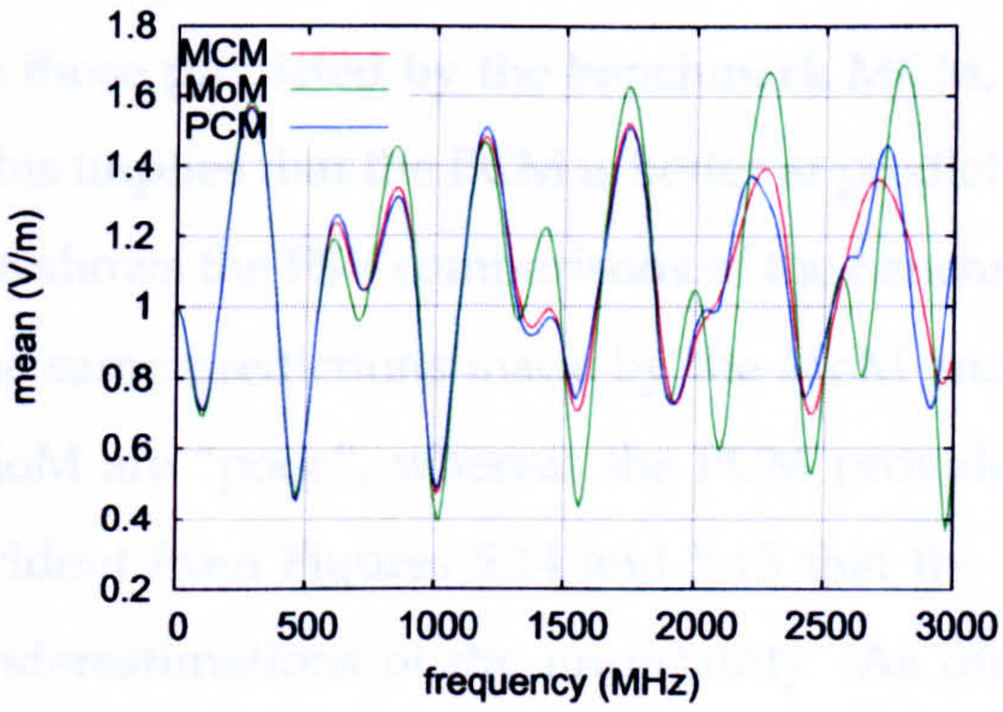

Figure 5.12: Mean normalised electric field for the coarse FDTD simulation.

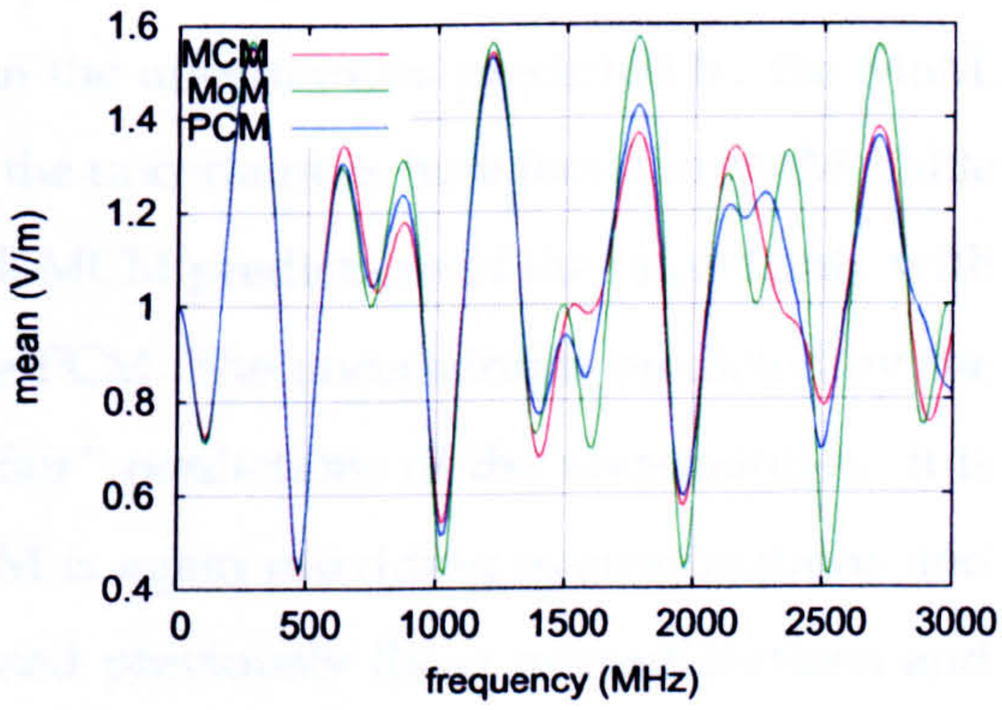

Figure 5.13: Mean normalised electric field for the fine FDTD simulation.

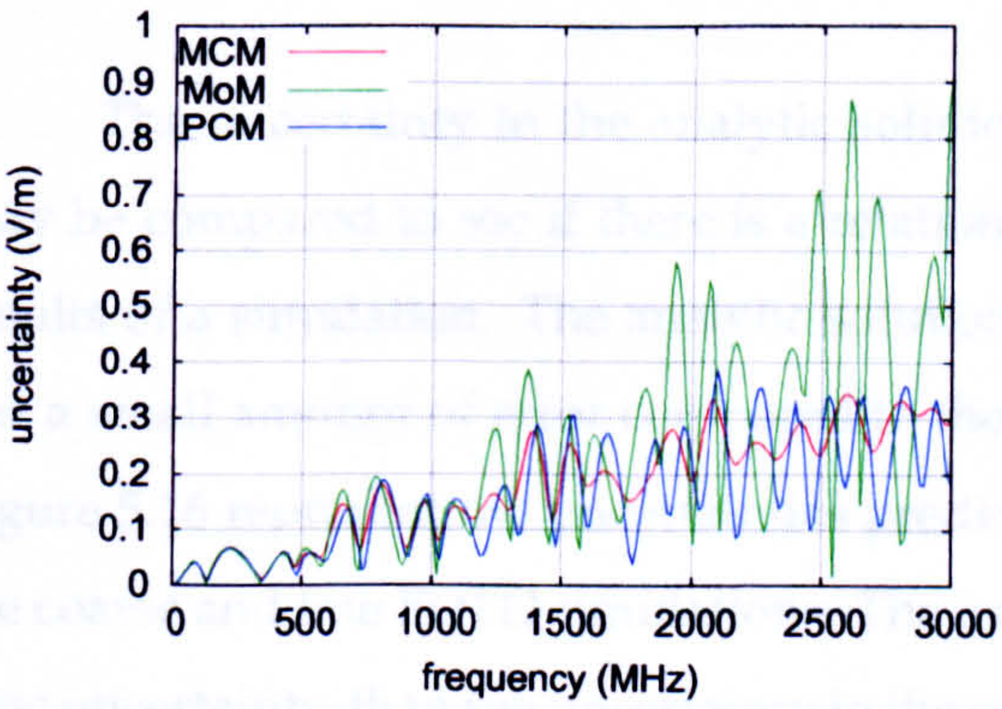

Figure 5.14: Uncertainty in the normalised electric field for the coarse FDTD simulation.

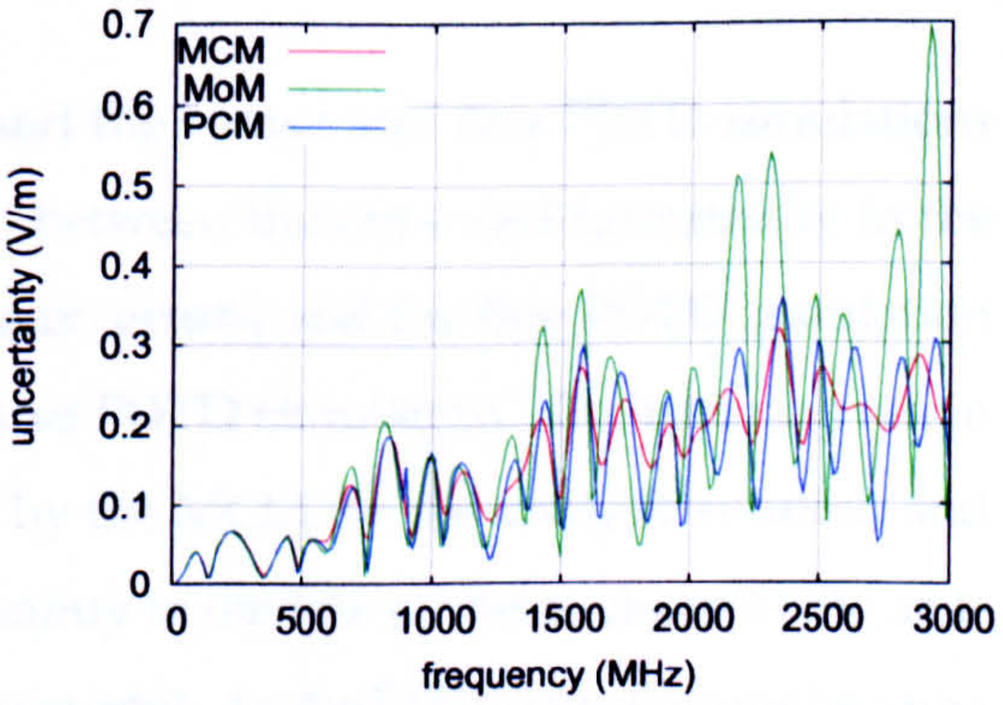

Figure 5.15: Uncertainty in the normalised electric field for the fine FDTD simulation.

Comparing the Predictions of the Mean						
Method	Applied To	ADM	FDM	GDM	GDM (1-6)	Qualitative
MoM	(2,2) Coarse	0.1979	0.3822	0.4637	4.1662	Fair
PCM	(2,2) Coarse	0.0720	0.1525	0.1831	2.8409	Very Good
MoM	(2,2) Fine	0.1676	0.2568	0.3332	3.6708	Good
PCM	(2,2) Fine	0.0960	0.1549	0.1973	2.9829	Very Good
Comparing the Predictions of the Uncertainty						
MoM	(2,2) Coarse	0.6322	0.8532	1.1414	5.4280	Poor
PCM	(2,2) Coarse	0.3265	0.5535	0.6922	4.7329	Fair
MoM	(2,2) Fine	0.5885	0.8247	1.1130	5.3925	Poor
PCM	(2,2) Fine	0.2961	0.5138	0.6498	4.6270	Fair

Table 5.6: FSV comparisons of the means and uncertainties predicted by the benchmark MCM and the other two UA methods.

coarse and fine FDTD simulations. The uncertainties predicted by all three methods tend to increase as the frequency increases. This suggests that there is a greater uncertainty in the results of the simulations at higher frequencies.

Figures 5.14 and 5.15 show that the PCM predicts uncertainties that are a lot closer to those predicted by the benchmark MCM, than the uncertainties predicted by the MoM. This implies that the PCM is better at predicting the uncertainties here than the MoM. Table 5.6 shows the FSV comparisons of the benchmark MCM predictions of the uncertainty with the same predictions made by the MoM and the PCM. The uncertainties predicted by the MoM are "poor", whereas the PCM provides "fair" predictions of the uncertainties. It is evident from Figures 5.14 and 5.15 that the MoM is again providing overestimations and underestimations of the uncertainty. As discussed previously these overestimations and underestimations arise because the MoM is less accurate for larger input uncertainties.

Analysing the Relationship Between Accuracy and Uncertainty

The uncertainty in the analytic solution, and the coarse and fine FDTD simulations may be compared to see if there is a relationship between the error and uncertainty in the results of a simulation. The analytic solution has no errors, and the fine FDTD simulation has a small amount of error compared to the coarse FDTD simulation. The three curves in Figure 5.16 represent the uncertainties predicted by the MCM for the analytic solution and the coarse and fine FDTD simulations. The uncertainty in the fine model is closer to the analytic uncertainty, than the uncertainty in the coarse model. As the FDTD simulations become more accurate, the uncertainty calculated for those simulations converges to the uncertainty in the analytic case. Therefore there is some relationship between the uncertainty in a model

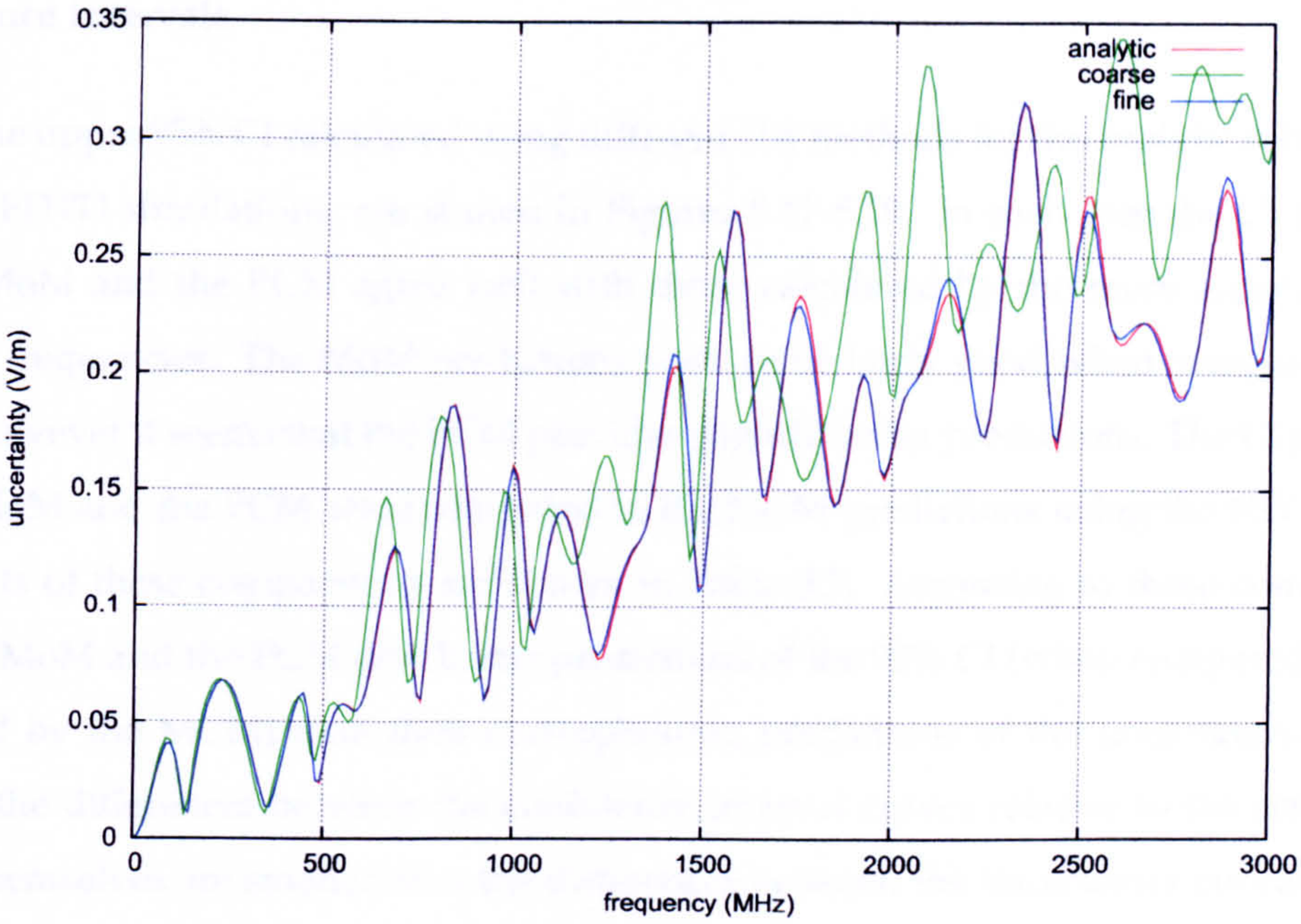

Figure 5.16: The uncertainty as predicted by the MCM for different implementations of the model.

and the accuracy with which that model is implemented. The features in the frequency response of the uncertainty in the coarse model, shown in Figure 5.16, differ from the features in the other two uncertainty curves. Overall however the sizes of the three uncertainty curves are similar. This suggests that there is only a small relationship between the size of the uncertainty in the model and the accuracy with which that model was implemented.

The uncertainty in the output depends on the uncertainty in the inputs, and the way in which that uncertainty is propagated through the simulation. The accuracy with which the model is implemented will affect how the uncertainty is propagated through the simulation. Accurate models will propagate uncertainties through the simulation in a similar manner to the analytic solution. Less accurate simulations will propagate the uncertainty through slightly differently. This is what causes the features of uncertainty curves, formed with a different level of accuracy, to differ. However, the overall size of the output uncertainty does not appear to differ significantly for simulations performed with different accuracies.

In the next section the mean and uncertainty, formed using the different UA methods, are used to estimate the 95% CI.

Confidence Intervals

The upper 95% CI calculated using different UA methods for the analytic solution and the two FDTD simulations, are shown in Figures 5.17-5.19. In each case the CI predicted by the MoM and the PCM agree well with those calculated by the more accurate MCM at lower frequencies. The MoM predictions seem to be fairly good when compared to the MCM, however it seems that the PCM provides slightly better predictions. The CI predicted by the MoM and the PCM were compared to the MCM predictions using the FSV method, the results of these comparisons are shown in Table 5.7. According to these comparisons both the MoM and the PCM give better predictions of the 95% CI (when compared to those predicted by the MCM) than their corresponding predictions of the uncertainty. This is because the differences between the confidence interval curves relative to the sizes of the curves themselves are smaller than the differences between the uncertainty curves relative to the sizes of the uncertainty curves. The FSV method normalises the difference measures, for the curves, to the sizes of the curves. This means that the smaller proportional differences in the confidence interval predictions result in the FSV method giving better comparisons. It is clear once again that the PCM is giving better predictions of the CI than the MoM, when compared to the MCM.

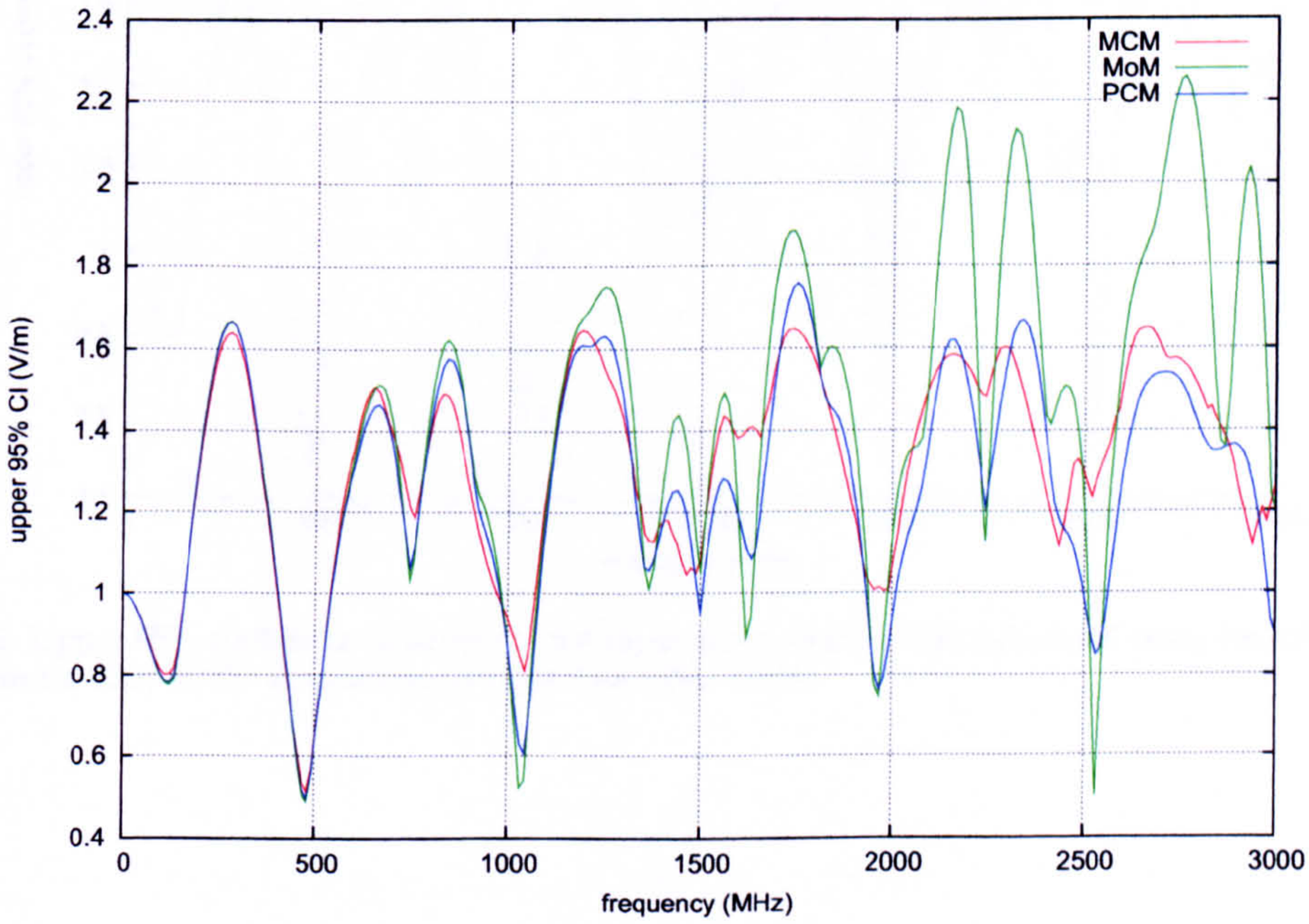

Figure 5.17: Upper 95% confidence interval for the normalised electric field calculated using the different UA methods, for the analytic solution.

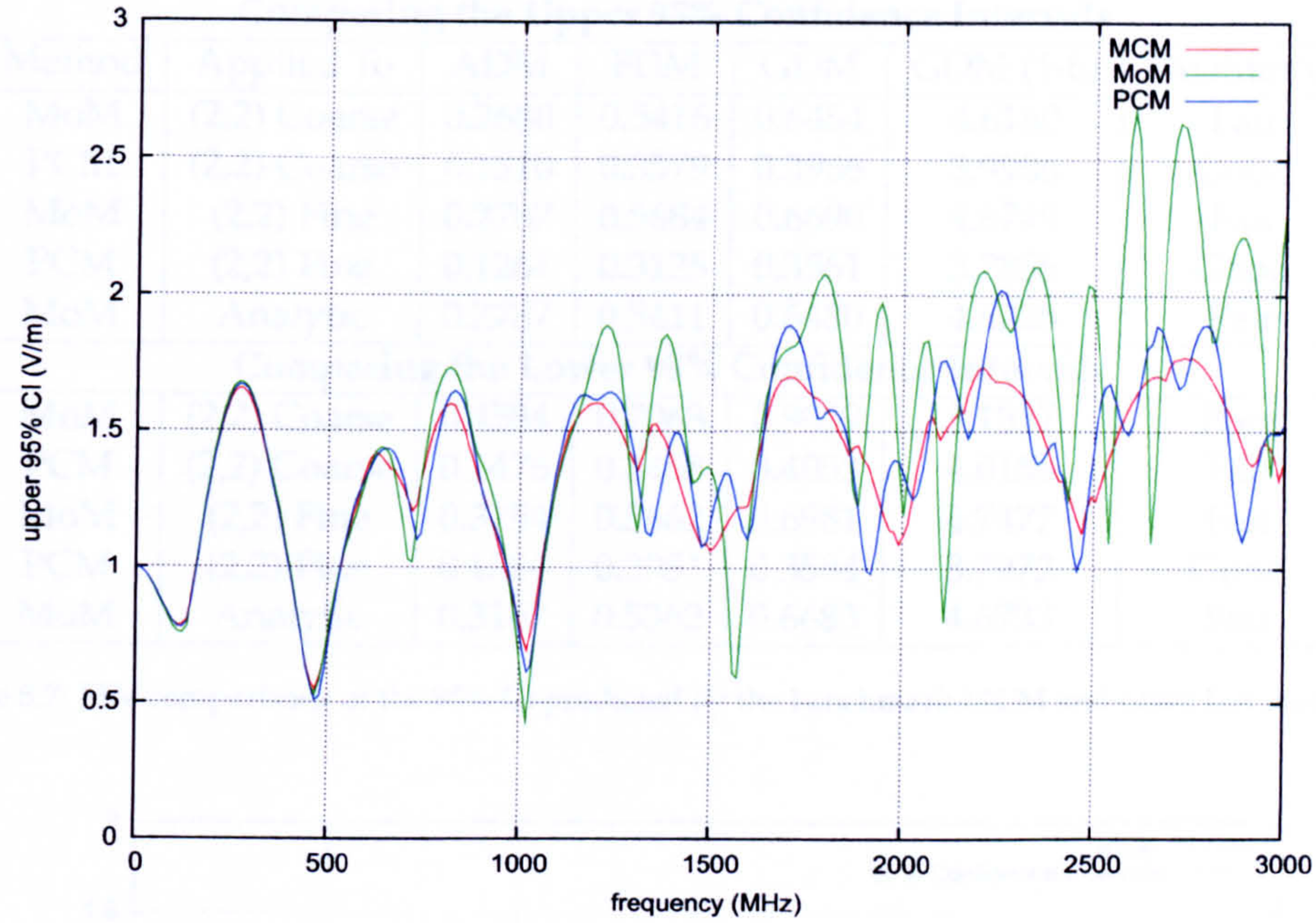

Figure 5.18: Upper 95% confidence interval for the normalised electric field calculated using the different UA methods, for the (2,2) FDTD simulation performed on a coarse mesh.

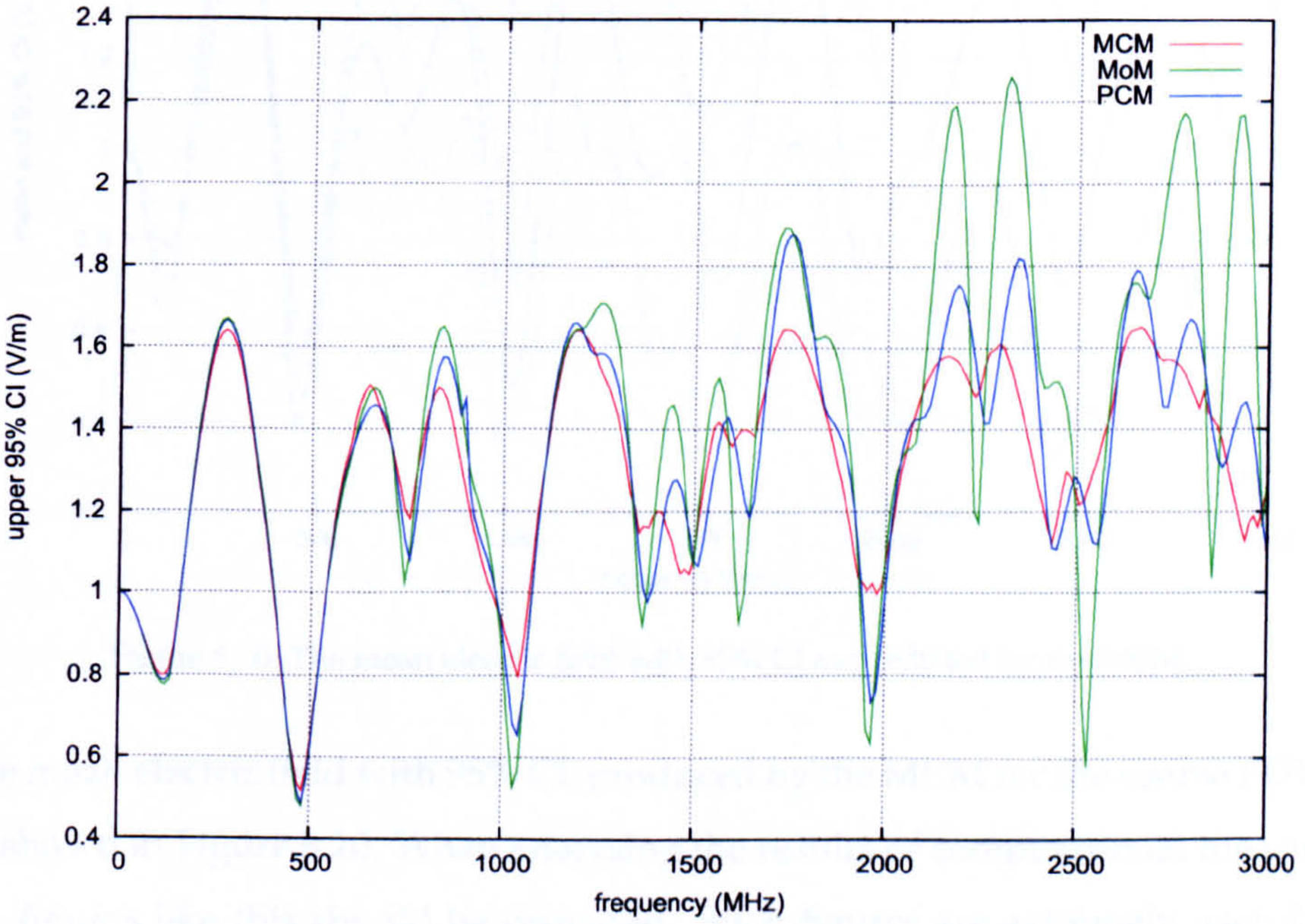

Figure 5.19: Upper 95% confidence interval for the normalised electric field calculated using the different UA methods, for the (2,2) FDTD simulation performed on a fine mesh.

Comparing the Upper 95% Confidence Intervals						
Method	Applied To	ADM	FDM	GDM	GDM (1-6)	Qualitative
MoM	(2,2) Coarse	0.2680	0.5416	0.6454	4.6160	Fair
PCM	(2,2) Coarse	0.1310	0.3579	0.3986	3.9986	Good
MoM	(2,2) Fine	0.2787	0.5684	0.6690	4.6749	Fair
PCM	(2,2) Fine	0.1264	0.3125	0.3561	3.7855	Good
MoM	Analytic	0.2787	0.5411	0.6480	4.6225	Fair
Comparing the Lower 95% Confidence Intervals						
MoM	(2,2) Coarse	0.4584	0.7063	0.9059	5.1337	Poor
PCM	(2,2) Coarse	0.1476	0.3468	0.4053	4.0158	Fair
MoM	(2,2) Fine	0.3154	0.5662	0.6981	4.7477	Fair
PCM	(2,2) Fine	0.1384	0.3051	0.3584	3.7972	Good
MoM	Analytic	0.3167	0.5362	0.6683	4.6733	Fair

Table 5.7: FSV comparisons of the 95% CI predicted by the benchmark MCM and other UA methods.

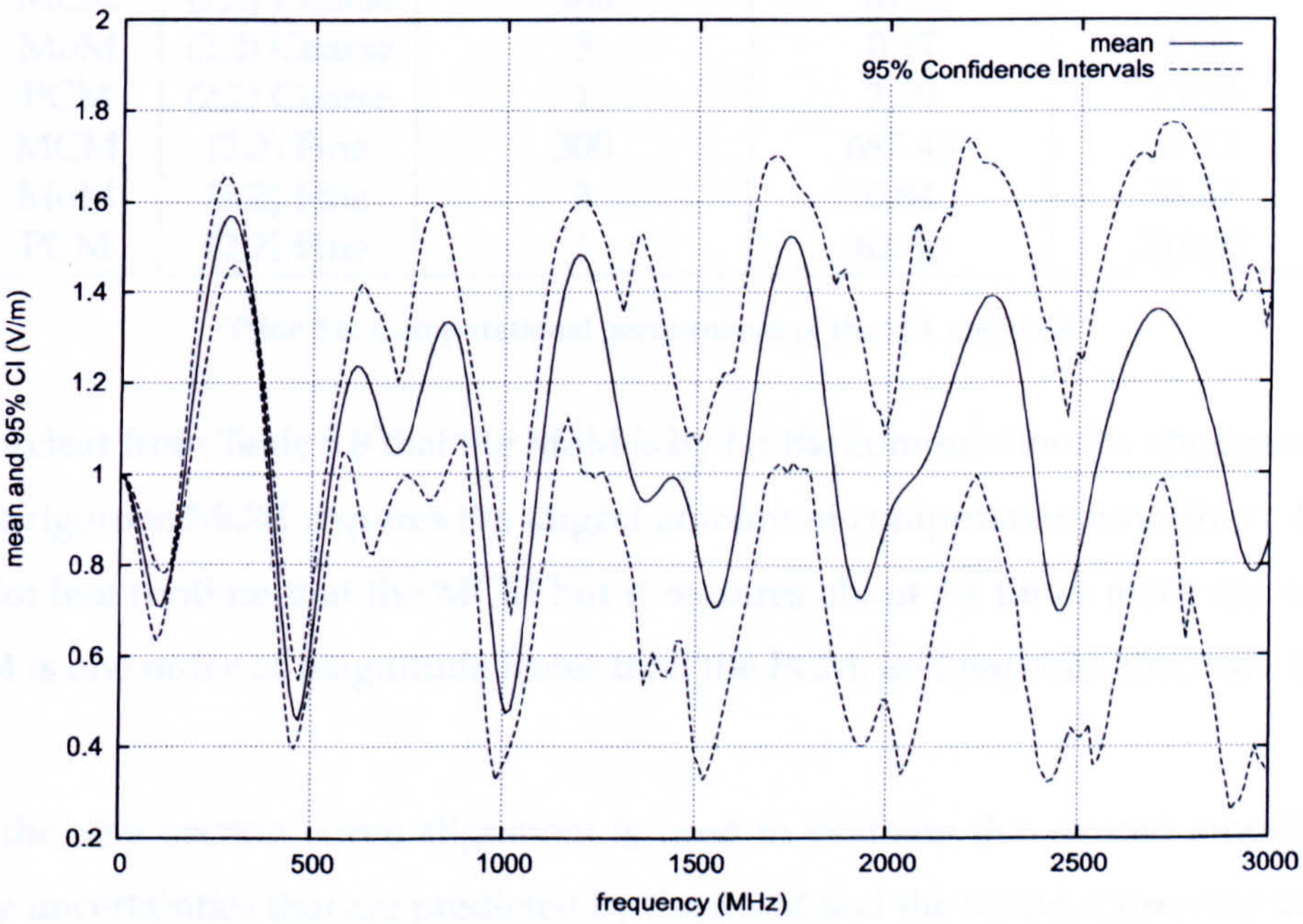

Figure 5.20: The mean electric field with 95% CI as predicted by the MCM.

The mean electric field with 95% CI, produced by the MCM for the coarse FDTD simulation, is shown in Figure 5.20. When analysing the results of computational measurements for EMC, figures like this should be provided. Such figures are extremely useful because they provide the quantitative level of confidence that can be held in the mean output value. For this example the experimenter can be confident that the electric field takes on a value close to the mean value for the lower frequencies. However at the higher frequencies there is less confidence to be held in the value of the electric field. This is because the 95% CI are larger at the higher frequencies.

5.4.6 The Computational Expense of The Uncertainty Analysis Methods

Thus far the relative performance of the UA methods have been compared in terms of their ability to predict the means, uncertainties and 95% CI in the output of the FDTD simulations. The three UA methods may also be compared in terms of their computational expense, when applied to the fine and coarse FDTD simulations. For this simple example none of the methods are computationally expensive, however investigating their relative computational expense provides an insight into the computational performance of the three methods for more complex examples. All of the analyses were performed on a Core2Duo processor working at 3.0GHz.

Method	Applied To	No. Simulations	Time Taken (s)	Memory (kB)
MCM	(2,2) Coarse	300	16.52	2.42
MoM	(2,2) Coarse	3	0.17	2.42
PCM	(2,2) Coarse	1	2.39	13.50
MCM	(2,2) Fine	300	687.40	38.42
MoM	(2,2) Fine	3	6.84	38.42
PCM	(2,2) Fine	1	62.30	216.00

Table 5.8: Computational performance of the UA methods.

It is clear from Table 5.8 that the MoM is by far the computationally cheapest method. The more rigorous MCM requires the largest amount of computational runtime. The PCM needs a lot less runtime that the MCM but it requires about six times more memory here. The MoM is one order of magnitude faster than the PCM, and requires about six times less memory.

In the next section curve alignment is used to evaluate the aligned amplitude and frequency uncertainties that are predicted by the MoM and the MCM. Currently there is no way of forming the aligned uncertainties for the PCM.

5.5 Evaluating the Uncertainties After Alignment

The three frequency response curves formed from the coarse FDTD simulations and used to obtain the prediction of the uncertainty, via the MoM, are shown in Figure 5.21. The curve produced by the reference simulation, where all input parameters take on their mean values, is very similar to the curve produced by the simulation with a perturbed permittivity.

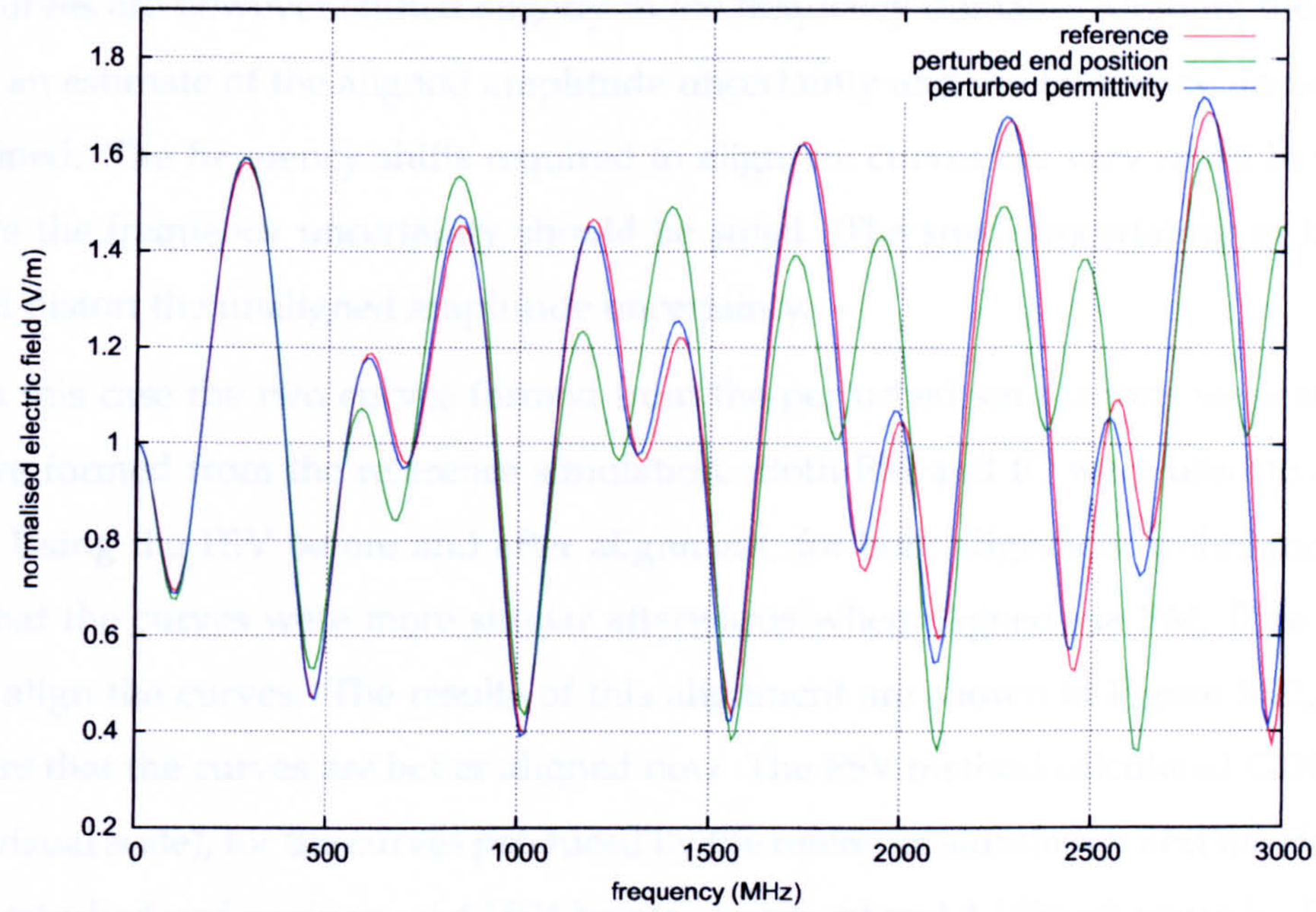

Figure 5.21: Frequency response of the electric field produced from the reference simulation and the simulations with perturbed input parameters.

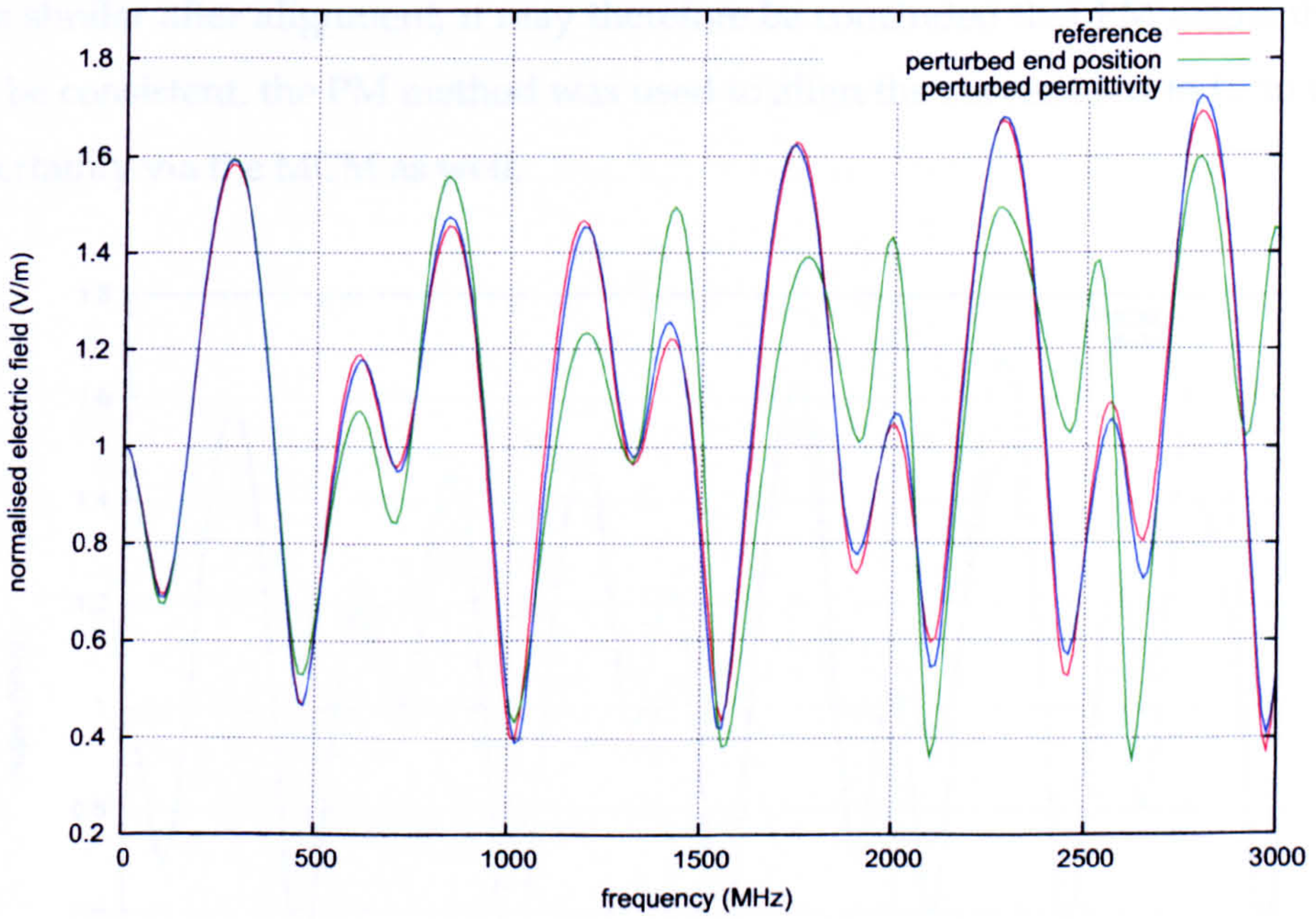

Figure 5.22: Frequency response of the electric fields produced by the simulations with perturbed input parameters, after alignment (via PM) to the response produced by the reference simulation.

These curves are however shifted slightly in the frequency domain. Aligning these curves enables an estimate of the aligned amplitude uncertainty and the frequency uncertainty to be obtained. The frequency shifts required to align the curves are very small in this case, therefore the frequency uncertainty should be small. The small uncertainty in frequency may still distort the unaligned amplitude uncertainty.

In this case the two curves formed from the perturbed simulations were aligned to the curve formed from the reference simulation. Both PM and IC were used to align the curves. Using the FSV before and after alignment, for both alignment techniques, it was found that the curves were more similar afterwards when aligned via PM. Thus PM was used to align the curves. The results of this alignment are shown in Figure 5.22, visually it appears that the curves are better aligned now. The FSV method calculated GDM values (on the visual scale), for the curves produced by the reference simulation and the simulation with a perturbed end position, of 4.1594 before alignment and 4.1426 afterwards. The GDM for the curves produced by the reference simulation and the simulation with a perturbed permittivity, were calculated as 2.2664 before alignment and 1.8327 afterwards. The curves are more similar after alignment, it may therefore be concluded that PM aligns the curves well. To be consistent, the PM method was used to align the curves used to form the mean and uncertainty via the MCM as well.

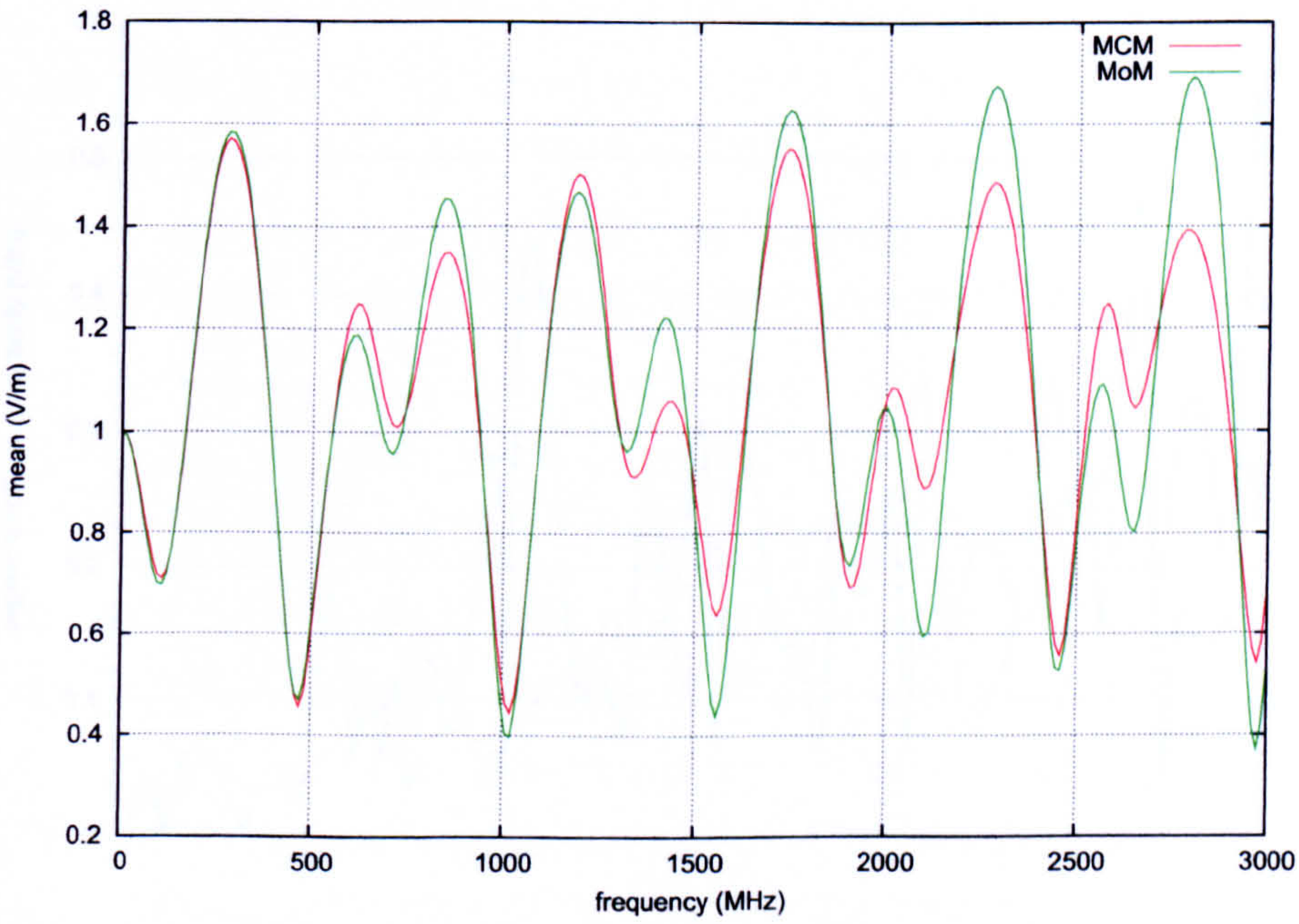

Figure 5.23: Frequency response of the mean electric field predicted by the MCM and the MoM after alignment via PM.

The mean calculated by the MoM is a lot closer to the mean predicted by the MCM after alignment. Figure 5.23 shows the means predicted by these two methods after alignment. Using the FSV method on the two curves from this figure determines that the similarity of the two curves is "good". Before alignment the means predicted by the two methods were determined to be a "fair" comparison. Thus, the means predicted by the MoM and the MCM are more similar after alignment has taken place.

The aligned amplitude uncertainties predicted by the MoM and the MCM for the coarse simulation are shown in Figure 5.24. By comparing Figure 5.24 with Figure 5.14 it is clear that the amplitude uncertainties predicted by the MoM are more similar to those predicted by the MCM after alignment. In the unaligned case the MoM overestimates and underestimates the actual uncertainty. Now that the curves have been aligned some of the nonlinear dependence of the output on the input parameters has been reduced. This means that the MoM, which assumes a linear dependence, will provide better estimates of the uncertainty after alignment. The overall sizes of the uncertainties predicted by the MoM and the MCM agree fairly well, however the curves are not very similar here. The FSV method agrees with this by returning a "poor" result for the comparison of the curves in the figure. This implies that the MoM gives a poor estimation of the uncertainty predicted by the more rigorous MCM. The detailed structure of the curves are not similar but the overall

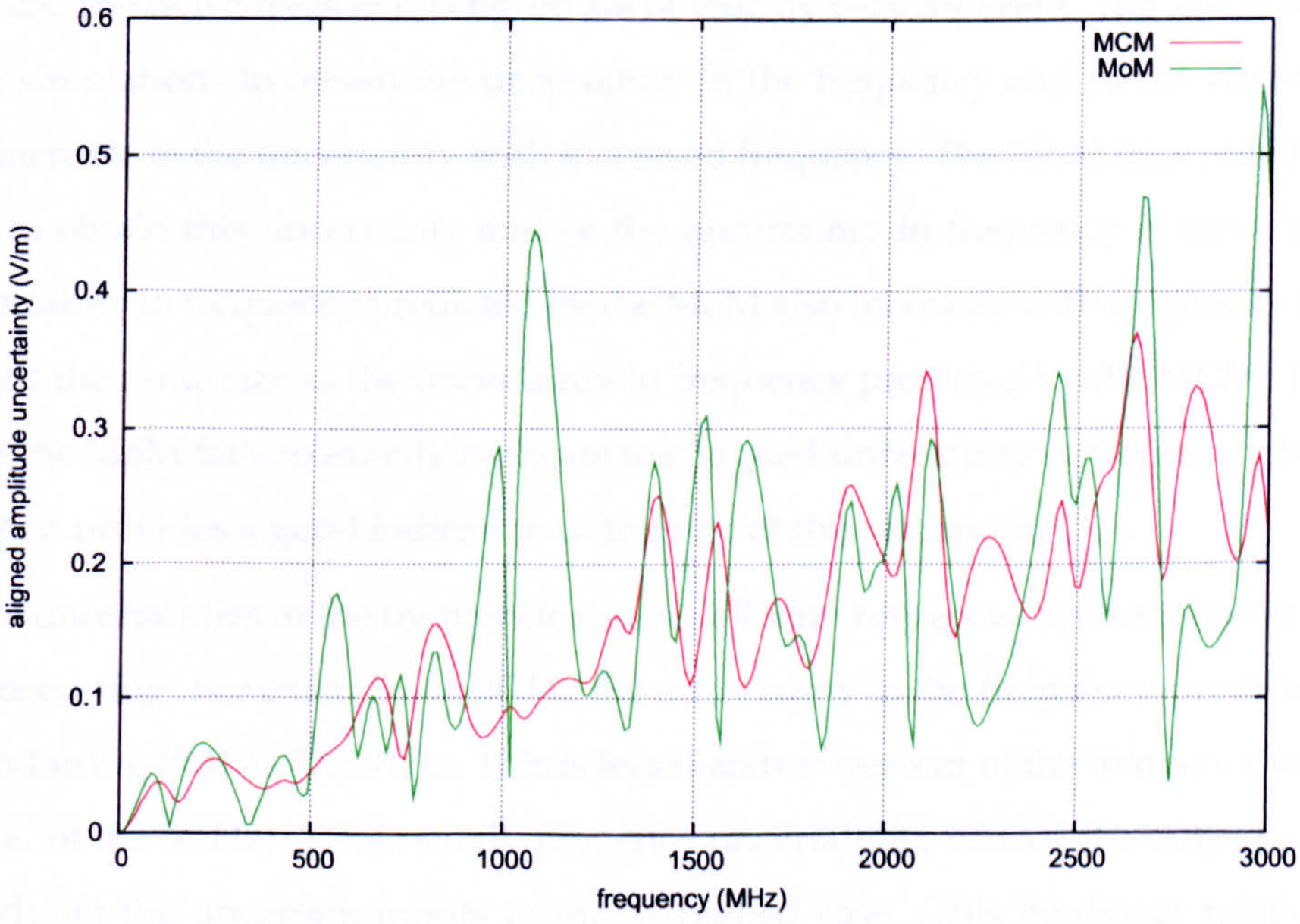

Figure 5.24: Frequency response of the uncertainty in the amplitude of the electric field predicted by the MCM and the MoM after alignment via PM.

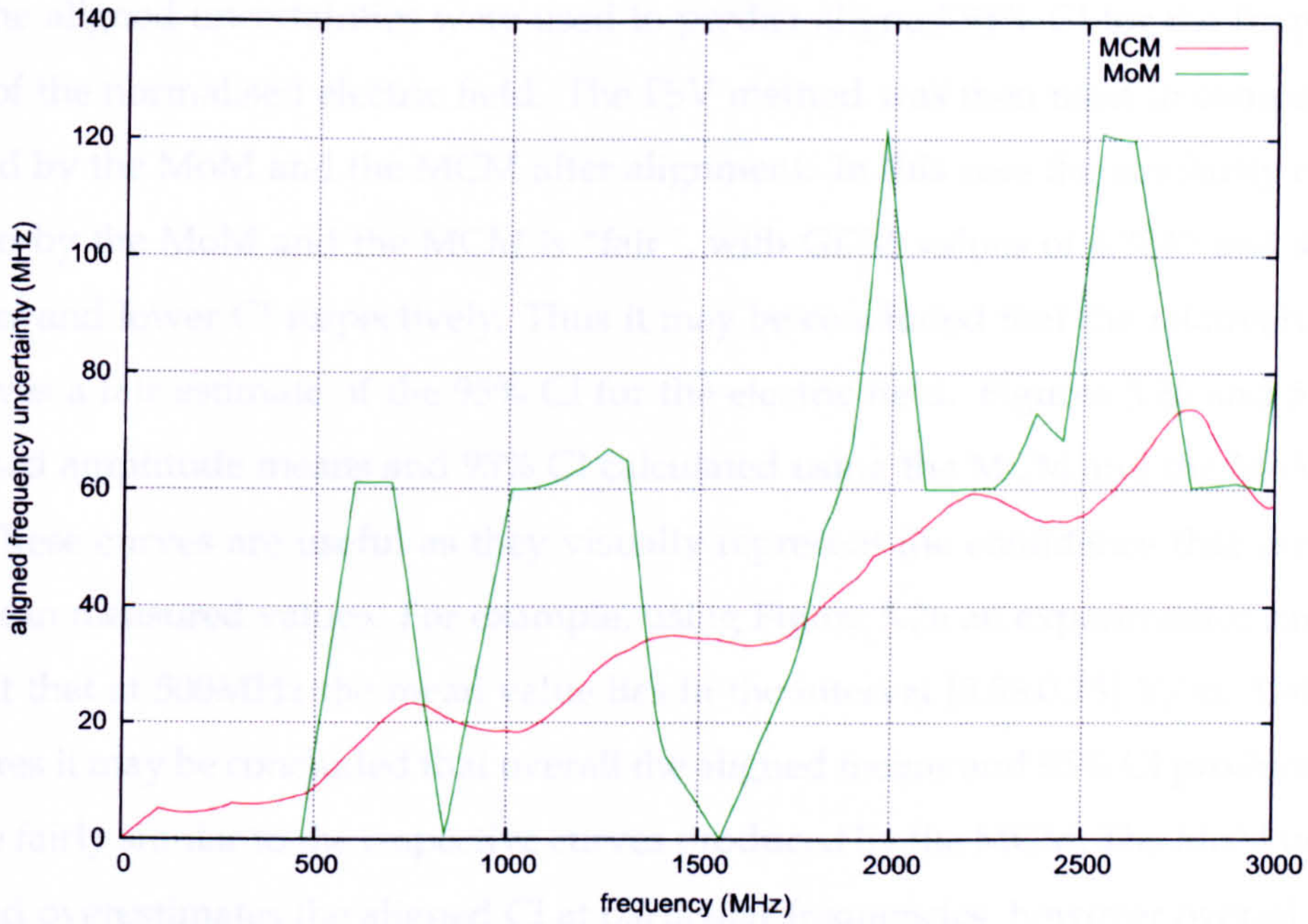

Figure 5.25: Uncertainty in the frequency predicted by the MCM and the MoM after alignment via PM.

sizes of the uncertainty are comparable. Since the MoM is much more computationally efficient than the MCM it is still useful for providing a prediction of the size of the output uncertainty in this example.

The aligned frequency uncertainties predicted by the two UA methods are shown in Figure 5.25. The two curves in this figure are obviously very different. The MCM uses many different simulations to obtain the uncertainty in the frequency and so the curve shows a smooth increase in the uncertainty with increased frequency. The MoM uses only three simulations to obtain this uncertainty and so the uncertainty in frequency is less continuous. The uncertainty in frequency predicted by the MoM also increases with frequency and overall is about the same size as the uncertainty in frequency predicted by the MCM. Therefore, although the MoM fails to exactly replicate the aligned uncertainty in frequency formed by the MCM, it provides a good indication of the size of this uncertainty.

The uncertainties in the frequencies are small with respect to the frequencies at which they are occurring. For example, at 3GHz the uncertainty in the frequency, predicted by the MCM (and using PM), is 57.5MHz. This is less than two percent of the frequency at which it occurs (i.e. of the 3GHz). These small frequency uncertainties caused the output to depend nonlinearly on the uncertain inputs in the unaligned case. This nonlinear relationship is reduced by aligning the curves, which explains why the MoM provides a better estimate of the amplitude uncertainty after alignment.

The aligned uncertainties were used to predict aligned 95% CI for the frequency response of the normalised electric field. The FSV method was then used to compare the CI predicted by the MoM and the MCM after alignment. In this case the similarity of 95% CI predicted by the MoM and the MCM is "fair", with GDM values of 4.3843 and 4.8484 for the upper and lower CI respectively. Thus it may be concluded that the relatively efficient MoM gives a fair estimate of the 95% CI for the electric field. Figures 5.26 and 5.27 show the aligned amplitude means and 95% CI calculated using the MCM and the MoM respectively. These curves are useful as they visually represent the confidence that can be held in the mean measured values. For example, using Figure 5.26 an experimenter can be 95% confident that at 500MHz the mean value lies in the interval [0.58,0.73] V/m. Using these two figures it may be concluded that overall the aligned means and 95% CI produced by the MoM are fairly similar to the respective curves produced by the MCM. The MoM underestimates and overestimates the aligned CI at particular frequencies, however overall the sizes of the means and 95% CI are similar to those produced by the MCM.

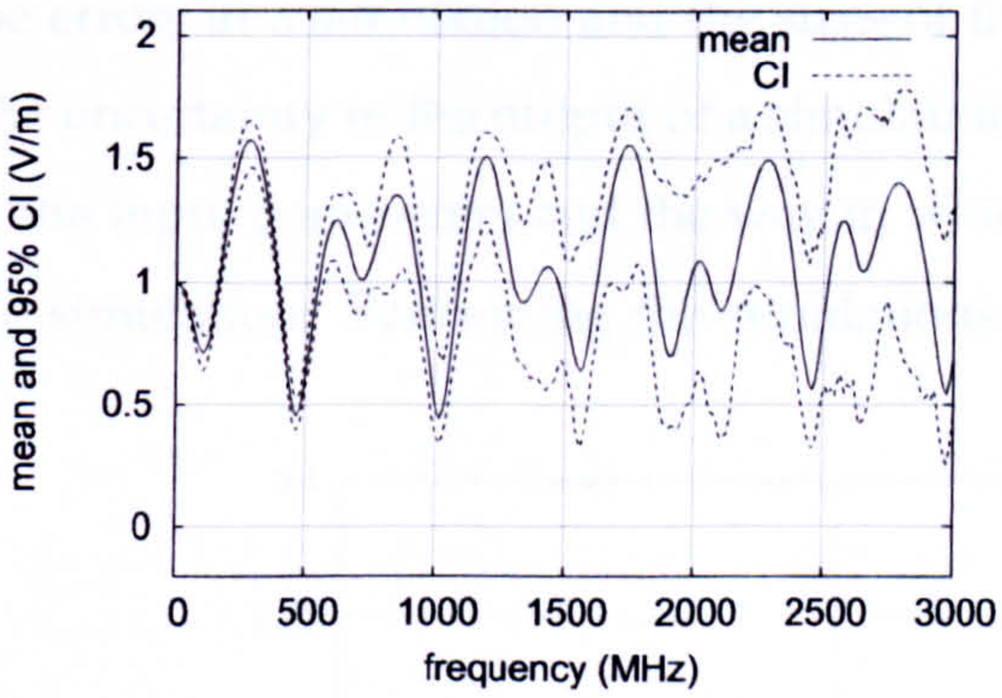

Figure 5.26: Mean amplitude and 95% CI calculated using the MCM after alignment via PM.

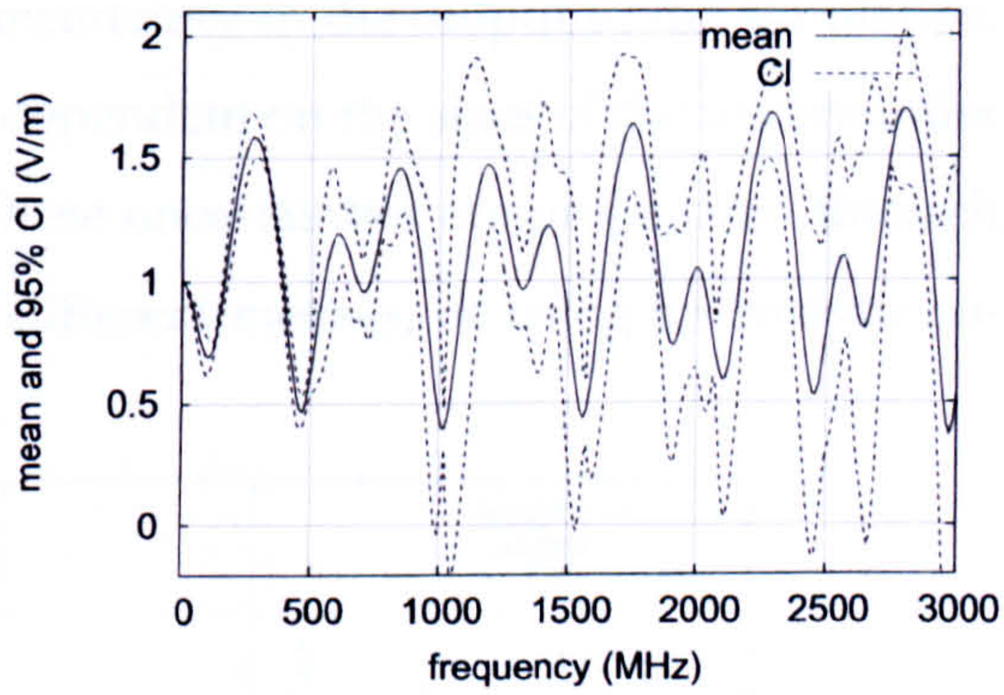

Figure 5.27: Mean amplitude and 95% CI calculated using the MoM after alignment via PM.

Now that curve alignment has been used it is possible to predict the 95% CI for the frequencies as well. The FSV method determines that MoM and MCM predict lower CI for the frequencies that are in "very good" agreement, with a GDM of 2.4729. The upper frequency CI, formed using the MoM and the MCM, are a "good" match with a GDM value of 3.0874. Thus the MoM gives a good prediction of the 95% CI for the frequencies, in this example. Figures 5.28 and 5.29 show the aligned mean and 95% CI of the frequencies calculated using the MCM and the MoM respectively. Although the specific detail of the CI predicted by the MoM and the MCM differ, both methods predict relatively small CI that increase with the frequency.

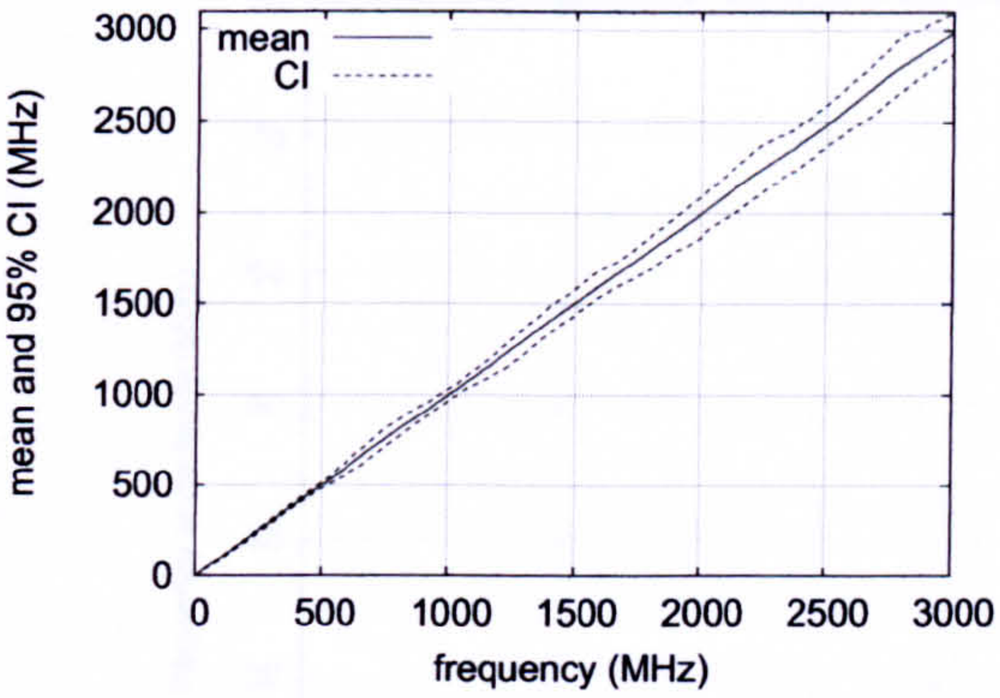

Figure 5.28: Mean frequency and 95% CI calculated using the MCM after alignment via PM.

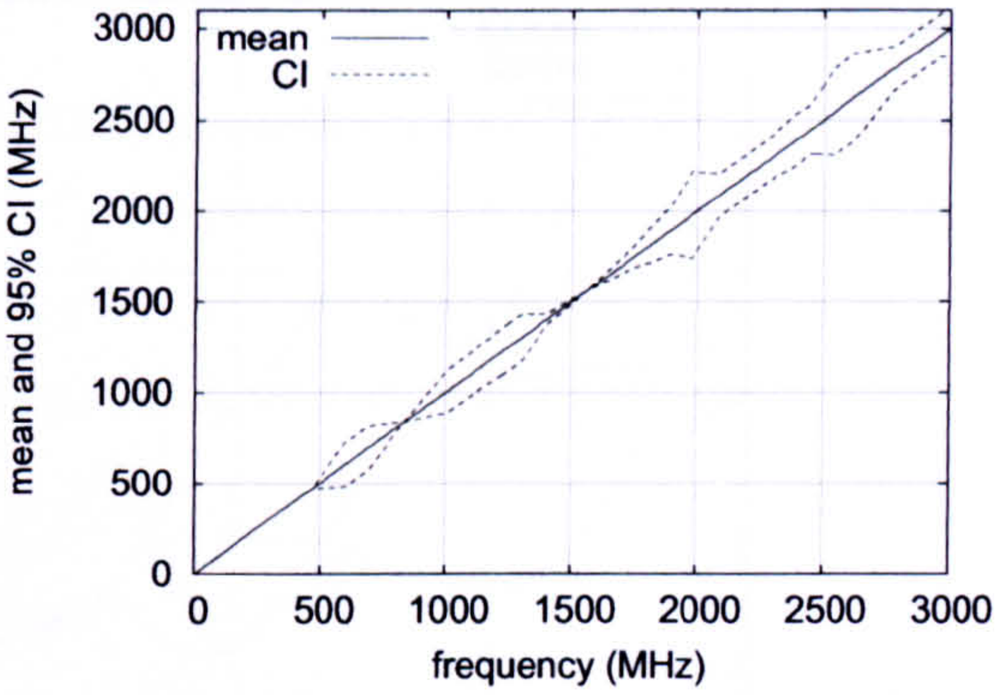

Figure 5.29: Mean frequency and 95% CI calculated using the MoM after alignment via PM.

Figures 5.30 and 5.31 show the aligned uncertainties predicted by the MCM for the analytic solution and both the coarse and fine FDTD simulations. The overall sizes of these uncertainties are similar, this implies that the uncertainties are only weakly dependent on the accuracy of the model used. Thus there is only a small relationship between the sizes of the errors in a simulation and the sizes of the uncertainty in the output of the simulation. The uncertainty in the output of a simulation is dependent on the sizes of the uncertainties in the input parameters and the way in which these uncertainties are propagated through the simulation. Performing the simulations on different meshes, or using an analytic so-

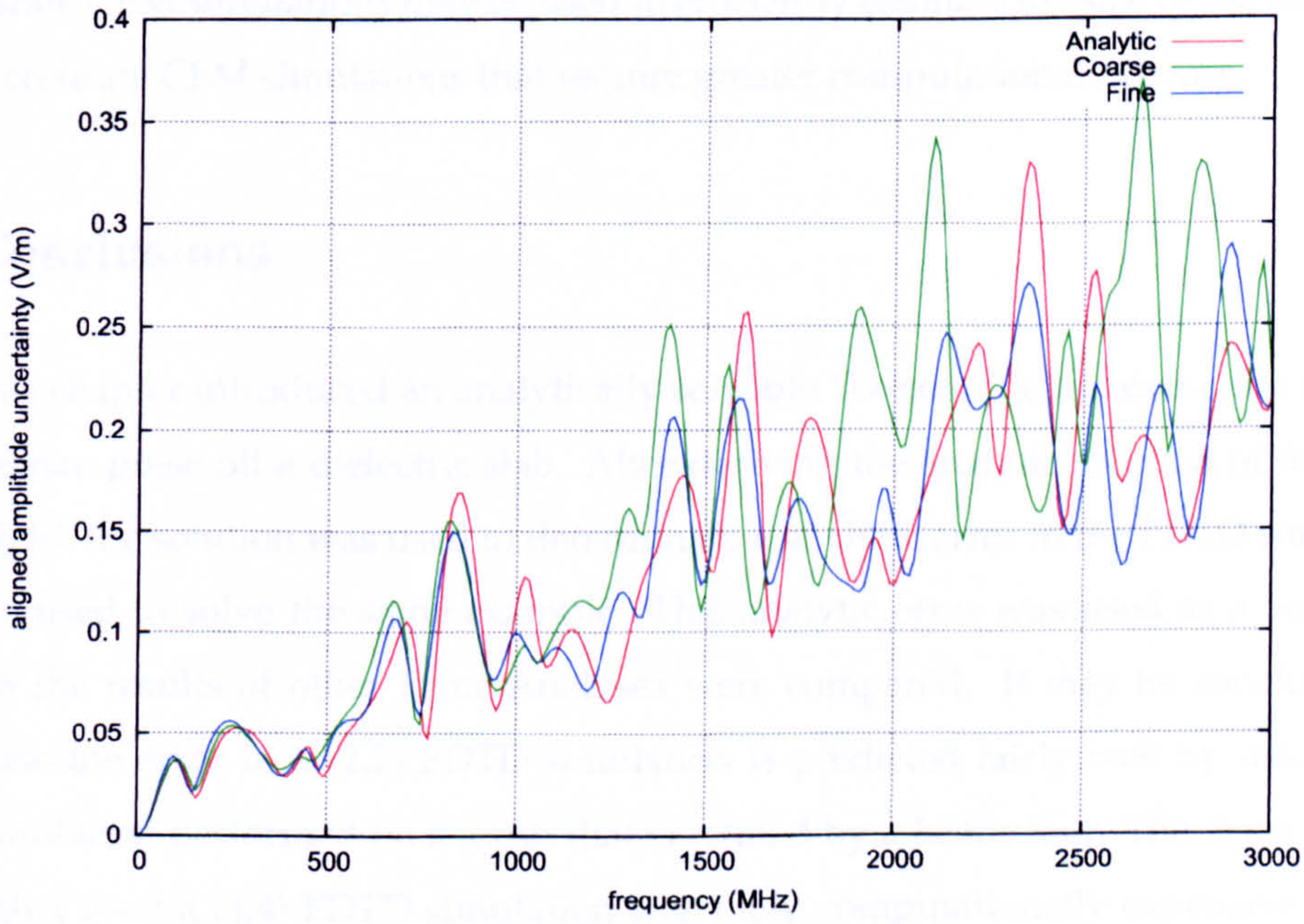

Figure 5.30: Aligned amplitude uncertainty predicted by the MCM for the analytic solution, and for the coarse and fine FDTD simulations.

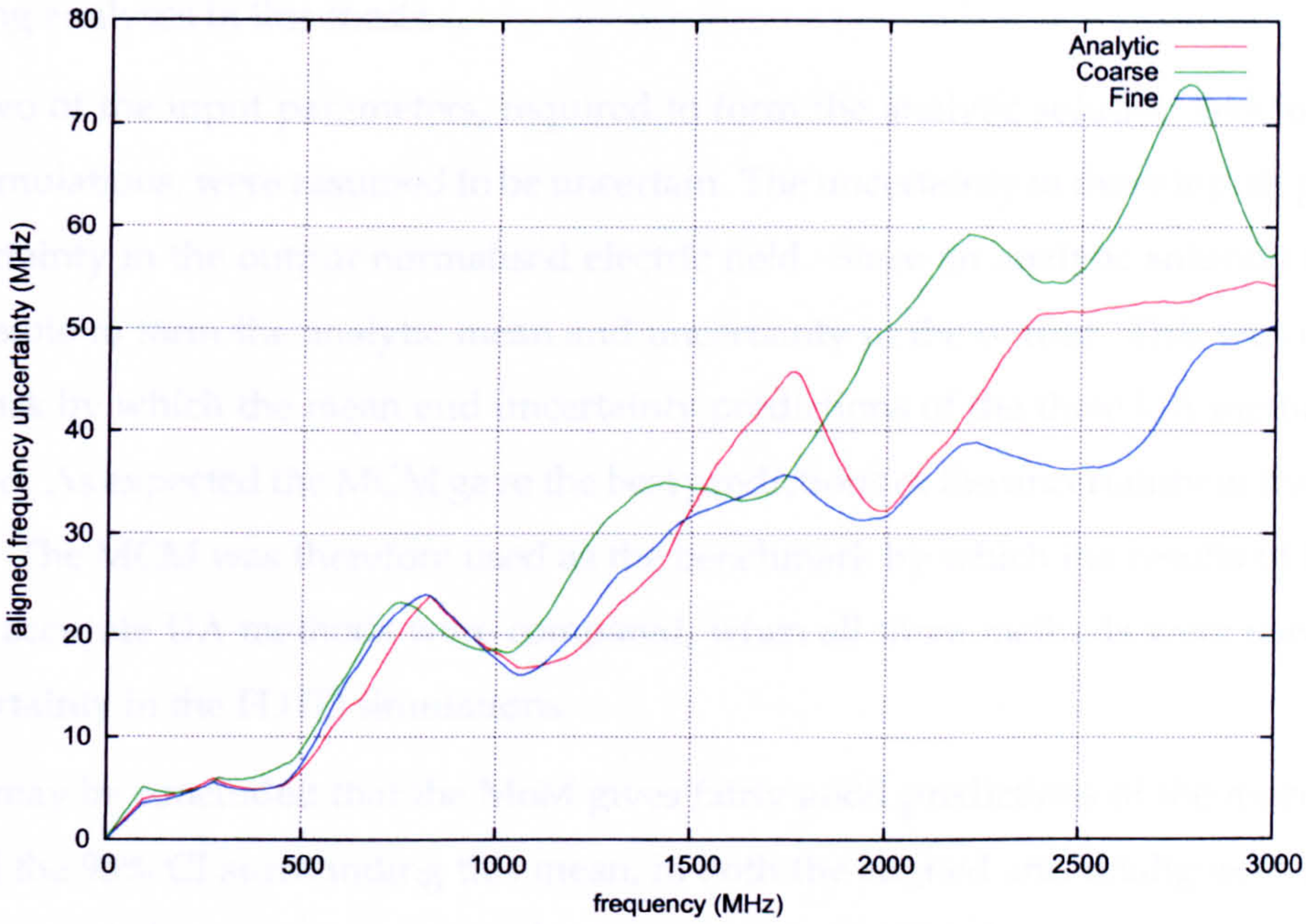

Figure 5.31: Aligned frequency uncertainty predicted by the MCM for the analytic solution, and for the coarse and fine FDTD simulations.

lution will affect how the uncertainty is propagated through. This results in the different detailed structure of the output uncertainty curves, as shown in Figures 5.30 and 5.31. However, these figures show that the size of the output uncertainty has little dependence on the accuracy of the simulation. This may mean that the uncertainty in computationally cheaper, less accurate CEM simulations may be used to efficiently estimate the size of the uncertainty in more accurate CEM simulations that require greater computational expense.

5.6 Conclusions

This chapter introduced an analytically solvable 1D example involving the reflection of a Gaussian pulse off a dielectric slab. After deriving the analytic solution of the output electric field, the solution was used to determine the analytic error in the FDTD simulations that were used to solve the same example. This analytic error was used as a benchmark by which the results of other Error Analyses were compared. It may be concluded that in this case the error in a (2,2) FDTD simulation is predicted fairly well by using a (2,2) FDTD simulation performed on a mesh that is refined by a factor four. The Error Analysis method that used a (4,4) FDTD simulation was more computationally expensive than the Error Analysis method that used (2,2) simulations, and provided only a marginally better estimation of the error. The (4,4) Error Analysis method will therefore not be used in the

remaining analyses in this thesis.

Two of the input parameters, required to form the analytic solution and to perform FDTD simulations, were assumed to be uncertain. The uncertainty in these inputs produced an uncertainty in the output normalised electric field. Since an analytic solution existed it was possible to form the analytic mean and uncertainty in the output. This was used as a benchmark by which the mean and uncertainty predictions of the three UA methods were compared. As expected the MCM gave the best predictions of the uncertainty in the analytic solution. The MCM was therefore used as the benchmark by which the results of the other two less accurate UA methods were compared, when all three methods were used to find the uncertainty in the FDTD simulations.

It may be concluded that the MoM gives fairly good predictions of the mean electric field and the 95% CI surrounding this mean, in both the aligned and unaligned cases. The MoM is about 100 times computationally faster than the MCM, for this example. However the method was shown to overestimate and underestimate the uncertainty in the normalised electric field at certain frequencies. It may be argued that despite these overestimations of the output uncertainty, the computational efficiency of the MoM means that it is still useful as an efficient method for approximately estimating the uncertainty.

The PCM is unable to use curve alignment to predict the aligned uncertainties. In the unaligned case the PCM was better at predicting the output uncertainties than the MoM, when compared to the uncertainties predicted by the benchmark MCM. The PCM is more computationally expensive than the MoM requiring more computational time and memory. The PCM requires less computational runtime than the MCM, but it does require more computational memory. In more complex simulations, with many uncertain inputs, the extra computational memory required may make this method unsuitable. In later chapters, certain examples are used to show that the PCM is not applicable in all scenarios.

For this example, the simulations for both the coarse and fine simulations require little computational runtime, it is therefore better to use the MCM to predict the uncertainties. The MCM does not require too much computational runtime here and it gives predictions of the uncertainty that were shown to be closest to the analytic uncertainty. For more complex simulations the MCM will be too computationally expensive. This thesis aims to determine whether the computationally efficient MoM and PCM can provide reliable estimates of the mean, uncertainty and 95% CI in these cases.

Using curve alignment it is possible to show that not all of the uncertainty in the nor-

malised electric field is due to amplitude differences, a proportion of the uncertainty is due to the frequency shifts between unaligned curves. For this example the uncertainty in the aligned frequency increases with frequency, this is as a result of poorer alignment of the output curves at the higher frequencies. Previously this brought about larger uncertainties in the unaligned amplitude of the electric field at the higher frequencies. Using alignment, it was shown that the uncertainties at the higher frequencies are also due to uncertainties in the frequency. The amplitude uncertainties predicted by the MoM reduced after the alignment process. The alignment process helped to reduce the nonlinearity in the relationship between the output and the input, thus making the MoM predictions more accurate.

In both the aligned and unaligned cases the relationship between the size of the output uncertainty and the size of the errors in a simulation is small. The uncertainty in the output of a simulation depends on both the sizes of the uncertainties associated with the input parameters and the way in which these uncertainties are propagated through the simulation. Performing the simulations on different meshes, or using an analytic solution will affect how the uncertainty is propagated through. Thus, different simulations that have different amounts of error will produce different output uncertainties. However, it has been shown that the uncertainty in the output of simulations that are performed with a different level of accuracy are similar in size for this example. Thus, the size of the output uncertainty has little dependence on the accuracy of the simulation, and is more dependent on the size of the uncertainties in the input parameters. If this is the case in general then computationally faster, less accurate CEM simulations may be used to efficiently estimate the uncertainty in more accurate, computationally expensive CEM simulations.

In this chapter the Error and Uncertainty Analyses were applied to a simple 1D analytic solvable example. In the next chapter these analyses will become more complex and computationally expensive as they are applied to a 3D analytically solvable example.

Chapter 6

Error and Uncertainty Analyses Applied to Three Dimensional Finite Difference Time Domain Simulations Involving Spheres

Contents

6.1 Introduction

In this chapter the different Error and Uncertainty Analysis methods are applied to 3D FDTD simulations. In the first example the backscattering of the electric field from a dielectric sphere is considered. This example has an analytic solution often known as the Mie series, a detailed description of which is given by Stratton in [91, p.563-567]. The sphere, in this example, is assumed to have an uncertain radius, permittivity and permeability.

As in the previous chapter, the analytic (exact) error in the output of a FDTD simulation is calculated by taking the difference between the FDTD simulated result and the analytic solution. An estimation of the error is obtained by using a (2,2) FDTD simulation performed on a refined mesh: this was shown to give good estimates of the error in the previous chapter. This estimate of the error is compared to the analytical error to determine the performance of the approximate Error Analysis method.

The analytic solution of the backscattered electric field is also used to obtain the mean and uncertainty analytically. These analytic results are compared to the means and uncertainties predicted by the three UA methods, when applied to the analytic solution of the backscattered field. These comparisons show that the MCM provides the best estimate of the uncertainty in the analytic solution. The MCM is therefore used as the benchmark method for the analysis of the uncertainty in the FDTD simulations. The MoM and the PCM are compared to the benchmark MCM in terms of their ability to accurately predict the mean, uncertainty and 95% CI in the output of the FDTD simulation. The three methods are also compared in terms of their computational expense.

A second example is introduced in Section 6.7, which considers the electric field backscattered from a PEC sphere with an uncertain radius. The PCM fails to provide a reliable estimate of the uncertainty in the output of the FDTD simulation, for this example.

6.2 Electric Field Scattering Off a Dielectric Sphere in Three Dimensions

In this 3D example a uniform plane wave electric field excitation is backscattered off a dielectric sphere in free space. The sphere has an uncertain radius, which is Normally distributed with a mean $\bar{a} = 0.1\text{m}$ and an uncertainty $\sigma_a = 0.005\text{m}$. The sphere also has an uncertain permittivity, which is Uniformly distributed in the interval $\epsilon_r = [3.7, 4.3]$, and an uncertain permeability, which is Uniformly distributed in the interval $\mu_r = [0.95, 1.05]$. The incident plane wave E_x^i propagates in the positive z direction, and is oriented in the x direction with a magnitude $E_0 = 1\text{V/m}$. The x-component of the backscattered field E_x^r is measured at a distance of 0.2m from the centre of the sphere. The setup of this example is shown in Figure 6.1. The absolute value of the backscattered field is transformed into the frequency domain, and normalised to the absolute value of the incident field in the frequency domain. The analytic Mie series solutions [92] may be used to calculate this normalised electric field analytically: these solutions are introduced in the next section.

The frequency response of the normalised electric field may also be calculated using

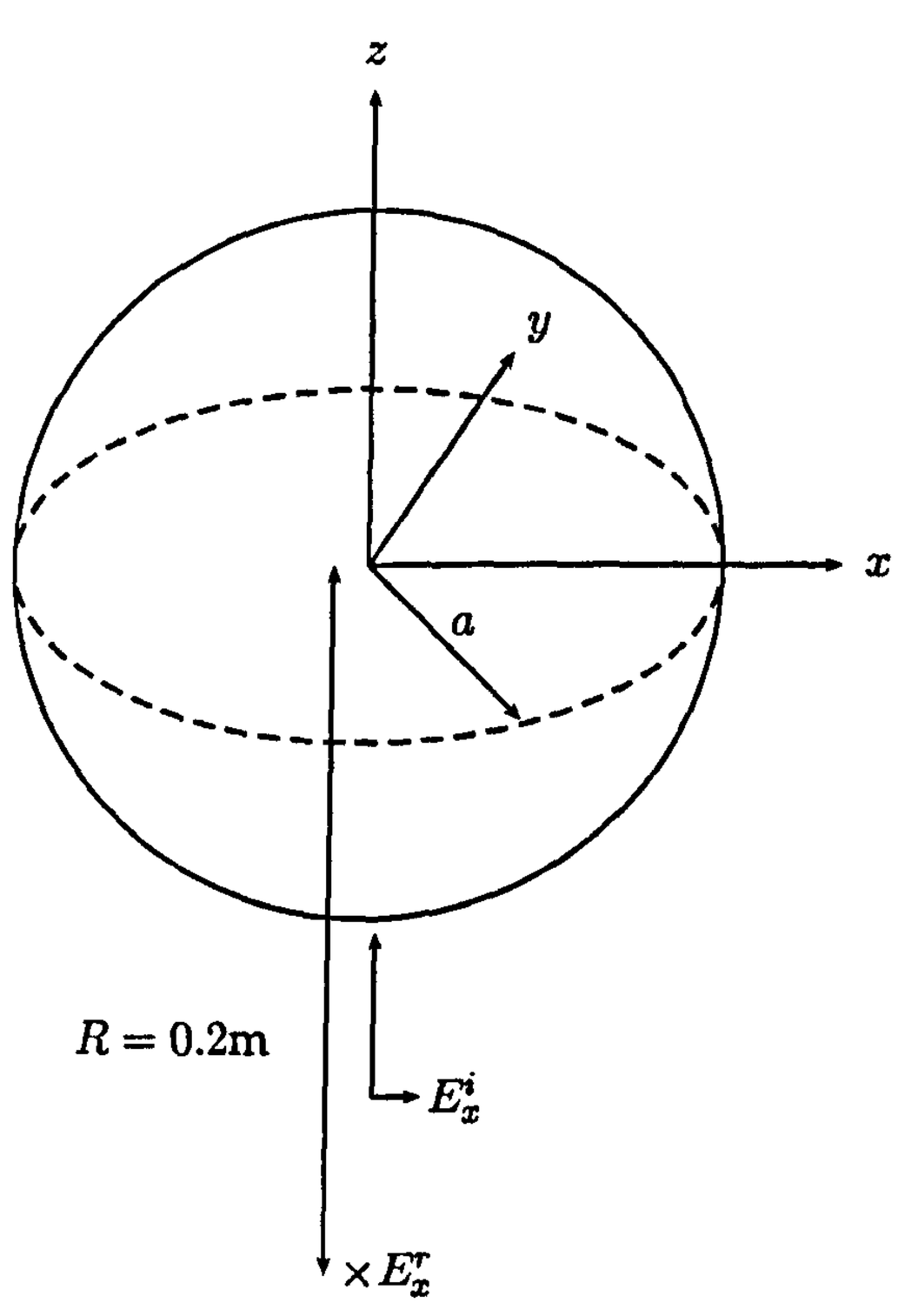

Figure 6.1: A three dimensional problem space containing a dielectric sphere. A plane wave is reflected off the sphere and observed at ×.

a FDTD simulation, with a broad Gaussian incident plane wave. A Huygen's surface [93] is used to simulate the incident electric field. The Huygen's surface is implemented so that it surrounds the sphere, but not the output point. This means that the total field recorded at the output point is only the reflected field E_x^r (and of course the error in this output). It is the reflected field that is used to calculate the normalised backscattered electric field.

6.2.1 The Analytic Solution

Consider a sphere, centred at the origin, with a radius a and propagation constant k_1 surrounded by a homogeneous material with a propagation constant k_2. The propagation constant k_1 is related to the free space frequency f of the travelling wave, the permittivity ϵ_1 and permeability μ_1 of the sphere as $k_1 = 2\pi f\sqrt{\epsilon_1\mu_1}$. The permittivity and permeability are in turn related to the relative permittivity ϵ_r and relative permeability μ_r as $\epsilon_1 = \epsilon_0\epsilon_r$ and $\mu_1 = \mu_0\mu_r$, where ϵ_0 and μ_0 are the permittivity and permeability of free space respectively. The propagation constant k_2 is formed similarly using the material properties of the media surrounding the sphere.

A plane wave that is incident upon this sphere, travelling along the positive z-axis and oriented in the positive x-direction, may be represented in terms of spherical wave functions as [91, p.564]

$$E_x^i\hat{x} = \hat{x}E_0e^{I(k_2z-\omega t)} = E_0e^{-I\omega t}\sum_{n=1}^{\infty} I^n\frac{2n+1}{n(n+1)}(\mathbf{m}_{o1n}^{(1)} - I\mathbf{n}_{e1n}^{(1)}) \tag{6.1}$$

where $I = \sqrt{-1}$, E_0 is the amplitude, ω is the angular frequency, z and t are the spatial and temporal coordinates, $\hat{x}$ is a unit vector in the x-direction and

$$\mathbf{m}_{o1n}^{(1)} = \frac{1}{\sin(\theta)}J_n(k_2R)P_n^1(\cos(\theta))\cos(\phi)\hat{\theta} - J_n(k_2R)\frac{\partial P_n^1}{\partial\theta}\sin(\phi)\hat{\phi} \tag{6.2}$$

$$\begin{aligned}\mathbf{n}_{e1n}^{(1)} =& \frac{n(n+1)}{k_2R}J_n(k_2R)P_n^1(\cos(\theta))\cos(\phi)\hat{R} + \frac{1}{k_2R}\left[k_2RJ_n(k_2R)\right]'\\ &\frac{\partial P_n^1}{\partial\theta}\cos(\phi)\hat{\theta} - \frac{1}{k_2R\sin(\theta)}\left[k_2RJ_n(k_2R)\right]'P_n^1(\cos(\theta))\sin(\phi)\hat{\phi}.\end{aligned} \tag{6.3}$$

In the above equations R, θ and ϕ are the spherical coordinates of the output point, $\hat{R}$, $\hat{\theta}$ and $\hat{\phi}$ are the corresponding unit vectors, and the prime denotes differentiation with respect to k_2R. The terms P_n^1 and J_n are the associated Legendre polynomials and spherical Bessel functions respectively.

The reflected electric field at a position $(R > a, \theta, \phi)$ may be written as [91, p.564]

$$E_x^r \hat{x} = E_0 e^{-I\omega t} \sum_{n=1}^{\infty} I^n \frac{2n+1}{n(n+1)} (A_n^r \mathbf{m}_{o1n}^{(3)} - I B_n^r \mathbf{n}_{e1n}^{(3)}) \tag{6.4}$$

where $\mathbf{m}_{o1n}^{(3)}$ and $\mathbf{n}_{e1n}^{(3)}$ are obtained by replacing the spherical Bessel functions $J_n(k_2 R)$ by the spherical Hankel functions $H_n^{(1)}(k_2 R)$ in equations (6.2) and (6.3). Similar equations to (6.1) and (6.4) may be obtained for the electric field transmitted to the interior of the sphere (ie. for $R < a$) and for the incident, reflected and transmitted magnetic fields. The coefficients A_n^r and B_n^r in equation (6.4) are obtained by asserting that the incident and reflected electric and magnetic fields are equal to the transmitted fields, at the boundary $R = a$. This produces two equations in the coefficients A_n^r and B_n^r, which may be solved to obtain [91, p.565]

$$A_n^r = -\frac{\mu_1 J_n(N\rho)[\rho J_n(\rho)]' - \mu_2 J_n(\rho)[N\rho J_n(N\rho)]'}{\mu_1 J_n(N\rho)[\rho H_n^{(1)}(\rho)]' - \mu_2 H_n^{(1)}(\rho)[N\rho J_n(N\rho)]'} \tag{6.5}$$

$$B_n^r = -\frac{\mu_1 J_n(\rho)[N\rho J_n(N\rho)]' - \mu_2 N^2 J_n(N\rho)[\rho J_n(\rho)]'}{\mu_1 H_n^{(1)}(\rho)[N\rho J_n(N\rho)]' - \mu_2 N^2 J_n(N\rho)[\rho H_n^{(1)}(\rho)]'} \tag{6.6}$$

where $N = k_1/k_2$ and $\rho = k_2 a$.

The expression for the reflected electric field is greatly reduced by considering the backscattered field on the z-axis, where $(\theta, \phi) = (\pi, \pi)$. At these angles $\sin(\phi) = 0$ and [94, p.656]

$$P_n^1(\cos(\theta))\Big|_{\theta=\pi} = 0 \tag{6.7}$$

$$\frac{P_n^1(\cos(\theta))}{\sin(\theta)}\bigg|_{\theta=\pi} = (-1)^n \frac{n(n+1)}{2} \tag{6.8}$$

$$-\frac{\partial P_n^1}{\partial \theta}\bigg|_{\theta=\pi} = (-1)^n \frac{n(n+1)}{2}. \tag{6.9}$$

Thus the backscattered electric field becomes

$$E_x^r = E_0 e^{-I\omega t} \sum_{n=1}^{\infty} I^n (-1)^n \frac{2n+1}{2} \left(-A_n^r H_n^{(1)}(k_2 R) - I B_n^r \frac{[k_2 R H_n^{(1)}(k_2 R)]'}{k_2 R} \right). \tag{6.10}$$

The magnitude of this scattered wave in the frequency domain is simply

$$|E_x^r| = E_0 \left| \sum_{n=1}^{\infty} I^n (-1)^n \frac{2n+1}{2} \left(-A_n^r H_n^{(1)}(k_2 R) - I B_n^r \frac{[k_2 R H_n^{(1)}(k_2 R)]'}{k_2 R} \right) \right|. \tag{6.11}$$

The normalised output electric field is formed by taking the ratio of $|E_x^r|$ to the 1V/m inci-

Refinements compared	ADM	FDM	GDM	GDM (1-6)	Qualitative
0.5 and 1	0.2051	0.3153	0.4100	4.0274	Fair
1 and 2	0.0591	0.1143	0.1405	2.4149	Very Good
2 and 4	0.0162	0.0330	0.0407	1.4073	Excellent

Table 6.1: FSV comparisons of simulated results calculated with different mesh refinements.

dent electric field excitation. The magnitude of this incident field is one for all frequencies and therefore the normalised electric field equals $|E_x^r|$.

This analytic solution was implemented into Matlab, making use of the spherical Bessel and Hankel functions that are programmed into the software. The infinite sum is impossible to calculate, the solution was therefore truncated after the first ten resonant modes. The frequency response of this normalised electric field is shown in the next section. Truncating the series causes the solution to be an approximation of the analytic solution, thus the truncated solution contains errors. The percentage difference between the solution produced with ten terms and the solution produced with 20 terms gave a maximum error of 0.0024% (over frequencies from 0GHz to 3GHz). Using ten terms in the series solution is therefore sufficient to produce an accurate approximation of the analytic solution. The approximate analytic solution (formed with ten terms) is regarded as the exact analytic solution in the discussion that follows. The uncertainty in this solution enters via the uncertainty in the radius a and the uncertainty in the propagation constant k_1, which is related to the uncertain permittivity ϵ_1 and the uncertain permeability μ_1.

6.2.2 Frequency response of the Backscattered Electric Field

It is possible to form a simulated solution for this example using the FDTD method. As in the previous chapter, multiple mesh refinements may be performed to determine when the simulated solution has reached convergence. This convergence is tested by using the FSV method to compare how similar the output normalised electric field curves are after each progressive mesh refinement. Table 6.1 shows the FSV comparisons of the output formed from simulations with different mesh refinements. The mesh refinement factor of one refers to a mesh with a cell size $\Delta l = 0.005$m, $100 \times 100 \times 100$ cells, and 10,000 time steps. It is clear from this table that the output converges for progressively finer meshes, as the curves become more similar.

The simulations were all performed on a Core2Duo processor at 3.0GHz. The time and memory required for the FDTD simulation with a refinement factor of one were 11 min-

utes and 31MB respectively. From Table 6.1 it may be concluded that the simulations are converging around a refinement factor of one, but full convergence is not reached until the refinement factor is two or four. Unfortunately each refinement causes the simulation to require eight times more memory (as there are eight times more cells), and 16 times more computational runtime (a factor eight times more cells to calculate for, and twice the number of time steps). The simulations therefore become very computationally expensive for refinement factors of two and above. Performing uncertainty analyses with these higher refinement factors would prove too costly. For example, a Monte Carlo simulation using 500 simulations with a refinement factor of two would take around 60 days. The FSV comparison has determined that the output formed from the simulations using refinement factors of one and two are very close. The simulation with a refinement factor of one is close to convergence and is computationally less expensive than the simulations using finer meshes. This simulation is therefore chosen for the subsequent Error and Uncertainty Analyses.

The frequency response of the analytic solution, and the FDTD simulated solutions are shown in Figure 6.2: these curves are all very similar. The output from the simulation performed with a refinement factor of four will be used to estimate the error in the simulation performed with a refinement factor of one, in the next section. From now on the simulation performed with a refinement factor of one will be referred to as the reference FDTD simulation. Similarly the simulation performed with a refinement factor of four will be referred to as the refined FDTD simulation.

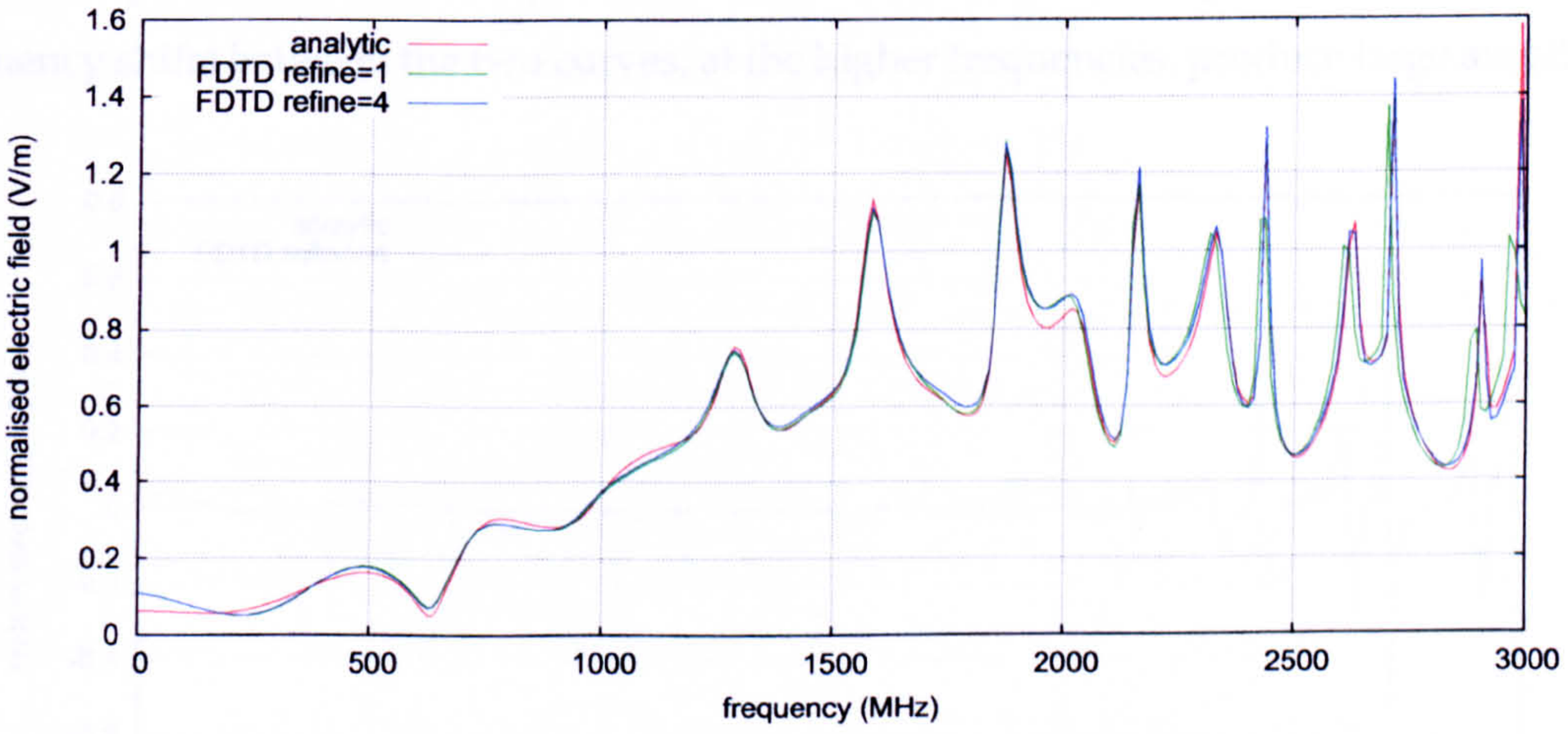

Figure 6.2: Frequency response of the normalised electric field

6.3 Error Analysis of the Finite Difference Time Domain Simulation

The analytic error is formed by taking the difference between the output of the reference FDTD simulation and the analytic solution. This provides the quantification of all the errors in the reference FDTD simulation. An approximate quantification of the errors may be formed by taking the difference between the output of the reference and refined FDTD simulations. The refined FDTD simulation contains fewer errors than the reference simulation, and so should highlight some of the errors in the reference simulation.

Figure 6.3 shows the analytical error and the approximate error formed using the refined FDTD simulation. It seems that the approximate Error Analysis method performs well at the higher frequencies but not so well at the lower frequencies, when compared to the analytic error. The errors in the refined FDTD simulation prevent the approximate Error Analysis method from identifying some of the errors in the reference FDTD simulation at the lower frequencies. This is confirmed by FSV comparisons of the analytic and approximate error predictions, which form GDM values on the visual scale of 6 (Very Poor) for frequencies below 2GHz, and 4.3105 (Fair) for frequencies between 2GHz and 3GHz. These comparisons may however be too harsh, visually the two curves seem to be similar. At the higher frequencies the two curves seem to be very similar. Removing the offset difference measure from the FSV method (as in the original implementation [68]) provides a GDM of 2.5663 (Very Good) for the comparison of the two curves at the higher frequencies. Small frequency shifts between the two curves, at the higher frequencies, produce large amplitude

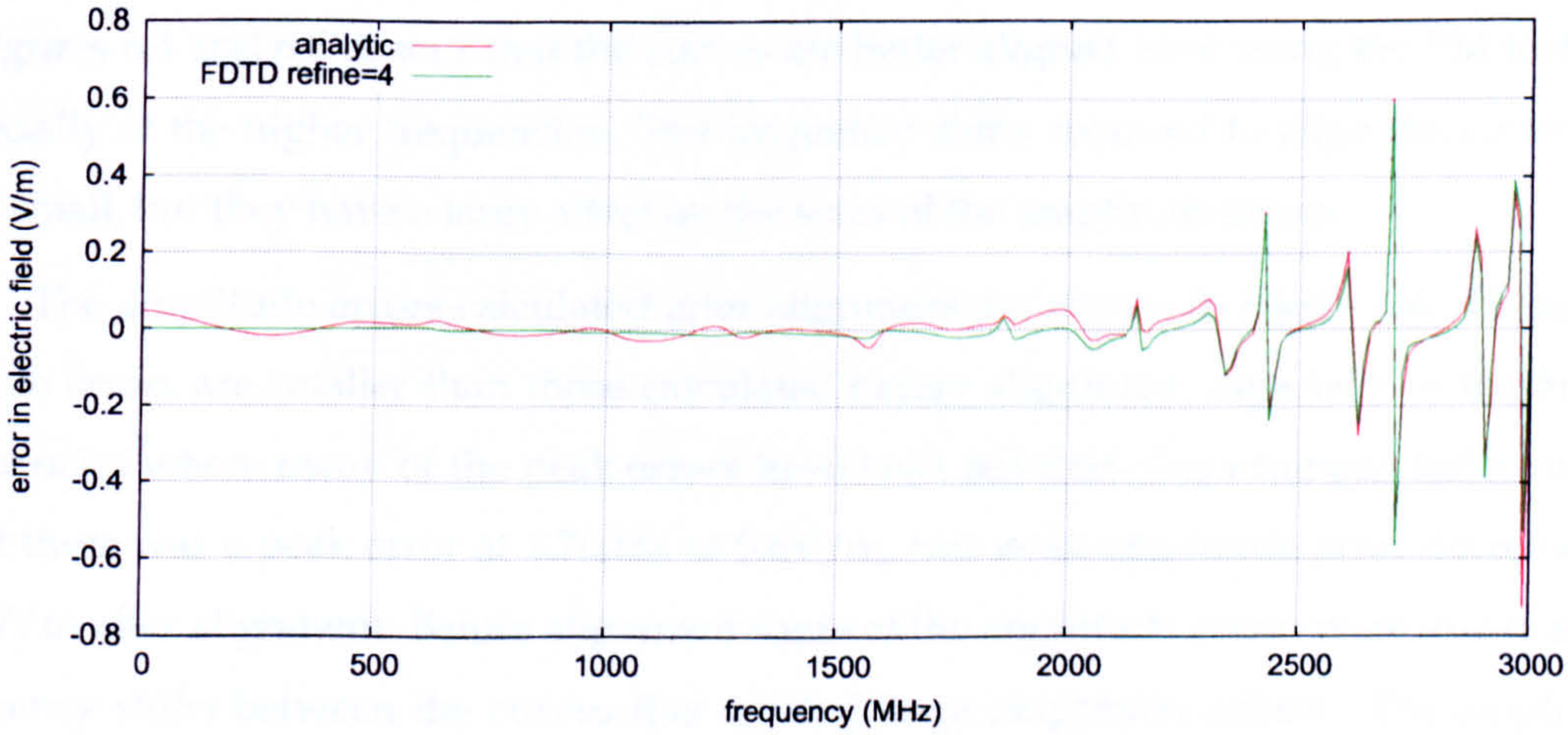

Figure 6.3: Frequency response of the error in the reference FDTD simulation, calculated analytically and using a FDTD simulation with a refinement factor of four

offsets. These amplitude offsets cause the FSV method to determine that the two curves are only fairly similar, when in fact it seems the curves are very similar at the higher frequencies. Using a curve alignment before the comparison would prevent these harsh comparisons from being produced, as described in Section 3.2.2.

Both Error Analysis methods agree that the errors in the reference FDTD simulation are relatively small at the lower frequencies. At the higher frequencies the errors become fairly large; the largest absolute error is 0.73V/m at 2.99GHz, which is 45.8% of the normalised electric field, calculated analytically at this frequency. From Figure 6.2 it appears that there is a small frequency shift between the reference FDTD simulated output and the other curves, at the higher frequencies. In the next section curve alignment is used to calculate the aligned amplitude and frequency errors in the reference FDTD simulation.

6.4 Evaluating the Errors After Alignment

Figures 6.4 and 6.5 show the normalised electric field, calculated using the reference FDTD simulation, before and after alignment to the analytic solution, and to the refined FDTD simulated solution. The PM method was used to align the curves in both cases. FSV comparisons of the output formed from the reference FDTD simulation and the analytic solution, provide GDM values on the visual scale of 3.1167 before and 2.7206 after alignment. The curves are more similar after alignment, this provides evidence that the alignment process has worked well. Similarly the comparison of the two FDTD simulated outputs before and after alignment are 2.6821 and 1.8990 respectively. Thus in both cases the PM has performed well, providing a good alignment of the curves. Visual comparisons of the curves in Figures 6.4 and 6.5 concur that the curves are better aligned after using the PM method, especially at the higher frequencies. The frequency shifts required to align the curves are only small, but they have a large affect on the sizes of the amplitude errors.

The amplitude errors calculated after alignment are shown in Figure 6.6. These amplitude errors are smaller than those calculated before alignment, especially at the higher frequencies where many of the peak errors have been reduced. For example, before alignment there was a peak error at 2.7GHz of 0.6V/m, this peak amplitude error decreases to 0.07V/m after alignment. Before alignment some of the amplitude errors were due to small frequency shifts between the curves that created large amplitude offsets. The amplitude errors are smaller after alignment because these small frequency shifts are removed.

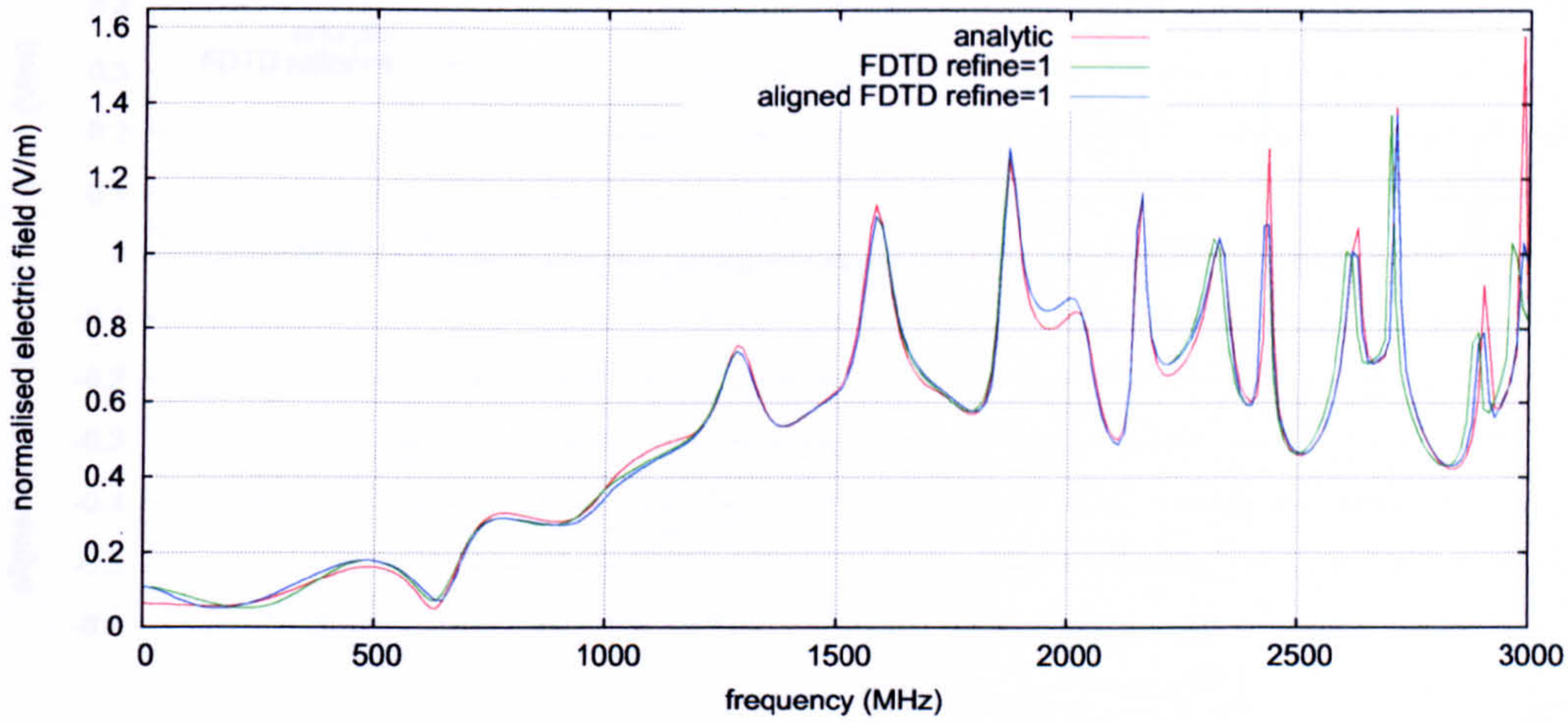

Figure 6.4: Analytic solution and reference FDTD solution before and after alignment.

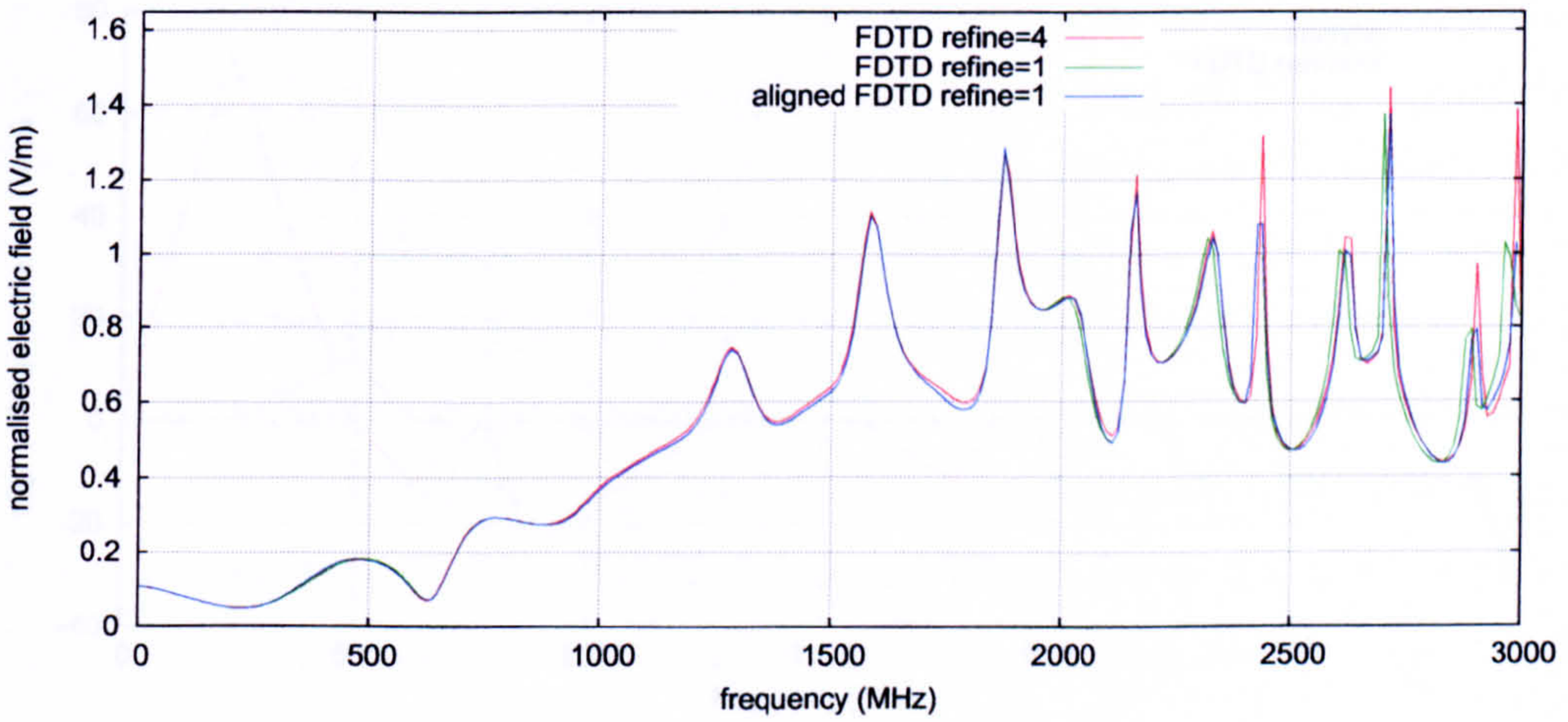

Figure 6.5: Refined and reference FDTD solutions before and after alignment.

The frequency errors calculated after alignment are shown in Figure 6.7. The largest frequency errors occur at the lowest and highest frequencies. These frequency shift errors are generally relatively small, however before alignment these frequency errors caused large amplitude differences between the curves. Now that the curves have been aligned it is possible to conclude that the errors in the FDTD reference simulation manifest themselves as moderately sized amplitude errors, and small frequency errors. It is difficult to acquire this knowledge, on the form of the output errors, without alignment.

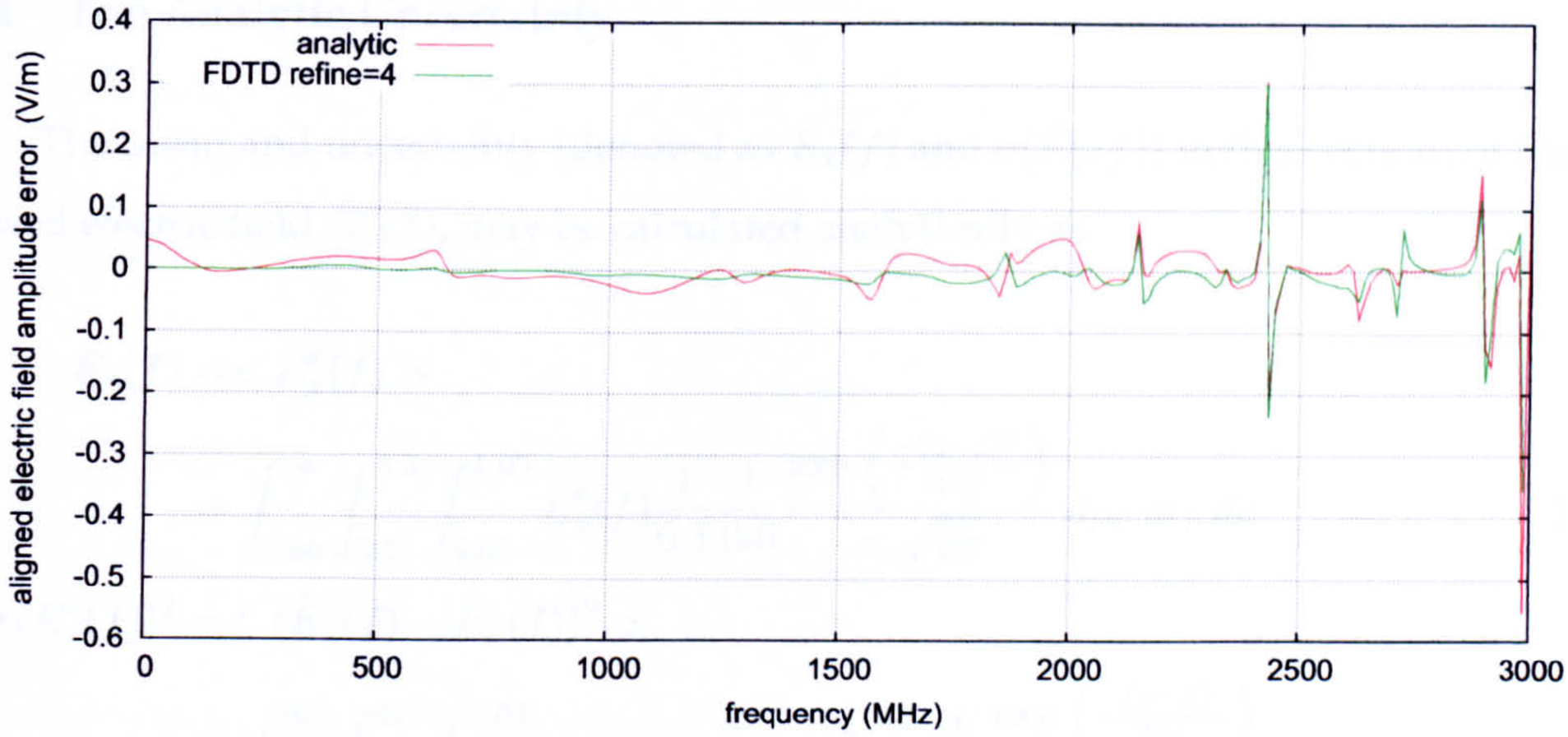

Figure 6.6: Frequency response of the amplitude error calculated after alignment.

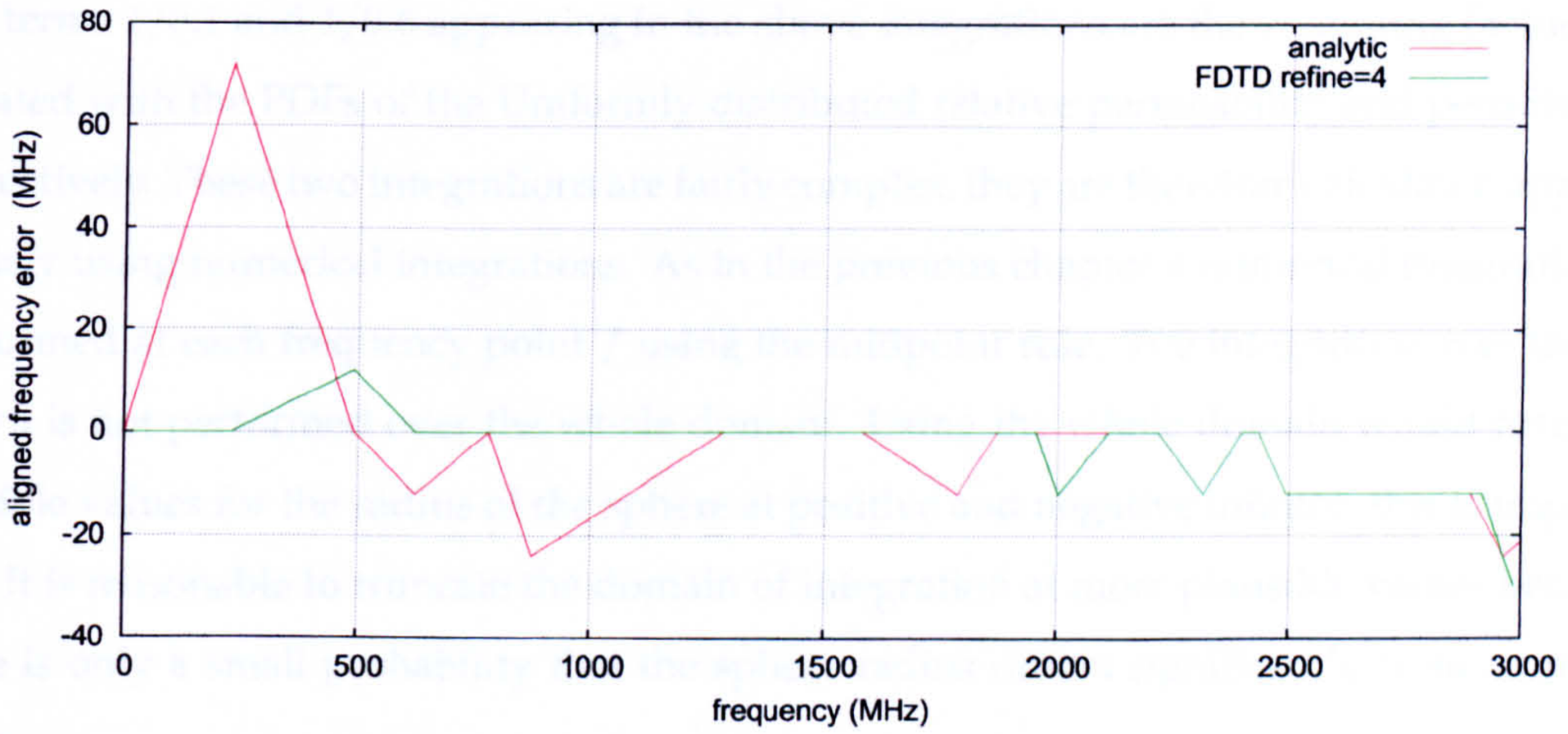

Figure 6.7: Frequency response of the frequency error calculated after alignment.

6.5 Uncertainty Analysis of the Backscattered Electric Field

In this section different UA methods are used to quantify the uncertainty in the output electric field. Firstly the application of each of the UA methods to this specific example is described. The methods are then compared in terms of their performance and their computational expense. The uncertainties in the analytic and reference FDTD simulated solutions are compared to determine whether there is a relationship between the errors and uncertainties in the FDTD simulations. The results of the UAs are then used to construct the 95% CI. Finally curve alignment is used to determine the uncertainty due to amplitude differences in the output, and the uncertainty due to frequency differences in the output.

6.5.1 The Analytic Uncertainty

The mean and uncertainty (denoted as $\bar{E}_x(f)$ and $\sigma(\tilde{E}_x^r(f))$ in this section) of the normalised electric field $\tilde{E}_x^r(f)$, may be calculated analytically as

$$\begin{aligned}\bar{E}_x(f) &=< \tilde{E}_x^r(f) > \\ &= \int_{-\infty}^{\infty}\int_{3.7}^{4.3}\int_{0.95}^{1.05} \tilde{E}_x^r(f)\frac{1}{0.1}\frac{1}{0.6}\frac{\exp\left(\frac{-(a-\bar{a})^2}{2\sigma_a^2}\right)}{\sigma_a\sqrt{2\pi}}\, d\mu_r\, d\epsilon_r\, da \qquad (6.12)\end{aligned}$$

$$\begin{aligned}\sigma(\tilde{E}_x^r(f))^2 &=< (\tilde{E}_x^r(f) - \bar{E}_x(f))^2 > \\ &= \int_{-\infty}^{\infty}\int_{3.7}^{4.3}\int_{0.95}^{1.05} (\tilde{E}_x^r(f) - \bar{E}_x(f))^2\frac{1}{0.1}\frac{1}{0.6}\frac{\exp\left(\frac{-(a-\bar{a})^2}{2\sigma_a^2}\right)}{\sigma_a\sqrt{2\pi}}\, d\mu_r\, d\epsilon_r\, da. \qquad (6.13)\end{aligned}$$

The terms 1/0.1 and 1/0.6 appearing in the above integrations are the weighting factors associated with the PDFs of the Uniformly distributed relative permeability and permittivity respectively. These two integrations are fairly complex, they are therefore calculated approximately using numerical integrations. As in the previous chapter a numerical integration is performed at each frequency point f using the midpoint rule. The integration over the radius a is not performed over the whole domain. Using the whole domain would result in possible values for the radius of the sphere at positive and negative infinity: this is unphysical. It is reasonable to truncate the domain of integration at more plausible values because there is only a small probability that the sphere radius differs significantly from its mean value.

6.5.2 The Monte Carlo Method

The LHS method was used to create 1,000 samples of the input parameters, based on the PDFs associated with the input parameters. These input parameter samples were used in the analytical solution and the FDTD reference simulation to create numerous output frequency responses of the normalised electric field. The mean and standard deviation (uncertainty) of these outputs were then calculated. The results of the Monte Carlo simulations were also used to calculate 95% CI, using the Kaplan-Meier empirical cumulative distribution function as discussed in Section 4.5.3.

The FSV method was used to determine when the MCM had reached convergence, as described in Sections 3.2.3 and 4.5.2. For this example it was found that convergence was reached after 850 simulations for the analytic solution and 700 for the reference FDTD

simulation. The MCM is the most rigorous method, it is also the most computationally expensive method: the 700 FDTD simulations took a total of 5.3 days.

6.5.3 The Method of Moments

The MoM was used as outlined below to obtain the mean and uncertainty in the analytic solution and the FDTD simulation. For the purposes of the discussion below, "simulation" refers to both the calculation of the analytic result and the FDTD simulation, depending on which one the MoM is being applied to.

The MoM required four simulations to calculate the output uncertainty for this example. One simulation was performed with the input parameters taking on their mean values, this represents the mean output of the normalised electric field. The second and third simulations were performed with the relative permittivity and permeability perturbed by $\Delta\epsilon_r = 0.12$ and $\Delta\mu_r = 0.03$ respectively, from their mean values. The final simulation was performed with the radius of the sphere being perturbed from its mean value by $\Delta a = 0.003$m. These perturbations were chosen since they are of a similar size to the uncertainty in each respective input parameter. This is in accordance with the calculation of the output uncertainty in practical EMC experiments [2]. The three sensitivity derivatives calculated from these four simulations were combined with the input uncertainties to calculate the uncertainty in the output, according to equations (4.51) and (4.53). The 95% CI are calculated using the mean and uncertainty as outlined in Section 4.6.3. Since only four simulations are required here to obtain the mean, uncertainty and 95% CI, this method is computationally much cheaper than the MCM.

6.5.4 The Polynomial Chaos Method

This section describes the steps required to calculate the uncertainty in the backscattered field using the PCM. Firstly the application of the PCM to the FDTD simulations is described. This is then followed by a description of how the PCM is applied to the analytic solution.

Application to the Finite Difference Time Domain Simulations

To perform an UA using the PCM, the uncertain input parameters need to be related to the material parameters in the FDTD chaotic update equations (4.111) and (4.112). The

terms in the update equations involving the material parameters are inner products, which are calculated as a preprocess using numerical integrations. The numerical integrations can be quite costly and add to the overall computational cost of this method.

Firstly the uncertainty in the relative permeability of the sphere must be related to θ_1, which follows a standard Uniform distribution over the interval $[-1, 1]$. Since the relative permeability is Uniformly distributed over the interval [0.95,1.05], the relative permeability is related to θ_1 as

$$\mu_r = \bar{\mu}_r + \frac{1.05 - 0.95}{2}\theta_1 = 1 + 0.05\theta_1. \tag{6.14}$$

Similarly the uncertainty in the relative permittivity of the sphere must be related to θ_2, which also follows a standard Uniform distribution. The following relation fits this purpose

$$\epsilon_r = \bar{\epsilon}_r + \frac{4.3 - 3.7}{2}\theta_2 = 4 + 0.3\theta_2. \tag{6.15}$$

The uncertainty in the radius of the sphere must be related to θ_3, which follows a standard Normal distribution. The following relation fits this purpose

$$a = \bar{a} + \sigma_a\theta_3 = 0.1 + 0.005\theta_3. \tag{6.16}$$

The uncertainty in the radius of the sphere must now be related to the uncertainty in the permittivity and permeability at positions around the mean radius of the sphere. If a point, in the problem space, is inside the sphere then $\mu_r = 1 + 0.05\theta_1$ and $\epsilon_r = 4 + 0.3\theta_2$, otherwise $\mu_r = 1$ and $\epsilon_r = 1$. Consider a point $(x, y, z) = (i\Delta l, j\Delta l, k\Delta l)$, which is a distance d from the centre of the sphere. This point is in the sphere if

$$d \leq a = 0.1 + 0.005\theta_3. \tag{6.17}$$

Thus (x, y, z) is in the sphere if

$$\theta_3 \geq \frac{d - 0.1}{0.005}. \tag{6.18}$$

The relative permeability at this point, represented by $\mu_r(d, \theta_1, \theta_3)$, is dependent upon two uncertain input parameters. The relative permittivity at the same point is also dependent on two uncertain parameters and is denoted by $\epsilon_r(d, \theta_2, \theta_3)$. These two material parameters become

$$\mu_r(d, \theta_1, \theta_3) = \begin{cases} 1 + 0.05\theta_1 & \text{for } \theta_3 \geq \frac{d-0.1}{0.005} \\ 1 & \text{otherwise} \end{cases} \tag{6.19}$$

and

$$\epsilon_r(d,\theta_2,\theta_3) = \begin{cases} 4+0.3\theta_2 & \text{for } \theta_3 \geq \frac{d-0.1}{0.005} \\ 1 & \text{otherwise.} \end{cases} \tag{6.20}$$

Thus, the material parameters $\gamma(d,\theta_1,\theta_3)$ and $\beta(d,\theta_2,\theta_3)$, used in the FDTD Polynomial Chaos update equations (4.111) and (4.112), are

$$\gamma = \gamma(d,\theta_1,\theta_3) = \begin{cases} \frac{\Delta t}{(1+0.05\theta_1)\Delta l \mu_0} & \text{for } \theta_3 \geq \frac{d-0.1}{0.005} \\ \frac{\Delta t}{\Delta l \mu_0} & \text{otherwise} \end{cases} \tag{6.21}$$

and

$$\beta = \beta(d,\theta_2,\theta_3) = \begin{cases} \frac{\Delta t}{(4+0.3\theta_2)\Delta l \epsilon_0} & \text{for } \theta_3 \geq \frac{d-0.1}{0.005} \\ \frac{\Delta t}{\Delta l \epsilon_0} & \text{otherwise.} \end{cases} \tag{6.22}$$

The input uncertainties follow Uniform and Normal distributions, therefore Legendre and Hermite polynomials must be used in the chaotic expansion of the electric and magnetic fields. If the uncertainty is sought to first order, then the chaotic expansion is terminated at $P = 4$. The first order polynomials required are

$$\psi_0 = 1 \tag{6.23}$$

$$\psi_1 = L_1(\theta_1) = \theta_1 \tag{6.24}$$

$$\psi_2 = L_1(\theta_2) = \theta_2 \tag{6.25}$$

$$\text{and} \quad \psi_3 = H_1(\theta_3) = \theta_3. \tag{6.26}$$

The orthogonality of the polynomials leads to the relations

$$< L_i(\theta_k) L_j(\theta_l) >= \delta_{ij}\delta_{kl}\frac{1}{2i+1} \tag{6.27}$$

and

$$< H_i(\theta_k) H_j(\theta_l) >= \delta_{ij}\delta_{kl}(i)!. \tag{6.28}$$

Thus the inner products of the different polynomials are given by

$$< \psi_i \psi_j > = 0 \quad \text{for} \quad i \neq j \tag{6.29}$$

$$< \psi_0 \psi_0 > = 1 \tag{6.30}$$

$$< \psi_1 \psi_1 > = \frac{1}{3} \tag{6.31}$$

$$< \psi_2 \psi_2 > = \frac{1}{3} \tag{6.32}$$

$$\text{and} \quad < \psi_3 \psi_3 > = 1. \tag{6.33}$$

The electric and magnetic fields are calculated using the update equations (4.111) and (4.112). Before these equations can be used, the inner products of the material parameters α, β and γ with the polynomials used in the chaotic expansion need to be calculated. The material parameter $\alpha = 1$ with zero uncertainty. The inner product of α with the polynomials ψ_i and ψ_j is therefore

$$< \alpha \psi_i \psi_j > = \alpha < \psi_i \psi_j > \tag{6.34}$$

where $i, j = 0, \ldots, 3$. The inner products required for γ and β are calculated using the integrals

$$\begin{aligned} < \gamma \psi_i \psi_j > &= \int_{-\infty}^{\infty} \left(\frac{1}{2} \int_{-1}^{1} \left(\frac{1}{2} \int_{-1}^{1} \gamma(d, \theta_1, \theta_3) \psi_i \psi_j d\theta_1 \right) d\theta_2 \right) \frac{\exp(-\frac{\theta_3^2}{2})}{\sqrt{2\pi}} d\theta_3 \\ &= \int_{-\infty}^{\infty} \left(\frac{1}{2} \int_{-1}^{1} \gamma(d, \theta_1, \theta_3) \psi_i \psi_j d\theta_1 \right) \frac{\exp(-\frac{\theta_3^2}{2})}{\sqrt{2\pi}} d\theta_3 \end{aligned} \tag{6.35}$$

$$\begin{aligned} \text{and} \quad < \beta \psi_i \psi_j > &= \int_{-\infty}^{\infty} \left(\frac{1}{2} \int_{-1}^{1} \left(\frac{1}{2} \int_{-1}^{1} \beta(d, \theta_2, \theta_3) \psi_i \psi_j d\theta_1 \right) d\theta_2 \right) \frac{\exp(-\frac{\theta_3^2}{2})}{\sqrt{2\pi}} d\theta_3 \\ &= \int_{-\infty}^{\infty} \left(\frac{1}{2} \int_{-1}^{1} \beta(d, \theta_2, \theta_3) \psi_i \psi_j d\theta_2 \right) \frac{\exp(-\frac{\theta_3^2}{2})}{\sqrt{2\pi}} d\theta_3. \end{aligned} \tag{6.36}$$

These integrations may be simplified using the properties of the material parameters and the orthogonal polynomials, this simplification has been left out here for brevity. The resulting improper integrals are calculated numerically using the extended midpoint rule, as in the previous chapter.

The inner products calculated using the above integrations are substituted into the update equations (4.111) and (4.112), which are then used to find the mean and uncertainty in the electric field at the output point. In this example the output quantity of interest is the absolute value of the electric field in the frequency domain relative to a 1 V/m input excitation. More numerical integrations are required to calculate the mean and uncertainty

in this output, which adds to the overall computational cost of this method. The 95% CI are calculated using the mean and standard deviation, in the same manner as for the MoM.

Application of the Polynomial Chaos Method to the Analytic Solution

The normalised output electric field $\tilde{E}_x^r(f)$ is expanded in terms of the uncertain input parameters θ_1, θ_2 and θ_3 as

$$\tilde{E}_x^r(f,\theta_1,\theta_2) = e_0(f) + e_1(f)\theta_1 + e_2(f)\theta_2 + e_3(f)\theta_3 \tag{6.37}$$

where $e_0,\ldots,e_3$ are constant coefficients. The uncertain parameters θ_1, θ_2 and θ_3, in equation (6.37), are related to the uncertain parameters μ_r, ϵ_r and a in the same manner as described by equations (6.14)-(6.16). The coefficient e_i is calculated using the inner product

$$\begin{aligned} e_i(f) &= \frac{<\tilde{E}_x^r(f,\theta_1,\theta_2),\psi_i>}{<\psi_i^2>} \\ &= \frac{1}{<\psi_i^2>}\int_{-\infty}^{\infty}\int_{-1}^{1}\int_{-1}^{1}\tilde{E}_x^r(f,\theta_1,\theta_2)\psi_i\frac{1}{2}\frac{1}{2}\frac{\exp(-\frac{\theta_3^2}{2})}{\sqrt{2\pi}}d\theta_1\,d\theta_2\,d\theta_3 \end{aligned} \tag{6.38}$$

where $i = 0,\ldots,3$. These inner products are calculated numerically, at each frequency f, using the midpoint rule. The numerical integration in θ_3 may be performed over a smaller domain of physically acceptable values.

Once the coefficients $e_0,\ldots,e_3$ are found, the mean normalised electric field $\bar{E}(f)$ and uncertainty $\sigma(\tilde{E}_x^r(f))$ may be calculated as

$$\bar{E}(f) = e_0 \tag{6.39}$$

$$\text{and}\quad \sigma(\tilde{E}(f)) = \sqrt{\sum_{i=1}^{3} e_i^2 <\psi_i^2>}. \tag{6.40}$$

Notice that the definition of the mean here is exactly the same as the definition of the analytic mean given by equation (6.12).

6.5.5 Comparing the Results of the Uncertainty Analysis Methods

The results obtained using the different UA methods are presented in this section, beginning with the mean and uncertainty in the analytic solution. Following this the mean and uncertainty in the output of the FDTD simulations are presented.

The Uncertainty in the Analytic Solutions

Figures 6.8 and 6.9 show the mean and uncertainty in the normalised electric field formed using the different UA methods, for the analytic solution. The analytic solution of the mean is exactly the same as the mean predicted by the PCM. This is as expected since the analytic solution of the mean (6.12) and the equation representing the PCM prediction of the mean (6.39) are equivalent. For this example it is clear that the MCM gives a better prediction of the analytic mean, than the MoM. The FSV method was used to compare the means and uncertainties predicted by the approximate UA methods with the analytic solutions. The results of these comparisons are given in Table 6.2.

Using Table 6.2 it is clear that the PCM provides the best prediction of the mean

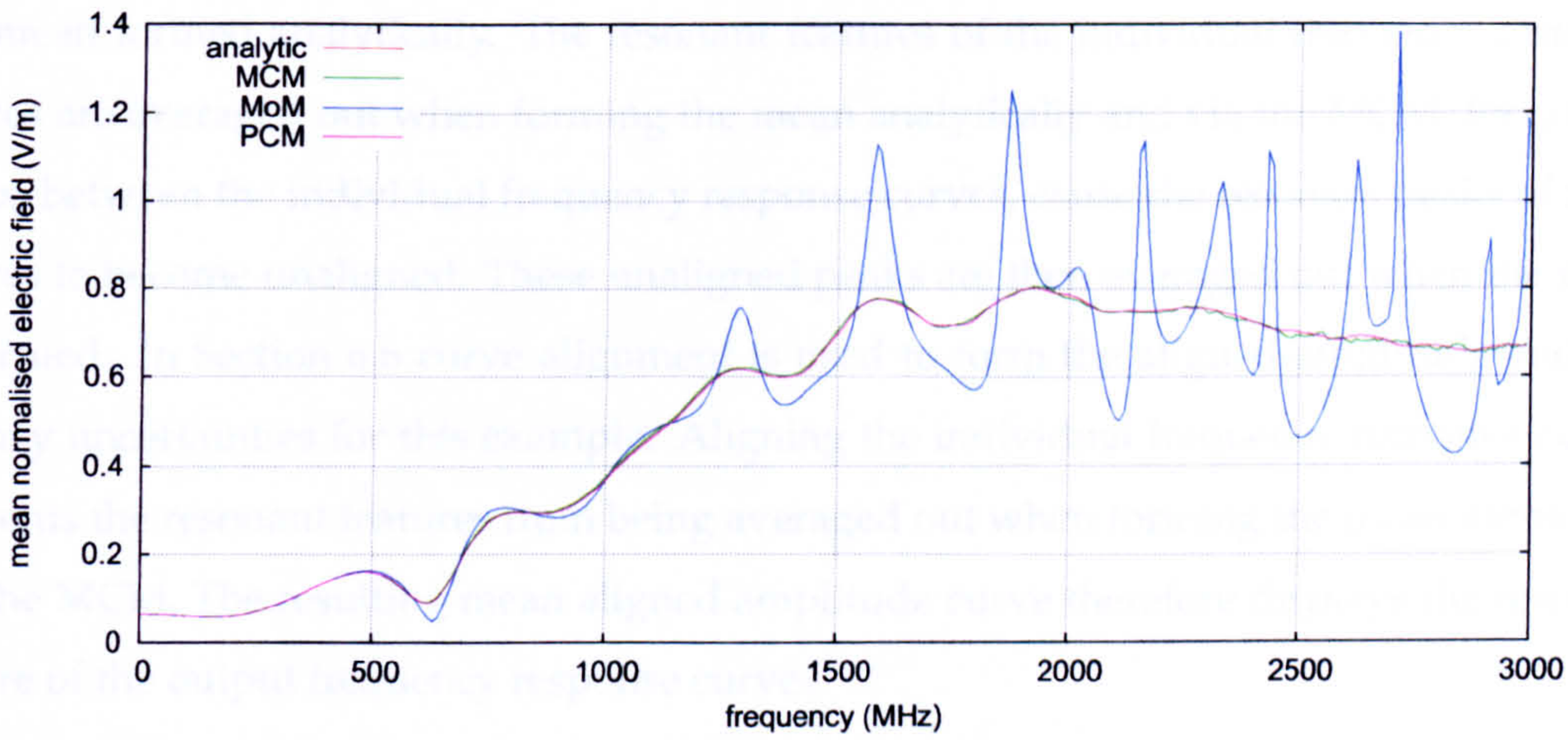

Figure 6.8: Mean normalised electric field calculated using the different UA methods, for the analytic solution.

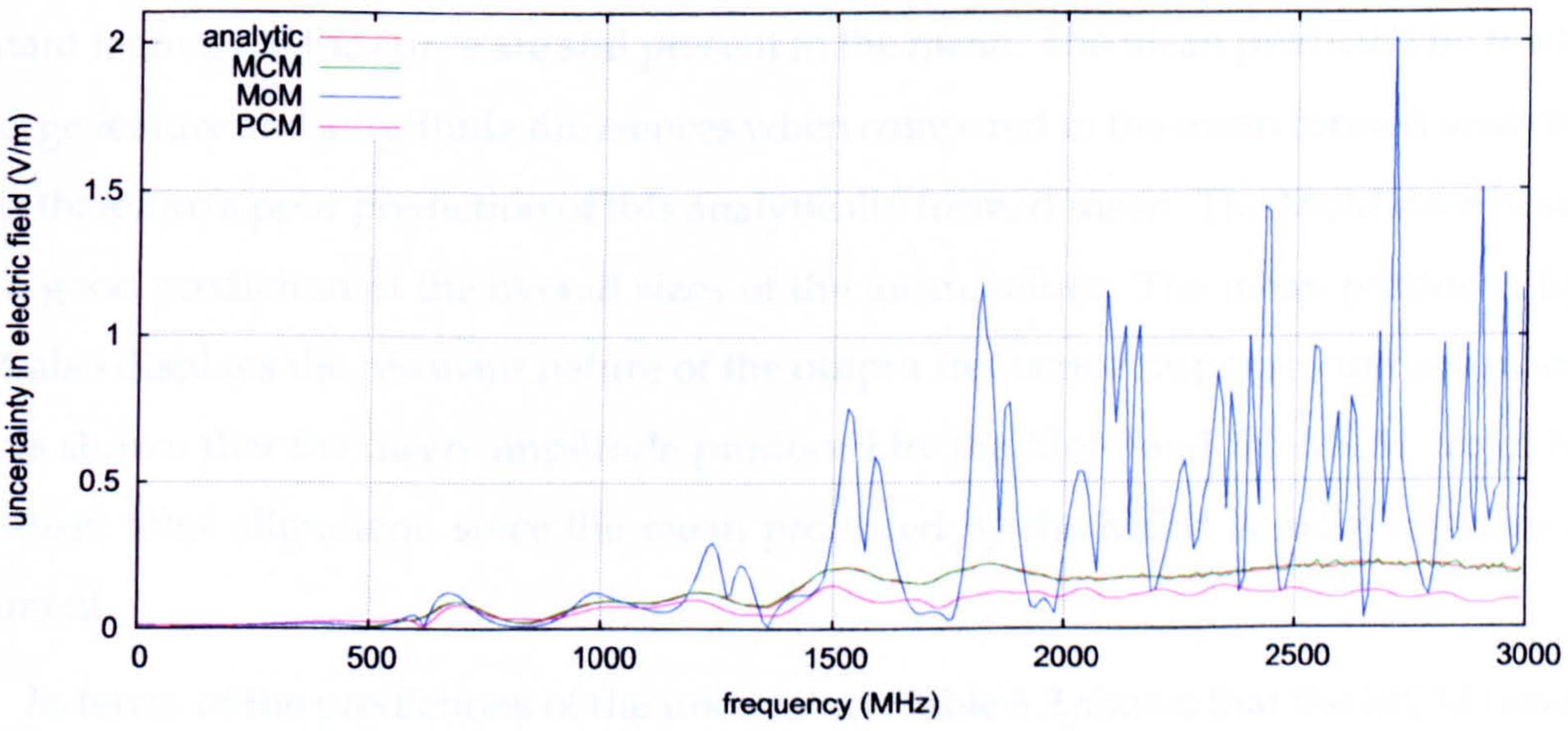

Figure 6.9: Uncertainty in the normalised electric field calculated using the different UA methods, for the analytic solution.

Comparing the Predictions of the Means					
Method	ADM	FDM	GDM	GDM (1-6)	Qualitative
MCM	0.0193	0.0835	0.0888	1.8884	Excellent
MoM	0.3753	0.9864	1.1243	5.4067	Poor
PCM	0	0	0	1	Excellent
Comparing the Predictions of the Uncertainty					
MCM	0.0335	0.2222	0.2327	3.1687	Good
MoM	3.5202	1.3983	3.9182	6	Very Poor
PCM	0.6208	0.4247	0.8142	5.0190	Poor

Table 6.2: FSV comparisons of the analytic solution of the mean and uncertainty in the normalised electric field, with the means and uncertainties predicted by the three UA methods.

formed analytically. The application of the PCM to the FDTD method is different however from the application to the analytic solution. The mean predicted by the PCM for the FDTD method may therefore be less accurate. The MCM also provides an excellent prediction of the mean formed analytically. The resonant features of the individual frequency response curves are averaged out when forming the mean analytically and via the MCM. Frequency shifts, between the individual frequency response curves, cause the resonant peaks of these curves to become unaligned. These unaligned peaks are then averaged out when the mean is formed. In Section 6.6 curve alignment is used to form the aligned amplitude and frequency uncertainties for this example. Aligning the individual frequency response curves prevents the resonant features from being averaged out when forming the mean amplitude via the MCM. The resulting mean aligned amplitude curve therefore displays the resonant nature of the output frequency response curves.

The MoM uses only one output curve to form the mean: the output formed by using the mean input parameter values in the analytic solution. Since only one curve is used the resonant features of the curve are still present in the mean. The mean predicted by the MoM has large feature and amplitude differences when compared to the mean formed analytically and is therefore a poor prediction of this analytically formed mean. The MoM does however give a good prediction of the overall sizes of the mean values. The mean produced by the MoM also displays the resonant nature of the output frequency response curves. In Section 6.6 it is shown that the mean amplitude produced by the MoM and the MCM are in better agreement after alignment, since the mean produced by the MCM is more resonant after alignment.

In terms of the predictions of the uncertainty, Table 6.2 shows that the MCM provides the best estimation of the uncertainty formed analytically followed by the PCM; the MoM provides a "very poor" estimation of the uncertainty for this example. These comparisons

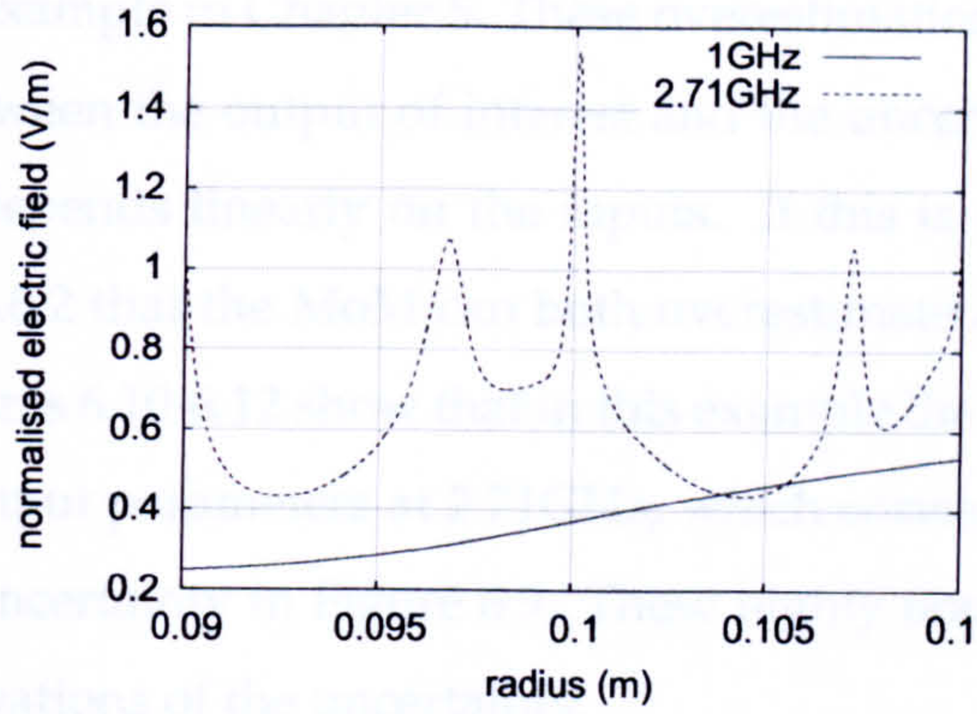

Figure 6.10: Normalised electric field for spheres with different radii.

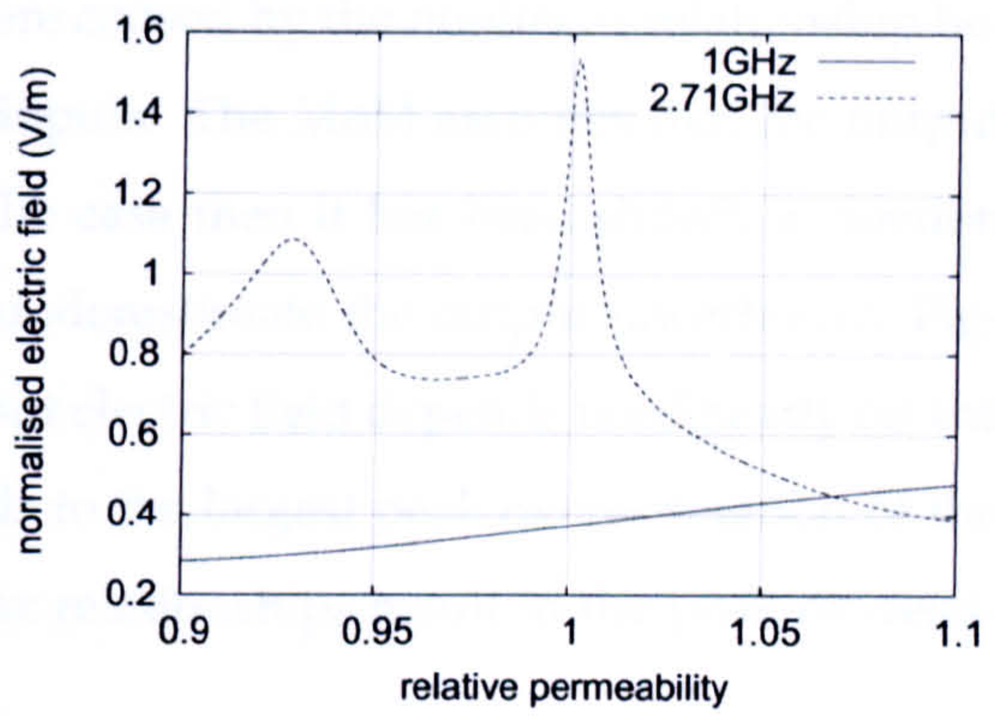

Figure 6.11: Normalised electric field for spheres with different relative permeabilities.

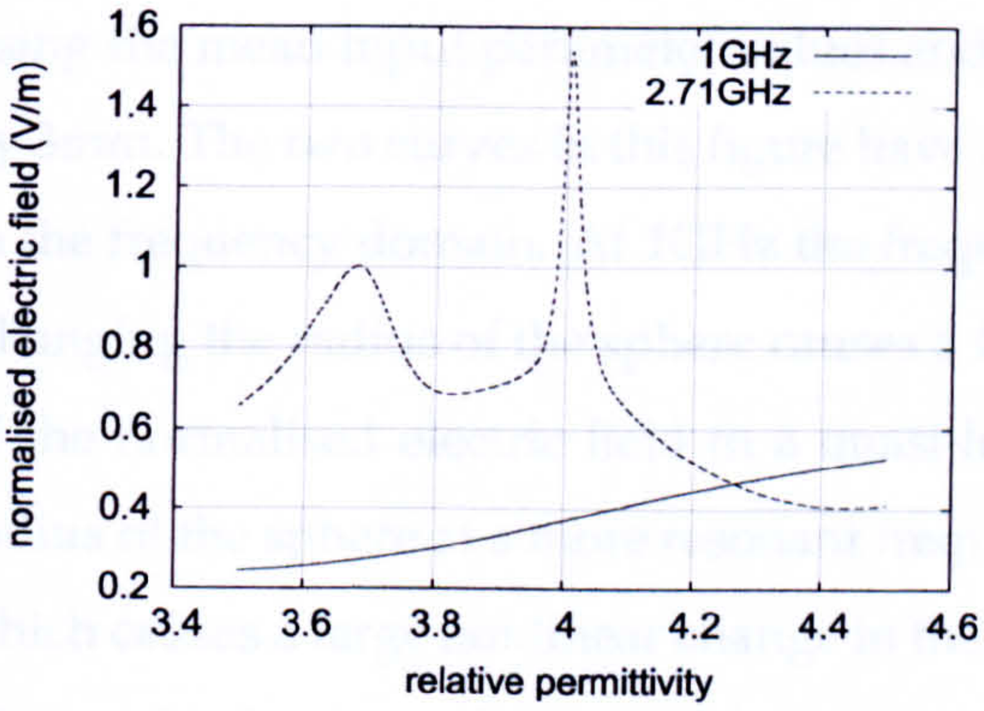

Figure 6.12: Normalised electric field for spheres with different relative permittivities.

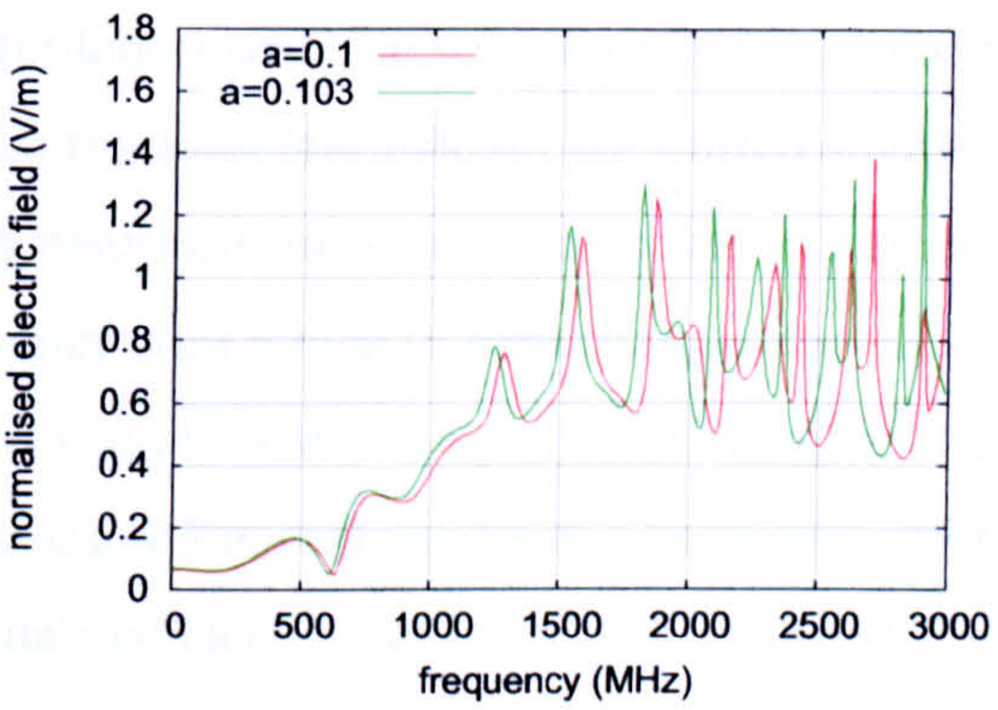

Figure 6.13: Frequency response of the normalised electric field for two spheres with different radii.

agree with the visual comparisons that can be made from Figure 6.9. The PCM prediction of the analytic uncertainty is "poor", however the GDM on the visual scale shows that the prediction is closer to being a "fair" estimate than a "very poor" estimate. As with the mean produced by the MCM, in Section 6.6 it is shown that the amplitude uncertainty formed after alignment via the MCM is more resonant.

Since the MCM provides by far the best estimations of the uncertainty for the analytic solutions it is chosen as the benchmark method. The MCM is used to test the performance of the other two approximate UA methods, when all three UA methods are applied to the FDTD simulation of this example. Once again it is important to remember that the PCM may not give as good predictions of the mean and uncertainty in the FDTD simulations, as it gave here for the analytic solutions. This is because the PCM is implemented differently in the FDTD simulations and the analytic solution.

The uncertainty predicted by the MoM, shown in Figure 6.9, clearly overestimates the output uncertainty at the higher frequencies. Similar overestimations were found in the

example in Chapter 5. These overestimations were caused by the nonlinear relationship between the output of interest and the uncertain inputs. The MoM assumes that the output depends linearly on the inputs. If this is not the case then it has been shown in Section 4.6.2 that the MoM can both overestimate and underestimate the output uncertainty. Figures 6.10-6.12 show that in this example the output electric field depends nonlinearly on the input parameters at 2.71GHz, which corresponds to the largest peak overestimation of the uncertainty in Figure 6.9. These highly nonlinear relationships result in the peak overestimations of the uncertainty.

Figure 6.13 shows the normalised electric field produced from a FDTD simulation using the mean input parameter values and a simulation with the sphere radius perturbed by 3mm. The two curves in this figure have similar resonant features but are shifted slightly in the frequency domain. At 1GHz the frequency response curve is less resonant in nature. Changing the radius of the sphere causes a frequency shift which in turn changes the value of the normalised electric field in a quasi-linear fashion, at this frequency. Changing the radius of the sphere at a more resonant frequency (e.g. 2.71GHz) results in a frequency shift which causes a large nonlinear change in the normalised electric field. Figure 6.10 shows the relationship between the normalised electric field and the radius of the sphere at 1GHz and 2.71GHz. At 1GHz the normalised electric field depends on the radius in a relatively linear fashion, whereas at 2.71GHz the normalised electric field depends on the radius in a highly nonlinear manner. Similar nonlinear relationships between the output electric field and the other uncertain inputs arise at frequencies where there is a high modal density, as shown in Figures 6.11 and 6.12. These nonlinear relationships cause the MoM to overestimate the uncertainty at particular frequencies.

The above discussion identifies that the nonlinear relationship between the outputs and the uncertain inputs is partly caused by the frequency shifts (in the frequency response of the normalised electric field) formed by perturbing the uncertain input parameters. In Section 6.6 curve alignments are used to determine the extent to which the output uncertainty is an amplitude uncertainty and a frequency uncertainty. Using curve alignment removes the frequency shifts between the aligned output amplitude curves. The relationship between the aligned output amplitude and the uncertain input parameters should therefore be more linear. Thus the MoM should not overestimate the aligned amplitude uncertainties by as much.

Forward difference approximations of the sensitivity derivatives, formed using the

curves in Figures 6.10-6.12, are highly dependent on the size of the perturbation used. The output uncertainty formed via the MoM is therefore dependent on the size of the chosen perturbation. For practical applications, with no analytic solution, it is impossible to determine the size of the perturbation that will give the most accurate estimate of the output uncertainty. It has been previously suggested that it is appropriate to choose a perturbation of around the same size as the input parameter uncertainty [2].

By applying the UA methods to the analytic solution it has been shown that the MCM provides the best prediction of the uncertainty in the output of this example. Some of the errors that arise from using the MoM have also been examined. The next section considers the performance of the UAs, when applied to the reference FDTD simulation.

The Uncertainty in the Finite Difference Time Domain Simulations

Figure 6.14 shows the means predicted by the three UA methods when applied to the reference FDTD simulations. As for the analytic case, the frequency response of the mean predicted by the MCM is less resonant due to the averaging of unaligned resonant peaks. It is not clear, from Figure 6.14, whether the MoM or the PCM is better at predicting the mean formed by the benchmark MCM result. The FSV comparisons of the means predicted by the MoM and the PCM, with the mean predicted by the MCM, are shown in Table 6.3. From this table it may be concluded that both methods provide "poor" estimates of the mean formed using the benchmark MCM. The biggest differences between the curves are the feature differences. Both the PCM and MoM predict mean curves with large peaks, the mean produced by the MCM does not have these resonances. The resonances have been

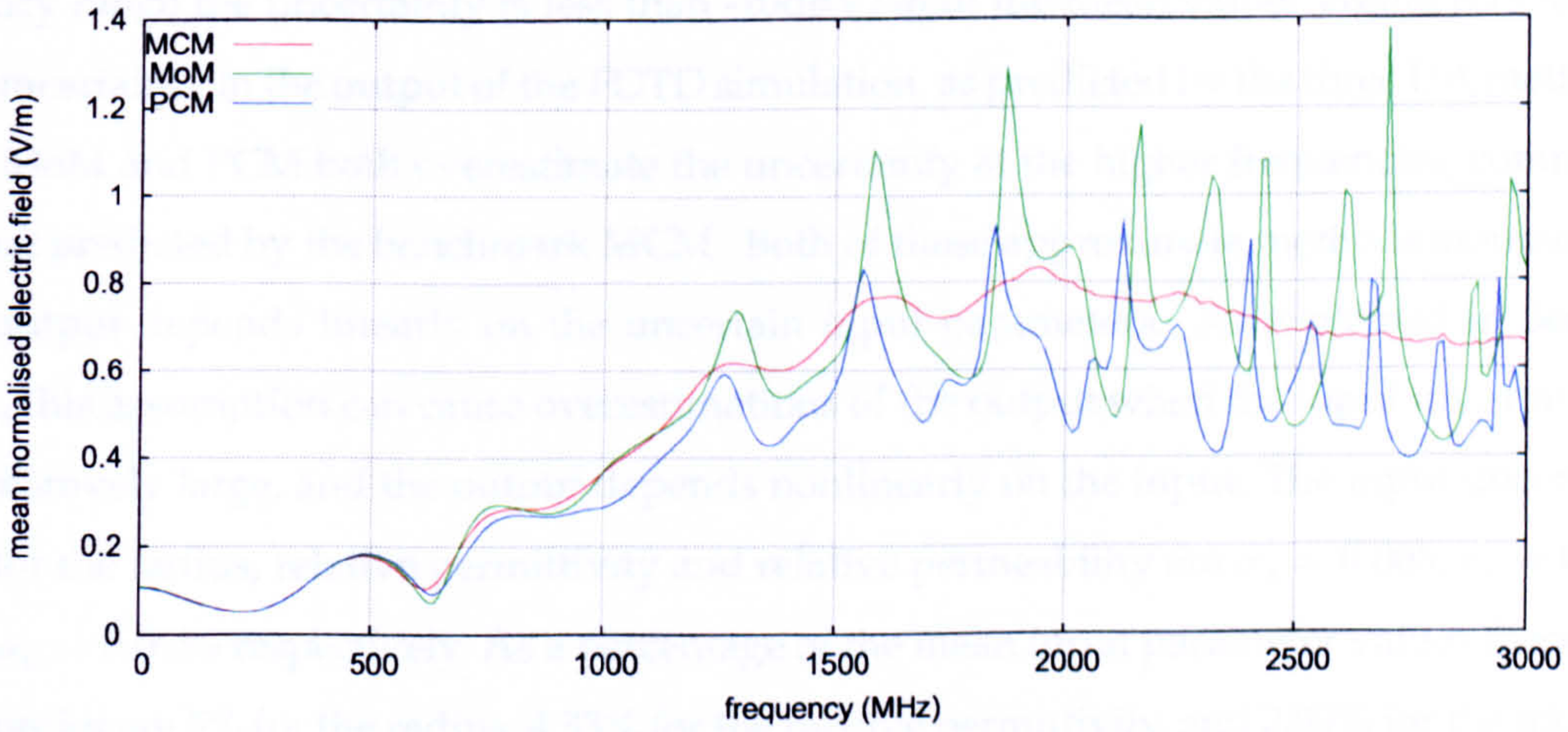

Figure 6.14: Mean normalised electric field calculated using the different UA methods for the FDTD simulation.

Comparing the Predictions of the Mean					
Method	ADM	FDM	GDM	GDM (1-6)	Qualitative
MoM	0.3682	0.9556	1.0923	5.3666	Poor
PCM	0.4268	0.7839	0.9701	5.2139	Poor
Comparing the Predictions of the Uncertainty					
MoM	1.5678	1.3430	2.1646	6	Very Poor
PCM	0.8751	0.8543	1.3210	5.6525	Poor

Table 6.3: FSV comparisons of the means and uncertainties predicted by the benchmark MCM and other two UA methods.

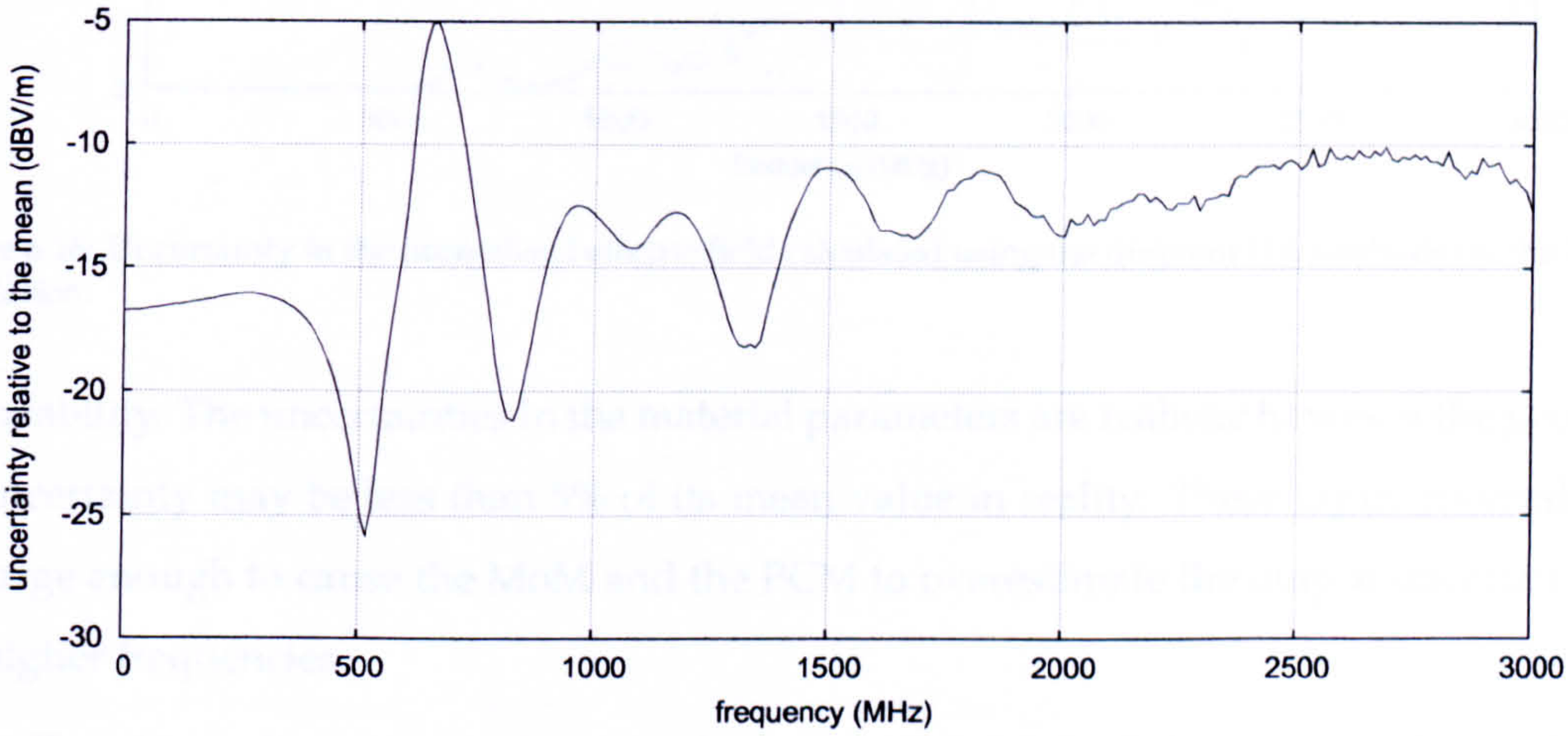

Figure 6.15: Uncertainty in the normalised electric field relative to the mean value, formed using the MCM.

averaged out by forming the mean using multiple simulated outputs that are shifted in frequency.

The frequency response of the uncertainty in the normalised electric field relative to the frequency response of the mean is shown in Figure 6.15. This figure shows that the uncertainty is always less than -5dBV/m of the mean value, and over the majority of the frequency range the uncertainty is less than -10dBV/m of the mean value. Figure 6.16 shows the uncertainty in the output of the FDTD simulation, as predicted by the three UA methods. The MoM and PCM both overestimate the uncertainty at the higher frequencies, compared to that predicted by the benchmark MCM. Both of these approximate methods assume that the output depends linearly on the uncertain input parameters. As explained in Section 4.6.2, this assumption can cause overestimations of the output when the input uncertainties are relatively large, and the output depends nonlinearly on the input. The input uncertainties for the radius, relative permittivity and relative permeability are $\sigma_a = 0.005$, $\sigma_\epsilon = 0.173$ and $\sigma_\mu = 0.0289$ respectively. As a percentage of the mean input parameter values these uncertainties are 5% for the radius, 4.33% for the relative permittivity, and 2.89% for the relative

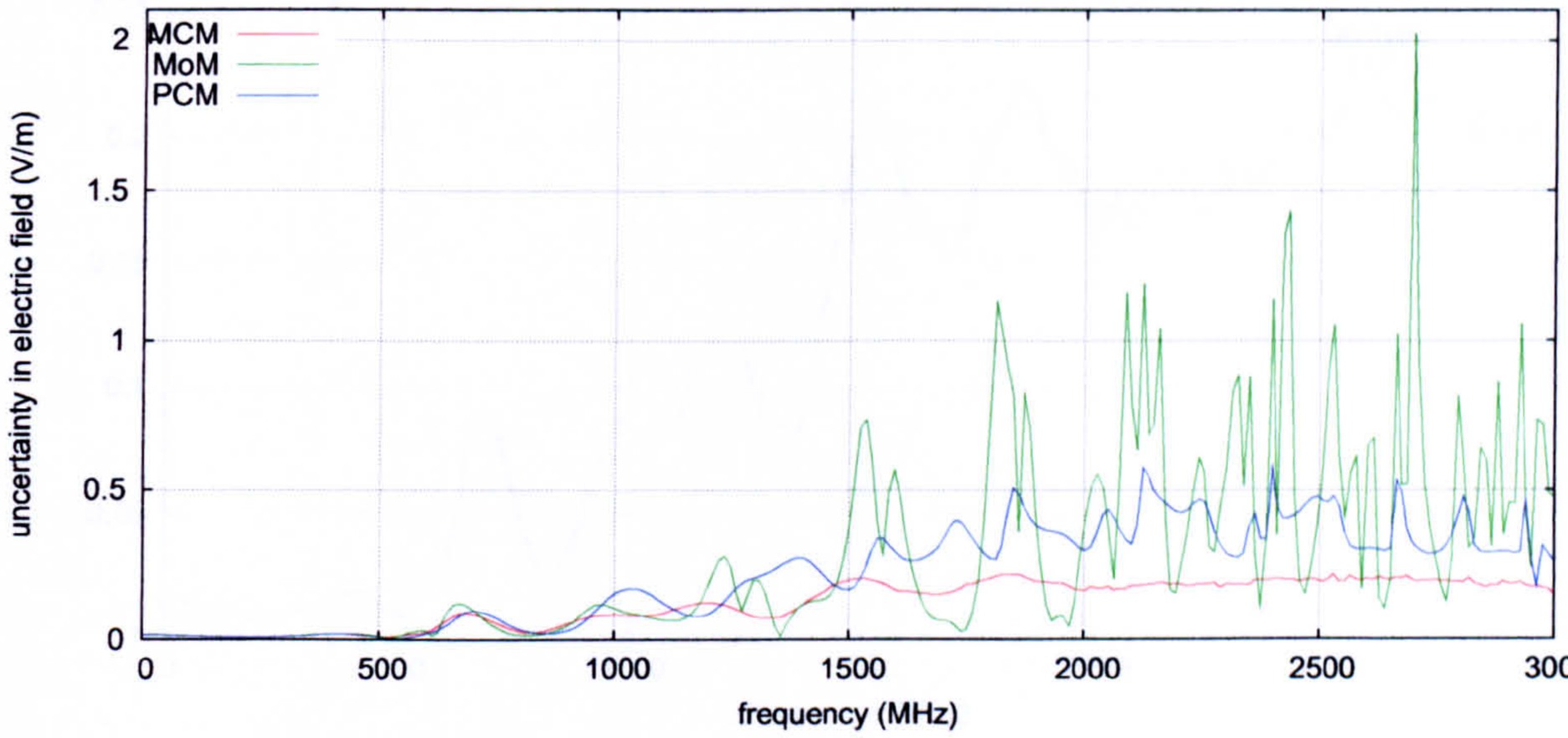

Figure 6.16: Uncertainty in the normalised electric field calculated using the different UA methods for the FDTD simulation.

permeability. The uncertainties in the material parameters are realistic however the geometric uncertainty may be less than 5% of its mean value in reality. These input uncertainties are large enough to cause the MoM and the PCM to overestimate the output uncertainty at the higher frequencies.

The above discussion points out that overestimations of the uncertainty, predicted by both the MoM and the PCM, are more prominent at the higher frequencies. Figure 6.16 shows that both the MoM and the PCM give better predictions of the uncertainty at the lower frequencies. This is confirmed by FSV comparisons of the uncertainty predicted by the MoM and the PCM, with the uncertainty predicted by the benchmark MCM, at the lower frequencies. The MoM uncertainty curve gives a "fair" comparison with the MCM uncertainty curve up to 1.21GHz. The PCM does slightly worse, giving a "fair" prediction of the uncertainty up to only 1.02GHz. The MoM gives an even better comparison for lower frequencies, up to 480MHz the similarity between the MoM uncertainty curve and the benchmark MCM uncertainty curve is "very good". In this same region the PCM only gives a "fair" prediction of the uncertainty. It may be concluded that the MoM, in particular, is good at predicting the uncertainty at lower frequencies, for this example. Figure 6.13 shows that the normalised electric field is less resonant at the lower frequencies and that the frequency shifts, caused by changes in the input parameters, are smaller. This implies that the output depends on the input in a more linear way, at the lower frequencies, and hence the MoM and the PCM provide better predictions of the uncertainty. In general in EMC the normalised electric field is less resonant in nature at the lower frequencies. The MoM and the PCM may therefore be useful for efficiently predicting the uncertainty in the output of

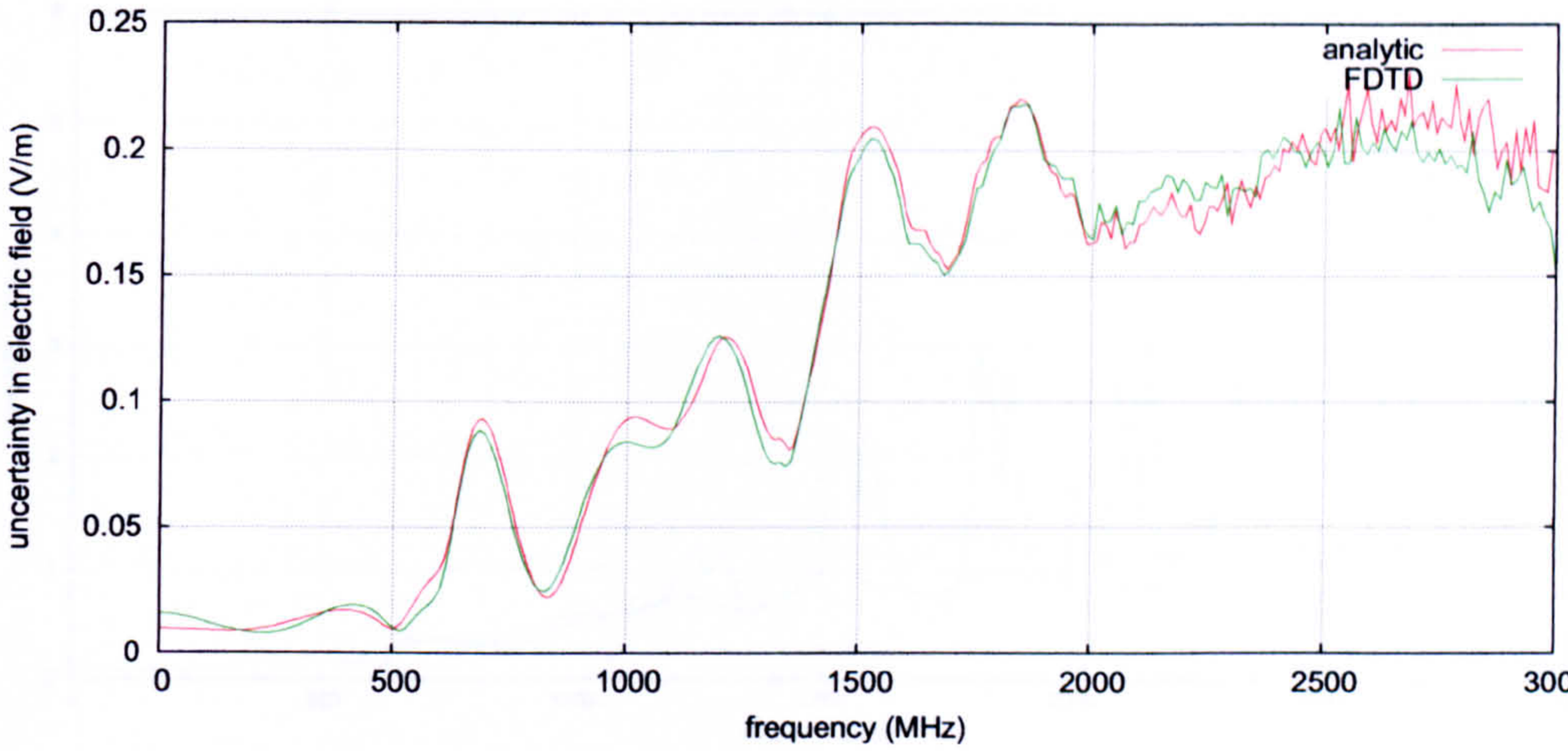

Figure 6.17: Uncertainty in the analytic solution and in the FDTD simulated solution calculated using the MCM.

CEM simulations of EMC problems at the lower frequencies, where the frequency response is less resonant. These UA methods may however provide poor estimates of the uncertainty in more resonant EMC data.

Analysing the Relationship Between Accuracy and Uncertainty

Thus far in this chapter, the uncertainty in the analytic solution and the reference FDTD simulated solution have been quantified. The analytic solution effectively has zero error whereas the FDTD simulated solution suffers from truncation and discretisation errors, as well as other sources of error. Comparing the uncertainty in these two solutions, as predicted by the MCM, provides some insight into the relationship between the errors and uncertainties.

The uncertainties in the analytic solution and the FDTD simulated solution are shown in Figure 6.17. The uncertainty curves in this figure are very similar, despite the FDTD simulation containing some errors. If the FDTD simulation had no errors then the two curves would be identical. There is therefore a small relationship between the errors and uncertainty. The uncertainty in the output is however more dependent on the sizes of the input uncertainties and the sensitivity of the output to changes in the different input parameters. The uncertainty will be more dependent on the errors as the size of the errors increase. When CEM simulations are used to perform an EMC analysis great effort is made to minimise the errors in CEM simulations. The uncertainties in accurate CEM simulations are thus likely to have only a small dependence on the errors in the simulations.

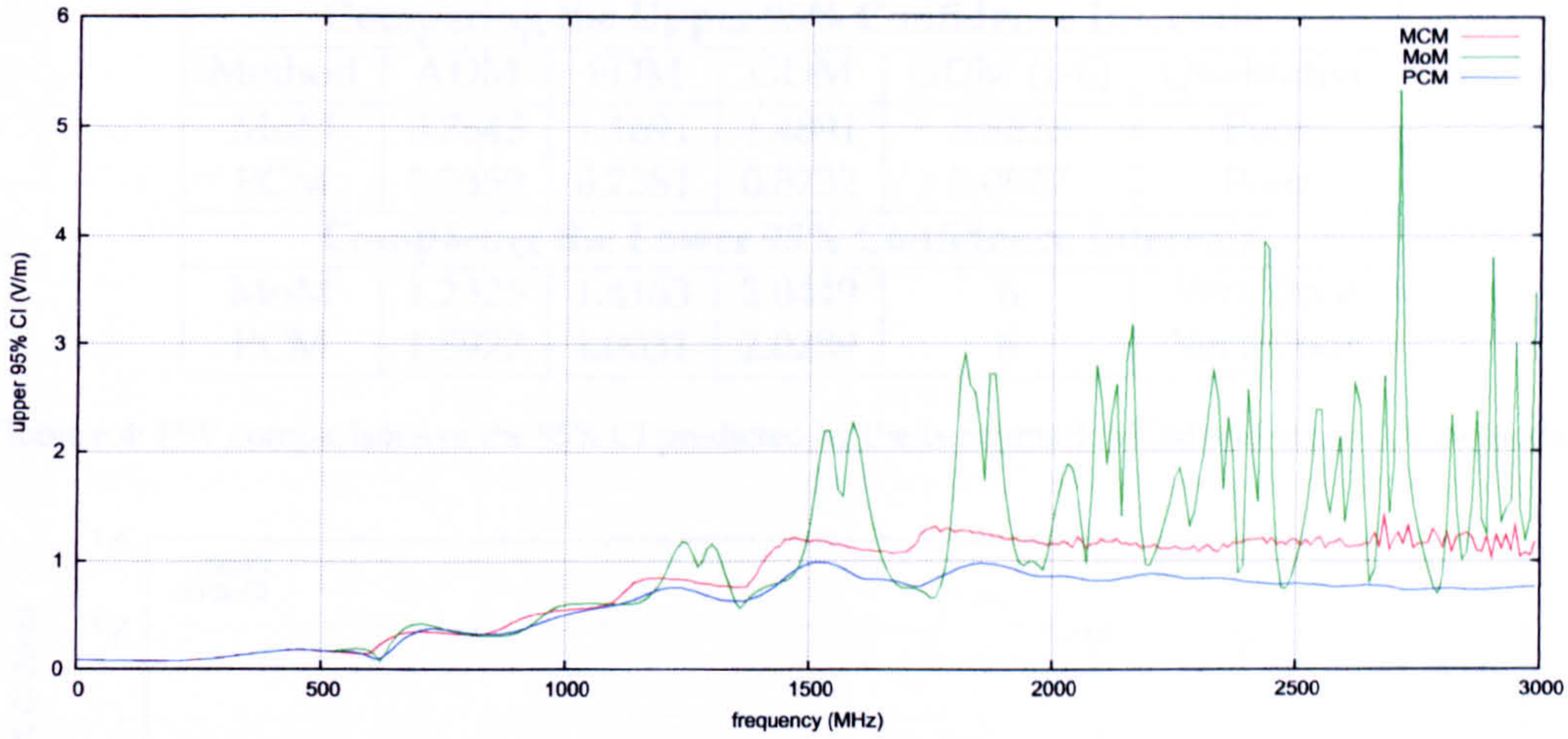

Figure 6.18: Upper 95% confidence interval for the normalised electric field calculated using the different UA methods, for the analytic solution.

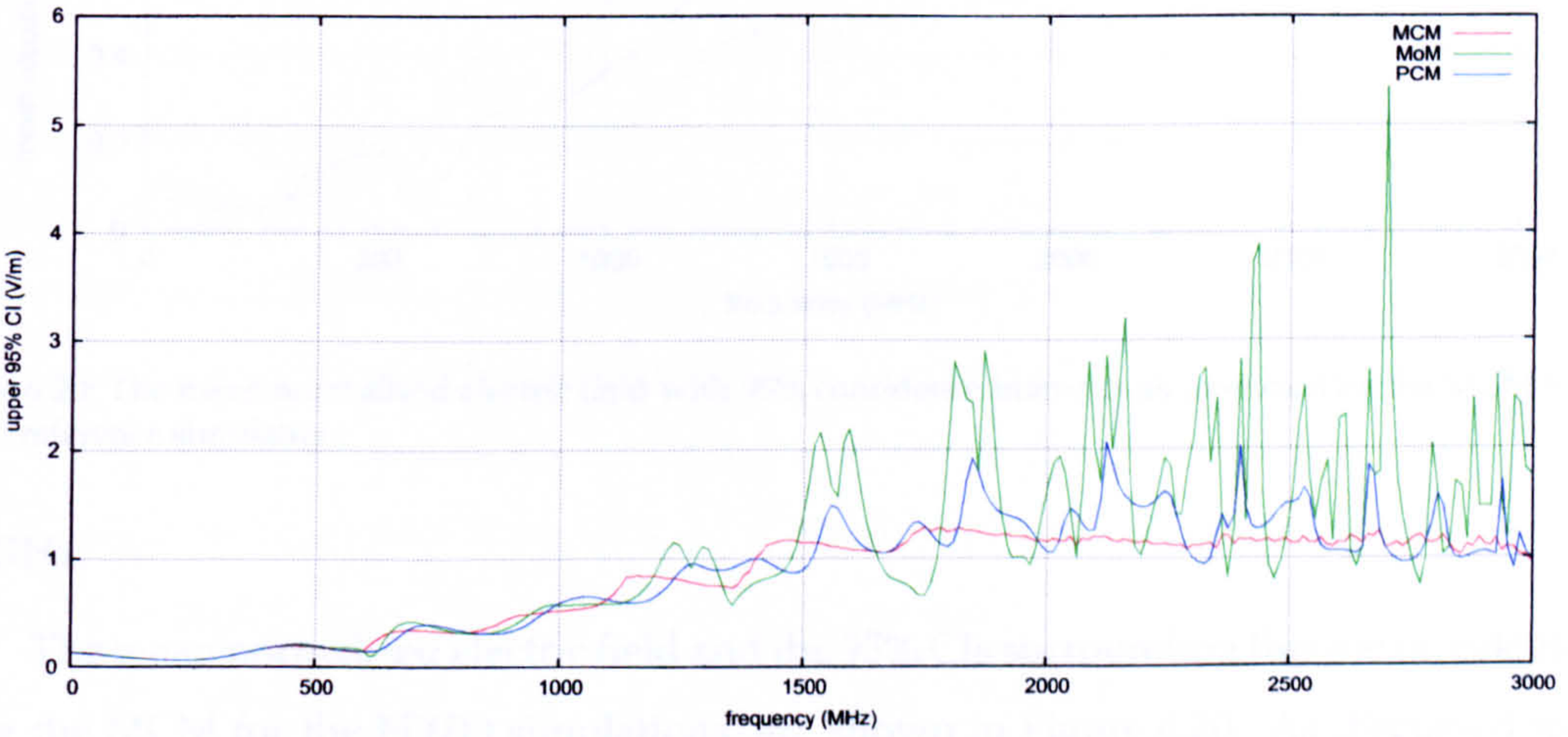

Figure 6.19: Upper 95% confidence interval for the normalised electric field calculated using the different UA methods, for the FDTD simulated solution.

Confidence Intervals

The upper 95% confidence intervals, calculated using different UA methods for the analytic solution and the FDTD simulation, are shown in Figures 6.18 and 6.19. The poor estimates of the uncertainty, by both the MoM and the PCM, lead to poor estimates of the 95% CI. The CI produced by the different UA methods were compared using the FSV method; these comparisons are shown in Table 6.4. The lower confidence intervals predicted by both the MoM and the PCM are "very poor" when compared to the lower CI calculated using the MCM. At lower frequencies, however, both the MoM and the PCM give better predictions of the 95% CI. FSV comparisons with the benchmark MCM show that the MoM gives "fair" predictions of the upper 95% CI up to 1.55GHz, and the PCM gives "fair" predictions up to

Comparing the Upper 95% Confidence Intervals					
Method	ADM	FDM	GDM	GDM (1-6)	Qualitative
MoM	0.7643	1.1691	1.4891	5.8626	Poor
PCM	0.3359	0.7381	0.8732	5.0927	Poor
Comparing the Lower 95% Confidence Intervals					
MoM	1.2325	1.4163	2.0449	6	Very Poor
PCM	1.5927	1.0031	2.0289	6	Very Poor

Table 6.4: FSV comparisons of the 95% CI predicted by the benchmark MCM and other UA methods.

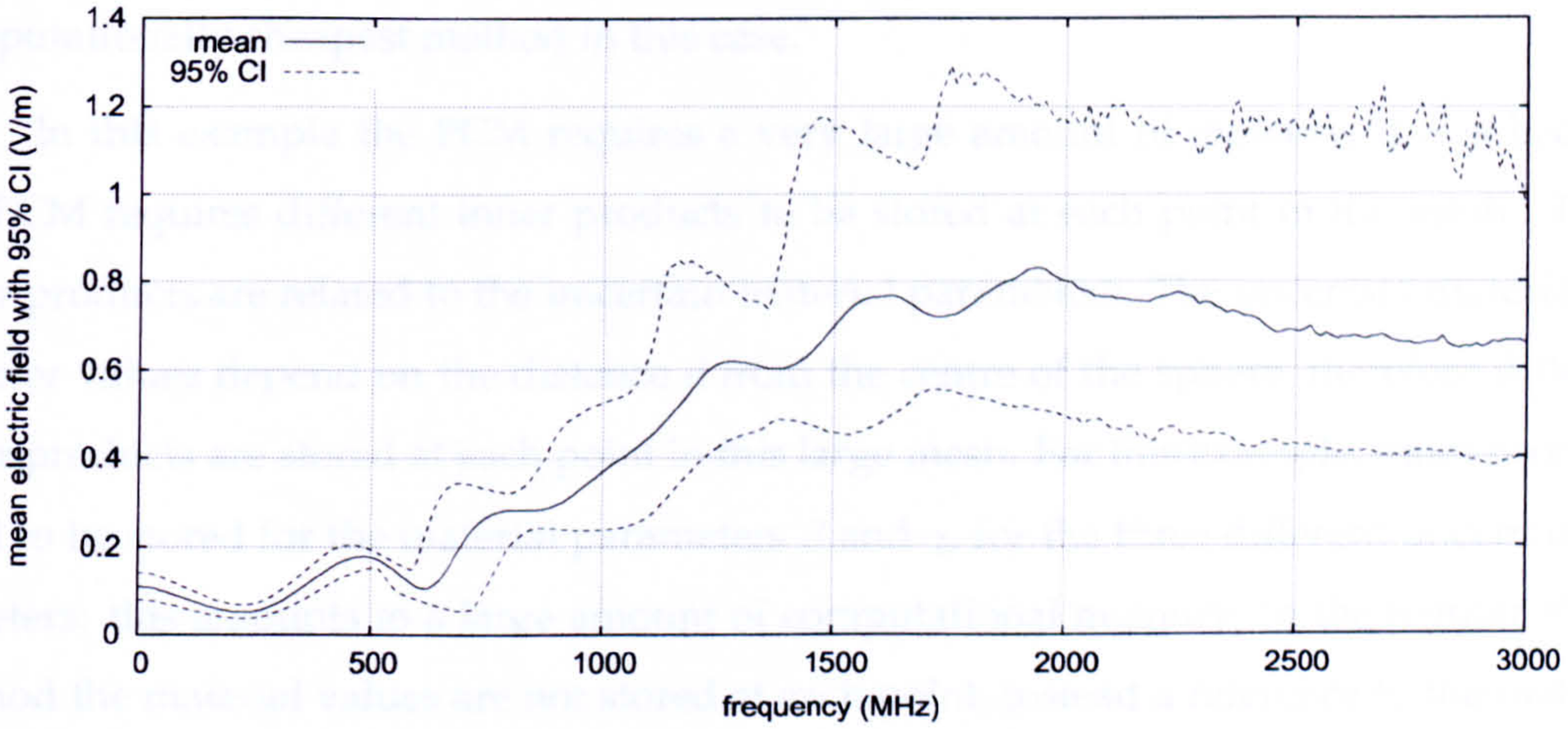

Figure 6.20: The mean normalised electric field with 95% confidence intervals as predicted by the MCM for the FDTD reference simulation.

2.12GHz.

The mean normalised electric field and the 95% CIs surrounding this mean, calculated using the MCM for the FDTD simulations, are shown in Figure 6.20. As discussed in the previous chapter, Figures such as this are extremely useful as they provide the quantitative level of confidence that can be held in the result of a CEM simulation. For this example the confidence that can be held in the mean value is lower at the higher frequencies. At the lower frequencies the confidence intervals are close to the mean value, however as the frequency increases so does the size of the overall confidence interval. The interval seems to converge towards the higher end of the frequency region.

6.5.6 The Computational Expense of the Uncertainty Analysis Methods

The UAs were all performed on a Core2Duo processor working at 3.0GHz. Table 6.5 displays the computational requirements of each UA method. From this table it can be deduced that the MoM is by far the computationally cheapest method. The more rigorous MCM requires the largest amount of computational time. The PCM needs a lot less time

Method	No. Simulations	Time Taken (hours)	Memory (MB)
MCM	700	126	31
MoM	4	0.72	31
PCM	1	8.9	680

Table 6.5: Computational requirements of the UA methods.

than the MCM but it requires significantly more memory. The MoM is one order of magnitude faster and requires about 20 times less memory than the PCM. It is therefore the computationally cheapest method in this case.

In this example the PCM requires a very large amount of memory, this is because the PCM requires different inner products to be stored at each point in the mesh. These inner products are related to the uncertain material parameters. The uncertain material parameter values depend on the distance d from the centre of the sphere, therefore different inner products are stored at each point in this large mesh. For this example, inner products need to be stored for the material parameters β and γ, for the three different uncertain parameters: this amounts to a large amount of computational memory. In the regular FDTD method the material values are not stored at each point, instead a reference to the material parameter at the point in the mesh is stored. This reduces the memory requirements of the FDTD simulation for small numbers of material types. It is difficult to minimise the memory requirements of the Polynomial Chaos FDTD simulation, for this example, because the material parameters are variable throughout the mesh. Since there are different parameters values at the different mesh points, many more parameter values need to be stored. The PCM therefore requires much more computational memory, in this case, than the other two methods. For more complex examples, the memory required to perform the Polynomial Chaos FDTD simulation may be too large.

In the next section curve alignment is used to determine the aligned amplitude and frequency uncertainties that are predicted by the MoM and the MCM. Currently there is no way of forming the aligned uncertainties for the PCM.

6.6 Evaluating the Uncertainties After Alignment

The four output curves used to calculate the uncertainty in the FDTD simulation, via the MoM, are shown in Figure 6.21. The reference curve refers to the simulation performed with all the input parameters taking on their mean values. The perturbed curves refer to the simulations performed with the aforementioned parameter perturbed from its mean value.

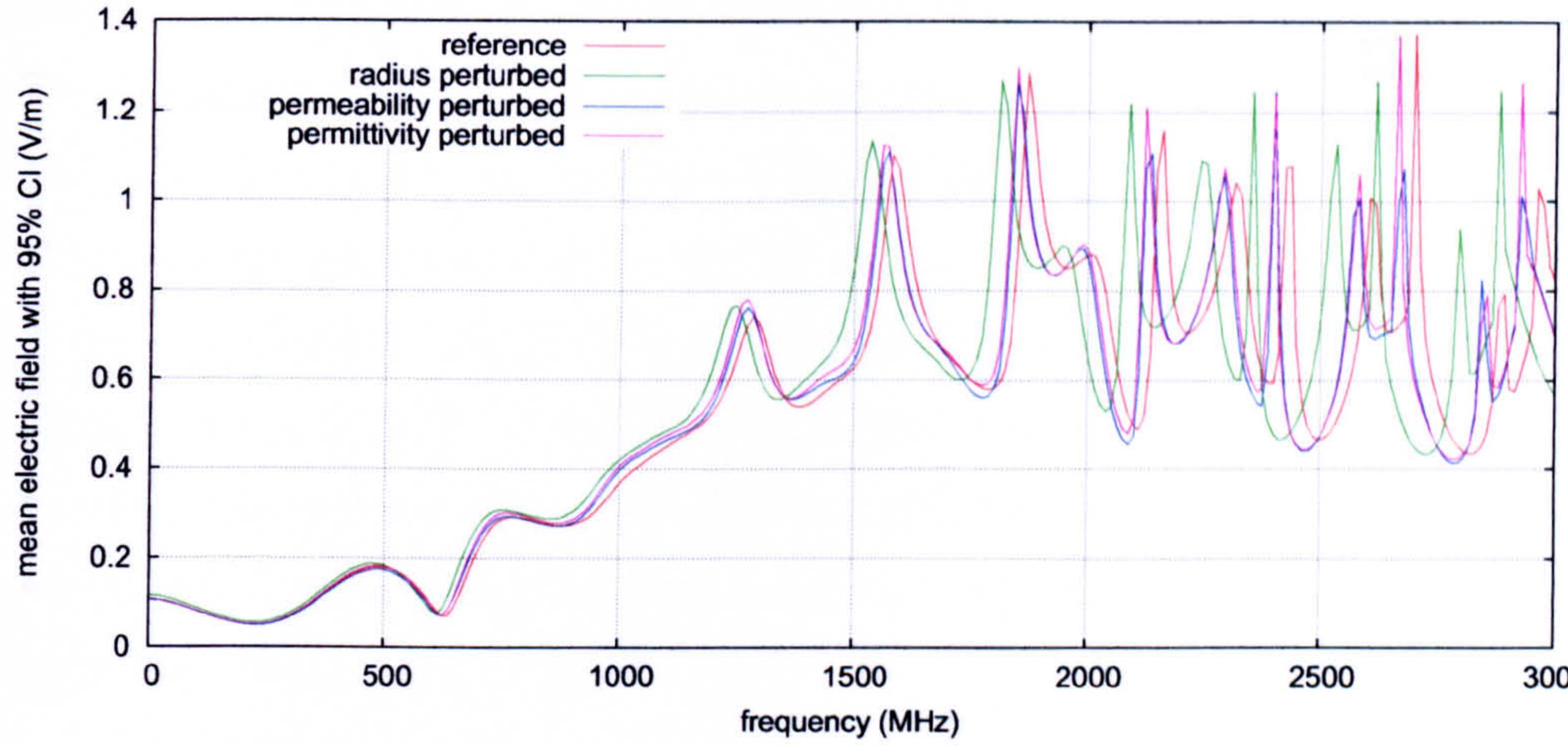

Figure 6.21: Frequency response of the normalised electric field produced from the reference simulation and the simulations with perturbed input parameters.

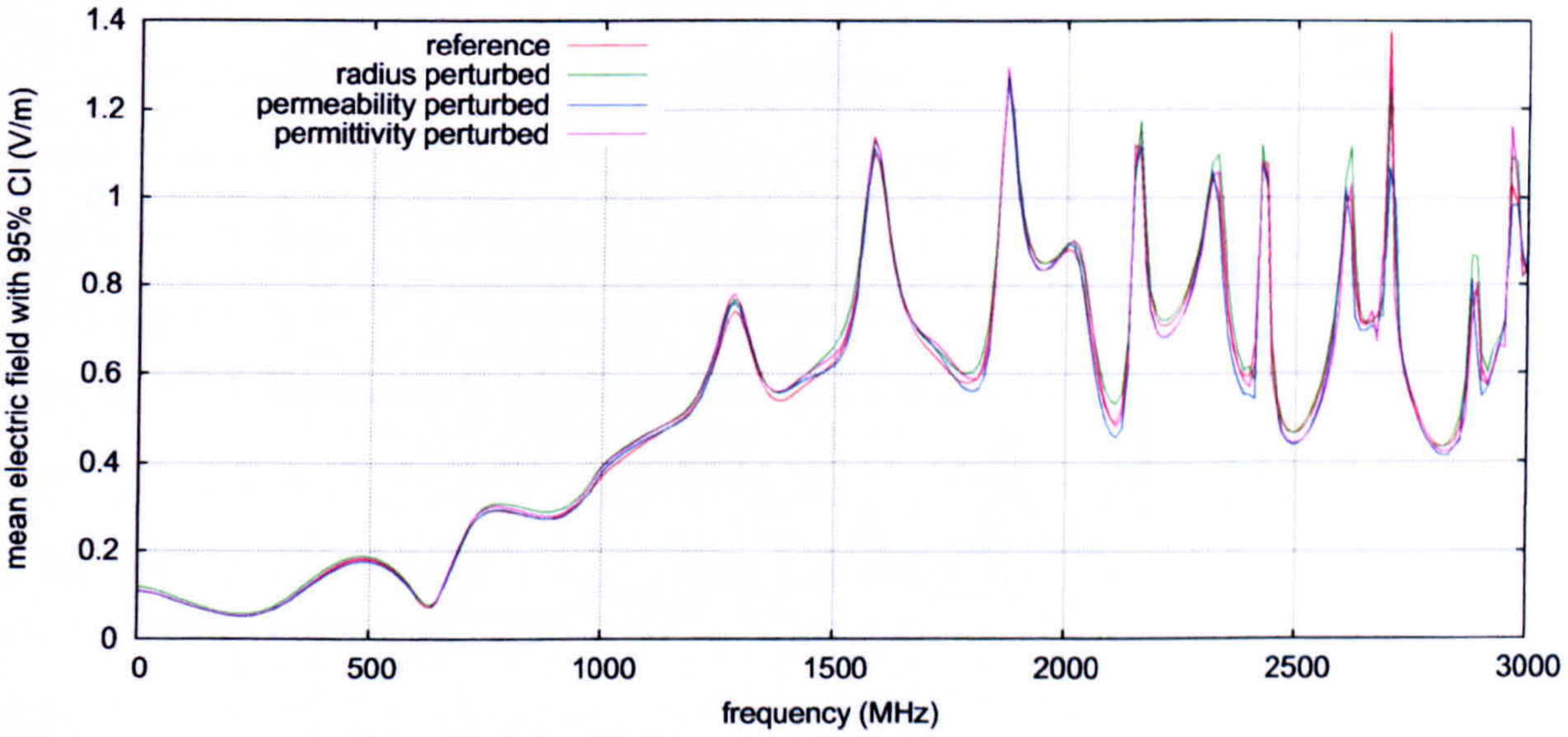

Figure 6.22: Frequency response of the normalised electric field produced by the simulations with perturbed input parameters, after alignment (via PM) to the response produced by the reference simulation.

These curves are very similar, but they are all shifted slightly in frequency. The uncertainty in the amplitude and frequency of the FDTD simulation can be calculated by aligning the output curves in 6.21. This provides more information as to how the uncertainty in the output manifests itself.

The three curves formed from the perturbed simulations were aligned to the curve formed from the reference simulation. The PM method is particularly suited to align such curves, as there are many well defined peaks that may be identified, matched and used to subsequently align the curves. The PM method was therefore used to align the curves in this example. The aligned curves are shown in Figure 6.22, it is clear from this figure that the PM method aligned the curves very well. These aligned curves were used to calculate the

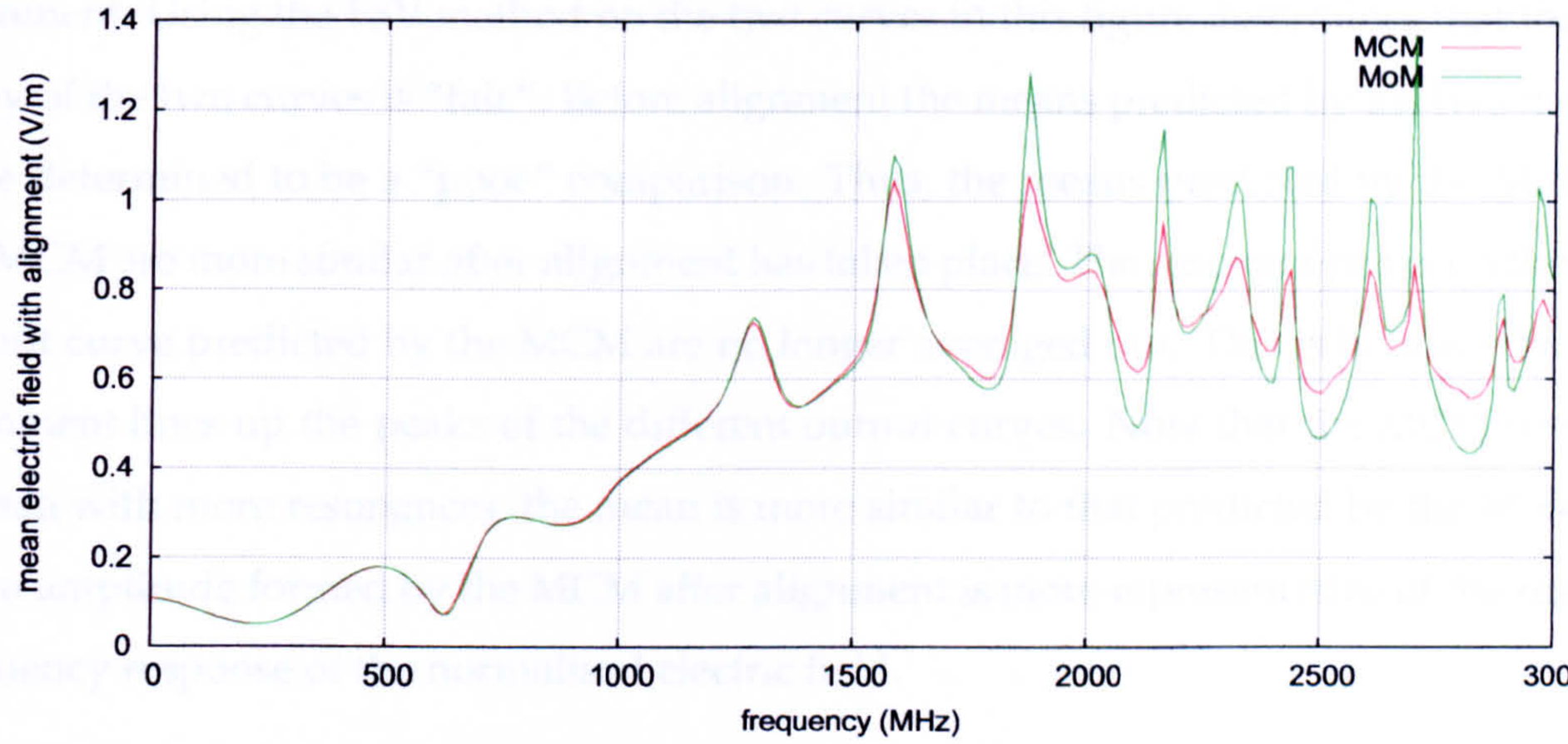

Figure 6.23: Frequency response of the mean normalised electric field predicted by the MCM and the MoM after alignment via PM.

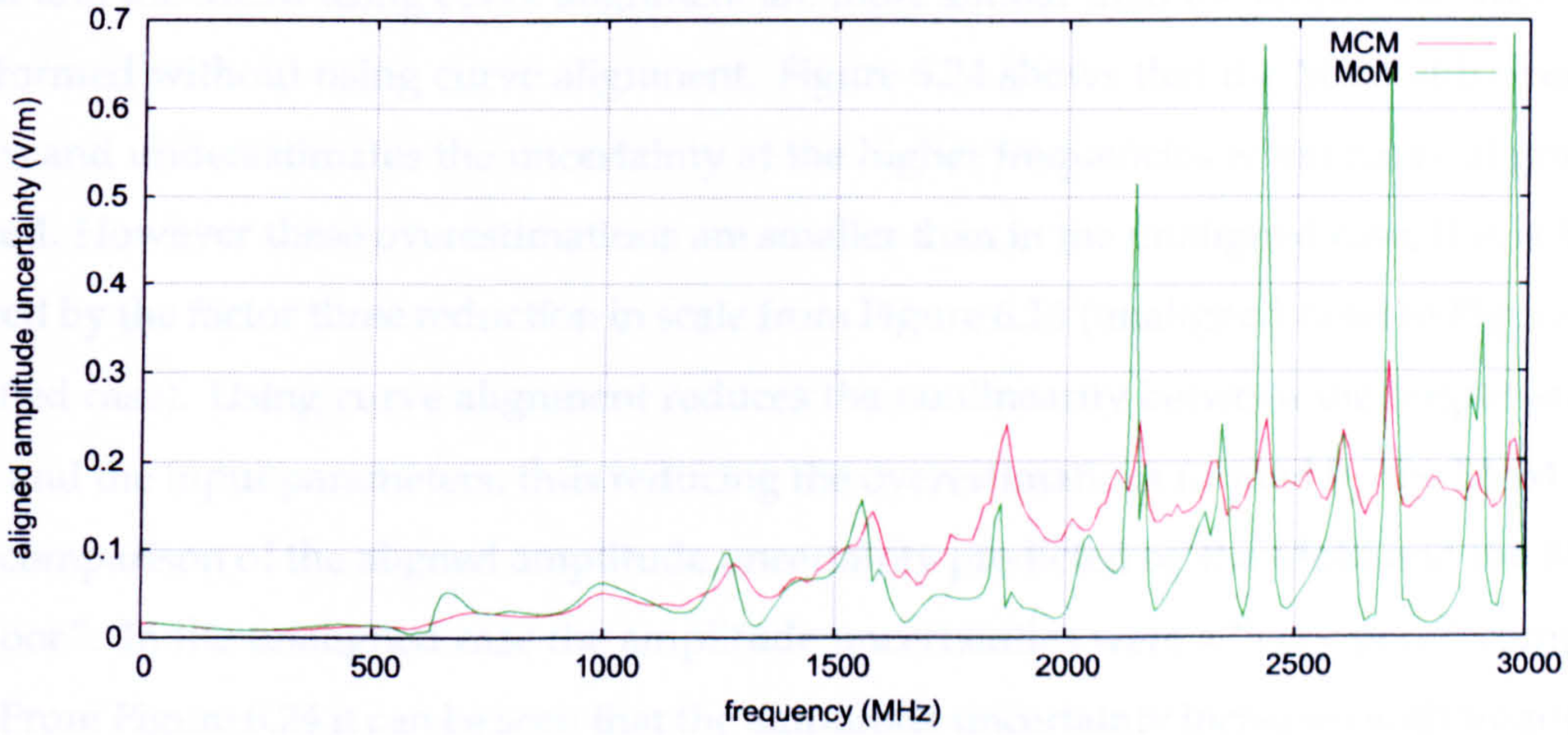

Figure 6.24: Frequency response of the uncertainty in the amplitude of the normalised electric field predicted by the MCM and the MoM after alignment via PM.

aligned uncertainty in the frequency and amplitude using the MoM. To be consistent, the PM method was also used when forming the aligned amplitude and frequency uncertainties via the MCM method. The MCM required only 400 simulations to form converged mean and uncertainty estimates. More simulations were required to form the mean and uncertainty without alignment (700 simulations). The individual frequency response curves are more similar after alignment, the means and uncertainties therefore change less when more MCM simulations are performed and thus convergence is reached more quickly in the aligned case.

The aligned amplitude mean predicted by the MoM is a lot closer to the mean predicted by the MCM. Figure 6.23 shows the means predicted by these two methods after

alignment. Using the FSV method on the two curves in this figure determines that the similarity of the two curves is "fair". Before alignment the means predicted by the two methods were determined to be a "poor" comparison. Thus, the means predicted by the MoM and the MCM are more similar after alignment has taken place. The resonant peaks on the mean output curve predicted by the MCM are no longer averaged out. This is because the curve alignment lines up the peaks of the different output curves. Now that the MCM produces a mean with more resonances, the mean is more similar to that predicted by the MoM. The mean amplitude formed by the MCM after alignment is more representative of the resonant frequency response of the normalised electric field.

The aligned amplitude uncertainties predicted by the MoM and the MCM for the FDTD simulation are shown in Figure 6.24. The amplitude uncertainties formed by the MoM and the MCM using curve alignment are more similar than the amplitude uncertainties formed without using curve alignment. Figure 6.24 shows that the MoM still overestimates and underestimates the uncertainty at the higher frequencies when curve alignment is used. However these overestimations are smaller than in the unaligned case, this is highlighted by the factor three reduction in scale from Figure 6.16 (unaligned case) to Figure 6.24 (aligned case). Using curve alignment reduces the nonlinearity between the output amplitude and the input parameters, thus reducing the overestimations formed by the MoM. The FSV comparison of the aligned amplitude uncertainty predicted by the MoM and the MCM is "poor". In the unaligned case the amplitude uncertainties were a "very poor" comparison. From Figure 6.24 it can be seen that the amplitude uncertainty increases with frequency for both methods; some of the features of the two uncertainty curves agree, but overall the curves are not very similar. At the lower frequencies, however, the two aligned amplitude uncertainties are in much better agreement. The FSV comparison of the amplitude uncertainties after alignment is again "very good" up to 480MHz, and is "fair" up to 1.69GHz. Before alignment the MoM was only able to give a "fair" estimate of the uncertainty up to 1.21GHz. Therefore, using curve alignment the MoM is able to give "fair" predictions of the amplitude uncertainty over a larger frequency range. The computational efficiency of the MoM means that it is useful for providing an approximate prediction of the aligned amplitude output uncertainty, for this example, especially up to 1.69GHz.

The uncertainties in the frequency formed using curve alignment (denoted as the aligned frequency uncertainties) via the MCM and the MoM are shown in Figure 6.25. These frequency uncertainty curves provide more insight into the form of the output uncertainty.

The frequency uncertainty increases with frequency for both UA methods. The larger frequency uncertainties at the higher frequencies manifest themselves as large amplitude uncertainties when curve alignment is not used. As discussed in Section 6.5.5, these large frequency shifts produced nonlinear relationships between the output electric field and the input parameters. This caused the MoM to overestimate the output uncertainty near the resonant peaks of the backscattered field, when curve alignment was not used. These overestimations are reduced by using curve alignment. Figure 6.25 shows that the MoM predicts larger frequency uncertainties than the more accurate MCM, at the higher frequencies. Thus the MoM still overestimates the aligned amplitude and frequency uncertainties at the higher frequencies. These overestimations are still present because the MoM is still an approximate method relying on the assumption that the output depends linearly on the uncertain inputs. The FSV comparison of the aligned frequency uncertainty produced by the benchmark MCM and the MoM is "fair" up to 2.70GHz. The MoM is therefore fairly accurate at predicting the aligned frequency uncertainties over the majority of the frequency range.

The aligned uncertainties are used to predict the aligned 95% CI for the mean frequency response of the electric field. Figures 6.26 and 6.27 show that the MoM gives an excellent prediction of the upper 95% CI for the aligned frequencies, when compared to the MCM, but a poorer prediction of the upper aligned amplitude 95% CI at the higher frequencies. The MoM predictions of the amplitude 95% CI are better at the lower frequencies. Using the FSV method, the MoM is determined to give "good" predictions of the aligned amplitude upper 95% CI up to 2.09GHz, when compared to the more accurate MCM. The FSV method was also used to compare the 95% CI of the aligned frequencies predicted by

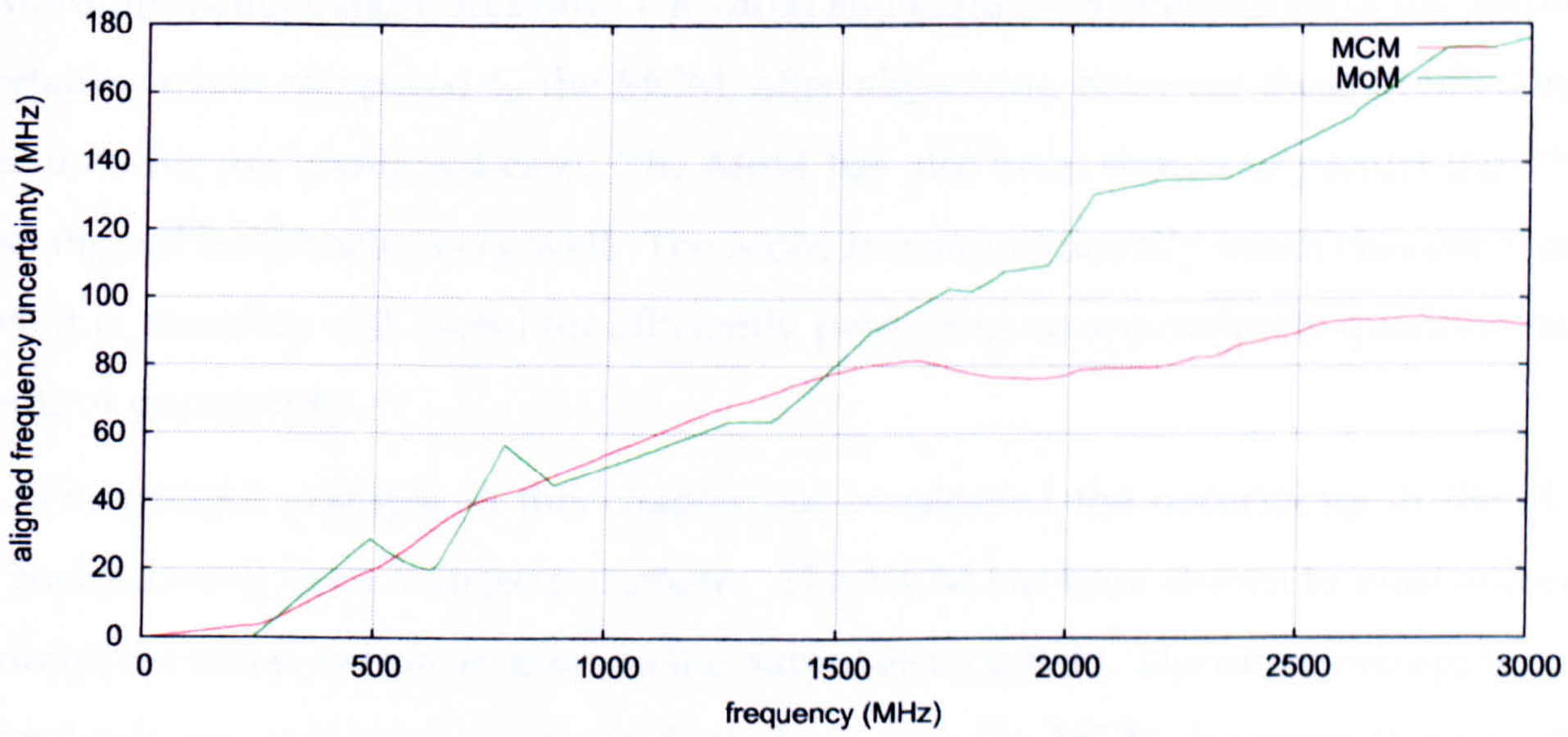

Figure 6.25: Frequency response of the uncertainty in the frequency predicted by the MCM and the MoM after alignment via PM.

both methods and determined that their similarity is "excellent". The MoM therefore gives an excellent prediction of the upper 95% confidence intervals for the frequencies, in this case.

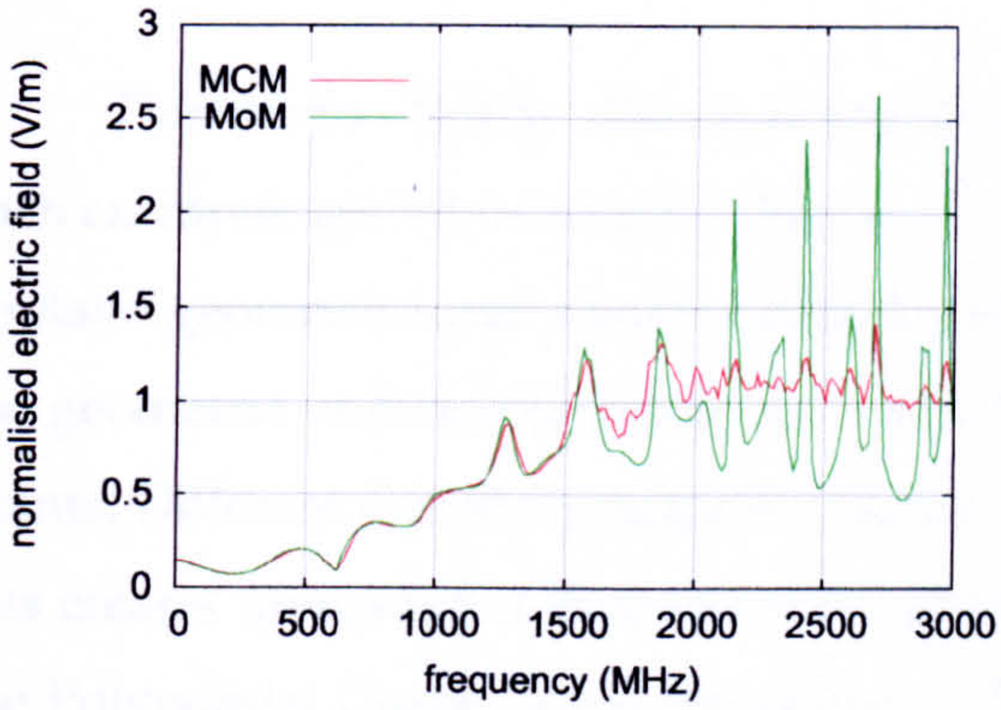

Figure 6.26: The upper aligned 95% CI for the amplitude.

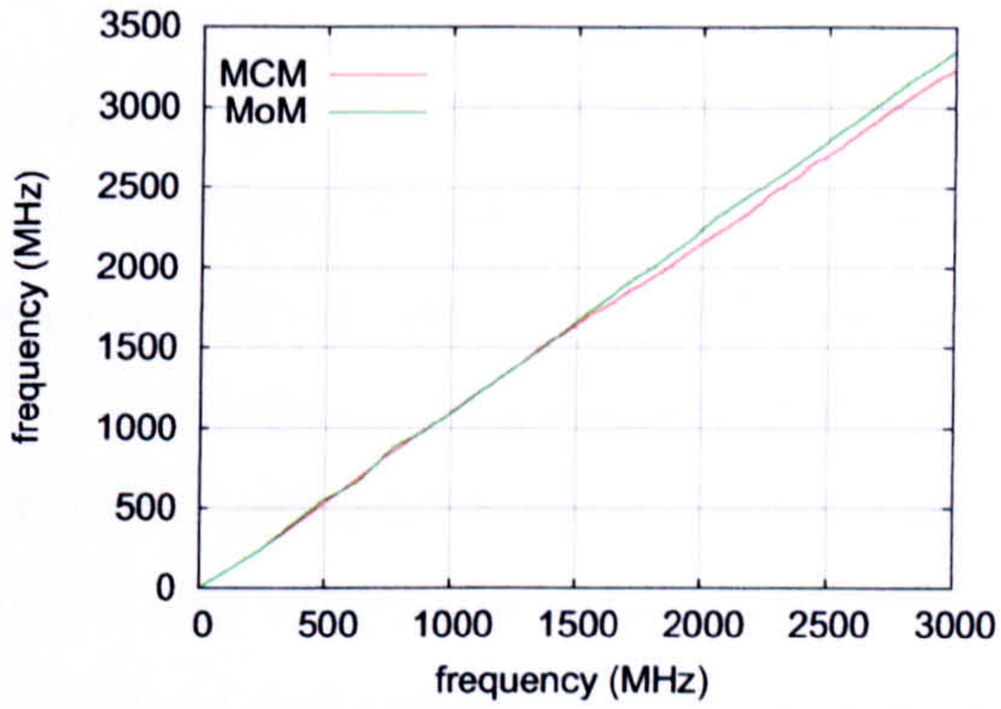

Figure 6.27: The upper aligned 95% CI for the frequency.

For the examples introduced in this chapter and in the previous chapter, it has been shown that the uncertainty in the electric field is due to both amplitude and frequency uncertainties. The aligned frequency increases with frequency, for both examples; this is as a result of poorer alignment of the output curves at the higher frequencies. These frequency shifts produce larger uncertainties in the unaligned amplitude of the electric field at the higher frequencies. Using alignment it is clear that the uncertainties at the higher frequencies are also due to uncertainties in the frequency. The overestimated amplitude uncertainties predicted by the MoM are reduced after the alignment process. The alignment process helps to reduce the nonlinearity in the relationships between the output and the inputs, thus making the MoM predictions more accurate. The MoM still gives poor predictions of the amplitude uncertainty when compared to the MCM, after alignment, however these predictions are better than for the unaligned case. The MoM has also been shown to predict the 95% CI of the aligned frequencies very well. The MoM is computationally much cheaper than the MCM, it is therefore still useful for efficiently predicting an approximate quantification of the output uncertainty.

The present example in this chapter has considered the uncertainty in the electric field backscattered from a dielectric sphere. The MCM has been shown to most accurately determine the mean and uncertainty in the output electric field. The other two approximate UA methods are computationally much cheaper than the MCM, however these methods provide poor estimates of the output uncertainty at higher frequencies. In the next section

it is shown that there are cases where the PCM does not work as an UA method.

6.7 A Perfectly Electrically Conducting Sphere

This section briefly discusses one example where the PCM is not applicable, other such examples are introduced in Chapter 7. The main problem with the PCM is with the way it relates geometric input uncertainties to material parameters. In the example in this section the geometric uncertainty causes a boundary to be distributed over a number of discrete points. Different material parameters values are assigned to the points near to the boundary, this creates unwanted reflections of the Polynomial Chaos field coefficients (e_i^n and h_i^n) in the Polynomial Chaos FDTD simulation. The purpose of this section is to demonstrate a limitation with the PCM, the MoM and MCM are therefore not considered in this section.

Consider a PEC sphere, with an uncertain radius, illuminated by a uniform plane wave excitation. The sphere is in free space, and the permittivity and permeability of the sphere take on the free space values. Suppose the radius of this sphere is Normally distributed with a mean $\bar{a} = 0.1$m and a standard deviation $\sigma_a = 0.005$m. The output of interest is the normalised electric field in the frequency domain, backscattered at a distance of 0.2m from the centre of the sphere. This field may be calculated analytically using the series solution given by Balanis [94, p.650-658], and using a FDTD simulation, with $100 \times 100 \times 100$ cells, a cell size $\Delta l = 0.005$m and 10,000 time steps. Figure 6.28 shows the analytic solution and the FDTD solution of this example. The two curves in Figure 6.28 are fairly similar, however it is clear that there are errors in the result of the FDTD simulation. The details on how the PCM is implemented into the FDTD simulation, for this example, are given next.

6.7.1 Implementing the Polynomial Chaos Method into the Finite Difference Time Domain Simulation

To perform an UA using the PCM the uncertain radius needs to be related to the material parameters in the FDTD chaotic update equations (4.111) and (4.112). Since the permittivity and permeability are constant throughout the problem space, the uncertain radius relates only to the uncertainty in the conductivity of points near to the mean radius of the sphere. Firstly the uncertainty in the radius a of the sphere must be related to θ, which

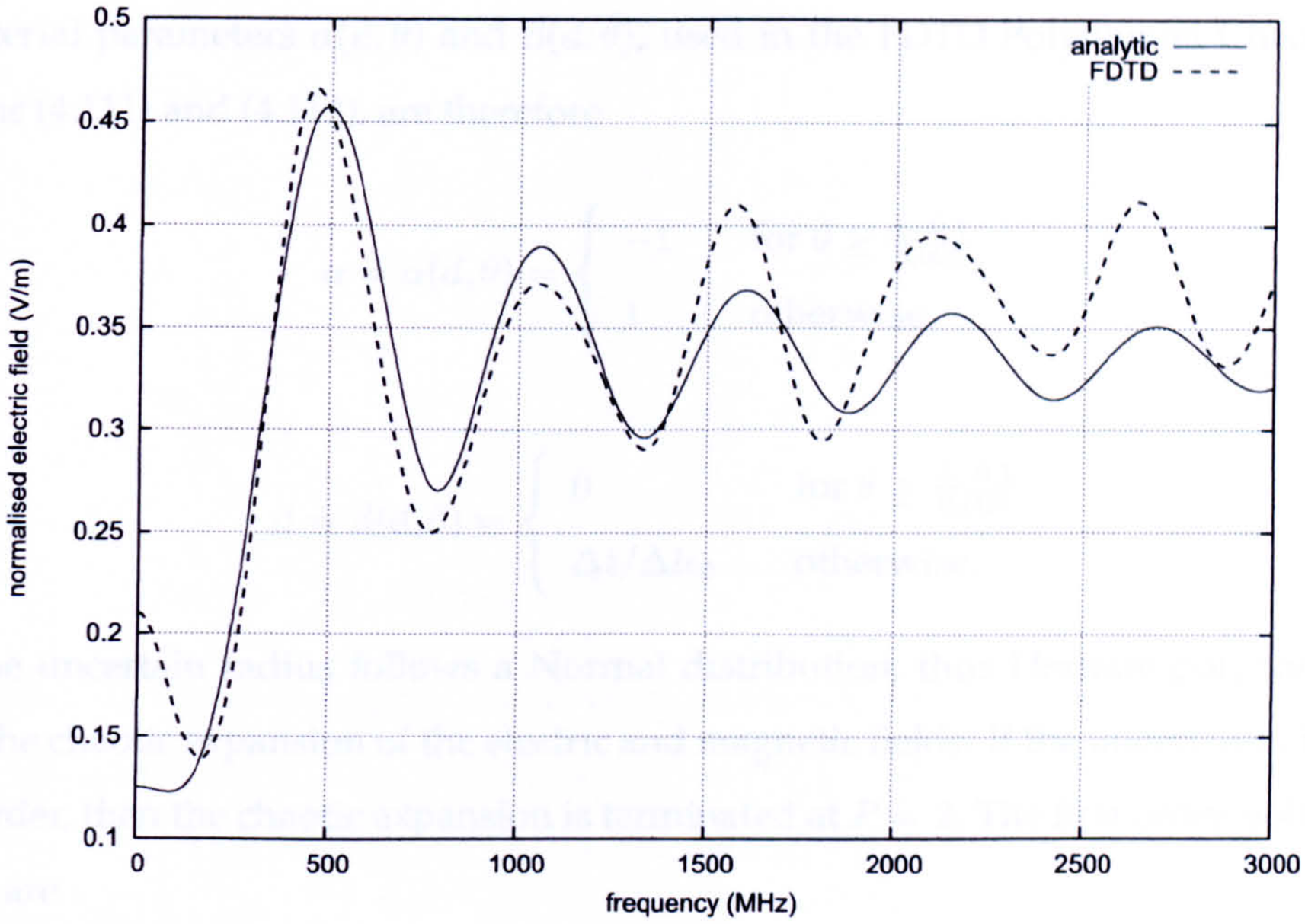

Figure 6.28: Frequency response of the normalised electric field backscattered from a PEC sphere.

follows a standard Normal distribution. The following relation fits this purpose

$$a = \bar{a} + \sigma_a \theta = 0.1 + 0.005\theta. \tag{6.41}$$

This uncertainty in the radius of the sphere must now be related to the uncertainty in the conductivity S at positions around the mean radius of the sphere. The term σ is the standard notation for the conductivity and the standard deviation (uncertainty); the conductivity has been denoted as S here to avoid any confusion with the notation. If a point in the problem space is inside the sphere then $S = \infty$, otherwise $S = 0$. Thus the material parameters are $\alpha = -1$ and $\beta = 0$ if the point is inside the sphere and $\alpha = 1$ and $\beta = \Delta t/\Delta l \epsilon_0$ if the point is outside the sphere. Consider a point $(x, y, z) = (i\Delta l, j\Delta l, k\Delta l)$, which is a distance d from the centre of the sphere. This point is in the sphere if

$$d \leq a = 0.1 + 0.005\theta. \tag{6.42}$$

Thus (x, y, z) is in the sphere if

$$\theta \geq \frac{d - 0.1}{0.005}. \tag{6.43}$$

The material parameters $\alpha(d,\theta)$ and $\beta(d,\theta)$, used in the FDTD Polynomial Chaos update equations (4.111) and (4.112), are therefore

$$\alpha = \alpha(d,\theta) = \begin{cases} -1 & \text{for } \theta \geq \frac{d-0.1}{0.005} \\ 1 & \text{otherwise} \end{cases} \tag{6.44}$$

and

$$\beta = \beta(d,\theta) = \begin{cases} 0 & \text{for } \theta \geq \frac{d-0.1}{0.005} \\ \Delta t/\Delta l \epsilon_0 & \text{otherwise.} \end{cases} \tag{6.45}$$

The uncertain radius follows a Normal distribution, thus Hermite polynomials are used in the chaotic expansion of the electric and magnetic fields. If the uncertainty is sought to first order, then the chaotic expansion is terminated at $P = 2$. The first order polynomials required are

$$\psi_0 = 1 \tag{6.46}$$

$$\text{and} \quad \psi_1 = H_1(\theta) = \theta. \tag{6.47}$$

The orthogonality of the polynomials leads to

$$< \psi_i(\theta_k)\psi_j(\theta_l) >= \delta_{ij}\delta_{kl}(i)!. \tag{6.48}$$

The electric and magnetic fields are calculated using the update equations (4.111) and (4.112). Before these equations can be used, the inner products of the material parameters α, β and γ with the polynomials used in the chaotic expansion need to be calculated. The material parameter $\gamma = \Delta t/\Delta l \mu_0$ with zero uncertainty, since the permeability is that of free space throughout the problem space. Thus the inner product of γ with the polynomials ψ_i and ψ_j is

$$< \gamma\psi_i\psi_j >= \gamma\delta_{ij}\delta_{kl}(i)! \tag{6.49}$$

where $i, j = 0, 1$. The inner products formed with α and β, at each point a distance d from

the sphere centre, are calculated using the integrals

$$\begin{aligned} < \alpha\psi_i\psi_j > &= \int_{-\infty}^{\infty} \alpha(d,\theta)\psi_i\psi_j \frac{\exp(-\frac{\theta^2}{2})}{\sqrt{2\pi}} d\theta \\ &= \int_{-\infty}^{\frac{d-0.1}{0.005}} \psi_i\psi_j \frac{\exp(-\frac{\theta^2}{2})}{\sqrt{2\pi}} d\theta + \int_{\frac{d-0.1}{0.005}}^{\infty} (-1)\psi_i\psi_j \frac{\exp(-\frac{\theta^2}{2})}{\sqrt{2\pi}} d\theta \end{aligned} \tag{6.50}$$

$$\text{and} \quad < \beta\psi_i\psi_j > = \int_{-\infty}^{\infty} \beta(d,\theta)\psi_i\psi_j \frac{\exp(-\frac{\theta^2}{2})}{\sqrt{2\pi}} d\theta$$

$$= \int_{-\infty}^{\frac{d-0.1}{0.005}} \frac{\Delta t}{\Delta l \epsilon_0} \psi_i\psi_j \frac{\exp(-\frac{\theta^2}{2})}{\sqrt{2\pi}} d\theta. \tag{6.51}$$

These improper integrals are calculated using numerical techniques [90, p.141-147]. The inner products calculated using the above integrations are substituted into the update equations (4.111) and (4.112), which are then used to find the mean and uncertainty in the electric field at the output point.

The above inner products represent the conductivity of the material through which the electromagnetic fields propagate. The uncertainty in the radius of the sphere results in different values for the inner products at the points surrounding the radius of the sphere. Figures 6.29 and 6.30 show how the inner products change with the cell position. In these figures, the cell positions are in the z-direction, with x and y both equal to $50\Delta l$, and the sphere centred at $(50\Delta l, 50\Delta l, 50\Delta l)$, with a radius of 20 cells. Notice that the inner product values take on different values at neighbouring cell positions. This corresponds to neighbouring cell positions having different conductivities, and hence different reflection coefficients. The Polynomial Chaos field coefficients e_i^n and h_i^n (used in the Wiener-Askey Chaos expansion of the electromagnetic fields) will therefore reflect between these neighbouring cells. These reflections occur over very small distances producing a large field gradient between neighbouring cells. These large field gradients couple in the Polynomial Chaos FDTD update equations resulting in a large rate of change of other Polynomial Chaos field coefficients. The amplitude of the coupled field coefficients increase as the time of the simulation increases, ultimately tending to infinity.

Figures 6.31-6.33 show three plots that represent how the amplitude of the Polynomial Chaos simulated solution increases to unphysical values. These plots represent the spatial variation of the Polynomial Chaos field coefficient e_0^n in the plane $x = 50\Delta l$ (the central plane). Figure 6.31 shows the field coefficient for time step 150. At this time step the plane wave has reached the sphere, the wave moves round the sphere and is backscattered from

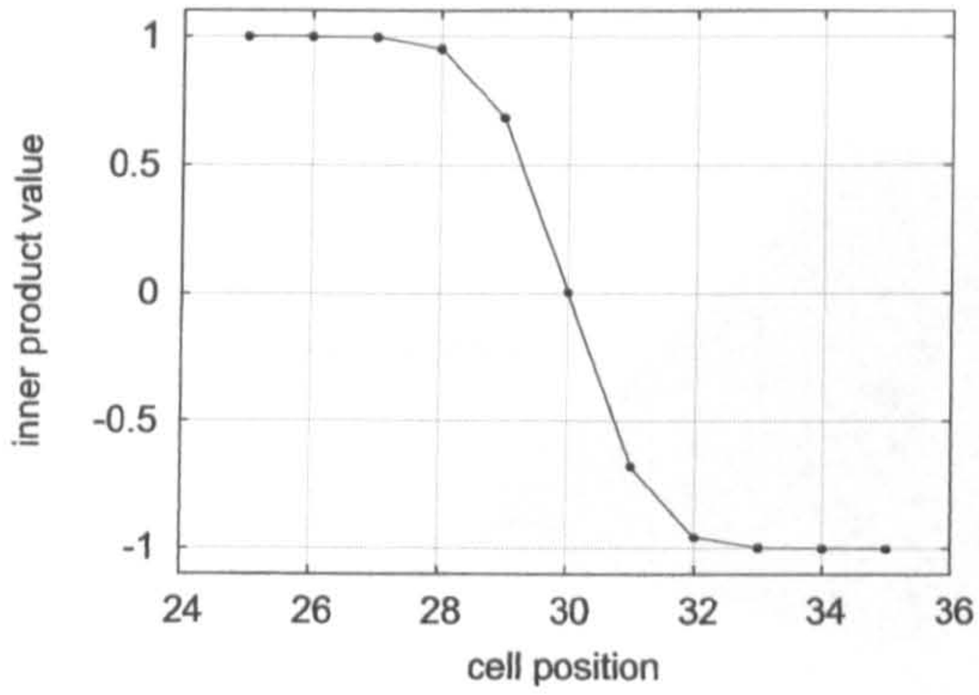

Figure 6.29: Inner product $< \alpha\psi_0\psi_0 >$ values for different cell positions.

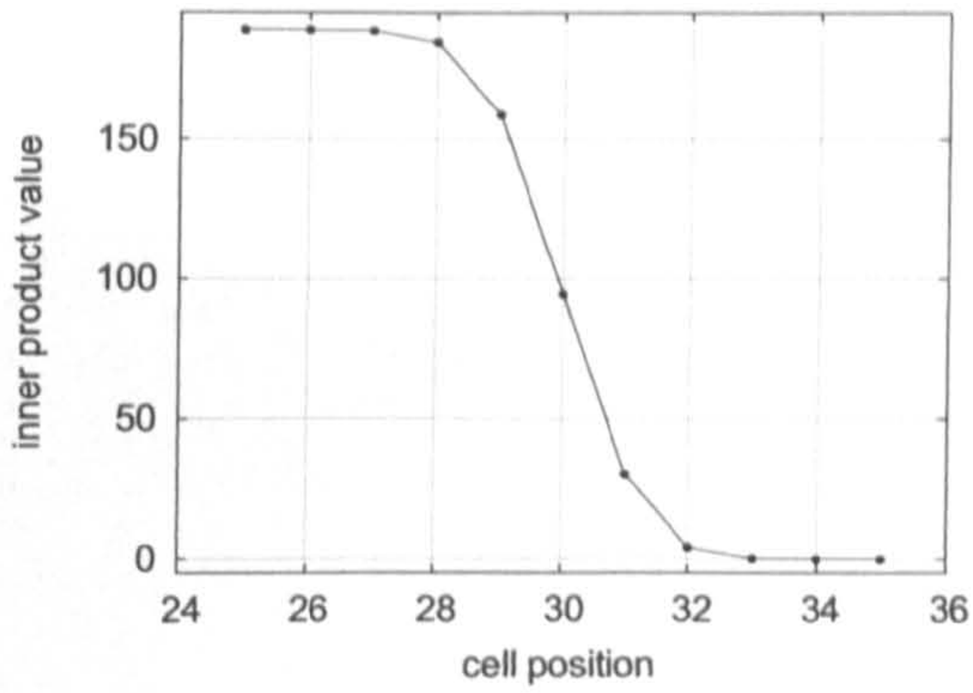

Figure 6.30: Inner product $< \beta\psi_0\psi_0 >$ values for different cell positions.

it. At points near the front of the sphere, where the wave was first incident, the electric field coefficient reflects between neighbouring cell positions and builds up. By time step 200 (Figure 6.32) these large fields propagate around the uncertain radius and begin to spread away from the sphere. Figure 6.33 shows how the field has increased to extremely large values that fill the whole problem space, ultimately rendering a nonsensical solution. Thus for this example the PCM cannot be used to obtain the uncertainty in the output of the FDTD simulation. In the next chapter a number of other examples will be introduced where the PCM cannot be used. These examples all have uncertain geometric input parameters.

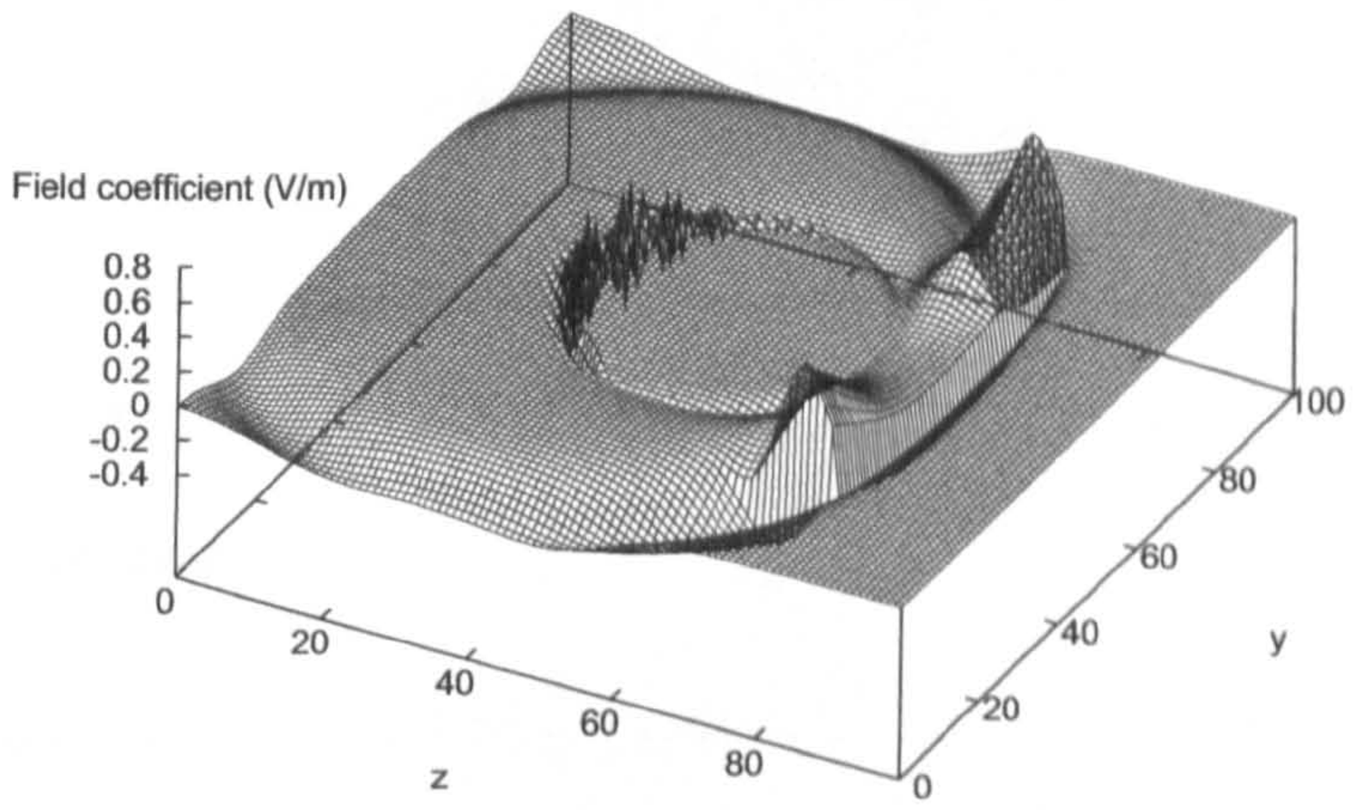

Figure 6.31: Planar response of e_0 at time step 150 for the central x-plane.

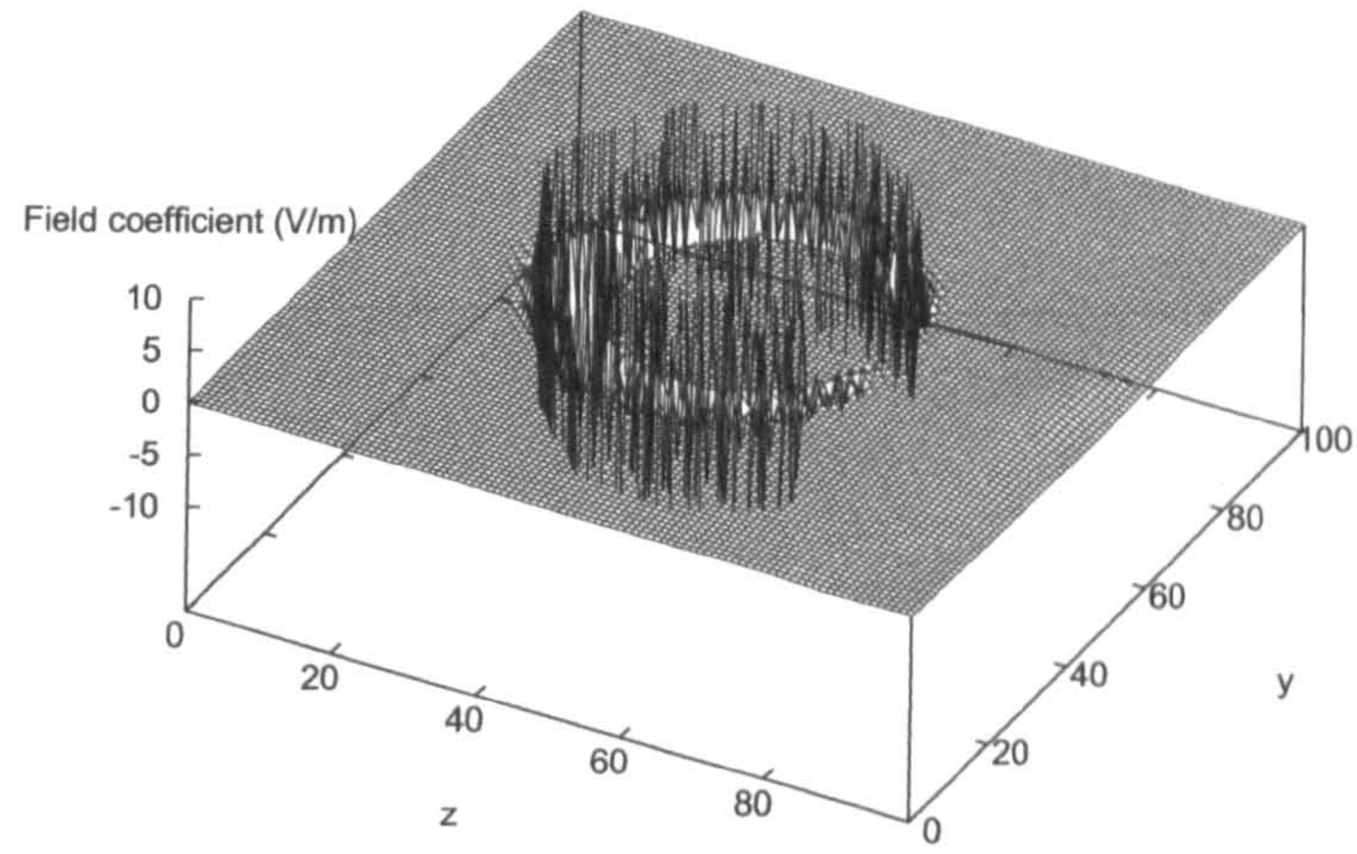

Figure 6.32: Planar response of e_0 at time step 200 for the central x-plane.

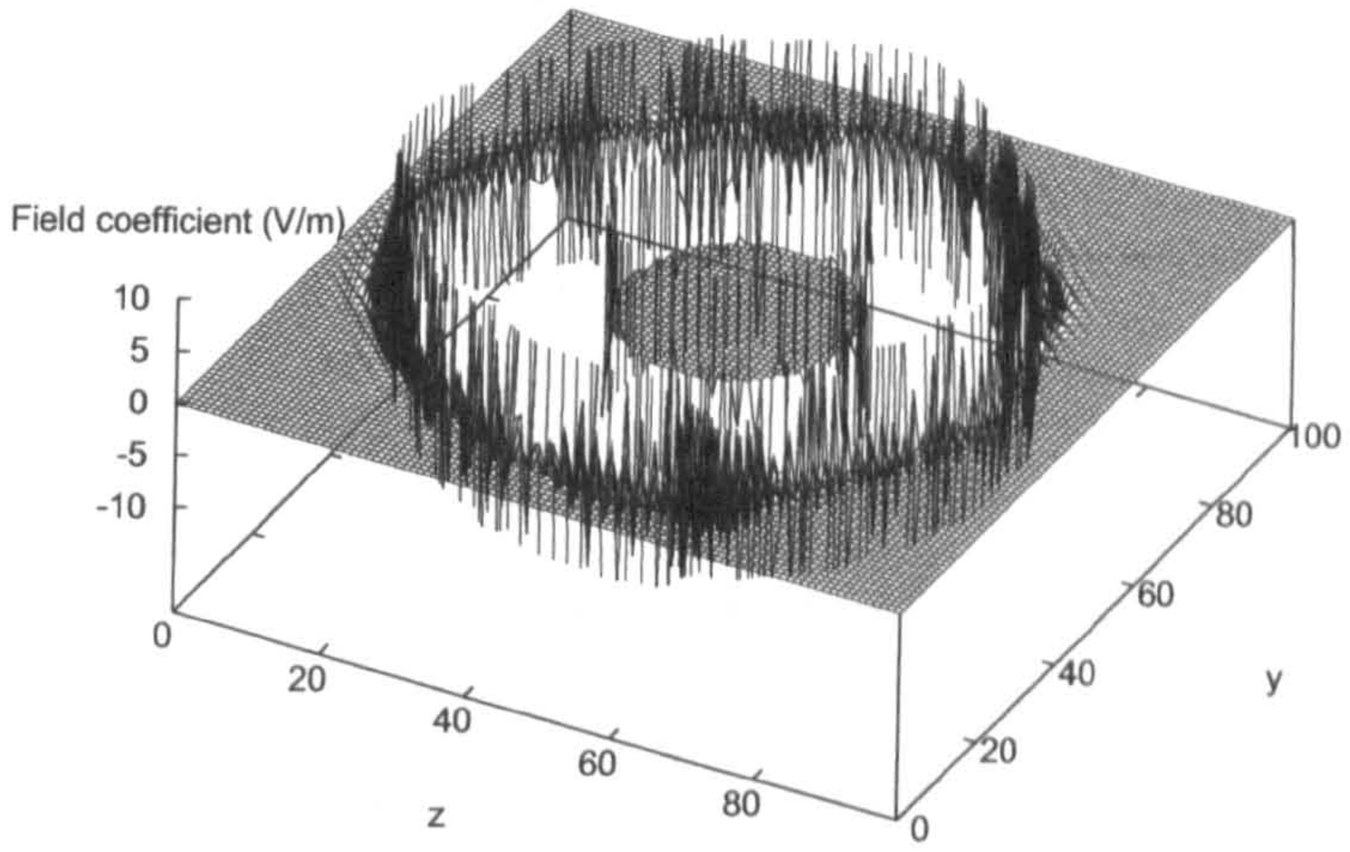

Figure 6.33: Planar response of e_0 at time step 300 for the central x-plane.

6.8 Conclusions

This chapter has investigated the performance of the different Error and Uncertainty Analysis methods, when applied to more complex 3D examples. In the first example the electric field backscattered off a dielectric sphere was considered. This example was chosen because it is analytically solvable.

The analytic solution was used to form the error, mean and uncertainty in the results of the FDTD simulation analytically. The error formed analytically was compared to the

error formed approximately using another FDTD simulation, performed on a refined mesh. The FSV method was used to perform this comparison, and determined that the two errors are fairly similar at the higher frequencies. Overall the error estimation, formed using the refined FDTD simulation, seemed to be a very good estimation of the actual error. The FSV comparison may have suffered from small frequency shifts creating large offsets between the curves. Ignoring the offset difference, the curves were determined to be very similar. The error estimation, formed from the refined FDTD simulation, did however underestimate the errors at the lower frequencies. These underestimations arise because the refined simulations are less accurate at the lower frequencies, and thus fail to highlight the errors in the coarse FDTD simulations.

At higher frequencies the error in the coarse FDTD simulation took on large peak values. It was shown that these large amplitude errors were partly due to frequency shifts, at the higher frequencies, that caused an unalignment of the characteristic resonant peaks. Using curve alignment it was shown that the aligned amplitude error was significantly lower at the higher frequencies and that there were errors due to frequency differences between the curves. Thus the error in the output of the FDTD simulation manifests itself as an amplitude and a frequency error. This information, on the form of the output uncertainty, is difficult to obtain without aligning the curves.

Uncertainty Analyses were applied to the analytic solution of the field backscattered from the dielectric sphere. The mean and uncertainty predicted by the MCM, the MoM and the PCM were compared to the mean and uncertainty obtained analytically. Through these comparisons it was shown that, of the three UA methods investigated in this thesis, the MCM most accurately predicts the uncertainty in the solution. The MCM was therefore used as the benchmark method, by which the performance of the other two methods were compared when all three UAs were applied to the FDTD simulated solution. The MoM was shown to give very poor predictions of the uncertainty at higher frequencies. It was argued that the nonlinear relationship between the output field and the frequency, along with the frequency shifts caused by the parameter perturbations, caused the output to depend on the input in a highly nonlinear way. This nonlinear relationship is most prominent around the frequencies at which the electric field is at a resonant peak. The MoM assumes that the output depends linearly on the input, this is therefore a poor assumption to make at the peak frequencies. Subsequently, at the resonant frequencies, the MoM prediction of the uncertainty is poor.

The means predicted by the MoM and the PCM were shown to be poor when compared to the mean predicted by the MCM for the FDTD simulation. The overall mean amplitudes, predicted by the three methods, were similar but the features predicted by the MoM and the PCM were different from those predicted by the MCM. Resonant features of the electric field are averaged out in the prediction formed by the MCM. There is no such averaging of the resonant features in the mean curves predicted by the other two methods. This results in the means predicted by the MoM and the PCM being poor estimations when compared to the means predicted by the MCM. The means produced by the MoM and the PCM do however represent the resonant nature of the frequency response of the normalised electric field.

In terms of the uncertainty predictions for the output of the FDTD simulations, the MoM produced a very poor prediction of the uncertainty and the PCM gave a poor prediction at the higher frequencies, when compared to the prediction formed using the benchmark MCM. Both the MoM and the PCM assume that the output depends linearly on the uncertain inputs; at higher frequencies the relationship was highly nonlinear. This caused the PCM and the MoM to overestimate the output uncertainty at the higher frequencies. Both the MoM and the PCM performed better at lower frequencies. The MoM and PCM were shown to give fair predictions of the uncertainty up to 1.21GHz and 1.02GHz respectively.

By comparing the uncertainty predicted by the MCM for the analytic and FDTD simulated solutions, it was shown that the uncertainty in the output of a simulated solution has only a small dependence on the accuracy with which that simulation is implemented. The larger the errors in the output of a simulation, the more the output differs from the output formed with zero error, and therefore the more the output uncertainty will also differ. For fairly accurate simulations, however, the uncertainty is more dependent on the size of the input uncertainties, and the sensitivity of the output to changes in those input uncertainties.

Confidence intervals were formed using the means and uncertainties predicted by the different UA methods. The confidence intervals provide the quantitative level of confidence that may be held in the mean output. For the dielectric sphere example it was shown that at lower frequencies a high level of confidence can be held in the mean output, whereas at higher frequencies the confidence in the value of the output mean reduces. The means and uncertainties predicted by the MoM and the PCM were poor, at the higher frequencies, which caused the predictions of the 95% CI to be poor as well. Both methods performed

better at the lower frequencies, giving fair predictions of the upper 95% CI up to 1.55GHz for the MoM and 2.12GHz for the PCM.

The three UA methods were also compared in terms of their computational expense. As with the example in the previous chapter, the MCM requires the most amount of computational time, the PCM requires significantly more memory than the other methods, and the MoM is by far the computationally cheapest method. For this example the MoM requires 175 times less computational time than the MCM, and about a factor 20 times less memory than the PCM. The MoM has been shown to give good predictions of the uncertainty over certain frequencies, it is also by far the computationally cheapest method. The MoM is therefore useful in obtaining an efficient estimate of the uncertainty in the output of CEM simulations, especially when the output depends on the inputs in a more linear fashion.

Curve alignment was used to determine the form of the output uncertainty. Currently it is not possible to determine the aligned uncertainty using the PCM. Using the PM method it was shown that the uncertainty in the output is due to both frequency and amplitude uncertainties. The amplitude uncertainties before alignment were larger at the higher frequencies. This is because small frequency shifts at the higher frequencies created large amplitude offsets between the curves. Using curve alignment reduces the aligned amplitude uncertainty, and provides an estimation of the frequency uncertainty. Both the aligned amplitude and frequency uncertainties were shown to increase with frequency.

The overestimations of the uncertainty predicted by the MoM were reduced slightly by using curve alignment. This is because the frequency shifts of the resonant frequency response curves were reduced, which meant that the output depended on the inputs in a more linear fashion. Thus the MoM assumption that the output depends linearly on the inputs was a better assumption. The aligned amplitude and frequency uncertainties estimated by the MoM were still poor at the higher frequencies. At the lower frequencies, however, the MoM performed better predicting fair aligned amplitude and frequency uncertainties up to 1.69GHz and 2.70GHz respectively. The MoM gave an excellent prediction of the aligned frequency upper 95% CI over the whole frequency range, and a good prediction of the aligned amplitude upper 95% CI up to 2.09GHz: this is much better than before alignment. It may be concluded that, for this example, the MoM provides better approximations of the uncertainty and the 95% CI at lower frequencies and when curve alignment is used.

The aligned mean calculated using the MoM was determined to be a fairly good estimate of the aligned mean calculated by the MCM. The alignment process lines up the

resonant features in the curves produced by the MCM simulations. Thus, the resonant features are no longer averaged out in the mean obtained from the MCM. This causes the two means to be more similar than before alignment. For this example it can be concluded that the MoM gives a fairly good prediction of the aligned mean, when compared to the aligned mean produced by the MCM.

Section 6.7 introduced a similar 3D example where the PCM did not work. The example involved the scattering of an electric field plane wave off a PEC sphere with an uncertain geometry. The PCM deals with this uncertainty by distributing the conductivity values of the sphere over a small number of discrete points. Different conductivity values at neighbouring points caused the Polynomial Chaos field coefficients to reflect over small distances. This induced a large rate of change of the field coefficients, which were coupled by the Polynomial Chaos FDTD update equations. The high rate of change of one field coefficient induced the high rate of change of other field coefficients. This resulted in the amplitude of the field coefficients increasing rapidly in size. Unrealistic field coefficients resulted, which could not be used to form a sensible mean or uncertainty for the output of the FDTD simulation.

In the next chapter the UA methods will be applied to CEM simulations of more realistic EMC examples. These examples do not have analytic solutions and it is therefore not possible to determine the performance of the approximate error and uncertainty analyses by comparisons with analytic results. The approximate error analysis will be used to estimate the error in the output of the FDTD simulations, this method has been shown to work quite well in the previous analytic examples. The MCM has been shown to be the best predictor of the uncertainty in the output of the analytic solution. This method will therefore be used as the benchmark method by which the results of the other two approximate methods are compared.

Chapter 7

Error and Uncertainty Analyses Applied to Electromagnetic Compatibility Examples.

Contents

7.1 Introduction

The examples used in this chapter represent more realistic EMC scenarios that have no analytic solution and are subsequently solved using CEM simulations. The MCM, MoM and PCM are applied to these CEM simulations to quantify the mean, uncertainty and 95% CI associated with the output of the simulations. As in the previous chapter the MCM is used as the benchmark method by which the performance of the other two UA methods are compared. The approximate error analysis method is also used to provide an estimate of the errors in the FDTD simulations.

In the first example an electromagnetic wave is radiated from a dipole antenna and is incident upon a personal computer. There is an aperture in the front face of this computer, where the compact disc drive would be placed. This forms the usual EMC setup of a shielded box with an aperture. The shielded box contains an output point and a Printed Circuit Board (PCB), which has a number of electrical components situated upon it. These components absorb a small amount of the field that penetrates the box and therefore the board and its components may be modelled as a thin material block with a certain reflection coefficient. There is however an uncertainty in the reflection coefficient of the board, which results in an uncertainty in the normalised electric field recorded at the output point. The three UA methods are used to quantify this uncertainty and produce the 95% CI that surround the mean output. This example is modelled using the FDTD method.

The second example considers the uncertainty in the shielding effectiveness of an enclosure with uncertain aperture coordinates. The third example also considers the uncertainty in the shielding effectiveness of a box, but this time with ten geometric uncertain parameters. This third example is used to test the performance of the UA methods when there is a larger number of uncertain parameters. These last two examples are modelled using the FDTD method and the ILCM method. A comparison of the uncertainty in the output of these different methods is provided. The PCM cannot be used in these last two

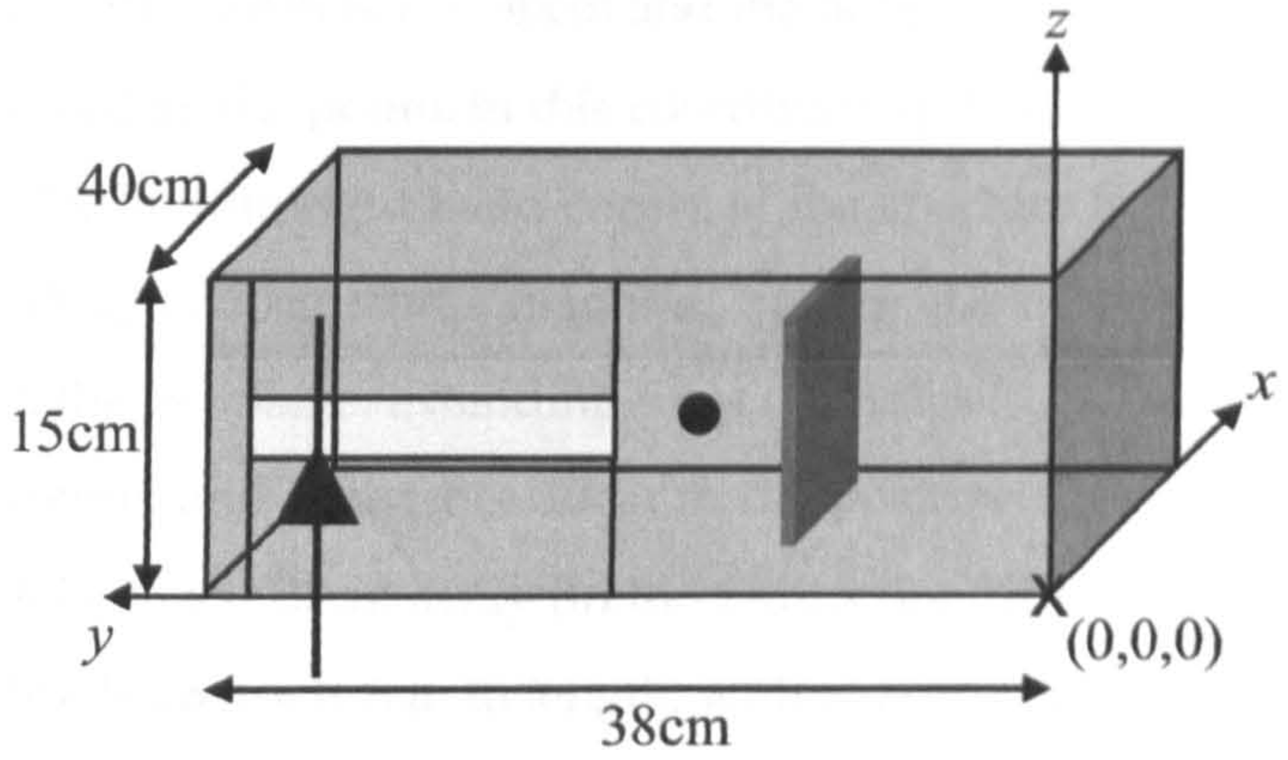

Figure 7.1: Shielded box containing a PCB, illuminated by an electromagnetic pulse from a dipole.

examples; the PCM would implement the uncertain geometries as different inner product field coefficients of varying conductivity, over a small number of points. This would result in a nonsensical solution as in the example in Section 6.7.

7.2 A Printed Circuit Board in a Shielded Enclosure

Figure 7.1 shows the setup of the first EMC example. An electric field is excited from a dipole (oriented in the z-direction) and scattered off a shielded enclosure, which has an aperture in the front face. This shielded enclosure represents the shielding exterior of a personal computer. A PCB is situated inside the computer, absorbing some of the electric field that penetrates the enclosure and is incident upon the board. The PCB may be modelled as a thin dielectric block with a certain reflection coefficient [95]. The absolute value of the reflection coefficient is not exactly known, but it is assumed to take a value from the interval

$$\Gamma = [0.91, 0.97]. \tag{7.1}$$

Notice that the reflection coefficient described by equation (7.1) is uncertain, it follows a Uniform distribution. The uncertainty in this input will cause there to be an uncertainty in the frequency response of the normalised electric field recorded at the centre of the enclosure. This normalised electric field $\tilde{E}_z$ is the absolute value of the z-component of the electric field observed at the centre of the box relative to a 1 V/m input excitation.

To describe the coordinates of this example the origin is assigned to the bottom right hand corner of the front face of the enclosure, which itself is in the y-z plane. The width of

the box is $y = 38$cm, the depth is $x = 40$cm and the height is $z = 15$cm. For the purposes of the following discussion, the points in this coordinate system have units of cm, referenced from the origin. The bottom right hand corner of the aperture is at the point $(0, 19, 5)$ and extends by a width $a_y = 15$cm and a height $a_z = 4$cm. Using this coordinate system, the PCB is oriented in the x-z plane, extending from the point (5,14,2) a distance $x_b = 30$cm in the positive x-direction and a distance 10cm in the positive z-direction. The centre of the dipole is at (-20,26,7), this is 20cm away (in the x-direction) from the centre of the aperture. The arms of the dipole are each 7cm in length, with a radius of 1mm. The voltage source at the centre of the dipole has an amplitude of $V_0 = 2$V over a load of 50Ω. The input excitation is a Gaussian of the form

$$V = V_0 \exp\left(\frac{-4\ln 2(t - t_0)^2}{fwhh^2}\right), \tag{7.2}$$

where $t_0 = 6.67 \times 10^{-10}$s is the onset time and $fwhh = 2.78 \times 10^{-10}$s is the full width of the Gaussian pulse at half the height of the maximum amplitude.

The reflection coefficient of the PCB is set by assigning certain material parameters to the PCB. In this example the frequency dependent reflection coefficient is set for a frequency of 1.8GHz: this is one of the main frequencies at which mobile phones operate in the United Kingdom. An analytic expression exists that relates the reflection coefficient of a uniform plane wave incident upon a lossy dielectric slab in free space, to the material parameters and thickness of that slab [94, p.235-236]. In the FDTD simulation of this example, the PCB is modelled as a thin boundary with an associated conductivity, permittivity and permeability. The thickness of the PCB is not well defined and therefore the analytic expression cannot be used to obtain the material parameters that are associated with the required reflection coefficient.

To obtain the correct material parameters of the PCB, the relationship between the reflection coefficient and the conductivity of the board was formed through a number of FDTD simulations. The board was assumed to have a relative permittivity of four and a relative permeability of one. The conductivity required to obtain the correct reflection coefficient was determined by using efficient one dimensional FDTD simulations. These simulations involved propagating a Gaussian pulse down the x-axis towards a thin boundary representing the PCB. By recording the electric field reflected back from the board, transforming this field into the frequency domain and taking the ratio of the resultant field to the incident excitation, it is possible to determine the reflection coefficient of the board at 1.8GHz. Varying the conductivity of the board allowed a relationship between the reflection coefficient and

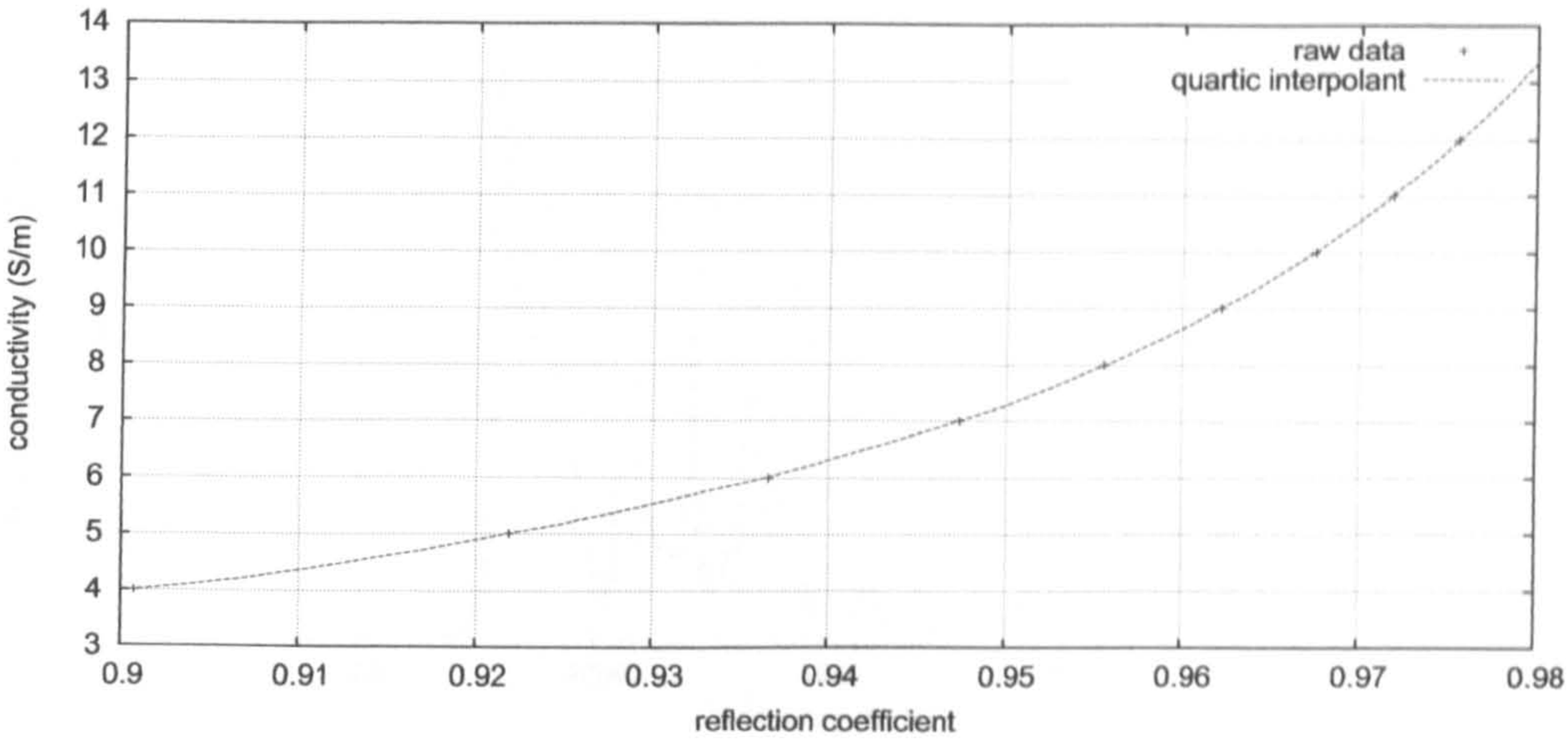

Figure 7.2: Relationship between the reflection coefficient and the conductivity.

the conductivity to be formed.

Figure 7.2 shows the reflection coefficient values associated with the different conductivities of the PCB. A quartic function was interpolated using these data points: this quartic is also shown in Figure 7.2. Visually the interpolant fits the data points extremely well. The observed raw data points and the expected points, evaluated from the quartic interpolant, produce a Chi-square value of $\chi^2 = 1.1039^{-4}$. This Chi-square value is extremely small and it may therefore be concluded that the quartic interpolant fits the data very well in this case. The quartic interpolant relates the reflection coefficient Γ to the conductivity S as

$$S = 10^6 \left(0.26969667\Gamma^4 - 0.99480063\Gamma^3 + 1.3765588\Gamma^2 - 0.84684980\Gamma + 0.19541786\right). \quad (7.3)$$

It is important to maintain the numerical accuracy of these coefficients, using less significant figures results in a poor fit to the raw data points. This quartic interpolant is used later to relate the uncertain reflection coefficient of the board to the uncertain conductivity of the board.

The frequency response of the normalised electric field at the centre of the enclosure was obtained using a FDTD simulation. This simulation was set up with a problem space containing $100 \times 100 \times 100$ points, with a cell size of 1cm and 10,000 time steps. The dipole and enclosure were modelled at the centre of this problem space. For the purposes of the discussion that follows this FDTD simulation is referred to as the reference simulation.

Figure 7.3 displays the frequency response of the normalised electric field as performed on the reference FDTD mesh and two meshes refined by factors of two and four.

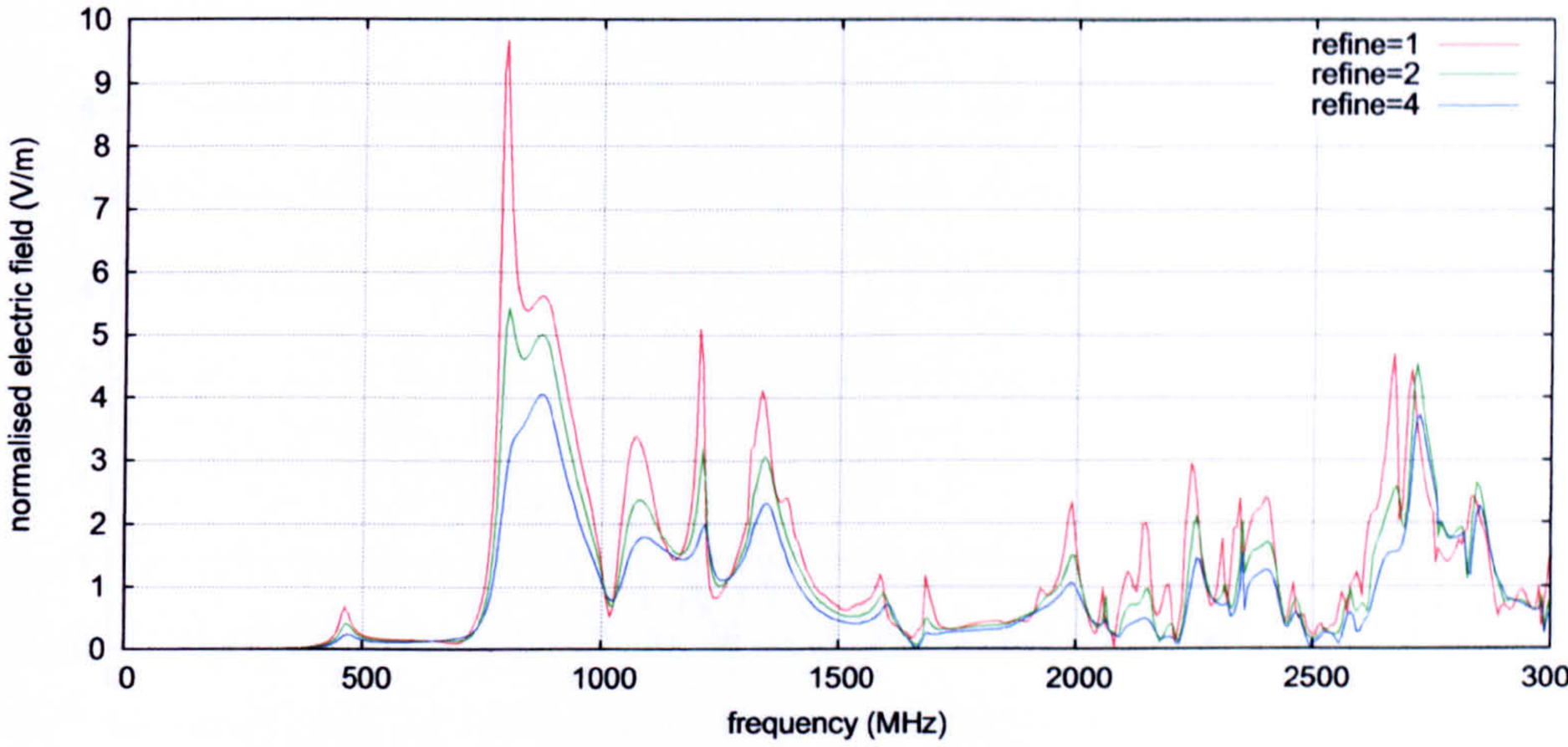

Figure 7.3: The normalised electric field formed from FDTD simulations performed on progressively refined meshes.

The curves in this figure have a similar modal structure but differ in their amplitude. Convergence of the output of the progressively refined FDTD simulations has not been reached: the FSV comparison of the electric field produced with refinement factors of two and four is only "fair". Despite this absence of a converged solution, the reference simulation is used in the UAs that follow. The refined simulations are too computationally expensive to be used in the UAs. The reference FDTD simulation took around 11 minutes, which resulted in a MCM simulation that took around 18 hours. Refining the mesh by a factor two would have caused this MCM simulation to take about 12 days. One of the problems with the MCM is its computational expense when applied to real, computationally expensive CEM simulations. This highlights the need for computationally efficient UA methods that can be used to estimate the uncertainty in real CEM simulations.

For this example the different UAs were applied to the results of the reference simulation. An estimation of the error in the output of this reference simulation is determined in the next section.

7.2.1 Error Analysis of the Finite Difference Time Domain Simulation

In the previous two chapters an approximate Error Analysis method was shown to give a fairly accurate estimate of the error in the FDTD simulation. This error prediction method uses a FDTD simulation performed on a mesh that is refined by a factor four, with respect to the reference FDTD mesh. Taking the difference between the output of the reference simulation and the refined simulation gives an estimate of the error in the output of

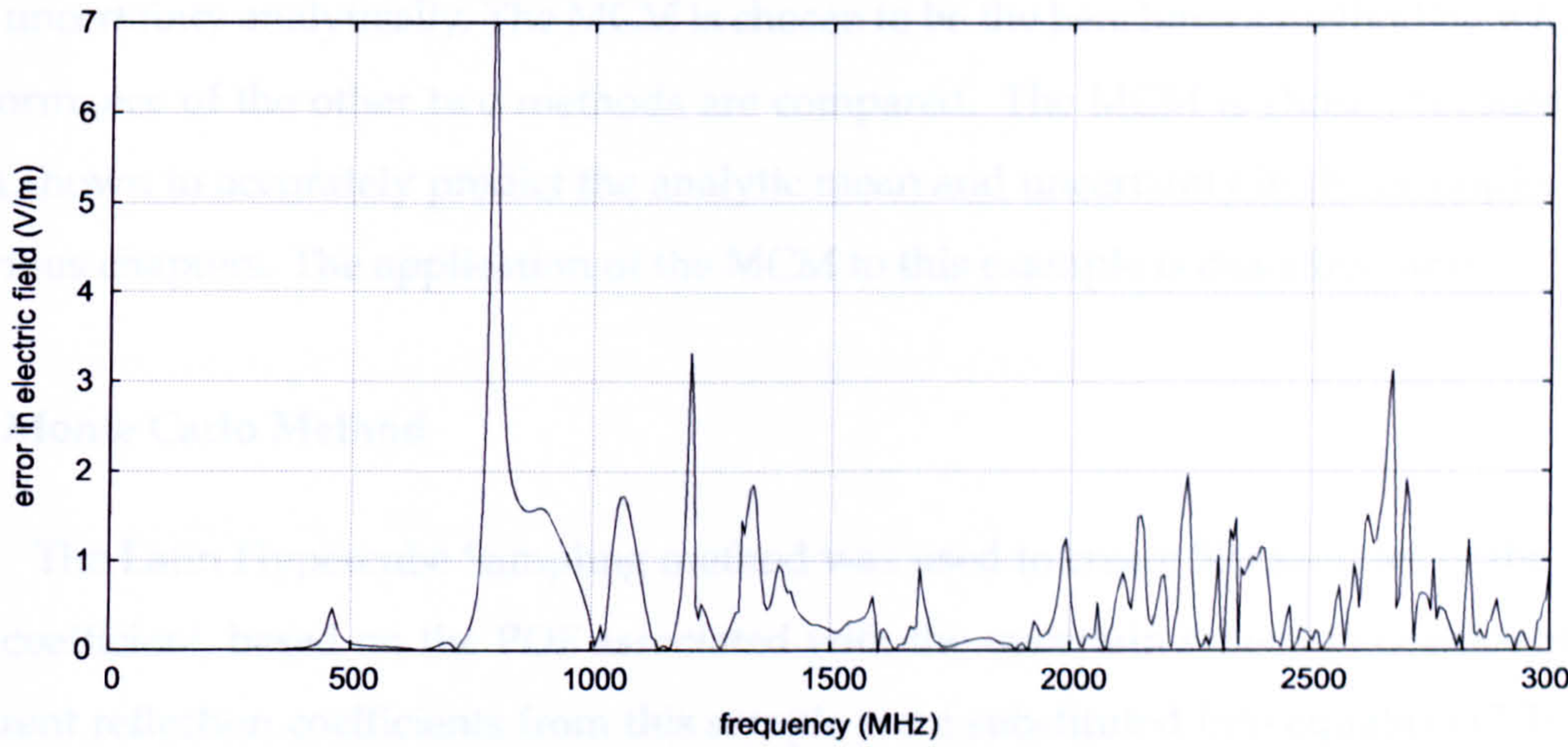

Figure 7.4: Estimate of the error in the normalised electric field.

the reference simulation. These output errors are mainly due to the discretisation errors and dispersion errors that are formed from the approximations used to create the FDTD method.

Figure 7.4 shows the absolute error predicted in the reference simulation. At certain frequencies there are relatively large peak errors. At our frequency of interest (1.8GHz) the error is 41% of the normalised field formed from the FDTD simulation with a refinement factor of four. This large percentage error is due to the fact that the output FDTD simulations, performed on progressively refined meshes, have not yet converged. Figure 7.3 shows that the differences between the output of the reference and refined FDTD simulations are mainly due to amplitude differences. There will be a small frequency error, however the majority of the error is due to the differences in the amplitudes. Curve alignment is therefore not used in this example to quantify the aligned amplitude and frequency errors.

This section has determined that the estimated error in the reference FDTD simulation is fairly large. In the next section the uncertainty in the output of the reference FDTD simulation is quantified.

7.2.2 Uncertainty Analysis of the Normalised Electric Field

In this section the three different UA methods are used to quantify the uncertainty in the output electric field. Firstly the application of each of the UA methods to this specific example are described. The methods are then compared in terms of their ability to accurately estimate the output uncertainty and in terms of their computational expense.

Since no analytic solution exists for this example there is no way of forming the mean

and uncertainty analytically. The MCM is chosen to be the benchmark method by which the performance of the other two methods are compared. The MCM is chosen because it has been shown to accurately predict the analytic mean and uncertainty in the examples in the previous chapters. The application of the MCM to this example is described next.

The Monte Carlo Method

The Latin Hypercube Sampling method was used to create 500 samples of the reflection coefficient, based on the PDF associated with the uncertain reflection coefficient. The different reflection coefficients from this sample were substituted into equation (7.3) to obtain the corresponding sample of conductivities for the PCB. This set of conductivities forms the input parameter sample for the FDTD simulations.

The input parameter sample was used in the FDTD reference simulation to create numerous output frequency responses of the normalised electric field. The FSV method was used to determine when the MCM had reached convergence, as described in Sections 3.2.3 and 4.5.2. For this example it was found that convergence was reached after only 100 FDTD simulations. The MCM is still the most computationally expensive method, however fewer simulations were required here compared to in previous examples. This example contains only one uncertain input with a relatively small associated uncertainty. The outputs formed from the different MCM simulations are therefore fairly similar, which causes the means and uncertainties to converge quickly.

The Method of Moments

The MoM required only two simulations to calculate the output uncertainty for this example. One simulation was performed with the reflection coefficient taking on its mean value $\bar{\Gamma} = 0.940$, to three significant figures. The conductivity corresponding to this value was found using the same one dimensional FDTD simulations that were used to find the relationship between the conductivity and the reflection coefficient. The second simulation was performed with the reflection coefficient taking on a perturbed value $\Gamma = 0.951$, to three significant figures. Once again the conductivity corresponding to this reflection coefficient was found using the 1D FDTD simulations. This perturbation is a similar size to the uncertainty in the reflection coefficient. It has been previously suggested that using a perturbation of a similar size to the uncertainty in the input parameter is appropriate when

using the MoM.

The sensitivity derivative calculated from the results of the two FDTD simulations was combined with the input uncertainty to calculate the mean and uncertainty in the output, according to equations (4.51) and (4.53). Since only two simulations are required here, this method is computationally much cheaper than the MCM.

The Polynomial Chaos Method

To perform an UA using the PCM the uncertain input parameter needs to be related to the material parameters in the FDTD chaotic update equations (4.111) and (4.112). The uncertainty in the reflection coefficient of the PCB is related to θ, which follows a standard Uniform distribution over the interval $[-1, 1]$. Since the reflection coefficient is Uniformly distributed over the interval [0.91,0.97], it is related to θ as

$$\Gamma = \bar{\Gamma} + \frac{0.97 - 0.91}{2}\theta = 0.94 + 0.03\theta. \tag{7.4}$$

Using equation (7.3) the uncertain reflection coefficient is related to the uncertain conductivity of the PCB as

$$\begin{aligned} S(\theta) = 10^6 \big(&0.26969667(0.94 + 0.03\theta)^4 - 0.99480063(0.94 + 0.03\theta)^3 \\ &+1.3765588(0.94 + 0.03\theta)^2 - 0.84684980(0.94 + 0.03\theta) + 0.19541786\big)\,. \end{aligned} \tag{7.5}$$

The material parameters α and β, both have some dependence on the conductivity. The material parameters α and β may therefore be written as

$$\alpha = \frac{1 - S(\theta)\Delta t/2\epsilon}{1 - S(\theta)\Delta t/2\epsilon} \tag{7.6}$$

$$\text{and} \quad \beta = \frac{\Delta t}{\Delta l \epsilon (1 + S(\theta)\Delta t/2\epsilon)} \tag{7.7}$$

where $S(\theta)$ is given in equation (7.5) and $\epsilon = 4\epsilon_0$.

The reflection coefficient follows a Uniform distribution, Legendre polynomials must therefore be used in the chaotic expansion of the electric and magnetic fields. If the uncertainty is sought to first order, then the chaotic expansion is terminated at $P = 2$. The first

order polynomials required are

$$\psi_0 = 1 \tag{7.8}$$

$$\text{and} \quad \psi_1 = L_1(\theta) = \theta. \tag{7.9}$$

The orthogonality of the polynomials leads to the relations

$$< L_i(\theta_k) L_j(\theta_l) >= \delta_{ij}\delta_{kl}\frac{1}{2i+1}. \tag{7.10}$$

The electric and magnetic fields are calculated using the update equations (4.111) and (4.112). Before these equations can be used the inner products, of the material parameters (α, β and γ) with the polynomials (ψ_0 an ψ_1), need to be calculated. The material parameter $\gamma = \Delta t/\mu_0 \Delta l$ with zero uncertainty. The inner product of γ with the polynomials ψ_i and ψ_j is therefore

$$< \gamma\psi_i\psi_j >= \gamma < \psi_i(\theta_k)\psi_j(\theta_l) > \tag{7.11}$$

where $i, j = 0, 1$. The inner products required for α and β are calculated using the integrals

$$\begin{aligned} < \alpha\psi_i\psi_j > &= \frac{1}{2}\int_{-1}^{1} \alpha(\theta)\psi_i\psi_j d\theta \\ \text{and} \quad < \beta\psi_i\psi_j > &= \frac{1}{2}\int_{-1}^{1} \beta(\theta)\psi_i\psi_j d\theta \end{aligned} \tag{7.12}$$

where $\alpha(\theta)$ and $\beta(\theta)$ are given in equations (7.6) and (7.7). These integrals were calculated numerically using MAPLE. The material inner product values are only required at the mesh points of the PCB, this means that only six numerical integrations are required here. For the sphere examples, in the previous chapter, many different integrations were required at the different points in the problem space. This led to a greater computational expense for the PCM.

The inner products calculated using the above integrations are substituted into the update equations (4.111) and (4.112), which are then used to find the mean and uncertainty in the electric field at the output point. In this example the output quantity of interest is the absolute value of the electric field in the frequency domain relative to a 1 V/m input excitation. More numerical integrations are required to calculate the mean and uncertainty in this output, which adds to the overall computational cost of this method.

7.2.3 Results of the Uncertainty Analyses Applied to the Finite Difference Time Domain Simulations

The mean and uncertainty in the output electric field are shown in Figures 7.5 and 7.6 respectively. At 1.8GHz the uncertainty is very small (7.93×10^{-3} V/m) compared to the mean value (4.29×10^{-1} V/m) at this frequency. This means that the normalised electric field takes on a value that is close to its mean value. Performing the UAs provides us with the level of confidence that may be held in the mean output.

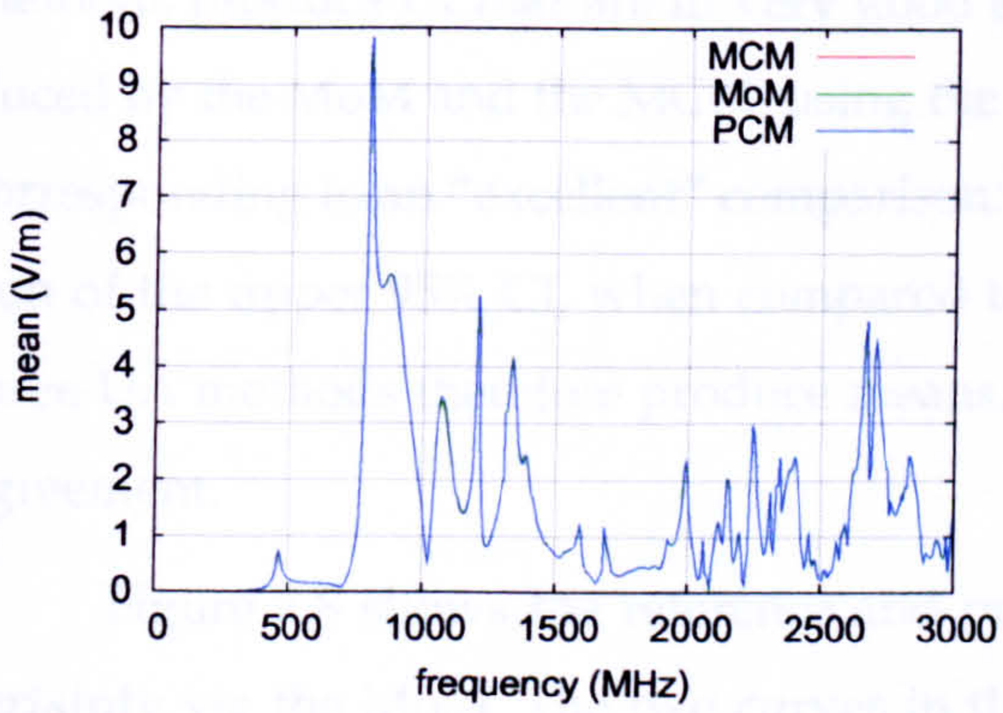

Figure 7.5: Mean normalised electric field as predicted by the three UA methods

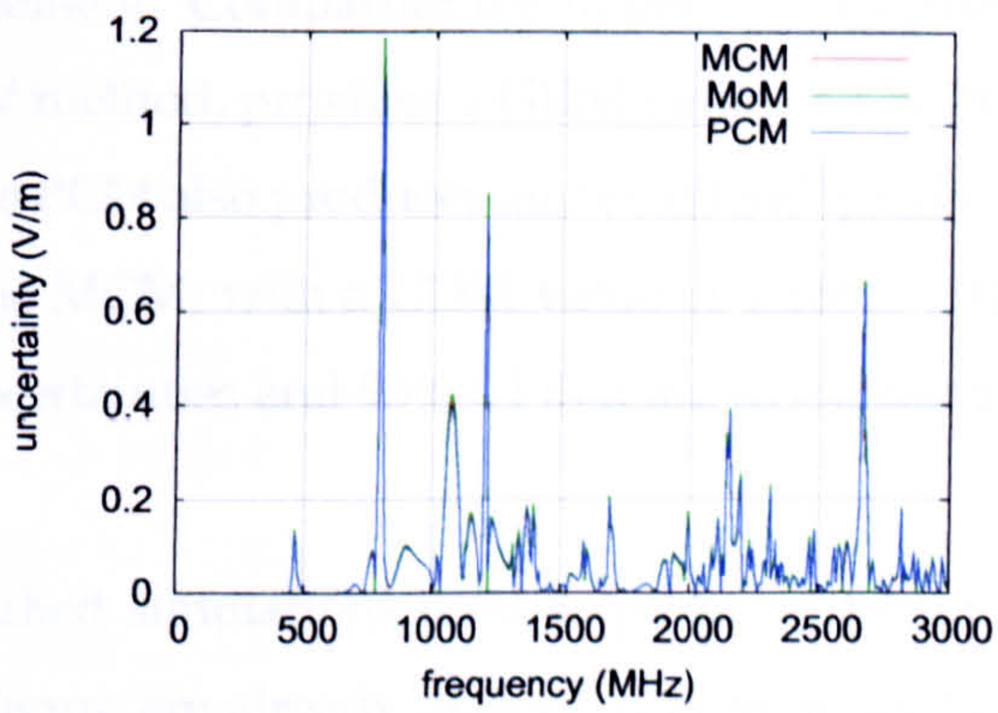

Figure 7.6: Uncertainty in the normalised electric field

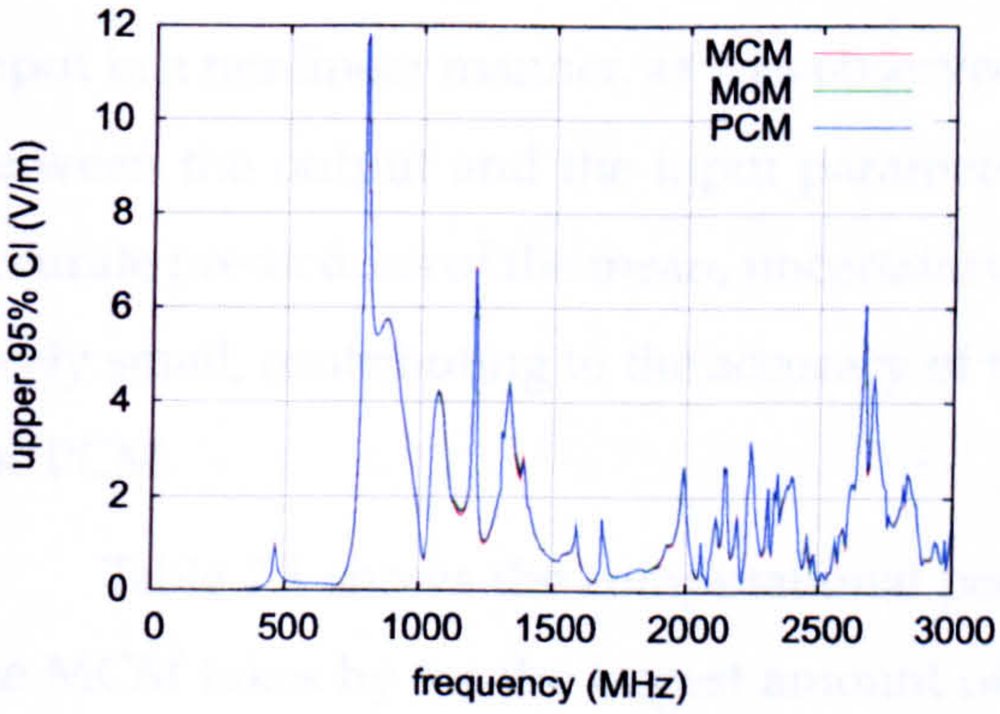

Figure 7.7: The upper 95% CI of the normalised electric field

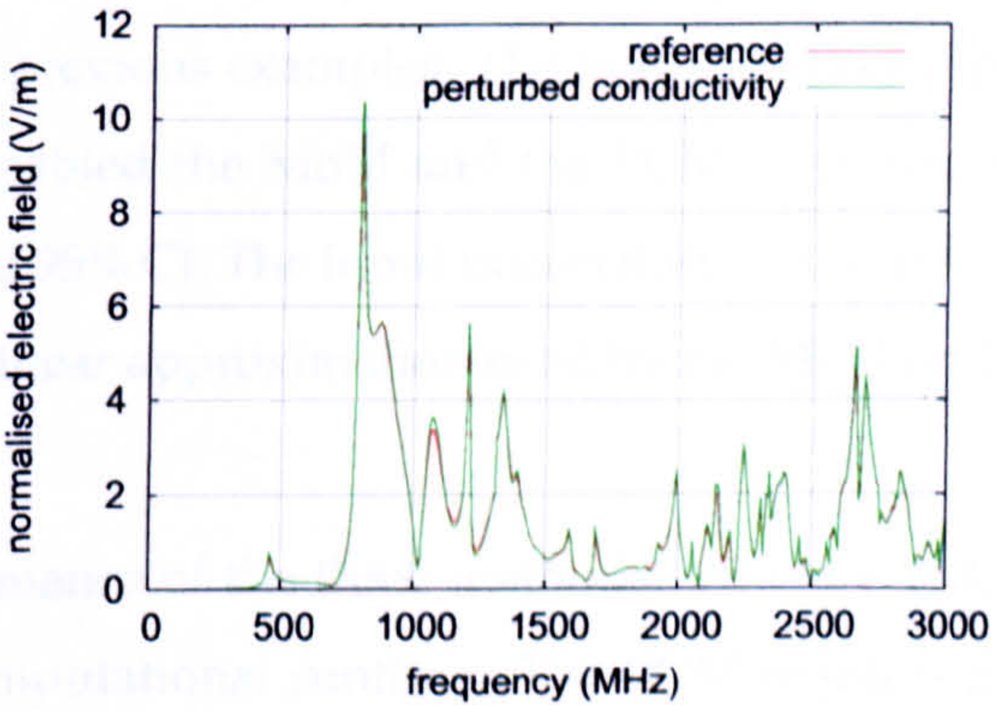

Figure 7.8: Output formed by the reference and perturbed simulations

The means and uncertainties predicted by the three methods are in excellent agreement: the curves in Figures 7.5 and 7.6 are so similar that they overlay each other. The FSV method was used to compare the curves in these figures. Both the MoM and the PCM formed means that were "excellent" matches to the mean curve produced by the MCM. The uncertainties formed using the MoM and the PCM were also "excellent" matches to the

Table 7.1: Computational requirements of the three methods.

Method	No. Simulations	Time	Memory
PCM	1	1.8 hours	62 MB
MoM	2	22 minutes	31 MB
MCM	100	18 hours	31 MB

uncertainty calculated by the benchmark MCM.

Figure 7.7 shows the upper 95% CI predicted by the three UA methods. The three UA methods produce CI that are in very good agreement. Comparing the upper 95% CI produced by the MoM and the MCM, using the FSV method, provides a GDM value of 1.7828, corresponding to an "excellent" comparison. The PCM also produces an "excellent" prediction of the upper 95% CI, when compared to the MCM, with a GDM value of 1.1805. All three UA methods therefore produce means, uncertainties and 95% CI that are in excellent agreement.

Figure 7.8 shows the reference and perturbed simulations used to produce the uncertainty via the MoM. The two curves in this figure are already aligned very well, curve alignment is therefore not needed in this example. The perturbation of the input parameter does not produce a frequency shift between the resonant curves. The resonant peaks on the two curves in Figure 7.8 are aligned and therefore the output does not depend on the input in a nonlinear manner, as was observed in previous examples. The linear relationship between the output and the input parameter enabled the MoM and the PCM to provide accurate predictions of the mean, uncertainty and 95% CI. The input uncertainty is also relatively small, contributing to the accuracy of the linear approximation used by the MoM and the PCM.

Table 7.1 shows the computational performance of the three methods. As expected, the MCM takes by far the largest amount of computational runtime. The PCM requires a factor 5 times more computational runtime than the MoM and a factor 2 times more memory. Therefore, for this example the MoM is the preferred method: the method gives excellent predictions of the mean and uncertainty and it is the most computationally efficient method.

Figure 7.9 shows the mean output electric field with 95% CI, as predicted by the MCM. These CI provide the quantitative level of confidence that may be held in the results of the simulation. At 1.8GHz the 95% CI are very small: the output field is in the region $E_z = [0.418, 0.444]$ V/m with 95% confidence. An experimenter may be very confident that at this

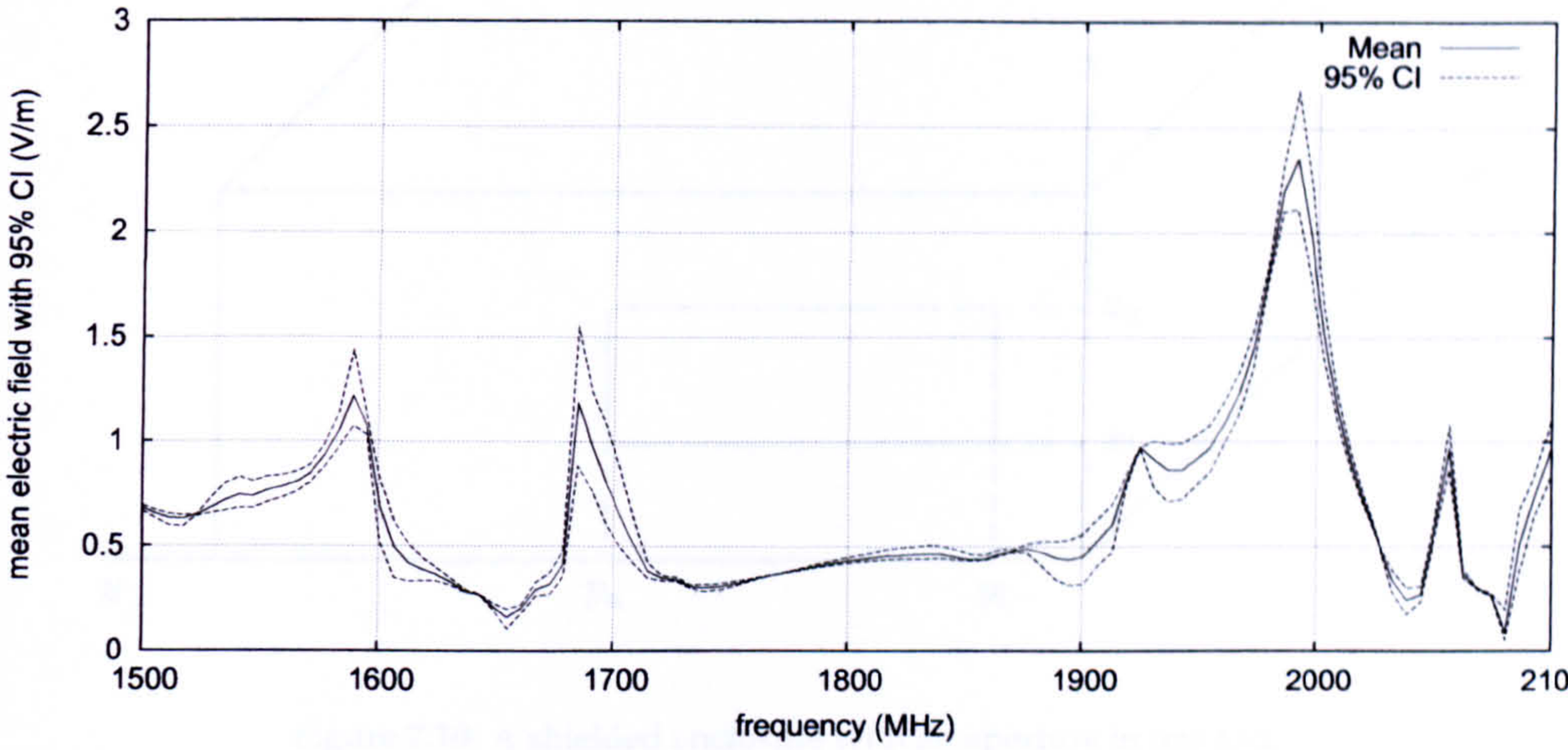

Figure 7.9: Mean output electric field with 95% CI.

frequency the output electric field is very close to its mean value $\bar{E}_z = 0.429$ V/m. The estimated error at this frequency, however, was around 40% of the value obtained from the refined FDTD simulation. Thus, the experimenter may be confident that the normalised electric field lies close to its mean value, but must be aware that there is a relatively large error in this mean value.

This example has shown that the computationally efficient UA methods (the MoM and the PCM) can provide excellent predictions of the uncertainty in CEM simulations of EMC scenarios. This example was however fairly simple with only one uncertain input parameter with a relatively small associated uncertainty. The next section introduces another EMC example with more uncertain input parameters.

7.3 A Shielded Enclosure With an Uncertain Aperture Geometry

Another well studied EMC example involves calculating the SE of a metallic box with a rectangular aperture. The shielding enclosure is illuminated by an electromagnetic wave and some of the energy of this wave penetrates through the aperture of the enclosure. The SE of the enclosure is measured by taking the ratio of the electric field present at a point inside the enclosure, to the field present at the same point when the enclosure is not present. In this example a shielded enclosure is considered with an uncertain aperture geometry. This uncertainty in the aperture causes an uncertainty in the output SE of the enclosure. Uncertainty Analyses are used to quantify the uncertainty in this output.

A similar coordinate system to that used in the last example, is used here to explain

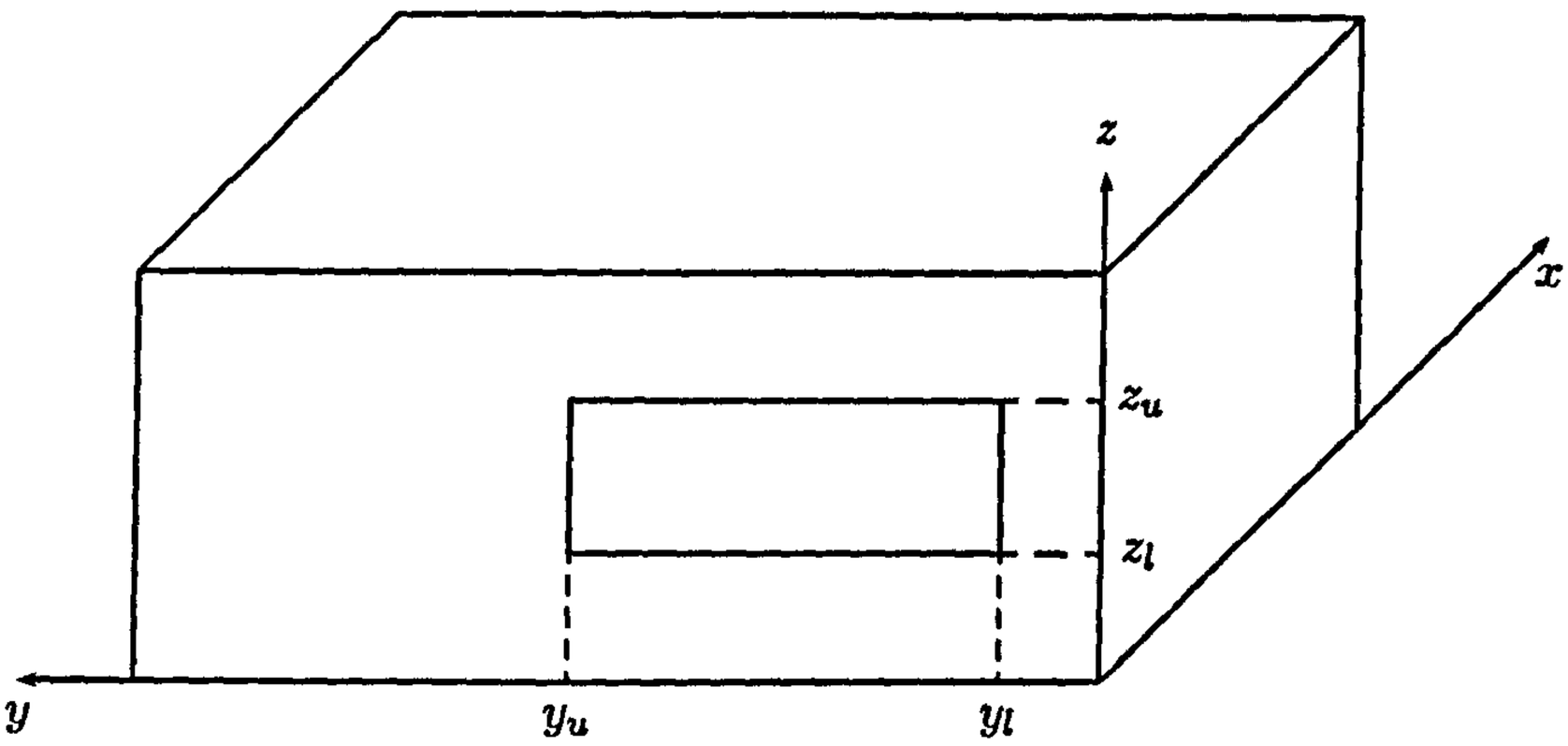

Figure 7.10: A shielded enclosure with an aperture in one face.

the geometries of the shielding enclosure. The front face of the box, which contains the rectangular aperture, is situated in the y-z plane with the bottom right hand coordinate situated at the origin. The width of the box is $y = 38$cm, the depth is $x = 40$cm and the height is $z = 16$cm. For the purposes of the following discussion, the points in this coordinate system have units of cm, referenced from the origin. In this example the aperture has uncertain coordinates. The coordinates of the sides of the aperture have average values of $\bar{y}_l = 4$cm for the lower y-coordinate, $\bar{y}_u = 21$cm for the upper y-coordinate, $\bar{z}_l = 5$cm for the lower z-coordinate and $\bar{z}_u = 11$cm for the upper z-coordinate. These uncertain aperture coordinates all follow Normal distributions with standard deviations (uncertainties) of 1cm. Figure 7.10 shows the setup of this example.

The shielded box is illuminated with a plane wave excitation, which is modelled in the FDTD simulation using a Huygen's surface. The Huygen's surface minimises the source fields propagating towards the boundary, allowing the external boundary of the problem space to be situated closer to the shielded box. Reducing the size of the problem space increases the efficiency of the FDTD simulations. The Huygen's surface is situated at five cells in from the boundary of the problem space and creates a plane wave Gaussian excitation of the form

$$E = E_0 \exp\left(\frac{-4\ln 2(t-t_0)^2}{fwhh^2}\right) \tag{7.13}$$

where $E_0 = 1$V/m, $t_0 = 6.67 \times 10^{-10}$s is the onset time and $fwhh = 2.78 \times 10^{-10}$s is the full width of the Gaussian pulse at half the height of the maximum amplitude.

The output of interest, for this example, is the SE of the electric field observed at the centre of the box: the point (20,19,8) in the above coordinate system. The time response of

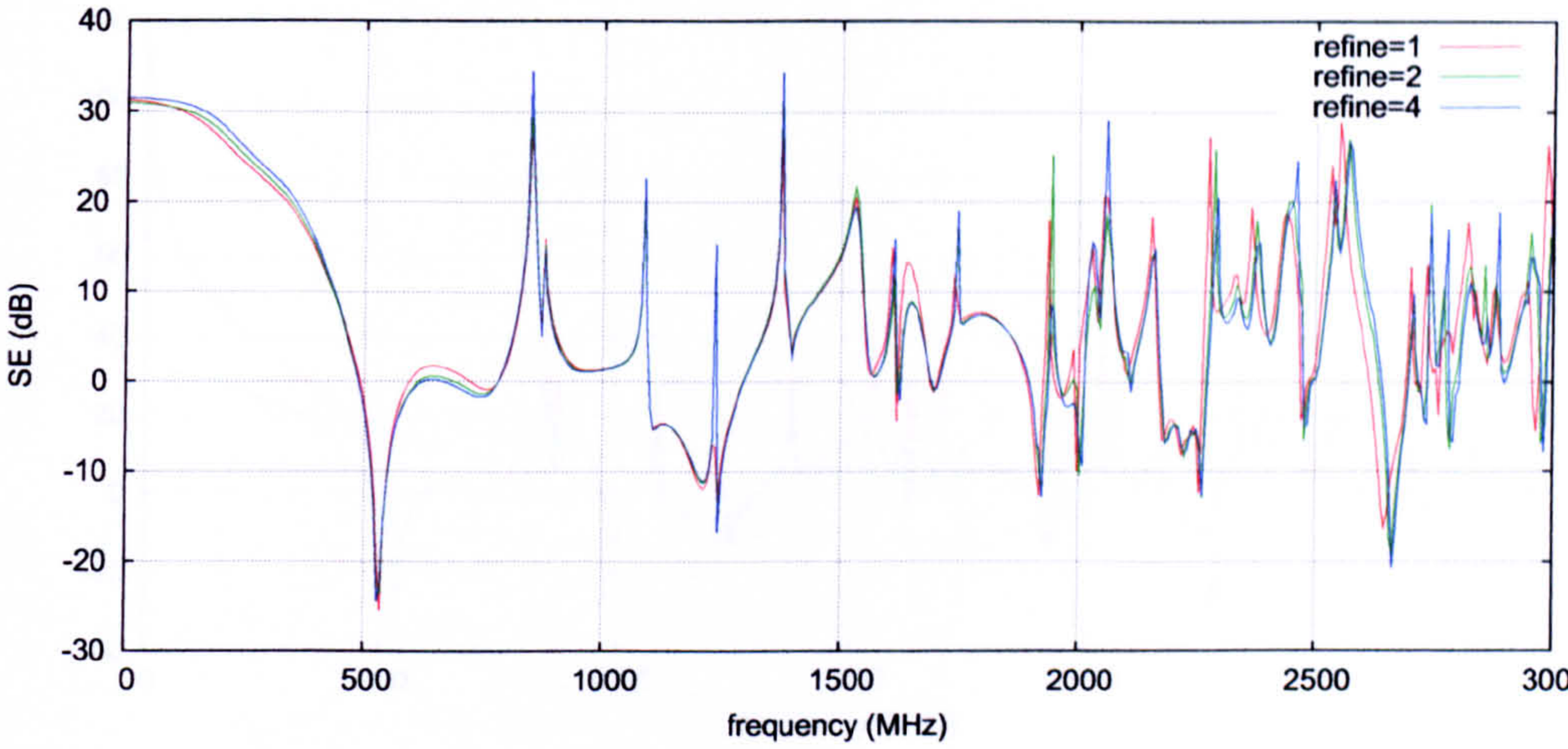

Figure 7.11: Frequency response of the SE obtained using FDTD simulations on meshes with different refinement factors.

the z-coordinate of the electric field was recorded at this output point. This electric field time response was then transformed into the frequency domain via an FFT to form $E_{box}(f)$. The frequency response of the electric field in the absence of the box $E_{free}(f)$ was then obtained for the same output point. The SE of the box, at the output point, is defined as

$$SE(f) = -20 \log_{10} \left(\frac{|E_{box}(f)|}{|E_{free}(f)|} \right). \tag{7.14}$$

The FDTD simulation was set up with a problem space containing $60 \times 60 \times 60$ points, with a cell size of 1cm and 10,000 time steps. The enclosure was modelled at the centre of this problem space, surrounded by the Huygen's surface. For the purposes of the discussion that follows this FDTD simulation is referred to as the reference simulation, performed on a mesh with a refinement factor of one. Figure 7.11 shows the output of the FDTD simulations performed on progressively refined meshes. The frequency response of the SE formed by the reference simulation was determined to be a "good" match (with a GDM of 3.3862) to the frequency response produced by a simulation using a refinement factor of two. It may therefore be concluded that the reference simulation has converged sufficiently. The error in this FDTD simulation was found approximately by using the FDTD simulation performed on a mesh with a refinement factor of four.

The SE was also formed using the ILCM method, which is described in Section 2.2.3. Quantifying the uncertainty in the output of these two different methods provides information on whether the output uncertainty is dependent on the method used. Figure 7.12 displays the frequency response of the SE of the box, calculated using the reference FDTD

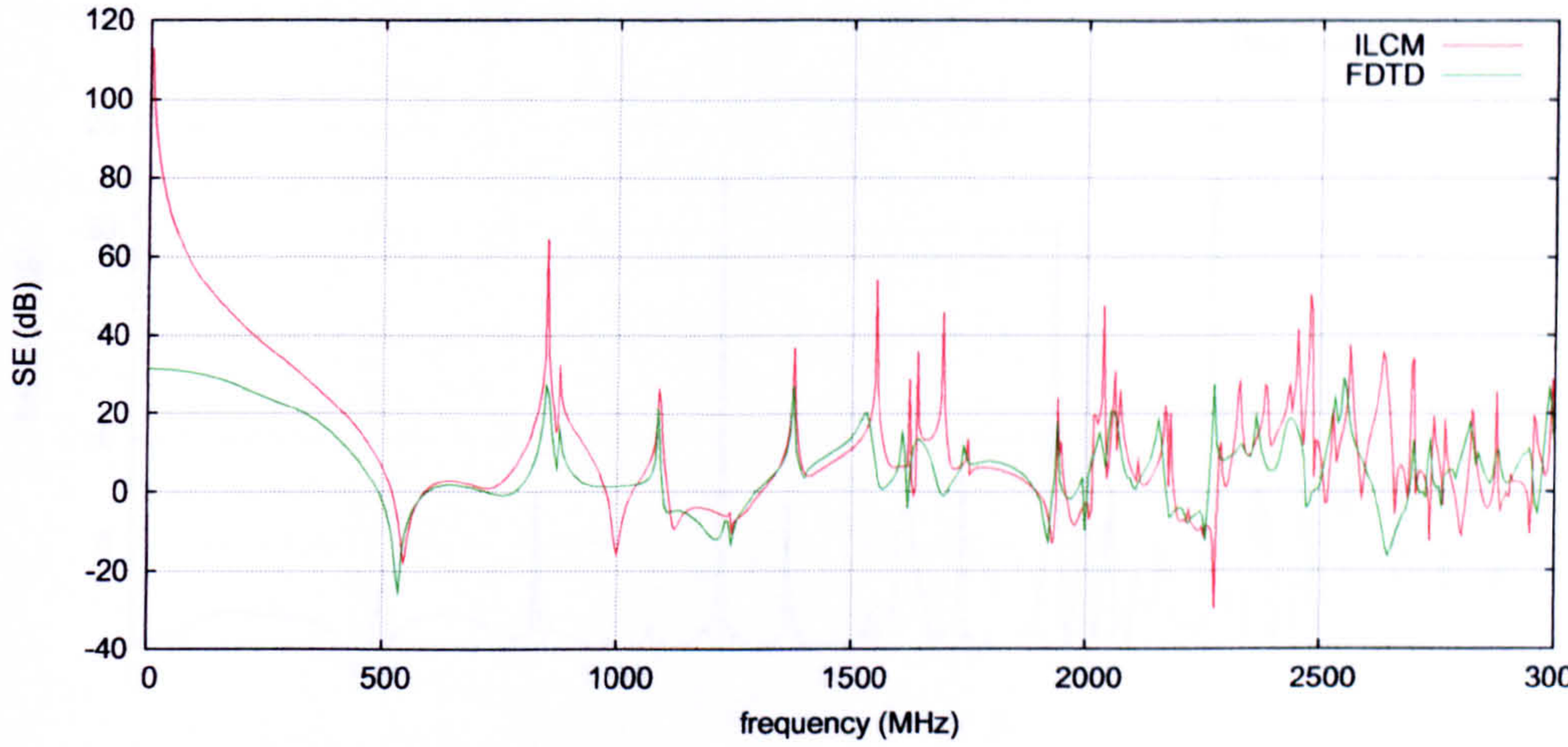

Figure 7.12: Frequency response of the SE obtained via the reference FDTD simulation and the ILCM method.

simulations and using the ILCM method. The overall form of these curves is similar however some of the features differ. The FSV comparison agrees with this providing a GDM of 4.9795, for the two curves in Figure 7.12, corresponding to a "fair" comparison. The error in the output of the reference FDTD simulation is quantified in the next section.

7.3.1 Quantifying the Error in the Output of the Finite Difference Time Domain Simulation

The absolute value of the error in the reference FDTD simulation was obtained approximately by taking the absolute difference between the output of the reference FDTD simulation and the simulation performed with a refinement factor of four. The results of this approximate error analysis are shown in Figure 7.13. The estimated error takes on large peak values at particular frequencies and is significantly lower at surrounding frequencies. The curves used to form the output error curve are shown in Figure 7.11. At certain frequencies, on these curves, one curve is at a resonant peak value and the other curve is not. Taking the difference between the two curves at these frequencies results in a large peak error value being formed. The highly resonant nature of the frequency response of the SE results in an error curve with peak values at particular frequencies. The error in the reference FDTD simulation, shown in Figure 7.13, is therefore small at most of the frequencies but takes on large peak values at some of the frequencies.

At the higher frequencies, the frequency responses of the SE in Figure 7.11 suffer from a small amount of misalignment. The SE obtained using the reference and refined FDTD simulations were aligned using the PM method. The results of this alignment are shown

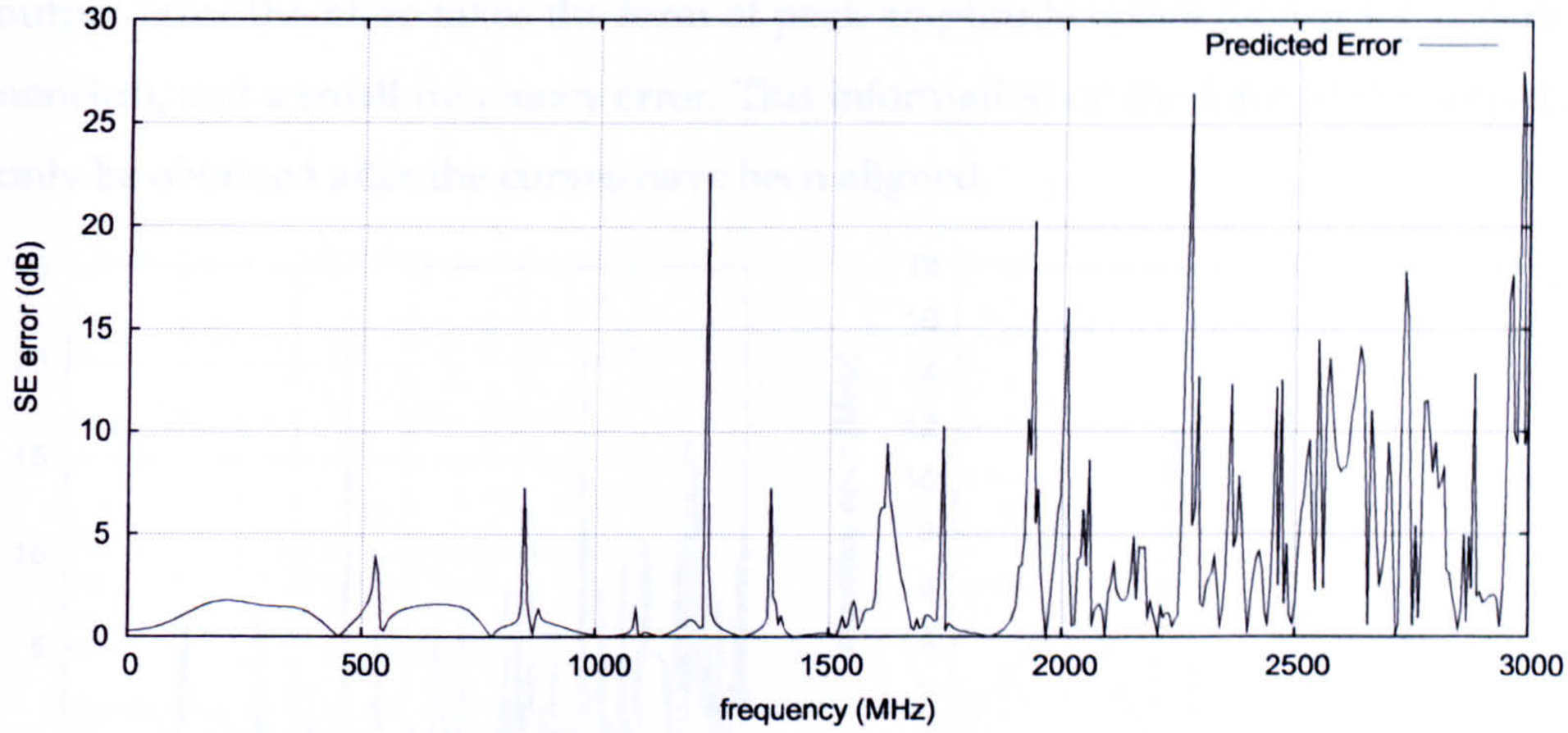

Figure 7.13: Frequency response of the estimated error in the output of the reference FDTD simulation.

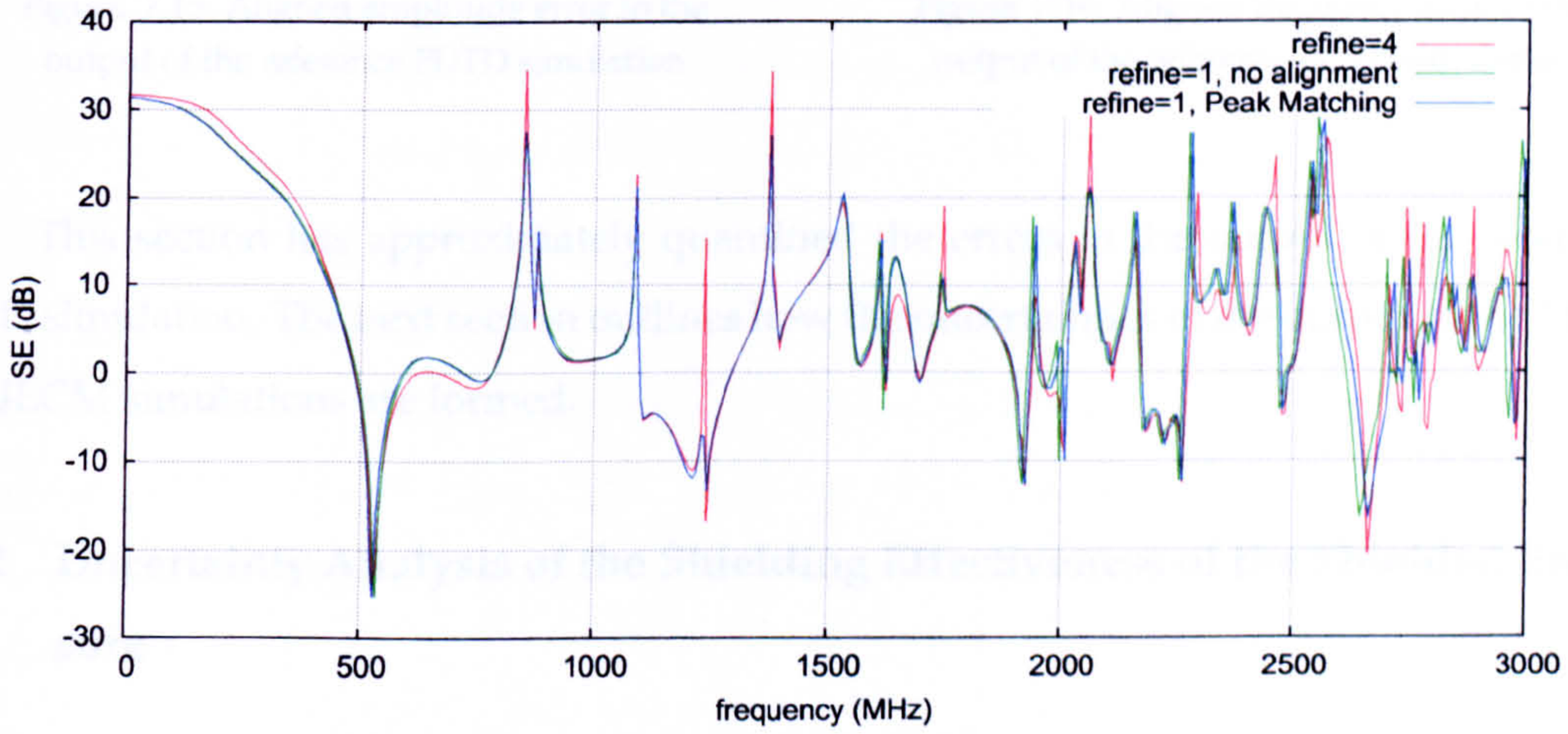

Figure 7.14: Frequency response of the SE, formed from the reference FDTD simulation, before and after alignment to the SE formed from the refined FDTD simulation.

in Figure 7.14, it is clear from this figure that the curves are aligned better after alignment via the PM method. The FSV method was used to test the similarity of the two curves before and after alignment. The GDM obtained for the two curves reduced from 3.5552 before alignment to 3.2333 after alignment. It may therefore be concluded that the curves are more similar after alignment, and therefore that the PM method has aligned the curves well. The subsequent aligned absolute amplitude and frequency errors are shown in Figures 7.15 and 7.16 respectively. A number of the peak amplitude errors, occurring at the higher frequencies (such as the peak error at 2.98GHz), are reduced after alignment. At certain frequencies the peak amplitude errors have not been reduced after alignment, this is because the curves were already aligned fairly well at these frequencies. The aligned frequency errors are all very small, these errors increase slightly with the frequency. The majority of

the output error therefore takes the form of peak amplitude errors (occurring at particular frequencies), and a small frequency error. This information on the form of the output error can only be obtained after the curves have been aligned.

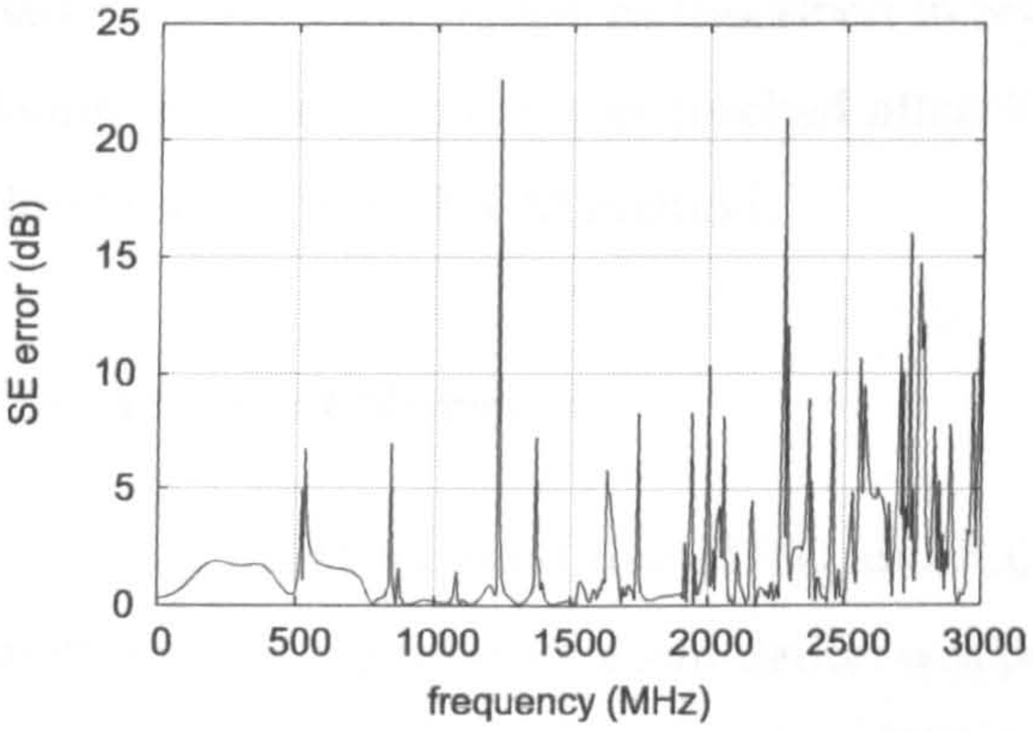

Figure 7.15: Aligned amplitude error in the output of the reference FDTD simulation

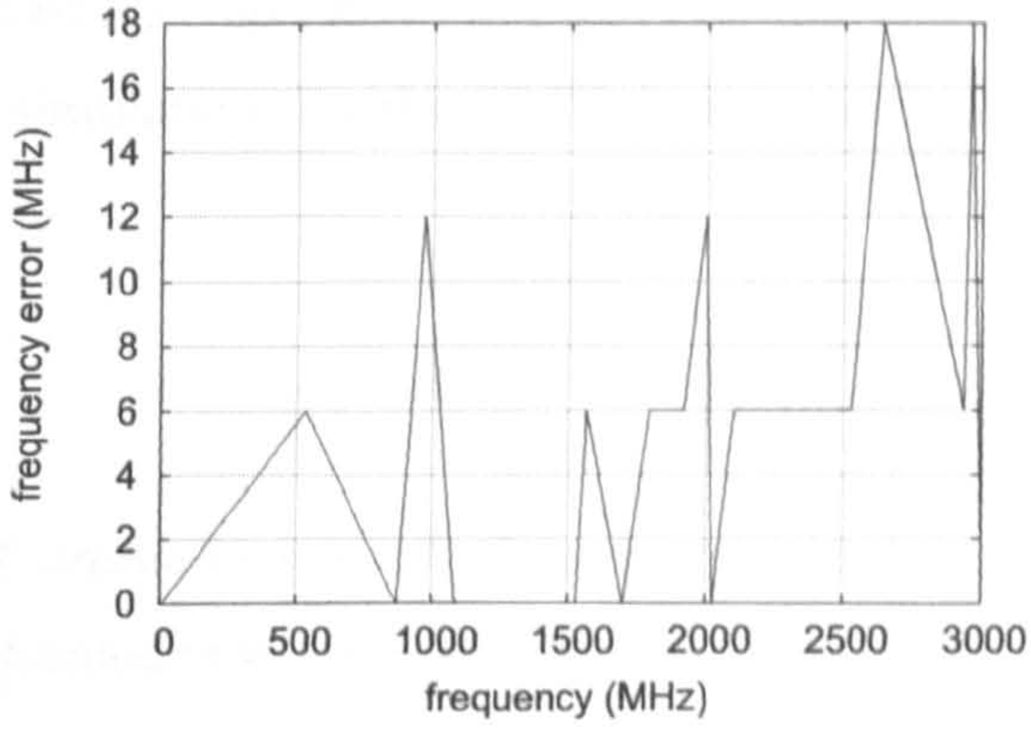

Figure 7.16: Aligned frequency error in the output of the reference FDTD simulation

This section has approximately quantified the errors in the output of the reference FDTD simulation. The next section outlines how the uncertainties in the output of the FDTD and ILCM simulations are formed.

7.3.2 Uncertainty Analysis of the Shielding Effectiveness of the Shielded Enclosure

The uncertainty in the SE of the shielded enclosure will be quantified in this section. The PCM is not used to quantify the uncertainty as it has been previously shown (in Section 6.7) to be unable to estimate the output uncertainty due to uncertain geometric inputs involving conducting bodies. The MCM is once again used as the benchmark method as it has been shown to most accurately determine the output uncertainty, in previous examples. The MCM will be used to test the performance of the more computationally efficient MoM. This section begins by detailing the implementation of the MCM and the MoM into the FDTD and ILCM simulations. Following this the uncertainties in the output of the FDTD and ILCM simulations are obtained.

The Monte Carlo Method

The LHS method was used to create 5,000 samples of the uncertain input parameters. A Python script automatically created 5,000 input files, for the two CEM methods, using

these samples. The different input files were used to perform the different FDTD and ILCM simulations. These simulations created numerous output frequency responses for the SE of the shielded enclosure. The FSV method was used to determine when the MCM simulations had reached convergence, as described in Sections 3.2.3 and 4.5.2. For this example it was found that convergence was reached after 300 simulations for the FDTD method and 400 simulations for the ILCM method.

The Method of Moments

The MoM required five FDTD and ILCM simulations to calculate the output uncertainty for this example. One simulation was performed with the aperture parameters taking on their mean values. The other four FDTD and ILCM simulations were performed with each of the aperture parameters (y_l, y_u, z_l and z_u) perturbed from their mean values by 1cm (one FDTD cell) in the positive coordinate direction. This perturbation is the same as the uncertainty in the input parameters.

The sensitivity derivatives calculated from the five simulations, formed via the FDTD and ILCM method, were combined with the input uncertainties to calculate the mean and uncertainty in the output according to equations (4.51) and (4.53). Since only five simulations were required to obtain these uncertainties, the MoM is computationally much cheaper than the MCM.

7.3.3 Results of the Uncertainty Analyses applied to the FDTD and ILCM method

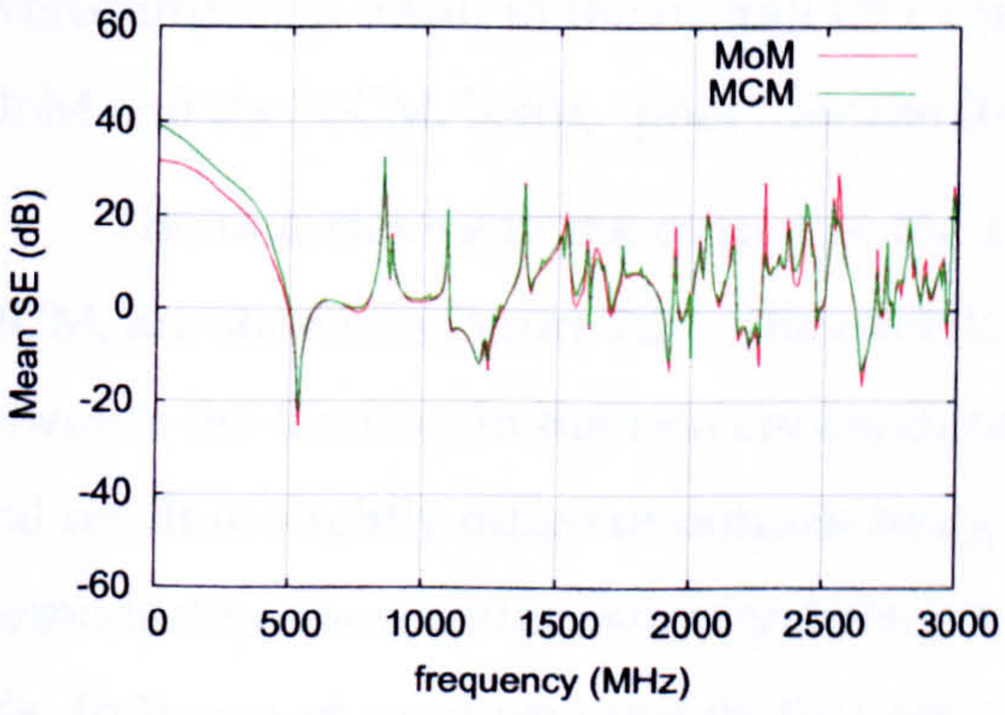

Figure 7.17: Mean SE formed from the FDTD simulations.

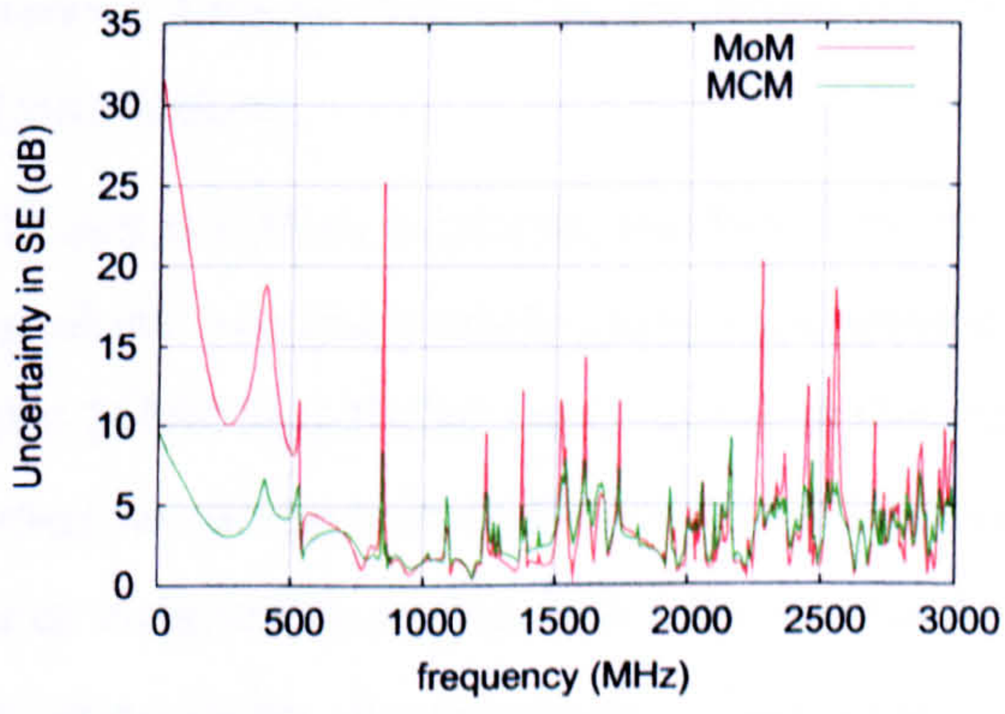

Figure 7.18: Uncertainty in the SE obtained from the FDTD simulations.

Figures 7.17 and 7.18 show the means and uncertainties predicted by the MCM

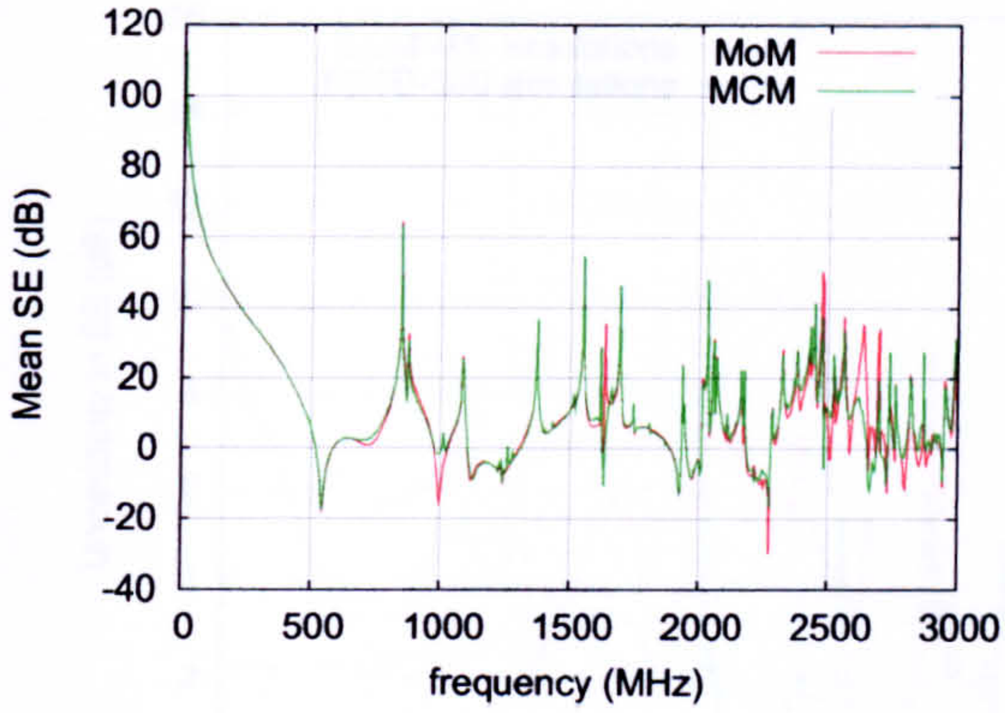

Figure 7.19: Mean SE formed from the ILCM simulations.

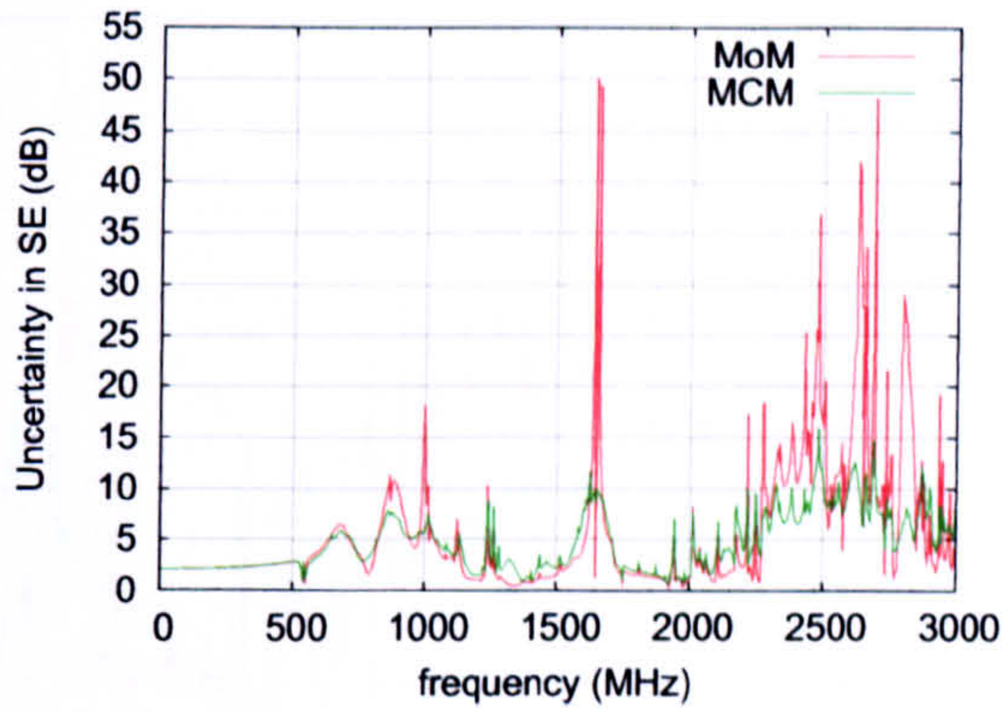

Figure 7.20: Uncertainty in the SE obtained from the ILCM simulations.

and the MoM for the results of the FDTD simulations. It is clear that the means predicted by the MoM and the MCM are in good agreement. This is confirmed by the FSV comparisons of the means predicted by the MoM and the MCM, which returns a GDM value of 3.1620. The FSV comparison of the uncertainty predicted by the MoM and the MCM returns a GDM of 5.8475, which corresponds to a "poor" comparison. The MoM underestimates and overestimates the uncertainty predicted by the more accurate MCM. As described in previous chapters, these underestimations and overestimations arise from the linear approximation used by the MoM. The mean and uncertainty in the output of the ILCM simulations are shown in Figures 7.19 and 7.20. As for the FDTD simulations, the MoM and the MCM predict means that are in "good" agreement, with a GDM of 3.1824. The uncertainties predicted by the MoM and the MCM, for the ILCM simulations, are in fairly good agreement apart from at certain frequencies, where the MoM overestimates the output uncertainty. These overestimations result in the overall FSV comparison of the uncertainties, predicted by the MoM and the MCM, being "poor" for the ILCM simulations.

The uncertainty in the output of the FDTD and ILCM simulations, predicted by the MCM, are shown in Figure 7.21. The overall sizes of the two uncertainty curves are similar, however the features in the two curves differ. The FDTD and ILCM methods are different and result in slightly different outputs being formed, as can be seen in Figure 7.12. The two methods therefore produce slightly different output uncertainty curves. The different methods do however produce outputs that are of the same order of magnitude, which results in the output uncertainties (produced by the two methods) also being of the same order of magnitude. It is interesting that for this example the ILCM simulations have a greater uncertainty at the higher frequencies than the FDTD simulations, whereas below about 500MHz

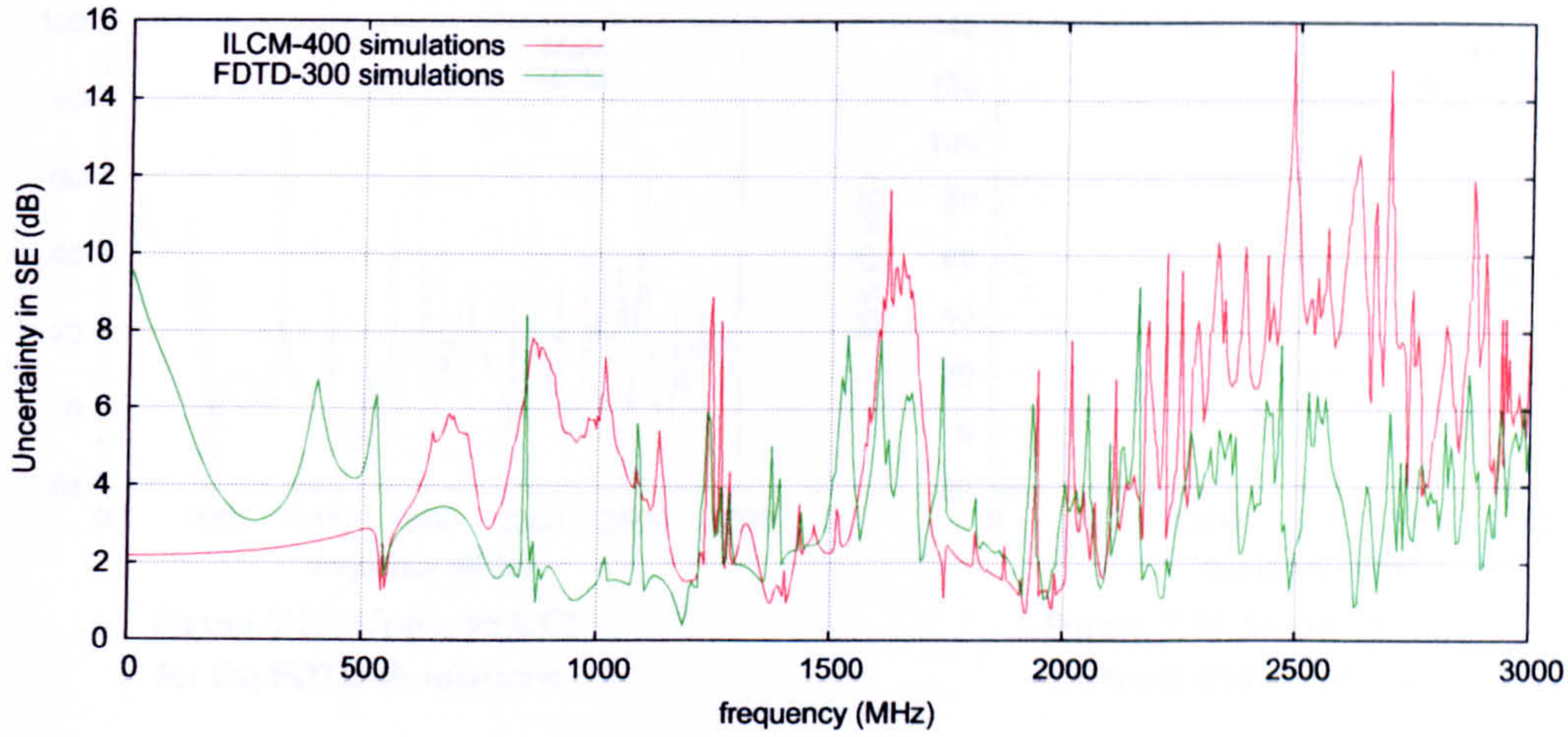

Figure 7.21: Uncertainty in the SE for the FDTD and ILCM simulations, formed using the MCM.

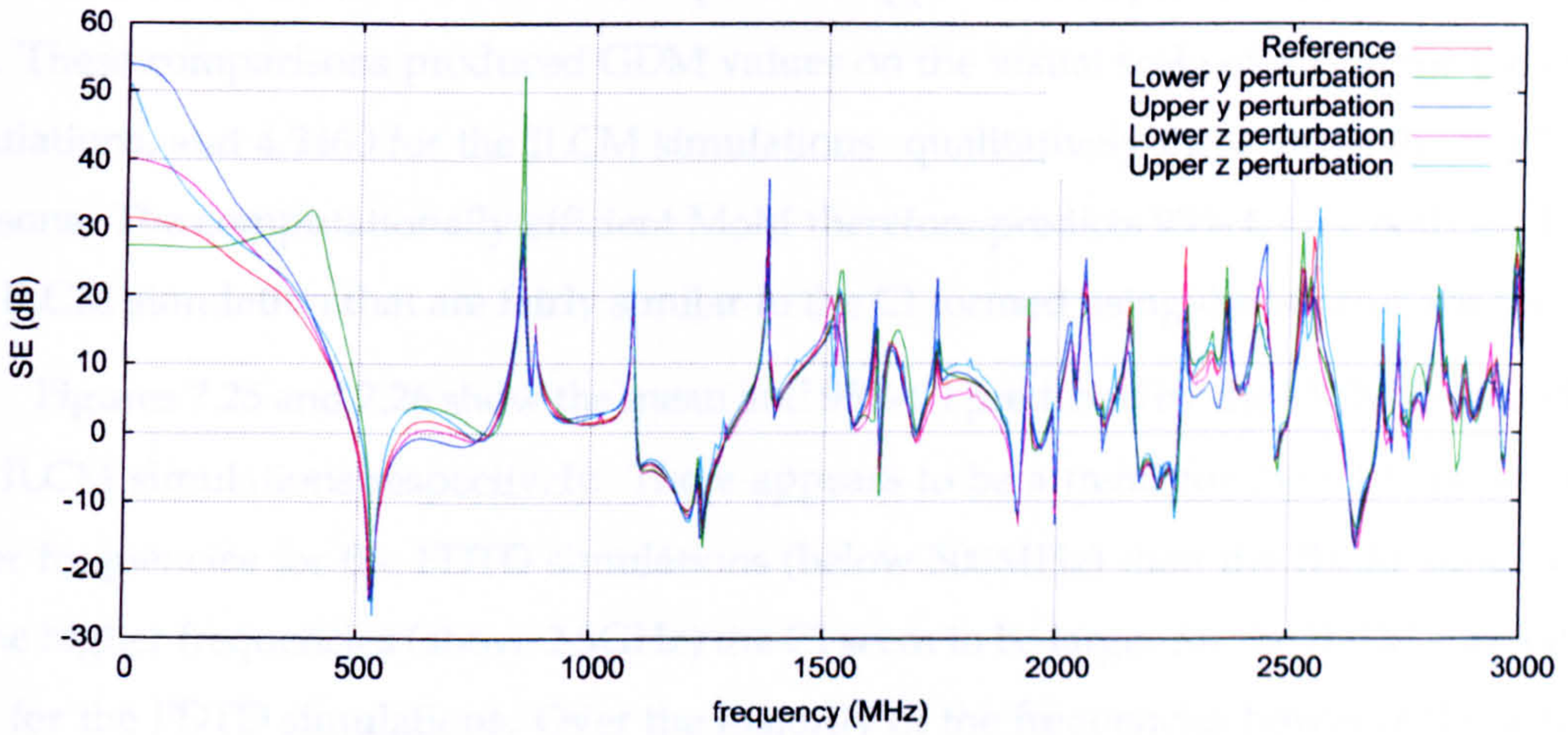

Figure 7.22: The frequency response curves that are used to form the uncertainty in the output of the FDTD simulations via the MoM.

the FDTD simulations are more uncertain than the ILCM simulations.

Figure 7.22 shows the different curves, formed using the FDTD method, that are used by the MoM to quantify the output uncertainty. It is evident that these curves are already aligned extremely well. It is very difficult to provide a better alignment of these curves. Performing an alignment would show that the frequency uncertainty is extremely small and that the aligned amplitude uncertainty is only slightly smaller than the unaligned amplitude uncertainty. For these reasons, curve alignment is not used in this example to obtain the aligned amplitude and frequency uncertainties.

The upper 95% CI predicted by both the MoM and the MCM, for the FDTD and ILCM simulations, are shown in Figures 7.23 and 7.24 respectively. The MoM and MCM predictions of the upper 95% CI are in fairly good agreement in both cases. This is confirmed by

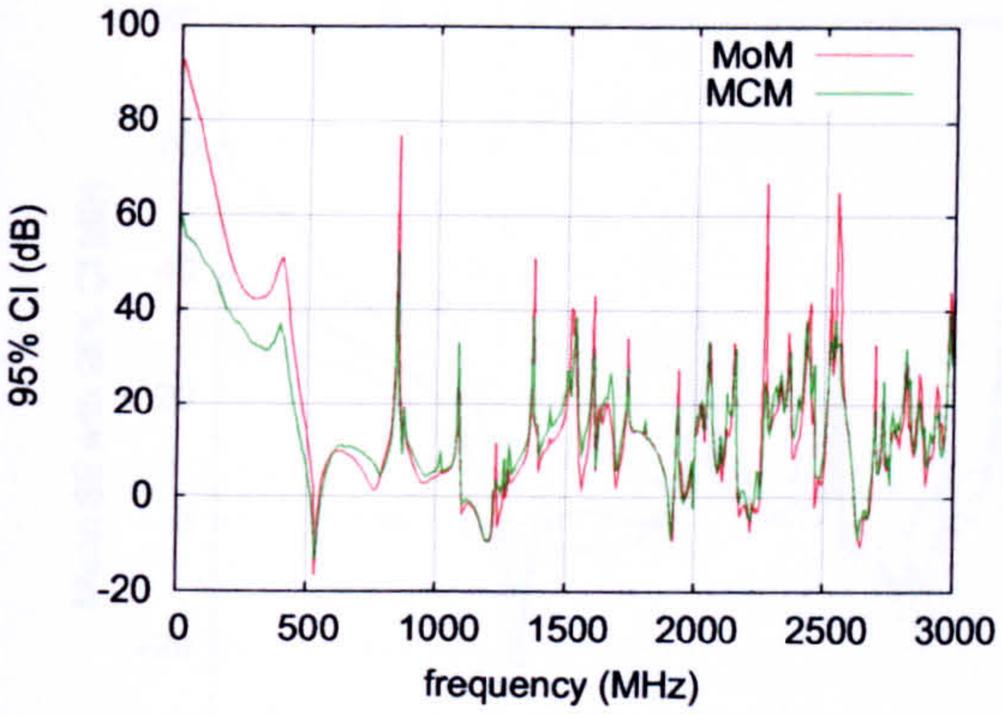

Figure 7.23: Upper 95% CI for the FDTD simulations.

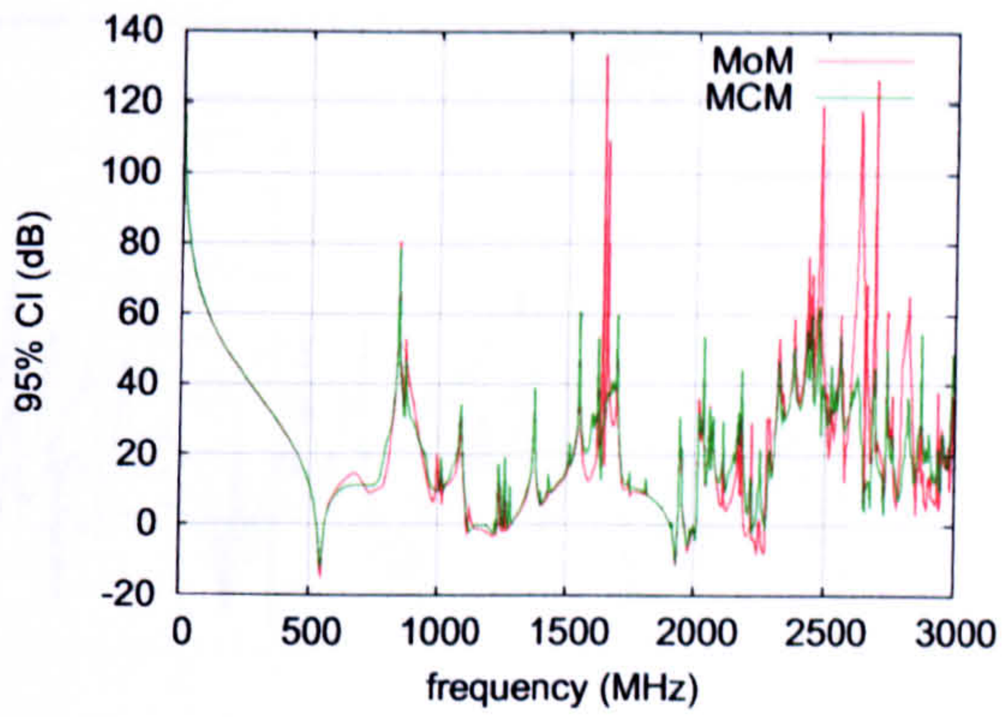

Figure 7.24: Upper 95% CI for the ILCM simulations.

the FSV method, which was used to compare the upper 95% CI predicted by both UA methods. These comparisons produced GDM values on the visual scale of 4.2778 for the FDTD simulations, and 4.3460 for the ILCM simulations: qualitatively these are both "fair" comparisons. The computationally efficient MoM therefore predicts 95% CI for both the FDTD and ILCM simulation that are fairly similar to the CI formed using the benchmark MCM.

Figures 7.25 and 7.26 show the mean and 95% CI predicted by the MCM for the FDTD and ILCM simulations respectively. There appears to be a trend for the CI to be larger at lower frequencies for the FDTD simulations (below 500MHz) than the ILCM simulations. At the higher frequencies (above 2.5GHz) the CI seem to be larger for the ILCM simulations than for the FDTD simulations. Over the majority of the frequencies however the detailed structure and amplitude of the mean and 95% CI are similar for both the FDTD and ILCM simulations. In general the 95% CI are fairly close to the mean values and therefore the SE will take on a value fairly close to the mean value. The CI in Figure 7.25 and 7.26 allow the experimenter to determine how confident they can be in the results of the SE at particular frequencies. For example, at 850MHz the SE is above 20dB for both the FDTD and ILCM simulations with at least 95% confidence.

The MoM requires only five simulations to perform the UAs in this example. This takes 14 minutes for the FDTD simulations and only 4 seconds for the ILCM simulations. The MCM takes longer to perform the UA for the FDTD simulations, requiring 13.8 hours. The MoM is therefore the preferred UA method for quantifying the uncertainty in output of the FDTD simulations in this example. The MoM is computationally faster than the MCM and provides estimates of the mean, uncertainty and 95% CI that are fairly similar to those produced by the MCM, in this example. The MoM does however underestimate and over-

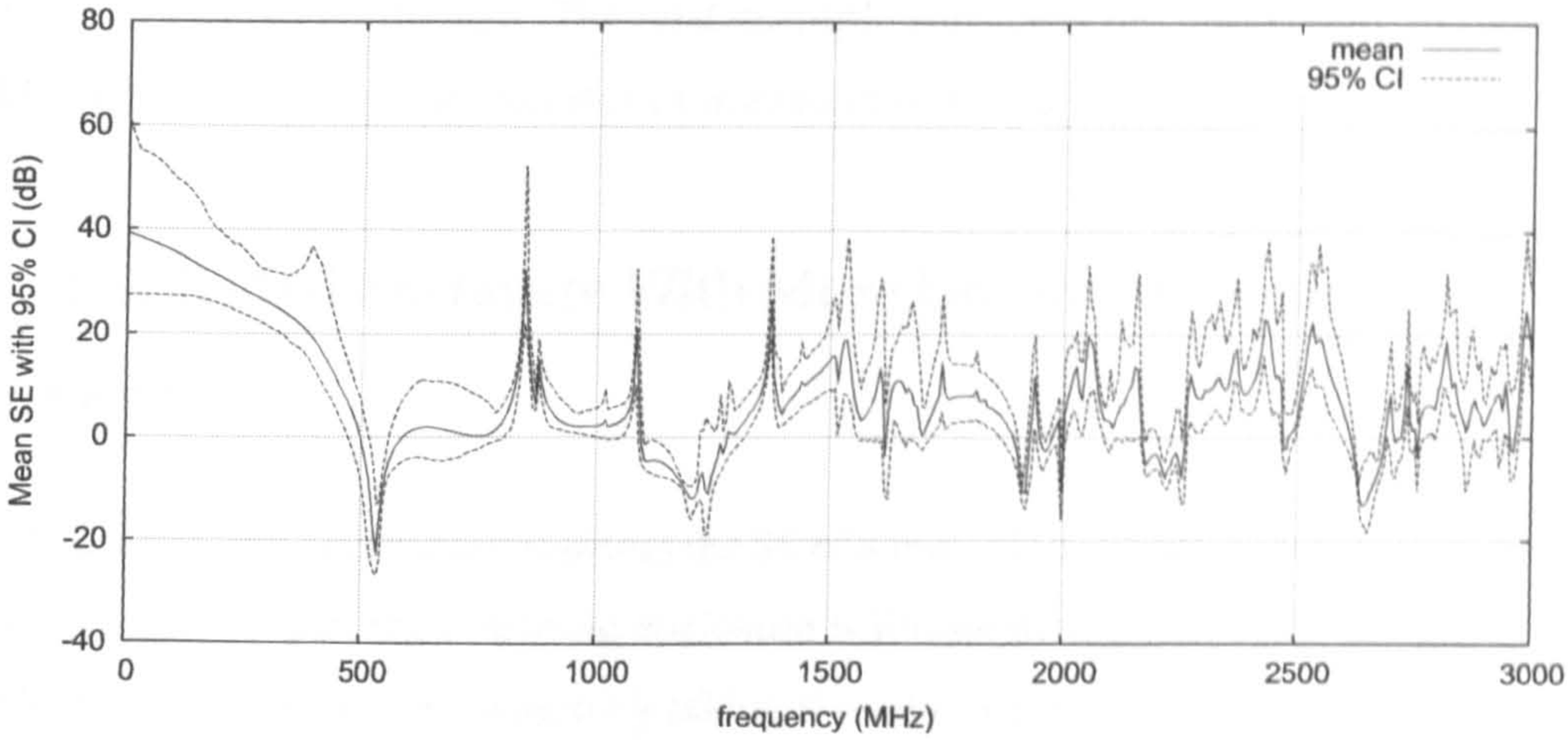

Figure 7.25: Mean and 95% CI for the FDTD simulations.

estimate the uncertainty formed using the benchmark MCM, at certain frequencies.

The MCM required only 6 minutes to determine the uncertainty in the ILCM simulations. This is because the ILCM simulations are computationally fast. It was shown that the ILCM and FDTD simulations predicted similar means, uncertainties and 95% CI. There were some differences but overall the mean, uncertainty and 95% CI formed using the benchmark MCM were of a similar order of magnitude for both the ILCM and FDTD simulations. This suggests that it may be possible to use the accurate MCM with the computationally efficient ILCM method to determine an estimate of the mean, uncertainty and 95% CI in the FDTD simulations. This uncertainty estimate will not contain the same underestimations and overestimations that are formed via the MoM.

This example considered the uncertainty in the SE of a shielded enclosure, caused by

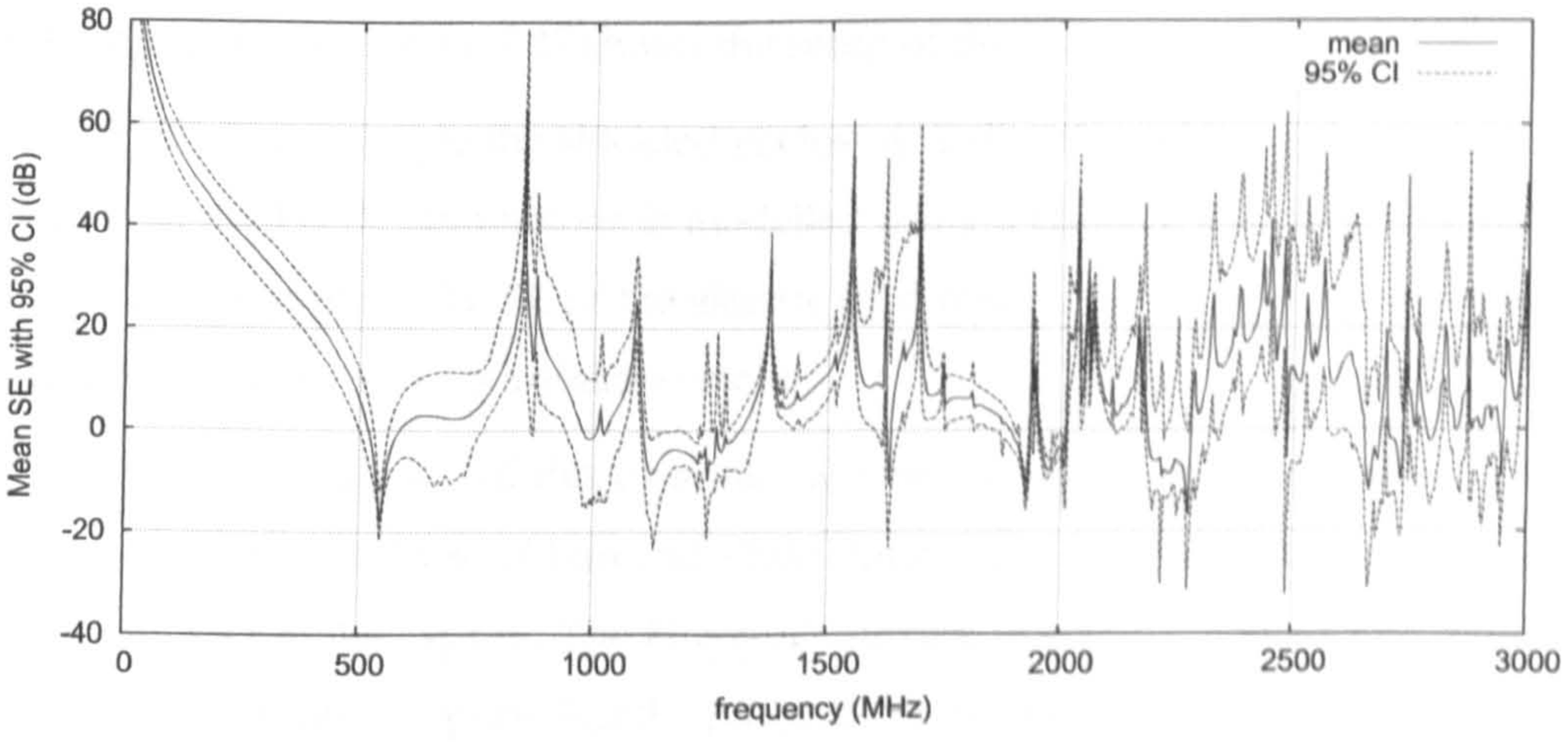

Figure 7.26: Mean and 95% CI for the ILCM simulations

uncertain aperture coordinates. The next example considers the uncertainty in the SE of a shielded box due to a greater number of uncertain input parameters.

7.4 A Shielded Enclosure With More Uncertain Geometric Coordinates

The final EMC example considers the SE of a metallic box with a rectangular aperture. As in the last example, the shielding enclosure is illuminated by an electromagnetic wave. The SE of the enclosure is measured by taking the ratio of the electric field present at a point inside the enclosure to the field present at the same point when the enclosure is not present. This example considers a metallic box with an uncertain geometry. There are ten uncertain input parameters including four coordinates describing the location of the aperture and six coordinates describing the size of the enclosure. The uncertainty in the geometry of the structure produces an uncertainty in the output SE of the enclosure.

The same coordinate system, as that used in the last example, is used here to explain the geometries of the shielding enclosure. The front face of the box, which contains the rectangular aperture, is situated in the y-z plane with the bottom right hand coordinate situated at the origin. The mean lower x, y and z coordinates of the metallic box are $\bar{x}_l = 0$cm, $\bar{y}_l = 0$cm and $\bar{z}_l = 0$cm respectively. The mean upper x, y and z coordinates of the metallic box are $\bar{x}_u = 40$cm, $\bar{y}_u = 38$cm and $\bar{z}_u = 16$cm respectively. The average coordinates of the sides of the aperture are $\bar{y}_{al} = 4$cm and $\bar{y}_{au} = 19$cm for the lower and upper y-coordinates respectively, and $\bar{z}_{al} = 6$cm and $\bar{z}_{al} = 10$cm for the lower and upper z-coordinates respectively. These uncertain coordinates follow Normal distributions with standard deviations (uncertainties) of 1cm. Figure 7.27 shows the setup of this example.

As in the last example the shielded enclosure is illuminated by a plane wave excitation, which in the FDTD simulations is modelled using a Huygen's surface. The output of interest in this example is the SE of the electric field observed at the centre of the box: the point (20,19,8) in the above coordinate system.

The FDTD simulation, of this example, was set up with a problem space containing $60 \times 60 \times 60$ points, a cell size of 1cm and 10,000 time steps. The enclosure was modelled at the centre of this problem space. The Huygen's surface was implemented five cells within the exterior of the problem space. For the purposes of the discussion that follows this FDTD simulation is referred to as the reference simulation, performed on a mesh with a refinement

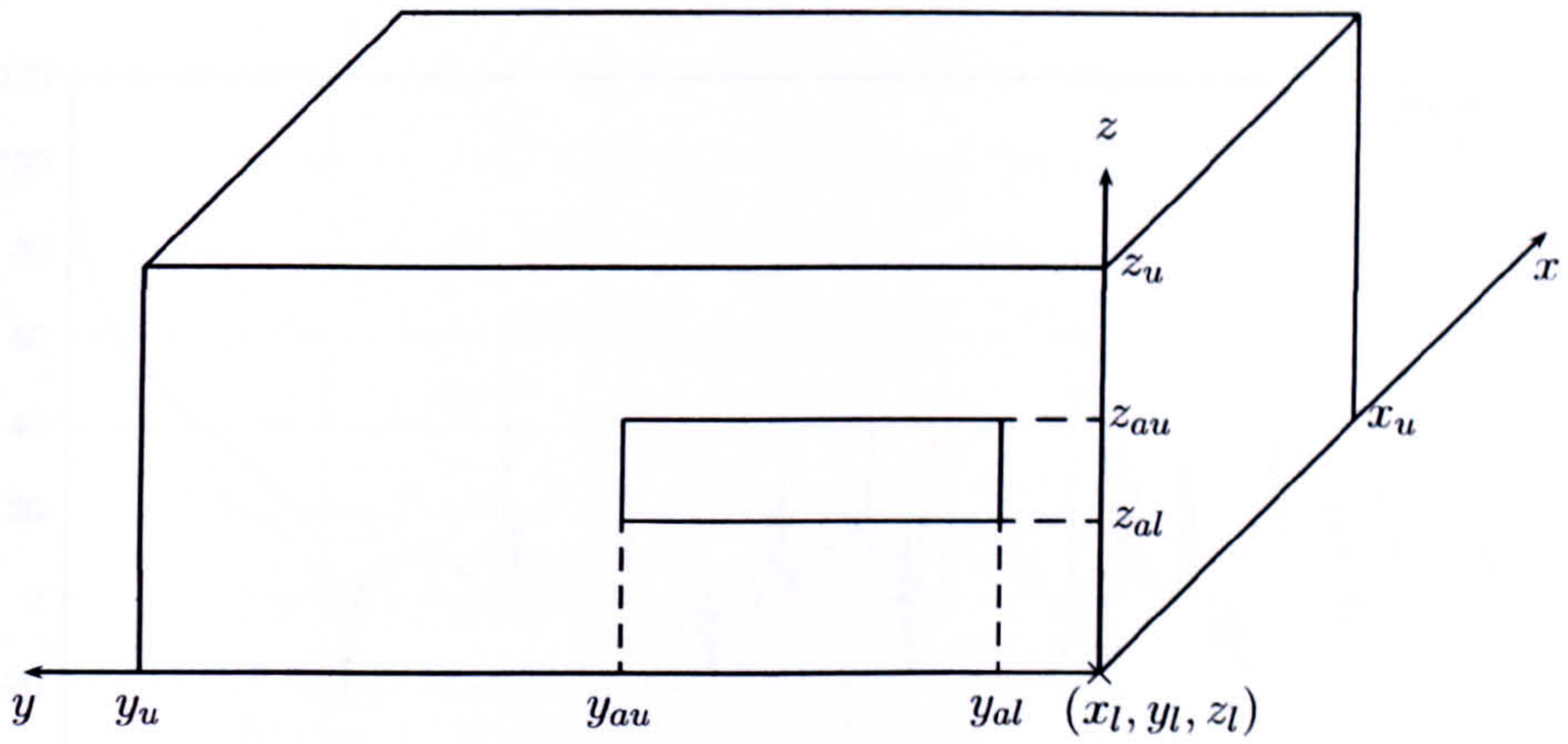

Figure 7.27: A shielded enclosure with an aperture in one face.

factor of one. Figure 7.28 shows the output of the FDTD simulations performed on progressively refined meshes. These curves are all fairly similar: the FSV comparison of the curves produced with a refinement factor of one and two returns a GDM of 3.4265 corresponding to a "good" comparison. It may therefore be concluded that the reference simulation has converged sufficiently. The error in this FDTD simulation was found approximately by using the FDTD simulation performed on a mesh with a refinement factor of four.

The frequency response of the SE was also formed using the ILCM method. Figure 7.29 displays the frequency response of the SE of the box, calculated using the reference FDTD simulation and the ILCM simulation. Overall the detailed structure of these two curves is similar and both curves have similar amplitudes. These two curves differ significantly for frequencies below 500MHz. When compared using the FSV method, the two

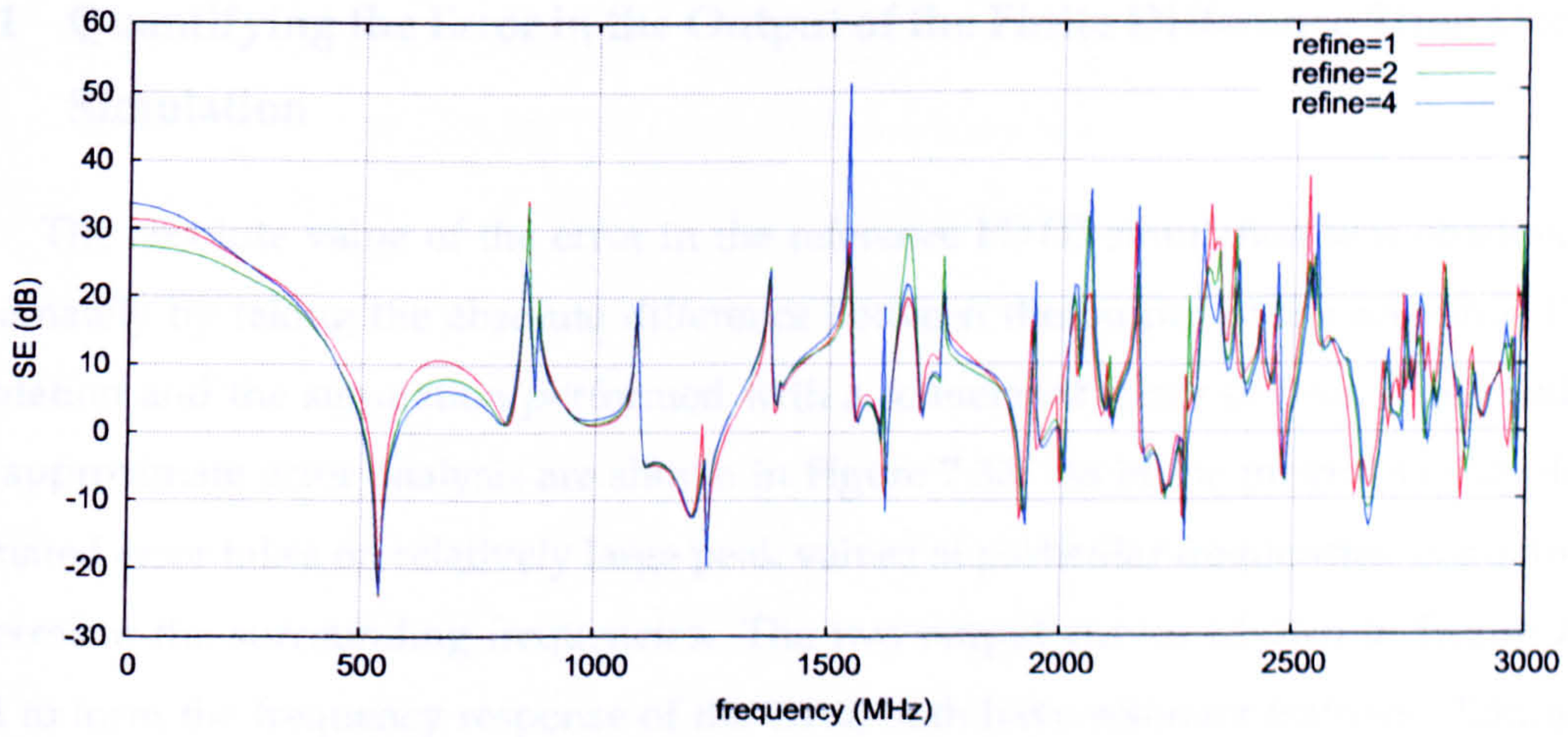

Figure 7.28: Frequency response of the SE obtained using FDTD simulations on meshes with different refinement factors.

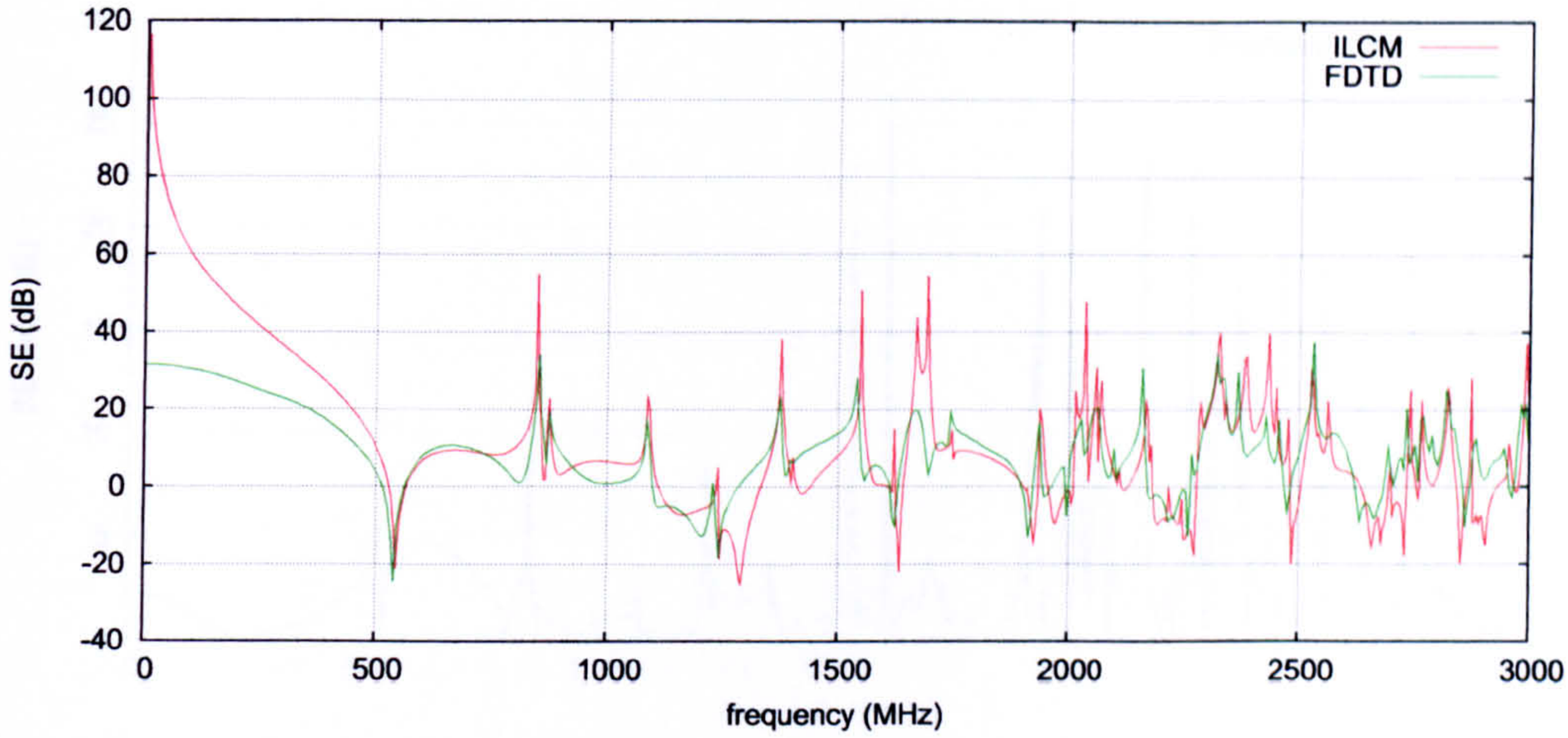

Figure 7.29: Frequency response of the SE obtained via the reference FDTD simulation and the ILCM method.

curves are determined to be a "poor" comparison with a GDM of 5.2704. Above 500MHz the curves are fairly similar with a GDM of 4.7438. The differences in the two output frequency responses are due to the errors associated with each method. The ILCM method is known to be less accurate when used to model enclosures with apertures that are fairly square. In this example, the aperture is not square but the height of the aperture is still about one quarter of the size of the aperture width. The FDTD simulation also suffers from errors including boundary, discretisation and dispersion errors. The slight differences in the output of the FDTD and ILCM simulations will result in slightly different associated output uncertainties being formed for the two methods. An estimation of the error in the output of the reference FDTD simulation is quantified in the next section.

7.4.1 Quantifying the Error in the Output of the Finite Difference Time Domain Simulation

The absolute value of the error in the reference FDTD simulation was obtained approximately by taking the absolute difference between the output of the reference FDTD simulation and the simulation performed with a refinement factor of four. The results of this approximate error analysis are shown in Figure 7.30. As in the previous example the estimated error takes on relatively large peak values at particular frequencies, compared to the error at the surrounding frequencies. The two output curves (shown in Figure 7.28), used to form the frequency response of the error, both have resonant features. Taking the difference between the two curves results in relatively large errors at certain frequencies. The frequency response of the error has fewer peaks at the lower frequencies, this is because

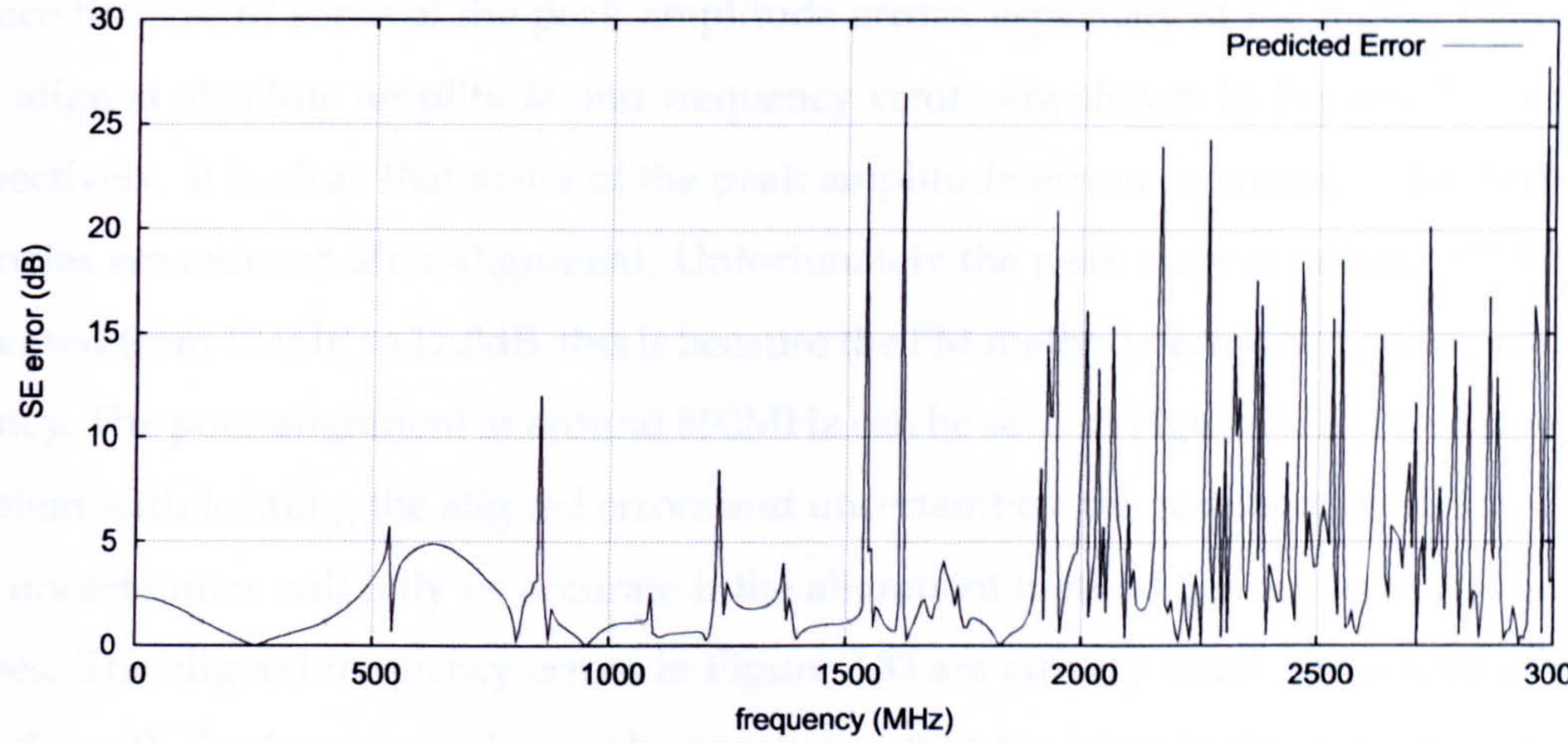

Figure 7.30: Frequency response of the estimated error in the output of the reference FDTD simulation.

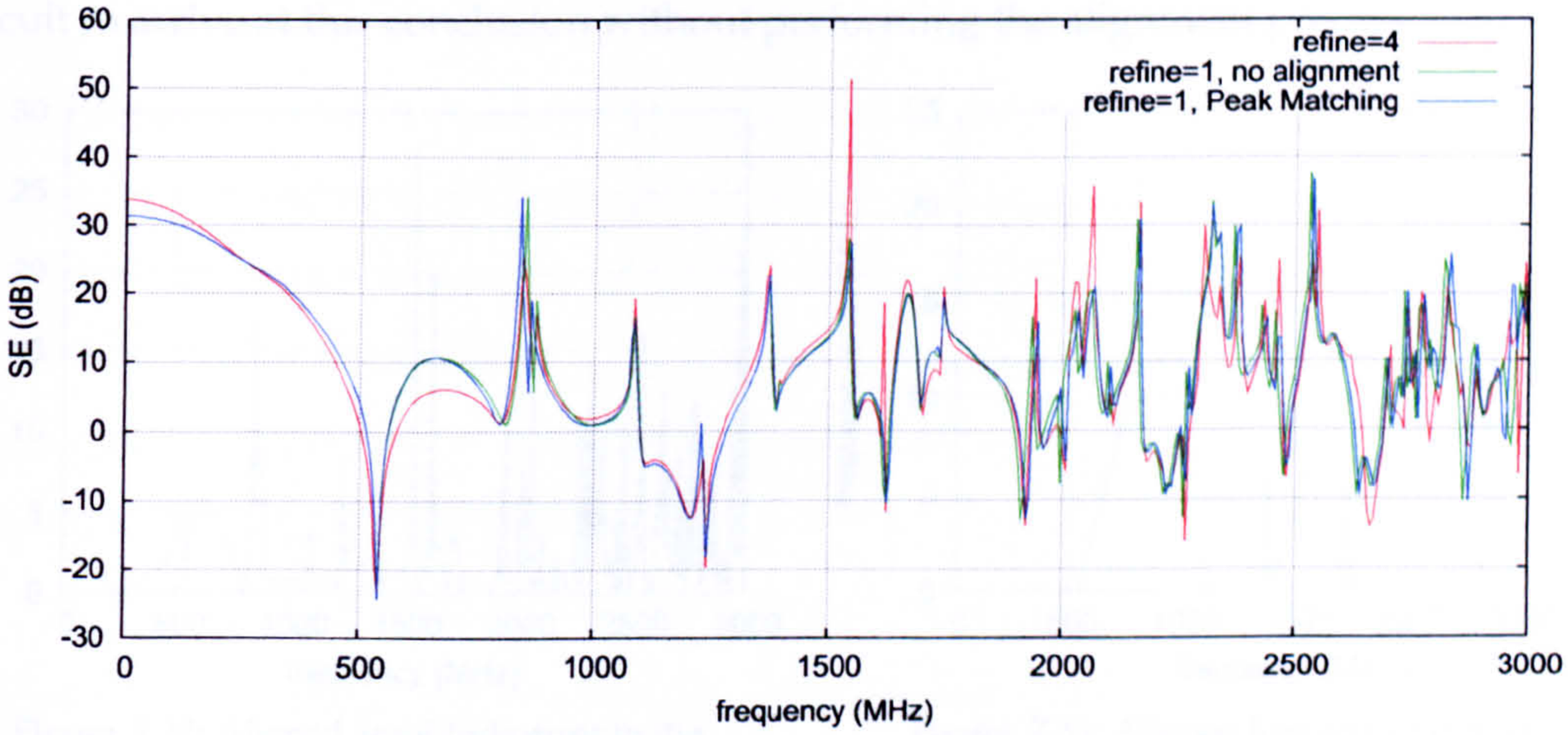

Figure 7.31: Frequency response of the SE formed from the reference FDTD simulation, before and after alignment to the SE formed from the refined FDTD simulation.

the two curves used to form the error curve are less resonant at the lower frequencies. It can be seen from Figure 7.30 that the baseline error in the reference FDTD simulation is fairly small but the error takes on large peak values at some of the frequencies.

It may be argued that at the higher frequencies the frequency responses of the SE in Figure 7.28 suffer from a small amount of misalignment. Aligning these peaks via the PM method may help to reduce the size of some of the peak errors at the higher frequencies. The SE obtained using the reference and refined FDTD simulations were aligned using the PM method. The results of this alignment are shown in Figure 7.31. The improvement in alignment is small: comparisons between the response formed with the reference FDTD simulation and with a refinement factor of four results in a GDM of 3.7121 before alignment and 3.6460 after alignment. This small improvement in alignment is however sufficient to

reduce the size of some of the peak amplitude errors, especially at the higher frequencies. The aligned absolute amplitude and frequency errors are shown in Figures 7.32 and 7.33 respectively. It is clear that some of the peak amplitude errors occurring at the higher frequencies are reduced after alignment. Unfortunately the peak error at around 850MHz has increased from 12.0dB to 17.0dB, this is because the PM method performed poorly at this frequency. The poor alignment at around 850MHz can be seen in Figure 7.31. This highlights a problem with forming the aligned errors and uncertainties: the results of the aligned errors and uncertainties will only be accurate if the alignment method has accurately aligned the curves. The aligned frequency errors in Figure 7.33 are all very small, these errors increase slightly with the frequency. It may be concluded that the error in the output of the reference FDTD simulation is a series of peak amplitude errors, and a small frequency error. It is difficult to arrive at this conclusion without performing the alignment process.

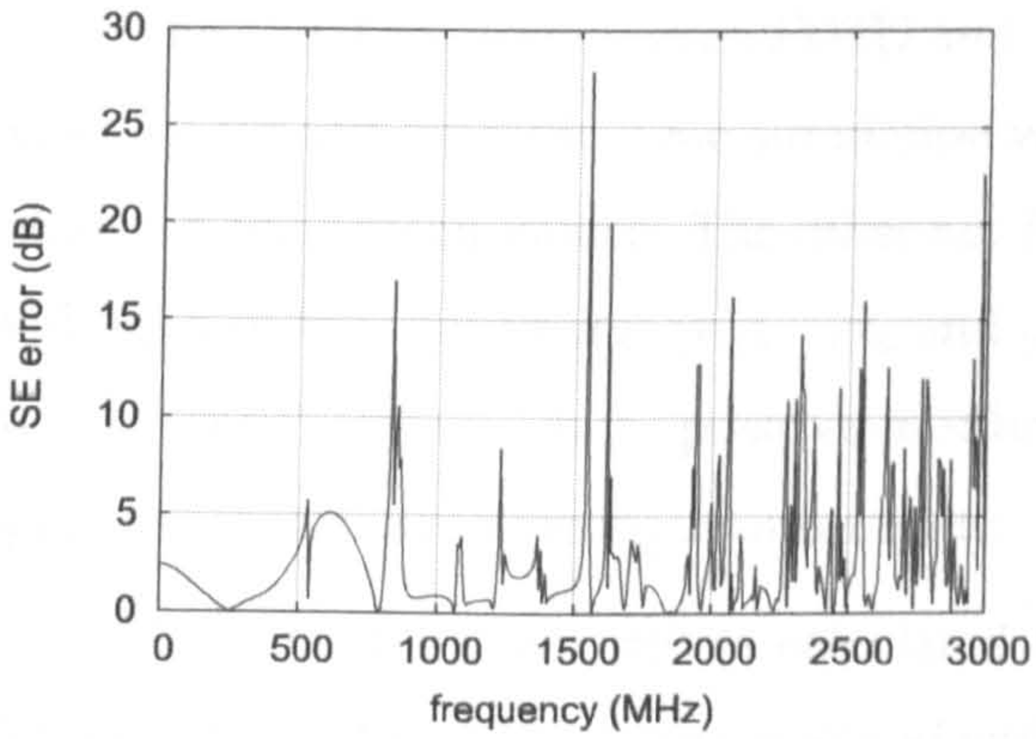

Figure 7.32: Aligned amplitude error in the output of the reference FDTD simulation

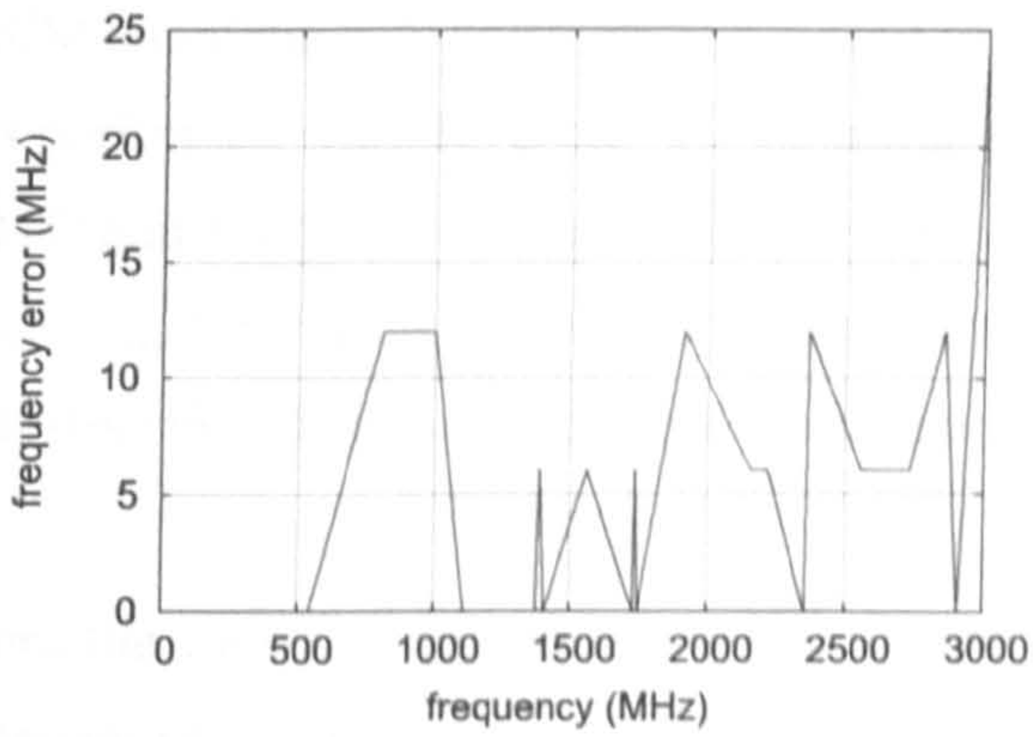

Figure 7.33: Aligned frequency error in the output of the reference FDTD simulation

7.4.2 Uncertainty Analysis of the Shielding Effectiveness of the Shielded Enclosure

The uncertainty in the SE of the shielded enclosure will be quantified in this section. As in the last example, the PCM is not used to quantify the output uncertainty as it has been previously shown (in Section 6.7) to be unable to estimate the output due to uncertain geometric inputs involving conducting bodies. The MCM is once again used as the benchmark method to test the performance of the computationally efficient MoM.

The Monte Carlo Method

The implementation of the MCM into the FDTD and ILCM simulations is similar to the implementation detailed in Section 7.3.2, for the previous example. The only difference is that the 5,000 Latin Hypercube Samples were formed for all ten uncertain geometric parameters. That is the four uncertain aperture coordinates and the six uncertain coordinates of the sides of the metal box. The FSV method was used to determine when the MCM simulations had reached convergence, as described in Sections 3.2.3 and 4.5.2. For this example it was found that convergence was reached after 600 simulations for the FDTD method and 1,000 simulations for the ILCM method.

The Method of Moments

The MoM required eleven FDTD and ILCM simulations to calculate the output uncertainty, for this example. One simulation was performed with the geometric coordinates taking on their mean values. The other ten FDTD and ILCM simulations were performed with each of the coordinates ($x_l, \ldots, z_u$ and $y_{al}, \ldots, z_{au}$) perturbed from their mean values by 1cm (one FDTD cell) in the positive coordinate direction. The chosen perturbation is once again the same size as the input uncertainty.

The sensitivity derivatives calculated from the eleven simulations, formed via the FDTD and ILCM method, were combined with the input uncertainties to calculate the mean and uncertainty in the output according to equations (4.51) and (4.53). Since only eleven simulations were required to obtain these uncertainties, the MoM is computationally much cheaper than the MCM.

7.4.3 Results of the Uncertainty Analyses applied to the FDTD and ILCM methods

Figures 7.34 and 7.35 show the means and uncertainties predicted by the MCM and the MoM for the results of the FDTD simulations. The means predicted by the MoM and the MCM are of a similar overall size, but the features are very different. The resonant peaks have been averaged out in the means predicted by the MCM. No such averaging occurs for the mean formed by the MoM, which is produced by one simulation with all parameters taking on their mean values.

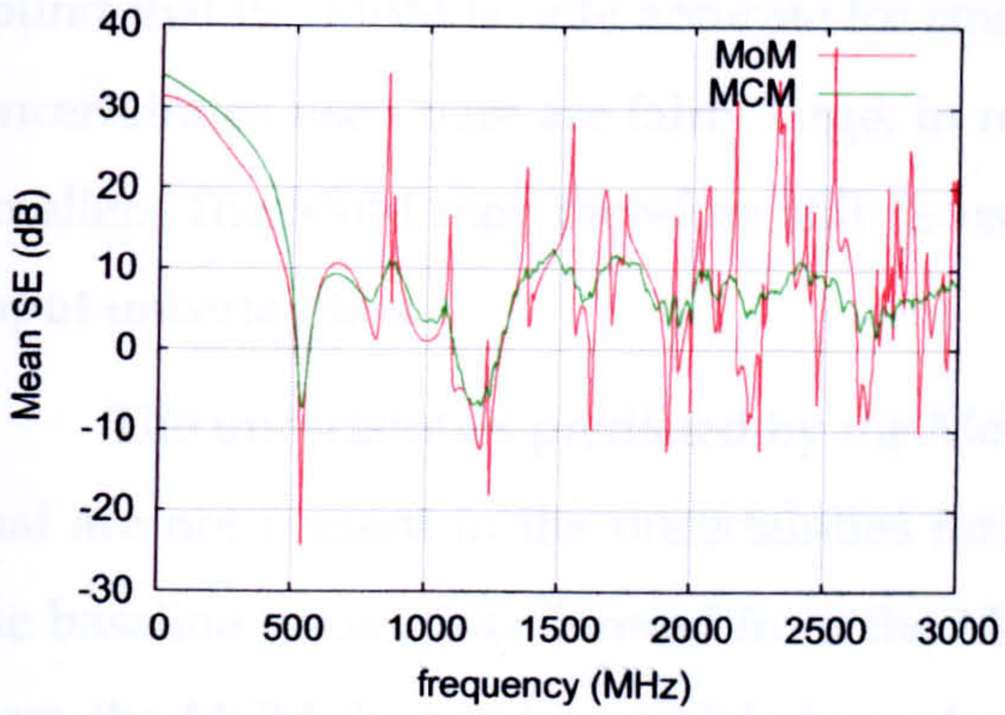

Figure 7.34: Mean SE formed from the FDTD simulations.

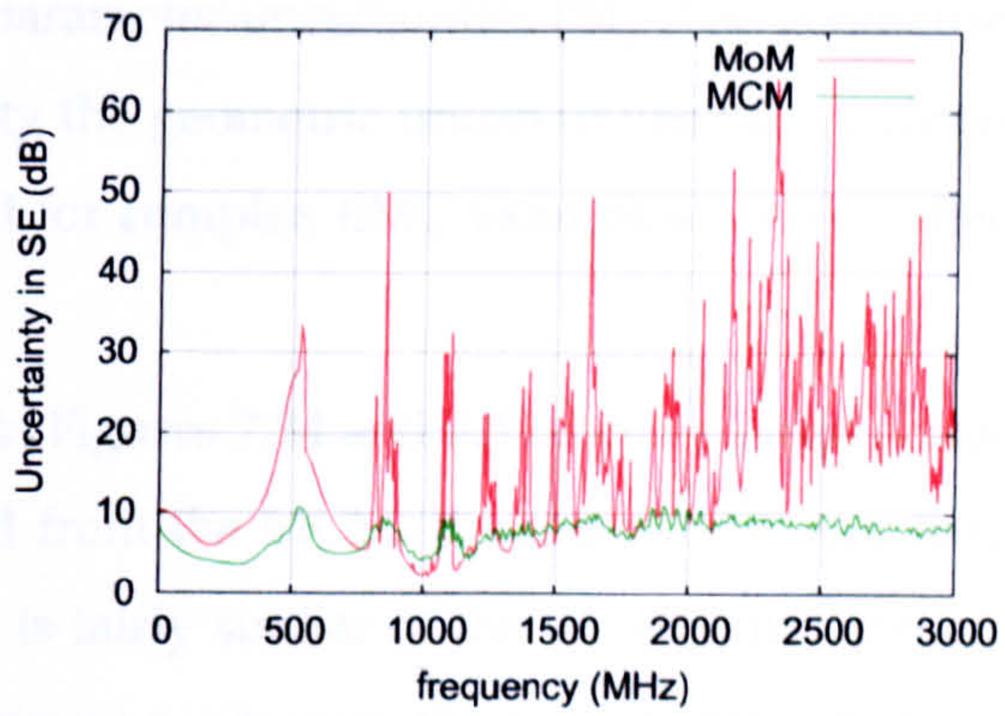

Figure 7.35: Uncertainty in the SE obtained from the FDTD simulations.

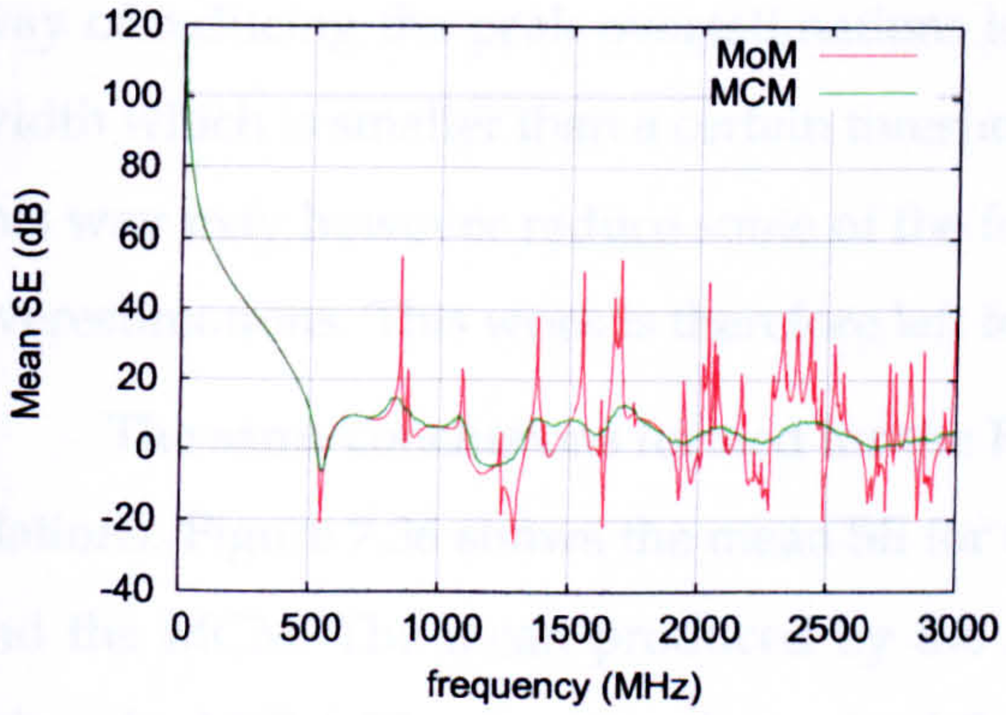

Figure 7.36: Mean SE formed from the ILCM simulations.

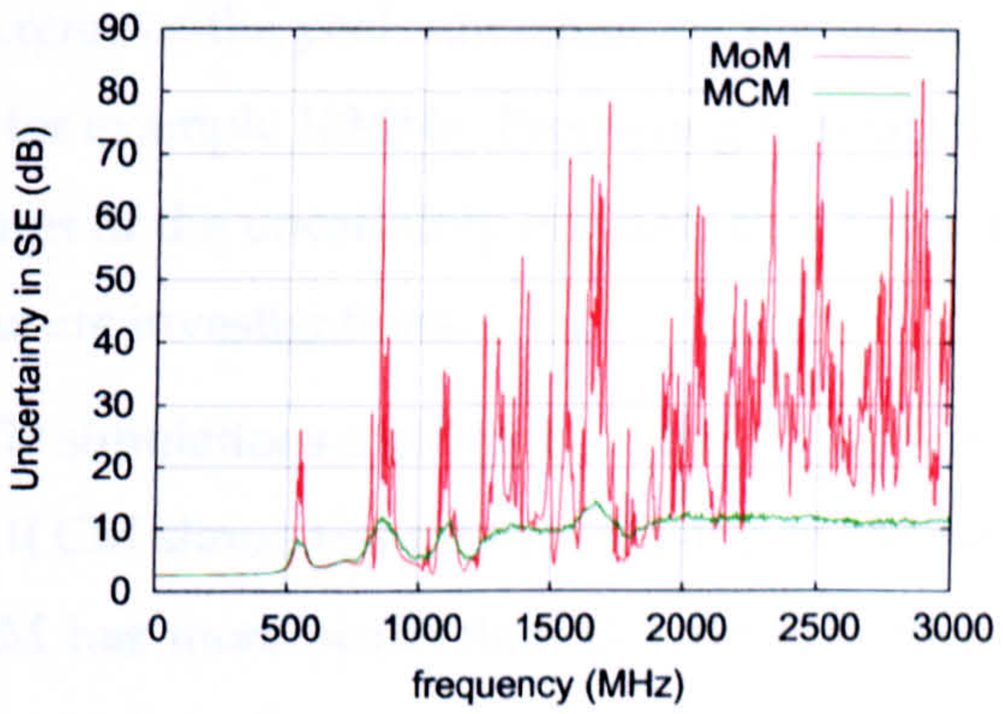

Figure 7.37: Uncertainty in the SE obtained from the ILCM simulations.

The FSV comparison of the means and uncertainties predicted by the MoM and the MCM, for the FDTD and ILCM simulations, are shown in Table 7.2. These FSV comparisons show that the uncertainties predicted by the MoM and the MCM, for the FDTD simulations, are in "very poor" agreement. As discussed previously, the MoM assumes that the output depends linearly on the uncertain inputs. This assumption clearly introduces errors into the MoM uncertainty estimation. The MoM may well be an efficient UA method but its overestimations of the uncertainty in the FDTD simulations are too large for the method to be used in examples such as this more complex EMC example. Previous research has

Metric	ADM	FDM	GDM	GDM (1-6)	Qualitative
FDTD mean	0.3294	0.8255	0.9470	5.1850	Poor
FDTD uncertainty	1.3500	1.2850	2.0218	6	Very Poor
ILCM mean	0.2996	0.8836	0.9737	5.2253	Poor
ILCM uncertainty	1.3687	1.3208	2.0349	6	Very Poor

Table 7.2: FSV comparisons of the different metrics predicted by the benchmark MCM and the MoM.

found that the MoM is only accurate for small parameter uncertainties [84]. The geometric uncertainties used here are fairly large, in reality the geometric uncertainties may well be smaller. The MoM may therefore still be useful for complex EMC examples with smaller input uncertainties.

The uncertainties predicted by the MoM in Figures 7.34 and 7.35 contain large peaks that are not present in the uncertainties formed from the MCM. It appears however that the baseline uncertainty formed from the MoM is fairly similar to the uncertainty formed from the MCM. It may be possible to perform a post process on the uncertainty estimate, formed from the MoM, to remove the peak overestimations and therefore provide an efficient estimate of the uncertainty that is in better agreement with the MCM. One possible way of reducing the peak overestimations is to remove the peak uncertainties that have a width which is smaller than a certain threshold, for example 10MHz. Processing the data in this way may however reduce some of the features of the uncertainty estimate that are not overestimations. This work is therefore left for future investigations.

The same conclusions formed for the FDTD simulations also apply to the ILCM simulations. Figure 7.36 shows the mean SE for the ILCM simulations, formed using the MoM and the MCM. The mean produced by the MoM has more peaks than the mean formed using the MCM. The resonant features of the curves have been averaged out in the mean produced by the MCM. This results in a "poor" comparison between the means produced by the two UA methods.

Figure 7.37 shows the uncertainty in the output of the ILCM simulations predicted by the MoM and the MCM. As for the FDTD simulations, the MoM overestimates the uncertainty in the ILCM simulations. These overestimations are more prominent at the higher frequencies. The MoM prediction of the uncertainty in the ILCM simulations is therefore "very poor" when compared to the uncertainty formed by the benchmark MCM. There are many large peak overestimations formed by the MoM, one such peak occurs at 1.55GHz (see Figure 7.37). This overestimation is now investigated further using the ILCM method.

Figure 7.38 shows the frequency response of the SE, around 1.55GHz, for the reference ILCM simulation and a perturbed ILCM simulation.The perturbed simulation was performed with the lower x-coordinate of the box perturbed 1cm from its mean value. Using Figure 7.38 it can be seen that the SE, formed from the reference simulation, is at a resonant peak at 1.55GHz. The resonant frequency of the SE, formed from the perturbed simulation, is at a slightly higher frequency and a slightly lower amplitude. The small perturbation in

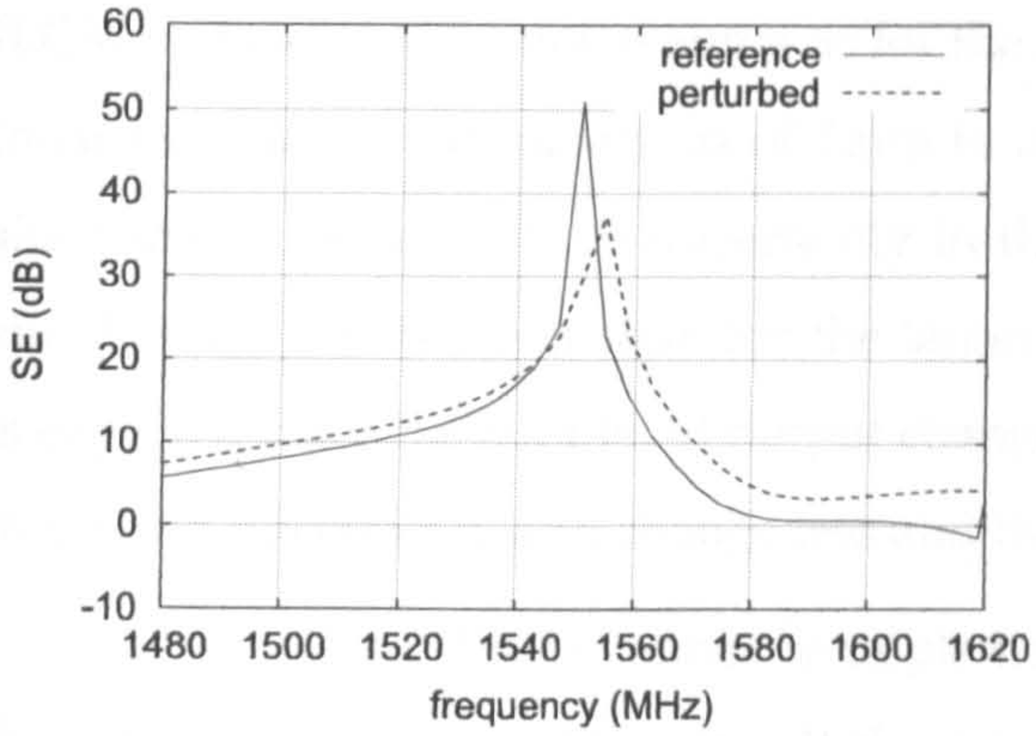

Figure 7.38: The SE obtained from the reference simulation and a simulation with x_l perturbed.

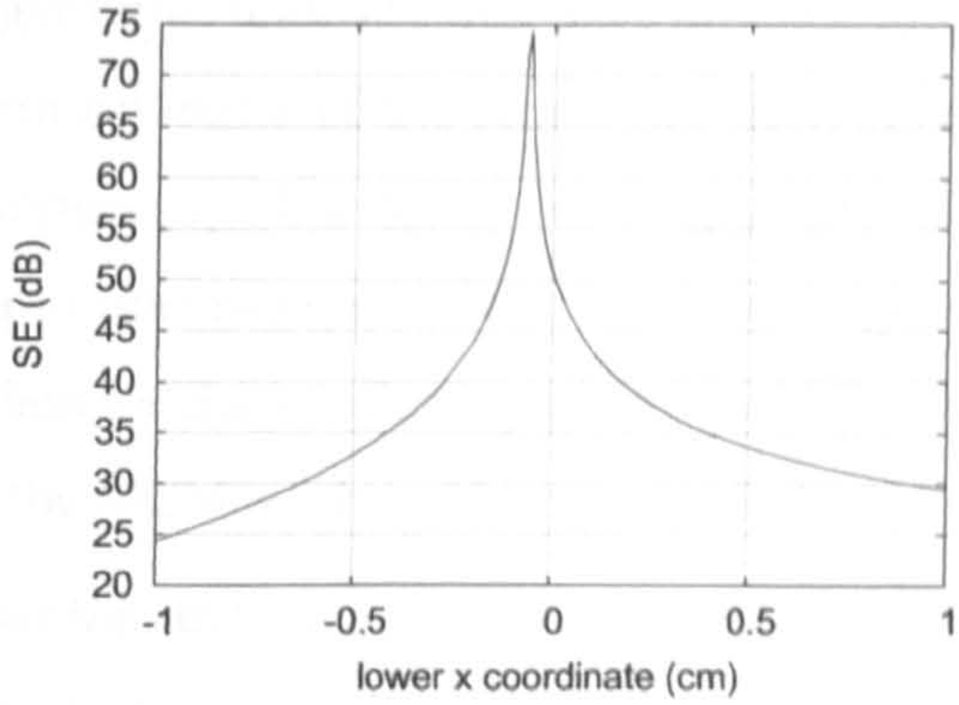

Figure 7.39: Relationship between the output SE and the coordinate x_l at 1.55GHz.

the input parameter creates a large difference between the two curves at 1.55GHz. The output SE is therefore very sensitive to changes in the input parameter at the resonant frequency (1.55GHz). The MoM assumes that the output depends linearly on this input parameter. The sensitivity derivative, of the SE with respect to the input parameter, is large at the resonant frequency and the MoM therefore predicts that the uncertainty (due to this uncertain input parameter) at this frequency is also large.

Figure 7.39 shows how the SE varies with the uncertain input parameter at 1.55GHz. The SE has a highly nonlinear dependence on the uncertain input parameter. The linear assumption used by the MoM is clearly poor when there is such a nonlinear relationship. Similar nonlinear relationships were also observed for the dielectric sphere example in Chapter 6. Unfortunately EMC data can often exhibit highly resonant features. Approximating the relationship between the resonant output and the uncertain inputs linearly will result in poor estimations of the output uncertainty. Higher order approximations may improve the accuracy, however it will always be difficult to accurately represent nonlinear relationships (such as that shown in Figure 7.39) using polynomials. Previously work has found that the MoM estimate of the output uncertainty is more accurate if the input uncertainties are smaller. This is investigated, for this example, in the next section.

Smaller Input Uncertainties

To investigate whether the MoM performs better for small parameter uncertainties, the uncertainty in the geometric inputs of this example are reduced to 1mm. It is perhaps more realistic that the shielded enclosure developed smaller geometric uncertainties of the order of 1mm in the manufacturing process. The MCM and the MoM were applied to the

ILCM method in the same manner as for the larger input uncertainties. This time the MoM must use smaller perturbations of 1mm to obtain estimates of the sensitivity derivatives, since this is the size of the uncertainty in the inputs [2]. The MCM converged after 350 simulations, this is fewer than for the larger input uncertainties. This faster convergence is expected since the simulated output changes less for the smaller input uncertainties; the mean and uncertainty also change less and thus the MCM reaches convergence faster.

The standard MCM cannot be implemented into the reference FDTD simulations for these smaller input uncertainties. If the uncertainty in a geometric position is small then standard sampling methods will select input values that are close to the mean geometric position. The FDTD simulations have to be performed with geometric perturbations that coincide with the FDTD mesh. Rounding the sampled parameter values to the nearest cell position results in all of the geometric input parameters taking on their mean values. It is therefore difficult to use the standard MCM to determine the output uncertainty formed from the FDTD simulations on the current mesh. For Normally distributed geometric input parameters, 95% of the sampled values are with 1.96 standard deviations from the mean. An FDTD mesh therefore needs to have cell positions within the 95% interval to obtain a prediction of the output uncertainty using the standard MCM. This identifies one problem with using the MCM to estimate the output uncertainty of FDTD simulations due to small uncertain geometric input parameters.

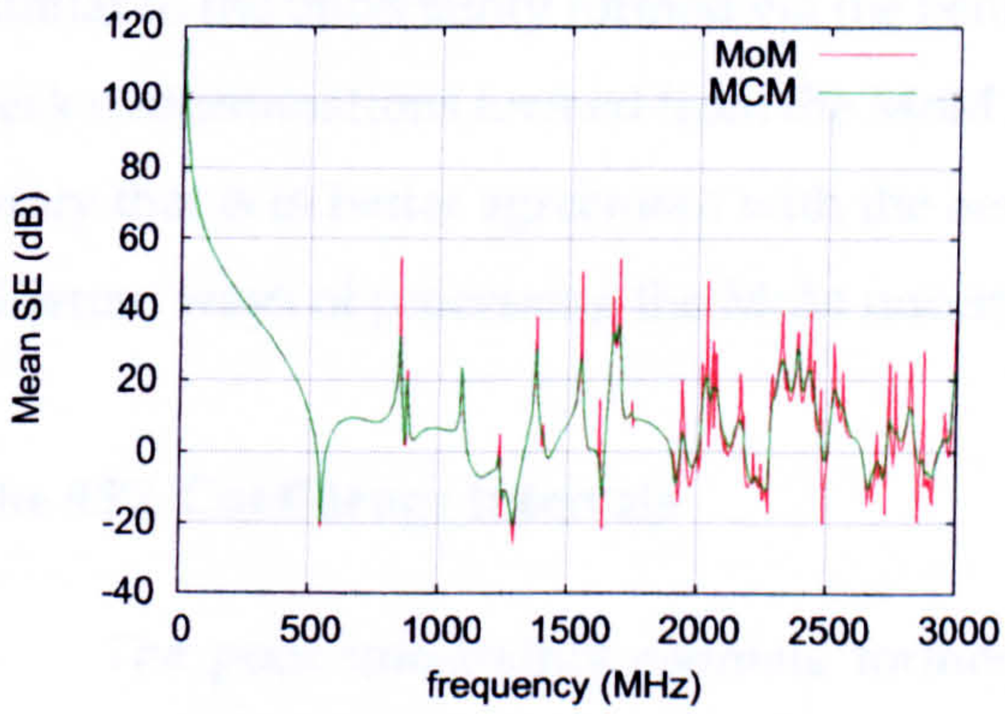

Figure 7.40: Frequency response of the mean SE formed using the ILCM method.

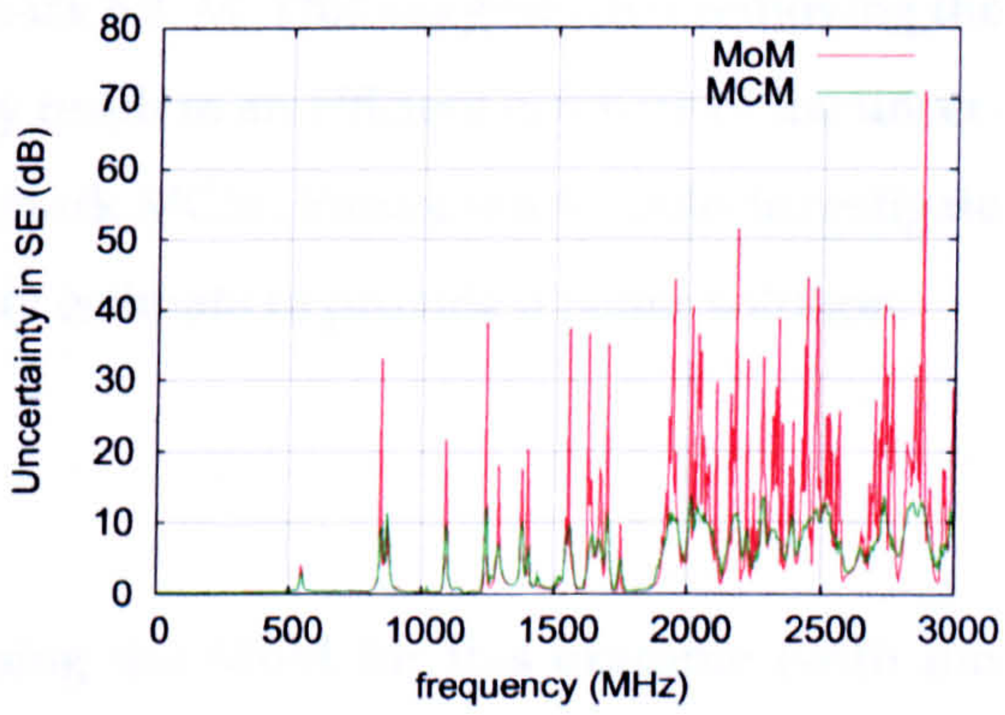

Figure 7.41: Frequency response of the uncertainty in the SE formed using the ILCM method.

The problem outlined above does not occur when using the ILCM method. The ILCM method can simulate perturbations of any size, being limited only by the numerical precision used in the implementation of the method. The frequency responses of the mean and uncertainty in the output SE, formed using the ILCM method, are shown in Figures 7.40 and

7.41 respectively. It is clear that the mean predicted by the MoM and the MCM for smaller input uncertainties (Figure 7.40) are in much better agreement than when the input uncertainties were larger (Figure 7.36). The FSV comparisons agree with this determining that the similarity between the mean curves is "good" when the input uncertainties are small. The uncertainty curves produced by the MoM and the MCM are in better agreement when the input uncertainties are small, however the MoM still produces large peak overestimations of the uncertainty. The FSV method determines that the similarity of the two uncertainty curves is "poor". Therefore the estimates of the uncertainty, formed via the MoM, still suffer from the resonant nature of the output EMC data curves despite the input uncertainties being smaller.

The computationally efficient MoM provides better estimations of the uncertainty when the input uncertainties are smaller. It is difficult to use the MCM to obtain the uncertainty in the output of FDTD simulations when there are small geometric input uncertainties. The MoM is therefore the preferred UA method to use when estimating the uncertainty in the output of FDTD simulations due to small geometric input uncertainties. Unfortunately the results of CEM simulations of EMC scenarios often have resonant features, and the input uncertainties are not necessarily small. In these cases the MoM provides a poor estimation of the output uncertainty.

Notice once again that the baseline uncertainty formed by the MoM in Figure 7.41 is similar to the uncertainty formed via the benchmark MCM. This suggests that removing the peak overestimations formed from the MoM may result in an efficient estimate of the uncertainty that is in better agreement with the benchmark MCM. Future work could investigate different ways of processing the MoM uncertainty estimate to provide a better solution.

The 95% Confidence Intervals

The poor uncertainty estimate formed using the MoM for this example (with the larger input uncertainties), results in a poor estimation of the 95% CI. The MoM uses the uncertainty prediction directly to obtain the 95% CI, thus poor uncertainty estimates result in poor estimates of the CI. In the case of the smaller input uncertainties, the agreement between the 95% CI produced by the MoM and the MCM is much better. The mean and uncertainty estimates produced by the MoM and the MCM are more similar, when the input uncertainties are small, the resulting 95% CI are therefore also more similar. The FSV comparison of the upper 95% CI produced by the MoM and the MCM, for the case when

the input uncertainties were smaller, is "fair" with a GDM on the visual scale of 4.3460.

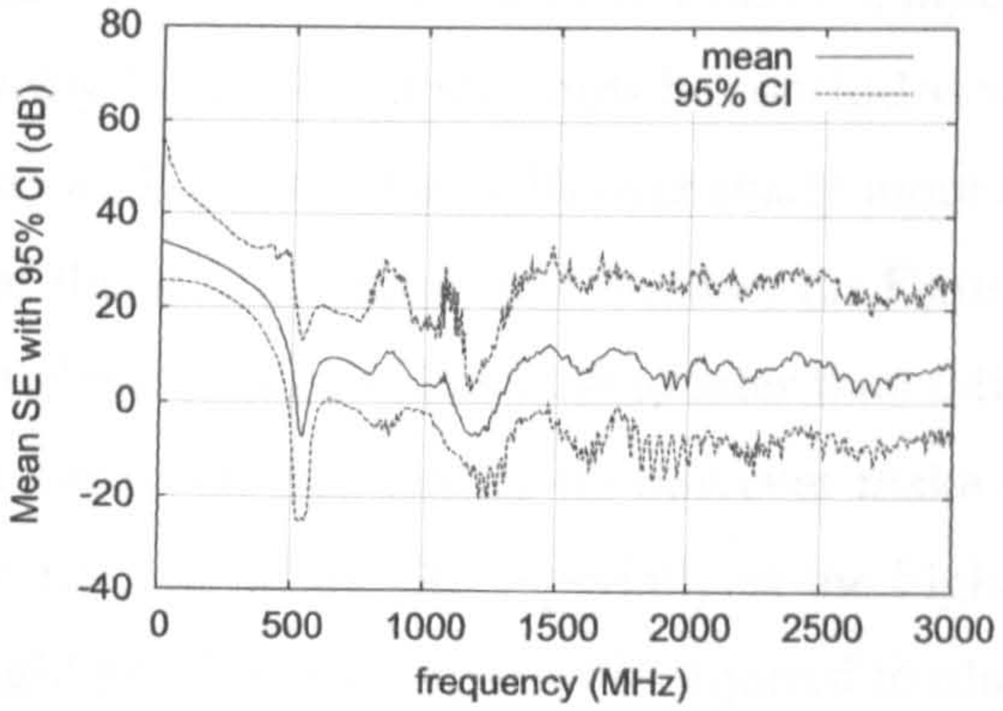

Figure 7.42: Mean and 95% CI for FDTD simulations with larger input uncertainties, formed via MCM.

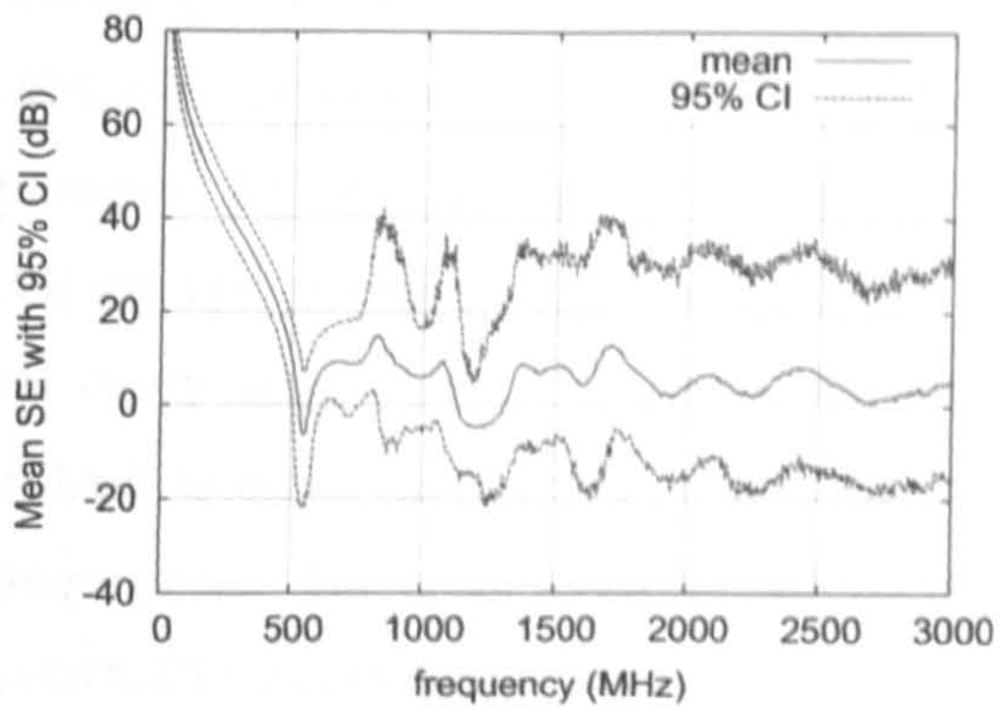

Figure 7.43: Mean and 95% CI for ILCM simulations with larger input uncertainties, formed via MCM.

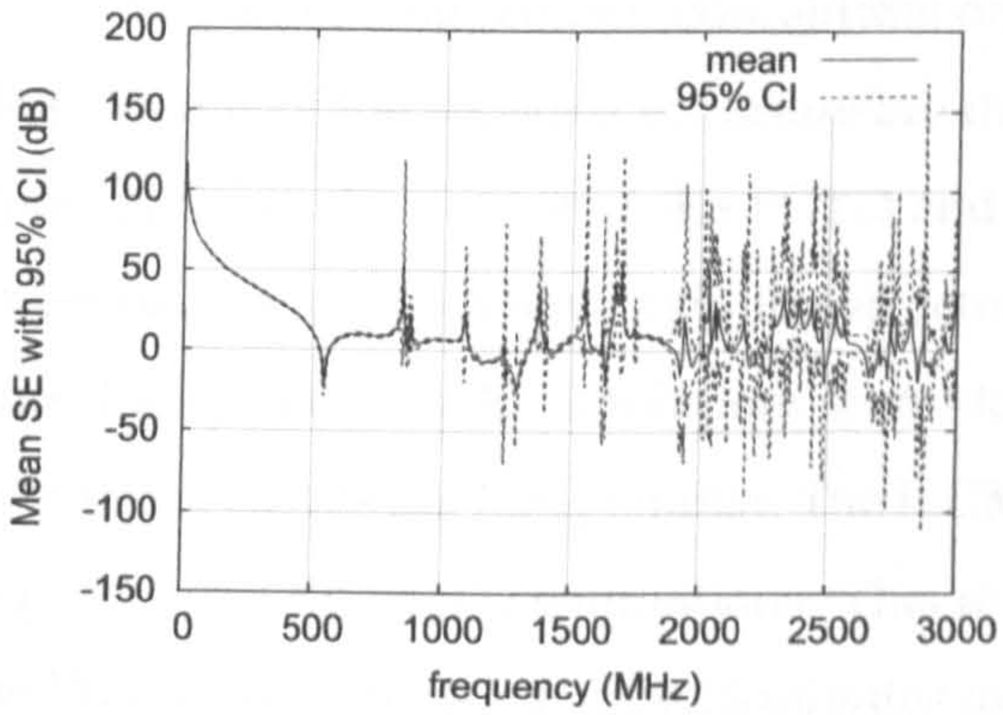

Figure 7.44: Mean and 95% CI for ILCM simulations with smaller input uncertainties, formed via MoM.

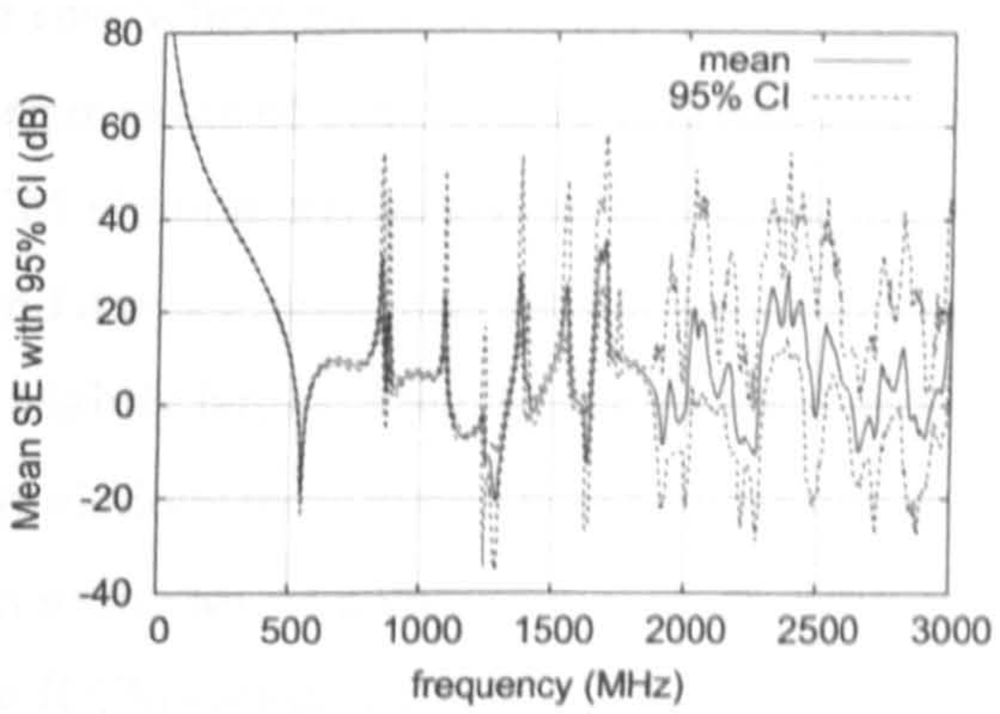

Figure 7.45: Mean and 95% CI for ILCM simulations with smaller input uncertainties, formed via MCM.

Figures 7.42 and 7.43 show the mean and 95% CI for the FDTD and ILCM simulations, with the larger input uncertainties, formed using the MCM. The CI are similar for both the FDTD and ILCM simulations, but seem to be slightly larger for the ILCM simulations at the higher frequencies. Figures 7.42 and 7.43 show that the SE can vary quite considerably from its mean value over the majority of the frequency range. With 95% confidence it may be concluded that the SE produced by the FDTD simulations is between -20dB and 40dB for most of the frequencies. The enclosure may be required to have a SE above 0dB over most of the frequencies. Using Figures 7.42 and 7.43 it may be concluded that the shielded enclosure does not meet that required standard with 95% confidence. This demonsatrates how useful the UAs are at quantifying the level of confidence that may be held in the results of the CEM simulations.

Figures 7.44 and 7.45 show the mean and 95% CI for the ILCM simulations with

smaller input uncertainties, formed via the MoM and the MCM respectively. It is clear that the 95% CI are much smaller when the input uncertainties are smaller: this is as expected. Using Figure 7.45 it may now be concluded with 95% confidence that the shielded enclosure has a SE greater than 0dB over many more frequencies. The 95% CI formed via the MoM for the smaller input uncertainties (in Figure 7.44) are also useful for concluding that the shielded enclosure has a SE greater than 0dB over many frequencies. The overestimations at particular frequencies do however make it difficult to make more accurate conclusions on the size of the SE, especially at the higher frequencies. The large overestimations are highlighed by the larger scale required to plot the 95% CI formed via the MoM.

Comparing the Uncertainty in the FDTD and ILCM Simulations

The remaining sections concentrate on the case where the uncertainty in the geometric positions of the shielded enclosure are the larger value of 1cm. Figure 7.46 displays the uncertainty in the output of the FDTD and ILCM simulations as predicted by the MCM. These two curves both have a similar structure and are of a similar order of magnitude. The uncertainty in the ILCM simulations seems to be slightly larger at the higher frequencies but overall the curves are fairly similar. The ILCM simulations require much less computational expense than the FDTD simulations. This results in the MCM analyses taking 28 hours for the FDTD simulations but only 13 minutes for the ILCM simulations. In fact the MCM analysis of the ILCM simulations is computationally faster than the MoM analysis of the FDTD simulations which took around 31 minutes. Using the MCM with the ILCM simulations provides an efficient way to estimate the uncertainty in the output of the FDTD simulations

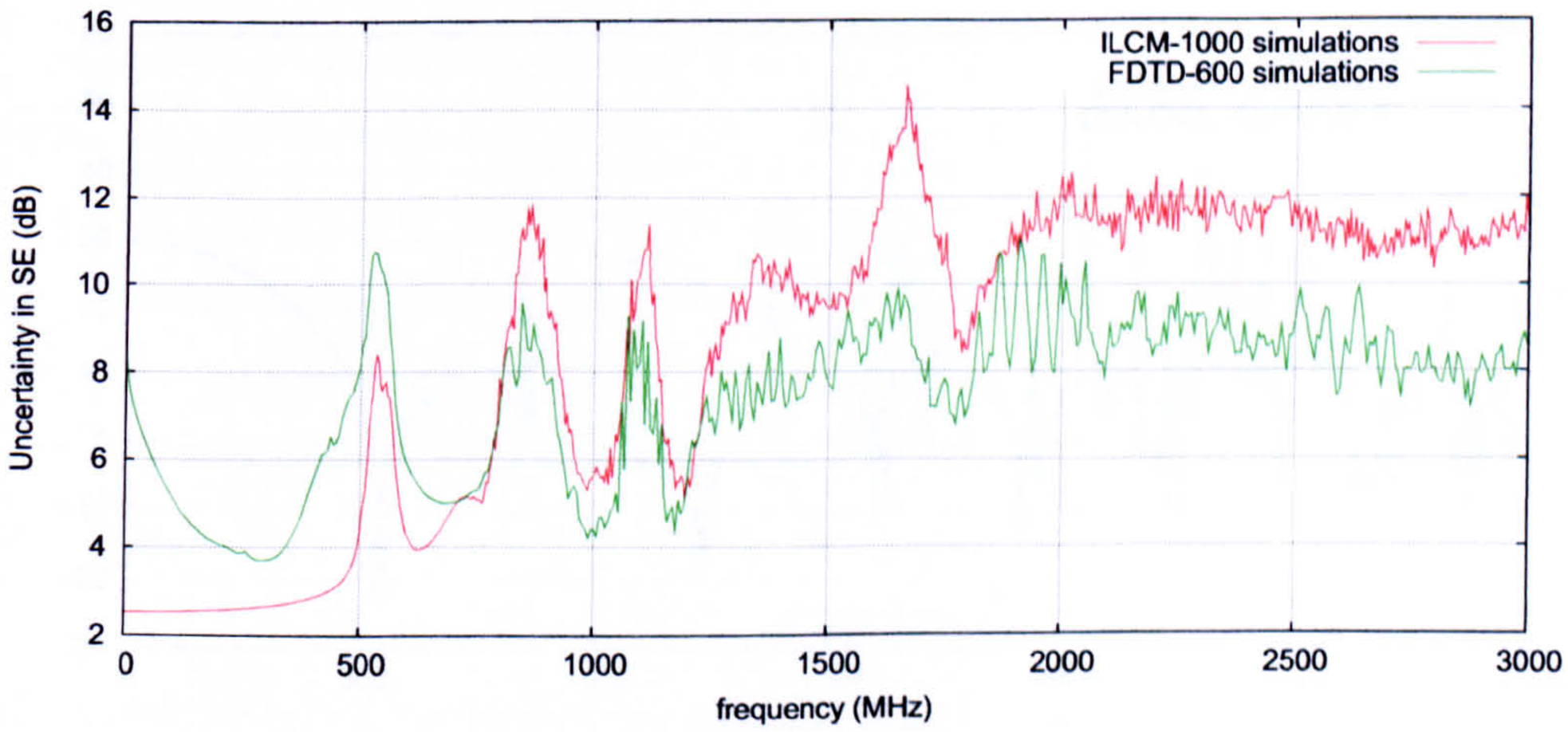

Figure 7.46: Uncertainty in the SE formed from the FDTD and ILCM simulations.

in this example. This analysis is computationally faster than performing a MoM analysis with FDTD simulations, and does not form large peak overestimations of the uncertainty.

Evaluating the Aligned Uncertainties

Figure 7.47 shows the results of the FDTD simulations performed with the mean parameter values (reference simulation), and with the coordinate y_u perturbed by one cell position. The IC method was used to align the curves in this example because it was found to provide a better alignment than the PM method. The problem with the PM method is that it relies on being able to identify peaks that should be matched. In more complicated data such as that formed from EMC analysis it is often quite difficult to establish which peaks should be matched. The alignment in Figure 7.47 has been successful at many of the frequencies, however at other frequencies (for example at 1.37GHz and 1.54GHz) the alignment process has worked less well. It can be very difficult to align real EMC data. The aligned curves were therefore tested to see whether there was a greater AAAD between the curves before alignment or after alignment. If there was a greater AAAD between the curves after alignment then it was concluded that the alignment process did not work. In this case the alignment was better before the IC method was used and so the original curve (before alignment) was used in any subsequent analyses. Thus the aligned uncertainties were formed using a mixture of aligned curves and curves that are already aligned fairly well but have not undergone alignment.

After alignment the means produced by the MoM and the MCM are in better agreement for both the FDTD and ILCM simulations, as seen in Figures 7.48 and 7.49. The align-

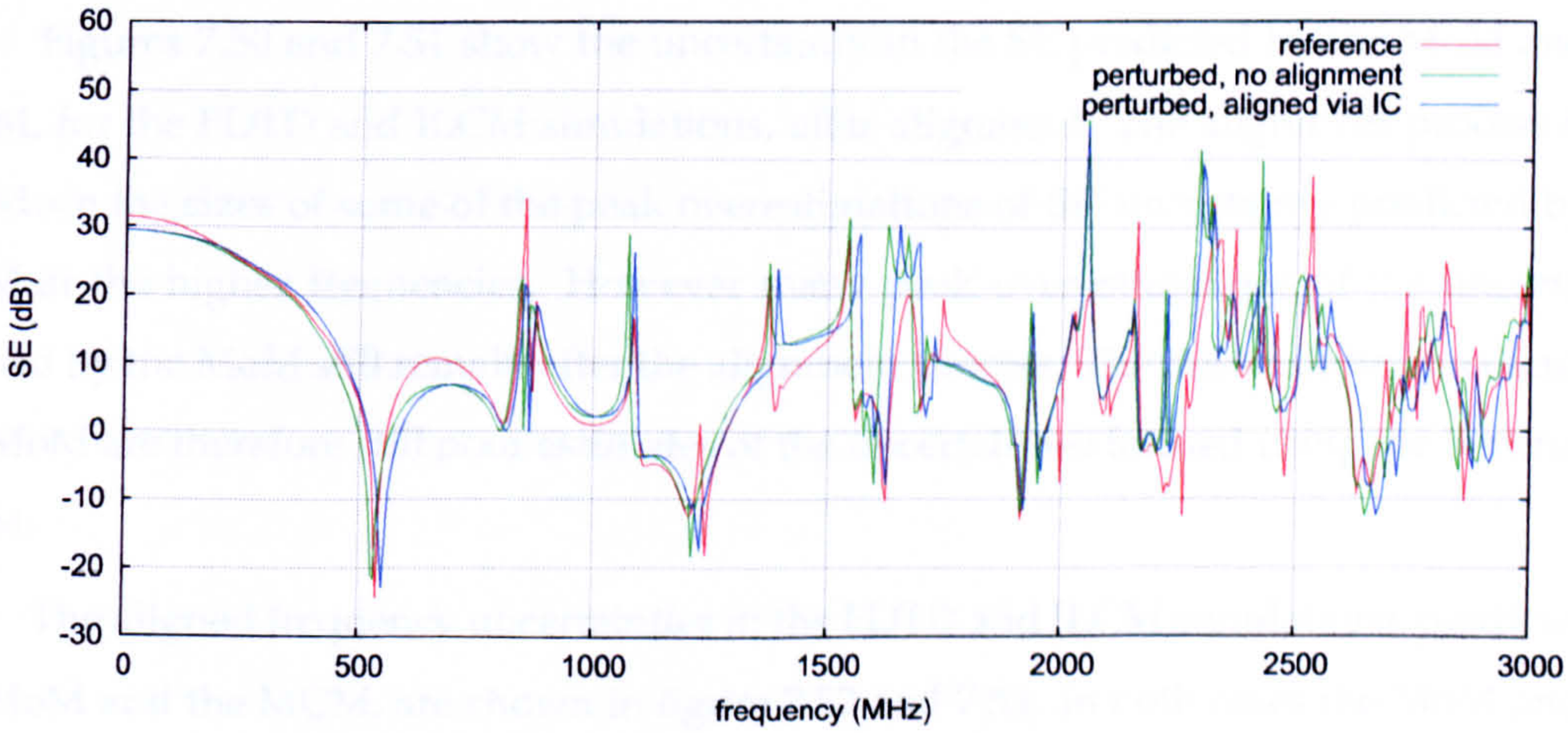

Figure 7.47: SE obtained from the reference FDTD simulation and a simulation with y_u perturbed.

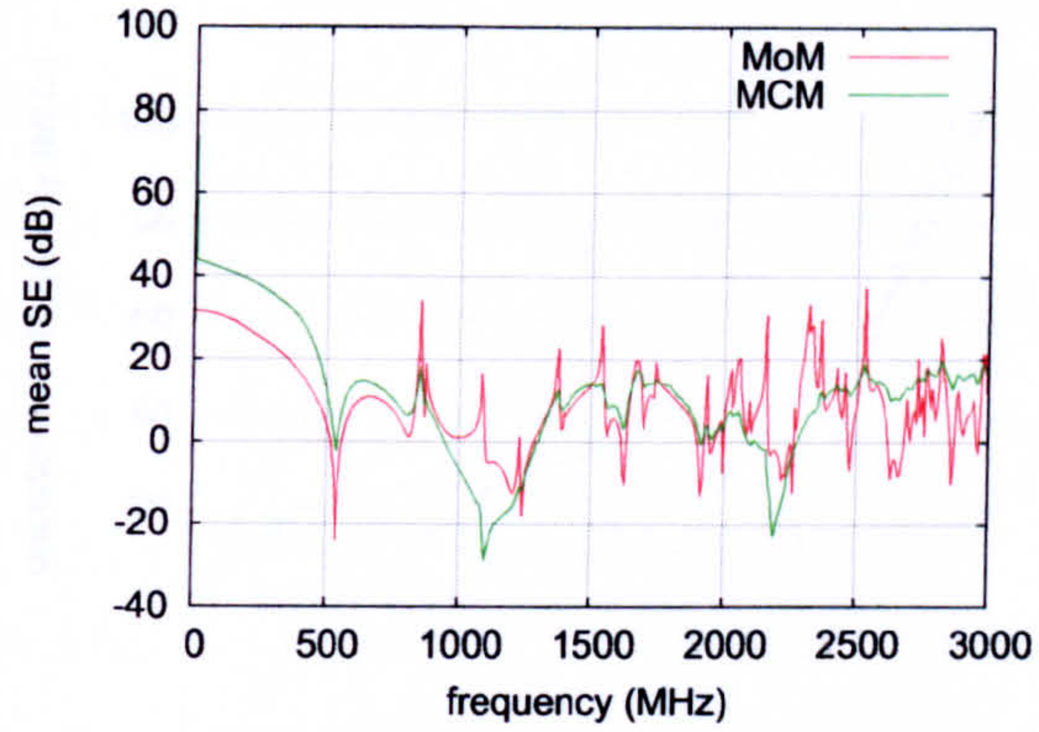

Figure 7.48: Mean SE formed from FDTD simulations with curve alignment.

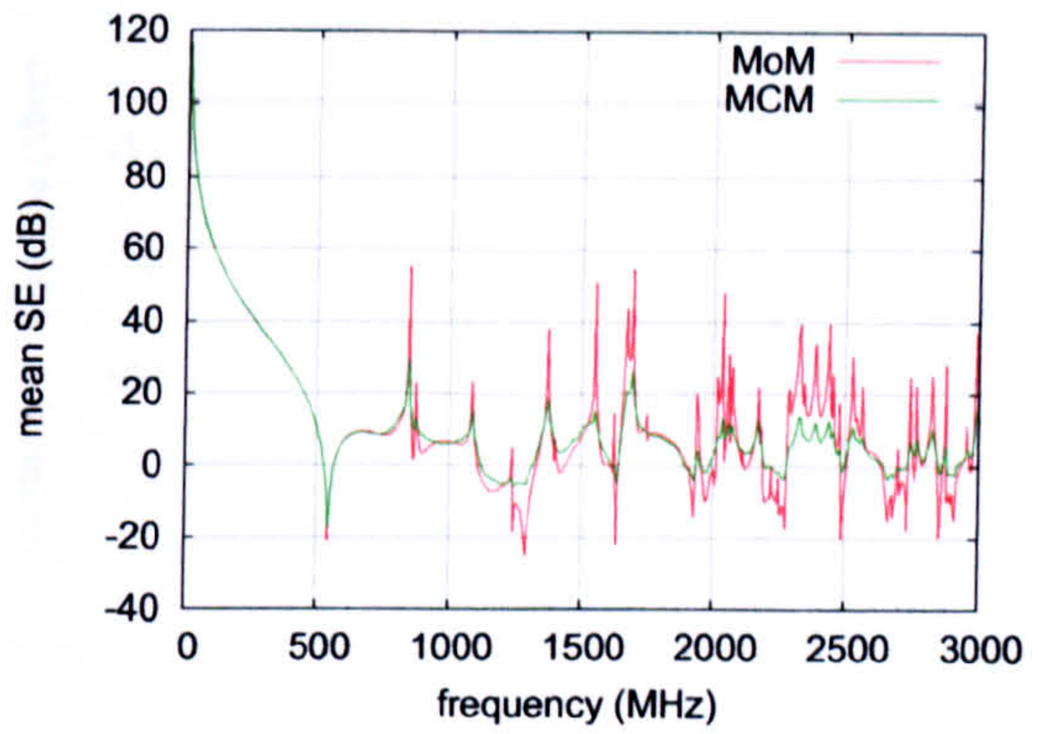

Figure 7.49: Mean SE formed from ILCM simulations with curve alignment.

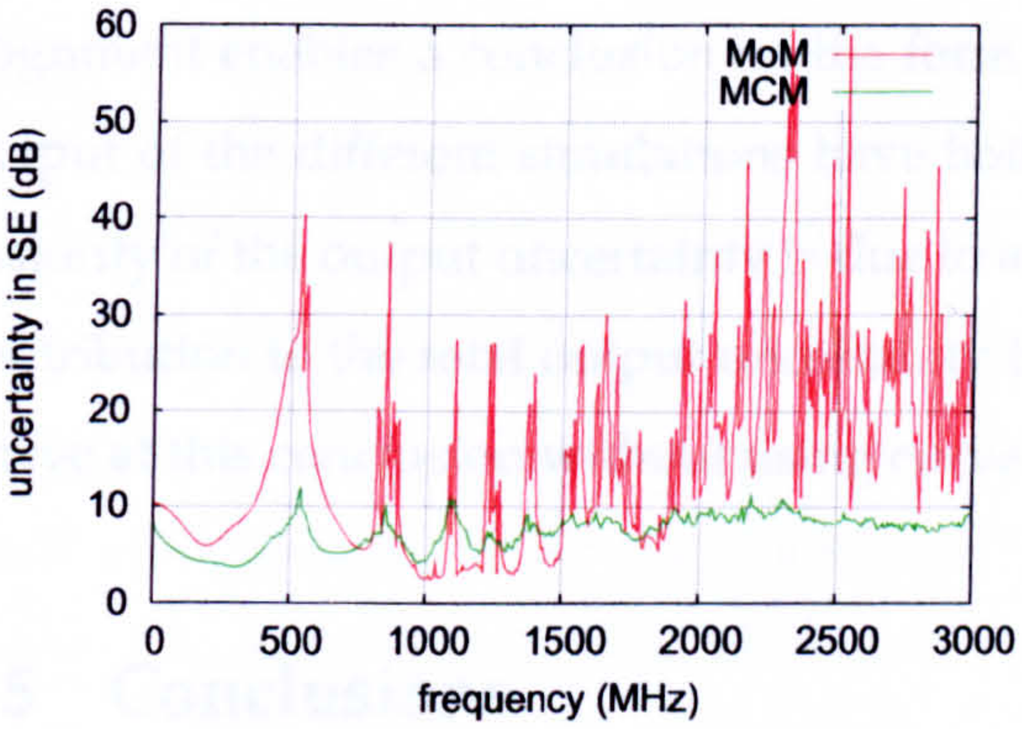

Figure 7.50: Uncertainty in the SE formed from FDTD simulations with curve alignment.

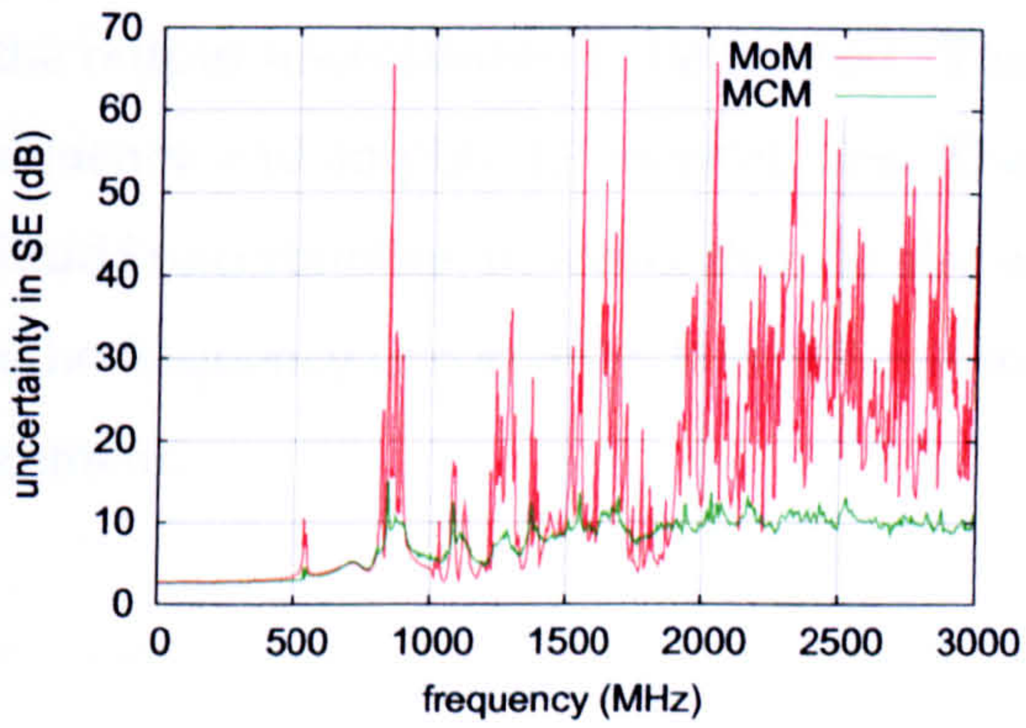

Figure 7.51: Uncertainty in the SE formed from ILCM simulations with curve alignment.

ment of the output curves, formed by the many MCM simulations, helps to reduce the averaging of the resonant peaks. This makes the mean predicted by the MCM more similar to the mean predicted by the MoM after alignment.

Figures 7.50 and 7.51 show the uncertainty in the SE predicted by the MoM and the MCM, for the FDTD and ILCM simulations, after alignment. The alignment process helps to reduce the sizes of some of the peak overestimations of the uncertainty predicted by the MoM at the higher frequencies. However many peak overestimations of the uncertainty formed by the MoM still remain after the alignment process. The uncertainties predicted by the MoM are therefore still poor estimates of the uncertainties formed using the benchmark MCM.

The aligned frequency uncertainties in the FDTD and ILCM simulations, predicted by the MoM and the MCM, are shown in figure 7.52 and 7.53. In both cases the MoM and the MCM predict that the uncertainty in the frequency increases with frequency. Using curve

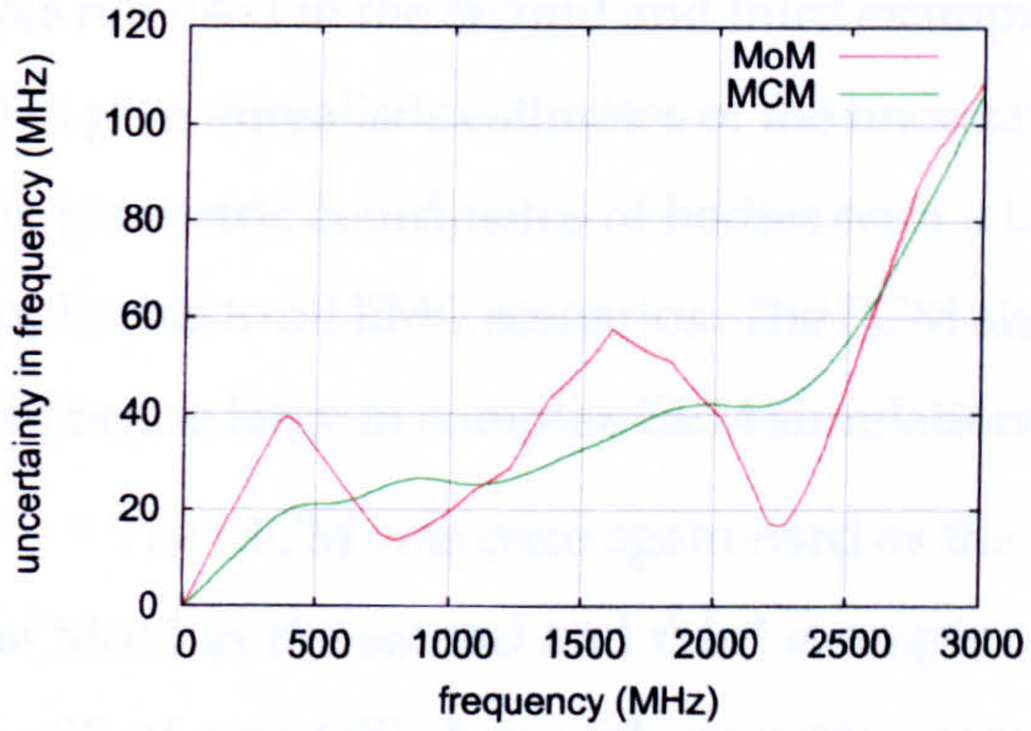

Figure 7.52: Aligned frequency uncertainty for FDTD simulations.

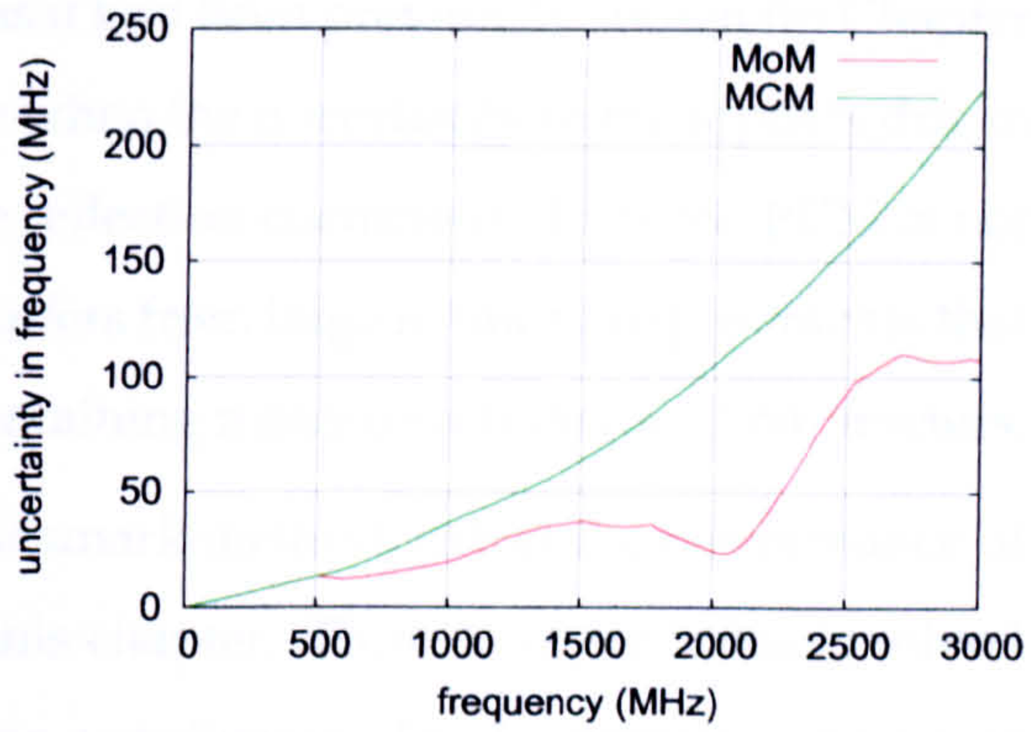

Figure 7.53: Aligned frequency uncertainty for ILCM simulations.

alignment enables a conclusion on the form of the output uncertainties to be formed. The output of the different simulations have both frequency and amplitude uncertainties. The majority of the output uncertainty is due to amplitude uncertainties, however there is also a contribution to the total output uncertainty from the frequency uncertainty. It is difficult to arrive at this conclusion without using curve alignment.

7.5 Conclusions

Once again the examples in this chapter have shown the merits of performing Error and Uncertainty Analyses on the output of CEM simulations. In the first example, where a PCB was modelled as having an uncertain reflection coefficient, the uncertainty at the frequency of interest (1.8GHz) was shown to be small. There was a high level of confidence that the normalised electric field took on a value close to its mean value. The approximate Error Analysis, however, showed that the estimated error in this mean value is fairly large. A proper evaluation of the results can only be made after the error and uncertainty in the results is quantified. Using the results of the UAs in the third example (with the larger input uncertainties) it was concluded that, with 95% confidence, the SE of the box was not greater than 0dB over the majority of the frequency range. This information is essential if an experimenter is to use the results with confidence.

Through the more realistic EMC examples, introduced in this chapter, the performance of the different UA methods were determined. All three UA methods were in very good agreement for the first example. The MoM was shown to be the most computational efficient method and therefore the preferred method for use in this first example. The PCM

was not used in the second and third examples as it had been previously shown (in Chapter 6) to give unrealistic estimates of the uncertainty when the uncertainty in the input is due to the geometric coordinates of bodies with a large reflection coefficient. Thus the PCM is not applicable to all EMC scenarios. The PCM also suffers from large memory requirements that will be too large in complex CEM simulations containing many uncertain input parameters.

The MCM was once again used as the benchmark method, to test the performance of the MoM in the second and third examples of this chapter. These two examples involved the SE of a metallic box with uncertain geometric coordinates. The frequency response of the SE was highly resonant in nature. Near to these resonances it was shown that the SE also depended on the uncertain input in a highly nonlinear manner. The MoM assumes that the output depends linearly on the uncertain inputs. The nonlinear relationships found in these examples caused the MoM to predict large peak overestimations of the output uncertainty, when compared to the benchmark MCM.

Previous research has shown that the MoM performs better when the input uncertainties are small. This was corroborated by the third example in this chapter. However, the MoM still produced overestimations of the uncertainties at certain frequencies, even with the smaller input uncertainties. Resonant features on the output frequency response curve caused the linear approximation used by the MoM to be poor at certain frequencies. This resulted in the peak overestimations predicted by the MoM. Despite these overestimations of the output uncertainty, the MoM did improve overall when the input uncertainties were smaller. In reality the input uncertainties are not always small, and simulations used to model different EMC experiments often produce frequency responses that are highly nonlinear. There is a risk that the MoM will overestimate the uncertainty in the output of these simulations at certain frequencies.

The MCM is applicable to most EMC scenarios, its application is however limited by the large computational runtime required to perform the MCM simulations. Complex CEM simulations often take days or weeks to run, performing multiple MCM simulations will be too computationally expensive in these cases. The MCM is best suited to simple examples that require only a small amount of computational runtime. The MCM was also shown to be unsuitable when determining the uncertainty in the output of FDTD simulations due to geometric inputs that have an associated uncertainty that is small with respect to the size of the FDTD mesh. In such cases the MoM may be used to give an approximate estimate of the uncertainty, as it has been shown to perform better when the input uncertainties are small.

This discussion leads to the conclusion that the MoM may be used in cases where the input uncertainties are very small. This method is computationally the most efficient method and it has been shown to perform more accurately when the input uncertainties are very small. The MoM does still predict large overestimations of the uncertainty at certain frequencies, even when the input uncertainty is small. This must be taken into account when using the results of the MoM uncertainty analysis.

A possible way of reducing the uncertainty overestimations formed from the MoM is to perform a post process on the MoM uncertainty estimate. The baseline uncertainty predicted by the MoM appears to be similar to the uncertainty formed via the MCM. Removing the peak overestimations from the MoM uncertainty estimate may therefore result in a more accurate estimate of the output uncertainty being formed. Different methods that may be used to accurately remove the peak overestimations need to be investigated. These investigations are left for future work.

The examples in this chapter have highlighted the extra computational effort that is required to obtain the estimates of the uncertainty. The MoM is the computationally cheapest method, the computational runtime required by the MoM scales with the number of uncertain input parameters. Further research is required to determine whether it is possible to obtain accurate estimates of the uncertainty, in the output of complex CEM simulations, using more computationally efficient methods. Some of these ideas are discussed in more detail in the final chapter of this thesis.

In previous chapters it has been shown that the uncertainty in the output of a simulation has only a small dependence on the accuracy with which the simulation is performed. This suggests that a computationally cheaper estimate of the output uncertainty may be obtained by using computationally cheaper CEM simulations. In the last two examples of this chapter the ILCM and FDTD method were used to calculate the SE of the shielded enclosures. In both examples the uncertainty in the FDTD and ILCM simulations were similar in size, although the uncertainty in the ILCM simulations were slightly larger at the higher frequencies. The computationally efficient ILCM method may therefore be used to obtain an efficient estimate of the uncertainty in the FDTD simulations, for the specific example of a shielded enclosure. Since the MCM most accurately estimates the output uncertainty, and the ILCM method is extremely computationally efficient, the MCM can be used to obtain the estimate of the uncertainty in the output of these simulations.

Throughout this thesis the use of curve alignment has been considered as a way of de-

termining the amplitude and frequency errors and uncertainties in the output. Once again in this chapter curve alignment was used to show that the output errors and uncertainties are not solely due to amplitude differences. The frequency errors and uncertainties in the output of the different simulations in this chapter were small, and in some cases it was deemed that curve alignment was not needed. The output curves obtained from the EMC examples were often more complicated and resonant in nature, making curve alignments more difficult. It was noted that the accuracy of the aligned amplitude and frequency errors and uncertainties relies on the accuracy of the method used to align the curves. In some cases the curve alignments performed less well and the subsequent aligned errors and uncertainties contained some errors. In most cases, however, the curve alignments performed well and provided information on the proportions of the output uncertainty that were an uncertainty in the amplitude and an uncertainty in the frequency.

This concludes the results obtained for this thesis. The final chapter will discuss the main conclusions of this work and propose some of the future work that is required to make the UAs more practical for use with real CEM simulations of EMC experiments.

Chapter 8

Conclusions and Future Work

Contents

8.1 Discussion and Conclusions

Uncertainty analyses provide the quantitative level of confidence that may be held in the results of a measurement or computational simulation. Without a determination of this confidence it is impossible to form valid conclusions based on these results. For example, in the last example of the previous chapter a measurement of the SE of a shielded enclosure was obtained. An experimenter may have required that the SE was greater than a certain level (e.g. 0dB) for frequencies up to 3GHz. By performing an UA and obtaining the 95% CI it was concluded that the SE was not above 0dB with 95% confidence. It would have been impossible to make such a conclusion without performing an UA.

This thesis has investigated three different probabilistic UA methods that may be used to quantify the uncertainty in the output of CEM simulations. Some of the novel aspects

of this work include the application of the PCM to the FDTD method, the use of the FSV method to test for convergence in the MCM and the use of curve alignment methods to distinguish between the amplitude and frequency errors that are present in the outputs of interest. The following sections outline some of the main findings of this work commenting on the performance of the different UA methods, the information gathered from using curve alignments, and the dependence of the output uncertainty on the CEM model used and the errors associated with that model.

8.1.1 The Performance of the Uncertainty Analysis Methods

The probabilistic methods that were used in this thesis are the MCM, the MoM and the PCM. These methods were applied to a number of FDTD and ILCM simulations, which were used to determine the performance of these different methods in terms of their accuracy and computational expense. Analytic solutions existed in the first two examples, these solutions were used to form the output uncertainty analytically (denoted as the analytic uncertainty here). The MCM was shown to most accurately predict the analytic uncertainty and was therefore chosen as the benchmark method by which the performance of the other two UA methods were compared for more complex and realistic EMC examples. The MCM may well be the most accurate method investigated in this thesis, but it is also the most computationally expensive method. The computational expense of the MCM usually prevents it from being used in more complex EMC scenarios involving many uncertain input parameters.

All three UA methods were shown to be in good agreement for the EMC example involving a shielded enclosure containing a PCB, which had an uncertain reflection coefficient (in Section 7.2). The output mean, uncertainty and 95% CI predicted by the three methods were all very similar. The MoM was shown to be by far the computationally most efficient method and is therefore the preferred method to use in this example. In more realistic EMC examples the MoM was shown to produce large resonant overestimations of the uncertainty at certain frequencies. These overestimations arise, in part, because the linear approximation used by the MoM is poor at certain frequencies, as discussed below.

Small perturbations in the input parameters, of some of the CEM examples in this thesis, caused frequency shifts in the frequency response of the output of interest. The shifts in the frequency can cause large changes in the resonant output of interest at certain frequencies. This means that the output of interest can have a highly nonlinear dependence on the

input parameters at particular frequencies. These nonlinear relationships usually occur near to the resonant frequencies of the output curves. The MoM, used in this thesis, relied on the assumption that the output depended on the inputs in a linear manner. It was shown that the nonlinear relationships caused the MoM to overestimate and underestimate the actual uncertainty at certain frequencies.

Previous research has found that the MoM is more accurate for smaller input uncertainties. This was corroborated by the example in Section 7.4. In this example the output uncertainty produced by the MoM was in better agreement with that produced by the benchmark MCM when the input uncertainties were smaller. The MoM did however still produce resonant overestimations of the uncertainty at particular frequencies, even when the input uncertainties were small. An experimenter using the efficient MoM must therefore be aware that it may produce overestimations and underestimations of the output uncertainty at particular frequencies. In the last example of this thesis it appeared that the baseline uncertainty formed via the MoM was similar to the uncertainty formed by the MCM. It may therefore be possible to provide a more accurate estimate of the uncertainty by processing the uncertainty estimate formed via the MoM to remove the large peak overestimations.

The PCM has previously been shown to efficiently and accurately quantify the uncertainty in the output of CFD simulations [13],[14], and in specific areas of CEM [18]. The novel implementation of the PCM into the FDTD method was presented in this thesis. In the example in Section 7.2, involving a PCB with an uncertain reflection coefficient, the PCM provided an efficient and accurate estimate of the output uncertainty. The PCM performed less well however in a number of the other examples. In this thesis the PCM linearly approximated the relationship between the output of interest and the uncertain inputs. This approximation was poor at frequencies with a high modal density, and subsequently the PCM produced overestimations of the uncertainty at these frequencies. These uncertainty overestimations were, however, less pronounced than the overestimations formed by the MoM. The PCM required less computational runtime than the MCM, but significantly more computational memory. In more complex examples the memory required by the PCM may be too large. Overall the MoM is computationally more efficient than the PCM and was shown to provide estimates of the uncertainty that were of a similar level of accuracy.

The PCM fails to provide a sensible estimate of the uncertainty in the output of FDTD simulations involving the uncertain geometric coordinates of a conducting object. In the example involving a PEC sphere with an uncertain radius the PCM distributed the con-

ductivity of the sphere over a number of points, near to the boundary of the sphere. This distribution of conductivities caused the uncertain field coefficients to reflect over short distances. The high rate of change of the field coefficients coupled in the update equations to cause other field coefficients to increase in amplitude. The amplitude of the field coefficients increased to nonsensical values preventing the method from being used to estimate the uncertainty in the output. The PCM would have had a similar problem when quantifying the uncertainty due to the uncertain geometric positions of the shielded enclosure (Sections 7.3 and 7.4). This problem with the PCM arises because of the discretisation used in the FDTD method. The discrete FDTD mesh forces the PCM to distribute the material parameters, of bodies with an uncertain geometry, over a discrete number of points. The neighbouring points therefore have different material properties and different reflection coefficients. This problem may not arise if the material parameters were distributed continuously, however it is rare that a CEM method will allow for continuously distributed parameters.

The discretisation of the FDTD method can also affect the uncertainty estimates formed by the MCM and the MoM. Geometric perturbations used to form the sensitivity derivatives, in the MoM, are confined to positions on the FDTD mesh. The size of the perturbation used has an effect on the output uncertainty, and it has been previously suggested that the perturbations used should be of a similar size to the uncertainty of the input parameter [2; 16]. The size of the FDTD mesh may prevent the perturbation from being of a similar size to the input uncertainty and thus the MoM may not provide its best estimate of the output uncertainty. The MCM produces a number of input parameter samples to represent the uncertainty in a geometric coordinate. Unfortunately these samples must be rounded to the nearest cell position on the FDTD mesh, thus preventing the MCM from forming its most accurate estimate of the uncertainty. In the example in Sections 7.4 it was shown that the MCM could not be used to quantify the uncertainty when the geometric input uncertainties were much smaller than the size of the FDTD mesh. It was suggested that the FDTD mesh must have multiple cell positions within two standard deviations of the mean cell position to enable the MCM to determine the uncertainty in the output.

In conclusion, the analyses in this thesis show that the MoM is the preferred method for efficiently quantifying the uncertainty in the output of CEM simulations. The MCM is generally the most accurate method but its computational expense make it impractical for use with more complex CEM simulations. The PCM predicts uncertainties with a similar level of accuracy as the MoM, but it is computationally more expensive and cannot be

used in certain situations. The MoM is computationally efficient and can provide good estimates of the output uncertainty. It can however predict large resonant overestimations of the uncertainty, which must be taken into account when using this method to estimate the uncertainty in the resonant output of a CEM simulation.

One of the most prominent results of this project is the extra computational runtime required to perform UAs. The most efficient UA investigated was the MoM, the computational runtime required for this method scales linearly with the number of uncertain inputs. If a single simulation with N uncertain input parameters takes T amount of time to run, then the MoM analysis will require $(N+1)T$ amount of computational runtime. For complex simulations, as N and T increase, the computational runtime required may become too expensive.

8.1.2 Using Curve Alignments

Curve alignment methods have been used in this thesis to determine the form of the errors and uncertainties in the output curves. The errors and uncertainties in the output take the form of amplitude and frequency errors and uncertainties. Without using curve alignment it is difficult to determine the size of the frequency errors and uncertainties. In general the errors and uncertainties in the frequencies were shown to be small, but often had a significant impact on amplitude uncertainty formed without curve alignment. A novel mathematical derivation was presented in this thesis, which provided relationships between the errors and uncertainties formed with and without curve alignment. These relations were verified using real data, and were shown to be accurate so long as the frequency errors and uncertainties were small. It is therefore concluded that no information is lost by analysing errors and uncertainties using curve alignment.

Two curve alignment methods (the PM and IC methods) were developed during this project. The PM method was shown to align curves well and with much less computational expense than the IC method. The DTW method was also shown to align curves very well, but at the expense of severely distorting the curves. The PM method was therefore used to align the output curves in the majority of examples in this thesis. Using curve alignment it was shown that the errors and uncertainties in the output curves were predominantly amplitude errors and uncertainties, and small frequency errors and uncertainties, which generally increased with frequency.

8.1.3 The Uncertainty in Different Computational Electromagnetic Models

Estimates of the error in the output of different FDTD simulations have also been formed through this thesis. It has been confirmed that a useful way of estimating many of the output errors in a FDTD simulation is to take the difference between the results of the simulation and the results of a simulation performed on a refined mesh. Error analyses are also important when forming conclusions based on the results of CEM simulations. However, nowadays CEM simulations are often performed with a high level of accuracy. It may therefore be argued that time consuming error analyses will simply conclude that the results contain only small errors.

This project has shown that uncertainties in the output of CEM simulations will be present even if the CEM simulations are performed at a high level of accuracy. In a number of examples in this thesis, UAs were applied to FDTD simulations performed with a different level of accuracy and to analytic solutions. These UAs were used to investigate the dependence of the uncertainty, in the output of a simulation, on the accuracy with which that simulation is implemented. It was found that the simulations performed with different levels of accuracy had slightly different output uncertainty curves. The uncertainty curves did however follow a similar form and were of a similar size. Thus there is no significant relationship between the error in a model and the output uncertainty.

UAs were also performed on simulations using different CEM methods. Both ILCM and FDTD simulations were used in the examples in Sections 7.3 and 7.4. Using these examples it was shown that the uncertainty in the ILCM simulations was slightly larger than the uncertainty in the FDTD simulations at higher frequencies, although overall the uncertainty in the ILCM and FDTD simulations were similar. It is concluded that the CEM technique used had some effect on the output uncertainty, however the overall size of the output uncertainty was very similar for both methods.

The uncertainty in the output of a CEM simulation appears to be very similar for simulations performed with different levels of accuracy and for different CEM methods. This may mean that computationally cheaper, less accurate CEM simulations may be used to obtain an estimate of the uncertainty in computationally expensive CEM simulations. This presents a promising avenue for future research into accurate and computationally efficient UA methods.

In summary the research conducted in this thesis, along with the results obtained,

provide a number of novel contributions to the field of research. The results obtained in this thesis show that, of the three uncertainty analysis methods investigated, the MCM is the most accurate method providing the best estimates of the uncertainty in various CEM simulations. This method is also shown to be the most computationally expensive method, as expected. The MoM is the most practical method to use to obtain an estimate of the uncertainty due to its computational efficiency. However, at resonant frequencies the MoM forms large peak overestimations of the uncertainty. These overestimations are due, in part, to the resonant nature inherent in EMC data coupled with small frequency variations in the output. The PCM can provide slightly more accurate estimates of the output uncertainty than the MoM, but there are situations when this method cannot be used. The PCM is also found to be computationally more expensive than the MoM.

The work in this thesis shows that there is no relationship between the overall size of the output uncertainty in a simulation and the underlying model used to form this simulation, or the accuracy with which the simulation is performed. This suggests that it is possible to decrease the computational expense of the UAs by using computationally cheaper less accurate CEM methods to estimate the uncertainty in the output of a simulation which uses a computationally more expensive CEM method. If a fast CEM method is used then the MCM is preferred as it will keep the accuracy of the uncertainty estimate as high as possible. One of the most consistent findings of this work is that the uncertainty analyses are computationally expensive when compared to performing a single simulation using only the the mean input parameters of the system. Looking for computationally efficient ways of quantifying the output uncertainty is one of the key areas for future research.

The importance of quantifying the frequency errors and uncertainties as well as the amplitude errors and uncertainties is also confirmed by the results in this thesis. This is especially important in EMC where small frequency variations can cause large amplitude variations due to the resonant nature of the output data. The novel curve alignment methods proposed in this thesis enable the successful analysis of these frequency errors and uncertainties. The research conducted in this thesis also suggests that considering the frequency or x-domain differences between two curves provides a useful additional measure (the XDM) that can be used to improve the FSV method.

8.2 Future Work

This section outlines some of the future investigations that could be carried out on this project. These investigations include improvements to the accuracy and efficiency of the UA methods used in this thesis, and improvements to the curve alignment and FSV methods.

8.2.1 Performing Post Processing on the Results Obtained by the MoM

The baseline uncertainty predicted by the MoM appears to be similar to the uncertainty formed via the MCM. Removing the peak uncertainty overestimations (often formed by the MoM) will therefore result in an efficient and accurate estimate of the output uncertainty. It may be possible to reduce the size of these overestimated peaks by applying a moving point average over the MoM uncertainty estimate. Alternatively peak overestimations may be removed by removing peaks that have a width smaller than a threshold value, for example 10MHz. Processing the data may however have undesired effects and thus more work is needed to determine the best method for processing the data and the associated gains and risks involved with performing the post processing.

8.2.2 More Efficient Uncertainty Analysis Methods

The current UA methods used in this project may be too expensive to be used for more complex CEM problems. Innovative techniques therefore need to be identified that provide computationally efficient ways of estimating the uncertainty in the output of complex CEM simulations. This project has already shown that different CEM methods and CEM simulations performed with a different level of accuracy produce similar output uncertainties. One possible way of reducing the computational expense of UAs is to apply the chosen UA method to less accurate, computationally faster simulations. The uncertainty in the output of the less accurate simulations could be used to provide an estimate of the uncertainty in more accurate CEM simulations. This will effectively reduce the size of the computational runtime T of the CEM simulation, and therefore significantly reduces the computational expense of the UA.

Similar techniques have already been applied in the optimisation of design parameters in electromagnetic based Computer Aided Design [96]. This work performed optimisation on less accurate, more efficient CEM simulations. The optimised parameters were then successfully transformed to more accurate CEM simulations using space mapping tech-

niques.

The uncertainty in the output of ILCM and FDTD simulations were also shown to be similar in size. The ILCM simulations are computationally much faster than the FDTD simulations, and may therefore be used to efficiently estimate the uncertainty in the output of the FDTD simulations. The MCM may be used to estimate this uncertainty as it has been shown to be the most accurate UA method used in this thesis. In computationally expensive simulations the MCM may require too much computational runtime. The ILCM simulations are extremely efficient and thus the overall expense of the MCM simulations will be acceptable. The ILCM method may not be applicable to other more complex CEM scenarios, in these cases other efficient CEM techniques will be required to estimate the output uncertainty. Further work is needed to investigate efficient CEM methods that may be used in more general EMC scenarios.

The computational expense of the MoM may be reduced by reducing the number of uncertain parameters N used in the UA. Less accurate simulations may be used to determine which input parameters contribute most significantly to the output uncertainty. Once these parameters are identified the more accurate simulations may be used to determine the output uncertainty due to only these most important parameters. This method reduces the size of N and therefore the computational expense of the MoM. Unfortunately the MoM can often form large resonant overestimations of the uncertainty. These overestimations may make it difficult to accurately determine which parameters are contributing most to the output uncertainty. It may be possible to use the baseline uncertainty, formed by the MoM, to determine the contribution of the individual uncertain parameters to the output uncertainty. Further work is needed to determine whether this method can be used to increase the overall efficiency of the UAs, and whether the resulting uncertainty estimates are accurate.

A final novel method that may help to increase the efficiency of the MoM uses a database to store different sensitivity derivatives formed from previous UAs of CEM simulations. The database may be used to interpolate sensitivity derivatives for a new MoM UA. This technique is an expert update technique: UAs will learn from the results of previous analyses, to save computational effort. If it is not possible to interpolate certain sensitivity derivatives, then the derivatives may be obtained in the conventional way, these results may then be fed back into the database. It is clear that different scenarios may produce very different sensitivity derivatives for the input parameters. For example, it may be difficult to interpolate the sensitivity derivatives for a wire in an enclosure using previous results

where the enclosure may have had a completely different Q factor. Nonlinear relationships between the output results and the different input parameters, formed from different scenarios, may also affect the sensitivity derivatives that are obtained using this method. It is clear that more work is needed to determine the applicability of these efficient UA methods to complex CEM simulations of realistic EMC scenarios.

8.2.3 Improvements to Curve Alignment Methods

In some cases, in this thesis, it was difficult to align the output curves. The aligned amplitude and frequency errors and uncertainties are only as accurate as the curve alignment methods used to form them. Further work is needed to improve the curve alignment techniques. Currently all the curve alignment techniques assume that the first two points on the curves, undergoing alignment, are already aligned: this may not always be the case. The curve alignment methods may be modified so that the first two points on the output curves are free to move, to allow a better alignment.

The PM method used in the majority of this thesis was shown to align curves well in many cases. In some cases however it failed to accurately identify the corresponding peaks on the two curves that should be matched. Further work is needed to increase the accuracy of the peak matching algorithm. The DTW method was shown to align curves extremely well, however it was concluded that this method manipulated the data too severely. The DTW method could be modified by constraining the movement of the points when aligning the curves. If the DTW method was restricted to moving the points in a smoother fashion then it may still provide excellent alignments, without distorting the data too severely. Further work is needed to determine whether these curve alignment methods can be improved.

8.2.4 Modifications to the Feature Selective Validation Method

Possible modifications to the FSV method were proposed through the work in this project. It was shown that the FSV method determined that curves formed from the sine and cosine functions were very poor matches. It is clear that these curves are actually very similar and only differ by a constant phase shift. It was proposed that by first aligning the curves an additional difference measure could be used to compare the two curves. This difference measure (XDM) represents the difference between each curve in their frequency domain (or x-domain). The difference measure is formed by analysing how much the curves

need to be shifted in their x-domain to align the curves. Using this difference measure it was shown that the sine and cosine curves are in fact an excellent match however they are shifted slightly in their frequency domain. More work is needed to determine the way in which the XDM should be implemented into the current FSV scheme. Further optimisation is required to form agreement between the comparisons made by the modified FSV scheme and by the engineers in [69].

8.2.5 Quantifying Model Form Uncertainty

The work in this thesis concentrated on quantifying the parametric uncertainties in the output of CEM simulations. The model form uncertainty is not considered through this work. The model form uncertainty is the uncertainty in the output of a simulation due to the uncertainty in how well the model used represents reality. This uncertainty is more difficult to quantify. One source of model form uncertainty arises from the uncertainty in the orientation of a structure, in a FDTD simulation, which will give the best agreement with reality. For regular geometries it is known that certain orientations will reduce the amount of staircasing errors introduced and will thus give the best agreement with reality. However, for less regular geometries it is more difficult to determine the correct orientation to use. This uncertainty could be quantified by obtaining the variance in the output formed from different orientations of the geometry in the model. More work could be carried out to determine the model form uncertainty in different CEM simulations.

Of all the proposed work discussed in this section the greatest reward would be obtained from forming methods that more efficiently estimate the uncertainty in the output of complex CEM simulations. This work also comprises the most difficult work proposed in this section. There is a relatively high risk that the proposed efficient UA methods may provide poorer estimates of the output uncertainty. Currently the most promising technique is to use the uncertainty in computationally cheaper CEM simulations to predict the uncertainty in computationally more expensive CEM simulations. The analysis in this thesis suggests that the uncertainty in more accurate CEM simulations is very similar to the uncertainty in computationally cheaper, less accurate simulations of the same scenario.

Appendix A
Uncertainty Analyses in the Finite Difference Time Domain Method

Uncertainty Analyses in the Finite Difference Time Domain Method

Robert S. Edwards, Andy C. Marvin, *Senior Member, IEEE,* and Stuart J. Porter *Member, IEEE,*

***Abstract*—Providing estimates of the uncertainty in results obtained by Computational Electromagnetic (CEM) simulations is essential when determining the acceptability of the results. The Monte Carlo Method (MCM) has previously been used to quantify the uncertainty in CEM simulations. Other computationally efficient methods have been investigated more recently, such as the Polynomial Chaos Method (PCM) and the Method of Moments (MoM). This paper introduces a novel implementation of the PCM and the MoM into the Finite Difference Time Domain (FDTD) method. The PCM and the MoM are found to be computationally more efficient than the MCM, but can provide poorer estimates of the uncertainty in resonant Electromagnetic Compatibility (EMC) data.**

***Index Terms*—Uncertainty Analysis, FDTD, Computational Electromagnetism, Monte Carlo, Polynomial Chaos, Method of Moments.**

I. Introduction

COMPUTATIONAL Electromagnetic (CEM) simulations rely on sets of input parameters, which often have an associated uncertainty. These uncertainties may arise from a lack of precise knowledge of the material parameters or geometries that are being modelled. Uncertainties in these input parameters lead to uncertainties in the output of the CEM simulations. This type of uncertainty is often known as parameter uncertainty. In this paper a determination of the parameter uncertainty in the results of Finite Difference Time Domain (FDTD) simulations will be made. Quantifying the uncertainty in the output of interest amounts to quantifying the standard deviation of the output. Uncertainty Analyses provide the quantitative level of confidence that may be held in the results of CEM simulations. This information is essential when determining whether the results are acceptable or useful.

Previous research has already highlighted the importance of quantifying uncertainty in CEM [1]–[4]. This research uses the Monte Carlo Method (MCM), which is generally accepted as being an accurate UA method, to test the performance of other computationally efficient Uncertainty Analysis (UA) methods. Chauvière published work involving the implementation of the Polynomial Chaos Method (PCM) into a higher order discontinuous Galerkin solution of Maxwell's Equations [1]. The PCM was found to accurately quantify the output uncertainty, whilst being more computationally efficient than the MCM. Chauvière's work, however, only estimated the output uncertainty due to one uncertain input parameter. The accuracy and computational efficiency of this method with increased numbers of uncertain input parameters needs to be analysed.

More recently Ajayi has discussed the use of a Direct Solution Technique (DST) to quantify uncertainty [2]. This technique applies the probabilistic Method of Moments (MoM) [5], [6] into different CEM schemes, such as the Transmission Line Matrix (TLM) method. Ajayi used the DST to estimate the uncertainty in the frequency of the first resonance for simple electomagnetic problems [2]. The DST was found to work well for small parameter variations, giving results that are in agreement with results obtained from the MCM [2].

The present paper outlines novel implementations of the PCM and the MoM into the FDTD method. These Uncertainty Analysis (UA) methods are used to obtain the uncertainty in the output electric field viewed in the frequency domain. In the first of two examples, the UA methods are used to estimate the uncertainty in the electric field that penetrates a shielded enclosure containing a Printed Circuit Board (PCB), at around 1.8GHz. This example is fairly simple having only one uncertain input parameter and encompassing only a few resonant features. The second electrically large example considers three uncertain inputs, encompassing many more resonant modes. The PCM and the MoM are compared to the MCM in terms of their ability to accurately quantify the uncertainty, and in terms of their compuatational expense.

In this paper, the uncertainty in the output of interest is a frequency response curve. The Feature Selective Validation (FSV) method [7], [8] is used in the present paper to determine the similarity of the uncertainty curves formed from the different UA methods. This method is a numerical technique, which determines how similar two curves are in terms of their amplitude and feature differences. The amplitude and feature differences between the curves are combined to give a General Difference Measure (GDM). This method currently forms part of a draft standard for the verification and validation of CEM models [9].

II. Uncertainty Analysis (UA) Methods

A. Monte Carlo Method (MCM)

To determine the uncertainty in a FDTD simulation via the MCM, the Probability Density Functions (PDFs) associated with the uncertain input parameters must first be sampled many times. In this paper Latin Hypercube Sampling (LHS) [10] is chosen as the preferred sampling method. This has been shown to produce a converged solution more quickly than other sampling methods [10]. The samples, obtained from the PDFs, form sets of input parameter values: one FDTD simulation is performed for each set. The outputs formed from each simulation are combined to form the output mean and standard deviation. The uncertainty in the output is represented by the standard deviation.

It is well know that the MCM has slow convergence and as such it is a computationally expensive method. The mean

and uncertainty, formed using the MCM, converge for large numbers of samples. Once convergence has been reached, using more samples does not change the mean and uncertainty significantly. In this paper the FSV method is used, in a novel way, to determine when the MCM has reached convergence. The mean and uncertainty formed in this paper are frequency response curves. The FSV method is used to compare the respective mean and uncertainty frequency response curves after every N simulations. Convergence is reached when the mean and uncertainty curves are determined to be "excellent" matches to the respective mean and uncertainty curves produced N simulations previously. In the examples in this paper $N = 50$ and convergence is reached when the comparisons of the respective mean and uncertainty curves produce a GDM< 1.5. This novel way of using FSV provides an accurate, consistent and impartial way of determining convergence, when the output of interest is a curve.

B. Polynomial Chaos Method (PCM)

The concept of Homogeneous Chaos was first introduced by Wiener [11]. Homogeneous Chaos uses Hermite polynomials to represent stochastic processes that depend on uncertain input parameters, which follow Normal distributions [12]. The PCM is a more generalised method for dealing with inputs that are not necessarily Normally distributed. In the PCM certain orthogonal basis polynomials are selected depending on the distributions of the random input variables [12]. A function depending on the uncertain random variables can be expanded in terms of the selected polynomials. This expansion, which is known as the Wiener-Askey chaotic expansion [12], casts the uncertainty in the output into the orthogonal polynomials alone. The orthogonality of the polynomial basis set can reduce stochastic differential equations to a set of deterministic differential equations that can be solved numerically [12].

Xiu and Karniadakis [12] found the PCM to be computationally cheaper than the MCM. They noted however that the method's efficiency is problem specific [13].

1) Wiener-Askey Chaos: Any second order random process X depending on some random event θ, can be represented as [12]

$$X(\theta) = \sum_{i=0}^{\infty} c_i \psi_i(\zeta(\theta)) \tag{1}$$

where c_i are constant coefficients and

$$\zeta(\theta) = (\zeta_1(\theta), \zeta_2(\theta), \ldots) \tag{2}$$

represents a vector containing an infinite number of independent random variables [12]. The polynomial basis set $\{\psi_i\}$, corresponding to the random variables $\zeta(\theta)$, are chosen from the Askey-scheme, which can be found in [12].

The polynomial basis sets are all orthogonal, which implies that

$$< \psi_i \psi_j > = < \psi_i^2 > \delta_{ij} \tag{3}$$

where δ_{ij} is the Kronecker delta and the inner product $< ., . >$ is defined as [12]

$$< f(\zeta) g(\zeta) > = \int f(\zeta) g(\zeta) w(\zeta) d\zeta. \tag{4}$$

The weighting function $w(\zeta)$ corresponds to the choice of polynomial basis $\{\psi_j\}$.

2) General Polynomial Chaos: The Weiner-Askey chaotic expansion (1) can be used to solve stochastic differential equations [12]. Let $u(x, t, \theta)$ be a solution of the stochastic differential equation

$$\mathcal{L}(x, t, \theta) u(x, t, \theta) = f(x, t, \theta) \tag{5}$$

where x, t and θ represent position, time and some random event respectively. The symbol $\mathcal{L}$ represents some differential operator and f is a source term [12]. The solution u may be regarded as a random process and expanded as [12]

$$u(x, t, \theta) = \sum_{i=0}^{P} u_i(x, t) \psi_i(\zeta(\theta)). \tag{6}$$

For practical applications the infinite sum in (1) has been truncated at P here. If d is the order of the highest order polynomial used in the expansion, and n is the dimension of the random variable ζ, then

$$P + 1 = \frac{(n + d)!}{n! d!}. \tag{7}$$

Substituting the expansion of u into equation (5) yields

$$\mathcal{L}(x, t, \theta) \sum_{i=0}^{P} u_i(x, t) \psi_i(\zeta(\theta)) = f(x, t, \theta). \tag{8}$$

The inner product of both sides of this equation can be formed with ψ_k to give

$$\left\langle \mathcal{L}(x, t, \theta) \sum_{i=0}^{P} u_i(x, t) \psi_i(\zeta(\theta)), \psi_k \right\rangle = < f(x, t, \theta), \psi_k > . \tag{9}$$

The orthogonality of the basis polynomials reduces equation (9) to a set of $(P + 1)$ differential equations: one for each u_i [12]. These equations are deterministic [12] and can therefore be solved numerically. Once each u_i is found, the mean and variance of $u(x, t, \theta)$ can be calculated. The mean is calculated as [1]

$$\begin{aligned} \bar{u}(x, t, \theta) &= < u(x, t, \theta), 1 > = \sum_{i=0}^{P} u_i < \psi_i, 1 > \\ &= \sum_{i=0}^{P} u_i < \psi_i, \psi_0 > = \sum_{i=0}^{P} u_i \delta_{i0} = u_0 \end{aligned} \tag{10}$$

using the fact that $\psi_0 = 1$ for all polynomial bases. The variance can be obtained in a similar way by first calculating

$$\begin{aligned} < u(x,t,\theta), u(x,t,\theta) > &= \sum_{i=0}^{P} \sum_{j=0}^{P} u_i u_j < \psi_i, \psi_j > \\ &= \sum_{i=0}^{P} \sum_{j=0}^{P} u_i u_j \delta_{ij} < \psi_i^2 > = \sum_{i=0}^{P} u_i^2 < \psi_i^2 > . \end{aligned} \tag{11}$$

The variance of $u(x, t, \theta)$ is therefore [1]

$$\begin{aligned} \sigma^2 &= < u(x, t, \theta), u(x, t, \theta) > - < u(x, t, \theta), 1 >^2 \\ &= \sum_{i=0}^{P} u_i^2 < \psi_i^2 > - u_0^2 = \sum_{i=1}^{P} u_i^2 < \psi_i^2 > . \end{aligned} \tag{12}$$

The uncertainty in $u(x, t, \theta)$ is the standard deviation σ.

3) General Polynomial Chaos in FDTD: General Polynomial Chaos has already been successfully applied to Computational Fluid Dynamics (CFD) [14], [15], and to specific areas of Computational Electromagnetics (CEM) [1]. The application of General Polynomial Chaos to 1D FDTD is given here, these arguments can be easily generalised to 3D.

Maxwell's Equations for a wave propagating in a linear isotropic homogeneous material along the x-axis in 1D are

$$\frac{\partial H_z}{\partial t} = -\frac{1}{\mu}\frac{\partial E_y}{\partial x} \tag{13}$$

$$\frac{\partial E_y}{\partial t} = -\frac{1}{\epsilon}\left(\frac{\partial H_z}{\partial x} + \sigma E_y\right). \tag{14}$$

As usual $H_z(x,t)$ represents the magnetic field oriented in the z direction, at a position x and time t. Similarly E_y represents the electric field oriented in the y direction. The symbols μ, ϵ and σ represent the permeability, permittivity and conductivity of the medium in which the electromagnetic fields propagate. CEM models seek to solve these two coupled equations, to find approximations for $H_z(x,t)$ and $E_y(x,t)$. If there are uncertain input parameters, then the solutions will depend on some random event θ. The uncertain field solutions can therefore be represented as $H_z(x,t,\theta)$ and $E_y(x,t,\theta)$. The solutions to Maxwell's Equations may be found by using the FDTD scheme, first proposed by Yee [16].

In Yee's scheme the temporal and spatial partial derivatives in Maxwell's Equations are approximated using central difference approximations. The problem space is discretised into cells of length Δx, and time is split into discrete intervals Δt. This yields two update equations, which form the basis of the 1D FDTD solution. The update equations formed are

$$H_z^{n+\frac{1}{2}}\left(j+\frac{1}{2},\theta\right) = H_z^{n-\frac{1}{2}}\left(j+\frac{1}{2},\theta\right) - \gamma[E_y^n(j+1,\theta) - E_y^n(j,\theta)] \tag{15}$$

and

$$E_y^{n+1}(j,\theta) = \alpha E_y^n(j,\theta) + \beta\left[H_z^{n+\frac{1}{2}}\left(j-\frac{1}{2},\theta\right) - H_z^{n+\frac{1}{2}}\left(j+\frac{1}{2},\theta\right)\right]. \tag{16}$$

The shorthand notation $H_z^n(j,\theta) = H_z(j\Delta x, n\Delta t, \theta)$, is used in the above equations, where j and n are positive integers. The material properties of the medium in which the fields propagate are represented by

$$\alpha = \alpha(x,\theta) = \frac{1-\sigma(x,\theta)\Delta t/2\epsilon(x,\theta)}{1+\sigma(x,\theta)\Delta t/2\epsilon(x,\theta)}, \tag{17}$$

$$\beta = \beta(x,\theta) = \frac{\Delta t}{\Delta x \epsilon(x,\theta)(1+\sigma(x,\theta)\Delta t/2\epsilon(x,\theta)} \tag{18}$$

$$\text{and } \gamma = \gamma(x,\theta) = \frac{\Delta t}{\Delta x \mu(x,\theta)}. \tag{19}$$

The material properties μ, ϵ and σ all depend on the uncertain parameter θ. This dependence is defined by the PDFs of the input parameters.

The 1D FDTD update equations defined above are used to obtain solutions for the electric and magnetic field, subject to some electric field source. The field solutions can be expanded in terms of the appropriate orthogonal polynomials $\{\psi_i\}$, to separate the dependence of the field on the random parameter θ from the dependence on time and position. The field solutions are expanded as

$$E_y^n(j,\theta) = \sum_{i=0}^{P} e_i^n(j)\psi_i(\zeta(\theta)) \tag{20}$$

$$\text{and } H_z^n(j,\theta) = \sum_{i=0}^{P} h_i^n(j)\psi_i(\zeta(\theta)). \tag{21}$$

The coefficients $e_i^n(j)$ and $h_i^n(j)$ must be found so that the mean and uncertainty of the output fields can be formed. The following discussion outlines how to obtain the field coefficients $e_i^n(j)$ and $h_i^n(j)$.

Expansions (20) and (21) can be substituted into equations (15) and (16) to obtain

$$\sum_{i=0}^{P} h_i^{n+\frac{1}{2}}(j+1/2)\psi_i(\zeta(\theta)) = \sum_{i=0}^{P}\left[h_i^{n-\frac{1}{2}}(j+1/2)\psi_i(\zeta(\theta)) - \gamma\left(e_i^n(j+1) - e_i^n(j)\right)\psi_i(\zeta(\theta))\right] \tag{22}$$

and

$$\sum_{i=0}^{P} e_i^{n+1}(j)\psi_i(\zeta(\theta)) = \sum_{i=0}^{P}\left[\alpha e_i^n(j)\psi_i(\zeta(\theta)) + \beta\left(h_i^{n+\frac{1}{2}}(j-1/2) - h_i^{n+\frac{1}{2}}(j+1/2)\right)\psi_i(\zeta(\theta))\right]. \tag{23}$$

At this point the electric field source E_s may be added into equation (23). If this field source has some associated uncertainty then it may be expanded as

$$E_s^n(j,\theta) = \sum_{i=0} e_{i,s}^n(j)\psi_i(\zeta(\theta)). \tag{24}$$

Adding this source term into equation (23) yields

$$\sum_{i=0}^{P} e_i^{n+1}(j)\psi_i = \sum_{i=0}^{P}\left[\alpha e_i^n(j)\psi_i + e_{i,s}^n(j)\psi_i + \beta\left(h_i^{n+\frac{1}{2}}(j-1/2) - h_i^{n+\frac{1}{2}}(j+1/2)\right)\psi_i\right]. \tag{25}$$

Taking the inner product of both sides of equations (22) and (25) with some test polynomial ψ_k, where k is an integer in the range $0 \le k \le P$, reduces the equations to

$$h_k^{n+\frac{1}{2}}(j+1/2) = h_k^{n-\frac{1}{2}}(j+1/2) - \frac{1}{<\psi_k^2>}\sum_{i=0}^{P}\left[\left(e_i^n(j+1) - e_i^n(j)\right) < \gamma\psi_i\psi_k >\right] \tag{26}$$

and

$$e_k^{n+1}(j) = e_{k,s}^{n+1}(j) + \frac{1}{<\psi_k^2>}\sum_{i=0}^{P}\left[e_i^n(j) < \alpha\psi_i\psi_k > + \left(h_i^{n+\frac{1}{2}}(j-1/2) - h_i^{n+\frac{1}{2}}(j+1/2)\right) < \beta\psi_i\psi_k >\right]. \tag{27}$$

The above two equations make use of the orthogonality relation set out in equation (3). The material properties α, β and γ remain in the inner products due to their dependence on θ.

Equations (26) and (27) can be used to calculate $e_k^n(j)$ and $h_k^{n+1/2}(j+1/2)$ for all n and j, and $k=0,\ldots,P$. In order to do this the inner products $<\alpha\psi_i\psi_k>$, $<\beta\psi_i\psi_k>$ and $<\gamma\psi_i\psi_k>$ must first be calculated for all $i,k=0,\ldots,P$. These can be calculated using numerical integrations as a pre-process; the update equations can then be used in a similar manner to the leapfrog scheme used in conventional FDTD. The source term must also be calculated at each time step as

$$e_{k,s}^n(j)=\frac{1}{<\psi_k^2>}<E_s^n(j,\theta)\psi_k(\zeta(\theta))>. \tag{28}$$

To complete the scheme, update equations are required at the boundary. The examples in this paper consider the scattering of electromagnetic fields in free space and therefore the first order Mur absorbing boundary condition [17] is chosen as a relevant boundary condition. At the lower boundary (where $j=0$) the usual Mur update equation is

$$E_y^{n+1}(0)=E_y^n(1)+\sqrt{\frac{\beta(1)\gamma(1)-1}{\beta(1)\gamma(1)+1}}\left(E_y^{n+1}(1)-E_y^n(0)\right). \tag{29}$$

Introducing uncertainty into this equation via dependence on θ yields

$$E_y^{n+1}(0,\theta)=E_y^n(1,\theta) \tag{30}$$
$$+\sqrt{\frac{\beta(1,\theta)\gamma(1,\theta)-1}{\beta(1,\theta)\gamma(1,\theta)+1}}\left(E_y^{n+1}(1,\theta)-E_y^n(0,\theta)\right).$$

As before, the field terms can be expanded using the chaotic expansion, and an inner product of both sides of the resulting equation can be taken with ψ_k. Carrying out these two steps gives

$$e_k^{n+1}(0)=e_k^n(1) \tag{31}$$
$$+\frac{1}{<\psi_k^2>}\sum_{i=0}^{P}\left(e_i^{n+1}(1)-e_i^n(0)\right)<\xi(1,\theta)\psi_i\psi_k>$$

where ξ is defined as

$$\xi(1,\theta)=\sqrt{\frac{\beta(1,\theta)\gamma(1,\theta)-1}{\beta(1,\theta)\gamma(1,\theta)+1}}. \tag{32}$$

Usually at the boundaries the properties of the medium are those of free space: there is no uncertainty in the parameter values near the boundary. Thus ξ has no θ dependence and $<\xi\psi_i\psi_k>=\xi\delta_{ik}<\psi_k^2>$. The update equation for the electric field at the lower boundary reduces to

$$e_k^{n+1}(0)=e_k^n(1)+\xi(1)\left(e_k^{n+1}(1)-e_k^n(0)\right) \tag{33}$$

for $k=0,\ldots,P$. Using a similar argument the electric field update equation at the upper boundary ($j=N$) is

$$e_k^{n+1}(N)=e_k^n(N-1)+\xi(N-1)\left(e_k^{n+1}(N-1)-e_k^n(N)\right). \tag{34}$$

The coefficients $e_k^n(j)$ may now be calculated using equations (26), (27), (33), and (34). Similar equations to (10) and (12) are formed for the mean value of $E_y^n(j,\theta)$

$$\bar{E}_y=e_0^n(j) \tag{35}$$

and the variance

$$\sigma^2=\sum_{i=1}^{P}(e_i^n(j))^2<\psi_i^2>. \tag{36}$$

The PCM is easily applied to FDTD because the update equations follow a very similar form to those in conventional FDTD. The only extra step comes in calculating the integrals that correspond to the inner products in the update equations (26) and (27). The application of the PCM to FDTD given here may be easily generalised to 3D.

One problem with the PCM arises when trying to form the mean and uncertainty of some related quantity, which does not depend linearly on $E_y^n(j,\theta)$. For example the output of interest may be the absolute value of $E_y^n(j,\theta)$. The mean μ of this ouput is formed as

$$\mu=<|E_y^n(j,\theta)|,1>=\left\langle\left|\sum_{i=0}^{P}e_i^n(j)\psi_i(\zeta(\theta))\right|\psi_0\right\rangle. \tag{37}$$

The absolute value within the inner product prevents the orthogonality of the basis polynomials from being used to form a simple relationship for the mean. The mean will have to be calculated using a numerical integration over the uncertain parameter space θ. This presents a problem with the PCM: the calculation of the mean of the output of interest is not always trivial. Some of the mathematical simplicity of the PCM has been lost by trying to form the mean of the quantity $|E_y^n(j,\theta)|$. The mean must be calculated using a numerical integration at each frequency point, which requires extra computational time. This extra computational expense is however small compared to the PCM simulation runtime. Once this mean has been calculated the variance σ^2 may be calculated using the standard definition

$$\sigma^2(|E_y^n(j,\theta)|)=<(|E_y^n(j,\theta)|-\mu)^2>. \tag{38}$$

Further numerical integrations are required to obtain this variance. The uncertainty in $|E_y^n(j,\theta)|$ is the square root of this variance.

The PCM performs one large simulation, storing a factor $(P+1)$ more field coefficients and $(P+1)^2$ more material parameter values (via the inner products) than the MoM and the MCM. If there are, for example, three uncertain inputs and the Wiener-Askey chaos expansion is truncated at first order then $P=3$ and the PCM will require around 16 times more memory than the MoM and the MCM to store the material inner products. The PCM should however require less computational runtime than the MCM.

C. Method of Moments (MoM)

The MoM is another approximate UA method, which is similar to the method outlined in [6] for the determination of uncertainty in practical EMC measurements. It is the internationally accepted method outlined in [5], for the propagation of uncertainties through a model.

The MoM uses a first order Taylor series expansion of the output electric field E_y about the mean input parameter values,

$$E_y(p_1,\ldots,p_n)=c_1p_1+\ldots+c_np_n, \tag{39}$$

where the c_i represent the sensitivity derivatives of each parameter p_i evaluated at the mean parameter values $\bar{p}_i$. For the purposes of this discussion there are assumed to be n input parameters for the FDTD simulation.

The mean output electric field $\bar{E}_y$ is calculated by performing one simulation with all input parameters taking on their mean values [5], [6]. To calculate the sensitivity derivative c_i, in equation (39), an FDTD simulation must be performed with all parameters taking on their mean values, except for the parameter p_i. In this simulation the parameter p_i is perturbed slightly from its mean value to give $p_i = \bar{p}_i + \Delta$. This simulation will produce a perturbed output electric field E_y^i. The sensitivity derivative c_i is calculated using the finite difference approximation

$$c_i = \frac{E_y^i - \bar{E}_y}{\Delta}. \tag{40}$$

If u_i is the uncertainty in the parameter p_i, determined from the PDF of p_i, then the uncertainty in the mean output of the FDTD simulation is calculated as [5], [6]

$$\sigma = \left(\sum_{i=1}^{n} c_i^2 u_i^2 \right)^{\frac{1}{2}}. \tag{41}$$

The accuracy of the uncertainty estimate relies on the relationship between the uncertain inputs and the output of interest being linear. The method is also dependent on the size of the perturbation Δ that is used. It has been previously suggested that using a perturbation $\Delta = u_i$ is appropriate [5], [6].

The MoM requires the same amount of computational memory as the MCM. For a simulation with n uncertain input parameters, the MoM requires $n + 1$ FDTD simulations.

In the next section the UA methods described above are used to determine the mean and uncertainty in the output of an EMC example. The output of interest in the following examples is the frequency response of the normalised electric field. This normalised field is formed by taking the ratio of the absolute value of the specified electric field to the input excitation, in the frequency domain. The FDTD simulations are all performed with $100 \times 100 \times 100$ cells and 10,000 time steps.

III. Example 1: An EMC Example

Figure 1 shows the setup of the EMC example. An electric field is excited from a dipole (oriented in the z-direction) and scattered off a shielded enclosure, with an aperture in the front face. To describe the coordinates of the shielded enclosure and the aperture the origin is assigned to the bottom right hand corner of the front face, which itself is in the y-z plane. The width of the box is $y = 38$cm, the depth is $x = 40$cm and the height is $z = 15$cm. For the purposes of the following discussion, the points in this coordinate system have units of cm, referenced from the origin. The bottom right hand corner of the aperture is at the point $(0, 19, 5)$ and extends by a width $a_y = 15$cm and a height $a_z = 4$cm. Using this coordinate system the centre of the dipole is at (-20,26,7), this is 20cm away (in the x-direction) from the centre of the aperture. The arms of the dipole are each 7cm in length, with a radius of

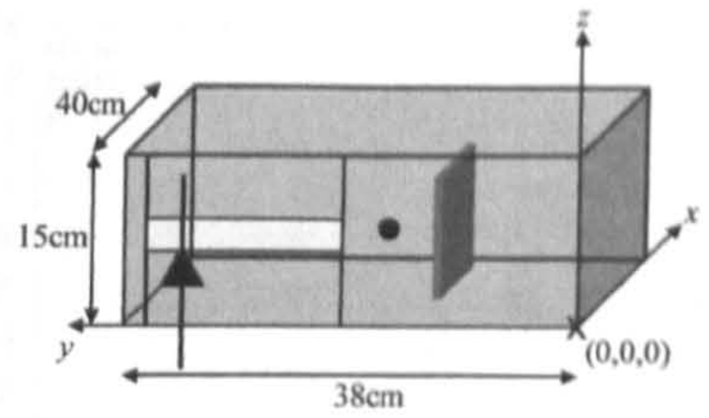

Fig. 1. A FDTD simulation of shielded enclosure with an aperture, containing a Printed Circuit Board.

1mm. The voltage source at the centre of the dipole has an amplitude of $V_0 = 2$V over a load of 50Ω. The input excitation is a Gaussian of the form

$$V = V_0 \exp\left(-\frac{4 \ln 2 (t - t_0)^2}{fwhh^2} \right), \tag{42}$$

where $t_0 = 6.67 \times 10^{-10}$s is the onset time and $fwhh = 2.78 \times 10^{-10}$s is the full width of the Gaussian pulse at half the height of the maximum amplitude.

The enclosure represents the shielding exterior of a typical electronic system containing a PCB. Using the coordinate system outlined above, the PCB is oriented in the x-z plane, extending from the point (5,14,2) a distance $x_b = 30$cm in the positive x-direction and a distance 10cm in the positive z-direction. The components on the PCB will absorb some of the electric field that penetrates the enclosure and is incident upon the board. The PCB may therefore be modelled as a thin dielectric block with a reflection coefficient [18]. For this example the reflection coefficient Γ is Uniformly distributed in the interval

$$\Gamma = [-0.91, -0.97]. \tag{43}$$

This reflection coefficient is optimised for a frequency of 1.8GHz by changing the material parameters of the PCB. The reflection coefficient will however be accurate for a small frequency range around 1.8GHz. Notice that the reflection coefficient described by equation (43) is uncertain, it follows a Uniform distribution. The uncertainty in this input will cause there to be an uncertainty in the output.

The output z-component of the electric field is observed at the centre of the box. A FDTD simulation was used to obtain the normalised electric field at this point using a uniform cell size of 0.01m.

Figure 2 shows the mean output electric field with 95% CI, as predicted by the MCM. Figures such as this one are extremely useful when determining the quantitative level of confidence that may be held in the results of a simulation. At 1.8GHz the 95% CI are $E_z = [0.418, 0.444]$ V/m. Thus, 95% of the sampled data was within about $\pm 3\%$ of the mean value.

The uncertainty in the output electric field is shown in Figure 3. The uncertainties predicted by all three methods are in very good agreement. The uncertainty curves were compared using the FSV method over frequencies up to 3GHz. The uncertainty predicted by the PCM is a "very good" match to the uncertainty predicted by the MCM, with a GDM of 2.3568. The MoM performs even better, the frequency

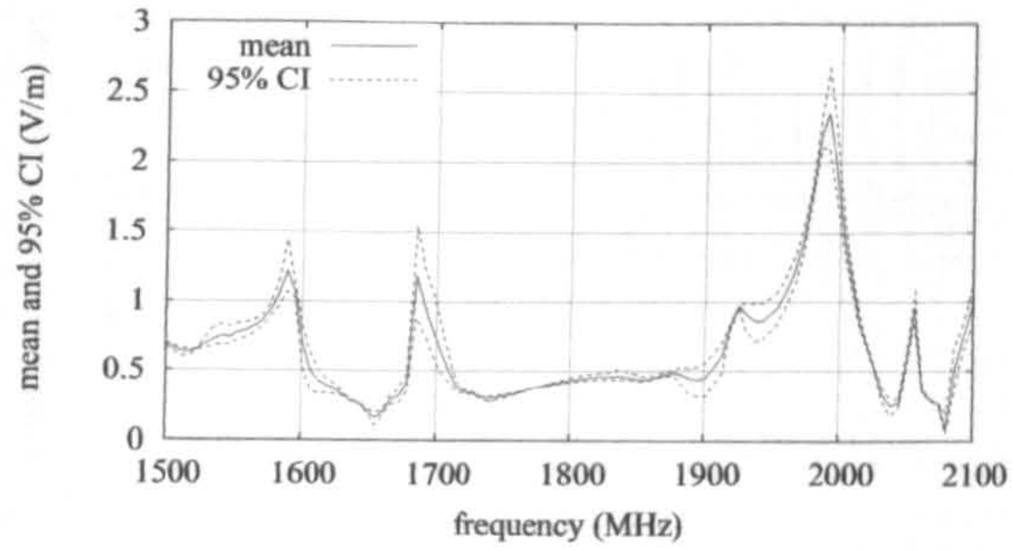

Fig. 2. Mean normalised electric field at the centre of the shielded enclosure and the 95% CI.

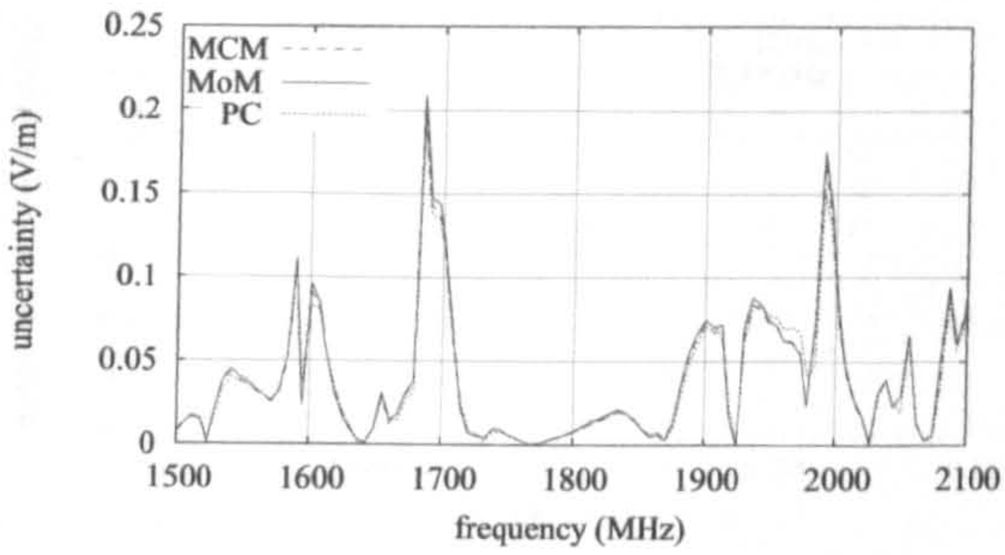

Fig. 3. Uncertainty in the normalised electric field, at the centre of the shielded enclosure, formed via the three UA methods.

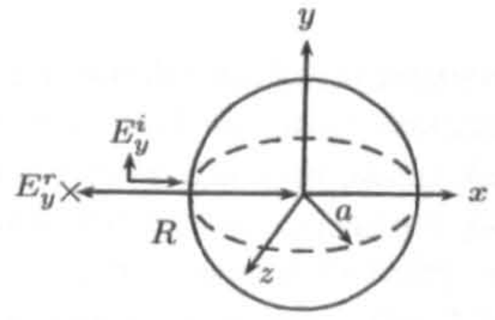

Fig. 4. A three dimensional problem space containing a dielectric sphere. A uniform plane wave is reflected off the sphere and observed at $\times$.

response of the uncertainty formed from the MoM and the MCM are an "excellent" match, having a GDM of 1.4755. Therefore, for this example, both efficient UA methods provide uncertainty estimates that are very close to the uncertainty formed using the MCM.

IV. Example 2: A Dielectric Sphere

This example considers the reflection of a uniform plane wave off a dielectric sphere in free space. The incident electric field E_y^i propagates in the positive x direction, and is polarised in the y direction with a magnitude $E_0 = 1$V/m. The y-component of the backscattered field E_y^r is calculated at a distance $R = 0.2$m from the centre of the sphere. This backscattered electric field is normalised relative to the input excitation to form the normalised electric field. This backscattered field may be solved for analytically using the Mie series [19].

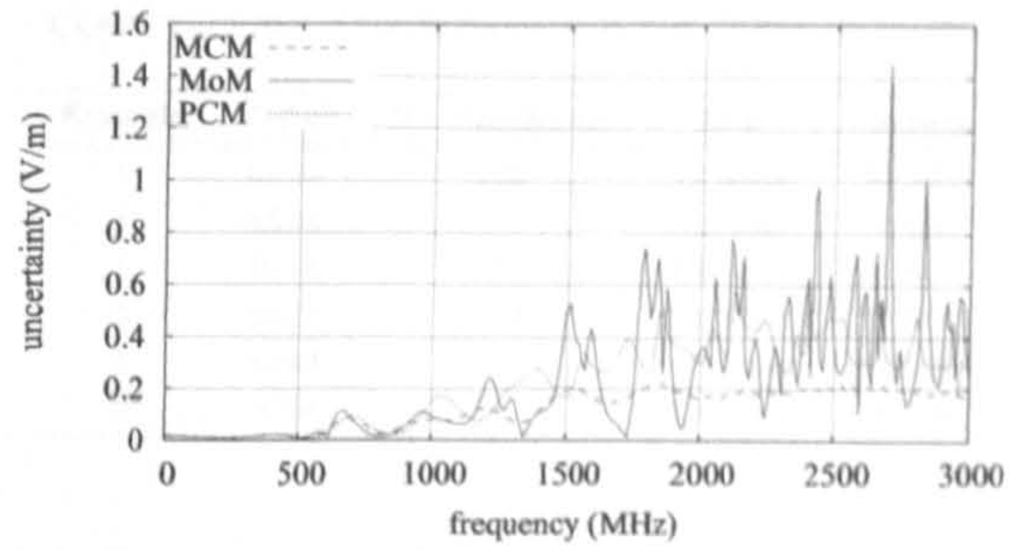

Fig. 5. Uncertainty in the normalised field backscattered from a dielectric sphere.

In this example the sphere parameters are uncertain: the radius is Normally distributed with a mean $\bar{a} = 0.1$m and an uncertainty $\sigma_a = 0.005$m, the relative permittivity is Uniformly distributed in the interval $\epsilon_r = [3.7, 4.3]$ and the relative permeability is Uniformly distributed in the interval $\mu_r = [0.95, 1.05]$. These uncertain input parameters will produce an uncertainty in the output normalised electric field. The setup of this example is shown in Figure 4.

The normalised electric field in the frequency domain was calculated using FDTD simulations, with a uniform broad Gaussian incident plane wave and a uniform cell size of 0.005m. Figure 5 shows the uncertainty in the FDTD simulations calculated using the three UA methods. At the lower frequencies the uncertainties produced by the three methods are in good agreement. However, at the higher frequencies the PCM and the MoM both overestimate the uncertainty, when compared to the uncertainty produced by the MCM. These qualitative comparisons are confirmed using the FSV method. The PCM gives a "fair" estimate of the MCM uncertainty up to 1.02GHz and a "poor" estimate of the uncertainty between 1.02GHz and 3GHz. The MoM does slightly better at the lower frequencies providing a "fair" estimate of the MCM uncertainty up to 1.21GHz. At the higher frequencies however the MoM performs less well, with a "very poor" estimate of the uncertainty between 1.21GHz and 3GHz.

Figure 6 shows the normalised electric field produced from a FDTD simulation using the mean input parameter values and a simulation with the sphere radius perturbed by 5mm. The two curves in this figure have similar resonant features but are shifted slightly in the frequency domain. At 1GHz the frequency response curve is less resonant in nature. Changing the radius of the sphere causes a frequency shift which in turn changes the value of the normalised electric field in a quasi-linear fashion, at this frequency. Changing the radius of the sphere at a more resonant frequency (e.g. 2.71GHz) results in a frequency shift which causes a large nonlinear change in the normalised electric field. Figure 7 shows the relationship between the normalised electric field and the radius of the sphere at 1GHz and 2.71GHz (calculated using the Mie Series solution). At 1GHz the normalised electric field depends on the radius in a relatively linear fashion, wheras at 2.71GHz the normalised electric field depends on the radius in a highly

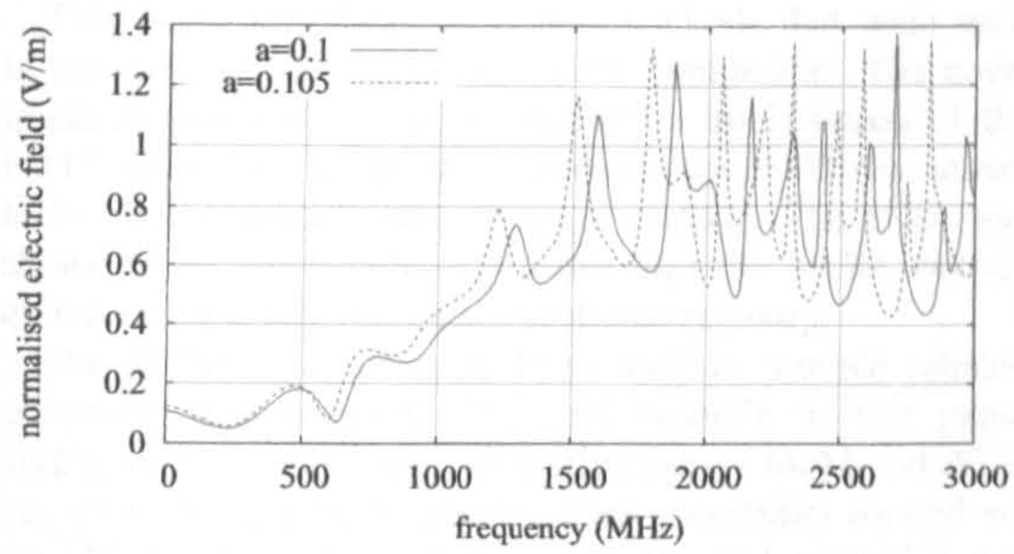

Fig. 6. Normalised field backscattered from two dielectric spheres with with different radii.

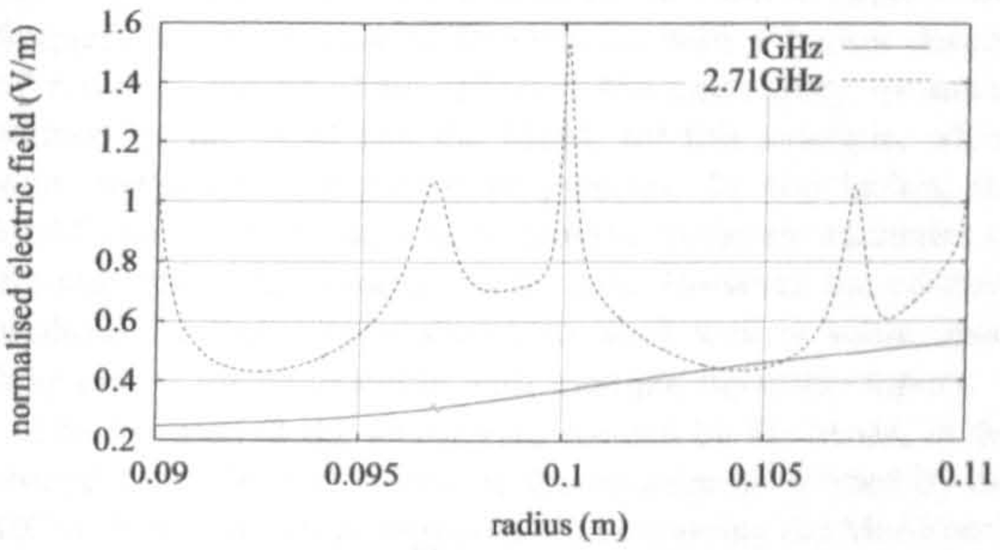

Fig. 7. The normalised electric field backscattered from dielectric spheres with different radii, at 1GHz and 2.71GHz.

nonlinear manner. Similar nonlinear relationships between the output electric field and the other uncertain inputs arise at frequencies where there is a high modal density.

In this example the chaotic expansion used by the PCM is truncated at $P = 3$; the output is therefore assumed to depend linearly on the uncertain inputs. The MoM also assumes a linear relationship between the output and the uncertain inputs. At subresonant frequencies (e.g. at 1GHz), the linear assumption is valid and the subsequent predictions of the uncertainty formed via the PCM and the MoM are similar to the uncertainty formed via the MCM. The linear assumption used by the PCM and the MoM is poorer at frequencies where the frequency response of the electric field is more nonlinear (e.g. at 2.71GHz). This explains the poor estimations of the uncertainty produced by the PCM and the MoM at such frequencies. The resonant nature of EMC data may prevent efficient UA methods, such as the PCM and the MoM, from being used to accurately quantify the uncertainty in the frequency response of the electric field formed from CEM simulations of EMC examples. The MoM and the PCM may still be useful for quantifying the uncertainty at subresonant frequencies.

In Figure 5, it appears that the baseline of the uncertainty formed by the MoM is similar to the uncertainty formed by the MCM. Removing the peak uncertainty overestimations (e.g. by using a moving point average) may result in a more accurate estimation of the uncertainty. Processing the data, in this way, may however result in the loss of some of the uncertainty peaks that are not overestimations.

TABLE I
COMPUTATIONAL REQUIREMENTS OF THE THREE METHODS.

Example	Method	No. Simulations	Time	Memory
1	MCM	100	18 hours	31 MB
1	MoM	2	0.36 hours	31 MB
1	PCM	1	1.8 hours	62 MB
2	MCM	700	126 hours	31 MB
2	MoM	4	0.72 hours	31 MB
2	PCM	1	8.9 hours	680 MB

V. COMPUTATIONAL REQUIREMENTS

Table I shows the computational performance of the three methods. All FDTD simulations were performed on a computer with a Pentium 4 processor running at 3.0GHz. The table shows that the MoM requires the least amount of computational expense. The MCM requires much more computational runtime than the PCM and the MoM, highlighting the need for efficient methods of quantifying the uncertainty in CEM simulations. Table I displays the extra computational memory required by the PCM, compared to that required by the MCM and the MoM. In the second example significantly more memory is required for the PCM. The MCM and the MoM use an optimised FDTD method; the material parameter values are not stored at each point in the problem space but a reference to the parameter value is stored. Conversely for the PCM, material values need to be stored at all points in the problem space. The uncertainty in the sphere radius causes the material parameter inner product values, used by the PCM, to be different at different points in the problem space. This means that the full inner product values have to be stored at each point in the problem space, requiring significantly more memory. In more complex examples the computational memory requirements may be too large to allow the PCM to be used.

To obtain the uncertainty of these (and any other) CEM simulations, extra computational runtime is needed. This extra runtime will be significant for complex problems with many uncertain input parameters. Uncertainty budgets provide essential information to help determine whether the results of a measurement are acceptable, and should not be discounted because of the extra computational expense. This paper has investigated two efficient UA methods (the PCM and the MoM), highlighting some of the strengths and limitations of these methods.

VI. CONCLUSION

Estimates of the uncertainty in the results of CEM simulations provide the scientific community with the quantitative level of confidence that may be held in the results. In the first example of this paper it may be concluded that there is a 95% chance that the output value lies within 3% of its mean value. It is impossible to determine this level of confidence without performing an UA.

This paper introduced three UA methods that were used to quantify the uncertainty in FDTD simulations. The novel implementation of the PCM required a modification of the FDTD algorithm. Of the three methods, the MoM was shown to be the computationally cheapest method. The PCM was shown to be computationally faster than the MCM, but required significantly more computational memory.

The MCM has previously been used to provide reliable estimates of uncertainty. The first example in this paper highlighted that the computationally cheaper MoM and PCM can give very good estimations of the uncertainty formed via the MCM. The efficient MoM and PCM, implemented in this paper, both rely on the assumption that the output of interest depends linearly on the uncertain inputs. In the second example it was shown that this assumption is valid at subresonant frequencies, but poorer at frequencies with a higher density of resonant modes. This reflected the uncertainty estimates formed by the PCM and the MoM, for this example, which were better at subresonant frequencies. In conclusion, the MoM and the PCM may only provide moderate estimates of the uncertainty in resonant EMC data. However the efficient methods have also been shown to work well at subresonant frequencies for an example with multiple uncertain inputs.

The baseline of the uncertainty formed by the MoM, in the second example, was similar to the uncertainty formed by the MCM. It was therefore suggested that removing the MoM peak uncertainty overestimations may result in a better estimation of the uncertainty. Investigations into such post processing comprises one of the future directions of this work.

REFERENCES

[1] C. Chauvière, J. S. Hesthaven and L. Lurati, "Computational modeling of uncertainty in time-domain electromagnetics," *SIAM Journal on Scientific Computing*, vol.28, no. 2, pp. 751-775, Jul. 2006.

[2] A. Ajayi, P. Ingrey, P. Sewell and C. Christopolous, "Direct computation of statistical variations in electromagnetic problems," *IEEE Trans. Electromagn. Compat.*, vol. 50, no. 2, pp. 751-775, May. 2008.

[3] J. Pereira, L. de Menezes and A. Borges, "Statistical analysis of induced ground voltage using the TLM+UT method," *IEEE International Symposium on Electromagnetic Compatibility, 2008. EMC 2008.* , pp. 1-4, 2008.

[4] L. de Menezes, A. Ajayi, C. Christopoulos, P. Sewell and G. A. Borges, "Efficient extraction of statistical moments in electromagnetic problems solved with the method of moments," *Microwave and Optoelectronics Conference, 2007. IMOC 2007. SBMO/IEEE MTT-S International*, pp. 757-760, 2007.

[5] "Guide to the expression of uncertainty in measurement," ISO, Geneva, Switzerland, 1993 (ISBN 92-67-10188-9).

[6] "The expression of uncertainty in EMC testing," UKAS publication LAB 34, Edition 1, 2002.

[7] A. P. Duffy, A. J. M. Martin, A. Orlandi, G. Antonini, T. M. Benson and M. S. Woolfson, "Feature selective vaidation (FSV) for validation of computational electromagnetics (CEM). Part I The FSV Method," *IEEE Trans. Electromagn. Compat.*, vol. 48, no. 3, pp. 449-459, Aug. 2006.

[8] A. P. Duffy, A. Orlandi and H. Sasse, "Offset difference measure enhancement for the Feature-Selective Validation method," *IEEE Trans. Electromagn. Compat.*, vol. 50, no. 2, pp. 413-415, May 2008.

[9] "Validation of computational electromagnetics computer modeling and simulation", IEEE Standards, to be published.

[10] M.D. McKay, W.J. Conover and R.J. Beckman. "A comparison of three methods for selecting values of input variables in the analysis of output from a computer code," *Technometrics,* vol.21, no. 2, pp. 239-245, May 1979.

[11] N. Wiener. "The homogeneous chaos". *American Journal of Mathematics*, vol. 60, pp.897-936, 1938.

[12] D. B. Xiu , G. E. Karniadakis, "The Wiener-Askey polynomial chaos for stochastic differential equations." *SIAM Journal on Scientific Computing*, vol. 24, no. 2, pp. 619-644, 2002.

[13] J. Faragher. "Probabilistic methods for the quantification of uncertainty and error in computational fluid dynamics simulations," DSTO Air Vehicles Division, DSTO-TR-1633, 2004.

[14] D. B. Xiu , G. E. Karniadakis, "Modeling uncertainty in flow simulations via generalized polynomial chaos." *Journal of Computational Physics*, vol. 187, no. 1, pp. 137-167, 2003.

[15] O. M. Knio and O. P. Le Maître, "Uncertainty propagation in CFD using polynomial chaos decomposition ," *Fluid Dynamics Research*, vol. 38, no. 9, pp. 616-640, 2006.

[16] K. S. Yee, "Numerical solution of initial boundary value problem involving Maxwell's equations in isotropic media," *IEEE Trans. Antennas and Propagat.*, vol. 14, no. 3, pp. 302-307, 1966.

[17] G. Mur, "Absorbing boundary conditions for the finite-difference approximation of the time-domain electromagnetic-field equations." *IEEE Trans. Electromagn. Compat.*, vol. 23, no. 4, pp. 377-382, 1981.

[18] M. P. Robinson and S. J. Porter and P. Op gen Oorth, "Reflection and Transmission Coefficients of Printed Circuit Boards," *4th European Symposium on Electromagnetic Compatibility, Bruges, September 11-15, 2000*, pp. 209-213, 2000.

[19] G. Mie, "Beiträge zur Optik trüber Medien, speziell kolloidaler Metallösungen." *Annalen der Physik*, vol. 330, no. 3, pp. 377-445, 1908.

Robert Edwards received the M.Math degree (with first class honours) in maths and physics in 2005 from the University of York, York, U.K., where he is currently working towards the Ph.D. degree in electronic engineering. He received the P.B. Kennedy Prize and the Oliver Heavens Award in 2005 for achieving the highest academic record by an undergraduate in the Maths Department and the Physics Department at York.

His current research interests include computational electromagnetics and statistical methods.

Andrew C. Marvin For a detailed biography see IEEE Trans. Electromagn. Compat., VOL. 50, NO. 4, pp. 770-782, 2008.

Stuart J. Porter is a senior lecturer and member of the Physical Layer Research Group at the Department of Electronics, University of York, UK. He received his BSc and DPhil degrees from the University of York, Department of Physics in 1985 and 1991.

His research interests include computational electromagnetics; antenna design and the application of evolutionary computation optimisation methods to antenna design and EMC.

Glossary

AAAD	-Average Absolute Amplitude Difference
ABC	-Absorbing Boundary Condition
ADM	-Amplitude Difference Measure
CEM	-Computational Electromagnetism
CFD	-Computational Fluid Dynamics
CI	-Confidence Intervals
DTW	-Dynamic Time Warping
ECDF	-Empirical Cumulative Distribution Function
EFIE	-Electric Field Integral Equation
EMC	-Electromagnetic Compatibility
EMI	-Electromagnetic Interference
FDM	-Frequency Difference Measure
FDTD	-Finite Difference Time Domain
FEM	-Finite Element Method
FFT	-Fast Fourier Transform
FSV	-Feature Selective Validation
GDM	-General Difference Measure
GTD	-Geometrical Theory of Diffraction
HIRF SE	-High Intensity Radiated Fields in Synthetic Environments
IA	-Interval Analysis
IC	-Interval Correlation
IEMoM	-Integral Equation Method of Moments
ILCM	-Intermediate Level Circuit Model
LHS	-Latin Hypercube Sampling

MCM -Monte Carlo Method

MFIE -Magnetic Field Integral Equation

MoM -Method of Moments

NWP -Numerical Weather Prediction

ODM -Offset Difference Measure

PCB -Printed Circuit Board

PCM -Polynomial Chaos Method

PDF -Probability Density Function

PEC -Perfectly Electrically Conducting

PM -Peak Matching

PML -Perfectly Matched Layer

SE -Shielding Effectiveness

TLM -Transmission Line Matrix

TWIE -Thin Wire Integral Equation

UA -Uncertainty Analysis

XDM -x-domain Difference Measure

References

[1] "Genereal requirements for competence of testing and calibration laboratories," tech. rep., ISO/IEC 17025, 1999.

[2] "The expression of uncertainty in EMC testing," UKAS publication LAB 34, Edition 1, UKAS, 2002.

[3] "IEEE P1597.1 draft standard for validation of computational electromagnetics computer modeling and simulation," *IEEE standards*, 2008.

[4] M. R. Allen and D. A. Stainforth, "Towards objective probabalistic climate forecasting," *Nature*, vol. 419, p. 228, 2002.

[5] J. M. Murphy, D. M. H. Sexton, D. N. Barnett, G. S. Jones, M. J. Webb, and M. Collins, "Quantification of modelling uncertainties in a large ensemble of climate change simulations," *Nature*, vol. 430, pp. 768–772, 2004.

[6] D. A. Stainforth, T. Aina, C. Christensen, M. Collins, N. Faull, D. J. Frame, J. A. Kettleborough, S. Knight, A. Martin, J. M. Murphy, C. Piani, D. Sexton, L. A. Smith, R. A. Spicer, A. J. Thorpe, and M. R. Allen, "Uncertainty in predictions of the climate response to rising levels of greenhouse gases," *Nature*, vol. 433, pp. 403–406, 2005.

[7] M. Allen, P. Stott, J. Mitchell, R. Schnur, and T. Delworth, "Quantifying the uncertainty in forecasts of anthropogenic climate change," *Nature*, vol. 407, pp. 617–620, 2000.

[8] M. Ehrendorfer, "Predicting the uncertainty of numerical weather forecasts: a review," *Meteorologische Zeitschrift*, vol. 6, no. 4, pp. 147–183, 1997.

[9] F. Molteni, R. Buizza, T. N. Palmer, and T. Petroliagis, "The ECMWF ensemble prediction system: Methodology and validation," *Quarterly Journal of the Royal Meteorological Society*, vol. 122, no. 529, pp. 73–119, 1996.

[10] R. W. Walters and L. Huyse, "Uncertainty analysis for fluid dynamics with applications," ICASE Report no. 2002-1, NASA/CR-2002-211449, REC Warangal, 2002.

[11] "AIAA, Guide for the verification and validation of computational fluid dynamics simulations," Report no. g-077-1998, American Institute of Aeronautics and Astronautics, 1998.

[12] D. B. Xiu and G. E. Karniadakis, "Modeling uncertainty in steady state diffusion problems via generalized polynomial chaos," *Computer Methods in Applied Mechanics and Engineering*, vol. 191, no. 43, pp. 4927–4948, 2002.

[13] D. B. Xiu and G. E. Karniadakis, "Modeling uncertainty in flow simulations via generalized polynomial chaos," *Journal of Computational Physics*, vol. 187, no. 1, pp. 137–167, 2003.

[14] O. M. Knio and O. P. L. Maître, "Uncertainty propagation in CFD using polynomial chaos decomposition," *Fluid Dynamics Research*, vol. 38, no. 9, pp. 616–640, 2006.

[15] J. Faragher, "Probabilistic methods for the quantification of uncertainty and error in computational fluid dynamics simulations," Report no. DSTO-TR-1633, DSTO Air Vehicles Division, 2004.

[16] "Guide to the expression of uncertainty in measurement," ISO, Geneva, Switzerland, International Standards Organization, 1993. ISBN 92-67-10188-9.

[17] R. F. Harrington, *Field Computation by Moment Methods*. IEEE Press, 1993.

[18] C. Chauvière, J. S. Hesthaven, and L. Lurati, "Computational modeling of uncertainty in time-domain electromagnetics," *SIAM Journal on Scientific Computing*, vol. 28, pp. 751–775, July 2006.

[19] P. I. A. Ajayi, P. Sewell, and C. Christopoulos, "Direct computation of statistical variations in electromagnetic problems," *IEEE Transactions on Electromagnetic Compatibility*, vol. 50, pp. 751–775, May 2008.

[20] J. Pereira, L. de Menezes, and A. Borges, "Statistical analysis of induced ground voltage using the TLM+UT method," *IEEE International Symposium on Electromagnetic Compatibility, 2008. EMC 2008.*, pp. 1–4, 2008.

[21] L. de Menezes, A. Ajayi, C. Christopoulos, P. Sewell, and G. A. Borges, "Efficient extraction of statistical moments in electromagnetic problems solved with the method

of moments," *Microwave and Optoelectronics Conference, 2007. IMOC 2007. SBMO/IEEE MTT-S International*, pp. 757–760, 2007.

[22] C. Christopoulos, P. Sewell, K. Biwojno, J. Wykes, J. D. Paul, D. W. P. Thomas, A. Ajayi, and L. de Menezes, "Multi-scale problems and complexity in computational electromagnetics," *Computational Electromagnetics Workshop*, pp. 44–48, 2007.

[23] A. Ajayi, *Direct computation of statistical variations in electromagnetic problems*. PhD thesis, Nottingham University, Nottingham, UK, 2008.

[24] R. S. Edwards, M. P. Robinson, J. F. Dawson, A. C. Marvin, and S. J. Porter, "Aligning curves for more accurate curve comparisons," *The 23rd Annual Review of Progress in Applied Computational Electromagnetics, ACES*, 2007.

[25] D. Poljak, *Advanced Modeling in Computational Electromagnetic Compatibility*. John Wiley & Sons, 2007.

[26] I. D. Flintoft, P. Favier, I. Bertino, C. Anastasiou, J.-P. Parmantier, C. Girard, S. Sarto, M. Bozzetti, J.-P. Moreau, and A. C. Marvin, "The high intensity radiated field synthetic environment research programme," *9th Ultra-Wideband Short-Pulse Electromagnetics Conference (UWB SP9) at European Electromagnetics (EUROEM)*, 2008.

[27] F. M. Tesche, M. V. Ianoz, and T. K. Karlsson, *EMC Analysis Methods and Computational Models*. John Wiley & Sons, 1997.

[28] T. Konefal, J. F. Dawson, A. C. Marvin, M. P. Robinson, and S. J. Porter, "A fast multiple mode intermediate level circuit model for the prediction of shielding effectiveness of a rectangular box containing a rectangular aperture," *IEEE Transactions on Electromagnetic Compatibility*, vol. 47, no. 4, pp. 678–691, 2005.

[29] J. B. Keller, "Geometrical theory of diffraction," *Journal of the Optical Society of America*, vol. 52, pp. 116–130, 1962.

[30] R. G. Kouyoumjian and P. H. Pathak, "A uniform geometrical theory of diffraction for an edge in a perfectly conducting surface," *Proceedings of the IEEE*, vol. 62, no. 11, pp. 1441–1461, 1974.

[31] R. F. Harrington, "Matrix methods for field problems," *Proceedings of the IEEE*, vol. 55, no. 2, pp. 136–149, 1967.

[32] "Numerical electromagnetics code." NEC http://www.nec2.org/.

[33] A. F. Peterson, S. L. Ray, and R. Mittra, *Computational Methods for Electromagnetics*. John Wiley & Sons, 1998.

[34] J. R. Brauer, *What Every Engineer Should Know about Finite Element Analysis*. Marcel Dekker, 1993.

[35] M. J. Turner, R. W. Clough, H. C. Martin, and L. J. Topp, "Stiffness and deflection analysis of complex structures," *Journal of the Aeronautical Sciences*, vol. 23, no. 9, pp. 805–823, 1956.

[36] R. W. Clough, "The finite element in plane stress analysis," *Proceedings of 2nd Conference on Electronic Computation, ASCE*, 1960.

[37] P. P. Silvester and R. L. Ferrari, *Finite Elements for Electrical Engineers*. Cambridge University Press, 1983.

[38] I. D. Flintoft, N. L. Whyman, J. F. Dawson, and T. Konefal, "Fast and accurate intermediate level modeling approach for EMC analysis of enclosures," *IEE Proceedings Science, Measurement and Technology*, vol. 149, no. 5, pp. 281–285, 2002.

[39] T. Konefal, J. F. Dawson, A. C. Denton, T. M. Benson, C. Christopoulos, A. C. Marvin, S. J. Porter, and D. W. P. Thomas, "Electromagnetic coupling between wires inside a rectangular cavity using multiple mode analogous transmission line circuit theory," *IEEE Transactions on Electromagnetic Compatibility*, vol. 43, no. 3, pp. 273–281, 2001.

[40] T. Konefal, J. F. Dawson, A. C. Denton, T. M. Benson, C. Christopoulos, A. C. Marvin, S. J. Porter, and D. W. P. Thomas, "Electromagnetic fields produced by pcb stripline and microstrip inside a screened rectangular enclosure: a circuit approach," *Proceedings 4th European Symposium on Electromagnetic Compatibility*, vol. 1, pp. 587–592, 2000.

[41] J. A. Kong, *Electromagnetic Wave Theory*. John Wiley & Sons, 1986.

[42] P. B. Johns and R. L. Beurle, "Numerical solution of 2-dimensional scattering problems using a transmission-line matrix," *IEE Proceedings*, vol. 118, no. 9, pp. 1203–1208, 1971.

[43] C. Christopoulos, *The Transmission-Line Modeling Method : TLM*. John Wiley & Sons, 1995.

[44] P. B. Johns, "A symmetrical condensed node for the TLM method," *IEEE Transactions on Microwave Theory and Techniques*, vol. 35, no. 4, pp. 370–377, 1987.

[45] P. B. Johns, "On the relationship between TLM and Finite-Difference methods for Maxwell's equations (short paper)," *IEEE Transactions on Microwave Theory and Techniques*, vol. 35, no. 1, pp. 60–61, 1987.

[46] K. S. Yee, "Numerical solution of initial boundary value problems involving Maxwell's equations in isotropic media," *IEEE Transactions on Antennas and Propagation*, vol. 14, no. 3, pp. 302–307, 1966.

[47] W. J. Duffin, *Electricity and Magnetism*. W. J. Duffin Publishing, 2001.

[48] P. D. Lax and B. Wendroff, "Systems of conservation laws," *Communications on Pure and Applied Mathematics*, vol. 13, no. 2, pp. 217–237, 1960.

[49] A. Taflove and S. C. Hagness, *Computational Electrodynamics: The Finite-Difference Time-Domain Method 2nd Edition*. Artech House, 2000.

[50] B. Engquist and A. Majda, "Absorbing boundary conditions for the numerical simulation of waves," *Mathematics of Computation*, vol. 31, no. 139, pp. 629–651, 1977.

[51] G. Mur, "Absorbing boundary conditions for the finite-difference approximation of the time-domain electromagnetic-field equations," *IEEE Transactions on Electromagnetic Compatibility*, vol. 23, no. 4, pp. 377–382, 1981.

[52] A. Taflove, *Advances in Computational Electrodynamics: The Finite-Difference Time-Domain Method*. Artech House, 1998.

[53] L. N. Trefethen and L. Halpern, "Well-posedness of one-way wave equations and absorbing boundary conditions," *Mathematics of Computation*, vol. 47, no. 176, pp. 421–435, 1986.

[54] R. L. Higdon, "Absorbing boundary conditions for difference approximations to the multi-dimensional wave equation," *Mathematics of Computation*, vol. 47, no. 176, pp. 437–459, 1986.

[55] J. P. Berenger, "A perfectly matched layer for the absorption of electromagnetic-waves," *Journal of Computational Physics*, vol. 114, no. 2, pp. 185–200, 1994.

[56] D. S. Katz, E. T. Thiele, and A. Taflove, "Validation and extension to three dimensions of the Bérenger PML absorbing boundary condition for FD-TD meshes," *IEEE Microwave and Guided Wave Letters*, vol. 4, no. 8, pp. 268–270, 1994.

[57] J. P. Bérenger, "Improved PML for the FDTD solution of wave-structure interaction problems," *IEEE Transactions on Antennas and Propagation*, vol. 45, no. 3, pp. 466–473, 1997.

[58] J. Fang, *Time domain finite difference computation for Maxwell's equations*. PhD thesis, Univ. California, Berkeley, CA, 1989.

[59] M. R. Spiegel, *Schaum's Outline of Calculus of Finite Differences and Difference Equations*. McGram-Hill, 1971.

[60] K. L. Shlager, J. G. Maloney, S. Ray, and A. Peterson, "Relative accuracy of several FDTD methods in two and three dimensions," *IEEE Transactions on Antennas and Propagation*, vol. 41, no. 12, pp. 1732–1737, 1993.

[61] K. L. Shlager and J. B. Schneider, "Comparison of the dispersion properties of several low-dispersion finite-difference time-domain algorithms," *IEEE Transactions on Antennas and Propagation*, vol. 51, no. 3, pp. 642–653, 2003.

[62] A. C. Cangellaris and D. B. Wright, "Analysis of the numerical error caused by the stair-stepped approximation of a conducting boundary in FDTD simulations of electromagnetic phenomena," *IEEE Transactions on Antennas and Propagation*, vol. 39, no. 10, pp. 1518–1525, 1991.

[63] A. Akyurtlu, D. H. Werner, V. Veremey, D. J. Steich, and K. Aydin, "Staircasing errors in FDTD at an air-dielectric interface," *IEEE Microwave and Guided Wave Letters*, vol. 9, no. 11, pp. 444–446, 1999.

[64] R. Holland, "Pitfalls of staircased meshing," *IEEE Transactions on Electromagnetic Compatibility*, vol. 35, no. 4, pp. 434–439, 1993.

[65] P. J. Roache, *Verification and Validation in Computational Science and Engineering*. Hermiosa Publishers, 1998.

[66] J. S. Hesthaven and T. Warburton, "High-order nodal methods on unstructured grids. I. Time-domain solution of Maxwell's equations," *Journal of Computational Physics*, vol. 181, pp. 1–34, 2002.

[67] A. J. M. Martin, *Quantitative data validation (automated visual evaluations)*. PhD thesis, De Montfort Univ., Leicester, U.K., 1999.

[68] A. P. Duffy, A. J. M. Martin, A. Orlandi, G. Antonini, T. M. Benson, and M. S. Woolfson, "Feature selective validation (FSV) for validation of computational electromagnetics (CEM). Part I. the FSV method," *IEEE Transactions on Electromagnetic Compatibility*, vol. 48, pp. 449–459, Aug 2006.

[69] A. Orlandi, A. P. Duffy, B. Archambeault, G. Antonini, D. E. Coleby, and S. Connor, "Feature selective validation (FSV) for validation of computational electromagnetics (CEM). Part II. assessment of FSV performance," *IEEE Transactions on Electromagnetic Compatibility*, vol. 48, pp. 449–459, Aug 2006.

[70] A. P. Duffy, A. Orlandi, and H. Sasse, "Offset difference measure enhancement for the feature-selective validation method," *IEEE Transactions on Electromagnetic Compatibility*, vol. 50, pp. 413–415, May 2008.

[71] C. J. Macdonald-Bradley, P. A. Jennings, R. J. Ball, P. H. Lever, and S. D. Baker, "A statistical approach for computational electromagnetics," *WROCLAW 2000 15th Int. Wroclaw Symposium on Electromagnetic Compatibility, Wroclaw, Poland*, 2000. ISBN 83-901999-0-4.

[72] H. Sakoe and S. Chiba, "Dynamic programming algorithm optimisation for spoken word recognition," *IEEE Transactions on Acoustics, Speech and Signal Processing*, vol. ASSP-26, no. 1, pp. 43–49, 1978.

[73] G. C. Hsiao and R. E. Kleinman, "Mathematical foundations for error estimation in numerical solutions of integral equations in electromagnetics," *IEEE Transactions on Antennas and Propagation*, vol. 45, no. 3, pp. 316–328, 1997.

[74] R. E. Moore, *Interval Analysis*. Prentice-Hall, 1966.

[75] S. S. Rao and L. Berke, "Analysis of uncertain structural systems using interval analysis," *AIAA Journal*, vol. 35, no. 4, pp. 727–735, 1997.

[76] J. Cruz, *Constraint Reasoning for Differential Models*. IOS Press, 2005.

[77] L. A. Zadeh, "Fuzzy sets," *Information and Control*, vol. 8, no. 3, pp. 338–353, 1965.

[78] K. Tanaka, *An Introduction to Fuzzy Logic for Practical Applications*. Springer, 2004. 0387948074.

[79] A. Kaufmann and M. M. Gupta, *Introduction to Fuzzy Arithmetic: Theory and Applications*. Electrical/Computer Science and Engineering Series, Van Nostrand Reinhold Company, New York, 1985.

[80] M. D. McKay, W. J. Conover, and R. J. Beckman, "A comparison of three methods for selecting values of input variables in the analysis of output from a computer code," *Technometrics*, vol. 21, pp. 239–245, May 1979.

[81] E. Saliby, "Descriptive sampling - a better approach to Monte-Carlo simulation," *Journal of the Operational Research Society*, vol. 41, no. 12, pp. 1133–1142, 1990.

[82] E. L. Kaplan and P. Meier, "Nonparametric estimation from incomplete observations," *Journal of the American Statistical Association*, vol. 53, no. 282, pp. 457–481, 1958.

[83] M. G. Morgan, M. Henrion, and M. Small, *Uncertainty: A Guide to Dealing with Uncertainty in Quantitative Risk and Policy Analysis*. Cambridge University Press, 1990.

[84] A. Ajayi, P. Ingrey, P. Sewell, and C. Christopoulos, "Direct computation of statistical variations in electromagnetic problems," *IEEE Transactions on Electromagnetic Compatibility*, vol. 50, pp. 325–332, May 2008.

[85] A. Papoulis, *Probability, Random Variables, and Stochastic Processes*. McGraw-Hill, 1965.

[86] N. Wiener, "The homogeneous chaos," *American Journal of Mathematics*, vol. 60, pp. 897–936, 1938.

[87] T. E. Lovett, F.Ponci, and A. Monti, "A polynomial chaos approach to measurement uncertainty," *IEEE Transactions on Instrumentation and Measurement*, vol. 55, no. 3, pp. 729–736, 2006.

[88] R. G. Ghanem and P. Spanos, *Stochastic Finite Elements: a Spectral Approach*. Springer, 1991.

[89] R. H. Cameron and W. T. Martin, "The orthogonal development of non-linear functionals in series of Fourier-Hermite functionals," *The Annals of Mathematics*, vol. 48, no. 2, pp. 385–392, 1947.

[90] W. H. Press, S. A. Teukolsky, W. T. Vetterling, and B. P. Flannery, *Numerical Recipes in C*. Second Edition, Cambridge University Press, 1994. First edition 1988.

[91] J. A. Stratton, *Electromagnetic Theory*. McGraw-Hill, 1941.

[92] G. Mie, "Beiträge zur optik trüber medien, speziell kolloidaler metallösungen," *Annalen der Physik*, vol. 330, no. 3, pp. 377–445, 1908.

[93] D. E. Merewether, R. Fisher, and F. W. Smith, "On implementing a numeric Huygen's source scheme in a finite difference program to illuminate scattering bodies," *IEEE Transactions on Nuclear Science*, vol. 27, no. 6, pp. 1829–1833, 1980.

[94] C. A. Balanis, *Advanced Engineering Electromagnetics*. John Wiley & Sons, 1989.

[95] M. P. Robinson, S. J. Porter, and P. O. gen Oorth, "Reflection and transmission coeffi-cients of printed circuit boards," *4th European Symposium on Electromagnetic Compatibil-ity, Bruges, September 11-15, 2000*, pp. 209–213, 2000.

[96] J. W. Bandler, R. M. Biernacki, S. H. Chen, P. A. Grobelny, and R. H. Hemmers, "Space mapping technique for electromagnetic optimization," *IEEE Transactions on Microwave Theory and Techniques*, vol. 42, no. 12, pp. 2536–2544, 1994.